Analysis of the Varying-period Folded Waveguide

Ao Xu, **Wen-Xiang Wang**, **Yan-Yu Wei**, **and Yu-Bin Gong**

National Key Laboratory of High Power Vacuum Electronics
School of Physical Electronics, University of Electronic Science and Technology of China
Chengdu 610054, China

Abstract— The dynamic velocity tapering is widely used to improve the efficiency of the beam-wave interaction in the slow wave structure of the TWTs. As an application of this technique, the varying-period folded waveguide has a series of the advantages such as the mode selection and the wide bandwidth. In this paper, the principle of taking a space harmonic to synchronize with the electron beam in the whole interaction process in a varying-period folded waveguide is present, the varying-period folded waveguide is analyzed by the simulation software, and the efficiency improvement is obtained.

1. INTRODUCTION

The linear theory of traveling wave tubes (TWT) predicts an exponential growth of the electromagnetic field along the interaction domain, provided that the average velocity of the electrons is close to the phase velocity of the electromagnetic wave in the empty structure, this is the resonance condition. As the electromagnetic energy increases, the total kinetic energy associated with the electron motion decreases, therefore their average velocity decreases. If the slow-wave structure is uniform, the resonance condition is no longer satisfied and the energy transfer is drastically reduced. This situation has to be avoided if we wish to construct a high gain and high efficiency TWT [1–3].

As the one of the slow-wave structures, the folded waveguide slow-wave structure has advantages over others in low-cost fabrication, high reproducibility, high-power handling capability with a moderate bandwidth in the millimeter wave frequency range [4, 5]. Therefore, it is important to avoid the situation in which the resonance condition is no longer satisfied in the folded waveguide.

To prevent this non-resonance, there must be some additional spatial control that will either reimburse the beam for energy given up or slow the circuit wave simultaneously to maintain a favorable phase relationship with the slowing beam. The first can be accomplished by providing an accelerating dc gradient, the second by tapering the circuit velocity [6, 7]. The varying-period fold waveguides are the applications of the tapering the circuit velocity. Therefore, comparing to the periodic folded waveguides, the varying-period folded waveguides are possible to obtain to the higher gain and the higher efficiency. In this paper, the space harmonic in the varying-period folded waveguide is analyzed, the condition to maintain the microwave synchronizing the electron beam in the whole interaction process is obtained, and this condition is proved by the software simulation. So, it is determined that the efficiency can be improved if the varying-period folded waveguide satisfied the condition which obtained in this paper.

2. THEORETICAL ANALYSIS

A schematic drawing of a varying-period folded waveguide is depicted in Fig. 1, where Q is the number of periods, $L_q = l_{q-1} + l_q$ is the period length of the qth "period", and $p_q = L + h_q + h_{q-1}$ is the length along the waveguide of the qth "period", where $q = 1, 2, \ldots, Q$. It is assumed that this structure is no loss, and propagates the TE_{10} mode. The longitudinal electric field can be expressed as follows:

$$E(z) = \begin{cases} E_0 e^{j\beta_0 z}, & z_q + b/2 > z > z_q - b/2 \\ 0, & z_{q+1} - b/2 > z > z_q + b/2, \quad q = 1, 2, \ldots, Q \end{cases} \tag{1}$$

Consulting the definition of the space harmonic of the folded waveguide, the space harmonic of the varying-period folded waveguide can be expressed as follows:

$$\begin{cases} E(z) = \frac{L_{sum}}{2\pi} \int\limits_{-\infty}^{+\infty} E(\beta) e^{j\beta' z} d\beta \\ E(\beta) = \frac{1}{L_{sum}} \int_0^{L_{sum}} E_0 e^{-j\beta z} dz \end{cases} \tag{2}$$

where β' is the phase constant of the space harmonic in the varying-period folded waveguide, analogous to the $\beta_n = \beta_0 + 2n\pi/L$ in the periodic folded waveguide, it can be expressed as $\beta' = \beta_0 + \beta$, β_0 is the phase constant of the fundamental wave, β is similar to $2n\pi/L$ in the periodic folded waveguide.
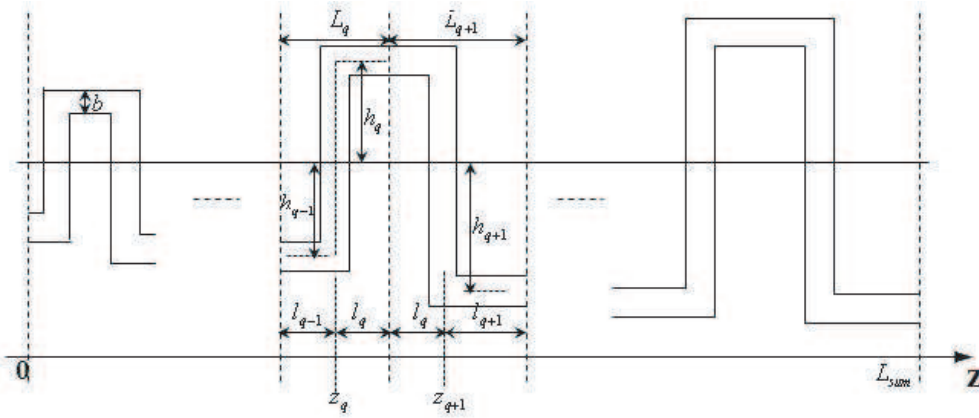

Figure 1: Varying-period folded waveguide.

Assuming that the change of the velocity of the electron beam in a varying-period folded waveguide is: it has no change in one "period", but is changed as $A(q)v_0$ at the initial point of each "period", where $A(q)$ is the coefficient of the change of the velocity of the electron beam, v_0 is the velocity of the electron beam at the entrance of this structure, where $q = 1, 2, \ldots, Q$. Because the velocity of the electron beam is decrease with the increase of the period number q, one can obtain $1 > A(q) > A(q+1) > 0$.

If a varying-period folded waveguide exists a space harmonic synchronizing with the electron beam in the whole interaction process, one can obtain:

$$\beta' = \beta_0 + \beta = \frac{\omega}{A(q)v_0} \quad q = 1, 2, \ldots, Q \tag{3}$$

It is found that the phase constant β' of this space harmonic should increase with the decrease of the velocity of the electron beam.

Where, in the periodic folded waveguide, the $2n\pi/L$ of the nth space harmonic is related to L because the periodicity of the regular folded waveguide. However, in the varying-period folded waveguide, the phase constant of the space harmonic can be obtained by Fourier transform. It can be found that β is also related to the number of the space harmonic, but can not be expressed as $2n\pi/L$, since there is no unitary L in the varying-period folded waveguide. Thus, β will only be decided by the whole structure and the number of harmonics but not L_q. Therefore, for one definite special space harmonic in a definite structure, β is a constant. As a result, the phase constant of the fundamental wave in each "period" must increase with the decrease of the velocity of the electron.

Direction of the electric field changes one time for each "period" in the varying-period folded waveguide, i.e.,:

$$\beta_{0q}L_q = \beta_{wg}p_q + \pi \quad q = 1, 2, \ldots, Q \tag{4}$$

where β_{0q} is the phase constant of the fundamental wave in the qth "period", β_{wg} is the phase constant of the microwave propagating along the waveguide.

The cut off wavelength of the TE_{10} mode in the straight waveguide is $2a$, thus:

$$\beta_{wg} = \frac{2\pi f}{c}\sqrt{1 - \left(\frac{c}{2af}\right)^2} \tag{5}$$

where a is the length of the cross section of the waveguide, c is the velocity of the light.

According to (3) (4) and (5), one can obtain:

$$\frac{2f_s}{c}\sqrt{1-\left(\frac{c}{2af_s}\right)^2}\left(\frac{p_{q+1}}{L_{q+1}} - \frac{p_q}{L_q}\right) + \left(\frac{1}{L_{q+1}} - \frac{1}{L_q}\right) = \frac{2f_s}{v_0}\left[\frac{1}{A(q+1)} - \frac{1}{A(q)}\right] \quad q = 1, 2, \ldots, Q \tag{6}$$

where f_s is the frequency of the microwave mode synchronizing with the electron beam. Actually, there are many modes with different frequencies exist in the varying-period folded waveguide. But only a mode with a specific frequency can synchronize with the electron beam. And this frequency should not be changed in any "period".

It is found that (6) is a unary quadratic equations about f_s, and f_s should be a unique value. According to the theorem of mathematic, the condition of existing solution of Equation (6) is the discriminant $\Delta = 0$. It is written as:

$$
\Delta = 16 \left[\frac{1}{a^2 c^2} \left(\frac{p_{q+1}}{L_{q+1}} - \frac{p_q}{L_q} \right)^4 + \frac{1}{c^2} \left(\frac{p_{q+1}}{L_{q+1}} - \frac{p_q}{L_q} \right)^2 \left(\frac{1}{L_{q+1}} - \frac{1}{L_q} \right)^2 \right.
$$
$$
\left. - \frac{1}{a^2} \left(\frac{p_{q+1}}{L_{q+1}} - \frac{p_q}{L_q} \right)^2 \left[\frac{1}{A(q+1)v_0} - \frac{1}{A(q)v_0} \right]^2 \right]
$$
$$
= 0 \tag{7}
$$

According to (7), there are two cases as follows:

$$
\frac{p_{q+1}}{L_{q+1}} = \frac{p_q}{L_q} \quad \text{and} \quad f_s = \frac{\frac{1}{L_{q+1}} - \frac{1}{L_q}}{2 \left[\frac{1}{A(q+1)v_0} - \frac{1}{A(q)v_0} \right]} \tag{8}
$$

Or

$$
\frac{p_{q+1}}{L_{q+1}} = \frac{p_q}{L_q} \pm ac \sqrt{ \frac{1}{a^2} \left[\frac{1}{A(q+1)v_0} - \frac{1}{A(q)v_0} \right]^2 - \frac{1}{c^2} \left(\frac{1}{L_{q+1}} - \frac{1}{L_q} \right)^2 }
$$
$$
\text{and} \quad f_s = \frac{c^2 \left[\frac{1}{A(q+1)v_0} - \frac{1}{A(q)v_0} \right]}{2a^2 \left(\frac{1}{L_{q+1}} - \frac{1}{L_q} \right)} \tag{9}
$$

It is obviously found that the mode according with condition (8) and (9) will synchronize with the electron beam in the whole interaction process in this varying-period folded waveguide.

3. SOFTWARE SIMULATION

A practical varying-period folded waveguides is simulated by HFSS, and they are used to compare the results with that of the calculation.

The output power is almost exponentially in the slow wave structure of the TWT. Therefore, it is known that the loss of the kinetic energy of the electron beam increases exponentially in the whole

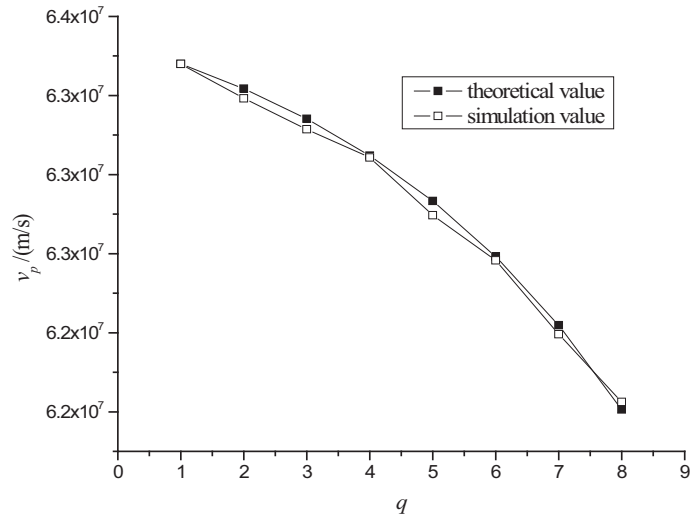| q	L /mm	p /mm
1	0.5	1.4
2	0.49835	1.3954
3	0.49633	1.3897
4	0.49386	1.3828
5	0.49084	1.3744
6	0.48715	1.364
7	0.48263	1.3514
8	0.4771	1.3359

Table 1.

Figure 2: Phase velocity in each period.

interaction process. Thus, we can assume that the initial velocity of the electron beam at each "period" can be expressed as $A(q + 1) = [A(q) * A(q) - 0.004e^{0.2q}]^{-1/2}$. The physical dimension for this example is: "period" amount is $Q = 8$, the wide side and the narrow side of the cross section of the waveguide are $a = 2\,\mathrm{mm}$, $b = 0.3\,\mathrm{mm}$ respectively, the channel radius of the beam is $r = 0.15\,\mathrm{mm}$, the length of the first "period" is $L = 0.5\,\mathrm{mm}$, and the length along the waveguide of the first "period" is $p_1 = 1.4\,\mathrm{mm}$ and $v_0 = 63700000\,\mathrm{m/s}$. Then, assuming the fundamental wave of the mode with the frequency $f = 86.1\,\mathrm{GHz}$ synchronizes with the electron beam at the first "period". According to the condition (8), the physical dimension of this structure is shown in Table 1.

In Table 1, q is the "period" number, L is the "period" length, and p is the length along the waveguide of one "period". It is found that the variety of the $\Delta L(q) = L_q - L_{q+1}$ and $\Delta p(q) = p_q - p_{q+1}$ are not rigorously proportional to the change of the electron beam velocity $\Delta v(q) = A(q)v_0 - A(q + 1)v_0$.

In Fig. 2, the theoretical value is the velocity of the electron beam in each "period" i.e., $A(q)v_0$ and the simulation value is the phase velocity of the special mode in each "period". Considering the calculation error, it is proved that the velocity of the electron beam is equal to the phase velocity of the special mode in each "period", i.e., if a space harmonic synchronizes with the electron beam in the first "period" and the physical dimension of this structure satisfies the condition (8), this space harmonic can synchronize with the electron beam in the whole interaction process in this structure.

4. CONCLUSIONS

The non-synchronization between the space harmonic and the electron beam in the slow wave structure of the TWTs is a terrible problem. The dynamic velocity tapering is the most important application to improve this problem. The conditions to maintain the synchronization between a space harmonic and the electron beam in a varying-period folded waveguide in the whole interaction process are present in this paper, and the result of the software simulation proves that the conditions are valid. Conclusively, the conditions obtained in this paper are useful to improve the efficiency of the beam-wave interaction and it is useful to the further studies on the varying-period folded waveguide.

REFERENCES

1. Jung, S.-S., A. Soukhov, B. Jia, et al., "Positive phase-velocity tapering of broadband helix traveling-wave tubes for efficiency enhancement," *Appl. Phys. Lett.*, Vol. 80, No. 16, 3000–3002, 2002.
2. Solntsey, V. A., "Mode selection in pseudoperiodical waveguides and slow-wave structures," *Proc. SPIE Int. Soc. Opt. Eng.*, Vol. 2250, 399, 1994.
3. Schachter, L. and J. A. Nation, "Slow-wave amplifiers and oscillators: A unified study," *Phys. Rev.*, Vol. 45, No. 12, 8820–8832, 1992.
4. Ha, H.-J., S.-S. Jung, and G.-S. Park, "Theoretical study for folded waveguide traveling wave tube," *International Journal of Infrared and Millimeter*, Vol. 19, No. 9, 1229–1245, 1998.
5. Booske, J. H., M. C. Converse, C. L. Kory, et al., "Accurate parametric modeling of folded waveguide circuits for millimeter-wave traveling wave tubes," *IEEE Trans. Elec. Devi.*, Vol. 52, No. 5, 685–694, 2005.
6. Meeker, J. G. and J. E. Rowe, "Phase focusing in linear-beam devices," *IRE Trans. Elec. Devi.*, Vol. 9, 257–266, 1962.
7. Xu, A., W.-X. Wang, Y.-Y. Wei, et al., "The study of synchronization in the periodic nonuniform folded waveguide," *Chinese Physics B*, accepted and to be published.

Behavior Study of Simultaneously Defected Microstrip and Ground Structure (DMGS) in Planar Circuits

M. Kazerooni, G. Rezai Rad, and A. Cheldavi

College of Electrical Engineering, Iran University of Science and Technology (IUST)
Narmak, Tehran, Iran

Abstract— In this paper several simultaneously defected microstrip and ground structures (DMGS) are proposed in order to study the behavior of these novel circuits by displacement of the defected patterns in circuit or ground planes. Investigation shows that the cascaded defects in one or two planes, makes to degrade the frequency response particularly in the high frequency, but by using the DMGS circuit enhances the stopband for wide range of frequency. Also the circuit parameters that related to the physical circuit configurations are extracted. The proposed DMGS circuit has larger effective inductance with respect to conventional DGS or DMS. These circuits have been analyzed and the performance of these circuits has been compared.

1. INTRODUCTION

Recently, there has been considerable research effort in the areas of photonic band gap (PBG) [1, 2], electromagnetic band gap (EBG) structure (previously termed photonic band gap) [3–6] and defected ground structures (DGSs) [7, 8]. In a defected microstrip structure (DMS), there is no etching in ground plane. DMS is made by etching a uniform or non uniform slit or pattern and etching the very small slits perpendicular to the main slits over the signal strip. This defect causes a band stop frequency response. The DGS structure consisting of the dumbbell cell that etched from the ground plane. If compared DGS to DMS, DGS occupies more area and the ground plane should be perforated. For getting the more stopband, cascaded two or more defected patterns on the circuit or ground planes is necessary but in the high frequency the response may be more affected by the large coupling. In this paper we have presented the novel DMGS circuit that yields the very wide stopband frequency response.

2. FREQUENCY RESPONSE OF DMS AND DGS STRUCTURES

Compared to DGS, the DMS has no radiated EMI ground noise but generally its radiation is nearly equal. For substantiation of this claim, two DMS and DGS circuits have designed (Fig. 1) with the same resonant frequency as shown in Fig. 2. Fig. 2 shows that the DMS structure provides good cutoff frequency characteristic and stop band effect with respect to DGS. The line width is chosen to have 50 ohm. These circuits were simulated using Ansoft HFSS v.11 (a full wave simulator). In order to obtain good insight into the series inductance due to the physical parameters of the cell, the narrow gap g, which determines the gap capacitance, was kept equal to 0.2 mm for both cases (DMS and DGS). The proposed structures are designed on a substrate with relative permittivity $\varepsilon_r = 2.33$ and thickness $H = 0.787$ mm.
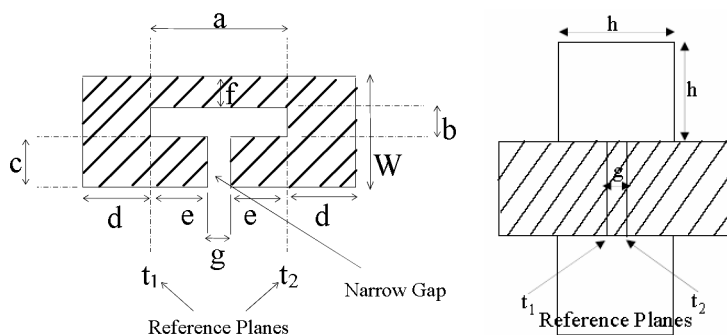

Figure 1: Unit cell DMS parameters with $a = 5$ mm, $b = 0.5728$ mm, $c = 1.3572$ mm, $d = 1.9$ mm, $e = 3$ mm, $f = 0.4$ mm, $g = 0.2$ mm and $h = 2.9346$ mm.
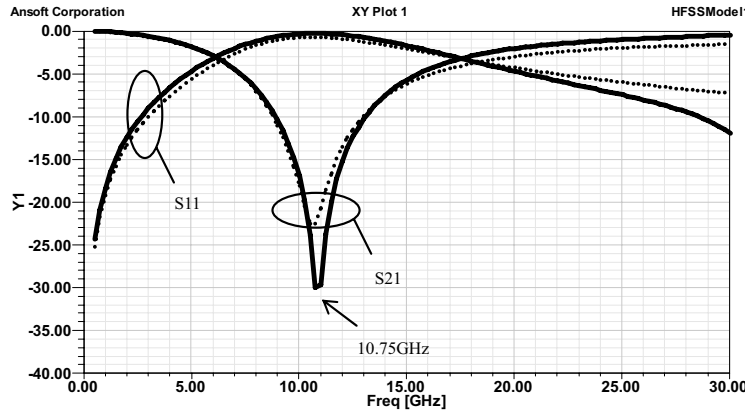
Figure 2: Frequency response of two DMS (solid line) and DGS (dot line) circuit with the same resonant frequency. In DMS, $a = 5$ mm, $b = 0.5728$ mm and $g = 0.2$ mm. In DGS, $a = b = 2.9346$ mm (dumbbell sides) and $g = 0.2$ mm.

3. EQUIVALENT CIRCUIT PARAMETERS OF DMS AND DGS

Based on EM simulation results, the circuit models of the DMS and DGS are established and the lumped elements of these models are extracted using circuit theory. The equivalent circuits of the proposed DMS and DGS can be expressed as a parallel RLC circuit. The center frequencies of the stop bands for the proposed DMS and DGS is determined by the resonance frequencies of these defects. Thus, the cutoff and stop band characteristics for the proposed DMS and DGS can be easily estimated. Equations (1)–(7) present the extracted equivalent circuit (RLC) parameters for a single DMS or DGS cell. The parallel capacitance and inductance value for the given DMS or DGS cell can be extracted from the attenuation pole location, which is a parallel LC resonance frequency, and prototype Butterworth low pass filter characteristics:

$$C = \frac{f_c}{200\pi \left(f_0^2 - f_c^2 \right)} \tag{1}$$

$$L = \frac{1}{4\pi^2 f_0^2 C} \tag{2}$$

$$Y = \frac{1}{Z} = \frac{1}{R} + j \left(\omega C - \frac{1}{\omega L} \right) \tag{3}$$

$$z_{in} = Z + Z_0 \tag{4}$$

$$S_{11} = \frac{z_{in} - z_0}{z_{in} + z_0} = \frac{1}{1 + 2z_0 y} \tag{5}$$

where f_0 and f_c are resonant frequency and 3-dB cutoff frequency respectively, and Z_0 is the characteristic impedance of the circuit. For simplicity we ignore the frequency dependence of R and use a constant value for R obtained in $\omega = \omega_0$. Using

$$S_{21} = \frac{2Z_0}{2Z_0 + Z}, \tag{6}$$

for $\omega = \omega_0$, $Z = R$ and then R is given as

$$R = 2Z_0 \frac{1 - S_{21}(\omega_0)}{S_{21}(\omega_0)}. \tag{7}$$

The extracted R, L, and C values for DMS and DGS are 4.19 kΩ, 1.56 nH, 0.14 pf and 1.23 kΩ, 1.6 nH, 0.13 pf, respectively. These values show that the L and C parameters in DMS and DGS circuit are nearly equal but resistance in DMS due to higher density of current is more than 3 times of another circuit in the resonant frequency.

4. FREQUENCY RESPONSES OF DMGS CONFIGURATIONS AND EMC EFFECT

Figure 3(a) shows the proposed DMGS circuit, which is loaded to the microstrip line and ground plane with dimensions as shown in Fig. 1. The simulation result for DMGS is shown in Fig. 3(a).

The extracted R, L, and C values for DMGS are $7.41\,\mathrm{k\Omega}$, $3.27\,\mathrm{nH}$, and $0.053\,\mathrm{pf}$. So it is easy to conclude that the series inductance of the DMGS circuit is much more than the series inductance of the only single cell DMS/DGS circuit. This high effective series inductance in the DMGS introduces a cutoff characteristic at a lower frequency and we obtain the wide stop band frequency. For the comparison of the different DMGS structures we have changed a to $2\,\mathrm{mm}$. The result is shown in Fig. 3(b).
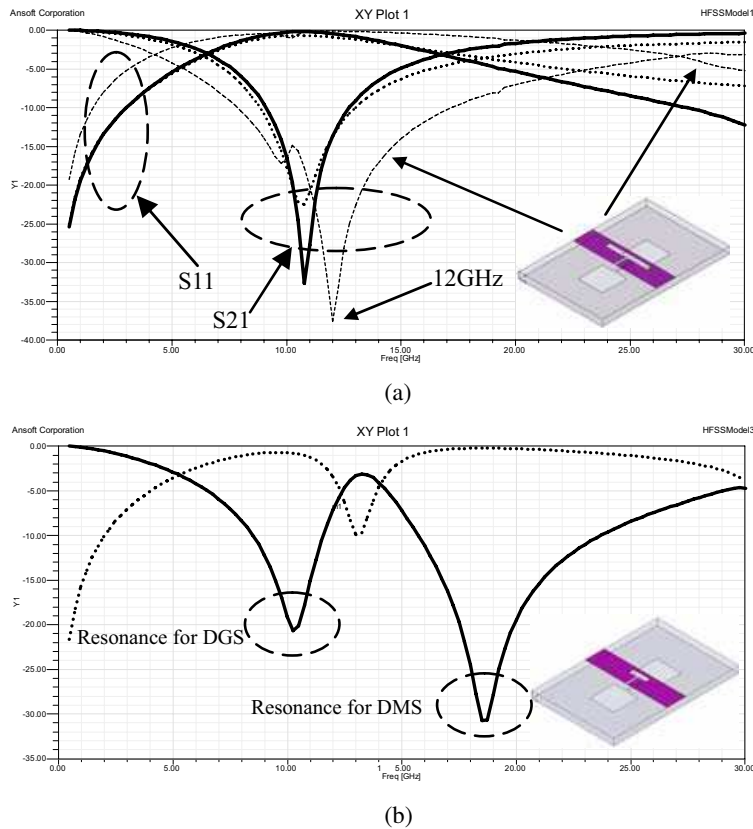

(a)

(b)

Figure 3: (a) 3D view of the DMGS and the comparison of simulated magnitude of S_{11} and S_{21} between DMGS (dashed line), DMS (bolded solid line) and DGS (dotted line). (b) S-parameter magnitude for a DMGS with defects that not to be same frequency response.

For investigation of EMC problem in these two circuits the radiation pattern is a good gauge. Fig. 4 shows the radiation patterns in E-plane. According to the Fig. 4 the EMC problem in DMS circuit can be nearly equal with respect to the DGS circuit. However the radiation from DMS and DGS circuit can be solved by housing the circuit board in the metal case but in DGS the circuit should be suspended. The radiation from the circuit plane of the DMGS is less than the radiation from the DMS. Also there is a not significant change in the radiation from the ground plane. In the Table 1 DMGS has been compared to DMS and DGS structure.

Table 1: Qualitative characteristics of three circuits.

Qualitative Characteristics / Type of Circuits	EMI noise due to defected ground	Easy to integration with other components	Application on microstrip miniature/milli-wave circuits	Width of Stop band bellow -10 dB (1st. cut off to 2 st. cut off)	Value of effective inductance	Value of capacitance
DGS	Moderate	moderate	Moderate	4.25 GHz (12.5 GHz)	Moderate	Moderate
DMS	No	Fine	Compatible	3.75 GHz (10.25 GHz)	Moderate	Moderate
DMGS	Moderate	moderate	Moderate	9.5 GHz (22.75 GHz)	High	Small

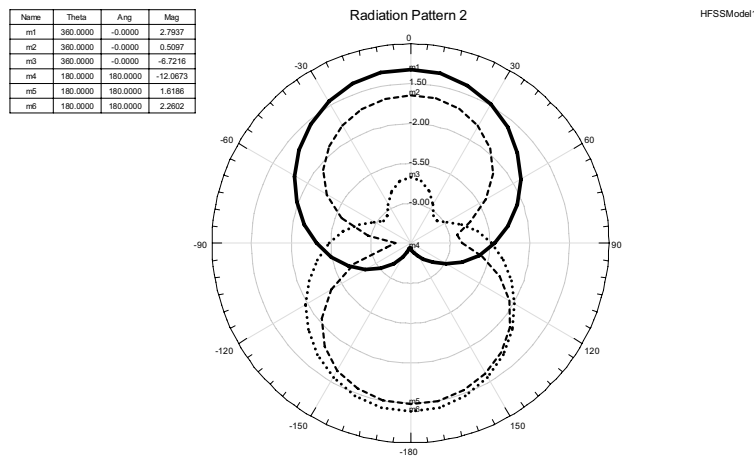| Name	Theta	Ang	Mag
m1	360.0000	-0.0000	2.7937
m2	360.0000	-0.0000	0.5097
m3	360.0000	-0.0000	-6.7216
m4	180.0000	180.0000	-12.0673
m5	180.0000	180.0000	1.6186
m6	180.0000	180.0000	2.2602

Figure 4: Comparison of the radiation pattern (IEEE gain) in E-plane at the resonant frequency. Dashed line is for DMGS (12 GHz), solid line is for DMS (10.75 GHz) and dotted line is for DGS (10.7 GHz) circuit.

5. DESIGN AND ANALYSIS OF THE CASCADED DMS (CDMS), CASCADED DGS (CDGS) AND COMPARED WITH DMGS

In order to show that the cascaded defects on circuit or ground plane don't play role of DMGS two circuits have designed and analyzed. For a cascaded DMS or DGS (CDMS or CDGS) structures, the central frequency of stopband can be roughly determined as follow formula [9]:

$$f_0 = \frac{c}{\lambda_g} \cdot \frac{1}{\sqrt{\varepsilon_{eff}}} \qquad (8)$$

where c is the speed of light in free space, $\lambda_g = 2 \cdot L$ is the Bragg condition and L is the period of CDMS or CDGS. Recently, a more accurate expression for the Bragg condition has been proposed [10], which takes into account the change in the effective dielectric constant of the microstrip line ε_{eff} produced by the pattern etched in the for example ground plane. For a microstrip line with etched pattern in microstrip or ground plane, the effective dielectric constant ε_{eff} can be estimated
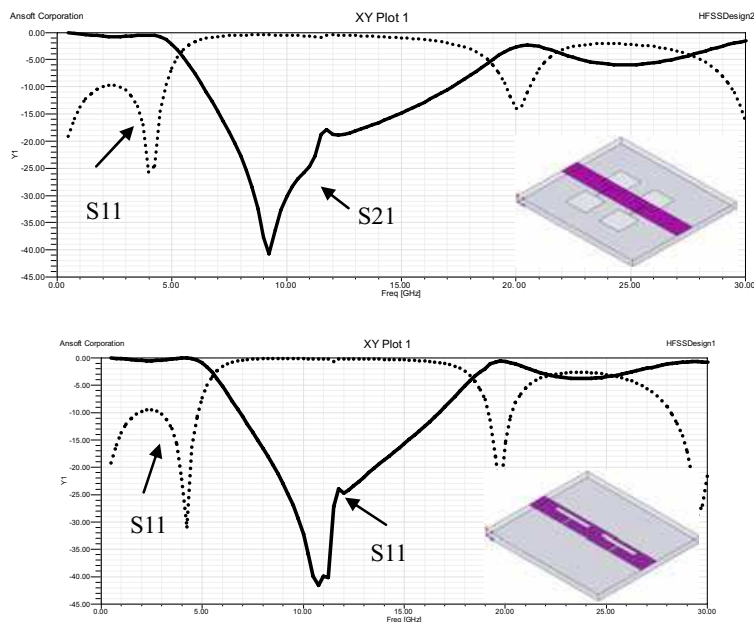

Figure 5: Frequency responses of CDMS and CDGS.

as that of the line with unperturbed microstrip circuit, i.e.,

$$\varepsilon_{eff} = \frac{\varepsilon_r + 1}{2} + \frac{\varepsilon_r - 1}{2} \left(1 + 12\frac{h}{w}\right)^{-0.5} \tag{9}$$

where d and w are the thickness of the substrate and the width of the line, respectively. In our design for obtaining stopband center frequency about 12 GHz in CDMS and CDGS, the value of L becomes 9 mm. The frequency responses of these circuits are shown in Fig. 5. As can be seen in the figures, the frequency response of these circuits is completely different from DMGS frequency response. Also this case tested for an uncommon DMGS that defects is cascaded, as demonstrated in Fig. 6. These disagreements are due to their different equivalent circuits. The related equivalent circuits have been shown in Fig. 7. Based on Fig. 7, these differences are absolutely revealed. Also at the high frequency the mutual coupling is tending to be larger and frequency response will be too degraded. This bad effect starts around the 20 GHz.
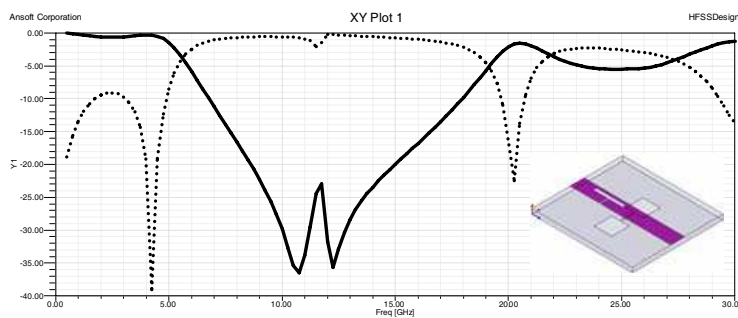

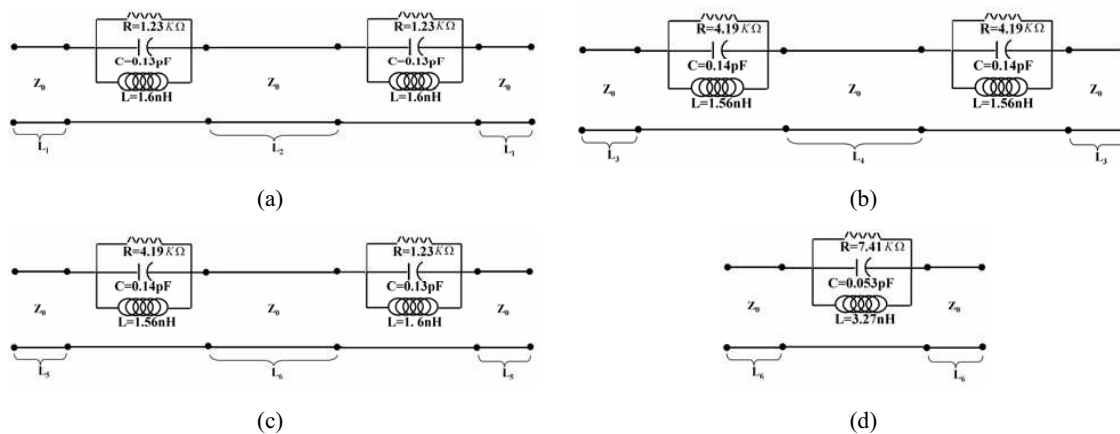Figure 6: Frequency responses of an uncommon DMGS.

Figure 7: The equivalent circuit of (a) DGS, (b) DMS, (c) uncommon DMGS and (d) DMGS.

6. CONCLUSION

The behavior of DMGS structures with etched simultaneously patterns on circuit and ground planes are studied. It is shown that the associated stop band in DMS and DGS can be joined together to form a very wide stopband characteristic by placing the etched patterns on the circuit and ground planes with the same frequency response as a novel circuit called by DMGS. Also the EMC effect, which is immediate interest for the design of band stop filters, was presented and analyzed.

This novel device can be used to perform broad band filtering of undesired frequencies, overcoming the narrowband techniques commonly used today. Other possible applications, such as filters and antenna structures are the future works of the authors.

REFERENCES

1. Rahman, M. and M. A. Stuchly, "Transmission line-periodic circuit repersentation of planar microwave photonic bandgap structures," *Microw.Opt. Technol. Lett.*, Vol. 30, 15–19, July 2001.
2. Radisic, V., Y. Qian, and T. Itoh, "Broadband power amplifier using dielectric photonic bandgap structure," *IEEE Microwave Guide Wave Lett.*, Vol. 8, 13–14, Jan. 1998.
3. Yang, F. and Y. Rahmat-Samii, "Reflection phase characterization of an electromagnetic band-gap (EBG) surface," *Proc. IEEE AP-S Dig.*, Vol. 3, 744–747, June 2002.
4. Yang, F. and Y. Rahmat-Samii, "Mutual coupling reduction of microstrip antennas using electromagnetic band-gap structure," *IEEE Antennas Propagat. Soc. Dig.*, Vol. 2, 478–481, 2001.
5. Fan, M., R. Hu, Z. H. Feng, X. X. Zhang, and Q. Hao, "Advance in 2D-EBG structures' research," *J. of Infrared Millimeter Waves*, Vol. 22, No. 2, 2003.
6. Yang, F. and Y. Rahmat-Samii, "Microstrip antennas integrated with electromagnetic band-gap structures: A low mutual coupling design for array applications," *IEEE Trans. Antennas and Propagation*, Vol. 51, 2936–2946, Oct. 2003.
7. Kim, C. S., J. S. Lim, J. S. Park, D. Ahn, and S. W. Nam, "A 10 dB branch Line Coupler Using Defected Ground Structure," *European Microwave Conference Digest*, 68–71, 2000.
8. Yun, J. S., G. Y. Kim, J. S. Park, D. Ahn, K. Y. Kang, and J. B. Lim, "A design of the novel coupled line bandpass filter using defected ground structure," *IEEE MTT-S Digest*, 327–330, 2000.
9. Coccioli, R., F. R. Yang, K. P. Ma, and T. Itho, "Aperture-coupled patch antenna on UC-PBG substrate," *IEEE Trans. Microwave Theory Tech.*, Vol. 47, 2123–2130, Nov. 1999.
10. Laso, M. A. G., T. Lopetegi, M. J. Erro, D. Benito, M. J. Grade, and M. Sorolla, "Novel wideband photonic bandgap microstrip structures," *Microwave Opt. Technol. Lett.*, Vol. 5, 357–360, 2000.

Design of 3.1 to 10.6 GHz Ultra-wideband Low Noise Amplifier with Current Reuse Techniques and Low Power Consumption

Pou-Tou Sun, **Shry-Sann Liao**, **Hung-Liang Lin**, **Chung-Fong Yang**, and **Yu-Hsuan Hsiao**

RF/MW Circuits Design Laboratory, Department of Communication Engineering
Feng-Chia University, 100, Wen-Hua Rd., Taichung 407, Taiwan, R.O.C.

Abstract— This paper presents a 3.1 to 10.6 GHz ultra-dwideband (UWB) low noise amplifier (LNA) using a current-reused technique and wideband input matching network is proposed. The implemented LNA presents a maximum power gain of 12.8 dB, and a good input matching in the required band. An excellent noise figure (NF) of 2.97 to 6.04 dB was obtained in the frequency range of 3.1 to 10.6 GHz with a power dissipation of 10.13 mW under a 1.8-V DC power supply. The finished chip size is $1.26 \times 1.05 \, \text{mm}^2$. The proposed UWB LNA is implemented by TSMC $0.18 \, \mu\text{m}$ CMOS technology.

1. INTRODUCTION

In the year of 2002, the Federal Communication Commission (FCC) in U.S. has approved Ultra-Wideband (UWB) radio technology for commercial applications. Ultra-wideband (UWB) applications in the 3.1–10.6 GHz frequency range [1], the related technologies have attracted much attention from both industry and academia. This new standard provides low cost, low complexity, low power consumption, high security, and high data-rate wireless communication capabilities, which can be used in wireless personal area network (WPAN), medical-image systems, and vehicular communications. The design of the low noise amplifier is one of the challenges in radio frequency receivers, which needs to provide a good input impedance match, a flat power gain, and a low noise figure (NF) within the required band.

In this design, wideband technique with a simple wideband matching filter for the input matching network is adopted, and the current-reused structure proposed in narrow-band LNA design [2] has been successfully extended to UWB applications. Combining these techniques, an UWB LNA implemented by standard TSMC $0.18 \, \mu\text{m}$ CMOS technology demonstrates an excellent NF as low as 2.97 dB with a power gain of 12.8 dB and low power consumption of 10.13 mW.

2. LNA TOPOLOGY AND CIRCUIT DESIGN

The circuit schematic of UWB LNA is shown in Figure 1 which the proposed CMOS UWB LNA with the current-reused technique and the wideband matching filter, the inter-stage network composed of the inductors L_G, L_D and capacitor C_G performs a current-reused function to achieve low power consumption and high power gain. In addition, an inductor L_B is connected between the M_3 and M_4 FET for the further bandwidth extension due to a series LC resonance with the gate capacitance of M_4 FET.

2.1. Current Reused Technique [3]

The current-reused configuration can be considered as a two stage cascade amplifier, where the first stage is the CS amplifier M_1, and the second stage is the cascode amplifier M_2 and M_3 with an additional buffer stage M_4 at the output. M_3 is the common-gate stage of the cascode configuration, which eliminates Miller effect and provides a better isolation from the output return signal. The purpose of using L_G and C_G is to perform a series-resonant with C_{gs} of M_2 for a low impedance path, while the impedance of L_D is adequately large in the desired bandwidth to provide a high impedance path to block the signal. The simulation results indicate that the current-reused function can work properly as L_D exceeds a certain value, and is not affected by the selection of C_G and L_G. As a consequence, the input signal can be amplified twice under the same current structure.

2.2. Input and Output Matching Design

In order to active the input matching, we use the source inductive degeneration method combined with shunt and series LC circuit to get a wideband matching. When impedance is matched, the real part of the input impedance is equal to the source impedance.

At the output matching, we used a source follower output buffer to active the output matching. Figure 2 is show the structure of source follower. The output impedance R_i of the source follower
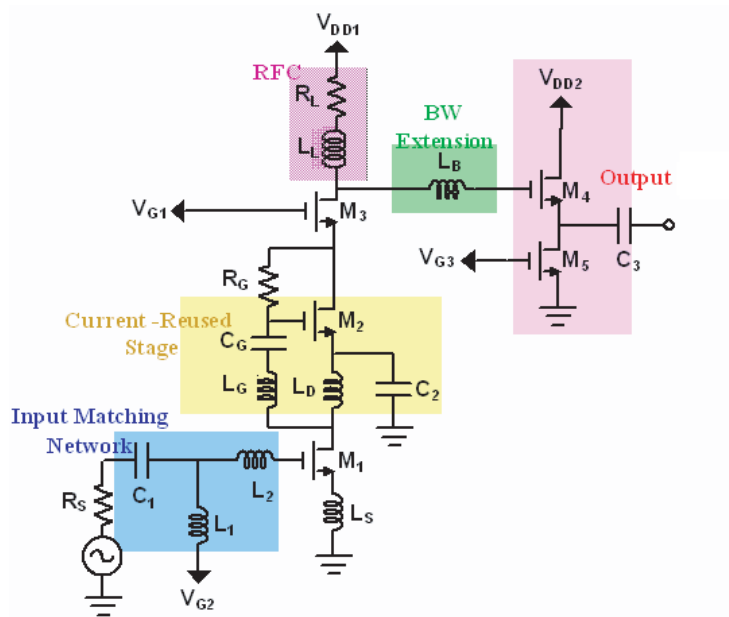
Figure 1: Circuit schematic of UWB low-noise amplifier.

is given by the equation

$$R_i = R_1 // R_2 = \frac{1}{g_{m1}} // r_{O1} // r_{O2}$$

$$r_{O1}, r_{O2} \geq \frac{1}{g_{m1}}$$

$$R_i \approx \frac{1}{g_{m1}}$$

$$I_D \approx \frac{1}{2} \mu_n C_{ox} \frac{W}{L} (V_{GS} - V_{TH})^2 (1 + \lambda V_{DS}) \tag{1}$$

$$g_{m1} = \mu_n C_{ox} \frac{W}{L} (V_{GS} - V_{TH}) (1 + \lambda V_{DS})$$

$$\frac{1}{g_{m1}} = \left[\frac{2 \mu_n C_{ox} \frac{W}{L} I_D}{1 + \lambda V_{DS}} \right]$$

$$R_i \approx \frac{1}{g_{m1}} = \left[\frac{2 \mu_n C_{ox} \frac{W}{L} I_D}{1 + \lambda V_{DS}} \right]^{-1/2}$$

So we can choose the gm of the M_1 to achieve wideband output matching.
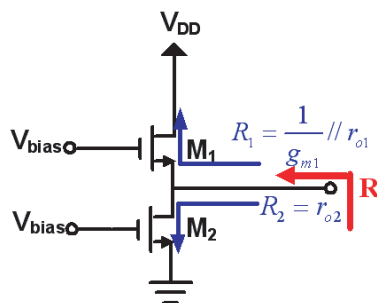

Figure 2: The schematic of source follower.

2.3. Consider of Low Noise Figure

The current reused amplifier functions as a two-stage cascade amplifier. The NF of the second stage contributed from both the FETs (M_2 and M_3) and the inductors (L_G and L_D) can be reduced by the gain of the first stage. In addition, the NF originated from R_L, L_L, L_B and M_4 is reduced twice by the gains of the first and second stages. With this design technique, not only can a high gain be obtained, but a low NF can also be achieved simultaneously.

3. SIMULATION AND MEASURED RESULTS

The circuit performance is measured by using on-wafer test. The LNA gain (S_{21}) and input return loss (S_{11}) simulation and measurement results are shown in Figure 3 and Figure 4. The measured gain is 9.16 to 12.8 dB at 3.1 to 10.6 GHz and input return loss is less then -10 dB at 3.1 to 10.6 GHz. Figure 5 and Figure 6 shows the simulation and measurement results of S_{12} and S_{22}. The measured S_{12} is less then -30.34 dB at 3.1 to 10.6 GHz and S_{22} is -9.3 to -17.2 dB at 3.1 to 10.6 GHz. Figure 7 shows the simulation and measurement results of the noise figure. The

Table 1: Simulated and measured performance of 3.1 to 10.6 GHz 0.18 μm CMOS LNA.

| UWB Low-Noise Amplifier		
Band Width	3.1GHz ~ 10.6GHz	
VDD1	1.8 V	
VDD2	1.8 V	
VG1	0.7 V	
VG2	1.6 V	
VG3	0.7 V	
	Simulation	**Measurement**
Power Consumption	10.25mW	10.13 mW
Input Return Loss(S11)	<-10 dB	<-10 dB
Input Return Loss(S22)	<-10 dB	<-9.3dB
Gain(S21)	12.5~14.8 dB	9.16~12.8 dB
Isolation(S12)	<-29.3 dB	<-30.34 dB
Noise Figure	2.9~4.7 dB	2.97~6.03 dB
P1dB	-17dBm @ 3.1GHz -16 dBm @ 6.8GHz -18 dBm @ 10.6GHz	-15.5dBm @ 3.1GHz -15 dBm @ 6.8GHz -15 dBm @ 10.6GHz
IIP3	-10 dBm @ 6.8GHz	-9.5 dBm @ 6.8GHz
Stability	>1	>1
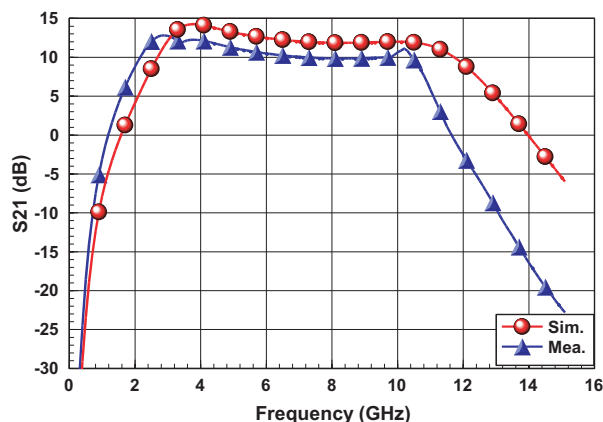
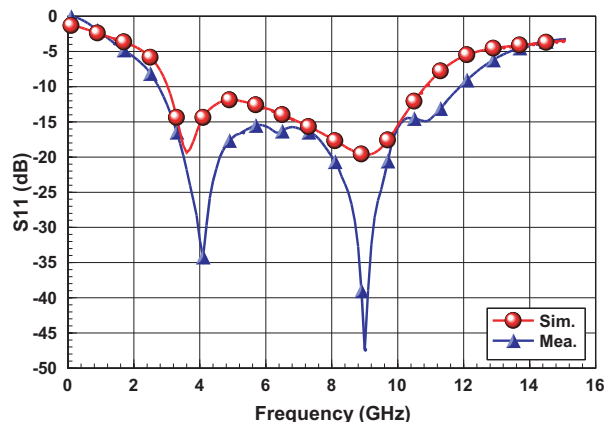Figure 3: Simulation and measurement results of the gain (S_{21}).

Figure 4: Simulation and measurement results of the input return loss (S_{11}).

measured noise figure is 2.97 to 6.04 dB at 3.1 to 10.6 GHz. The simulation and measurement results of $P_{1\,\mathrm{dB}}$ compression point and third order intercept point OIP3 are shown in Table 1. The power consumption is 10.13 mW at V_{DD} is 1.8 V. The total chip size is $1.26 \times 1.05\,\mathrm{mm}^2$ and the die photo is shown in Figure 8.
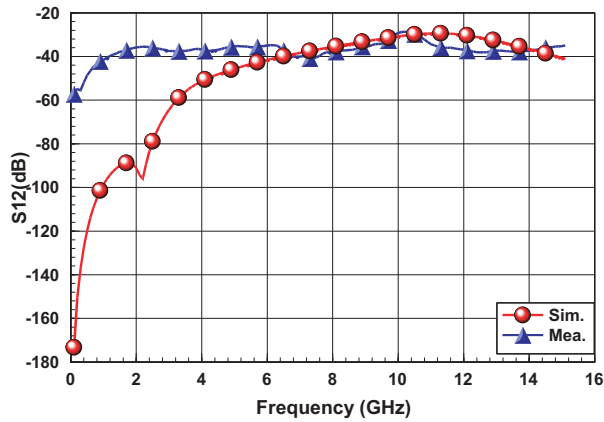

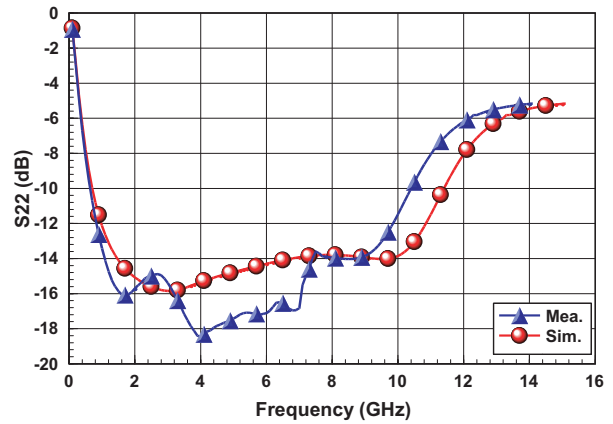Figure 5: Simulation and measurement results of the isolation (S_{12}).

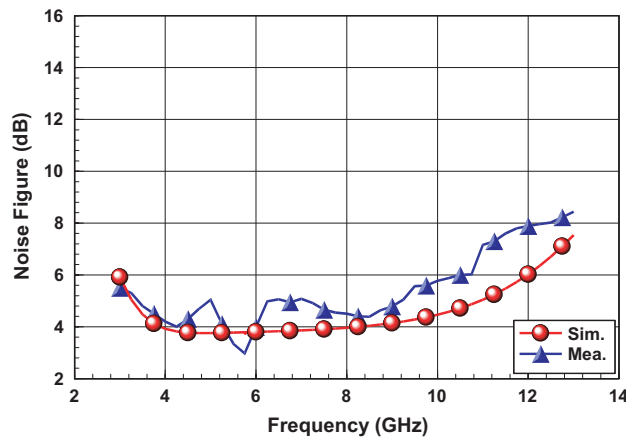Figure 6: Simulation and measurement results of the output return loss (S_{22}).

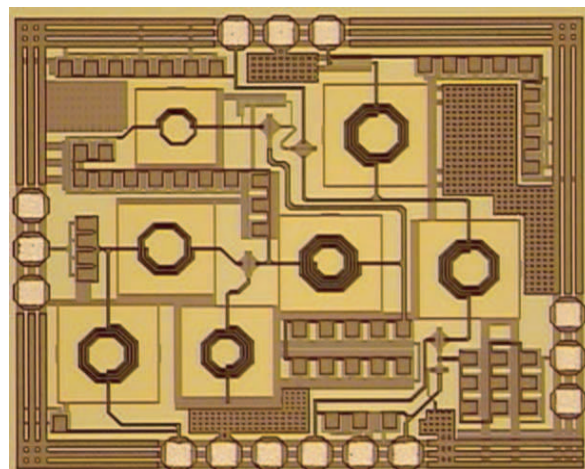Figure 7: Simulation and measurement results of the noise figure.

Figure 8: The die photo of 3.1 to 10.6 GHz 0.18 μm CMOS LNA.

4. CONCLUSION

A 3.1 to 10.6 GHz ultra-wideband (UWB) low noise amplifier (LNA) with a current-reused technique is fabricated in a TSMC 0.18 μm standard CMOS process. The LNA uses a current-reused technology to increase gain and save power consumption. The measurements are performed using on-wafer test. The LNA measurement at 3.1 to 10.6 GHz exhibits the minimum noise figure of 2.97 dB, maximum gain of 12.8 dB, input return loss is < -10 dB at 3.1 to 10.6 GHz and output return loss is < -9.3 dB at 3.1 to 10.6 GHz with a power consumption of 10.13 mW at V_{DD} is 1.8 V.

ACKNOWLEDGMENT

REFERENCES

1. WPAN High Rate Alternative PHY Task Group 3a (TG3a), IEEE802.15, 2007 [Online]. Available: http://www.ieee802.org/15/pub/TG3a.html
2. Bevilacqua, A. and A. M. Niknejad, "An ultra-wideband CMOS LNA for 3.1 to 10.6 GHz wireless receiver," *IEEE ISSCC Tech. Dig.*, 382–383, 2004.
3. Lin, Y.-J., S. S. H. Hsu, Member, IEEE, J.-D. Jin, and C. Y. Chan, "A 3.1–10.6 GHz ultra-wideband CMOS low noise amplifier with current-reused technique," Digest of Technical Papers, *IEEE Microwave and Wireless Components Letters*, Vol. 17, No. 3, Mar. 2007.
4. Shaeffer, D. K. and T. H. Lee, "A 1.5-V, 1.5-GHz CMOS low noise amplifier," *IEEE Journal of Solid-State Circuits*, Vol. 32, No. 5, May 1997.
5. Lee, J. and J. D. Cressler, "Analysis and design of an ultra-wideband low-noise amplifier using resistive feedback in SiGe HBT technology," *IEEE Trans. Microw. Theory Tech.*, Vol. 54, No. 3, 1262–1268, Mar. 2006.
6. Liu, R.-C., C. S. Lin, K.-L. Deng, and H. Wang, "A 0.5–14 GHz 10.6 dB CMOS cascode distributed amplifier," Digest of Technical Papers, *2003 Symposium on SI Circuits*, 139–141, June 12–14, 2003.
7. Cheng, K.-H. and C.-K. Wang, "A 3.1–10.6 GHz CMOS cascaded two-stage distributed amplifier for ultra-wideband application," Advanced System Integrated Circuits 2004, *Proceedings of 2004 IEEE Asia-Pacific Conference*, 296–299, Aug. 4–5, 2004.
8. Ismail, A. and A. A. Abidi, "A 3–10-GHz low-noise amplifier with wideband LC-ladder matching network," *IEEE Journal of Solid-State Circuits*, Vol. 39, Issue 12, 2269–2277, Dec. 2004.
9. Cha, C. Y. and S. G. Lee, "A 5.2-GHz LNA in 0.35-μm CMOS utilizing inter-stage series resonance and optimizing the substrate resistance," *IEEE Journal of Solid-State Circuits*, Vol. 38, 2003.

The Design of Low Noise Amplifier with Gain-controlled and Low Power Consumption for WLAN Applications

Pou-Tou Sun, **Shry-Sann Liao**, **Hung-Liang Lin**, **Chung-Fong Yang**, **and Tzu-Wei Yang**

RF/MW Circuits Design Laboratory, Department of Communication Engineering
Feng-Chia University, 100, Wen-Hua Rd., Taichung 407, Taiwan, R.O.C.

Abstract— This paper presents a 5.2 GHz, 0.18 µm CMOS Low-Noise Amplifier (LNA) with gain controlled and low power consumption for an IEEE 802.11a WLAN application. The LNA fabricated with TSMC 0.18 µm 1P6M standard CMOS process, the current-reuse technique is used to increase the gain and reduce power consumption. The circuit performance is measured by using on-wafer test. The LNA exhibits a noise figure 2.94 dB at 5.2 GHz, the maximum power gain of 13.6 dB, the gain control range is 5 dB, and the power consumption of 4.2 mW at $V_{DD} = 1.8$ V. The finished chip size is 1.0 mm × 0.9 mm.

1. INTRODUCTION

The proliferation of mobile computing devices has fueled the demand for wireless local area networks (WLANs). These data communication systems which are implemented as an extension or an alternative to wired local area networks are the most convenient way to establish high speed. Internet and intranet connections and distribute data throughout the workplace or at home. Worldwide standards such as IEEE 802.1 la, HIPERLANR and HiSWANa enable unlicensed deployment of WLAN devices in the 5.2-GHz band at data rates up to 54 Mb/s.

Consumer demand requires WLAN devices that are cheap, small size and light weight, as well as long battery life. These requirements can be met by utilizing a CMOS technology to integrate the RF front-end functions on a single die.

A crucial RF front-end building block is the low noise amplifier (LNA) which plays a critical role in determining the noise figure of the system. This paper presents the design and implementation of an LNA for 5.2-GHz WLAN applications fabricated in a standard 0.18 µm CMOS process. This LNA have lower power consumption by using current reused topology. This topology is made of a two-stage common source amplifier to share the operating current and reduce current consumption. In this paper, a current reused topology of a two-stage common source amplifier is adopted to share the operating current. The 5.2 GHz LNA is fabricated in a TSMC 0.18 µm standard CMOS process.
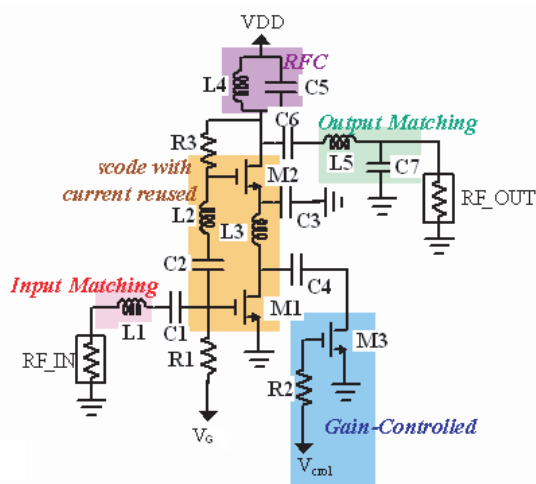

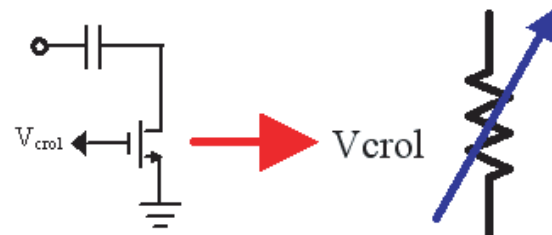Figure 1: Circuit schematic of a gain-controlled LNA with current reuse.

Figure 2: Circuit schematic of gain-controlled switch transistor.

2. LNA TOPOLOGY AND CIRCUIT DESIGN

Figure 1 illustrates the LNA with a current reuse topology. $M1$ and $M2$ transistors are both common source configurations, since the sources of $M1$ and $M2$ transistors are connected to signal ground separately. Cascade common source amplifiers share the same supply current to reduce dc current consumption. Overall transconductance of the LNA topology is the multiplication of the transconductances of the cascade amplifier. It provides gain expansion. V_G is that bias voltage of the first-stage common source amplifier. $R1$ and $R3$ are bias resistances. The bypass capacitance $C3$ achieves common source configuration of the second stage amplifier.
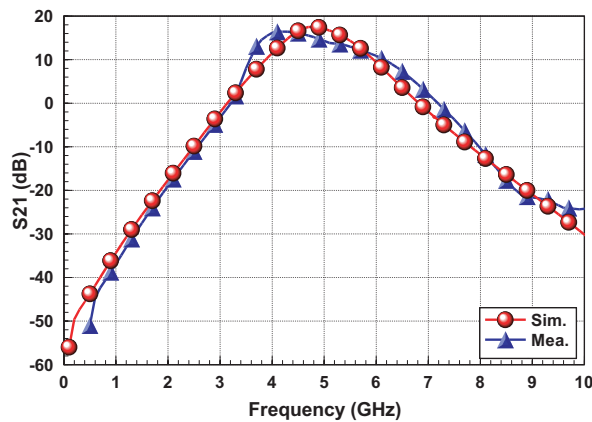

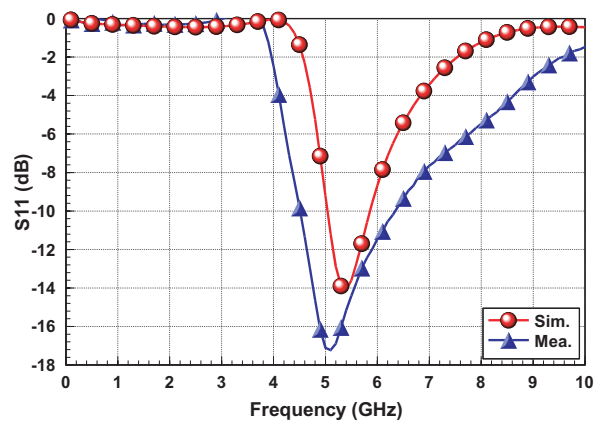Figure 3: Simulation and measurement results of the gain (S_{21}).

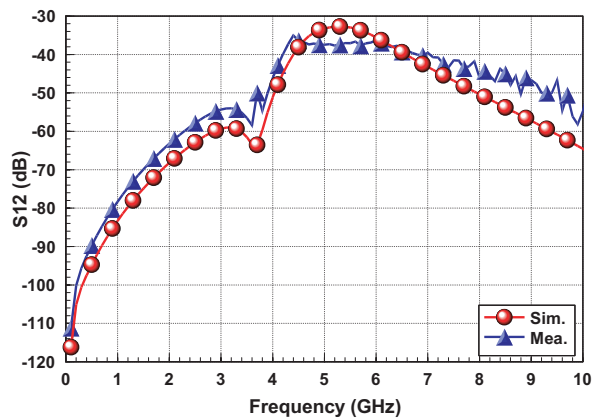Figure 4: Simulation and measurement results of the input return loss (S_{11}).

Figure 5: Simulation and measurement results of the isolation (S_{12}).
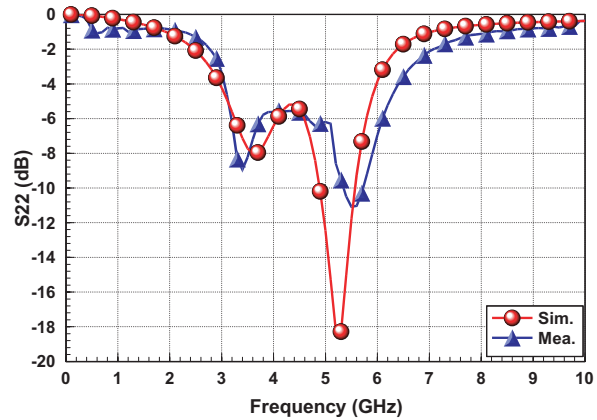

Figure 6: Simulation and measurement results of the output return loss (S_{22}).
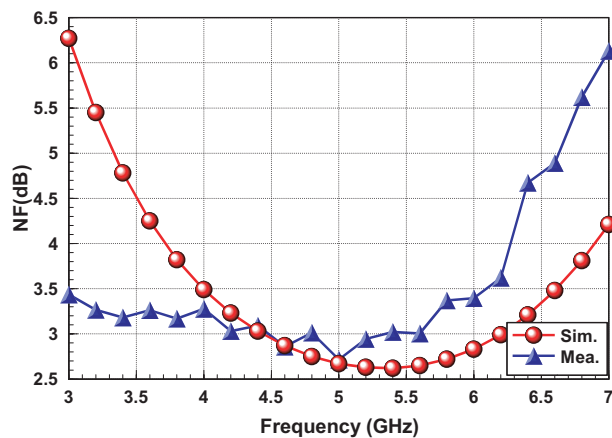

Figure 7: Simulation and measurement results of the noise figure.

2.1. Input/Output and Inter-stage Matching

From the sources of noise and how to determine the gate width of the first stage transistor can be known. Under power consumption limit, the chosen gate width of the first stage transistor $M1$ is $96\,\mu\text{m}$.

Multi-finger layout technology is used to reduce noise source of the transistor gate resistance. To achieve input matching to the $50\,\Omega$ characteristic impedance of the system, we use series the inductance $L1$ and the capacitance $C1$ to achieve the input matching.

The gate width of the second stage is chosen half of the first stage. Because of too large gate width will make the circuit unstable. On chip inductance $L3$ is used for the first stage inductive load. A choice of inductive load has another advantage which is no extra dc voltage drop. Series of on chip inductance $L2$ and capacitance $C2$ perform conjugated matching between the first and second stage [2]. Designing the parallel resonant frequency can be made by chose inductance $L4$ and capacitance $C5$ at operating frequency. Using series inductance $L5$ and shunt capacitance $C5$ performs output matching to the characteristic impedance of the system.

2.2. Gain-controlled Cell

Figure 2 illustrates the gain-controlled mechanism. The voltage V_{crol} applied to the switched transistor, which needs no extra dc current consumption [3].
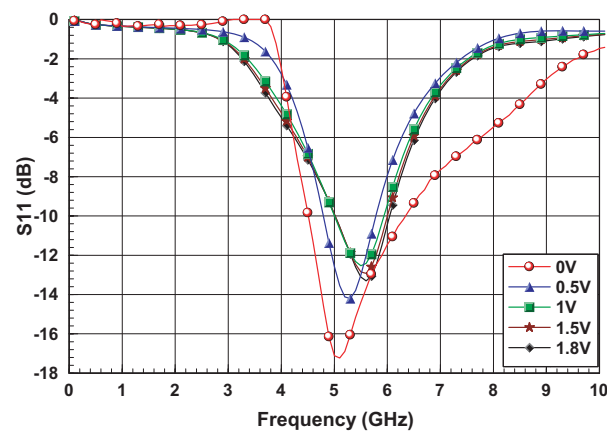
Figure 8: Measurement results of the S_{11} by control V_{crol} from $0\,\text{V}$ to $1.8\,\text{V}$.
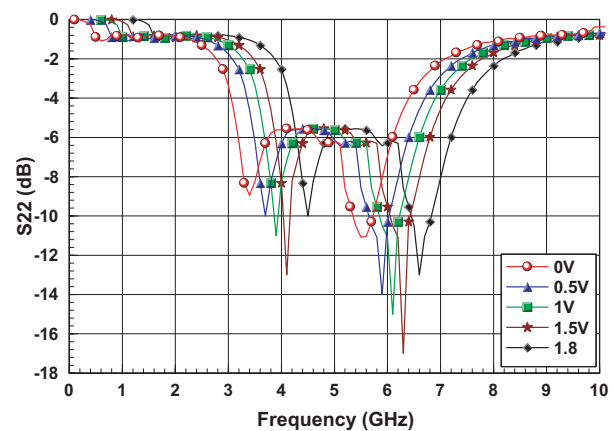
Figure 9: Measurement results of the S_{22} by control V_{crol} from $0\,\text{V}$ to $1.8\,\text{V}$.
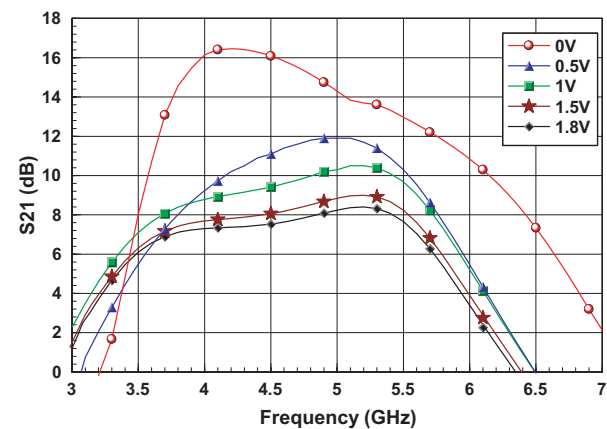
Figure 10: Measurement results of the gain (S_{21}) by control V_{crol} from $0\,\text{V}$ to $1.8\,\text{V}$.
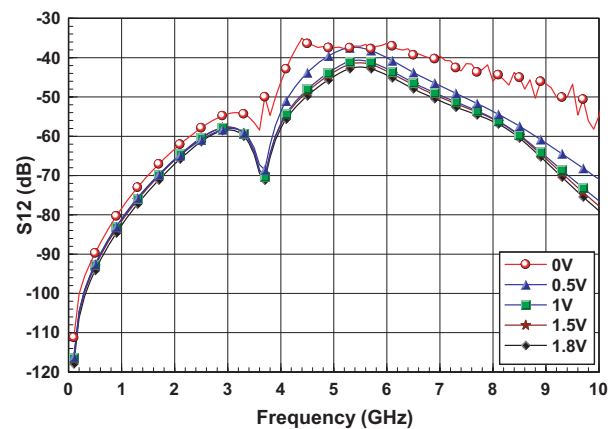
Figure 11: Measurement results of the S_{12} by control V_{crol} from $0\,\text{V}$ to $1.8\,\text{V}$.

3. SIMULATION AND MEASURED RESULTS

The circuit performance is measured by using on-wafer test. The LNA gain (S_{21}) and input return loss (S_{11}) simulation and measurement results are shown in Figure 3 and Figure 4. The measured

gain is 13.6 dB and input return loss is -16.6 dB at 5.2 GHz. Figure 5 and Figure 6 is shows the simulation and measurement results of S_{12} and S_{22}. The measured S_{12} is 37.7 dB and S_{22} is -8.6 dB at 5.2 GHz. Figure 7 shows the simulation and measurement results of the noise figure. The measured noise figure is 2.94 dB. The simulation and measurement results of P_{1dB} compression point and third order intercept point are shown in Table 1. The measured P_{1dB} is -20 dBm and OIP3 is -11 dBm. The gain control characteristic can be measured by the S-parameter for the control voltage V_{crol} from 0 V $\sim$ 1.8 V. The S-parameter measurement results are show in the Figures 8 to 11. The S_{11} is -11.2 to -16.6 dB, the S_{22} is -5.5 to -8.6 dB, the S_{21} is 8.4 to 13.6 dB and S_{12} is -37.7 to -41.52 dB. The measurement results by changing V_{crol} from 0 V to 1.8 V are summarizing in Table 2, which shows the gain control range is 5.2 dB. The power consumption is 4.2 mW at $V_{DD} = 1.4$ V. The total chip size is $1 * 0.9$ mm^2 and the die photo is shown in Figure 12.

5.2GHz Low-Noise Amplifier		
V_{D1}	+1.4 V	
V_{G1}	+0.64 V	
$V_{Control}$	0 ~ 1.8 V	
Performance	Simulation	Measurement
Center Frequency (GHz)	5.2 GHz	5.2 GHz
Power Consumption	4 mW	4.2mW
Input Return Loss (S_{11})	-12.9 dB	-16.6 dB
Output Return Loss (S_{22})	-18.3 dB	-8.6 dB
Gain (S_{21})	16.2 dB	13.6 dB
Isolation(S_{12})	-32.8 dB	-37.7 dB
Noise Figure	2.64 dB	2.94 dB
$P_{in,1dB}$	-22 dBm	-20 dBm
OIP3	-12dBm	-11 dBm
Stability	Unconditional Stability	Unconditional Stability

Table 1: Simulated and measured performance of 5.2 GHz 0.18 µm CMOS LNA.

Parameters	$V_{control}$= 0~1.8 V
Power Consumption	4.2 mW
Center Frequency (GHz)	5.2 GHz
S11 (dB)	-11.2 dB ~ -16.6 dB
S21 (dB)	8.4 dB ~ 13.6 dB
S12 (dB)	-37.7 dB ~ -41.52 dB
S22 (dB)	-5.5 dB ~ -8.6 B
NF (dB)	2.94 dB ~ 3.43 dB
Stability	>1
P1dB (dBm)	-20 dBm ~ -17.5 dBm@ 5.2 GHz
IIP3 (dBm)	-11 dBm ~ -6 dBm@ 5.2 GHz

Table 2: Measured performance of 5.2 GHz 0.18 µm CMOS LNA by control V_{crol} from 0 V to 1.8 V.
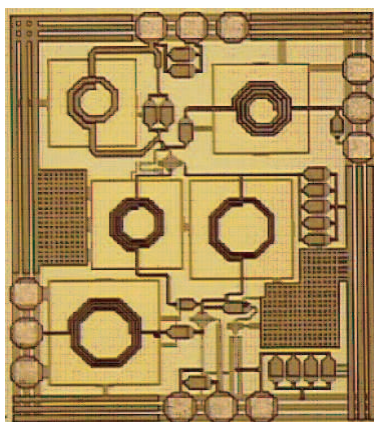
Figure 12: The die photo of the 5.2 GHz 0.18 µm CMOS LNA.

4. CONCLUSION

5.2 GHz CMOS LNA with gain-controlled and low power consumption is fabricated in a TSMC 0.18 µm standard CMOS process, for an IEEE 802.11a WLAN application is presented. The LNA uses a current-reuse technology to increase gain and save power consumption. The measurements are performed using on-wafer test. The LNA measurement at 5.2 GHz exhibits noise figure of 2.94 dB, gain of 13.6 dB, input/output return loss of -16.6 dB/-8.6 dB, P_{1dB} of -20 dBm, and gain control range is 5.2 dB with a power consumption of 4.2 mW at VDD is 1.4 V.

REFERENCES

1. Wang, X. and R. Weber, "Low voltage low power SiGe BiCMOS X-band LNA design and its comparison study with IEEE 802.11a LNA design," *Radar Conference, 2005 IEEE International*, 27–30, IEEE, 2005.
2. Wang, Y. S. and L.-H. Lu, "5.7 GHz low-power variable-gain LNA in 0.18-/spl mu/m CMOS," Vol. 41, No. 2, 66–68, Jan. 20, 2005.
3. Liao, C.-H. and H.-R. Chuang, "A 5.7-GHz 0.18-/spl mu/m CMOS gain-controlled differential LNA with current reuse for WLAN receiver," Vol. 13, No. 12, 526–528, Dec. 2003.
4. Tsai, M.-D., R.-C. Liu, C.-S. Lin, and H. Wang, "A low-voltage fullyintegrated 4.5–6-GHz CMOS variable gain low noise amplifier," *European Microwave Conf.*, 13–16, 2003.
5. Raja, M., T. Boon, K. Kumar, and S. Wong, "A fully integrated variable gain 575-GHz LNA with on chip active balun for WLAN," *IEEE RFIC Symp.*, 439–442, 2003.

Design of a SiGe BiCMOS Power Amplifier for WiMAX Application

Cheng-Chi Yu, **Yao-Tien Chang**, **Meng-Hsiang Huang**, **Luen-Kang Lin**, **and Hsiao-Hua Yeh**

Department of Communications Engineering, Feng-Chia University
100, Wen-Hua Rd., Taichung 407, Taiwan, R.O.C.

Abstract— Worldwide interoperability for microwave access (WiMAX) wireless communication system has been gradually popular in recent years. WiMAX mainly provides a high data rate, long transmission distance, wide coverage, and good quality of service technology to improve the drawback in wireless fidelity (Wi-Fi). Power amplifier is one of the most important components in WiMAX transmitter. A power amplifier operating at 3.5 GHz for WiMAX application is proposed in this paper. The TSMC 0.35-μm SiGe BiCMOS technology is used in this design. The choice of using SiGe BiCMOS technology for this design is based on its better breakdown robustness than CMOS and Si BJT (for same f_T), its technology availability and maturity, and its single-chip integration potential with multi-million gate digital CMOS. The proposed power amplifier is design with two stages open collector common-emitter amplifier. The results demonstrate that it can provide a reasonable efficiency, linearity and good output power.

1. INTRODUCTION

Recently, worldwide interoperability for microwave access (WiMAX) wireless communication system has been gradually popular in wireless communication market. This technology provides not only point to point (PTP) and point to multipoint (PMP) message services, it can also offer a high data rate and long transmission distance. Power amplifier is one of the key components in mobile communications. It needs some characteristics, such as high output power, high linearity and high power added efficiency (PAE). In the past, such implementations were predominantly made in more expensive compound semiconductor technology like Gallium Arsenide (GaAs) and Indium Phosphide (InP). The SiGe-heterojunction bipolar transistor (SiGe-HBT) technology is becoming popular in microwave applications due to its characteristics of low power consumption, high integration level, and low cost than GaAs and InP. Many papers on SiGe technologies of power amplifiers have been published in the past [1–3].

In this paper, a power amplifier operating at 3.5 GHz for WiMAX application is studied. A two stages open collector common-emitter amplifier with active linearity bias circuit is designed. The utility of active linearity bias circuit is for the purpose of obtaining both high efficiency and low nonlinear distortions [4, 5]. The TSMC 0.35-μm SiGe BiCMOS technology is used in this design.

2. CIRCUIT DESIGN

Figure 1 shows the schematic diagram of two stages WiMAX power amplifier. This power amplifier includes driver stage and power stage. In order to increase the available voltage swing at output, this topology utilizes high breakdown transistor for power transistor (Q2), and the power stage should be optimized for maximum power or efficiency. The power transistor (Q2) with emitter area $0.9 \times 20.3 \times 16\,\mu m^2$ HBTs, resulting in a total emitter area (A_E) of $292.32\,\mu m^2$, is used for power stage in this circuit. On the other hand, high gain and high speed transistor is use for the driver transistor (Q1) to simultaneously achieve both high gain and high output power for the power amplifier. The driver transistor (Q1) with emitter area $0.3 \times 20.3 \times 8\,\mu m^2$ HBTs, resulting in a total emitter area (A_E) of $48.72\,\mu m^2$, is used for driver stage.

The parasitic inductors of the bonding wires of each stage are also considered in circuit design. The input impedance consisting of a bonding inductor with high pass on-chip capacitor and inductor matching network (L1, C1, C2) is matched to 50 Ω. The inter-stage matching network contains L2, C3, and C4. The quarter-wavelength transmission lines of two stages are used to isolate the RF signal from the supply voltage. The output matching network can constrict the high-order harmonics in the output signal.

The schematic diagram of bias circuit is shown in Figure 2. The function of the bias circuit is to enhance linearity of power amplifier. When input power level is not big enough, the linearizer is not enabled. On the other hand, when at the high input power level, the impedance of the bias circuit is decreased by the capacitor Cb and the amount of RF power leaking into the bias circuit is increased. The linearizer shunt capacitor with the base-emitter diodes of the transistors compensates the decreased base bias voltage of the transistor (Q1). Therefore, the performance of 1-dB compression point will be improved.
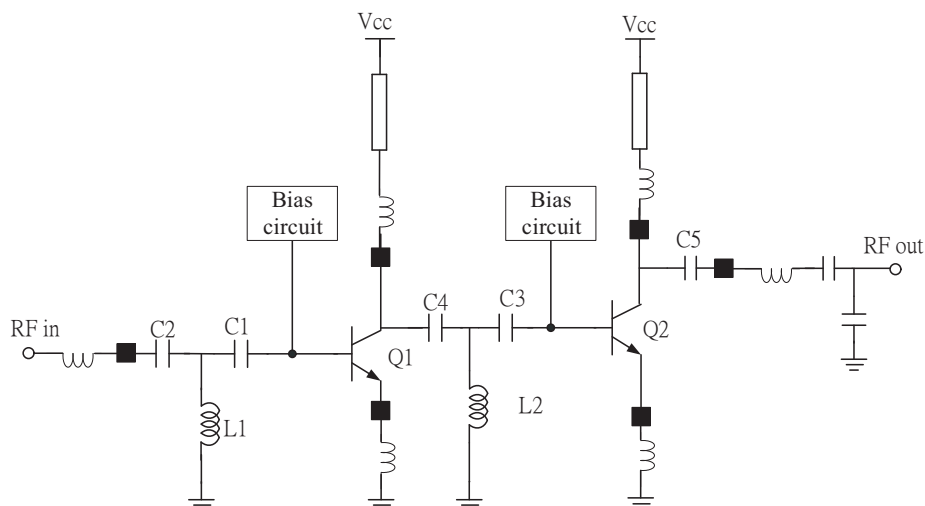
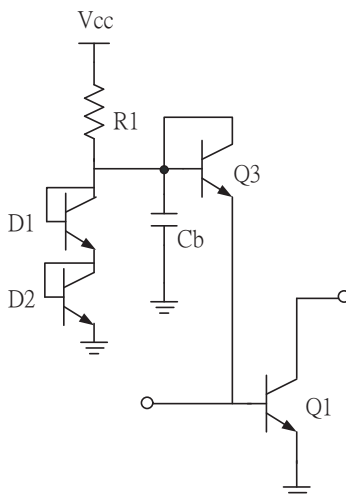Figure 1: Schematic diagram of two stages power amplifier.

Figure 2: Schematic diagram of the bias circuit.

3. LAYOUT TECHNIQUES

For high power design, a multitude of parallel devices were used to distribute large current among small unit devices. In ideal, the current is equally distributed through the devices. However, if devices are even slightly mismatched, one device will operate at a higher temperature than the others and draw a larger amount of current. Hence, the power gain is degraded by thermal effect.

Figure 3 illustrates the power cell of the power stage. Every power cell is connected with four subcells. This type of power cell can make subcells be fed in equal phase, and reduce thermal effect and the parasitic overlap capacitance of base-collector paths. The layout of the two stages power amplifier is shown in Figure 4. Total layout chip size of the power amplifier is $1.094 \times 0.792 \, \text{mm}^2$.

4. SIMULATION RESULTS

The WiMAX power amplifier is designed by TSMC 0.35-μm SiGe BiCMOS technology. The software Agilent ADS is used to simulate the circuit characteristics. The simulated results of the circuit are also including parasitic effects of microstrip lines.

The simulated S-parameters of the WiMAX power amplifier are depicted in Figure 5. The input return loss S_{11}, output return loss S_{22}, gain S_{21}, and reverse isolation S_{12} are -16 dB, -11 dB, 24.1 dB, and -49.7 dB, respectively. The output 1-dB compression point $P_{1\,\text{dB}}$ is 22.1 dBm at operating frequency of 3.5 GHz. A reasonable PAE of 44.5% is obtained, as shown in Figure 6. The supply voltage of the power amplifier is 3 V and the quiescent power consumption is 220 mW.
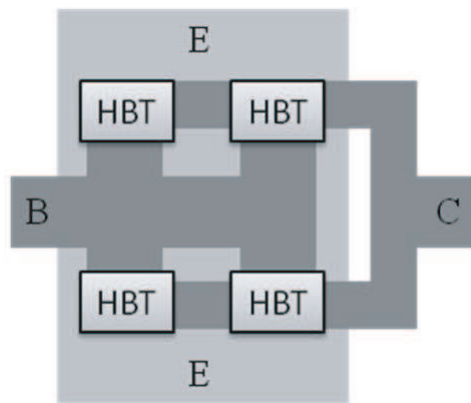
Figure 3: Power cell of the power stage.

Figure 4: Layout of the two stages power amplifier.
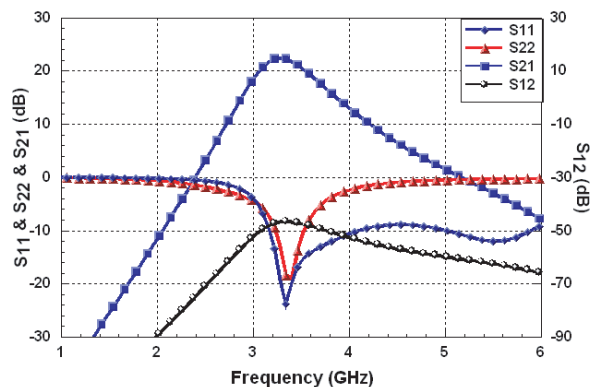
Figure 5: S-parameters of WiMAX SiGe power amplifier.
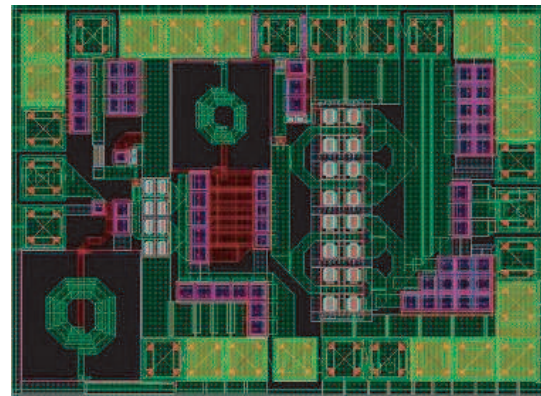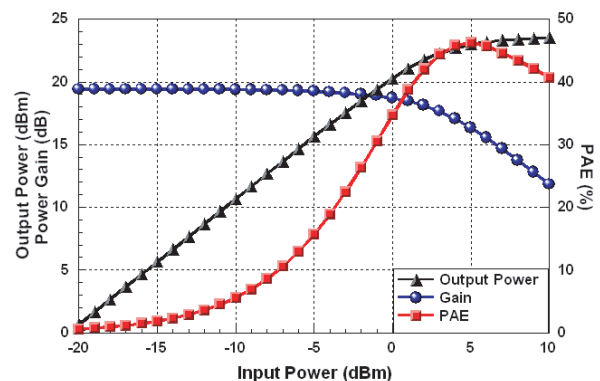
Figure 6: Output Power, Gain and PAE versus input power.

5. CONCLUSION

A SiGe BiCMOS power amplifier for WiMAX application is proposed. The chip area is $1.094 \times 0.792\,\text{mm}^2$. The active linearity bias is used to improve 1-dB compression point and achieve high linearity and efficiency. The power amplifier has 24.1 dB power gain, 46.3% PAE, 22.1 dBm output power at $P_{1\,\text{dB}}$, and 23.7 dBm maximum output power under 3 V operation voltage. The total quiescent power consumption of the power amplifier is 220 mW.

ACKNOWLEDGMENT

REFERENCES

1. Peng, Y.-J., J.-Y. Song, and Z.-G. Wang, "A 3.3 V SiGe HBT power amplifier for 5 GHz WLAN application," *8th International Conference on Solid-State and Integrated Circuit Technology, ICSICT '06*, 1541–1543, 2006.
2. Lin, C. H., Y. K. Su, Y. Z. Juang, C. F. Chiu, S. J. Chang, J. F. Chen, and C. H. Tu, "The optimized geometry of the SiGe HBT power cell for 802.11a WLAN applications," *Microwave and Wireless Components Letters*, Vol. 17, 49–51, IEEE, 2007.
3. Liao, H.-Y., K.-Y. Chen, J. D.-S. Deng, and H.-K. Chiou, "0.35-µm SiGe BiCMOS variable-gain power amplifier for WiMAX transmitters," 2007.
4. Y. Ping-Chun, L. Kuei-Cheng, C. Y. Lee, and C. Hwann-Kaeo, "A 1.8-V monolithic SiGe HBT power amplifier with a novel proposed linearizing bias circuit," *The 2004 IEEE Asia-Pacific Conference on Circuits and Systems, Proceedings*, Vol. 1, 305–308, 2004.
5. Sub, N. Y. and P. C. Soon, "PCS/W-CDMA dual-band MMIC power amplifier with a newly proposed linearizing bias circuit," *IEEE Journal of Solid-State Circuits*, Vol. 37, 1096–1099, 2002.

A Nut-type Ultrasonic Motor and Its Application on Focus System

Tieying Zhou[1], **Jun Zhang**[1], **Yu Chen**[1],
Cunyue Lu[1], **Deyong Fu**[1], **Yi Li**[2], **and Xiaoping Hu**[2]

[1]Department of Physics, Tsinghua University, Beijing 100084, China
[2]Boly Media Communications (Shen Zhen), Ltd., Shen Zhen 518031, China

Abstract— This article reports a screw driving polyhedron linear ultrasonic motor (USM) of a nut type. It consists of a stator of a threaded metal nut bonded piezoelectric plates and a rotor with external thread. The piezoelectric plates are bonded to the flat surface on the outside of the nut. A traveling wave in plane is stimulated on the stator when a harmonic electric signal is applied on the piezoelectric plates. The traveling wave drives the rotor to rotate and the threads transform the rotation into a linear motion. The lens could be fixed in the rotor and stator to obtain the auto focus and zoom and to realize the integrated design of focus system. This structure would omit retarder and directly drive to obtain a high accuracy of positioning and it is shockproof. The experiment data for a nut-type USM of M7 are obtained, when the applied voltages are 20–40 Vp-p and the working frequency 17 KHz for the second mode, the consumed power is 0.25 W, the moving speed is 0.5–1 mm/s in shaft direction, the driving force is about 5 g, and the response time less than 10 ms. A mini AF cellular phone module ($8.5 \times 8.5 \times 5.9 \, \text{mm}^3$) driven by this motor has been made. The image resolution of 3–5 Mp has been obtained in the module prototypes of the cellular phone.

1. INTRODUCTION

The explosive development of mobile phones makes it more and more necessary to bring auto focus into mobile phones so as to achieve better image quality. Tiny motors are needed to create auto focus and optical zoom in mobile phone which are far smaller than digital still cameras and with low cost, and could withstand high shock loads. Conventional electromagnetic motors become dramatically less efficient below 6 mm diameter [1] and require gear reduction, which have reached their practical limit of miniaturization.

Compared with conventional electromagnetic motors, an ultrasonic motor is a new type actuator which utilizes the inverse piezoelectric effect of piezoelectric materials to produce vibrations at ultrasonic frequencies. The outstanding features of low speed, high torque, quick response, self-hold without power, easy miniaturization and so on quite meet the requirements of mobile phone.

As early as 1980s, Canon Inc. had successfully utilized ultrasonic motors in the focus system of digital cameras and realized the industrialization of ultrasonic motors [2]. Zeng Daihien and Seok jin Yoon et al. have developed the small discreteness of lens [3, 4]. What is more, a named SQUIGGLE motor of New Scale Tech Inc. is 1.55×1.55 mm square and 6 mm long threaded nut, which uses the first bending vibration to rotate and drive a threaded screw. It is capable of sub-micrometer stepping and very cheap, but integrated module with lens is not capable.

The new nut-type linear ultrasonic motors presented here is developed to meet the requirements of mobile phone [5–7]. The excellent characters of this motor are follows: 1) lens assemblies could be fixed in the screw rotor or nut stator in order to create auto focus or optical zoom and realize the unique operating design of focus system; 2) The thread driving system directly drive the rotation of the rotor into the linear motion without gears or cams, which could obviously reduce the number of components and more cheap.

2. STRUCTURE AND OPERATING PRINCIPLE

2.1. Structure

A nut-type linear ultrasonic motor mainly includes 3 parts: a stator, a rotor and piezoelectric elements (as shown in Figure 1). The stator is a nut-typed metal tube, which has threads in the inner surface and several flat external surfaces (it could be 3, 4, 6, 8, 9, 12, and so on). And the rotor is a threaded screw, whose threads engage with the stator, so that the rotor could rotate freely to realize linear motion along the axial direction. The piezoelectric plates with same thickness and section are bonded on the flat external surfaces and their poling directions aligned along the normal direction of the external surfaces.
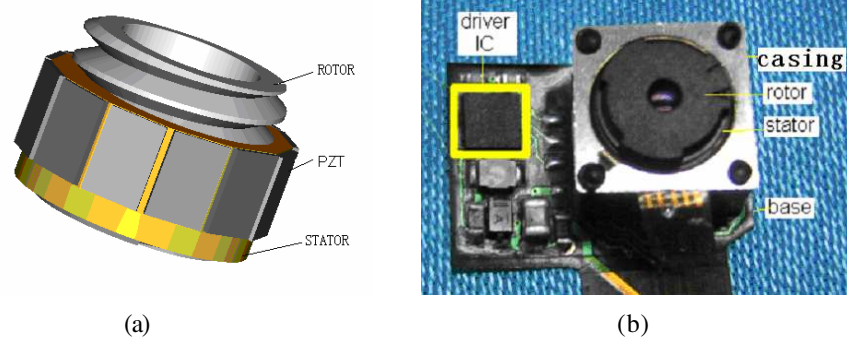
Figure 1: (a) Prototype of nut-type linear ultrasonic motor and (b) AF module.

2.2. Operating Principle

Firstly the vibration of the stator is discussed. As piezoelectric elements are quite thin, we ignore their effect on the stator and take the stator as a thin wall cylinder. According to the vibration theory [8], under the free boundary state, second mode ($n = 2$) or higher vibration modes ($n = 3, 4, 5 \ldots$) of the thin wall tube along the circumference direction are shown in Figure 2.
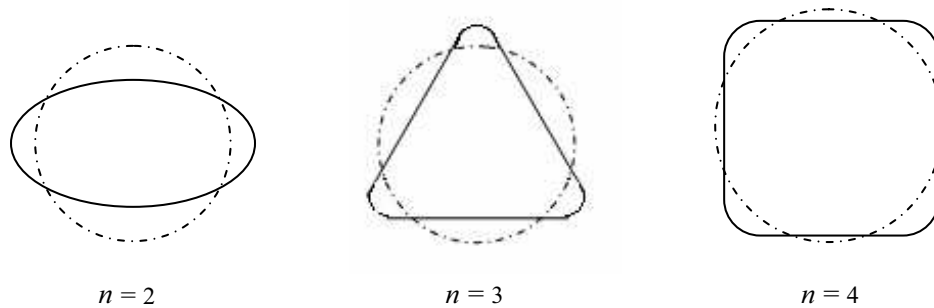
Figure 2: Schematic of vibration modes of cylinder after distortion-solid.

The higher the resonance frequency, the larger the vibration attenuation, so low order mode is preferably selected as the operation mode.

When an alternating current signal with one frequency is applied on the piezoelectric elements, bending vibration will be excited on walls of the stator. If it is assumed that a sine electrical signal is used for exciting one piezoelectric ceramic sheet, n order mode standing wave can be excited on the stator.

$$U_1 = A \sin(n\theta) \sin(\omega t). \tag{1}$$

where: A is amplitude, ω is frequency of the exciting signal, θ is polar coordinate (the angle of corresponding points on the stator walls) and the anticlockwise is defined as the positive direction.

In order to generate elliptic tracks for driving rotation of the rotor on surface points of the stator, proper combination of many piezoelectric elements is needed. For the stator whose cross section is an octagon (as shown in Figure 3). Eight piezoelectric elements are divided into two groups; $\sin \omega t$, $\cos \omega t$, $-\sin \omega t$ and $-\cos \omega t$ electric signals are applied on four piezoelectric elements in each group respectively, then eight piezoelectric elements can be excited for standing waves respectively. Total vibration of the stator is superposition of the eight standing waves.

$$U = \sum_{i=1}^{8} A \sin \left[n \left(\theta - \frac{i-1}{4} \pi \right) \right] f_i(\omega t) \tag{2}$$

When $n = 2$ (the second order vibration mode), eight standing wave vibrations U_1 to U_8 could

combine to form a traveling wave.

$$
\begin{aligned}
U &= U_1 + U_2 + U_3 + U_4 + U_5 + U_6 + U_7 + U_8 \\
&= A\{\sin(2\theta)\sin(\omega t) + \sin(2\theta - \pi/2)\cos(\omega t) - \sin(2\theta - \pi)\cos(\omega t) - \sin(2\theta - 3\pi/2)\cos(\omega t) \\
&\quad + \sin(2\theta - 2\pi)\sin(\omega t) + \sin(2\theta - 5\pi/2)\cos(\omega t) - \sin(2\theta - 3\pi)\sin(\omega t) - \sin(2\theta - 4\pi)\cos(\omega t)\} \\
&= A\left[4\sin(2\theta)\sin(\omega t) + 4\cos(2\theta)\cos(\omega t)\right] \\
&= 4A\cos(\omega t - 2\theta)
\end{aligned}
\tag{3}
$$

Same as the case of $n = 2$, the third order vibration mode $(n = 3)$ could also obtain a traveling wave by proper arrangements of drive signals. Under the arrangement of drive signals shown in Figure 3(b), the combined vibration is obtained as

$$
\begin{aligned}
U &= U_1 + U_2 + U_3 + U_4 + U_5 + U_6 + U_7 + U_8 \\
&= A\{\sin(3\theta)\sin(\omega t) + \sin[3(\theta - \pi/4)]\sin(\omega t) + \sin[3(\theta - \pi/2)]\cos(\omega t) + \sin[3(\theta - 3\pi/4)]\cos(\omega t) \\
&\quad - \sin[3(\theta - \pi)]\sin(\omega t) - \sin[3(\theta - 5\pi/4)]\sin(\omega t) - \sin[3(\theta - 3\pi/2)]\cos(\omega t) - \sin[3(\theta - 7\pi/4)]\cos(\omega t)\} \\
&= A[2\cos(\omega t - 3\theta)2\cos(\omega t - 3\theta + 3\pi/4)] \\
&= 2\sqrt{2 - \sqrt{2}}A\cos\left[\omega t - 3\theta + \cot^{-1}\left(\sqrt{2} - 1\right)\right]
\end{aligned}
\tag{4}
$$

which is 3rd order traveling wave.

In Figure 3(c)

$$
\begin{aligned}
U &= U_1 + U_2 + U_3 + U_4 + U_5 + U_6 + U_7 + U_8 \\
&= A\{\sin(3\theta)\sin(\omega t) - \sin[3(\theta - \pi/4)]\cos(\omega t) + \sin[3(\theta - \pi/2)]\cos(\omega t) + \sin[3(\theta - 3\pi/4)]\sin(\omega t) \\
&\quad - \sin[3(\theta - \pi)]\sin(\omega t) + \sin[3(\theta - 5\pi/4)]\cos(\omega t) - \sin[3(\theta - 3\pi/2)]\cos(\omega t) - \sin[3(\theta - 7\pi/4)]\sin(\omega t)\} \\
&= A[2\cos(\omega t - 3\theta) + 2\cos(\omega t - 3\theta + 9\pi/4)] \\
&= 2\sqrt{2 + \sqrt{2}}A\cos\left[\omega t - 3\theta + \cot^{-1}\left(\sqrt{2} + 1\right)\right]
\end{aligned}
\tag{5}
$$

which also is 3rd order traveling wave. Compared with the arrangement of Figure 3(b), the one of Figure 3(c) could provide the greater amplitude of vibration, which is optimal.

(a) $n = 2$ (b) $n = 3$ (c) $n = 3$
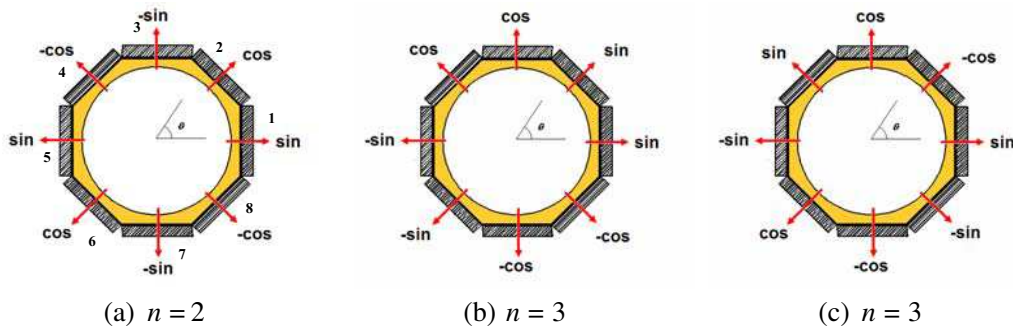
Figure 3: Motor drive signals for (a) traveling wave $n = 2$ and (b)(c) two kinds arrangements for $n = 3$.

Similarly, to the stators with different numbers of side surfaces, the proper arrangements of drive signals on piezoelectric elements are able to provide required traveling wave in the stator.

If the thin wall cylinder is cut along any one generatrix, then the cylinder can be expanded into a thin plate (as shown in Figure 4). If thickness of the thin plate is assumed as t, according to the vibration theory of thin plate, the x-y coordinate system is established by taking the neutral layer as the zero point. It is assumed that the neutral layer has not extension in y direction and displacement of point P on inner surface of the stator in x and y directions is u_x and u_y. According to above stated discussions, the traveling wave of cylinder can be expressed as

$$
u_x = u_0\cos(\omega t - ky),
\tag{6}
$$

where u_0 is the amplitude. Therefore, the displacement at y direction could be expressed as

$$u_y = -x\frac{\partial u_x}{\partial y} = -kxu_0\sin(\omega t - ky). \tag{7}$$

So

$$\left(\frac{u_y}{kxu_0}\right)^2 + \left(\frac{u_x}{u_0}\right)^2 = 1. \tag{8}$$

Obviously, the orbit of the particle P is an ellipse in the x-y plane, which is the foundation for the stator driving motion of the rotor on inner wall of the stator.
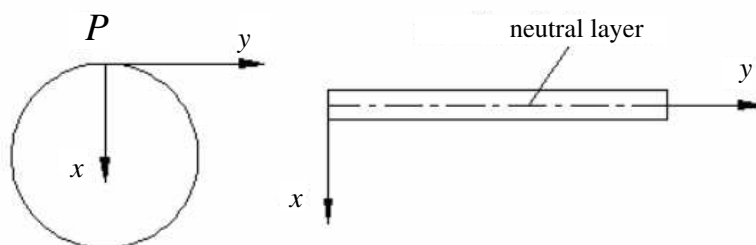
Figure 4: Schematic of the coordinate system.

3. STRUCTURE OPTIMIZATION DESIGN BY FEM

The vibration of a nut-type stator in the free condition was simulated using the finite element analysis (FEA) software to predict and verify its operation performance. A 8-side-surfaced stator, which 3.5 mm is in high, 0.25 mm in thick at the thinnest points and with the M7 threads in the inner wall and 0.25 mm in thick of piezoelectric plates at the outer side surfaces, has the 2nd vibration mode at 17.025 KHz.
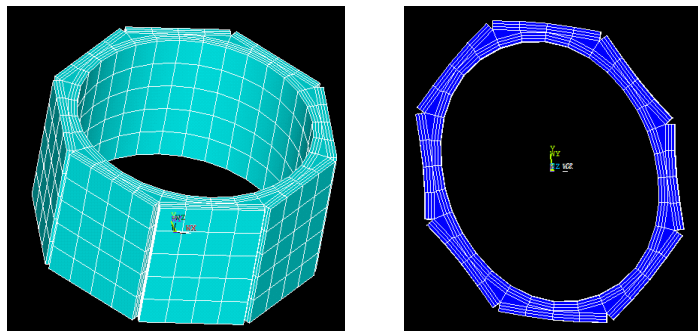
Figure 5: FEA modeling of the nut-type stator calculated by FEM software.

4. DRIVING MECHANICS

The contact mechanics is discussed following. Threads between the stator and rotor discussed here are the most common metric triangular threads shown in Figure 6, whose thread angle 2α is 60 degree. As the obliquity β of thread is quite small, it is roughly considered as zero, which is shown as Figure 7.

When a traveling wave is excited on the stator, the rotor contacts the stator at the peak. If there are l circles of threads in the contact region between the stator and rotor, and the number of contact points in a circle equals the order n of the mode, then there are $n \times l$ contact points. Considered the equivalence between the contact points, the rotor is taken as a mass point moving along a long side inclined plane. As shown in Figure 7, the coordinate system $o\xi\eta\zeta$ is established at the thread surface with ζ parallel to the normal direction of the surface and η to the y direction.
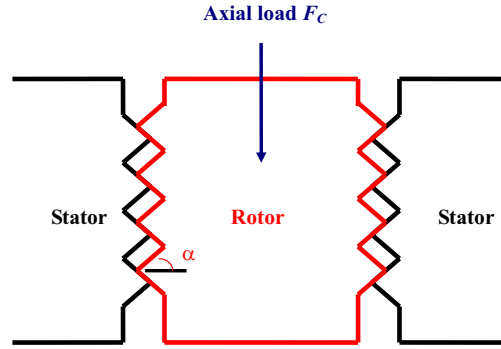
Figure 6: Profile of the nut-type USM.
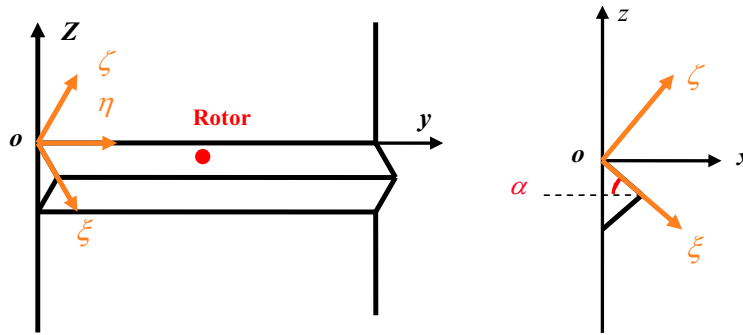
Figure 7: Equivalent contact mechanics of the stator and rotor.

Coordinate system $o\xi\eta\zeta$ and $oxyz$ have the relationship as followed:

$$\begin{cases} \hat{\xi} = \cos\alpha\hat{x} - \sin\alpha\hat{z} \\ \hat{\eta} = \hat{y} \\ \hat{\zeta} = \sin\alpha\hat{x} + \cos\alpha\hat{z} \end{cases} \quad \begin{cases} \hat{x} = \cos\alpha\hat{\xi} + \sin\alpha\hat{\zeta} \\ \hat{y} = \hat{\eta} \\ \hat{z} = -\sin\alpha\hat{\xi} + \cos\alpha\hat{\zeta} \end{cases}. \tag{9}$$

The rotor has an axial load Fc at the z direction, a support force Ns at the ζ direction, a load force $\mathbf{T}$ at the y direction and a friction force f which is parallel to the relative speed of the stator and rotor. During the static state and steady working state of the motor, Ns is equal to $Fc/\cos\alpha$ because of equilibrium condition of the rotor. Here the friction force is not resistance but a driving force.

Suppose that the stator and rotor are rigid and there is no deformation at the contact points. Therefore the contact point is the highest point of the elliptical motion of the particles on the surface of the stator as shown in Figure 8. At this time, the particles only has the speed of $v_{\eta\max}$ at the η direction, so that the friction force on the rotor is to right along the η direction. At the equilibrium state of the rotor, its tangential speed v_r equals $v_{\eta\max}$, while the load force equals the
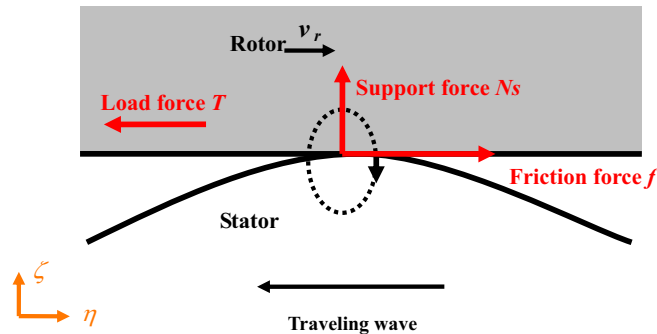
Figure 8: Driving mechanics between the stator and rotor.

static friction force at the contact surface. The greatest load force output by the motor should equals the maximum static friction force $\mu Fc/\cos\alpha$, where μ is the coefficient of static friction at the contact surface.

Also it could be calculated that the rpm and the linear feed speed v_l of the rotor are respectively equal to $30\,v_r/\pi r$ and $dv_r/2\pi r$ in which r is the rotor's radius and d is the thread pitch.

Here we suppose that both the stator and rotor are rigid, and more discussions on the viscoelastic friction layer and the contact pressure distribution can be seen in Reference [9].

5. EXPERIMENTS

About 1000 module prototypes of the cellular phone have been made. Main characteristics are shown Table 1. By now this new type motor has been experimentally applied in mobile phone AF systems [10, 11].

The experiment data for a nut-type USM of M7 are obtained, when the applied voltages are 20–40 Vp-p and the working frequency 17 KHz for the second mode, the consumed power is 0.25 W, the moving speed is 0.5–1 mm/s in shaft direct, the driving force is about 5 g, and the response time less than 10 ms. A mini AF cellular phone module ($8.5 \times 8.5 \times 5.9\,\text{mm}^3$) driven by this motor has been made. The image resolution of 3–5 Mp has been obtained in the module prototypes of the cellular phone, and the AF module is shown Figure 1(b).

Table 1: Main characteristics of several module prototypes of the cellular phone.

Type	BM620	BM631C	BM730	BM731C	BM850	BM851C
$L \times W$	7.8×7.8	7.5×7.5	8.8×8.8	8.5×8.5	10.5×10.5	9.5×9.5
Height (max)	5.6 mm	5.6 mm	5.9 mm	5.9 mm	8.5 mm	8.5 mm
Height (lensless)	4.7 mm	4.7 mm	5.2 mm	5.2 mm	6.2 mm	6.2 mm
Foot Print (PCB)	7.5×7.5	7.5×7.5	8.5×8.5	8.5×8.5	10.5×10.5	9.5×9.5
Motor	**screw driving polyhedron** USM					
Axial Resolution	2 μm	2 μm	2 μm	2 μm	2 μm	2 μm
Motor Speed	180 rpm	180 rpm	180 rpm	180 rpm	180 rpm	180 rpm
Response Time	< 10 ms	< 10 ms	< 10 ms	< 10 ms	< 10 ms	< 10 ms
Stall Force	5 g	5 g	5 g	5 g	10 g	10 g
Input Capacitance	< 0.65 nF	< 0.65 nF	< 1 nF	< 1 nF	< 1.3 nF	< 1.3 nF
Voltage	1.8–5 V	1.8–5 V	1.8–5 V	1.8–5 V	1.8–5 V	1.8–5 V
Frequency	22 KHz	22 KHz	17 KHz	17 KHz	15 KHz	15 KHz
Input/Holding Power	0.2/0.0 W	0.2/0.0 W	0.2/0.0 W	0.2/0.0 W	0.2/0.0 W	0.2/0.0 W
Temperature	$-20-+50°C$	$-20-+50°C$	$-20-+50°C$	$-20-+50°C$	$-20-+50°C$	$-20-+50°C$
Shock Resistance	> 5 g	> 5 g	> 5 g	> 5 g	> 5 g	> 5 g
Life Time	500000 cycles	500000 cycles	500000 cycles	500000 cycles	500000 cycles	500000 cycles
Weight	1.5 g	1.5 g	2 g	2 g	2.5 g	2.5 g

6. CONCLUSION

The lens assemblies could be fixed in the rotor or stator for nut-type USM, so that while the rotor revolves and moves along the axial direction, it would bring the lens assemblies backward and forward in order to create auto focus or optical zoom. Not only the motor has the outstanding features of ultrasonic motors (low cost, high efficiency, self-hold without power and so on), but also its unique operating design could reduce the linear speed and the number of components, and improve the precision. What is more, the nut-type ultrasonic motor could have more applications on the precise position systems which require compact structures and low cost.

ACKNOWLEDGMENT

REFERENCES

1. Henderson, D. A., "Simple ceramic motor, inspiring smaller products," *Actuator 2006, 10th International Conference on New Actuators*, Bremen, Germany, June 14–16, 2006.
2. Maeno, T., "Recent progress of ultrasonic motors in Japan," *The First International Workshop on Ultrasonic Motors and Actuators*, 15–17, Yokohama, Japan, 2005.
3. Zeng, D., et al., The small discreteness of lens, Chinese Patent Publication No. CN1664641A.
4. Yoon, S. J., "Development of linear ultrasonic motors," *The First International Workshop on Ultrasonic Motors and Actuators*, 7–8, Yokohama, Japan, 2005.
5. Lu, C., "The study and application of new types micro USM," The Postdoctoral Report, Department of Physics Tinghua University, Beijing, June 2006.
6. Zhou, T., K. Zhang, and K. Jiang, "Bending vibration piezoelectric cylindrical-type micro ultrasonic motor," Chinese Patent, Patent Grant No. ZL 001061720 (in Chinese) 2001-01-09.
7. Zhou, T., C. Lu, and Y. Chen, "A screw driving polyhedron ultrasonic motor Chinese Patent," Application No. 200510114849.2, Grant Patent No. CN1767347.
8. Ueha, S. and Y. Tomikawa, *Ultrasonic Motors: Theory and Application*, 11–25, Clarendon Press, Oxford, 1993.
9. Wallaschek, J., "Contact mechanics of piezoelectric ultrasonic motors," *Smart Mater. Struct.*, Vol. 7, 369–381, 1998.
10. Zhou, T., Y. Chen, C. Lu, et al., "The development, application and expectation of USM in lens focus," *Proceeding of the 11th China Small Motor Technology*, 141–147, Shanghsi, China, 2006.
11. Zhou, T., J. Zhang, Y. Chen, et al., "A nut-type ultrasonic motor and its application on focus system," *Chinese Science Bulletin*, Vol. 53, No. 11, 1251–1256, June 2008.

R&D of a New Type Piezoelectric Transformer with a Composite Structure

Weige Zhou, **Jinlong Du**, **and Bin Wu**

China Electronics Corporation WeiHua Research Center, Beijing, China

Abstract— Multi-layer piezoelectric transformers, regardless of thickness type or radial vibration type, currently have three basic structures: Monolithic-type, Composite structure (bonding method 1) and Composite structure (bonding method 2). The advantages and disadvantages of the piezoelectric transformers with different structures are summarized and bring forward a new composite structure of transformers. Experiments were conducted to verify the comparisons and developed a brand-new piezoelectric transformer with new composite structure.

1. INTRODUCTION

The trend of both miniaturization and integration of modern power electronic system makes the disadvantages of traditional magnetic components more and more obvious, and recently the study on a piezoelectric transformer as a substitution of a magnetic transformer has made great progress. Piezoelectric Transformers have the following main advantages over current largely used electromagnetic transformers: non-combustible, non-electromagnetic radiation, smaller size, simpler structure and higher conversion efficiency.

According to the different work patterns and shapes of piezoelectric transformers, piezoelectric transformers can be categorized into three types those are Rosen type with strip shape, thickness vibration type with rectangular shape and radial vibration-type with round shape. Among the three types, Rosen type piezoelectric transformers are most common.

Multi-layer thickness vibration type piezoelectric transformers were first supplied by NEC from Japan in 1990s. Their inputs and outputs are composed of longitudinal vibration mode piezoelectric stack components stacked each other in the thickness direction.

The structure, size, vibration mode and power output method of piezoelectric transformers will affect their own input and output impedance characteristics, thus affecting the output power and efficiency of power conversion. A multilayer radial vibration-type piezoelectric transformer is a developing piezoelectric transformer. Compared with the above two transformers, both the output power and conversion efficiency of a multilayer radial vibration-type piezoelectric transformer are increased significantly, meanwhile, its voltage transfer ratio is easier to be adjusted, this type transformers can meet the application requirements of both step-down and step-up. At the highest efficiency of the piezoelectric transformer, its optimal load impedance varies from several ohms to thousands ohms, which is in the middle value of Rosen type and the thickness vibration type optimal load impedance. A multilayer Radial vibration-type piezoelectric transformer has a broad range of applications, so it can be effectively used for DC/DC converter, AC/DC SMPS, adapters and electronic ballasts etc..

Multi-layer piezoelectric transformers, regardless of thickness type or radial vibration type, currently have the following basic structures:

1. Monolithic-type: namely, to obtain its structure by co-firing both ceramic raw embryo and Ag-Pd electrode plus polarization. Due to expensive Ag-Pd electrodes, in order to reduce material costs, electrode paste with smaller palladium content has inevitably be used, and it is inevitably necessary to reduce the sintering temperature, resulting in decreased performance of ceramic materials, therefore, it has greatly decreased the application range of transformers. As a result of post-polarization method, the defects generated during ceramic sintering are easier to appear in the end, if process control is not good enough, the defects will bring big losses. Also as a result of Co-firing, the electrical isolation of the transformer can only use ontology materials, which can not achieve high performance and result in restricting the application range of the transformer.

2. Composite structure (bonding method 1): the disadvantages of monolith method was abandoned., relatively inexpensive silver electrode was used as ceramic pieces, polarization qualified ceramic pieces are then combined into a transformer through an organic adhesive, thus a very

wide range of ceramic material can be used, and also ceramic material can be selected accord-
ing to design requirements, avoiding defects which possibly occur in the finished products,
therefore, the reliability of products can be improved. By using high temperature adhesives
with high quality, the temperature can reach 150°C, fully meeting the application requirements
now.

3. Composite structure (bonding method 2): the structure is between above two ones, the struc-
ture can be obtained by stick ceramic discs with organic or inorganic adhesives, which have
solidifying temperature up to more than 300°C and then polarize it The high-temperature
performance of adhesives is better than that of ordinary adhesives, but regarding to piezo-
electric ceramic materials whose Curie temperature is only about 300°C, its high temperature
performance is very difficult to take effect, and post- polarization would bring some problems,
just as monolithic structure have.

2. EXPERIMENT AND RESEARCH

Regarding to the advantages and disadvantages of piezoelectric transformers with different struc-
tures, a new type transformer with composite structure is developed, its output and input have
monolithic structure piezoelectric stack totally or partly, and then are combined into a transformer
by adhesives, glass pieces are incorporated between its output and input as isolating layers. Respec-
tively, tests were conducted using both new method and bonding method. Because of the different
manufacturing methods due to overall structures, the choices of materials are different, but the
transformers with same specifications have the same disc sizes. The following are the material
parameters and experimental designs of two materials:

2.1. Material Parameters

Table 1.

Symbols	Monolith structure	Bonding structure
$\varepsilon_{33}^T/\varepsilon_0$	1000	1850
tgδ(%)	0.8	0.25
Kp	0.6	0.65
$d_{33}(10^{-12}\,\text{m/V})$	225	460
Np (m/s)	2300	2000
Qm	700	400
σ	0.33	0.33
$\rho\,(\text{g/cm}^3)$	7.5	7.5
Tc(°C)	310	> 280

2.2. The Performance Comparison of the Transformers Manufactured by Two Methods

Using 20 w transformers as an example, several transformers are manufactures using both new
composite structure and bonding structure. The following are their structures in details.

2.3. A Brand-new Piezoelectric Transformer

A low input and output voltage piezoelectric transformer with new composite structure is manu-
factured.

Combining the advantages of both monolithic and the bonding structures, input and output use
monolithic piezoelectric stack, plus the isolation pieces, a brand-new transformer is formed using
adhesive, can meet the requirements of low voltage, high input current and high isolation.

3. RESULTS AND DISCUSSIONS

3.1. Performance of the Transformers with Different Temperatures

The relationship between capacitance, dielectric loss, $L1$, $R1$ and temperature are as followed:

3.1.1. Materials for the New Composite Structure Transformer

Figure 2 shows that within $-40°C \sim 125°C$ of ambient temperature, the capacitance C changes as
much as $20\% \sim 100\%$, in particular the dielectric loss above 80°C increase sharply, and transformer
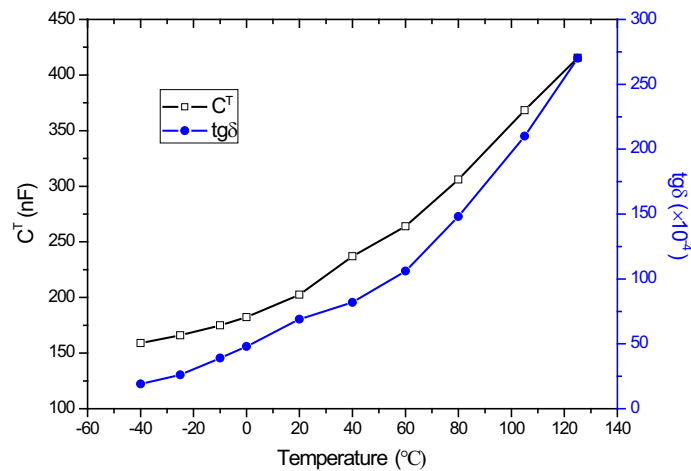
Figure 1: Dependence of capacitance, dielectric loss of new composite transformers on temperatures.
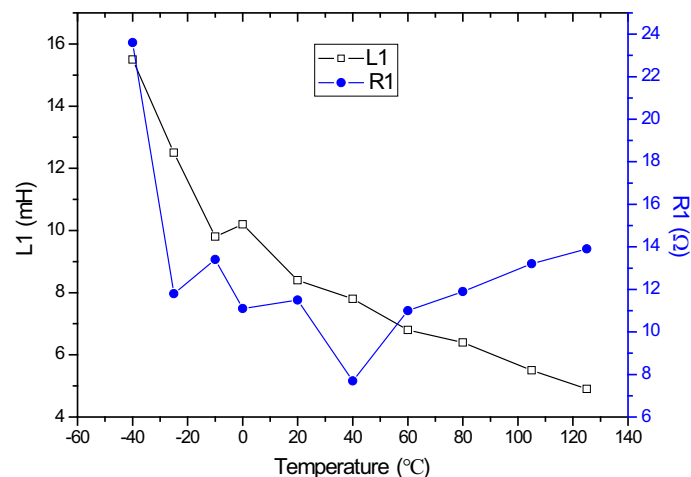

Figure 2: Dependence of $L1$, $R1$ of new composite transformers on temperatures.

dynamic resistance changes with temperature very greatly, especially when the temperatures are below $-30°$C and above $80°$C, resistance changes can up to 100%. Therefore, after high and low temperature tests, the performance of most transformers deteriorate, changes in temperature rise at room temperature are close to 100%, some can not work normally.

3.1.2. Materials for the Bonding Structure Transformer

Figure 4 shows that within $-40°$C $\sim 125°$C of ambient temperature, the capacitance C changes only 20% $\sim$ 60%, the overall level of dielectric loss is also lower than 80, the transformer dynamic resistance and inductance as a function of temperature also are relatively stable, so the transformer can work within $-40°$C $\sim 125°$C ambient temperature.

The transformers with two different structures have great different high-temperature performance, the reason for that is under different structure conditions the selectable range of the ceramic material varies. When monolithic structure is used, in order to decrease costs silver electrodes are used, accordingly reducing sintering temperature of ceramic materials, therefore greatly reducing the ceramic material performance at high temperature. If high temperature silver-palladium electrodes are used in order to improve sintering temperature, material costs would be greatly increased, reducing the transformer applicability and feasibility of large-scale production. Bonding structure transformers don't have this kind of restrictions, as long as ceramic discs and adhesives those meet application requirements are selected, they can work in a wide range of temperatures.

3.2. Performance Comparison of Different Structure of Transformer

Above table shows performance parameters of transformer at normal temperature. As for a 20 W 10 V transformer, in a certain temperature range, the performance of both transformers is similar, from the perspective of temperature rise, its temperature rise is not high, and they can
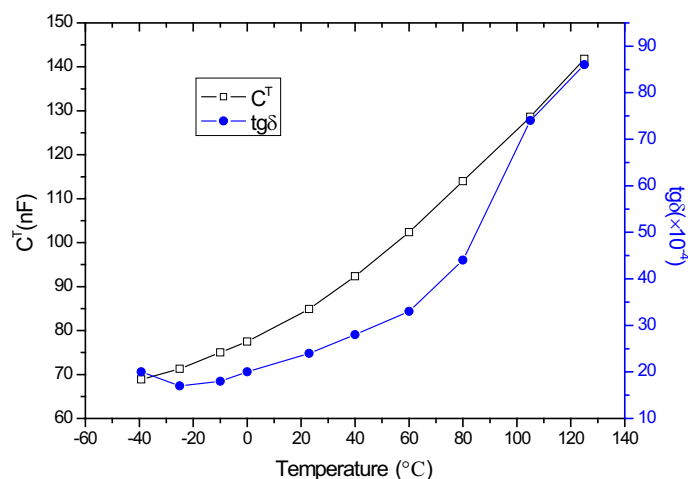
Figure 3: Dependence of capacitance, dielectric loss of bonding structure transformers on temperatures.
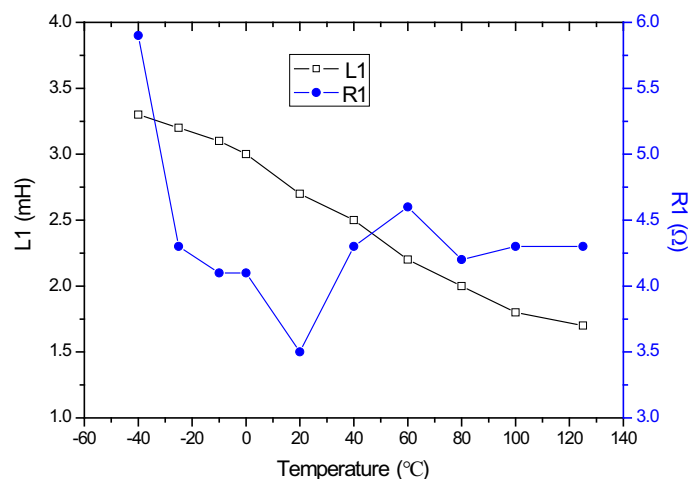
Figure 4: Dependence of $L1$, $R1$ of bonding structure transformers on temperatures.

be used normally. As we know, the transformer output voltages are relative to the thickness of ceramic disc of output part, generally speaking, the voltage increases with the thickness of disc. For both 20 W 20 V and 20 W 28 V transformers, the temperature rise of transformers with different structures change, the temperature rise of a new type ceramic monolith structure transformer with higher-thickness ceramic pieces is much higher than that of the transformer with bonding structure. The reason for that is the temperature rise is relative to higher-thickness of the single-layer of piezoelectric stack, lower density ceramics in production line due to cast and defects. With improved monolithic production processes, the problem will be resolved. We know that any kind of production methods has its limitations and advantages; monolithic cast technology method is very suitable for the production of thin disc. The input part of above-mentioned 20 W 7 V transformer has only 0.16 mm-thickness of each single-layer ceramic, if the transformer is made using bonding structure, production costs and control difficulty will be greatly enhanced, because it is too thin to handle by hand or machine during production process. Instead, if the transformer is made using new composite structures, the production process would be very simple and easy to be controlled.

Table 2 shows input/output isolation strength and leakage flow of the transformers with different structures, disadvantage of traditional monolithic structure transformer have been removed from the new composite structure transformer, which can be up to the isolation level of transformers with bonding structures.

3.3. Performance of a Brand-new Piezoelectric Transformer

From above analysis we can see, within a certain temperature range, high performance piezoelectric transformers with low input and output voltage requirements can be supplied by using new composite structures. Fig. 5 shows a new type composite structure transformer, its external diameter

Table 2.

Transformer	Input	Output	Isolation layer	Transformer Component mount structure
New composite structure	Single layer ceramic disc	monolithic piezoelectric ceramic stack	Glass pieces	bonding
Bonding structure	Single layer ceramic disc	piezoelectric ceramic stack by bonding	Glass pieces	bonding

Table 3.

Transformer structure	Num	f (kHz)	V_{in} (V_{RMS})	V_{out} (V_{RMS})	R_L (ohm)	η (%)	$\Delta T(^\circ C)$	Disc thickness t (mm)	Working temperature range($^\circ C$)
New composite structure	1	91	54.8	10	5.1	94.6	12	0.23	$-25 \sim 80$
		92	60.46	10	5.1	96.0			
		93	67.87	10	5.1	97.4	11		
		94	76.4	10	5.1	94.9			
	2	90	55.32	20	20.1	93.1		0.48	
		91	64.4	20	20.1	94.4	14		
		92	74.11	20	20.1	93.9			
		93	84.77	20	20.1	93.2	15		
	3	90	55.28	28	39.8	92.3		0.7	
		91	64.95	28	39.8	91.7			
		92	74.27	28	39.8	90.6	16		
		93	84	28	39.8	89.2			
	4	90	67.37	7	2.55	93.5	8	0.16	
		91	69.35	7	2.55	95.8			
		92	73.8	7	2.55	98.6	7.5		
		93	81.1	7	2.55	97.8			
Bonding structure	5	88	61.25	20	19.9	96.1		0.48	$-40 \sim 125$
		89	65	20	19.9	97.8	8.5		
		90	69.71	20	19.9	98.2			
	6	88	58.9	10	5	97.2	8	0.23	
		89	62.3	10	5	98.5			
		90	66.7	10	5	98.1			
	7	87	60.1	28	39.3	97.3	8.7	0.7	
		88	63.1	28	39.3	98.4			
		89	67.6	28	39.3	98.2	7		

Table 4.

transformer structure	input/output isolation strength (V/min)	leakage flow (μA)
Monolithic structure	1000	2000
new composite structure	3700	¡20
bonding structures	3700	¡20

is 13 mm, the overall thickness is 5 mm, output power is 10 W, and its electrical properties at room temperature are set in Table 5:

Table 5.

f (kHz)	V_{in} (V_{RMS})	I_{in} (A)	V_{out} (V_{RMS})	R_L (ohm)	$\eta(\%)$	$\Delta T(^\circ C)$
159.5	10.4	1.46	12	14.4	96.9	
161.5	10.11	1.34	12	14.4	97.6	
165	10.32	1.21	12	14.4	97.3	10.5
168	10.81	1.15	12	14.4	98.7	10.5

Figure 5: photograph of the piezoelectric transformer with a composite structure.

4. CONCLUSION

1. Based on the monolithic process, which is mature currently and can be used for large-scale production, when the temperature is above 80°C the performance of new transformers with composite structure becomes worse, which is relative to ceramic materials and monolith technology.

2. New type transformers with composite structures can work normally at -25°C $\sim 80^\circ$C, which is similar with the transformers with bonding structures, and can also achieve the same input/output isolation level with the bonding structures transformers.

3. When requested input/output voltage is low and the application temperature range is small, plus isolation intensity is great, the new composite structure transformers have the following main advantages over other transformers with different structure: a simpler structure, easier mass production process, and lower cost. This kind of transformers will have very high practical value.

REFERENCES

1. Rosen, C. A., "Ceramic transformers and filters," *Proc. Electronic Comp. Symp.*, 1956.
2. Uchino, K., B. Koc, et al., "Piezoelectric transformers — New perspective," *Ferroelectrics*, Vol. 263, 91–100, 2001.
3. Horsley, E. L., M. P. Foster, and D. A. Stone, "State-of-the-art piezoelectric transformer technology," *2007 European Conference on Power Electronics and Applications*, 1–10, Sept. 2–5, 2007.

Heavy Particle Collection by Ultrasonic Actuator

Junhui Hu, **Yanyan Liu**, **Tzehau Lam**, and **Huizhong Xu**

School of Electrical & Electronic Engineering, Nanyang Technological University

639798, Singapore

Abstract— This paper presents a new method to collect heavy particles by the ultrasonic actuator with two tapered metal strips. Heavy particles, such as medicine pills, can be trapped and transported in air by the actuator. We define the particle with a mass larger than 10 milligrams as heavy particle. A physical model is developed to explain the trapping mechanism. Effects of driving frequency, input voltage, particle size and weight, and structure of the actuator on the trapping capability are experimentally investigated.

1. INTRODUCTION

Ultrasonic manipulation of small particles, such as trapping, collection and transportation, has potential applications in bio-engineering, pharmaceutical industry, chemical engineering, material engineering, etc [1–4]. So far, only the trapping of light particles (mass/particle < 10 milli-gram) has been developed [5–8]. Therefore it is essential to seek a method to trap heavy particles. Here, we define particle with a mass larger than 10 milli-grams as heavy particle.

In this work, a new method of collecting heavy particles by ultrasonic actuator is proposed and developed. Heavy particles such as medicine pills, are able to be collected and transported in air by the actuator. To clarify the mechanism of collection, theoretical analyses are conducted. Effect of driving voltage and frequency, particle shape and weight, and structure of the actuator on the trapping capability are experimentally investigated.

2. STRUCTURE AND PHENOMENA

The actuator proposed for trapping heavy particles is shown in Fig. 1. Two identical L-shaped tapered metal strips with the shape and size shown in Figs. 1 (a) and (b) are clamped to a Langevin transducer shown in Fig. 1(c). The L-shape tapered metal strips are made of aluminum. Each L-shaped metal strip consists of a rectangular metal plate and a tapered metal strip. The rectangular metal plate has a size of $40\,\text{mm} \times 45\,\text{mm} \times 3\,\text{mm}$ with a $10\,\text{mm}$ diameter hole at its center. The metal strip with a length of $90\,\text{mm}$, width of $22.5\,\text{mm}$ and thickness of $3\,\text{mm}$, tapers off from the upper end to the lower end. The two identical L-shaped metal strips are stacked side by side, and fastened onto the Langevin transducer by M10 bolt. In this way, an air gap is formed between the two tapered metal strips. The Langevin transducer, consisting of 2 piezoelectric rings with $34\,\text{mm}$ outer diameter, is $79.5\,\text{mm}$ long, and has a resonance frequency of $25.3\,\text{kHz}$. When an AC voltage with frequency close to the resonance frequency of the ultrasonic actuator is applied to the actuator, a flexural vibration may be excited in the tapered metal plates.
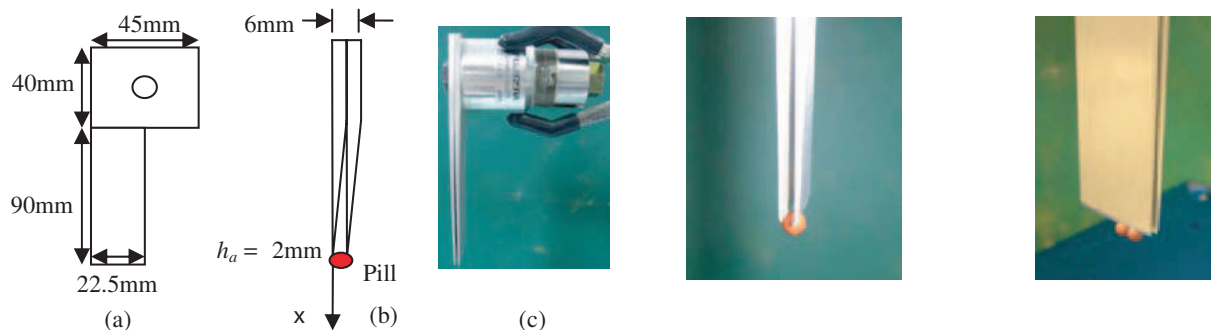
Figure 1: Structure and size of the actuator with two tapered metal strips.

Figure 2: Photos of trapped particles at the end of metal strips.

In the experiment, the two tapered metal strips in vibration were inserted into a collection of particles, and then lifted out. It was observed that particles were trapped to the sharp edges of the metal strips, as shown in Fig. 2. The number of particles trapped to the metal strips was counted

to express the trapping capability. It was found that heavy particles, such as medicine pills, could be trapped at the end of the metal plates in air successfully. By moving the actuator, these trapped particles on the metal strips could be transported from one location to another. The particles used in the experiments were red pills, brown pills, rectangular pills, circular pills, and cube pills, as shown in Fig. 3. The mass and size of them are shown in Table 1.

Table 1: Photos and sizes of the medicine pills.

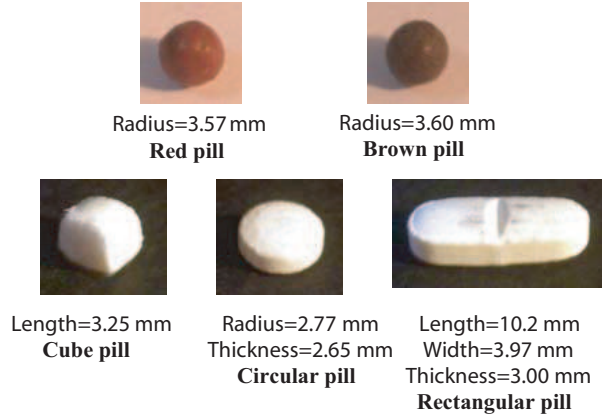| Particle Type	Mass (g)	Volume (cm^3)	Density (g/cm^3)
Red Pill	0.0259	0.1905	0.136
Brown Pill	0.0359	0.1954	0.168
Cube Pill	0.0350	0.0343	1.019
Circular Pill	0.0690	0.0639	1.080
Rectangular Pill	0.1196	0.1215	0.984

Figure 3: Photos and sizes of the medicine pills.
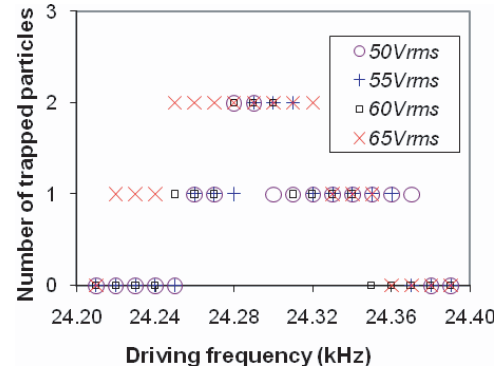
Figure 4: Relationship between number of trapped particles and driving frequency under different input voltages in air.

3. THEORETICAL ANALYSIS AND MECHANISM

When the metal strips are in ultrasonic vibration, there is a standing wave sound field between the two strips. Near the end of the tapered metal strips, the leaking sound field may have a large spatial gradient, which may generate a large enough acoustic radiation force to suck the pills.

Assuming the sound pressure of the traveling wave leaking from the sound field between the two strips is:

$$P = P_m e^{-\alpha x} \cos(kx - \omega t) \tag{1}$$

where α is the attenuation coefficient. In the leaking sound field, the relationship between the acoustic pressure and vibration velocity is [10]:

$$\rho_f \frac{\partial u}{\partial t} = -\frac{\partial P}{\partial x} \tag{2}$$

where ρ_f is the density of the fluid. Therefore the vibration velocity of the fluid in the leaking sound field near the metal strips is:

$$u = \frac{P_m^2 \sqrt{\alpha^2 + k^2}}{\rho_f \omega} e^{-\alpha x} \cos(kx - \omega t + \theta) \tag{3}$$

where $\theta = \tan^{-1} \frac{\alpha}{k}$. The acoustic radiation force acting on a particle in the leaking sound field is [11–14]:

$$\vec{F} = -\nabla U \tag{4}$$

where U is the time-averaged force potential of the sound field. When the wave number k and the radius of particle R satisfy $kR \leq 1$, the force potential U is:

$$U = V[-D < K_E > +(1 - \gamma) < P_E >] \tag{5}$$

where V is the volume of the particle sphere, $\langle K_E \rangle$ and $\langle P_E \rangle$ are the time-averaged kinetic and potential energy densities of the leaking sound field, respectively, D is a parameter determined by the densities of the particle sphere and fluid, and γ is the compressibility ratio between the particle sphere and fluid. D and γ can be calculated by

$$D = \frac{3(\rho_s - \rho_f)}{2\rho_s + \rho_f} \tag{6}$$

$$\gamma = \frac{\rho_f c_f^2}{\rho_s c_s^2} \tag{7}$$

where ρ_s and ρ_f are the densities of the particle sphere and fluid, respectively, and c_s and c_f are the sound speed in the particle sphere and fluid, respectively.

Therefore, the acoustic radiation force on a particle in the x-direction is:

$$\vec{F} = -\vec{i}\frac{V\alpha P_m^2 e^{-2\alpha x}}{2\rho_f}\left[\frac{D(\alpha^2 + k^2)}{\omega^2} + \frac{1 - \gamma}{c_f^2}\right] \tag{8}$$

In air, because $\rho_s \gg \rho_f$, $D \approx 1.5$, $\gamma \approx 0$. Therefore acoustic radiation force in air is simply into:

$$\vec{F} = -\vec{i}\frac{V\alpha P_m^2 e^{-2\alpha x}}{4\rho_f c_f^2} \tag{9}$$

Equation (9) shows that the force acting on a particle near the lower end of the air gap of the actuator points to the $-x$ direction, which traps particles at the end of the tapered metal plates.

4. EXPERIMENTAL RESULTS AND DISCUSSION

Trapping capability is expressed by the number of particles trapped.

Figure 4 shows the relationship between the number of trapped red pills and the driving frequency at different input voltages in air. It can be observed that the number of trapped particles reaches a maximum at a particular driving frequency or frequency range for a given voltage. This driving frequency or center of the frequency range is the resonance frequency, because at the frequency the input voltage and current are in phase and the input current is maximum.
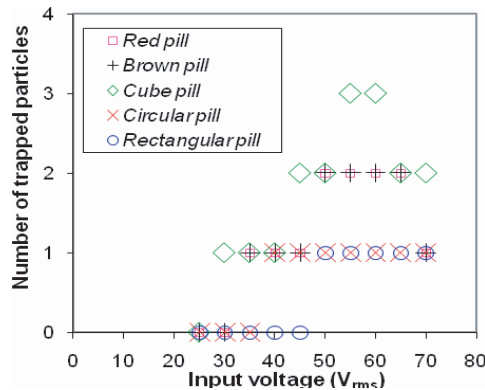
Figure 5: Relationship between number of trapped particles and input voltage for different particles in air.
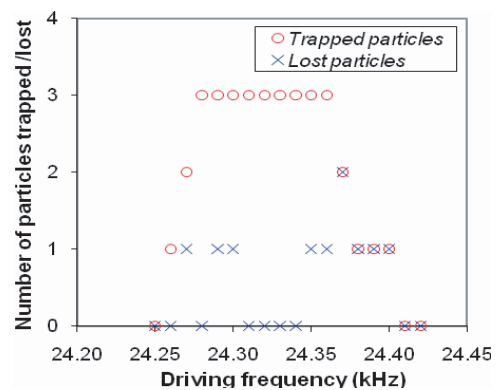
Figure 6: Relationship between number of trapped/lost particles and driving frequency in air.

Figure 5 illustrates the dependence of the number of trapped particles at resonance on the input voltage in air. It is seen that the maximum number of trapped particles at resonance increases as driving voltage increases. Also it is observed that it is easiest to trap cube pills among the pills

used in the experiment. From Table 1, it is known that cube pills have similar mass per particle with brown pills, but a much larger density than brown pills. If the shape of trapped particles had little effect on the trapping capability, the trapping capability for brown pills would be stronger than that for cube pills. So the experimental phenomenon indicates that the shape difference of the pills may have substantial effect on the trapping capability. For the circular and rectangular pills, although it is harder to be collected by the actuator because of a larger mass per particle, one rectangular (120 milli-gram/particle) or circular pill (69 milli-gram/particle) can still be sucked when the driving voltage is larger than 50 V_{rms}.

The trapped particles can be transported from one location to another in air by moving the actuator. Fig. 6 shows the number of trapped cube pills before transportation, and the number of lost cube pills during the transportation versus operating frequency at an average transportation speed of 10.7 cm/s, transportation distance of 60 cm, and input voltage of 55 V_{rms} in air. It seen that there exists a frequency range near the resonance in which no particle is lost during the transportation. Hence particle loss can be avoided during the transportation if a strong acoustic sound field is used.

5. SUMMARY

An ultrasonic actuator which is capable of trapping the medicine pills with a mass up to 120 milli-gram/particle has been developed. The trapping of pills may be caused by the leakage of the standing wave sound field between the two metal plates. The trapped particles can be transported at a speed of 10.7 cm/s from one location to another when the actuator is moved.

REFERENCES

1. Coakley, W. T., D. W. Bardsley, and M. A. Grundly, "Cell manipulation in ultrasonic standing wave fields," *J. Chem. Tech. Biotechnol.*, Vol. 44, 42–43, 1989.
2. Yasuda, K., S. Umemura, and K. Takada, "Concentration and fractionation of small particles in liquid by ultrasound," *Jpn. J. Appl. Phys. (Part I)*, Vol. 34, 2715–2720, 1995.
3. Ohtani, K., Y. Koike, S. Ueha, and H. Yokoi, "Novel wedge-shaped doubly inclined chamber for the flow-through separation of suspended particles," *Ultrasonics*, Vol. 38, 647–649, 2000.
4. Takeuchi, M. and K. Yamanouchi, "Ultrasonic micromanipulation of small particles in liquid," *Jpn. J. Appl. Phys.*, Vol. 33, 3045–3047, 1994.
5. Pui, P. W. S., F. Trampler, S. A. Sonderhoff, M. Groschl, G. Kilburn, and J. M. Piret, "Batch and semicontinuous aggregation and sedimentation of hybridoma cells by acoustic resonance fields," *Biotechnol. Progr.*, Vol. 11, 146–152, 1995.
6. Bohm, H., L. G. Briarty, K. C. Lowe, J. B. Power, E. Benes, and M. R. Davey, "Quantification of a novel h-shaped ultrasonic resonator for separation of biomaterials under terrestrial gravity and microgravity conditions," *Biotechnology and Bioengineering*, Vol. 82, No. 1, 74–85, 2002.
7. Doblhoff-Dier, O., T. Gaida, H. Katinger, W. Burger, M. Groschl, and E. Benes, "A novel ultrasonic resonance device for the retention of animal cells," *Biotechnol. Progr.*, Vol. 10, 428–432, 1994.
8. Hu, J. H., "Ultrasonic collection of small particles by tapered metal strip," *IEEE Trans. Ultrasonics, Ferroelectr. Freq. Control*, Vol. 53, No. 3, 571–578, 2006.
9. Morse, P. M. and K. U. Ingard, *Theoretical Acoustics*, McGraw-Hill, Vol. 243, 279–282, 1968.
10. Morse, P. M. and K. U. Ingard, *Theoretical Acoustics*, McGraw-Hill, Vol. 243, 358–359, 1968.
11. Gor'kov, L. P., "On the forces on a small particle in an acoustical field in an ideal fluid," *Sov. Phys.-Dokl.*, Vol. 6, 773–775, 1962.
12. Nyborg, W. L., "Radiation pressure on a small rigid sphere," *J. Acoust. Soc. Amer.*, Vol. 42, 947–952, 1967.
13. Hasegawa, T. and K. Yosioka, "Acoustic-radiation force on a solid elastic sphere," *J. Acoust. Soc. Amer.*, Vol. 46, 1139–1143, 1969.
14. Barmatz, M. and P. Collas, "Acoustic radiation potential on a sphere in plane, cylindrical, and spherical standing wave fields," *J. Acoust. Soc. Amer.*, Vol. 77, 928–945, 1985.

Modeling of the Potential Profile for the Annealed Polycrystalline PbSe Film

Gang Bi[1, 2], **Fanghai Zhao**[1], **Jiangang Ma**[1],
Shaibal Mukherjee[1], **Donghui Li**[1], **and Zhisheng Shi**[1]

[1]School of Electrical and Computer Engineering
University of Oklahoma, Norman, Oklahoma 73019, USA
[2]School of Information & Electrical Engineering
City College, Zhejiang University, Hangzhou 310015, China

Abstract— A new model for the mechanism of photoconductivity in annealed polycrystalline PbSe film is presented. The combined mechanism with respect to double heterojunction due to oxidation layer, dopant segregation and carrier trapping at grain-boundary is proposed. This letter focuses on characterizing the potential profile, which is extremely important from the viewpoint of carrier transport phenomena. A potential profile adjacent to the boundaries was calculated, and the effect of biased voltage was in detail discussed, which shows that the mechanism of photoconductivity of annealed polycrystalline PbSe film depends on properties of the grain boundaries.

1. INTRODUCTION

Narrow gap semiconductors such as lead salt materials are widely used to fabricate midinfrared optoelectronic devices [1, 2]. Thereinto, polycrystalline PbSe films grown on Si or SiO_2/Si substrates have attracted great interest mainly due to midinfrared imaging applications in the 3–5 and 8–12 μm atmospheric windows. Despite the continuous investigation of their properties, many aspects of the mechanism of photoconductivity in such films have not yet been completely resolved. Recently, we reported the photoluminescence intensity increased by more than two orders of magnitude at 4.5 μm after annealing PbSe in an O_2 atmosphere at 350°C [3]. The results show that the optical and electrical properties depend on the postgrowth processing significantly.

Modeling the mechanism of carrier transport for polycrystalline PbSe film such as their dependence on dopant concentration, type of dopant, and high-temperature processing becomes very important for the proper design of the devices. Most of the polycrystalline semiconductor devices are annealed structures with a complex potential relief, with which in such devices assigns its operational characteristics. Especially, potential profile is extremely important from the viewpoint of carrier transport phenomena. Therefore, the design of a potential relief of semiconductor devices is a topical question for engineering of new types and classes of devices.

Enormous analytical and numerical calculations [4, 5] for the electrical properties of a single Grain Boundary GB have been performed on polycrystalline based electrical conduction GB modeling. One of the big contrasts of polycrystalline PbSe compared with a numerical existing polycrystalline model is that much thicker oxide layer $PbSeO_3$ [3, 6] induces heavy overlap of complex barriers, as shown in Figure 1. Therefore, it is reasonable here to assume two heterojunction between n-type PbSe grain and P-type $PbSeO_3$ oxide layer both sides of GB, the defects in the crystallite and the $PbSeO_3$ insulator interface are assumed to be segregated to the GB. A wide range of continuous defects distribute in the GB with a peak density at the mid gap. Here, our discussion will focus on the developed potential profile in the active channel layer and its effect on the properties of PbSe optoelectronic devices, which will reflect the real microscopic view of PbSe polycrystalline thin film for photoconductivity actions.

We are also able to adequately estimate the unknown trap state densities inside the GBs comparing with the experimental values of field effect mobility μ, F_E and grain size L_g using this model.

2. SIMULATION METHODOLOGY AND MATERIAL PARAMETERS

Polycrystalline-silicon films were deposited by MBE at 250°C. The annealed condition is at 380°C for 20 hours. The double heterojunction due to the diffusion of O_2 at the grain boundary is formed, where n-type region in the semiconductor grain is packed by the p-type oxide at the grain boundary.

As an example we compute the potential relief for $PbSeO_3$/PbSe structure which is widely used in photonics and optoelectronics. The heterostructure is formed by annealing the PbSe.
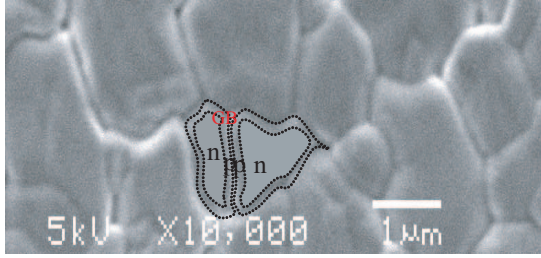
Figure 1: SEM image of a polycrystalline PbSe material at 10^4x magnification. In high quality material, grains extend throughout the film thickness.
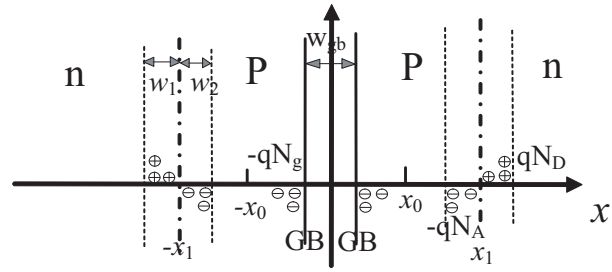

Figure 2: Charge depleted region.

Computation of potential profiles for bulk regions is based on analytical solution for Poisson's equation. The linear approximation of the potential relief is used within quantum well layers. Under simulation of biased potential profiles we also used analytical solution for Poisson's equation taking the voltage distribution into account.

If we know distribution of the voltage over the heterostructure, the Poisson's equation for single heterojunction can be solved. In compliance with various combinations of single heterojunctions solutions to the Poisson equation may be expressed as

$$\frac{\partial^2 \phi}{\partial x^2} = -\frac{q}{\varepsilon}\left(p(x) - n(x) + N_{D+}(x) - N_{A-}(x)\right) \tag{1}$$

where the concentrations of the free carriers n, p and ionized dopants $N_{D+}(x)$, $N_{A-}(x)$ are described by Fermi statistics:

$$n(x) = N_c F_{1/2}\left[(E_F - E_c + e\phi(x))/kT\right], \quad p(x) = N_v F_{1/2}\left[(E_v - E_F - e\phi(x))/kT\right] \tag{2a}$$

$$N_{D+}(x) = N_D(x) f\left[(E_F - E_D + e\phi)/kT\right], \quad N_{A-}(x) = N_A(x) f\left[(E_A - E_F - e\phi)/kT\right] \tag{2b}$$

where N_c, N_v are the effective density of states for electrons and holes, $N_D(x)$, $N_A(x)$ are the doping profiles; E_F is the common Fermi level; E_c is the conducting band edge, E_D, E_A are the donor and acceptor levels, respectively. Zero for the energy is set at the valence band edge. $f[]$ and $F_{1/2}[]$ are the Fermi function and Fermi-Dirac integral, respectively, T is the temperature and k is Boltzmann constant. Fermi level E_F is found from the electroneutrality of the whole sample. Fermi level E_F is found from the electro-neutrality of the whole sample

$$\int_V \left[p(x) - n(x) + N_{D+}(x) - N_{A-}(x)\right] = 0 \tag{3}$$

Substituting (2) into (1) and (3) the system of two equations is obtained with the unknown $\phi(x)$ and E_F. We imply Dirichlet zero boundary conditions for the potential at two opposite sides of the rectangular sample where the metallic contacts to the sample are assumed and Neuman boundary conditions along two other sides. The entirely area is separated into three segment, 1) nP heterojunction ($x > x_0$); 2) trapping segment ($-x_0 < x < x_0$); 3) Pn heterojunction ($x > x_0$). The boundary condition between segments should be piecewise continuity. Using conventional second order finite-difference scheme the system (1) and (3) is reduced to the system of nonlinear algebraic equations for digital point. The nonlinear system obtained is solved by means of Newton method. At each step of Newton iteration process we use advanced direct method for solving unsymmetrical sparse linear systems. This enabled us to use the grids having as much as 87 nodes and overcome numerical difficulties caused by very sharp concentration profiles being an inherent specific of the problem studied.

Material constants for n-type PbSe have been collected as follows: Bandgap $E_{g1} = 0.27\,\text{eV}$, Electron affinity $\chi_1 = 4.21\,\text{eV}$, Effective mass of electron in the conduction band $m_{e1}^* = 0.1994 m_0$, Effective mass of hole in the valence band $m_{h1}^* = 0.1658 m_0$, the charge carrier concentration $N_d = 1 \times 10^{17} - 5 \times 10^{17}\,\text{cm}^{-3}$, the carrier mobility $\mu_1 = 14000 - 20000\,\text{cm}^2/(\text{Vs})$, Dielectric constant $\varepsilon_1 = 21.06$, Work function $\Phi_1 = 4.26$. These for p-type PbSeO$_3$ have also been collected or calculated as follow: Bandgap $E_{g2} = 3.17\,\text{eV}$, Electron affinity $\chi_2 = 3.65\,\text{eV}$, Effective mass

of electron in the conduction band $m_{e2}^* = 0.20m_0$, Effective mass of hole in the valence band $m_{h2}^* = 0.18m_0$, charge carrier concentration $N_A = 2 \times 10^{18} - 8 \times 10^{18} \, \text{cm}^{-3}$, and the carrier mobility $\mu = 18000 - 22000 \, \text{cm}^2/(\text{Vs})$, dielectric constant $\varepsilon_2 = 4.58$, work function $\Phi_2 = 5.76$.

3. SIMULATION RESULTS

3.1. Potential Profile without Bias Voltage

In the section, we will discuss some features of the dependence of potential profiles ϕ on parameter nP heterojunction position x_1, dopant density and several trap densities at GB. In actually sample, layer of oxidation should thicken and dopant density should increase with annealing temperature and time increase in a specific range according to the behaviour of the polycrystalline annealing mechanism. In Figure 3, a single grain boundary structure of PbSe, applied with materials constants taken from above section, is modeled and treated as an nP-GB-Pn structure. In light of the varied annealing condition. Figure 3 points up the variation of ϕ with x for three heterojunction position $x_1 = 0.5 \times 10^{-4}$, 0.6×10^{-4} and 0.7×10^{-4} mm corresponding weak anneal, medial anneal and strong anneal, respectively. It is reasonable that the potential barrier V_b and the trapping depletion width W_g should increase with the x_1 increase, and vice versa. Figure 4 shows the corresponding energy
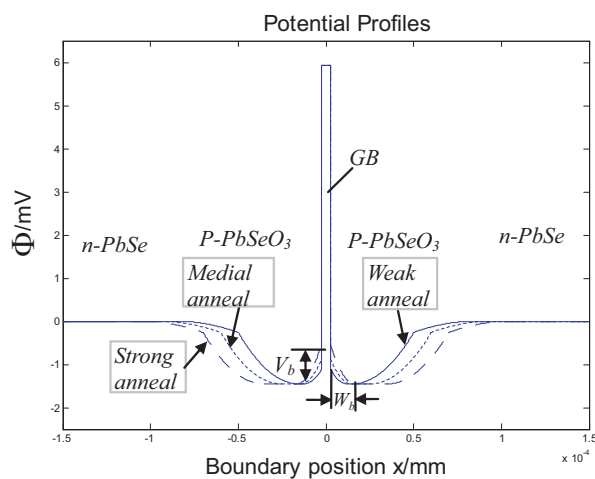

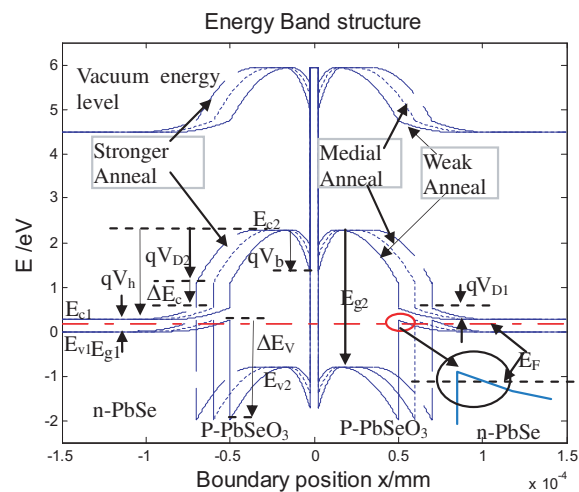Figure 3: Potential profile without bias voltage.

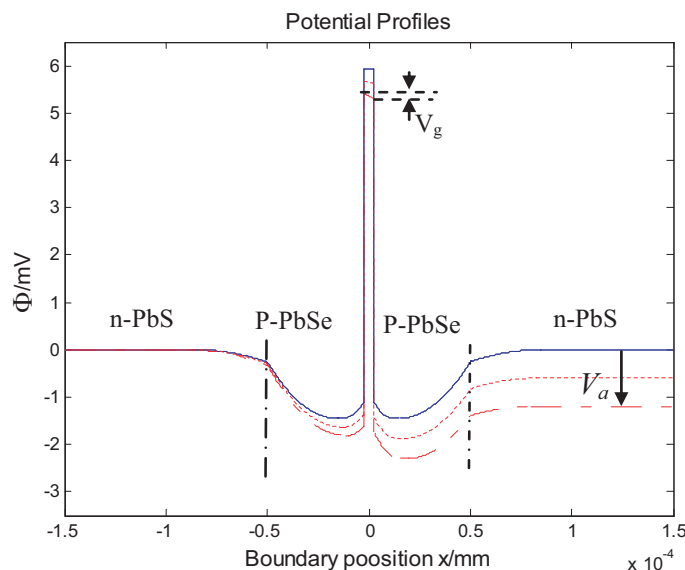Figure 4: Energy band diagram without bias voltage.

Figure 5: Potential profile with a bias voltage V_0.

band for different heterojunction position x_1. The V_b and W_g will tend to zero when x_1 decrease to a critical thickness, which is analogous to the situation with only carrier trapping model [7]. All energy levels defined in all Figures can be graphically represented by an energy level diagram including a GB energy band bending profile as also illustrated in Figure 4 and are referenced to the valence band edge $Ev1 = 0$. It's worth noting that an inversion layer will be form in the heterojunction area, as shown in the circle of the Figure 4, due to the energy band bending the narrow semiconductor compound such that the valence band edge is above the Fermi level (E_F). It can be seen from the Figure 4 that the barrier at GB is very sensitive to variation of the annealing condition which opens the possibility to influence on the electrical properties of the whole material.

3.2. Potential Profile without Bias Voltage

Let us consider V_a be the voltage drop across the complete grain boundary region. The voltage will be dropped across the grain boundary barrier region. This voltage will be dropped across the grain boundary barrier and the two depletion regions on either side of the grain boundary.

Figure 5 shows the potential profiles for different bias voltage the GB dopant (the bias voltage $0\,\mathrm{mV}$, $0.6\,\mathrm{mV}$, $1.2\,\mathrm{mV}$) obtained by the numerical simulation.

4. CONCLUSIONS

The potential profiles between polycrystalline grains are greatly influenced by the grain-boundary (GB), doping concentration and temperature, grain-boundary interface states density. In this paper, a novel model for computing the potential profile in polycrystalline PbSe film is developed. The model is based on the mechanism of double heterojunction due to O_2 diffusing into grain, grain-boundary trapping, and thermionic emission as well as tunnel transportation through the inter-grain energy barriers at grain boundary. Figure 1 shows SEM image of the polycrystalline PbSe prepared in our lab to be used for the calculation of potential profile.

REFERENCES

1. Springholz, G., Z. Shi, and H. Zogg, *Thin Films: Hetero Epitaxial: Systems*, edited by W. K. Liu and M. B. Santos, World Scientific, Singapore, 1999.
2. Khokhlov, D., *Lead Chalcogenides Physics and Applications*, Taylor and Francis, New York, 2003.
3. Zhao, F., S. Mukherjee, J. Ma, et al., "Influence of oxygen passivation on optical properties of PbSe thin films," *Applied Physics Letters*, Vol. 92, 211110, 2008.
4. Rozhansky, I. V., D. A. Zakheim, et al., "Modeling of the electrical properties of polycrystalline ceramic semiconductors with submicron grains," *Microelectronic Engineering*, Vol. 81, 494–502, 2005.
5. Yamaguchi, K., "Modeling and characterization of polycrystalline-silicon thin-film transistors with a channel-length comparable to a grain size," *J. Applied Physics*, Vol. 89, 590–595, 2001.
6. Tomaev, V. V., V. P. Miroshkin, L. N. Gar'kin, et al., "Dielectric properties and phase transition in the PbSe+PbSeO$_3$ composite material," *Glass Physics and Chemistry*, Vol. 31, 812–819, 2005.
7. Hossain, F. M., J. Nishi, S. Takagi, et al., "Modeling and simulation of polycrystalline ZnO thin-film transistors," *J. Applied Physics*, Vol. 94, 7768–7777, 2003.

Leaky Coplanar Waveguide Antenna with Tunable Beamwidth and Radiation Angle Using Composite Right/Left-handed Materials

Abdelaziz Hamdi[1], **Ammar B. Kouki**[2], **and Abdelaziz Samet**[3]

[1]Ecole National d'Ingénieurs de Sousse, Technopole de Sousse, Sahloul, Tunisia
[2]École de Technologie Supérieure
1100, rue Notre-Dame O. Montréal (Qc) H3C 1K3, Canada
[3]Ecole Polytechnique de Tunisie, B. P. 743, La Marsa, Tunis 2070, Tunisia

Abstract— A new field of physics has appeared with the emergence of materials known as "Left handed materials" (LHM) or "metamaterials". These materials show very particular characteristics. Their index of refraction has a negative value, which results in the reversal of Snell's law. Whereas, in traditional material the Poynting vector S always forms a right-handed triplet with E and H ($S = E \wedge H$). In the left handed media, the Poynting vector S and the wave vector K are in opposite directions. Thus, the wave moves in the direction opposite to the direction of the energy flow: phase speed and group speed are anti-parallel. Therefore, a left-handed media is artificial and does not exist in nature. Indeed, when these materials are inserted into a guided wave device, one obtains the backward-wave effect. The goal of this work is to study more in details this physical phenomenon. To undertake this study, this paper presents also the design of a 10 GHz beam-scanning CPW-Antenna fabricated on metamaterial support.

1. INTRODUCTION

Previously, it was proposed that materials with simultaneously-negative permittivity and permeability are physically permissible and possess a negative index of refraction [1]. Left-handed media (LHM) were stated because the vectors E, H and K would form a left-handed triplet instead of a right-handed triplet as is the case in conventional right-handed media (RHM). Although it has been known for some time that arrays of thin metallic wires, by virtue of their collective plasma-like behavior, can produce an effectively negative dielectric permittivity, how to produce a simultaneously-negative permittivity and permeability has not been clear. The recent development of the split-ring resonator (SRR) by Pendry et al. [2] was successful in this effort. Subsequently, three-dimensional (3-D) electromagnetic artificial dielectrics (metamaterials), consisting of an array of resonant cells, were developed to synthesize the simultaneously- negative permittivity and permeability required to produce a negative refractive index. Indeed, it successfully demonstrated reversed refraction [3, 4]. Consequently, the structures can achieve a negative index of refraction just within a narrow bandwidth. This paper offers a fresh perspective on the operation of LHM that enables the modeling and the design of a novel backward-wave CPW-Antenna with negative refractive index. It will first present the fundamentals of LHM. Then it will also describe how to model them using infinitesimal composite RHM/LHM unit cell (CRLH UC). Finally, we will carry out a feasibility study of a beam-scanning antenna on coplanar structure. The results show how the antenna radiates in backfire at low frequencies $F_L < F_o$, while in the high frequencies $F_o < F_R$, the antenna radiates in endfire. Whereas at the center frequency F_o, the structure radiates in broadside. Through this application, the metamaterial behavior has been clearly defined. All these results have been obtained with the Method of Moments used by ADS-Momentum.

2. COMPOSITE RIGHT/LEFT HANDED MEDIA UNIT CELL APPROACH

The unit-cell of the artificial lumped element (LE) and CPW topology implementation of the right/left handed transmission lines (RLH TL) are shown in this section.

2.1. Circuit Model

The ideal CRLH UC is represented in Figure 1. It consists of the combination of right-handed series inductance L_R and shunt capacitance C_R with left-handed series capacitance C_L and shunt inductance L_L.

The unit cell topology shown in Figure 1(b) is the most relevant model for practical applications, where the resonant serial branch $C_L L_R$ represents a series capacitor with parasitic shunt inductance, while the shunt antiresonant branch $L_L C_R$ represents a shorted shunt inductor. However, the model of Figure 1(c), shown the series connection of RHM and LHM sections. Naturally, from

an impedance perspective, imposing a negative L and C essentially exchanges their inductive and capacitive roles so that the series inductor becomes a series capacitor, and the shunt capacitor becomes a shunt inductor [5]. The emerging dual structure is recognized as having the topology of a high-pass filter network.
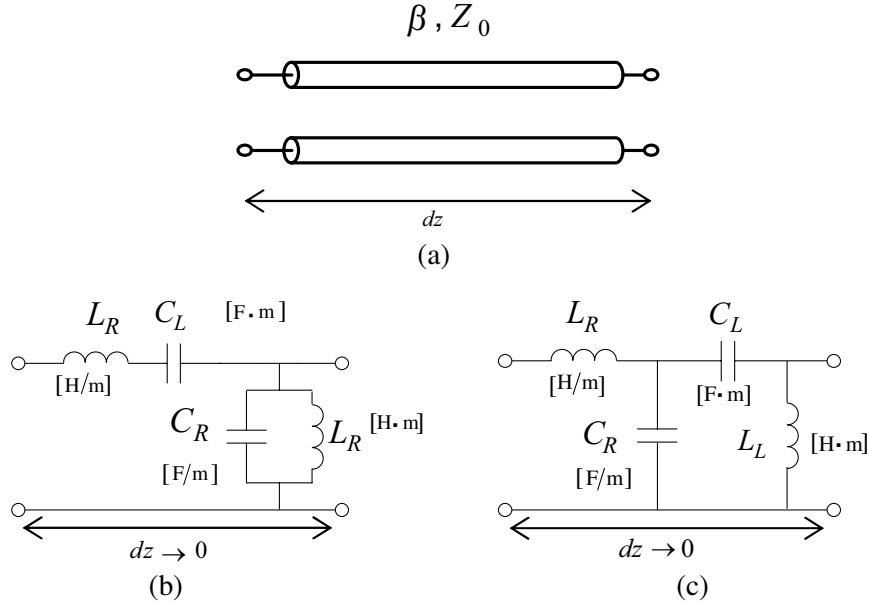

Figure 1: CRLH UC. (a) Transmission line with physique parameters, (b) infinitesimal circuit model, (c) infinitesimal circuit model in the balanced case ($L_RC_L = L_LC_R$).

For simplicity, we consider here only the lossless case, which can be straightforwardly extended to lossy case, we consider also the balanced case that defined by $L_RC_L = L_LC_R$ with the advantage of providing a more direct insight into the physical characteristics of the line [6]. The propagation constant γ or phase constant β of the unit cell of the Figure 1(a) can be obtained as

$$\gamma = j\beta = \sqrt{ZY} \tag{1}$$

where

$$Z = j\omega L_R + \frac{1}{j\omega C_L} \quad Y = j\omega C_R + \frac{1}{j\omega L_L} \tag{2}$$

which gives

$$\beta = s(\omega)\sqrt{\omega^2 L_R C_R + \frac{1}{\omega^2 L_L C_L} - \left(\frac{L_R}{L_L} + \frac{C_R}{C_L}\right)} \tag{3}$$

where

$$s(\omega) = \begin{cases} -1 & \text{if} \quad \omega < \omega_L = \min\left(\frac{1}{\sqrt{L_R C_L}}, \frac{1}{\sqrt{L_L C_R}}\right) \\ +1 & \text{if} \quad \omega > \omega_L = \min\left(\frac{1}{\sqrt{L_R C_L}}, \frac{1}{\sqrt{L_L C_R}}\right) \end{cases}$$

From the expression of the $s(\omega)$, it can be shown that:
— first case (LHM):

$$\frac{\partial \omega}{\partial \beta} < 0 \rightarrow v_g < 0 \quad \text{with} \quad \beta > 0 \rightarrow v_p > 0$$

— second case (RHM):

$$\frac{\partial \omega}{\partial \beta} > 0 \rightarrow v_g > 0 \quad \text{with} \quad \beta > 0 \rightarrow v_p > 0$$

In the balanced case,

$$L_R C_L = L_L C_R = LC \tag{4}$$

(3) simplifies to

$$\beta = s(\omega)\sqrt{\omega^2 LC + \frac{1}{\omega^2 LC} - 2} = \omega\sqrt{LC} - \frac{1}{\omega\sqrt{LC}} \tag{5}$$

The last expression immediately appears to be identical, under condition (4), to the propagation constant β_s of the model of Figure 1(c), which can be written as

$$\beta = \beta_R + \beta_L = \omega\sqrt{L_R C_R} - \frac{1}{\omega\sqrt{L_L C_L}} \tag{6}$$

The balanced condition (4) for the model of Figure 1(b) corresponds to the matched condition to extract the characteristic impedance Z_0 for the model of Figure 1(c).

$$\sqrt{\frac{L_R}{C_R}} = \sqrt{\frac{L_L}{C_L}} = Z_0 \tag{7}$$

Equation (6) clearly shows the composite nature of the line of Figure 1(a), characterized by negative left handed (LH) β a low frequencies. In the limits $\omega \to 0$ and $\omega \to \infty$, b tends to the purely LH β_L and to the purely RH dispersion β_R, respectively. The transition frequency [6] between the LHM and RHM ranges is obtained at $\beta = 0$ and is given by

$$\omega_0 = \frac{1}{\sqrt[4]{L_R C_R L_L C_L}} \xrightarrow{balanced \; case} \omega_0 = \frac{1}{\sqrt{LC}} \tag{8}$$

Form (6), we obtained the guided wavelength, phase velocity, and group velocity as

$$\lambda_g = \frac{2\pi}{\omega\sqrt{L_R C_R} - \frac{1}{\omega\sqrt{L_L C_L}}} \tag{9}$$

where $\lambda_g(\omega) = \infty$

$$v_p = \frac{\omega}{\omega\sqrt{L_R C_R} - \frac{1}{\omega\sqrt{L_L C_L}}} \tag{10}$$

and

$$v_g = \frac{1}{\sqrt{L_R C_R} - \frac{1}{\omega^2\sqrt{L_L C_L}}} \tag{11}$$

Equations (10) and (11) show that v_g is always positive, and that v_p is negative from dc to ω_o and positive from ω_o to ∞ respectively. It also can be interesting to note that

$$v_g(\omega \to \infty) = \frac{1}{\sqrt{L_R C_R}} = \frac{c}{n} \tag{12}$$

where $n = \sqrt{\varepsilon_r \mu_r}$ and c represents the speed of light. Equation (12) shows that the group velocity is always smaller than c, which alleviates the apparent paradox that in a purely LHM v_g may become larger than c [6]. In fact, a purely, LHM unit cell (only C_L and L_L) is not physical and can never be realized because the parasitic effects LR and CR (host media) become dominant as frequency is increasing so that all LHM effects dispear at high frequency, as shown by (12).

In this case, the periodicity is not necessary because of the fundamental computational and fabrication convenience. One possibility consists in periodically repeating an electrically small lumped unit cell, shown in Figure 2, into artificial line, as illustrated in Figure 2.

The artificial CRLH unit cell of Figure 2 is a bandpass filter with a stopband from dc to the LH cutoff

$$fc_L = \frac{1}{4\pi\sqrt{L_L C_L}} \tag{13}$$

and a stopband from the RH cutoff

$$fc_R = \frac{2}{\pi\sqrt{L_L C_L}} \tag{14}$$

Equations (13) and (14) are exact for infinitely periodic RH and LH UCs, respectively, but provide an excellent estimate of the cutoffs for the structures including over three cells, where
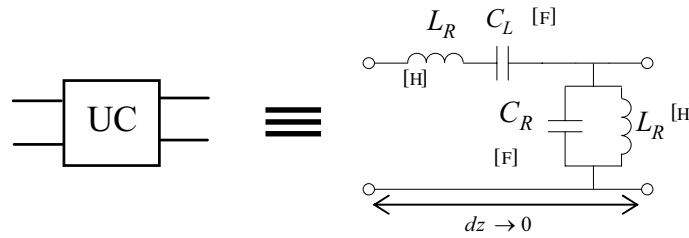
Figure 2: Practical artificial unit cell.

cutoffs become sharp enough so that they unambiguously correspond to a unique frequency. The dispersion relation of the CRLH UC of Figure 2 can be computed analytically in a conventional manner [6] by using the [ABCD] matrix formalism and Bloch-Floquet periodic boundary conditions

$$\beta = \frac{a\cos\left\{1 - \frac{1}{2}\left[\frac{1}{\omega^2 L_L C_L} + \omega^2 L_R C_R - \left(\frac{L_R}{L_L} + \frac{C_R}{C_L}\right)\right]\right\}}{l} \tag{15}$$

2.2. C_L-L_L Implementation

A layout of the C_L and L_L is shown in the Figure 3. The composite LH CPW section consists of value C_L and shunt inductors of value L_L, which are implemented by MOMENTUM. Here, the C_L is simply a gap on the center conductor of the CPW and metallic plate on opposite side of the substrate to reach the value of C_L as shown in Figure 3(a). For more compact design, the L_L consists of two meander microstrip line on each side of the CPW to keep the symmetric of the structure as shown in Figure 3(b).

(a)

(b)
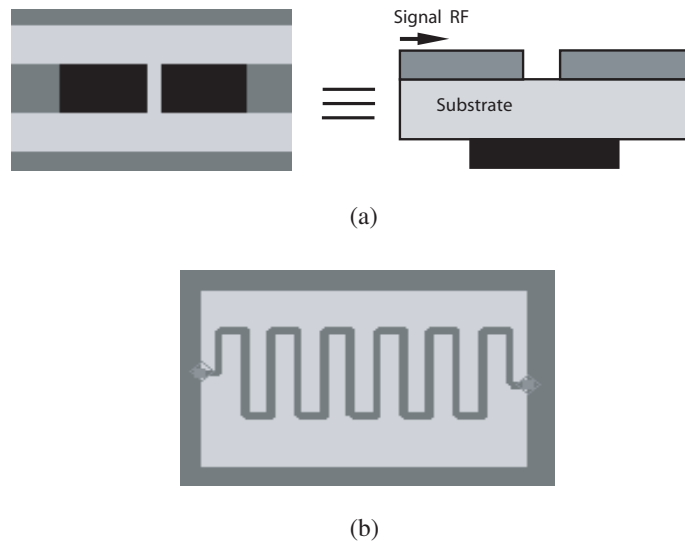
Figure 3: C_L-L_L implementation for the proposed design, (a) C_L layout, (b) L_L layout.

2.3. CPW Antenna Implementation

The CRLH UC topology shown in Figure 2 can be virtually implemented in any technology. The CRLH proposed in this paper will be based on the CPW implementation which is depicted by its unit cell in Figure 4.

The unit cell of the CRLH CPW-Antenna consists of a series capacitor of value CL and a shunt stub of a minder line inductor of value L_L shorted to the ground plane. Once these parameters are calculated, the structure will be built with localised elements and will be simulated from 1 to 20 GHz. A simulation in dispersive mode (full-wave) confirms the results obtained analytically. One finds the cut-off frequencies of the stop-band and pass-band filters. It is also noted that the propagation constant β sign changes at the transition frequency of $f_o = 10$ GHz.

3. SIMULATION RESULTS AND DISCUSSION

The parameter-extraction procedure consists of full-wave simulating or measuring separately the seriel capacitor and stub minder line-inductor of Figure 4, transforming their S-parameters into Y^{seriel} and Z^{stub} parameters, respectively, to obtain the the values of C_L and L_L. Excellent agreement can be observed, which shows that the circuit model proposed is accurate and can be potentially used in the more complicated problem of the coupler, which will be described in the following sections. It should be noted that, in practice, the UC is terminated in each side by a matched impedance of $50\,\Omega$ for symmetry and improved transmission characteristics.
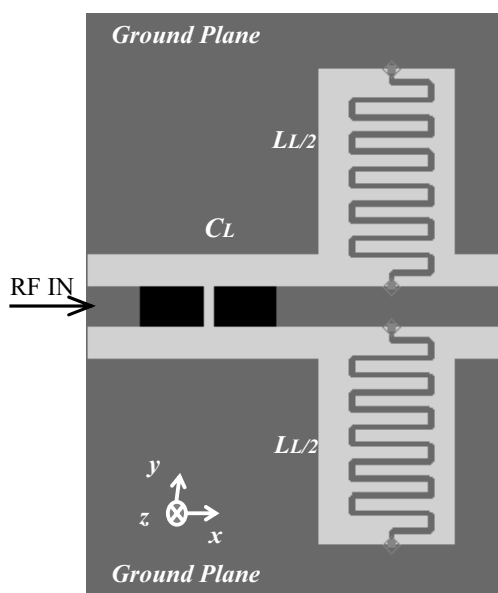
Figure 4: Layout of the unit cell of CPW-Antenna implementation on flexible substrate: Kapton, $h = 1\,\text{mil}$, $\varepsilon = 3.4@10\,\text{GHz}$.

The balanced CRLH UC dispersion diagram of Figure 5 shows how the CPW-Antenna radiates in backfire at low frequencies $7\,\text{GHz}$ "$F_L < 8\,\text{GHz}$ (region II), while in the high frequencies $8\,\text{GHz} < FR = 10\,\text{GHz}$, the antenna radiates in endfire (region III). Whereas at the center frequency $f_o = 8\,\text{GHz}$, the structure radiates in broadside, the E-plane and H-plane are illustrated in the Figure 6. Figure 6 shows the phase of the S-parameters in the CRLH CPW-Antenna, $\varphi\{S_{21}\} = 0$ at $\omega \to \infty$ (open circuit), and phase progressively accumulates as frequency decreases so that eventually $\varphi\{S_{21}\} = 0$ at $\omega \to 0$.
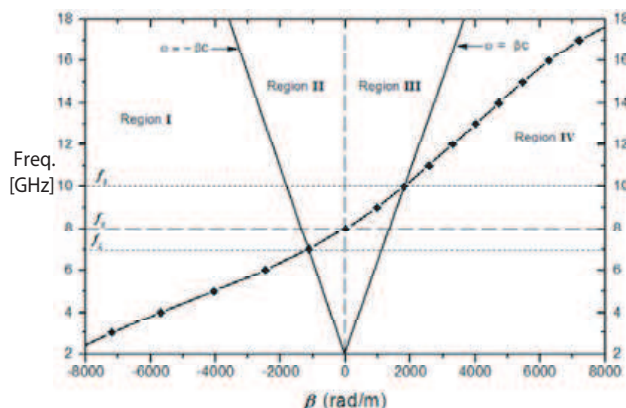
Figure 5: Dispersion diagram of the UC structure. Balanced case ($L_R = 1\,\text{nH}$, $C_R = 0.1\,\text{nF}$, $L_L = 2.5\,\text{nH}$, $C_L = 0.25\,\text{pF}$).
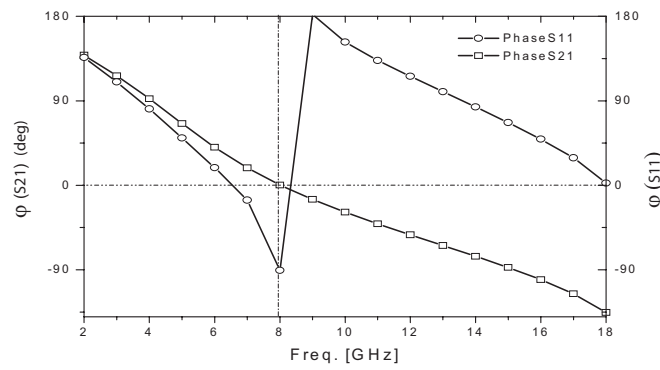
Figure 6: Theoretical scanning angle versus frequency.
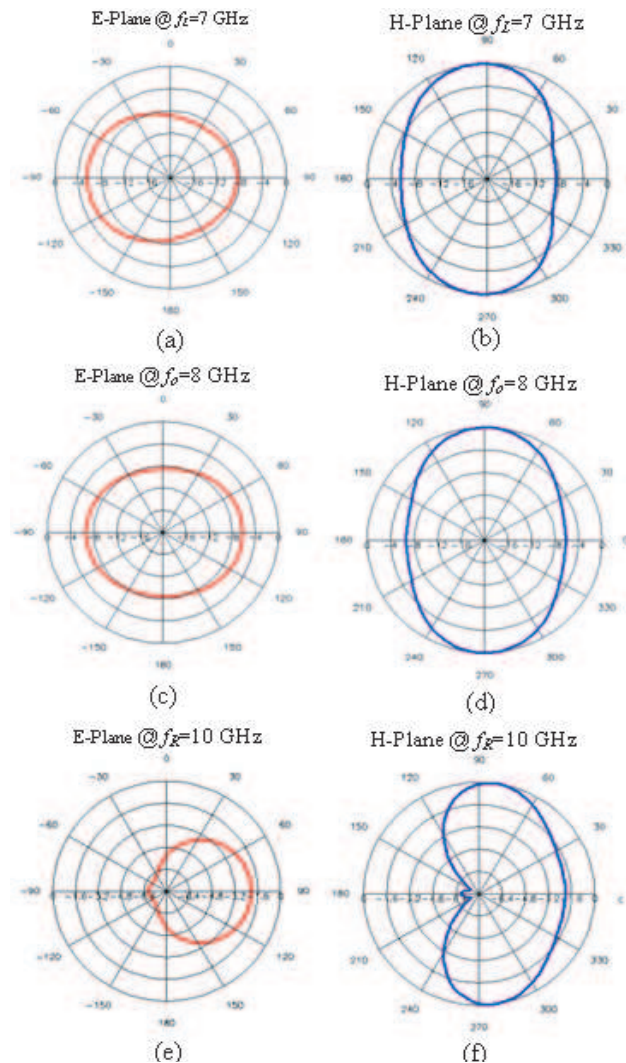
Figure 7: Simulation normalized E-plane and H-plane radiation 7 GHZ (Backfire), 8 GHz (Broadside) and 10 GHz (Endfire).

4. CONCLUSION

A novel CRLH backward-wave leaky CPW-Antenna broad bandwidth has been clearly presented. First, the isolated CRLH UC has been characterized mathematically and physically, and a CPW implementation of this UC has been demonstrated. A simple and accurate circuit model has been proposed and validated by full-wave simulations.

REFERENCES

1. Veselago, V. G., "The electrodynamics of substances with simultaneously negative values of "μ and ε," *Sov. Phys. Usp.*, Vol. 10, No. 4, 509–514, Jan.–Feb. 1968.
2. Pendry, J. B., A. J. Holden, D. J. Robins, and W. J. Stewart, "Magnetism from conductors and enhanced nonlinear phenomena," *IEEE Trans. Microwave Theory Tech.*, Vol. 47, 2075–2084, Nov. 1999.
3. Smith, D. R., W. J. Padilla, D. C. Vier, S. C. Nemat-Nasser, and S. Schultz, "Composite medium with simultaneously negative permeability and permittivity," *Phys. Rev. Lett.*, Vol. 84, No. 18, 4184–4187, May 2000.
4. Shelby, R. A., D. R. Smith, and S. Schultz, "Experimental verification of a negative index of refraction," *Science*, Vol. 292, 77–79, Apr. 2001.
5. Eleftheriades, G. V., A. K. Iyer, and P. C. Kremer, "Planar negative refractive index media using periodically L-C loaded transmission lines," *IEEE Trans. Microwave Theory Tech.*, Vol. 50, 2702–2712, Dec. 2002.
6. Caloz, C., A. Sanada, and T. Itoh, "A novel composite right-/left-handed coupled-line directional coupler with arbitrary coupling level and broad bandwidth," *IEEE Trans. Microwave Theory Tech.*, Vol. 52, 980–992, Mar. 2004.

Research on the Robotic Polishing Combined with Electromagnetic Field of Rapid Metal Tool

Guangchao Han[1], **Haiou Zhang**[2], **and Qichang Su**[2]

[1]School of Electronic Information & Mechanics, China University of Geosiences
Wuhan 430074, China
[2]School of Mechanical Science & Engineering
Huazhong University of Science and Technology
Hubei, Wuhan 430074, China

Abstract— In the rapid metal tooling, high efficient polishing process can improve the mould quality and shorten the lead time of the rapid tool, but the polishing process is frequently carried out manually. The application of industrial robot for the polishing process can minimize the production times and improve the working environment on a certain extent. In order to improve the robotic polishing efficiency continuously, the robotic polishing process combined with electromagnetic field is developed to fit for the application of commercial industrial robot, which is hard to be controlled online for its close control system. Free abrasive and soft polishing tool are also applied in the robotic polishing process to cooperate with the electromagnetic field. A minitype electromagnet is trial-manufactured and connected to the robotic end-effector, which can act on the polished surface along with the robotic moving. The electromagnet is coiled as solenoid that the polishing tool and the electrical spindle can be fixed in the hollow. A partition & flexible mapping method based on CAM is developed to generate the uniform robotic polishing path, which can compensate the elastic deformation and the abrasion of the soft polishing tool. Experiments are executed to test the influence between the electromagnetic field intensity and the polishing efficiency. The result shows that the polished material removal can increase over 50% when the ferromagnetic substrate is acted by the electromagnetic field about 170 Gs.

1. INTRODUCTION

Rapid spray metal tooling (RSMT) has attracted extensive attention in the automobile industries, because it can shorten the designing period of the new type automobile [1]. In the RSMT, high efficient polishing process can improve the mould quality and shorten the lead time of the rapid metal tool. But the polishing process is frequently carried out manually. These kinds of operations are iterative, time consuming and require experience. Automation can introduce cost reduction by minimizing production times on such manual finishing operations, which mostly includes the methods of industrial robot and NC machine. The industrial robot has more advantage than NC machine on polishing a large complex metal mould for its flexibility on machining fashion and machining range. This fact has attracted much research to investigate possible methods of designing and implementing robotic polishing systems. A robotic die polishing station controlled by a PC and a robot controller, which can exchange the grinding tool automatically so that the operation was completely unmanned [2]. The contact stress for an automated polishing process was modeled and analyzed, which determined the quality of the polished part, not the force exerted on the polishing tool [3]. A high precision polishing robot with a learning-based hybrid position/force controller was developed for polishing PET (Poly Ethylene Terephthalate) bottle molds [4]. An automatic mold polishing system (AMPS) was present, which integrates with mold geometry process kernel, path planner, process planner, and force control robot into a system [5, 6]. An automatic planning and programming system was developed based on data from a CAD system for a robotic polishing cell for mold manufacturing [7]. So the path planning and force control has become the research focus of the robotic polishing process now.

Most of the industrial robots in the market now, such as Motoman UP20 robots used for the RSMT, have a close control system that the user is hardly to intervene or adjust the robotic program when the robot is working, except terminating the machining process. (Not including the particular cell that has the open control system especially designed by the robot manufacturer). And a robotic polishing system with free abrasive and soft polishing tool has been developed to fit for the close system [8]. The stock removal of the ferromagnetic material in the grind test increased $5 \sim 21\%$ when the work piece were magnetized up to 16 mT by the alternating current [9]. In order to improve the robotic polishing efficiency continuously, the electromagnetic field up to 170 Gs is presented to the robotic polishing process in this paper.

2. ROBOTIC POLISHING SYSTEM

RSMT is a developing rapid metal tooling technology [10]. The schematic diagram of RSMT is shown in Fig. 1. Firstly, the master model is formed by the rapid prototyping method such as SLS or transformed from the part. Secondly, the silicon rubber mould is transformed from the master model and the original sprayed model is also produced from the silicon rubber mould. Then the metal film with excellent wear resistance is formed on the original model by robotic plasma spraying. The original model is no longer necessary after backup and then is broken and separated from the sprayed layer to obtain the metallic mold surface through the mechanical method. Finally, the sprayed surface is finished by robotic polishing process and the metal mould is gained, which can be applied to industrial production after assembly.
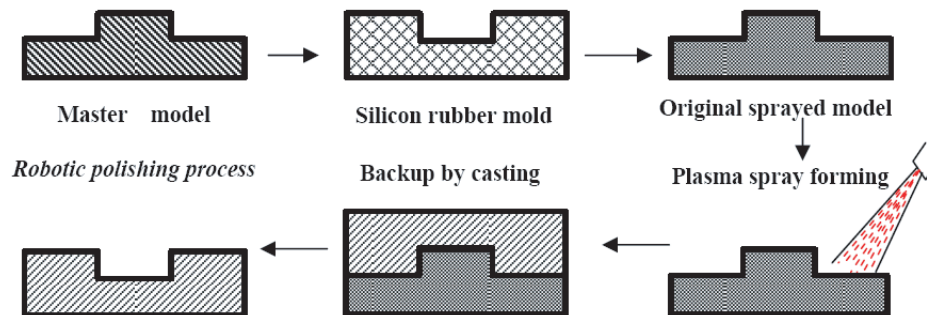

Figure 1: Schedule of the RSMT.

The robotic polishing process is an important step of the RSMT. The facilities of the robotic polishing system consist of a Motoman UP20 industrial robot, a high speed electrical polishing spindle and a numerical swivel table. Soft polishing tool (made up of unwoven cloth or wool) and free abrasive are also selected for the system. The CAD/CAM system (such as UG NX) is running on a separate workstation.

3. ELECTROMAGNETIC FIELD FOR THE POLISHING SYSTEM

In the robotic polishing system, the soft polishing tool and free abrasive are chosen for weakening the path error of the robotic moving. But the material removal efficiency of three-body abrasion process is decreased compared with the hard polishing tool. In order to enhance the polishing efficiency of the soft tool, the electromagnet is tried to combine with the robotic polishing process. The minitype electromagnet is coiled to form solenoid structure around the soft polishing tool and connected to the high speed electrical spindle, which are all connected to the robotic end-effector that the electromagnetic field can act on the polished surface along with the robotic moving. The electromagnet with robotic polishing system is shown in Fig. 2.

The complex polishing effect of material removal should be tested by the experiment. The 100 A/15 V DC electrical source is used for generating the electromagnet field, which is shown in

Figure 2: Robotic polishing process with electromagnetic field.

Figure 3: DC electrical source for the electromagnet.

Fig. 3. The experiment parameters are shown in Tabel 1. The Sketch of the experiment process is shown in Fig.4. It is formed an angle of 10° between the polishing tool axis and the normal direction of the polished surface which can be propitious to gain the maximum line speed of the rotating polishing tool and be helpful for expelling the abrasive chipping during the polishing process.
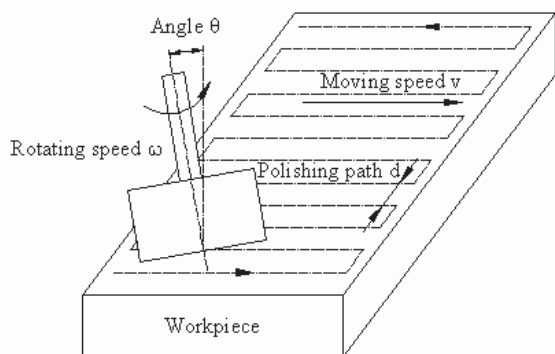

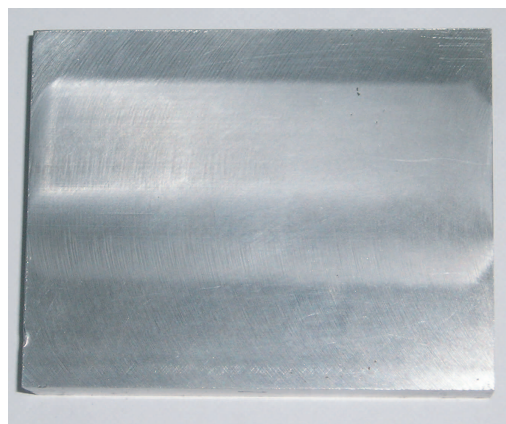Figure 4: Sketch of robotic polishing process.

Figure 5: Ferromagnetic substrate polished in the magnetic field.

In order to compensate the elastic deformation and the tool abrasion during the polishing process of the soft tool, the polishing path should be offset down about 1.0 mm along the negative normal direction of the polished surface basing on the original polishing position. And the position of the polishing tool should be offset down 0.1 mm every 175 mm polishing distance along the same direction [11]. The polishing force can be controlled between $10 \sim 20$ N, which is nearby to the situation of the man-made polishing force.

Table 1: Parameters of the robotic polishing experiment with magnetic field.

Free abrasive	Soft polishing tool	Tool diameter	Polished substrate
Green SiC	Unwoven cloth	30 mm	45# steel
Path interval (mm)	Path type	Moving speed (mm/s)	Tool rotating speed
0.1	Z type	10	3600 r/min

Different DC currents from 30 A to 50 A are used to generate magnetic fieldwhich can make the electromagnet keep normal working temperature. And the electromagnetic field intensity corresponding to the different currents have been demarcated before the experiment. The mass lost of the ferromagnetic substrate is tested after polished. The polished substrate is shown in Fig. 5 and the experiment results are shown in Table 2.

Table 2: Relation between the material removal and the magnetic field intensity.

No.	DC current (A)	Magnetic field intensity (Gs)	Material removal (g)
1	0	0	0.2
2	30	120	0.3
3	40	140	0.3
4	50	170	0.4

4. DISCUSSION AND CONCLUSIONS

According to the test results, it is shown that the material removal efficiency of the robotic polishing process is improved greatly over 50% with the increasing of the magnetic field intensity.

This is mostly caused by the magnetization of the electromagnetic field. The polished substrate is ferromagnetic material and the abrasive chipping polished from the substrate will mostly be magnetized and absorbed around the polishing scrape instead of being expelled by the rotating polishing tool. So the number of the free abrasive should be increased and three-body abrasive process is enhanced. Consequently, the robotic polishing efficiency is improved obviously. The higher magnetic field intensity and the interaction mechanism of the robotic polishing process will be made further studied in the future.

ACKNOWLEDGMENT

REFERENCES

1. Nagata, F., T. Hase, Z. Haga, et al., "CAD/CAM-based position/force controller for a mold polishing robot," *Mechatronics*, No. 17, 207–216, 2007.
2. Chen, H. and N. Xi, "Automated tool trajectory planning of industrial robots for painting composite surfaces," *International Journal of Advanced Manufacturing Technology*, Vol. 35, No. 7–8, 680–696, 2008.
3. Tse, W. C. and Y. H. Chen, "Implementation of a robot system for sculptured surface cutting. Part 1. Rough machining," *International Journal of Advanced Manufacturing Technology*, No. 15, 624–629, 1999.
4. Tse, W. C. and Y. H. Chen, "Implementation of a robot system for sculptured surface cutting. Part 2. Finish machining," *International Journal of Advanced Manufacturing Technology*, No. 15, 630–639, 1999.
5. Zhang, H., G. Wang, Y. Luo, et al., "Rapid hard tooling by plasma spraying for injection molding and sheet metal forming," *Thin Solid Films*, No. 390, 7–15, 2001.
6. Zhang, H., G. Han, and G. Wang, "Development of direct prototype spray tooling technology," *Die & Mould Technology*, Vol. 19, No. 7, 82–83, 2004.
7. Han, G.-C., H.-O. Zhang, and G.-L. Wang, "Numerical simulation & experiment study on the robotic plasma spray," *Journal of Huazhong Univ. of Sci. & Tech. (Nature Science Edition)*, Vol. 35, No. 7, 62–64, 2007.
8. Han, G., M. Sun, H. Zhang, et al., "Research on the robotic free abrasive polishing system for the rapid spray metal tooling," *Key Engineering Materials*, No. 373–374, 770–773, 2008.
9. Kumagai, K., O. Kamia, and T. Morita, "Magnetic effects on grinding of ferromagnetic materials effect of magnetic field on stock removal and grinding force," *JSPE*, Vol. 58, No. 10, 1679–1684, 1992.
10. Han, G.-C., H.-O. Zhang, and G.-L. Wang, "Robotic milling for rapid ceramic prototyping," *Journal of Harbin Institute of Technology (New Series)*, Vol. 12, No. 6, 674–679, 2005.
11. Han, G. and M. Sun, "Optimum path planning of robotic free abrasive polishing," *International Conference on Intelligent Robotics and Applications*, 906–915, Wuhan, China, October 2008.

Modeling of Thermal-metallurgical Behavior during Hybrid Plasma-laser Deposition Manufacturing

Fanrong Kong[1, 2], **Haiou Zhang**[1], **and Guilan Wang**[3]

[1]College of Mechanical Science and Engineering
Huazhong University of Science and Technology, Wuhan 430074, China
[2]Research Center for Advanced Manufacturing, Southern Methodist University
3101 Dyer Street, Dallas, Texas 75205, USA
[3]College of Material Science and Engineering
Huazhong University of Science and Technology, Wuhan 430074, China

Abstract— A three-dimensional nonlinear finite element method combining with Monte Carlo model was developed to investigate the temperature field and grain growth in the heat affected zone (HAZ) during the plasma-laser hybrid deposition manufacturing (PLDM) thin wall metal parts. The numerical study shows that the temperature gradient directly decides the grain growth speed in the HAZ of deposited wall. However, the effect of thermal impact due to continuous scanning of laser and plasma arc on the microstructure in the substrate material is negligible. This thermal-microstructure model could be further applied to study the variable high energy forming processes.

1. INTRODUCTION

Plasma-laser hybrid direct rapid manufacturing (PLDM) [1–3], consisting of fusion deposition forming based on plasma arc combined with laser beam, fine machining and surface treatment, belongs to dieless direct rapid manufacturing technology. PLDM could obviously reduce development cost and cycle of novelty product such as high temperature parts of aerospace engine. As compared with laser engineering net shape (LENS) technique, PLDM has many advantages, including high forming efficiency, low investment cost, facilitating to acquire full dense metal parts and finish the formed surface as the deposition forming. Moreover, it is available for controlling of concentration distribution of material composition in PLDM [2]. Therefore, PLDM has a huge potential of development in aerospace, energy, biological engineering, and environment protection fields for manufacturing difficulty-to-machine parts and functionally graded materials, even long-life mould with complex geometry.

It is noted that complicated thermal dynamic phenomena exist in the rapid forming metal parts process by PLDM; especially, when a layer of material is deposited, one or more previously deposited layers can be reheated or remelted, which under unfavorable process conditions may lead to undesired effects. For example, during the PLDM of steel, martensite can be reheated above the martensite start temperature, resulting in retaining of tempered martensite after finally cooling down. However, according to the previous literature [4], if the process parameters are controlled such that most of the part remains at temperature higher than the martensite start temperature, after cooling down this will lead to a uniform microstructure consisting of non-tempered martensite with minor proportions of retained austenite and carbides. Costa et al. [5] presented that short idle time and small substrate size can reduce the proportion of tempered martensite and result in a more uniform microstructure and mechanical property. This is because that "both short idle time and small substrate size are more probable to keep most of the part at temperature higher than the martensite state temperature" [4]. Wang et al. [4] also presented that "control of the molten pool determines the properties of the resulting solidified product". J. Choi et al. [6] studied the influence of preheating and power input on the microstructure and mechanical properties of deposited layer by using laser cladding. PLDM, as a recently developing forming technique, has a little bit difference with other ones. The addition of plasma arc make the energy input mode become more complicated, of which it is necessary being fully understood to make the simulation results reasonable.

Recently, the development of advanced computational science gives us an efficient way to simulate those grain growth by developing a thermal microstructure model. Great achievements have been made in the simulation of the grain growth or crystal evolution in the casting, laser welding, and electric arc welding process by applying the Monte Carlo model in cooperation with thermal

analysis that uses the finite element method or finite difference method [7–9]. The advantage of this thermal-microstructure model is that the temperature field analysis and the coupled microstructure simulation can be performed simultaneously.

In the proposed study, an experimentally based finite element model is used for studying the temperature distribution and grain growth in the HAZ during the PLDM processes, in which a new heat source model is developed. And the processing parameters influencing the thermal and metallurgical behaviors are also investigated in detail.

2. MATHEMATICAL MODELING

PLDM is accompanied with thermal-mechanical-metallurgical behaviors, including the interaction between laser and arc induced plasma, powder, shielding gas and substrate material. Some features in this process are shown as following:

(1) Effective energy distribution of PLDM depends on the plasma zone and varies with the powers and space location between the two ones.

(2) Rapid melting and cooling is followed by the motion of hybrid heat sources and induce a higher temperature and stress concentration as well as microstructure evolution around and in the molten pool zone.

(3) Free surface profile and fluid flow in the molten pool are related to the plasma arc pressure and surface tension due to temperature which act on the molten pool surface, and buoyancy force in the molten zone.

As shown in Fig. 1(a), in the deposition process, moved heat source radiates on the metal surface to form a melt pool and directionally conducting temperature field. Powder is melted and deposited on the substrate point by point, and then rapidly solidifies and metallurgically bonded with substrate and/or previous deposited layers.

(a) Experimental photo　　　　　　　　　　　　　　(b) Schematic view of PLDM
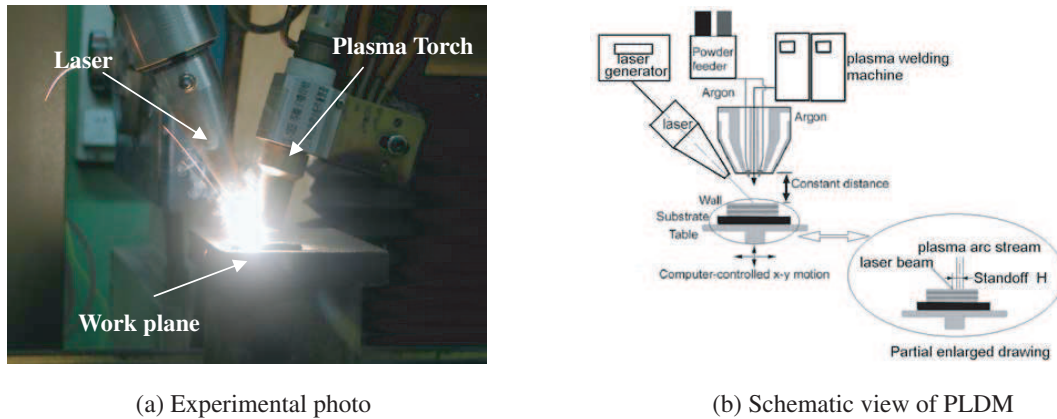
Figure 1: Representation of plasma laser hybrid deposition manufacturing (PLDM).

An uncoupled thermal-metallurgical analysis is implemented in this study. A thermal analysis is first performed to acquire temperature field data, which are then applied to the microstructure analysis by using Mont Carlo (MC) model. All calculations are realized based on ANSYS Parametric Design Language (APDL). And a "birth and death" technique is used to model the formed clad. The whole simulation zone consists of substrate and powder materials. To accurately simulate the thermal behavior of PLDM, temperature dependent material properties are used. In this model, the grain growth behavior in the melt pool has not been involved due to its much more complexity. However, it is also noted the heat affected zone is higher danger zone for thermal fracture induced. Therefore, it is of importance to study the grain growth behavior in HAZ for further understanding the forming mechanism in the PLDM. The whole microstructure analysis is performed by using Matlab code.

2.1. Finite Element Thermal Analysis

The governing equation used to analyze the temperature field can be specialized to a differential control volume and shown as follows:

$$\rho c \left(\frac{\partial T}{\partial t} + \{V\}^T \{L\} T \right) + \{L\}^T \{q\} = \ddot{q} \tag{1}$$

where, ρ is the density, c is the specific heat, and T is the location-time dependent temperature. $\{L\}$ is the vector operator, $\{L\} = \begin{Bmatrix} \frac{\partial}{\partial x} \\ \frac{\partial}{\partial y} \\ \frac{\partial}{\partial z} \end{Bmatrix}$; $\{V\}$ is the velocity vector for mass transport of heat, $\{V\} = \begin{Bmatrix} v_x \\ v_y \\ v_z \end{Bmatrix}$. $\ddot{q}$ is the heat generation rate per unit volume. $\{q\}$ is the heat flux vector, and Fourier's law is used to relate the heat flux vector to the thermal gradient:

$$\{q\} = -[D]\{L\}T \tag{2}$$

where conductivity matrix $[D]$ is given by:

$$[D] = \begin{bmatrix} K_{xx} & 0 & 0 \\ 0 & K_{yy} & 0 \\ 0 & 0 & K_{zz} \end{bmatrix} \tag{3}$$

K_{xx}, K_{yy}, K_{zz} are conductivity in the element x, y, and z direction, respectively.

Substituting Eq. (2) into Eq. (1) and ignoring the effect of fluid flow in the weld pool on the temperature field of the welded joint, i.e., letting $\{V\} = 0$, the governing equation of temperature field solution can be further shown below:

$$\rho c \left(\frac{\partial T}{\partial t} \right) = \{L\}^T ([D]\{L\}T) + \ddot{q} \tag{4}$$

In addition, the boundary conditions are considered.

(1) Specified heat flow input acting over the weld bead surface S_1:

$$\{q\}^T \{\beta\} = -q^* \tag{5}$$

where $\{\beta\}$ is unit outward normal vector; q^* is input heat flow due to laser/arc hybrid heat sources and given by $q^* = q_{arc}(x, y, z) \cdot \delta(x, y, z) + q_{laser}(x, y, z)$. The whole schematic view of hybrid heat sources in the welding system is shown in Fig. 1(b). And the plasma arc and laser hybrid heat source model in Ref. [3] is referenced in this study.

(2) Specified convection and radiation heat loss acting over surface S_2 (Newton's law of cooling):

$$\{q\}^T \{\beta\} = h_f(T_S - T_\infty) + \phi \ni (T_S^4 - T_\infty^4) \tag{6}$$

where, h_f is the heat convection coefficient acting on the surfaces of deposited wall, T_∞ is the bulk temperature of the surrounding air, and T_S is the surface temperature. ϕ is Stefan-Boltzmann constant, and $\ni$ denotes the effective emissivity.

Combining Eq. (4) with Eqs. (2), (5) and (6), and integrating them over the volume of the element, the governing equation of temperature field solution in this study can further yield as below:

$$\int_{vol} \left(\rho c \left(\frac{\partial T}{\partial t} \right) \delta T + \{L\}^T ([D]\{L\})T \right) d(vol)$$
$$= \int_{S_1} \delta T q^* dS_1 - \int_{S_2} \left\{ \delta T h_f(T - T_\infty) + \delta T \phi \ni (T^4 - T_\infty^4) \right\} dS_2 + \int_{vol} \delta T \ddot{q} \, d(vol) \tag{7}$$

where vol denotes volume of the element, δT denotes an allowable virtual temperature dependent of the location x, y, z, and time t.

2.2. Grain Growth Simulation of Heat Affected Zone Based on Monte Carlo Model

The concept behind the Monte Carlo method in grain growth simulation is both simple and fascinating: its only basis is the thermodynamic of atomic interactions. There are no other experimental or theoretical inferences, nor mathematical approximations. The first step is to represent the material as a 2D or 3D matrix, in which each site corresponds to a surface or volume element. The content of each element represents its crystallographic orientation. Contiguous regions (containing the same "number") represent the grains as shown in Fig. 2. The grain boundaries are fictitious surfaces that separate volumes with different orientations. After choosing the kind of matrix and filling it with an initial random content, the simulation itself begins. These are the four main steps of the algorithm:

1) Calculation of the free energy of an element of the matrix (G_i) with its present crystallographic orientation (Q_i) based on its neighborhood.
2) Random choice of a new crystallographic orientation for that element (Q_f).
3) New calculation of the free energy of the same element (G_f), but with the new crystallographic orientation (Q_f).
4) Comparison of the two values $(G_f - G_i)$. The orientation that minimizes the energy is chosen with transition probability W.

These four steps are repeated millions of times in random positions of the matrix. The overall result is a microscopic simulation of the free energy decay in the system, which is actually the main impelling force for grain growth. The Hamiltonian that describes the interaction among the closest neighbors, which represents the grain boundary energy, is:

$$H = -J \sum_{nn} (\delta s_i s_j - 1) \tag{8}$$

where, S_i is one of the Q possible orientations in the i element of the matrix and δ_{ab} is the *Kronecker-delta*, which is 1 when the two elements are equal and 0 otherwise. As a result, neighbors with a different orientation contribute J to the system energy and 0 when equal. The transition probability W is given by:

$$W = \begin{cases} \exp\left(-\frac{\Delta G}{k_b T}\right) \to \Delta G > 0 \\ 1 \to \Delta G \leq 0 \end{cases} \tag{9}$$

where, ΔG is the change in free energy due to the orientation alteration, k_b is the Boltzman constant, and T is the temperature. Thus the speed of the moving segment is given by:

$$v_i = C \left[1 - \exp\left(-\frac{\Delta G}{k_b T}\right) \right] \tag{10}$$

where, C is the boundary mobility.
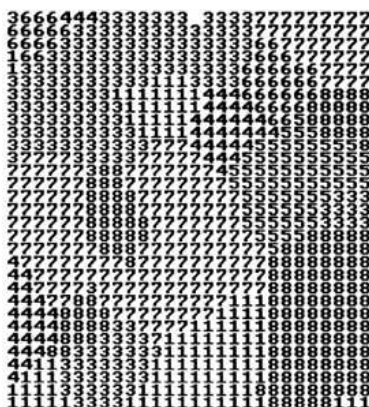

Figure 2: The grain structure represented by a 2D square matrix.

A continuous grain growth model is shown as follows [6]:

$$L^n - L_0^n = k(T)t \tag{11}$$

where L and L_0 are the initial and final mean grain sizes calculated with the linear intercept method, n is the grain growth exponent, and $k(T)$ generally given as an Arrhenius-type equation and its expression is shown as follows:

$$k(T) = k_0 \exp\left(-\frac{Q}{RT}\right) \tag{12}$$

where, k_0 is the pre-exponential coefficient, R is the gas constant, and Q is the activation energy for grain growth. The equation performs well in the simulation when the effect of grain boundary precipitates is small [7].

Monte Carlo simulation is an efficient way to model the grain growth under constant temperature or slow and uniform temperature evolution such as the casting process [7]. However, the PLDM process is a dynamic thermal process with a rapid melting and solidification evolution. In other words, there exist abrupt temperature gradient in the fusion zone and heat affected zone. In order to simulate microstructure evolution in HAZ of deposited wall, an experimentally data based (EDB) model [8] is used in this study to relate time and t_{MCS} in PLDM process.

$$L = K_1 \times \lambda \times (t_{MCS})^{n_1} \tag{13}$$

where λ is the grid point spacing, while K_1 and n_1 are constants. Through the regression calculation of t_{MCS} and the Monte Carlo simulating grain size, the value of K_1 and n_1 are respectively 0.715 and 0.477 [7]. In the EDB model, the relationship between the t_{MCS} and the real time temperature $T(t)$ is expressed as follows [8]:

$$(t_{MCS})^{2n} = \left(\frac{L_0}{K_1\lambda}\right)^n + \frac{K}{(K_1\lambda)^n} \exp\left(-\frac{Q}{RT(t)}\right)t \tag{14}$$

where n is the grain growth exponent and K is the model constant. The t_{MCS} varies with the thermal cycle as shown in Eq. (14). In order to unify the t_{MCS} in the simulation domain, a site selected probability P is employed here [7]:

$$P = \frac{t_{MCS}}{t_{MCSMAX}} \tag{15}$$

here, t_{MCSMAX} is the maximum of t_{MCS} in the simulation domain.

Table 1: Material physical parameters used in this study.

Temperature (°C)	Density (kg/m³)	Specific heat (J/(kg · K))	Thermal conductivity (W/(m · K))
0	7900	465	50
500	7700	618	39
1000	7450	780	25
1200	7350	610	26
1350	7240	550	27
1400	7200	460	28
1500	7130	390	29
1800	6950	400	29.5
2000	6840	410	30

3. NUMERICAL EXPERIMENT OF PLDM FORMING THIN WALL METAL PARTS

Figure 3 shows the finite element model. The material of substrate and powder used in this study are both nickel base high-temperature alloy. The computational zone used is half of solid model

according to the symmetry of geometry and boundary condition. The related physical parameters of material are shown in Table 1. A double-peak point distribution exists in the temperature & time curve during PLDM process; one is due to the laser radiation, the other is from the plasma arc. The temperature distribution is obviously influenced by the coupling of laser beam and plasma arc as shown in Fig. 4.
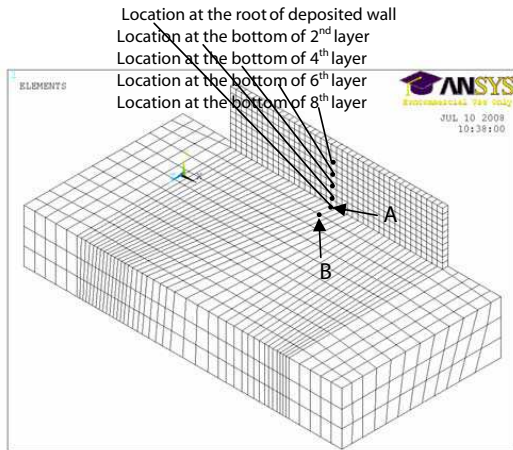
Figure 3: Finite element mesh.
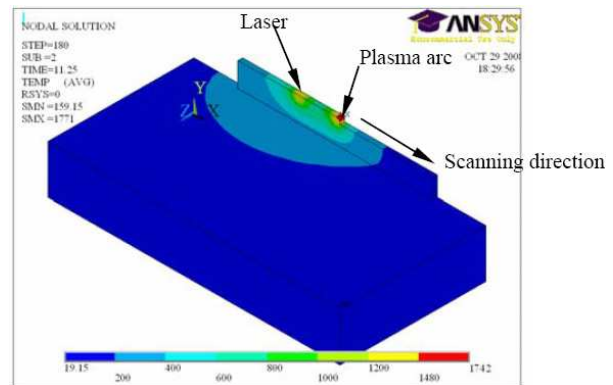
Figure 4: Temperature distribution of PLDM.
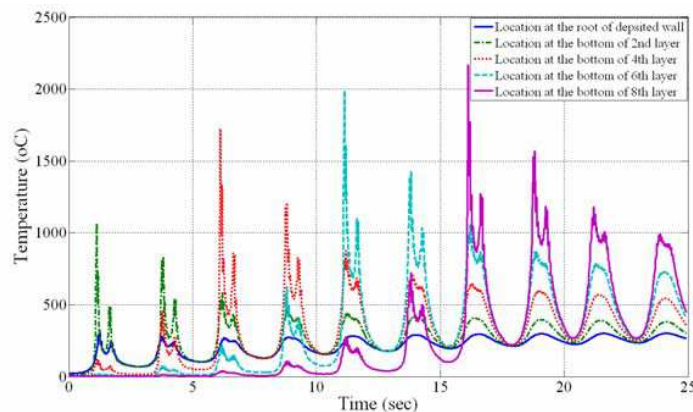
Figure 5: Effect of power ratio of laser to arc on the temperature distribution during PLDM (3000 W plasma arc +800 W laser, scanning speed is 8 mm/s).
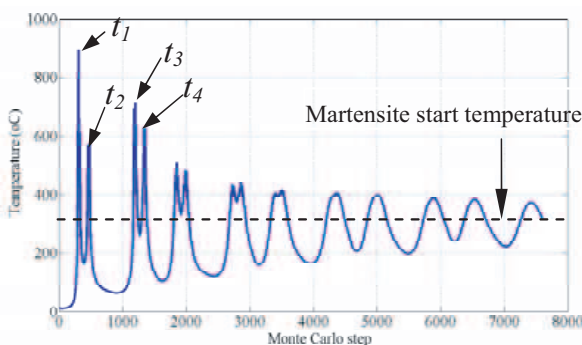
(a) Position **A** located at base metal
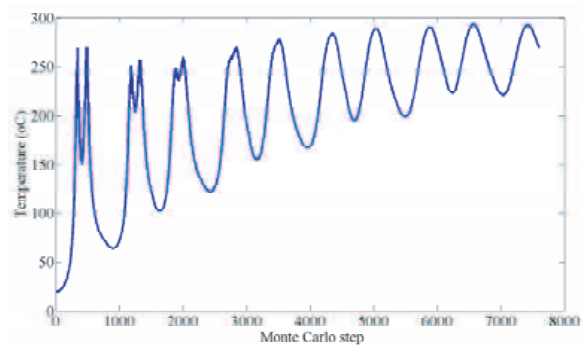
(b) Position **B** located at roof of deposited wall

Figure 6: The relation between the Monte Carlo step and real time & temperature during PLDM process.

The temperature evolution at locations at the different deposited layer is shown in Fig. 5. Numerical results clearly indicate that the double thermal impact exists in the deposited layer during PLDM process. Monte Carlo model then use the temperature data from the thermal analysis as loading. The relation between the Monte Carlo step and real time and temperature is shown in Fig. 6. According to the Ref. [5], the grain growth behavior exists when the temperature is higher than the martensite start point. From the results shown in Fig. 6(a), it is clearly seen that the influence of thermal impact due to deposition manufacturing on the microstructure of substrate is negligible. To further study the whole grain evolution in the PLDM, a characteristic location at the root of deposited layer is chosen (see Fig. 6(a)). And several moments in deposition manufacturing process are also picked, the relation between real time & temperature and MC step is listed in Table 2. Microstructure simulation results at location A during PLDM are shown in Fig. 7. Numerical results indicate that the grain growth speed depends on the temperature gradient and is inclined to slow down with the increasing of deposition time.

Table 2: Relation between real time & temperature and MC step.

Mark in Fig. 6	Real time (s)	Temperature (°C)	Monte Carlo step
t_1	1.01	895.12	305
t_2	1.56	573.45	476
t_3	3.88	695.34	1181
t_4	4.44	627.41	1352

(a) $t = t_1$　　　　　　　　　　　　(b) $t = t_2$

(c) $t = t_3$　　　　　　　　　　　　(d) $t = t_4$
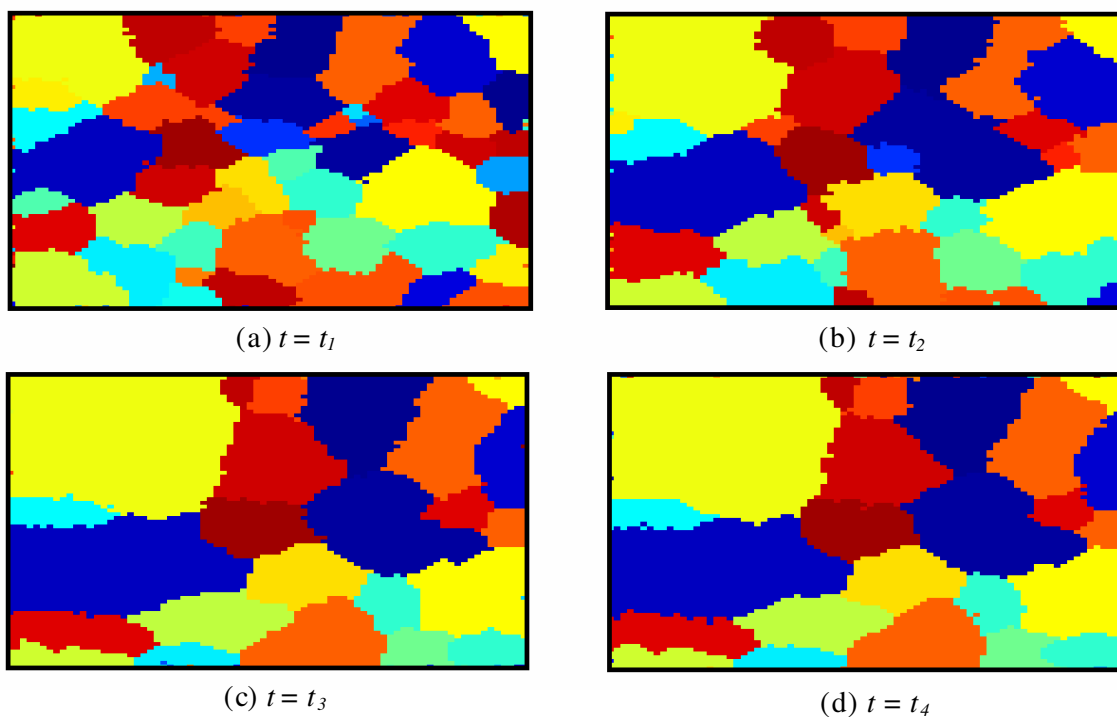
Figure 7: Microstructure simulation result at location A during PLDM.

4. CONCLUSIONS

(1) A three-dimensional thermal and metallurgical analysis based on finite element method combining with Monte Carlo model is developed to study the temperature field and grain growth in HAZ during the PLDM process.

(2) The thermal impact directly influences the grain size in the microstructure of deposited layers, but almost has no effect on the substrate material in the PLDM process. And the grain growth

speed in the HAZ depends on the temperature gradient and is inclined to slow down with the increasing of deposition time.

(3) The thermal-microstructure model could be further used to study the relation between temperature curve and the grain growth in the deposition manufacturing process by variable high energy beam techniques.

REFERENCES

1. Zhang, H., Y. Qian, G. Wang, and Q. Zheng, "The characteristics of arc beam shaping in hybrid plasma and laser deposition manufacturing," *Science in China: Series E Technological Sciences*, Vol. 49, No. 2, 238–247, 2006.

2. Zhang, H., Y. Qian, and G. Wang, "Study of rapid and direct thick coating deposition by hybrid plasma-laser manufacturing," *Surface and Coating Technology*, Vol. 201, 1739–1744, 2006.

3. Kong, F., H. Zhang, and G. Wang, "Numerical simulation of transient multi-phase field during hybrid plasma-laser deposition manufacturing," *ASME Journal of Heat Transfer*, Vol. 130, No. 112101, 1–7, 2008.

4. Wang, L. and S. Felicelli, "Influence of process parameters on the phase transformation and consequent hardness induced by the LENS process," *Material Processing Fundamentals*, Edited by P. Anyalebechi, TMS (The Minerals, Metals & Materials Society), 63–72, 2007.

5. Costa, L., R. Vilar, T. Reti, and A. M. Deus, "Rapid tooling by laser powder deposition: Process simulation using finite element analysis," *Acta Materialia*, Vol. 53, 3987–3999, 2005.

6. Choi, J., S. K. Choudhuri, and J. Mazumder, "Role of preheating and specific energy input on the evolution of microstructure and wear properties of laser clad Fe-Cr-C-W alloys," *Journal of Materials Science*, Vol. 35, 3213–3219, 2000.

7. Mishra, S. and T. Debroy, "Measurements and Monte Carlo simulation of grain growth in the heat-affected zone of Ti-6Al-4V welds," *Acta Materialia*, Vol. 52, 1183–1192, 2004.

8. Gao, J. H. and R. G. Thompson, "Real time-temperature models for Monte Carlo simulations of normal grain growth," *Acta Materialia*, Vol. 44, 4565–4575, 1996.

9. Kong, F., D. Lin, S. Santhanakrishnan, and R. Kovacevic, "A thermal-microstructure model to predict the grain growth of a dual-phase steel DP980 in laser heat-treatment," *2009 TMS Annual Meeting Exhibition*, San Francisco, California, USA, February 15–19, 2009.

A Flexible Synchronous Powder Feeder for Electromagnetism Compress Digital Manufacturing of FGM Metal Component

Haiping Zou, **Haiou Zhang**, and **Guilan Wang**

Huazhong University of Science and Technology, Wuhan 430074, China

Abstract— Archiving functionally gradient materials (FGM) fabrication via digital manufacturing methods has attracted considerable attention in recent years. In this paper, a new FGM powder feeder and its flexible numerical motors control solution used in electromagnetism compressed plasma deposition manufacturing process was developed. The motors control hardware circuit and its Superior computer control program was introduced and analyzed. The powder feeder unit was based on the timing belt driving and Pneumatic conveying principle. The Superior computer control program was based on lab windows/CVI program developing environment with good man-machine conversation interface. Tests were made with Ni-based alloy powders, Fe-based alloy powders and ceramic powders in the particle average diameter of 15–350 Microns. Results showed that powders mixtures obtained from the device are continuous and stable. The precision of delivering powders mixture can be within 2% error scope comparing to the desired mixture quality and the flexible proportion of mixture can be easy changed in the computer control program by synchronously controlling the powder feeder rotation speed.

1. INTRODUCTION

Functionally graded materials (FGM) are a new generation of engineering materials with continuous changes of microstructures and properties across the material [1]. The unique characteristics in structure distribution make FGM offer great promising characteristics such as low residual and thermal stresses and improved bonding strength between dissimilar materials. Generally the manufacturing processes that can fabricate FGM objects are Laser Engineered Net-Shaping (LENS) [2], Directed Light Fabrication (DLF) [3], Electron Beam Freeform Fabrication (EBF) [4], which are termed as rapid prototyping (RP) or layered manufacturing (LM). Electromagnetism compressed Plasma deposition manufacturing (PDM) [5], as a newly developed direct metal fabrication process, belongs to 3D welding. This technique is characterized by supply head delivering a well-defined flow rate of metal powder, which is deposited in molten pool formed by controlled plasma heating. Thereby full strength parts with the single or multifarious materials can be built up, layer by layer, by melting and rapid solidifying the feed material into the desired shape. Those fabrication techniques involve deposition of material to create objects, unlike conventional methods, where material is removed to obtain the final object [6]. The deposition of material can be explicitly controlled thereby providing unique opportunities to selectively deposit material. In other words, the material deposited can be varied continuously to yield a functionally graded material object with varying material distribution.

Powder feeder is the key apparatus for electromagnetism compressed FGM component fabricating. There are various powder feeders based on different principles having been developed at home and abroad. Screw feeder, turntable feeder and tub wheel feeder are used broadly in powder applications. But these feeders are not quite fit for the FGM component fabricating for the reason of blocking powders frequently, poor capability of deliver superfine powders, can not keep the powder flow continuous and steady especially in low feed speed. And most of all, these feeders can not realize numerical control to supply mixing powders with desired blend ratio at fabricating spot. So it is necessary to develop an apparatus which can well meet the requirement of electromagnetism compressed FGM component fabricating process.

2. PRINCIPLE OF FGM POWDER FEEDER UNIT

The flexible numerical control FGM powder feeder unit was based on the timing belt driving and Pneumatic conveying principle. It mainly consists of mechanism which can transport quantity powders accurately includes powder barrel, time belt, belt pulley, air vibrator, powder falling tube and its adjust device and so on; the powder feeder body; carrying gas channel; the step-motor and the control electro circuit. Fig. 1 shows the schematic drawing and photograph of powder feeder unit.

During the powder delivering process, material powders fall from powder barrel onto the timing belt by the gravity function. An air vibrator installed near the powder barrel shakes in a Vibration
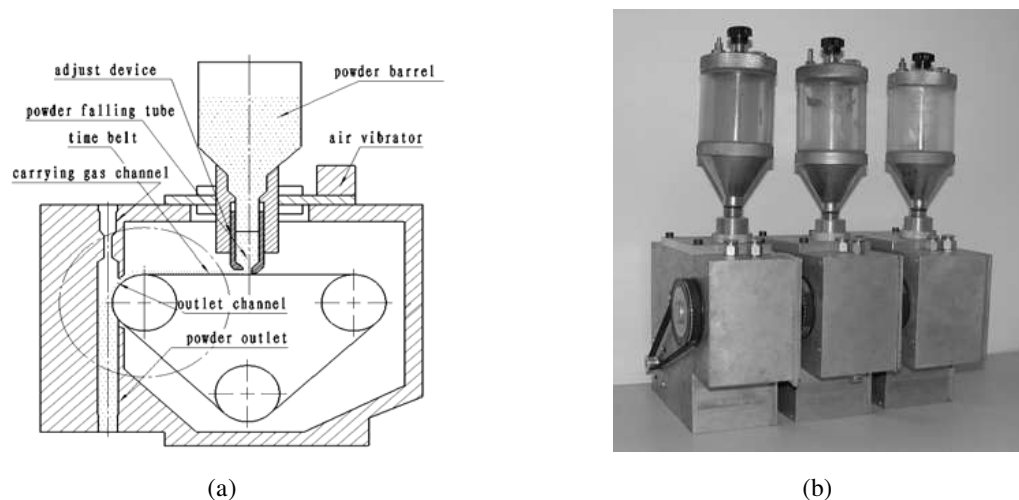
Figure 1: (a) Schematic drawing and (b) photograph of powder feeder unit.

frequency of 30000 vpm. The high frequency vibration of the powder barrel enhanced the flow ability of powders and avoided powders block as well as the powder bridging. The powder falling tube automatic adjust device eliminates the gap between powder falling tube and time belt, so the quantity measurement of delivered powders is decided by the through hole size at the bottom of falling tube which guarantees delivering the powders with accurate quantity. The time belt droved by belt pulley carries the material powders into the outlet channel at the one side of powder feeder body. The belt structure is able to ensure send the material powders on it to the powder outlet channel completely. The accelerated powder carrying gas is sent into the powder outlet channel through the gas inlet hole on the top of the powder feeder body. By using accelerated powder carrying gas, the material powders out of the feeder can keep good concentration after a long transportation distance.

3. REALIZATION OF FGM POWDER FEEDER MOTOLS CONTROL

3.1. Hardware Circuit

The motors control hardware circuit mainly includes the power source mold Block, D/A transformation module, V/F transformation module, display module as well as power failure memory replacement module and so on. The electrical principle is shown in Fig. 2. The monolithic integrated circuit ADUC812 as the core powder feeder motors control circuit, the TLC5620 as appended D/A transforms making up ADUC812's D/A channel insufficiency, the voltage/frequency transforms AD564 transforming 3-ways analogy output voltage signals frequency into pulse signals to actuate motors, Serial EEPROM X5165 as the power failure saves chip and The MAX232 chip achieving correspondence of ADUC812 and Superior PC machine.

3.2. The Superior Computer Control Program

The superior computer control program of FGM powder feeder was developed based on lab windows/CVI program developing environment with good man-machine conversation interface Fig. 3 shows the GUI of FGM powders feeder control system. The program realized communication between motors control circuit which installed in powder feeder control box and superior machine program through the serial port. By setting the figures of desired powder deliver quantity in the control program GUI (Graphical User Interface) panel, the computer control program sends out 3-ways electrical pulse signal unceasingly to the monolithic integrated circuit. The monolithic integrated circuit then actuates the step-motor to rotate at certain speed thus makes the time belt of powder feeder unit move in corresponding velocity and the material powders are sent out with the quantity as expected. The superior computer control program can also realize control of the powder feeders in both manual and automatic mode. It realizes two or three material gradient changes synchronously by adjusting the 3-ways output electrical pulse signal in the pre-defined mode corresponding to the materials gradient distribution.
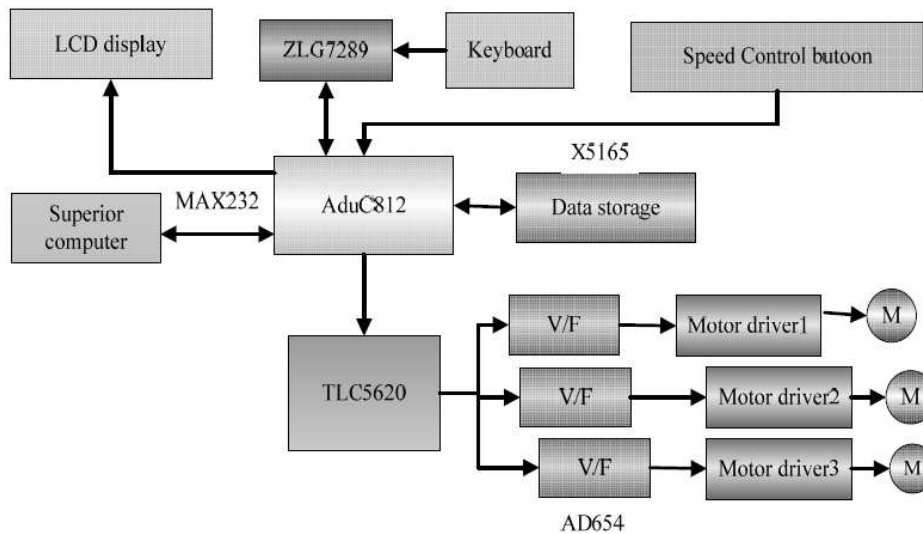
Figure 2: Schematic drawing of powder feeder control principle.
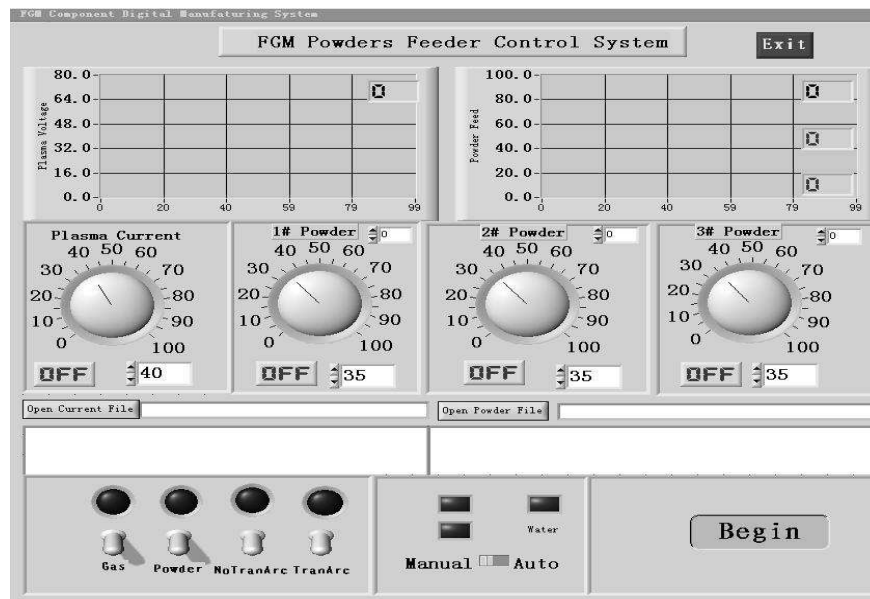
Figure 3: GUI of FGM powders feeder control system.

4. POWDER FEEDER EXPERIMENTS

During the FGM metal component digital manufacturing process, the quantity and the stability of delivered metal powders have great influences on the mechanical properties, the operating mode performance and the standard physical chemistry performance of the fabricated components. Therefore feeding the metal powder precisely and keeping the powder flow continuous and steady especially in low feed speed are the key factors to guarantee obtaining component with optimum performance.

In our paper, the powder mass of the new apparatus is determined by the density of the powder, the radius of through hole, the rotate speed of the step motor. The mass quantity of delivered powder per minute is shown in the formulary below.

$$m = \rho \times n \times \pi \times D \times \frac{1}{2} \times \pi \times r^2 \tag{1}$$

where m stands for Powder deliver quality; ρ stands for Powder density; n stands for deliver pulley rotational speed; D stands for diameter of deliver pulley and r stands for the radius of the through hole at the bottom of powder falling tube.

The powder feed precise tests were made with Ni-based alloy powders, Fe-based alloy powders and ceramic powders in the particle average diameter of 15–350 Microns with carrier Ar gas of $0.2\,\mathrm{m^3 \cdot h^{-1}}$. The powder mass is measured every 30 seconds and the results are shown in Fig. 4(a). The line is the measure data based linear least squares regression. The fitting equation is $M = Kt$. While M is powder mass (g), K is the proportion coefficient and t is the time (s). The proportion coefficient (K), correlation coefficient (R) and standard deviation (SD) is shown in Fig. 4(b).
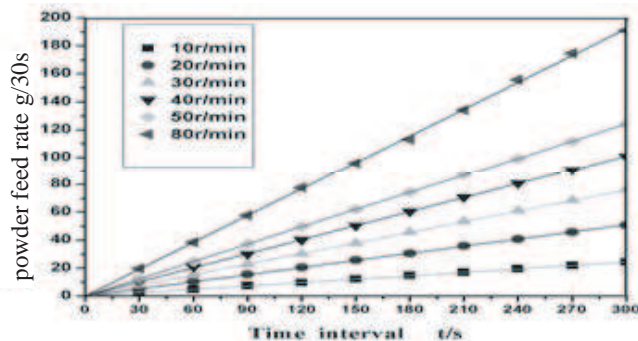
Motor feed rate			
n/(r/min)	K	R	SD
10	0.081	0.99999	0.08158
20	0.168	0.99998	0.22082
30	0.255	0.99999	0.18969
40	0.336	0.99998	0.43536
50	0.413	0.99999	0.16830
80	0.635	0.99999	0.28781

(a)   (b)

Figure 4: (a) Powder mass and motor ratio. (b) The results of fitting equation.

Experiments results show that powders obtained from the device were continuous and stable. The powder mass is stabilization and uniformity. Compared with traditional powder feeders, it has many merits such as low abrasion, broad range in adjusting powder mass, powder uniformity and the ability of delivering superfine powders etc. The precision of delivering powders could be within 2% error scope comparing to the desired quality and there is no evident difference between different powder feeder units. So the flexible proportion of mixture can be easy changed in the computer control program (Fig. 5) by synchronously controlling the powder feeder rotation speed.
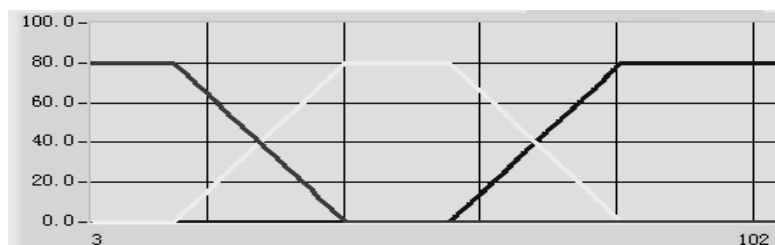
Figure 5: Schematic drawing of mixture powder feeding.

5. CONCLUSIONS

An approach to delivering multi-varieties powder precisely for electromagnetism compressed FGM component fabricating is presented. The apparatus unit is based on the timing belt driving and Pneumatic conveying principle. The feeding control hardware circuit was based on ADUC812 with appended TLC5620 D/A converter. The Superior computer control program was based on lab windows/CVI program developing environment with good man-machine conversation interface. Experiments results showed that powders mixtures obtained from the device are continuous and stable. The precision of delivering powders mixture can be within 2% error scope comparing to the desired mixture quality and the flexible proportion of mixture can be easy changed in the computer control program by synchronously controlling the powder feeder rotation speed to satisfying the need of FGM component fabricating.

REFERENCES

1. Banks, L., R. Eliasi, and Y. Berlin, "Modeling of functionally graded materials in dynamic analyses," *J. Composites Part B: Engineering*, Vol. 33, 7–15, 2002.
2. Griffith, M., D. M. Keicher, and C. L. Atwood, "Freeform fabrication of metallic components

using laser engineered net shaping (LENS)," *Proceedings of the Solid Freeform Fabrication Symposium*, 125–131, University of Texas at Austin, 1996.

3. Lewis, G., J. Milewski, and D. Thoma, "Properties of near-net shape metallic components made by the direct light fabrication process," *Proceedings of the Solid Freeform Fabrication Symposium*, 513–520, University of Texas at Austin, 1997.

4. Karen, M. B. and R. Taminger, "An electron beam freeform fabrication a rapid metal deposition process: A rapid metal deposition process," *Proceedings of the 3rd Annual Automotive Composites Conference*, 9–10, 2003.

5. Zhang, H., J. Xu, and G. Wang, "Fundamental study on plasma deposition manufacturing," *Surf. Coat.*, Vol. 171, 112–118, 2003.

6. Karapatis, N. P., J. P. Griethuysen, and R. Glardon, "Direct rapid tooling: A review of current research," *Rap Proto J.*, Vol. 4, 77–89, 1998.

Research on Relationship between arc Length and arc Voltage in the Plasma Deposition Manufacture Process

Haiou Zhang[1], Chao Wang[1], Guilan Wang[2], and Hui Ai[2]

[1]School of Mechanical Engineering
Huazhong University of Science and Technology, Wuhan 430074, China
[2]School of Materials Science and Engineering
Huazhong University of Science and Technology, Wuhan 430074, China

Abstract— The method of direct rapid metal prototyping and tooling can sharply shorten the lead-time and reduce the cost of product development, therefore it become the key technology in the RP&M. In this field, PDM (Plasma Deposition Manufacture) technology, based on low-cost and high efficiency plasma power resource caused attention. This paper analysis the present status of direct rapid metal prototyping by PDM technology, discusses how to control the process parameters in the molding process and the relationship between arc length and arc voltage. Experiments demonstrate that the hardware scheme is suitable for the friendly open system with satisfied operation and maintainability. In other hand, as it is difficult to measure the deposition height directly in the PDM process, a method for measuring deposition height by monitoring arc voltage is proposed because of the arc voltage is linear with arc length.

1. INTRODUCTION

The PDM (Plasma Deposition Manufacture) technology, based on low-cost and high efficiency plasma power resource, gathers plasma, laser, material, PC, auto-control system and so on. It is a melting accumulated process and the research of deposition height measure is very important in PDM. However, to measure the deposition height directly is difficult, after some experiments. It has been found that the arc voltage is linear with arc length.

2. HARDWARE ARCHITECTURE OF MOVEMENT CONTROL SYSTEM

In this PDM system, "PC+NC (numerical control) card" scheme is designed to realize movement control. It adopts PMAC movement card as core controller and Industrial Personal Computer (IPC) as host machine. The PMAC card's main function is interpolation, position control, handing velocity, PLC and other real time control. The main achievement of IPC is management function, it's also support using software to change CNC system's interface, graphic display, dynamic simulation, NC program, fault diagnose and so on. PMAC card is plugged in the PCI bus slot, the interface card transfers and isolate signal of the NC control informationfeedback information and PLC control information. Most of the hardware of NC system adopts common computer hardware except PMAC movement controller.

The PMAC can work independently. It can obey orders of the host machine too. To communication with the host machine it can use serial port or by the way of bus. When communicating through bus, it can also lead interrupt to host machine, therefore, to achieve flexible and effective management is possible. The PMAC movement control card in which the system is used have servo loop and calculate, IO function, memory management and PLC function.

Figure 1 shows the 5 Axis NC systems that this paper describes, it can divided into movement control parts and movement drive parts. The main part of movement parts is movement card, each axis servo equipments are in the drive part. In order to develop high degree of accuracy, high stability NC system, it needs many auxiliary electrical circuits, including power supply module, servo supply module, security loop module, auto zero module etc.

3. DEPOSITION HEIGHT MEASUREMENT

In the process of plasma deposition forming, there are more or less differences between the deposition height of the forming component and the deposition height which is presetting. As the deposition process continues, this deviation will accumulate. Hence, there will be two serious consequences: (1) the parts shape which is forming has large difference with the presetting, it can't meet the challenge. (2) When the multi-layer process is finished. The actual thickness of the Deposition may lower than the preset thickness. As this deviation accumulate, the distant between the deposition parts and
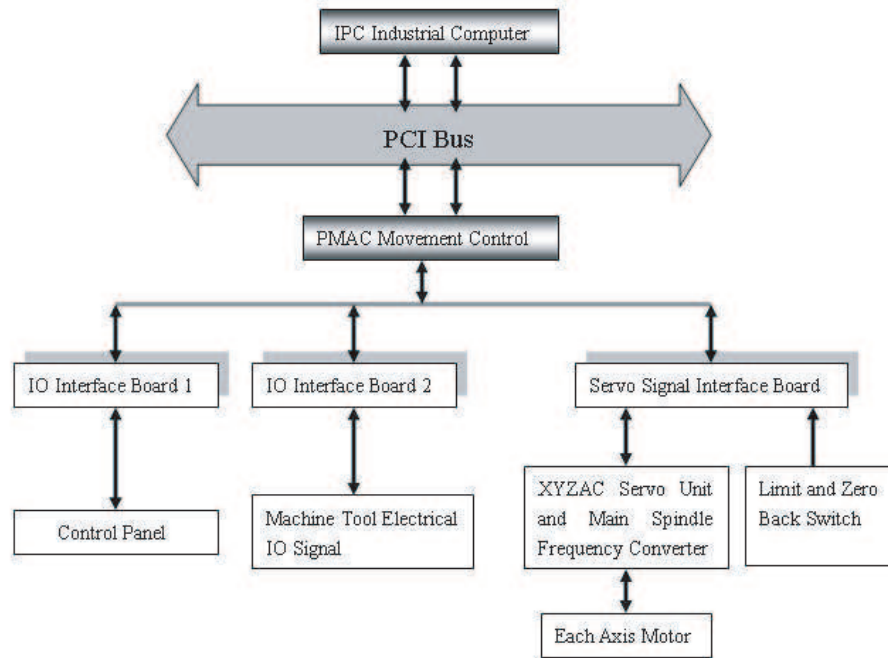
Figure 1: Five axis control system.

the torch will increase, as a result, the arc will be stretched or go out. Therefore, to detect the deposition height is very important. There are some design proposals as follow:

(a) Contact sensor measure

At the present, in contact sensors, the LVDT inductive sensor has high precision, anti –jamming ability. It is flexible, can accurate measure distance, Fig. 2 shows how the contact sensor measure the deposition height, but there are three problems in this method measuring the deposition height. (1) In the deposition process, the temperature is very high (often 800°C above), When using this method, the probe will distort or damage, the output of the measuring signal will distort. (2) The contact sensor can only measure single-point. Because of the difference between the parts, the deposition path is changing. Since putting the contact sensor behind the molten pool is very difficult, this method is difficult to measure the actual height. (3) Due to the high temperature of the molten pool, real time tracking molten pool is very difficult to measure the deposition height. Deposition forming and height measuring can't be simultaneously carried out. Hence, it can't satisfy the real-time requirement of the deposition height measure.

(b) Non-contact measurement

In the field of small distant and high precise non-contact measurement, there are two methods: laser measurement and ultrasonic measurement. Compare to contact measurement, non-contact measurement has many advantages such as the structure is simple, it will not cause interference or influence the deposition process, as the Fig. 3 shows. But the disadvantages can be seen in three aspects. (1) All the non-contact measurement is spot measurement. Because of the change with the deposition path it is hard to measure the resurfacing welding height. (2) Laser measurement has relationship with the surface temperature of the reflecting object and the absorption of objects. If the material to be deposited is different, the temperature is change, using the laser measurement may cause large measurement error. Another non-contact measurement method is ultrasonic measurement. It is greatly affected by the environmental temperature. But in the deposition field, the temperature will achieve more than 1000 degrees. So it is unsuitable to use the ultrasonic measurement method measuring the deposition height.

For the reasons that is analyzed above. We should find a method that it is affected little by environment and the change of path.

One of the important features of plasma arc is it has falling volt-ampere characteristic, it is because in the large current environment, magnet contraction effect will happen. When the current increase, the magnet contraction effect will be enhance. Also the ampere density and the arc temperature will increase. As a result, the arc resistance will decrease. The arc voltage will drop with the increasing current. Hence, the falling volt-ampere characteristic curved line will appear.
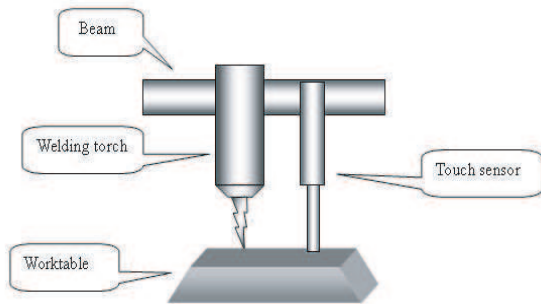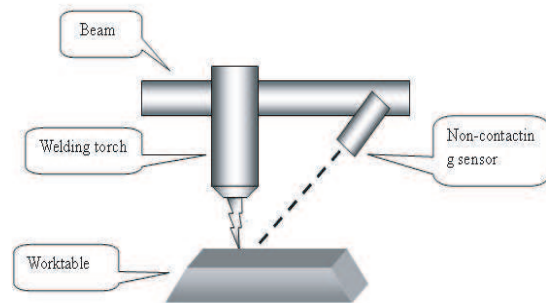
Figure 2: Touch sensor instrumentation plan.

Figure 3: Non-contacting sensor instrumentation plan.

But no all the situations are like this. When the current increase to a certain value, even or ascending volt-ampere characteristiccurved line will appear. Further more, in terms of the change of current will cause the change of arc resistance, the electric arc resistance is proportional to the arc stream. It's inversely proportional to the product of cross section of arc stream and electrical conductivity. It can be represented by

$$R = \frac{l}{\rho \cdot S} \tag{1}$$

where l is the arc length, ρ is the electrical conductivity of arc stream, S is the cross section of arc stream, R is the arc resistance.

Because of ρ and S is the function of current, so the arc resistance R can be represented by the function of current.

$$R = cf(I) \tag{2}$$

In order to conveniently analyze, it can be approximately represent by

$$R = \frac{c}{I^d} \tag{3}$$

where c and d are constant, so the voltage is $V = IR = cI^{(l-d)}$.

If the index $d > 1$, the current will increase and the arc voltage will decrease, the falling volt-ampere characteristic will be formed; If the index $d \approx 1$, the arc voltage will not change with the current, the even falling volt-ampere characteristic will be formed; If the index $d < 1$, the arc voltage will increase with the raise of current. The ascending falling volt-ampere characteristic will be formed.

The major elements that affect the volt-ampere characteristic of plasma arc are as follow: working gas flowphysical dimension of nozzle, arc length and the type of working gas etc. When the other parameters of plasma arc are kept constant, only increase the gas flow, the voltaic arc will rapid cooling, the compression degree of voltaic arc will increase, the cross section of arc stream will be thinner, the voltage of arc will rise. So the airstream will increase, as a result, the volt-ampere

The effects of airflow stress on VA characteristic.

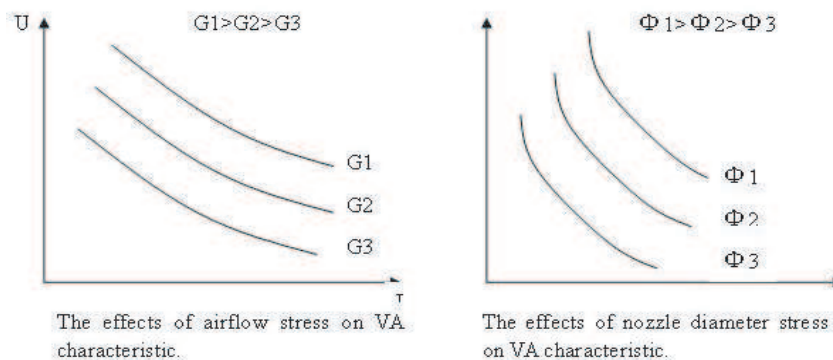The effects of nozzle diameter stress on VA characteristic.

Figure 4: VA characteristic curve.

characteristic will move to the upper right corner. But the increase of airstream should have certain restrictions, unless it will lead to decreased efficiency or extinguish voltaic arc.

The physical dimension of nozzle is nozzle pore diameter, channel length and compressed angle of nozzle. When other condition unchanged, decrease the pore diameter of nozzle or increase the channel length of nozzle and decrease the compressed angle of nozzle can lead the volt-ampere characteristic to the upper right corner. It is because that the compress and the cooling of arc stream are enhanced so that the arc stream will be thinned, the voltage will rise, as Fig. 4 shows.

Although many factors have affect the arc length, Include the intensity of current, the airflow and the diameter of the nozzle, but when this changes can be considered to be neglected, the change of arc length will linearly reflect the change of voltage. By measure the change of arc voltage to calculate the arc length, this method provide an important basis for acquire the height of deposition.

4. THE MEASUREMENT OF DEPOSIUTION HEIGHT EXPERIMENT OF PDM SYSTEM

Deposition height is the major token parameter of forming parts. The measure of deposition height is important basis for changing deposition parameter and planning deposition route. As mentioned above, by measuring arc voltage we can indirectly measure the deposition height. Two experiments are as follow. Table 1 shows when deposition current is different, the experiment of changing deposition height and measuring arc voltage data. Fig. 5 shows the line chart of this relationship. Table 2 shows when deposition height is different, the experiment of changing current intensity and measuring arc voltage data. Fig. 6 shows the line chart of this relationship.
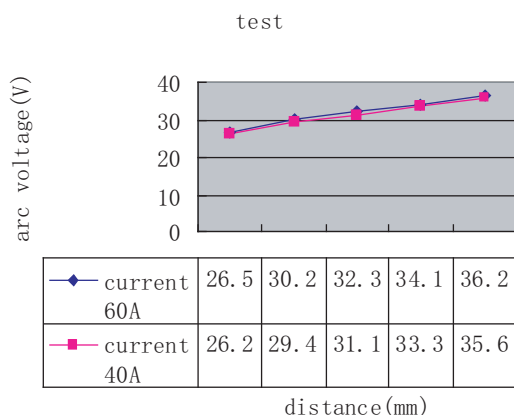
Figure 5: Test ling chart.
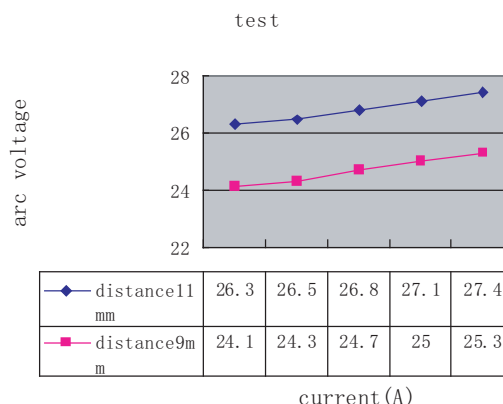
Figure 6: Test ling chart.

Table 1: The test of Arc voltage data.

Current (A)	Deposition interval (mm)	Arc voltage (V)	Current (A)	Deposition interval (mm)	Arc voltage (V)
40	9	26.2	60	9	26.5
40	11	29.4	60	11	30.2
40	13	31.1	60	13	32.3
40	15	31.3	60	15	34.1
40	17	35.6	60	17	36.2

It can be seen from the graph that the current intensity has little effect on the arc voltage. And it is approximately linearly proportional with the deposition height. This system uses the method which measures the arc voltage and according to current to do compensation to indirect measures the current deposition height. Fig. 7 is a diagram of computing deposition height.

From the graph it can be seen, where H is the actual height of deposition parts. H_S is the distance between nozzle and base plate. D_R is the actual interval between deposition part and

Table 2: The test of Arc voltage data.

Deposition interval (mm)	Current (A)	Arc voltage (V)	Deposition interval (mm)	Current (A)	Arc voltage (V)
9	40	26.2	9	40	26.2
11	40	29.4	11	40	29.4
13	40	31.1	13	40	31.1
15	40	31.3	15	40	31.3
17	40	35.6	17	40	35.6
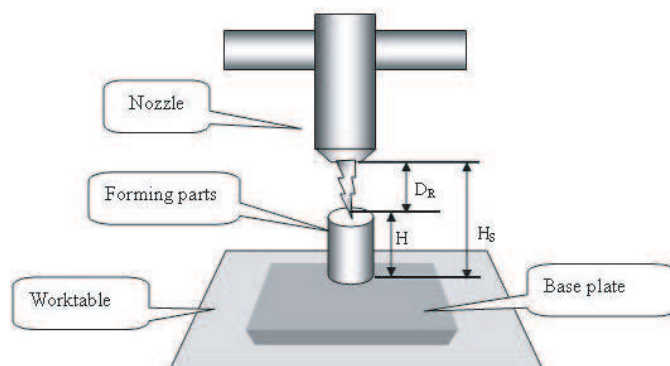
Figure 7: Deposition height computing diagram.

nozzle. Hereby, better measuring results can be acquired.

$$H = H_S - D_R \qquad (4)$$

5. CONCLUSION

This paper discusses how to control the process parameters in the molding process and the relationship between arc length and arc voltage. A method of measuring deposition height is developed in direct rapid metal prototyping and tooling. According to the quantitative relationship between arc voltage and arc length, the deposition height can be indirectly computed by experimental verification which measure the arc voltage to obtain arc length data. In the manufacture process, the metal prototyping and tooling height and other parameters including melting temperature, melting poor shape could be collected in due course and transmitted to IPC (industry PC). And then, according to these data, IPC might modulate movement track and deposition parameter to insure metal prototyping and tooling shape and performance.

ACKNOWLEDGMENT

REFERENCES

1. Hao, G., Q. S. Han, and Z. Y. Sun, *Research on Open CNC System Based on PMAC*, BJ. Ins. Mach., Vol. 18, No. 2, 24–28, 2003.
2. Zhang, F. J., *The Development and Advance Study of LabWindows*, Beihang University, Beijing, 2001.
3. Zhang, Y. G., *Programming Guide of Virtual Instrument Developing Environment LabWindows/CVI6.0*, China Machine Press, Beijing, 2002.
4. Song, Y. A., A. Park, and H. Jee, "3D welding and milling — A direct approach for fabrication of injection molds," *Proceedings of Solid Freeform Symposium*, 793–800, 1999.

Research of Electromagnetic Effects on the Compound Arc Beam in the Hybrid Plasma-laser Manufacturing Process

Ying-Ping Qian[1], **Hai-Ou Zhang**[2], **Gui-Lan Wang**[3], **and Guangchao Han**[4]

[1]School of Mechanical Engineering, Hubei University of Technology, 430068, China
[2]School of Mechanical Engineering, Huazhong University of Science and Technology, 430074, China
[3]School of Material, Huazhong University of Science and Technology, Wuhan 430074, China
[4]China University of Geosciences, China

Abstract— In this paper, the mechanism of electromagnetic influence on the compound arc column is analyzed theoreticly, and the influence rule of electromagnetic on the compound arc beam is studied experimentally. The experimental results show that the compound arc column can absorb electromagnetic waves, and electromagnetic waves can compress the compound arc column. The compound arc column can maintain the same patterns only when the magnetic compressure and the expansive power outward are balance.

1. THE PRINCIPLE OF HYBRID PLASMA-LASER DEPOSITION MANUFACTURE (PLDM)

The principle of PLDM technology is shown in Fig. 1. The shape, dimension and function of the conception model are gained by means of concept design, and then workout a CAD model with the help of shaping software. According to the requirement of the component's dimensional accuracy, the CAD model is dealt with slices and transferred into an STL document. In accordance with the shape of every layer, the control system draws up to route, generates the CNC code to control the movement of the NC machine [1–4]. On the one side of the plasma arc, the laser beam is focused on the plasma arc into the molten pool through adjusting the optical path for light transmitting and focusing. The deposition and shaping are then carried out under the control of the parameters such as movement of sending powder system, plasma arc-stream, shielding gas flow, sending powder gas flow, electric current according to the precious design. The high-temperature alloy powder is sent to the pool to melt and solidify into a compact metal layer rapidly then continues repeating the lamination until the entire three-dimensional component's layers are formed.
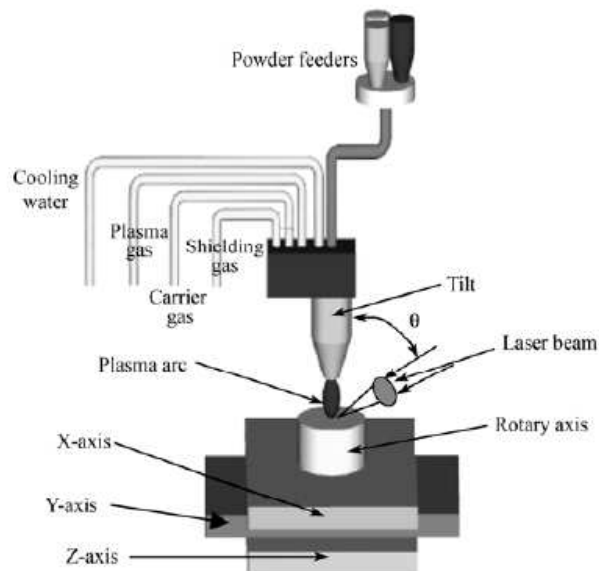

Figure 1: Schematic representation of the PLDM process.

2. THE CHARACTER OF THE COMPOUND ARC BEAM

The compound arc column is most plasma arc beam. Plasma is a kind of ionization gas which composes of a great deal of free electron and ion and behave whole electricity neuter, which is the fourth state except solid, liquid and gas. Simply speaking, plasma is a kind of high ionization gas. And high ionization means that the density of the electrification particle is enough high and the interaction of the positive and negative charged particle is quite strong. Commonly, the generation of the plasma is a complicated process which relate to many classical gas discharge theory, experiments, the atom microcosmic process and exterior effect. In addition, the producing way of the plasma sometimes close connects the plasma's restriction and application. The mainly mechanism of the plasma production include ionization caused by heating, gas discharge and the laser induction.

3. THE MAGNETISM SHRINK EFFECT OF THE COMPOUND ARC BEAM

In the compound arc beam, the plasma take up the finity area and keep the column, this is called the linear plasma column as Fig. 2. The angle magnetic field which circle itself will produce when mightiness electric current pass the plasma along the axis direction. The magnetic field interacts with the rapidly moving particle, which makes the plasma pressure increasing and the column radial decreasing. Appearancely, the plasma beam can reach balance till the plasma pressure is equal to the magnetism pressure [5].
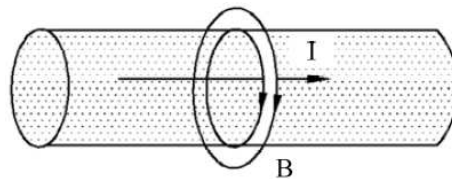
Figure 2: The balance of the linear plasma.

The balance factor of the linear shrinkage plasma is following:

$$<P> + \frac{<B_{zi}^2>}{2\mu_0} = \frac{B_{ze}^2}{2\mu_0} + \frac{B_{\theta e}^2}{2\mu_0} \tag{1}$$

Thereinto:

$$<P> = \frac{1}{\pi a^2} \int_0^a P(r) 2\pi r dr \tag{2}$$

$$<B_{zi}^2> = \frac{1}{\pi a^2} \int_0^a B_z^2(r) 2\pi r dr \tag{3}$$

In the formula, μ_0 is the magnetic conductivity in vacuum, B_{zi} and B_{ze} parting denote the inside and outside magnetic field intensityof plasma along the axial direction, $B_{\theta e}$ denotes the outside angle magnetic field intensity of plasma, P denotes the plasma pressure. The left of the formula (1) denotes the inner pressure and the average magnetic field intensity of the plasma beam. The right of the formula (1) denotes the external column axial direction and angle direction magnetism pressure. The balance condition shows, when the inside and outside plasma beam total magnetism pressure are equal, the plasma beam will reach balance.

When electric current flow through the parallel conducting wire, they will attract for each other. If regards the voltaic arc beam as numberless conducting wire with electric currents, and every conducting wire will receive a larenz force which produced by magnetism caused by electric current. Direction of Larenz force will attract for each other and towards the center of arc column, which like as a hank wire will become tighter more and more when electric current pass through, and the arc column diameter will decrease because of the self-magnetic compression.

The element force balance equation of arc column is following:

$$\frac{dP}{dr} + j_z \cdot B_\Phi = 0 \tag{4}$$

Thereinto P is the barometric pressure, j_z is axial direction electric current, B_Φ is the arc column self-magenetic field strength, and it always point to the tangential direction, and $j_z \cdot B_\Phi$ delegate the Lorenz power, the physical significance of the force balance equation formula (4) is that the Lorenz power in the arc column will be balanced by the pressure gradient. Because of the Lorenz power is centripetal, the result that the arc column center pressure is inevitable greater than the other place's pressure can be gained easily from the formula (4).

Because the arc column is pillar symmetrical, the relationship of magnetic density and electric current can be get by the Ampere's law as following:

$$\oint_l B \cdot dl = \mu_0 \sum I \tag{5}$$

Thereinto, μ_0 is vacuum magnetic permeability, $\sum I$ is the the electric current algebraic sum included in the closed circuit l. If make l as a circle with radius r, then the B and dl have the same direction, and $|B| = B_\Phi$, and they remain the constants in the circle, so the formula (5) can be predigested as the following:

$$B_\Phi = \frac{\mu_0}{r} \int_0^r j_z dr \tag{6}$$

To get the formula (2)–(4) substitude the formula (2)–(6):

$$dP = -\mu_0 \left(\frac{j_z}{r} \int_0^r j_z r dr \right) dr \tag{7}$$

To get the pressure p integrate from arc column edge to the interior, the edge pressure of the arc column should be the environmental pressure P_0, so:

$$P(r) - P_0 = -\mu_0 \int_{r^*}^r \frac{j_z}{r} \int_0^r j_z r dr \tag{8}$$

That is:

$$\Delta P(r) = -\mu_0 \int_{r^*}^r \frac{j_z}{r} \int_0^r j_z r dr \tag{9}$$

Thereinto, $\Delta P(r) = P(r) - P_0$ means the pressure increasing generated along the radial direction r because of the self magnetic compression. The formula (9) shows the relationship of the one dimention arc column self magnetism compression, appending pressure, the arc column diameter and the electric current. If the electric current density distributing form can be got, the relationship of the appending pressure of self magnetism compress and the electric current of arc beam can be gained too. Supposing the electric current density in the arc column is constant, ViZ.:

$$j_z = \frac{I}{\pi r_*^2} = const \tag{10}$$

The formula (9) simplified as following:

$$\Delta P(r) = \frac{\mu_0}{4\pi} \frac{I^2}{\pi r_*^2} \left(1 - \frac{r^2}{r_*^2} \right) \tag{11}$$

Supposing the arc column electric current density distributed like the parabola:

$$j_z = j_m \left(1 - \frac{r^2}{r_*^2} \right) \tag{12}$$

The formula (9) simplified as following:

$$\Delta P(r) = \frac{5}{3} \frac{\mu_0}{4\pi} \frac{I^2}{\pi r_*^2} \left(1 - \frac{12}{5} \frac{r^2}{r_*^2} + \frac{9}{5} \frac{r^4}{r_*^4} - \frac{2}{5} \frac{r^6}{r_*^6} \right) \tag{13}$$

In the arc column axis:

$$\Delta P(r) = \frac{5}{3} \frac{\mu_0}{4\pi} \frac{I^2}{\pi r_*^2} = \Delta P_{\max} \tag{14}$$

Above several expressions show that the self magnetism compress appending pressure and arc current's square have the direct ratio arelationship, and inverse proportion to the arc radius square, the appending pressure in the arc axes are will become higher with the electric current density distribute more steeper.

4. THE EXPERIMENT OF LASER INFLUENCE ON THE APPEARANCE OF THE COMPOUND ARC COLUMN

The appearance of plasma arc beam changed with the laser average power under the condition that the repeat frequency is 50 Hz and the pulse width is 1.0 ms is shown as Fig. 3. The relationship between plasma arc characteristic and laser average power is shown as Fig. 4. It is clear that the plasma arc is becoming smaller when the laser average power is increasing, which means that the laser has the compression effect on the plasma arc. The reason is that the increase of the laser average power makes the energy absorbed by the plasma arc increase, improves ionization and magnetic effect compression, and then results in the reduction of the plasma arc diameter.
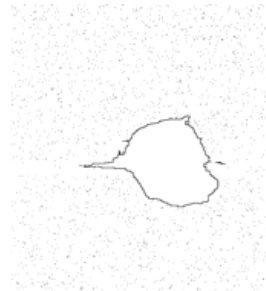
(a) The appearance of the single plasma arc beam

(Left: the original arc image. Right: the image figure)
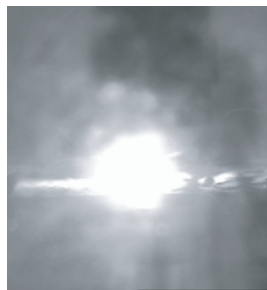
(b) The hybrid arc beam appearance under the condition of average power 4 W

(Left: the original image. Right: the image figure)
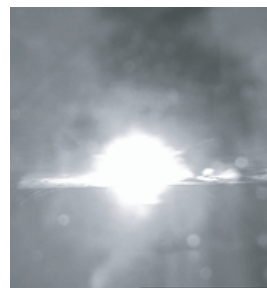
(c) The hybrid arc beam appearance under the condition of average power 39 W

(Left: the original arc image. Right: the image figure)

(d) The hybrid arc beam appearance under the condition average power 91 W

(Left: the original arc image. Right: the image figure)

(e) The hybrid arc beam appearance under the condition of average power 160 W

(Left: the original arc image. Right: the image figure)

(f) The hybrid arc beam appearance under the condition of average power 254 W

(Left: the original arc image. Right: the image figure)

Figure 3: The hybrid arc beam appearance under the condition of different laser average power (laser repetition frequency: 50 Hz, laser pulse width: 1.0 ms).
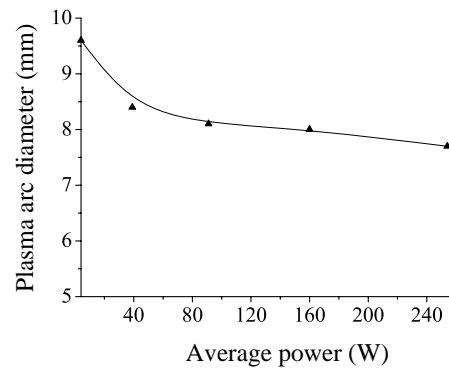
Figure 4: The relationship between laser average power and plasma arc diameter.

5. CONCLUSION

(1). Self magnetism compress appending pressure and arc current's square have the direct ratio arelationship, and inverse proportion to the arc radius square, the appending pressure in the arc axes are will become higher with the electric current density distribute more steeper.

(2). Only when the magnetic compression strength and the compound arc column outward expansion power are balance, the arc column can maintain a certain form of the same shape.

(3). The plasma arc is becoming smaller when the laser average power is increasing.

ACKNOWLEDGMENT

REFERENCES

1. Zhang, H., G. Wang, and Y. Luo, "Rapid hard tooling plasma spraying for injection molding and sheet metal forming," *Thin Solid Films*, Vol. 390, 7–11, 2001.
2. Chen, Y. B., J. Chen, L. Q. Li, et al., "Properties of arc and weld in laser-TIG hybrid process," *Transactions of the China Welding Institution*, Vol. 24, No. 1, 55–56, 60, 2003.
3. Chen, Y. B., L. Q. Li, and F. D. Chen, "Effect of laser-supported combustion on laser-TIG hybrid heat source," *Journal of Harbin Institute of Technology*, Vol. 35, No. 6, 695–697, 2003.
4. Wang, H. M., "Research progress on laser surface modifications of metallic materials and laser rapid forming of high performance metallic components," *Acta Aeronautica Etastronautica Sinca*, Vol. 23, No. 5, 473–478, 2002.
5. Sun, X., *Plasma and Application*, 1–106, Publishing Company of High Education, Beijing, 1983.

Multi-axis Path Planning for Electromagnetic-compressed Plasma Deposition Manufacturing Based on STL Format

Haiou Zhang[1], Jiang Jiang[2], Guilan Wang[2], Xinhong Xiong[2], and Guangchao Han[3]

[1]State Key Laboratory of Digital Manufacturing Equipment and Technology
Wuhan 430074, China
[2]State Key Laboratory of Plastic Forming Simulation and Die & Mould Technology
Wuhan 430074, China
[3]China University of Geosiences, China

Abstract— Super alloy was widely used in a variety of industry field such as aeronautics and astronautics, and plasma deposition manufacturing has provided an effective way in fabricating refractory and intractable parts e.g., super alloy parts directly from their digital models. However, there is much difficulty in fabricating parts with large obliquity because of the flowing of molten pool caused by gravity field. In this paper, an innovated method named electromagnetic-compressed plasma deposition manufacturing is presented which employs the electromagnetic field to decrease the effectiveness of the flowing of molten pool. The result shows that the complicated parts with big overhang structure and large obliquity could be fabricated under proper tool path and the help of electromagnetic. Some parts with complex shape were trial manufactured which proves that electromagnetic-assisted plasma deposition manufacturing is a promising technology in direct rapid manufacturing.

1. INTRODUCTION

Super alloy, a kind of refractory and intractable material, was widely used in industry, and plasma deposition manufacturing, one of the Solid Freeform Fabricating (SFF) technologies, has provided an effective way in fabricating parts made of super alloy with the help of the electromagnetic-compressed plasma arc. However, complex parts with overhang structure are often difficult to fabricate without support. P. Singh and D. Dutta [1] proposed a customized deposition system named Compliant Parallel Kinematical Machine (CPKM) and Multi-Direction Slicing (MDS) method to minimize the support structure. Jun Zhang and Frank Liou [2] investigated an adaptive slicing technology in which the slicing direction varied according to the normal vectors of the solid surface and the deposition of some overhang structure could be achieved based on two presented methods named "Transition Wall" and "Surface Tension". Jianzhong Ruan [3] et al. proposed a multi-axis slicing method to search the slicing direction based on centroidal axis computation. R. Dwivedi and R. Kovacevic [4–6] developed the Laser-based multi-axis direct metal deposition (LBDMD) technology in which the skeleton of the complex part is utilized to specify its building direction.

Electromagnetic-compressed plasma deposition manufacturing [8, 9], which employs the electromagnetic field to decrease the effectiveness of the flowing of molten pool, belongs to 3D welding and milling. This technique is characterized by the supply head delivering a well-defined flow rate of metal powder, which is deposited in the molten pool formed by controlled plasma heating. After deposition of a single layer, the powder delivery nozzle is incremented in the building direction, and another layer is deposited. Milling is intermittently adopted to remove the excessive portion of one or more deposited layers of the materials. Thereby, fully dense parts with the single or multifarious materials can be built up, layer by layer, by melting and rapid solidifying the feed material into the desired shape. Fig. 1 is the sketch of electromagnetic-compressed plasma deposition manufacturing system. This system is comprised of two sub-systems. One is electromagnetic-compressed plasma arc deposition system, the other is milling system. The whole system is established on a five-axis kinematical platform which consists of three linear axes (X, Y, Z) and two rotating axes (A, C) associated with a dual-axis rotary-tilting table.

Although many ways and means with great value have been suggested in the multi-axis path planning, they always belong to laser cladding; less literature has been found on multi-axis plasma arc deposition. Since the electromagnetic-compressed plasma deposition manufacturing is a kind of special technology which is based on "Slicing & Deposition", there must be always physical existence of a substrate as a "base" on which the materials can be deposited. In other words, "don't use support" mentioned above doesn't mean there is no support material under the subsequent layers, whereas the previously deposited layers always play a "support" role to prop the subsequent layers

from below. Hence, the principle of multi-axis strategy of electromagnetic-compressed plasma deposition manufacturing is to maintain the support relationship between the previously deposited layers and subsequent layers at any time in the fabrication process with the help of the kinematical system.
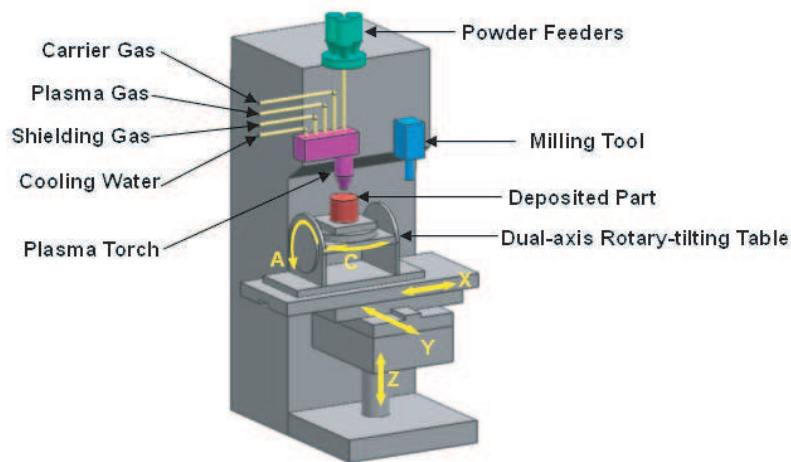
Figure 1: The sketch of electromagnetic-compressed plasma deposition manufacturing system.

2. STRATEGY OF PATH PLANNING FOR ELECTROMAGNETIC-COMPRESSED PLASMA DEPOSITION MANUFACTURING

In the path planning of SFF process, a STL model is usually adopted which is all comprised of small triangle faces. Each triangle face consists of four elements — three vertex of triangle and one normal vector of the face. In SFF process, slicing is the process that is represented as a set of layers formed by "slicing" a CAD model with a set of horizontal planes. The distance between planes is called "layer thickness". Differences in quality can be achieved by controlling the layer thickness. Research on 2.5D slicing procedures and deposition tool path for layered manufacturing processes has been widely conducted [3]. And in this paper, the multi-axis strategy will be emphasized.

After STL model is sliced, the 3D contour is generated which consists of the rings in the slicing plane and a set of surface normal vectors obtained by the intersection of the slicing plane with STL model.
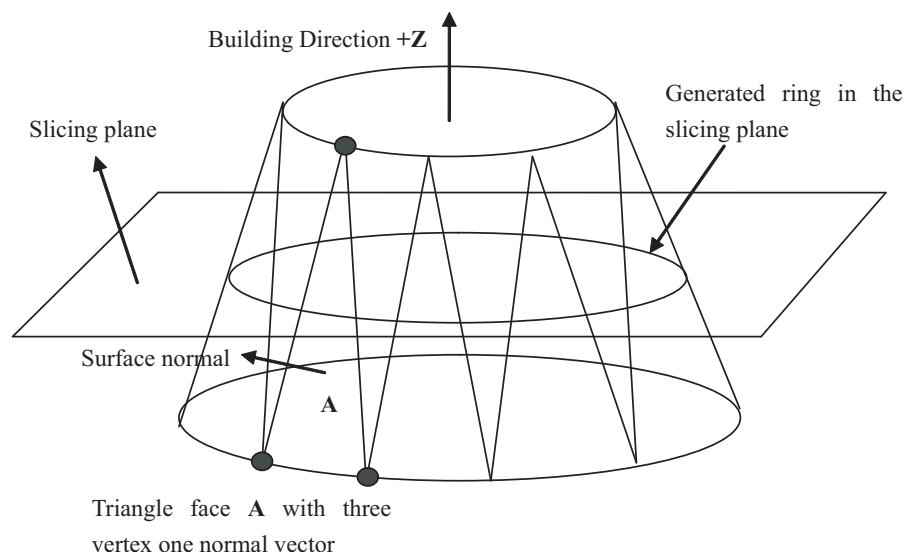
Figure 2: The sketch of STL model with triangle faces.

In some complex parts with large overhang structure, the deposition can't be achieved in the

$+Z$ building direction because of the flowing of molten pool caused by gravity field. So the torch direction should be adjusted during the process.

As it's shown in Fig. 3, V_{f1} and V_{f2} are the surface normal vectors of the STL model. Since the STL model is provided with large obliquity, the part can't be fabricated along the building direction. Whereas, the torch direction varies in a single layer which is vertical with respect to the surface normal vector. In Fig. 3, V_{t1} and V_{t2} are the vectors which represent the torch direction. It can be seen that when the path is along a certain segment $\boldsymbol{AB}$, the torch direction along V_{t1} is constant but lean to the $+Z$ direction. Each segment has its own torch direction in the deposition path. However, the transition between adjacent segments should be continuously. Thus, V_{i1} and V_{i2} are the interpolated vectors to keep the nozzle transforming from one direction to another continuously and stably. Therefore, the torch direction is kept changing in a single layer until the deposition is finished. So the five-axis path (Location Point) can be listed as follows:

$$(A_x, A_y, A_z, V_{t1_i}, V_{t1_j}, V_{t1_k})$$
$$(B_x, B_y, B_z, V_{t1_i}, V_{t1_j}, V_{t1_k})$$
$$(B_x, B_y, B_z, V_{i1_i}, V_{i1_j}, V_{i1_k})$$
$$(B_x, B_y, B_z, V_{i2_i}, V_{i2_j}, V_{i2_k})$$
$$\cdots$$
$$(B_x, B_y, B_z, V_{in_i}, V_{in_j}, V_{in_k})$$
$$(B_x, B_y, B_z, V_{t2_i}, V_{t2_j}, V_{t2_k})$$
$$(C_x, C_y, C_z, V_{t2_i}, V_{t2_j}, V_{t2_k})$$

where (A_x, A_y, A_z) represents the x, y, z components of point $\boldsymbol{A}$ respectively, and $(V_{t1_i}, V_{t1_j}, V_{t1_k})$ represents the i, j, k components of vector V_{t1} respectively.
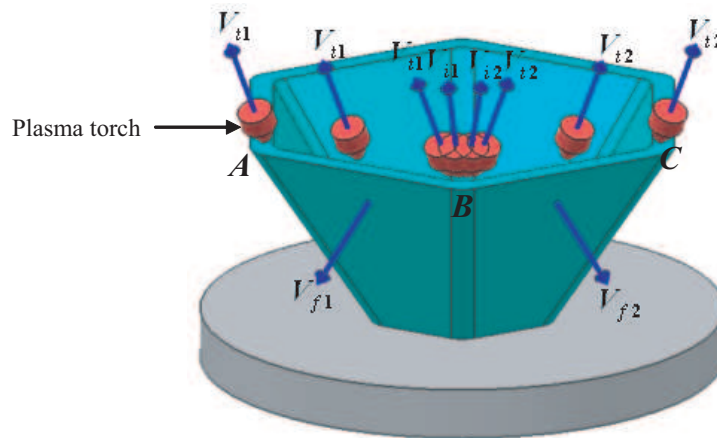
Figure 3: The Sketch of multi-axis strategy in electromagnetic-compressed plasma deposition manufacturing.
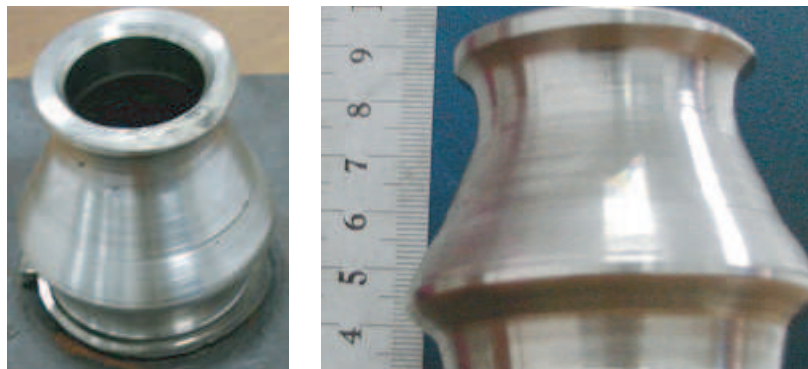
Figure 4: The thin wall sample trial manufactured by electromagnetic-compressed plasma deposition manufacturing.

3. EXPERIMENTAL VERIFICATION

The Fig. 4 above shows a thin wall sample with large obliquity. An initial observation suggests that this structure cannot be built along the $+Z$ direction without a support requirement. Thus, the multi-axis strategy is implemented to treat with this sample and the A axis is oblique to keep the plasma torch direction vertical with respect to the surface normal vector during the whole manufacturing process.

4. CONCLUSION

A new method named electromagnetic-compressed plasma deposition manufacturing is proposed which employs the electromagnetic field to decrease the effectiveness of the flowing of molten pool and adopts five-axis deposition strategy in fabricating super alloy parts with large obliquity. With the help of the electromagnetic field and five-axis deposition strategy, a thin wall sample with large overhang structure was successfully fabricated. The experiment result shows that electromagnetic-compressed plasma deposition manufacturing is capable of fabricating or depositing structures along multi-directions and it's also a valuable technology by which the super alloy parts with overhang structures can be fabricated directly from their digital models.

REFERENCES

1. Singh, P. and D. Dutta, "Multi-direction slicing for layered manufacturing," *Journal of Computing and Information Science and Engineering*, Vol. 2, 129–142, 2001.
2. Zhang, J. and F. Liou, "Adaptive slicing for a multi-axis laser aided manufacturing process," *Journal of Mechanical Design*, Vol. 126, 254–261, March 2004.
3. Ruan, J., T. E. Sparks, A. Panackal, et al., "Automated slicing for a multiaxis metal deposition system," *Journal of Manufacturing Science and Engineering*, Vol. 129, 303–310, April 2007.
4. Dwivedi, R. and R. Kovacevic, "An expert system for generation of machine inputs for laser-based multi-directional metal deposition," *International Journal of Machine Tools & Manufacture*, 1811–1822, Vol. 46, 2006.
5. Dwivedi, R., S. Zekovic, and R. Kovacevic, "A novel approach to fabricate uni-directional and branching slender structures using laser-based direct metal deposition," *International Journal of Machine Tools & Manufacture*, 1–11, 2006.
6. Kovacevic, et al., System and method for fabricating or repairing a part, United States Patent, No. 7020539, 2006.
7. Dwivedi, R. and R. Kovacevic, "Process planning for multi-directional laser-based direct metal deposition," *Proceedings of the Institution of Mechanical Engineers, Journal of Mechanical Engineering Science*, Vol. C219, 695–707, 2005.
8. Zhang, H.-O., X.-H. Xiong, G.-L. Wang, et al., "Direct manufacturing technology of metal parts by hybrid plasma deposition shaping and milling finishing," *China Mechanical Engineering*, Vol. 16, No. 20, 1863–1866, 2005.
9. Zhang, H.-O., X.-H. Xiong, and G.-L. Wang, "Directly manufacturing of superalloy double integrated impeller by hybrid plasma deposition & milling," *China Mechanical Engineering*, Vol. 18, No. 14, 1723–1726, 2007.

Integrated Robotic Plasma Spraying System for Advanced Materials Processing

Weisheng Xia[1,2], **Haiou Zhang**[2], **Gui-Lan Wang**[1],
Yunzhen Yang[1], **Guangchao Han**[3], **and Haiping Zou**[1]

[1]State Key Laboratory of Materials Processing and Die & Mould Technology
Huazhong University of Science and Technology, Wuhan 430074, China
[2]State Key Laboratory of Digital Manufacturing and Equipment Technology
Huazhong University of Science and Technology, Wuhan 430074, China
[3]China University of Geosciences, China

Abstract— During atmospheric plasma spraying (APS), to control the time dependent D.C. plasma jet behavior requires the comprehensive understanding of its electric, magnetic, thermal, thermodynamic phenomena. In this paper, influence of particles injection with the form of suspension on the fluctuation of plasma jet is analyzed, and a control approach is presented to eliminate the effect. Moreover, an integrated robotic plasma spraying system for advanced materials processing, i.e., rapid metal tooling and solid oxide fuel cell (SOFC), is developed, which combines a PC-based controller with a six-axis robot. The intelligent adaptive adjustment of robot spraying trajectories and self-dispatch of manufacturing strategies were carried out by the resultant system according to the feedback of the temperature and thickness of sprayed coatings and other information during plasma praying. The flexibility of the forming system was promoted by integrating plasma spray forming with robot motion control. Excellent control performance is observed and this system can be effective to meet the requirements of different materials processing techniques.

1. INTRODUCTION

Atmospheric plasma spraying (APS) has already been applied in widespread industries for a variety of applications due to its low cost and simplicity [1]. It can rapidly manufacture coatings with almost all kinds of materials, such as metals, alloys, ceramics and polymers. Hence, APS has successfully shifted from a traditional technology for surface engineering to a versatile material processing one, and drawn keen attention especially for its noteworthy application of solid oxide fuel cells (SOFCs) [2, 3].

Meanwhile, there is an increasing use of robot in industry domains because of its high flexibility and broad operating region [4, 5]. For further study on rapid tooling using plasma thermal spray technology, we conducted developmental research of combining the industry robotic technology and plasma thermal spray technology to establish integrated robotic rapid spray metal tooling process for manufacturing injection molding tools and sheet metal forming dies.

2. INTEGRATED ROBOTIC PLASMA SPRAYING SYSTEM

2.1. System Design and Setup

As a line-of-sight process, APS can fabricate satisfying coatings with complex geometries through holding spray guns by a robot. It is very easy and simple to generate a spray trajectory or modify processing parameters by using a programmable robot, such as spray angle, spray distance, scanning velocity and step, etc. Moreover, robotic plasma spraying has proved a feasible and high-efficient solution to ensure a high accuracy in process and coating repeatability.

System make-up of robotic plasma spraying system is shown in Fig. 1, which includes plasma jet generator, six-axis industrial robot and turning platform, powder injector, and PC+PLC based control system. Siemens S7-300 PLC was connected to the system through MPI (Multi-Point Interface), and the opening OPC (Ole for Process Control) protocol was applied for the data communication between PC and PLC. Communication between PC and UP-20 robot was established based on the data transmission medium of Ethernet, and the robot control software was developed for the host control and the exchanging of working jobs by PC. PC was chose as the central controller of the system with the help of process monitoring software with COM (Component Object Model) technology to meet with the multiple requirements of process monitoring and processing optimization, information storage, computing resources and so on. Hence, the superiorities of PLC over the stable and safe control of field apparatus and that of PC over process monitoring, data

storage, control algorithm were effectively integrated to enhance the system function. Finally, the robotic plasma spray forming system was established accompanied with forming process monitoring, intelligent adaptive adjustment of robot spraying trajectories, real-time control of robot and other functions. The intelligent adaptive adjustment of robot spraying trajectories and self-dispatch of manufacturing strategies were carried out by the resultant system according to the feedback of the temperature and thickness of sprayed coatings during plasma praying [6].
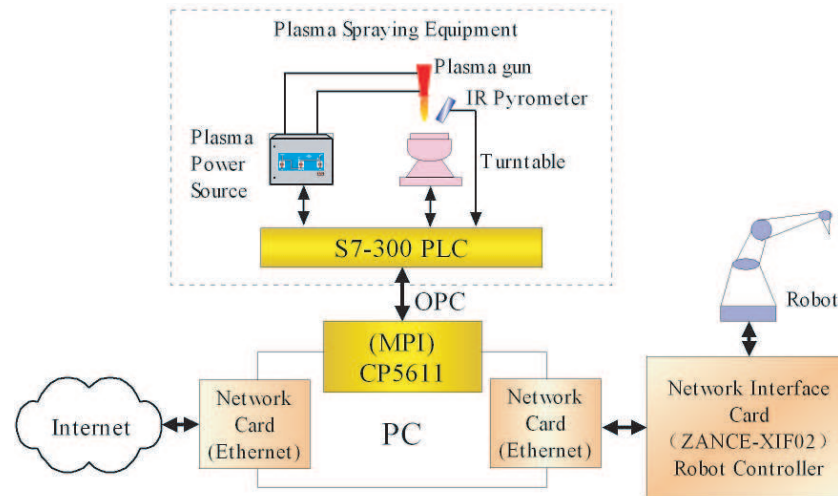
Figure 1: Schematic diagram of robotic plasma spray forming system.

2.2. Influence of Suspension Injection on the Fluctuation of Plasma Jet

During plasma spraying, to control the time dependent D.C. plasma jet behavior requires the comprehensive understanding of its electric, magnetic, thermal, thermodynamic phenomena. The arc fluctuations already have an important influence on particles velocities and temperatures. This influence is by far more important with the suspension injection because fluctuations act on drops or jet penetration, fragmentation, particle trajectories, heating and acceleration. Plasma properties (e.g., velocity, specific enthalpy, gas mass density) vary continuously along the plasma jet radius i.e., along the suspension penetration path toward the plasma jet axis [7]. The instabilities of the arc root of the D.C. torch involve high transient voltage fluctuations and thus dissipated power fluctuations, resulting in plasma jets varying continuously in length and position [8] with strong variations of their velocities in the axial direction.

(a)   (b)
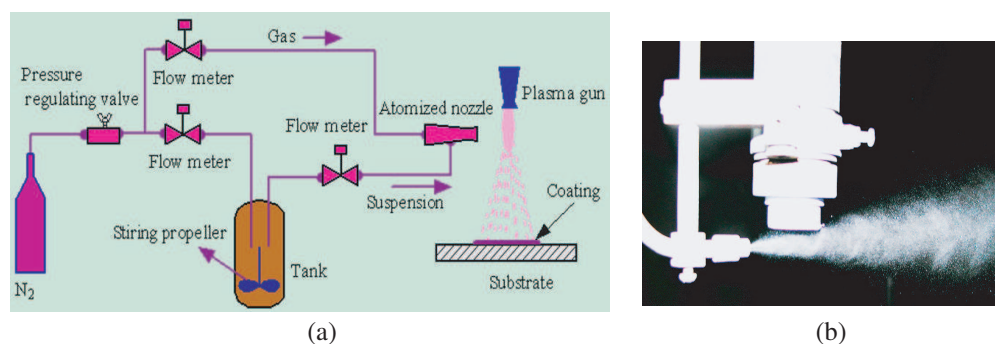
Figure 2: Experimental set-up of (a) SPS and (b) the atomization profile of suspension.

Figure 2(a) presents the scheme of the experimental system for SPS using in this study. The liquid feedstock system is composed of three stainless steel tanks, in which suspensions are stored, and stirred and mixed continually by the propeller fixed in the tank. During the process of SPS, tanks are pressured with compressed air (N_2) monitored and controlled with a rotor flow meter and pressure regulating valve. It is worth noting first that the momentum of the liquid droplets has to be high enough to ensure their penetration into the core of the plasma jet. Hence, the

atomized nozzle was self-designed with three inlets for suspensions and one inlet for the atomizing gas. Picture of suspension drops by the atomized nozzle is shown in Fig. 2(b). Hence, the liquid feedstock system can be used for the SPS process of three different suspension compositions, and the pressure of the tank of the suspension feeders can be varied to modify the drop velocities.

In this paper, images of plasma jet are collected by a charge-coupled device (CCD), and then grey values are calculated through the formal image processing and grey transform, finally, temperature field of plasma jet was obtained through the Abel transformation on the basis of the relationship between the grey value of images and the radiation intensity of plasma jet, which was established through the calibration experiment [9]. From the temperature field information, it is easy to establish optimal processing parameters, and also would further reduce costs and make spraying tooling more attractive, and furthermore, it can keep the forming process and quality of coatings. Different profiles of plasma jet during suspension injection are shown in Fig. 3. After the adjustment, the particle suspension flow fluently from the tank to the injector and it is also easy to penetrate into the center zone of plasma jet. This case is beneficial to enhance the deposition efficiency and the utilization ratio of powders.

(a)   (b)
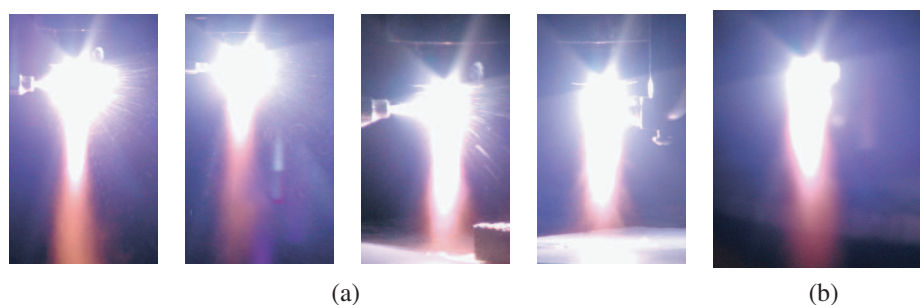
Figure 3: Different profiles of plasma jet influenced by suspension injection (a) during and (b) after adjustment process.

3. ADVANCED MATERIALS PROCESSING

3.1. An Application of SOFC

Figure 4 illustrates the surface line-scan photograph of the planar PEN (Positive-Electrolyte-Negative) coatings. The PEN was composed of anode, graded layer, electrolyte, graded layer and cathode. In the two graded layers between the respective electrode and the electrolyte, the material components gradually vary and every component layers contact tightly. The porosity of the anode graded layer changes gradually from high to low, and the porosity of the cathode graded layer gradually changes from low to high. The thicknesses of the anode, the electrolyte and the cathode are 200, 60, and 100 μm, respectively. In order to avoid increasing the resistance of cell, the graded layer only has the thickness of $20 \sim 30 \, \mu m$. According to the AC complex analysis results and comparison with the electrical conductivity of the PEN without the graded layers, the electrical conductivity of the one with the graded layers increased sharply.
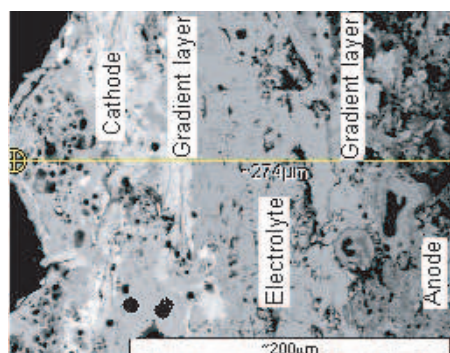
Figure 4: SEM of the planar PEN.

3.2. Rapid Metal Tooling

Rapid metal tooling has received widespread attention because die and mold-making of rapid tooling for both trial and mass production poses a problem in realizing the rapid development of new products. It has been demonstrated that thermal spraying process is an attractive method to manufacture metal molds of any size ranging from small to large.

Our integrated robotic rapid spray metal tooling process was based on the 6-DOF (Degree of Freedom) industry robot. This industrial robot was employed to perform the central content of the rapid metal tooling procedure. First, a ceramic block was fabricated into ceramic prototype mould through robotic milling procedure. Second, the ceramic mould surfaces were coated with iron-nickel-chromium alloy layers by robotic plasma spraying procedure, and then bismuth alloy, which undergoes little thermal expansion, or zinc alloy was cast to make the backup of the sprayed layer. Finally, the ceramic pattern was broken and removed, so that robotic polishing of the sprayed layer proceeded and the completion of the metal tools for injection molding or sheet metal forming was obtained [10].

Using the methods of generating robotic trajectory of milling, spray and polishing, the iron-nickel-chromium alloy spray automobile cover components die mould was experimentally made. Fig. 5 shows model and mould pictures of integrated robotic plasma spraying metal tooling process. The fabricated mould can satisfies the craft forming request completely.

(a)   (b)   (c)
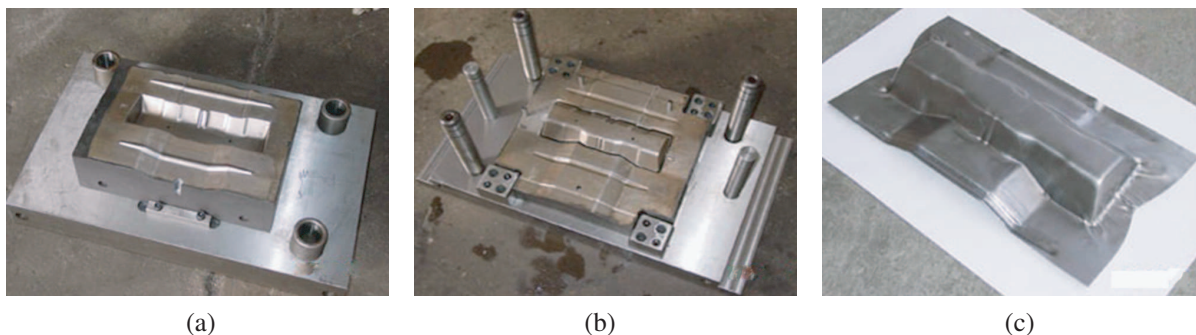
Figure 5: (a) Concave mould, (b) protruding mould assembling chart and (c) the product of the car panel.

4. CONCLUSIONS

1) In order to improve the process quality and reliability of plasma spray, an integrated RPS system is developed, which provides users with the high quality of spraying forming and coatings. This system can meet the requirement of advanced materials processing, and also has satisfying operation and fine control effects.

2) A control approach is presented to eliminate the influence of suspension injection on the plasma jet. It is helpful for users to achieve the optimal process parameters and develop process control in spraying process.

3) Fabrication experiments of the automobile cover component and the planar PEN of SOFC confirm the multipurpose uses of this system. It can enable spraying tooling large and medium mould with complex surface and the consistent production of those coatings.

ACKNOWLEDGMENT

REFERENCES

1. Fauchais, P., "Understanding plasma spraying," *J. Phys. D — Appl. Phys.*, Vol. 37, No. 9, R86–R108, 2004.

2. Hui, R., Z. Wang, O. Kesler, L. Rose, J. Jankovic, S. Yick, R. Maric, and D. Ghosh, "Thermal plasma spraying for SOFCs: Applications, potential advantages, and challenges," *J. Power Sources*, Vol. 170, No. 2, 308–323, 2007.

3. Henne, R., "Solid oxide fuel cells: A challenge for plasma deposition processes," *J. Therm Spray Technol.*, Vol. 16, No. 3, 381–403, 2007.

4. Nassenstein, K. and D. Luckenbach, "Progress in thermal spray processes," *Thermal Spray Connects: Explore Its Surfacing Potential!*, 378–382, Basel, Switzerland, 2005.

5. Vergeest, J. S. M. and J. W. H. Tangelder, "Robot machines rapid prototype," *Ind. Robot*, Vol. 23, No. 5, 17–20, 1996.

6. Xia, W.-S., H.-O. Zhang, G.-L. Wang, Y.-Z. Yang, and Y. Zou, "Open architecture robotic plasma spray forming system based on Ethernet," *Robot*, Vol. 30, No. 1, 17–21, 2008 (in Chinese).

7. Etchart-Salas, R., V. Rat, J. Coudert, P. Fauchais, N. Caron, K. Wittman, and S. Alexandre, "Influence of plasma instabilities in ceramic suspension plasma spraying," *J. Therm Spray Technol.*, Vol. 16, No. 5, 857–865, 2007.

8. Coudert, J. F., M. P. Planche, and P. Fauchais, "Characterization of D.C. plasma torch voltage fluctuations," *Plasma Chem. Plasma Process.*, Vol. 16, No. 1, S211–S227, 1995.

9. Xia, W., H. Zhang, G. Wang, and D. Liu, "Plasma jet temperature field diagnostics for process control in rapid plasma spray tooling," *ICMA 2004 — International Conference on Manufacturing Automation: Advanced Design and Manufacturing in Global Competition*, 771–776, Wuhan, China, 2004.

10. Zhang, H., G. Wang, Y. Luo, and T. Nakaga, "Rapid hard tooling by plasma spraying for injection molding and sheet metal forming," *Thin Solid Films*, Vol. 390, No. 1–2, 7–12, 2001.

Numerical Simulation of Electromagnetic Flux Leakage in Application of Internal Defects Prediction of Metal Parts

H. O. Zhang[2], Y. Z. Yang[1], G. L. Wang[1], and Haiping Zou[3]

[1]State Key Laboratory of Material Processing and Die & Mould Tech.
Huazhong University of Sci. & Tech., Wuhan 430074, China
[2]State Key Laboratory of Digital Manufacturing Equipment and Tech.
Huazhong University of Sci. & Tech., Wuhan 430074, China

Abstract— Metal products were widely used at a variety of industry, so it is essential to predict the security and the usability without the destructive testing for the desired production efficiency under the different their working conditions. Recently, the plasma deposition dieless manufacturing process (PDM) is an innovative and promising application of plasma heat source with extensive industrial potential for refractory and intractable material part or prototype, rebuilding of worn components and especially the direct rapid fabrication of functionally graded materials (FGMs). However, Residual stress and distortion induced by the highly localized transient heat and strongly nonlinear temperature distributions would likely promote undesired and unpredictable warps and cracks in this process. Thus, to distinguish the internal defect from the significant discontinuities during the nondestructive testing of the metal parts, in this paper, the finite-element method (FEM) was applied to predict the electromagnetic distribution. According to the difference the magnetic flux leakage analysis, distinction threshold was built by the ratio of the peak-to-peak amplitudes of the raw inspecting signal anomaly. Computational results show that it is potential to decrease the testing period and improve the security of metal parts, in particular, the micro-raw and hole in the metal parts can be predicted, thus the possibly-intended breakage would be improved.

1. INTRODUCTION

Tubular products are widely used at a variety of industry. Considering their working condition, nondestructive testing (NDT) stands essential for both the desired production efficiency and security [1–3]. As a popular testing method used for the steel pipes' testing, MFL was supposed intuitively to provide more health information sufficiently. During the real-time inspection, other factors, such as shape and orientation could contribute significantly for the defect's location characteristics, leading the location identification disorder. This problem has been attached more and more importance during the evaluation system of the steel pipes' health information in their supplying and in their service. To assess the severity of the flaw in the tubular product, Perazzo et al. have improved the signal processing and extracted more features. They also suggested some additional threshold for the reliable inspection [4]. The desired differentiation has yet been achieved in our experimental inspections to the artificial defects' designed with different shape and machined at the same surface of the reference materials with regular wall-thicknesses, respectively. With the help of the noise-decreasing process, J. Etcheverry et al. threw some light on the signal-processing to the raw MFL signal. Harmonic functions were used to eliminate the disturbance from the noise, and transformation was carried out from the inspected vector series into the normalized scalars, which the latter could function as the index, presenting more information about the flaws. In fact, signal procession is popular in the defect identification, such as wavelet analysis and neural-network algorithm. Although some promising progress has been taken to identify the artificial discontinuities' shape characterization, further work needs carrying to achieve the desired inspection, especially to their application on the natural flaws' evaluation. Any biased evaluation desperately leads either the danger in its service or the un-expected production cost after the inspection. As a kind of signal processing method, the differentiating index provided in this paper focuses on the ratio between the peak-to-peak amplitudes of the original-signal anomaly and its difference component at second order, instead of some single index inspected or some component originating from some transformation in conventional MFL techniques. Verified by the experimental inspections on the transverse notches and pits artificially machined on the drill pipe with 9.35 mm in wall-thickness and 88.7 mm in outer diameter, this method presents the advantage, which is irrespective of the defects' critical physical size and shapes, comparing with the currently applied methods. This alternative discrimination index could be used in the conventional MFL testing system, providing more information about the inspection result with the minimum cost.

2. CHARACTERISTIC ANALYSIS OF THE FLUX LEAKAGE

MFL testing probe is designed to scan along the outer surface of the pipe, with some desired lift-off distance. Any discontinuity in the specimen under magnetic saturation could be taken as a kind of magnet-dipole, As illustrated in Figure 1, M_1–M_{11} was used for the magnetic dipole simulation, which configures the magnetic flux anomaly in the vicinity of the defects. As a kind of nonlinear and micro-spatial sector, specific flux strength distribution is decomposed to normal and tangential components i.e., H_X and H_Y at the A and A_p points, which are raised by the external discontinuity and the internal one respectively and denoted through the formulas below:

$$H_X = \int_0^h dH_{M_1} + \int_0^h dH_{M_{11}}$$
$$= 2\sigma_s \cdot \left[\arctg \frac{h \cdot (x+b)}{(x+b)^2 + y \cdot (y+h)} - \arctg \frac{h \cdot (x-b)}{(x-b)^2 + y \cdot (y+h)} \right] \quad (1)$$

$$H_Y = \int_0^h dH_{M_1} + \int_0^h dH_{M_{11}}$$
$$= \sigma_s \cdot \ln \frac{\left[(x+b)^2 + (y+h)^2\right] \cdot \left[(x-b)^2 + y^2\right]}{\left[(x+b)^2 + y^2\right] \cdot \left[(x-b)^2 + (y+h)^2\right]} \quad (2)$$
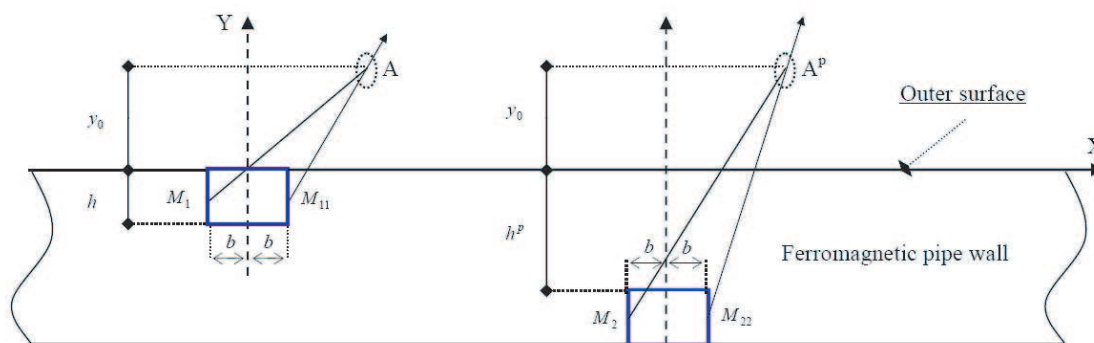
Figure 1: Illustration of the magnetic flux leakage field dipole model.

3. RESULTS AND DISCUSS

As the conventional MFL inspection illustrating, the peak-to-peak amplitude was always used as the index to calibrate against to build the threshold. Induced by the discontinuity at the opposite surface, the flux anomaly is ferrous influenced, and presents being smoothed and weakened, comparing to those at the scanning surface. As illustrated in Figure 1. With the help of FEA (Finite Element Analysis) simulation to the 2-dimensional axis-symmetric model, we could find the relation quantitatively about the amplitudes of the signal anomalies, arising from the simulated defects with comparable physical size but different location. According to the wall thickness of 5.50 mm, 9.35 mm, and 12.00 mm, the discontinuities were designed with the depths varying with 5%, 10% and 15% of the wall-thickness. The analyzing results were listed in Table 1, and it could be obviously found that the amplitude index, induced by the discontinuities at the outer surface, approximately twice the counterpart of the discontinuities at the inner surface.

Table 1: Ratio of the peak-to-peak amplitudes from the simulated internal defects and the external ones.

Wall-thickness (mm)	N5 (5%) V_{ED}/V_{ID}	N10 (10%) V_{ED}/V_{ID}	N15 (16%) V_{ED}/V_{ID}
5.50	2.30	2.13	2.50
9.35	2.12	2.06	2.23
12.00	2.06	2.04	2.08

The external notches are commonly set as the reference signal source in the most MFL equipments' calibration, and some characteristic components were used to assess the severity of the imperfection in the specimen during the real time production inspection, such as peak-to-peak amplitude and other indexes corresponding to the anomaly single. But is it available to identify the flaws' location? As shown in the formula (1) and (2) and illustrated in the Figure 1, the lift-off distance could not be ignored for the defects' location identification. In fact, the permeability change happening at the media, which separates the material with high permeability (steel wall) and the far lower one (air), conventional proportion-approximating procedure and the linear simulation will definitely distort the inspecting subject with biased inspection result.
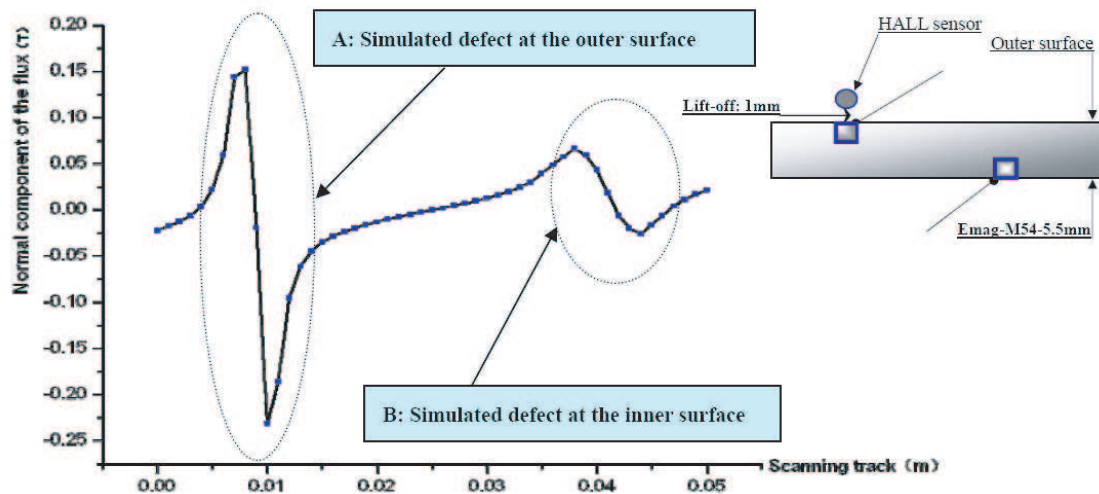
Figure 2: Dissimilar characteristics between the signal anomalies.
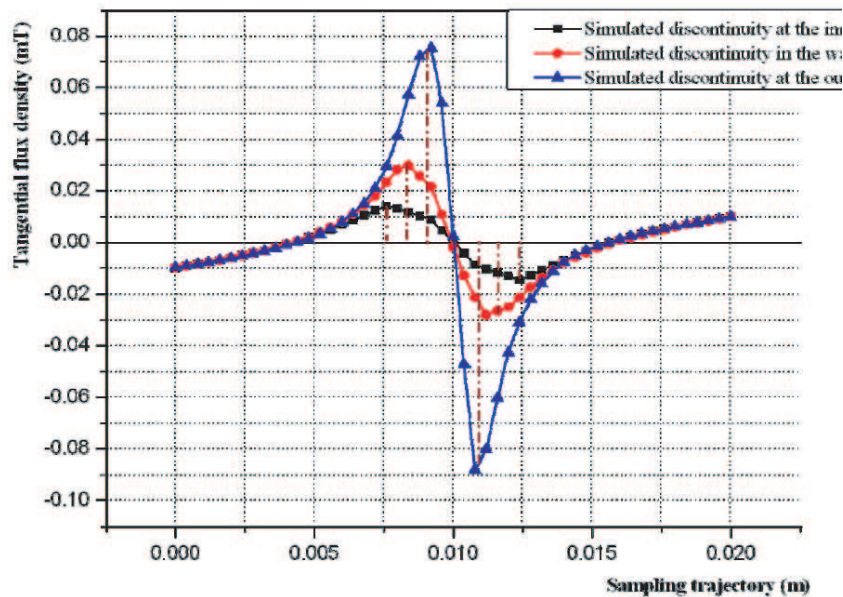
Figure 3: Tangential flux density induced by defects with the same physical size but at different surface.

As the signal anomaly illustrating at the calibration and real-time inspection, the external flaw corresponds to some relative sharper flux anomaly than that from the internal one. Based on this, ad hoc triggering thresholds shall be set independent of each other corresponding to the external and internal defects during the calibration. As the essential index, width between the crests of

signal anomaly was discussed below. With the help of 2-dimensional axis-symmetric model FEA (Finite Element Analysis) model, some flaws were designed at the inner surface, subsurface and the outer surface, showing the variation of the signal anomaly due to its location. Obviously the width between the adjacent crests in vicinity of the designed flaws shows their inherent characteristic in the Figure 3.

4. CONCLUSIONS

Based on the analysis on the original inspected signals belong to the spatial domain and the spectral domain, the ratio index was formulated by the peak-to-peak amplitudes of raw signal and its second difference component, supplying an alterative accessing index. To be exempt of the disturbance from the defects' physical size and shape during the MFL inspection in field, some procedures were built and fabricated into the defects' location identification in this paper, by resort of the further difference process, the first process, i.e., feature extracting capability could be assessed.

ACKNOWLEDGMENT

REFERENCES

1. Stanley, R. K., "Electromagnetic tubular inspection during well servicing," *Proceedings of the 13th World Conference on NDT*, 1992.
2. Kang, Y. and X. Wu, *Numerical Magnetic NDT Technique*, China Machine Press, Beijing, January 2007.
3. Lord, W., "Applications of numerical field modeling to electromagnetic methods of nondestructive testing," *IEEE Transaction on Magnetics*, Vol. 19, No. 6, November 1983.
4. Perazzo, R., A. Pignotti, S. Reich, and P. Stickar, "Feature extraction in MFL signals of machined defects in steel tubes," *Review of Progress in Quantitative Nondestructive Evaluation*, Vol. 20a, 619–626, D. O. Thompson and D. E. Chimenti, eds., American Institute of Physics, Melville, New York, 2000.

Influence of Calcium Cyclotronic Resonance on the Developmental Rates of *Xenopus Laevis* Tadpoles

M. Severini[1], **C. Giliberti**[3], **G. Tarantino**[2], **M. Loy**[2], **M. Bonori**[2],
A. Congiu Castellano[2], **A. Bedini**[3], **R. Palomba**[3], **and L. Giuliani**[3]

[1]Department of Ecology and Economical Sustainable Development
Tuscia University, Viterbo, Italy
[2]Physics Department, University La Sapienza, Rome, Italy
[3]Institute for Prevention and Work Safety (ISPESL), Rome, Italy

Abstract— Recent *in vivo* and *in vitro* studies suggest that exposures to a weak ELF magnetic field close to Larmor frequency of Ca^{2+} could have a role in changing the development rate of cells and animals. Several experiments have been performed to assess the influence of specific exposure conditions on the *Xenopus laevis* tadpoles development rate. In our study, the exposition to a weak ELF magnetic field close to Ca^{2+} cyclotronic resonance, doesn't seem to affect the developmental rates of the tadpoles. Otherwise, under exposure conditions different from those of Ca^{2+} cyclotronic resonance, a significant retard seems to occur. Comparing these results, it can be deduced that probably the geomagnetic field B_0 plays an important role in the activation of some processes connected with the development rate of this specie. In order to find an interpretation of the interaction mechanisms occurring between the magnetic fields and the biological matter at microscopic level, according to the Zhadin effect, an estimation of the energies associated to the most important ions involved in the intra/extra cellular activities (K^+, Ca^{2+}, Mg^{2+}) under different exposure conditions, has been performed.

1. INTRODUCTION

The investigation on the effects of weak magnetic fields on biological systems starts in 1985, after the remarkable works by Liboff [1] and Blackman [2]. Ever since, the attention has been focused on the effects of an extremely low frequency (ELF) AC magnetic field that manifested themselves as a change in free calcium concentration in extra and intra cellular media. The results turned out to be highly dependent on the simultaneous presence and magnitude of a DC magnetic field. The DC and AC fields were very weak and comparable to the natural geomagnetic one in their magnitudes. The greatest effect was observed at the AC field frequency close to the cyclotron frequency corresponding to the charge-to-mass ratio of a Ca^{2+} ion and to the applied DC field. Subsequently, various experiments confirmed the existence of these effects [3]. Recent experiments suggest that a weak extremely low frequency (ELF) magnetic field, tuned to the Ca^{2+} cyclotron resonance (ICR), can induce evidence of various effects on living systems. In particular, Lisi et al. [4] find an increase of the differentiation and maturation of human epithelial cells, while Gerardi et al. [5] show that these exposure conditions influence the metabolism of rats, causing a rise in body weight, blood glucose and fatty acid metabolism. The interpretation of the interaction mechanisms occurring between magnetic fields and living systems at microscopic level is discussed in the scientific community, and several models based on the resonance idea have been proposed. Among them, the model of multiple splitting of resonance peak has been proposed by Zhadin first in 1998 [6] and later in deep studies [7–9]. This model showed the splitting of the natural frequency of ion thermal oscillation (ω_0) within a macromolecule under the influence of combined DC and AC magnetic fields into a multiple series of new resonant peaks, which exert influence on ion motion. The combined action of DC and AC magnetic fields at specific frequencies yields changes in the energy of the ion thermal motion. The numerical estimation revealed the sufficiency of the resonance energy to change a macromolecule conformation state at the fields compared with the geomagnetic one; a number of free ions statistically different from that in presence of the only DC field, can be released by the macromolecule for intra/extra cellular processes. The theoretical analysis is valid for a damping coefficient $\gamma \ll \omega_L$ where

$$\omega_L = qB_0/2m \tag{1}$$

is the Larmor frequency. In this paper, the *Xenopus laevis* tadpoles (Daudin) have been used to investigate the role of a particular frequency-amplitude combination of ELF magnetic fields on their developmental rates. This specie has become the most important amphibian model in the biomedical research, thanks also to the ease of its management in captivity after hormonal stimulation. The

results of three different expositions of *Xenopus laevis* tadpoles to different combinations of AC and DC ELF magnetic fields are here presented. The possibility that the geomagnetic field B_0 plays an important role in the activation of some processes connected with the development rate of this specie has been investigated. The results have been discussed according to the Zhadin model [7–9], estimating the energies associated to the most important ions involved in the intra/extra cellular activities (K^+, Ca^{2+}, Mg^{2+}).

2. MATERIAL AND METHODS

Two sets of experiments with *Xenopus laevis (Daudin)* tadpoles have been accomplished, each one made by 3 tests; for each test, a cohort (68 individuals) was reared in two aquariums under the sinusoidal magnetic field produced by a solenoid (*"exposed cohort"*). The maturation times of *Xenopus laevis* tadpoles have been compared with those of three corresponding *"control cohorts"* (68 individuals), grown in two unexposed aquariums. The tadpoles have been managed after hormonal stimulation. Each test was performed employing individuals obtained from the same spawning; in different tests the same pair of adults were not used. By using a stereomicroscope and according to Nieuwkoop & Faber table [10], the individuals were daily classified in the various stages of their life-cycle until stage 58 (maturation stage). The expositions have been carried out under controlled conditions of temperature ($24.0 \pm 0.2°C$). The geometrical characteristics of the aquariums used for the *exposed* and *control cohorts* were identical: 0.26 m (height), 0.26 m (width), 0.40 m (length), $0.027 \, \text{m}^3$ (volume). The dimensions of the solenoid were: length 1.60 m and diameter 0.38 m. It was made of 1600 copper wire turns (diameter 0.001 m), it had a resistance of $43 \, \Omega$ and an inductance of 200 mH. The magnetic induction was measured periodically in the exposed aquariums centre by EFA3 (Wandel & Goltermann). In the laboratory, static magnetic field was $25 \, \mu\text{T}$, measured by the APS 520 A Fluxgate Magnetometer. One experiment was carried out fixing the static field (B_0) at $65 \, \mu\text{T}$ (obtained by adding a DC component to the AC component of the current generator) in order to tune the Calcium cyclotron frequency resonance to the frequency (50 Hz) of the sinusoidal field applied ($B_{ac} = 100 \, \mu\text{T}$). The other experiment was carried out employing the geomagnetic field in the laboratory ($B_0 \equiv B_{geomag} = 25 \, \mu\text{T}$), while the sinusoidal magnetic field was $100 \, \mu\text{T}$ (B_{ac}) at 50 Hz. The results of these two experiments have been compared with the data of Severini et al. [11], where three cohorts of *Xenopus laevis* were reared in an aquarium under the "sawtooth" magnetic field produced by a television. The magnetic field was the superimposition of two perpendicular saw-tooth components; the first harmonic of the horizontally polarized component was 50 Hz, and that of the other was 15.797 Hz.

The results of the daily observations of these three experiments were utilized to obtain the *growth times* of the tadpoles, measured in days from the birth. The data have been analysed by the Analysis of Variance (ANOVA) Two-Ways, assuming a double dependence of the samples *growth times* from the oviposition of the specie and the treatment applied (magnetic fields). The results have been discussed according to the Zhadin model [7–9] and the average energy of the ions at the resonance (E_m) has been calculated, assuming that the combined action of DC and AC magnetic fields gives the multiple splitting of the resonance peaks of the ion. The most effective action of the magnetic fields takes place when the ratio ω_{ac}/ω_L (ω_L ion Larmor frequency) is a whole number m. If it doesn't occur, a correction of the ion energy has to be applied (E_i), taking into account the *characteristic function* of a resonant system around the resonance. For three possible values of the damping coefficient γ, an estimation of the ratio E_i/E_0 has been performed, where E_0 is the ion average energy under the influence of the static field B_0. This ratio has been calculated for K^+, Ca^{2+}, Mg^{2+}, that are the most important ions involved in the intra/extra cellular activities.

3. RESULTS

Table 1 shows the results of three experiments, performed with *X. Laevis* exposed to various combinations of weak magnetic fields (B_{ac}) and static fields (B_0). Experiment A refers to an exposition to a weak low frequency magnetic field close to Ca^{2+} cyclotronic resonance conditions. The calculated significativity level shows that these exposure conditions don't seem to affect development rates of tadpoles. The results of Experiments B and C (Table 1), performed with magnetic fields at frequencies far from those involved in the development or in the enzymatic activity, show that ELF magnetic fields retard developmental rates of *X. Laevis* tadpoles with statistically significant mean delays.

Table 1: Summary of the results obtained for the *X. Laevis* exposed to weak magnetic field.

		Grow time of X. laevis (in days)						Analysis of Variance, F-test			
		Test1		Test2		Test3		400 individuals for experiments			
		Control	Exposed	Control	Exposed	Control	Exposed		Free Degrs	F	Significativity
Experiment A	Mean	35.0	36.1	33.5	34.2	34.9	35.5				
B_o=65 μT	St.Dev	3.9	5.7	3.5	3.8	3.9	4.3	Oviposition	2	6.91	<< 0.005
B_{ac}: Sinusoidal	Mean Delay	1.1		0.7		0.6		Treatment	1	3.98	0.047
50 Hz,100μT	Total Mean Delay	**0.8**									
Experiment B	Mean	32.5	35.3	30.8	31.7	35.6	38.7				
B_o=B_{geom}=25 μT	St.Dev	5.3	5.7	5.1	5.3	5.7	6.2	Oviposition	2	30.4	<< 0.001
B_{ac}: Sinusoidal	Mean Delay	2.8		0.9		3.2		Treatment	1	13.5	<< 0.01
50 Hz,100 μT	Total Mean Delay	**2.3**									
Experiment C	Mean	43.4	48.6	39.6	44.2	40.4	46.4				
B_o=B_{geom}=25μT	St.Dev	4.9	6.3	6.6	7.1	3.7	4.3	Oviposition	2	27.6	<< 0.001
B_{ac}: sawtooth	Mean Delay	5.2		4.6		6.0		Treatment	1	134.0	<< 0.001
50 Hz, 30 μT 15 kHz [11]	Total Mean Delay	**5.3**									

4. DISCUSSION

The data in Table 1 can be realized by means of the results of Learch et al. [12], which suggest that ELF Ca^{2+} cyclotron resonance depress pineal melatonin in the adults rats, with a rise in their development rate. For amphibians, melatonin acts as an antagonist of the thyroid hormone, essential for the development rate of the tadpoles, while the role of Ca^{2+} in the synthesis of melatonin has to be more investigated. Then it might be hypothesized that, a statistically significant delay between *exposed* and *control cohorts* doesn't occur in Experiment A because of a compensation mechanism between the inhibitory effect induced by weak fields and the probable rise effects on the development rate due to frequency Ca^{2+} cyclotron resonance. Comparing the experiments in *non-resonance* conditions (Experiments B and C) with the *resonance* one (Experiment A), it might be deduced that probably B_0 plays an important role in the activation of some processes connected with the development rate of *X. Laevis*. In particular, Experiments A and B were carried out with the same B_{ac} and different B_0; statistically significant differences between the *exposed cohorts* could then be attributed to B_0. It is important to remark that all the tests have been carried out with the same number of treatment for test, dimension of the sample, boundary conditions (as temperature, alimentation, etc.), in order to guarantee the comparison. According to the Zhadin model, the energies of the ions in resonance condition ($\omega_{ac}/\omega_L = m$, with m whole number) can be calculated. The evaluation of the energies for ions in *non-resonance* conditions (E_i) requires a correction, performed by using the *characteristic function* $L(Z)$ of a resonant system around the resonance:

$$L(Z) = 1/\left[(2Z/\gamma)^2 + 1\right] \qquad (2)$$

where Z is the distance between the actual ion pulsation (ω_L) and the pulsation of the closest resonance (ω_{Lris}).

In Table 2, the evaluations of the ratio E_i/E_0 for the ions K^+, Ca^{2+}, Mg^{2+} in correspondence of three possible values of the damping coefficient γ are reported together with the estimation of Z. For the damping coefficient γ, the values hypothesized by Muesham et al. [13] have been assumed. The data in Table 2, according to the Zhadin model, show that in *resonance* conditions (Experiment A), Calcium and Magnesium ions seem to undergo an alteration of their energies (positive for the Ca^{2+}, negative for the Mg^{2+}). The increase of Ca^{2+} energy could represent a confirmation of the melatonin depression hypothesis — And the consequent increase of developmental rate — Caused by a larger number of Ca^{2+} ions present in the intra/extra cellular processes. Moreover, considering the antagonist role of Mg^{2+} in respect to the Ca^{2+}, the reduction of the Mg^{2+} energy (Table 2,

Experiment A) could confirm the above mentioned hypothesis.

Table 2: Evaluation of E_i/E_0 for the ions K^+, Ca^{2+}, Mg^{2+} for three possible values of the damping coefficient γ.

		Experiment A			Experiment B		
		Exposure conditions: $B_0=65\,\mu T$; $B_{ac}=100\,\mu T$; $50\,Hz$; $\omega_{ac}=314$			**Exposure conditions:** $B_0=25\,\mu T$; $B_{ac}=100\,\mu T$; $50\,Hz$; $\omega_{ac}=314$		
Ions		K^+	Ca^{2+}	Mg^{2+}	K^+	Ca^{2+}	Mg^{2+}
q/m		2.47E+06	4.81E+06	7.93E+06	2.47E+06	4.81E+06	7.93E+06
ω_L		80.1	156.3	257.7	30.8	60.1	99.1
$\omega_{ac}/\omega_{Lris}=m$		4	2	1	10	5	3
ω_{Lris}		78.5	157.0	314.0	31.4	62.8	104.7
		K^+	Ca^{2+}	Mg^{2+}	K^+	Ca^{2+}	Mg^{2+}
E_m/E_0		1	1.70	1.23	1	1	1
Z		1.6	0.7	56.3	0.6	2.7	5.5
E_i/E_0	$\gamma=10$	0.91	1.67	0.01	0.99	0.78	0.45
	$\gamma=40$	0.99	1.69	0.14	1.00	0.98	0.93
	$\gamma=120$	1	1.7	0.66	1.00	1.00	0.99

5. CONCLUSIONS

The *Xenopus laevis* tadpoles (Daudin) have been used to investigate the role of a particular frequency-amplitude combination of ELF magnetic fields in their developmental rates. The results show that B_0 plays an important role in the activation of some processes connected with the development rate of this specie. According to the Zhadin model, the ion kinetic energy has been calculated in *resonance conditions*, showing an increase of Ca^{2+} ion energy. In *non-resonance conditions*, an approximation based on the *characteristic function* of a resonant system, has been implemented and discussed.

REFERENCES

1. Liboff, A. R., "Geomagnetic cyclotron resonance in living cells," *J. Biol. Phys.*, Vol. 9, 99–102, 1985.
2. Blackman, C. F., S. G. Benane, D. E. House, and W. T. Joines, "Effects of ELF (1–120 Hz) and modulated (50 Hz) RF fields on the efflux of calcium ions from brain tissue in vitro," *Bioelectromagnetics*, Vol. 6, 1–11, 1985.
3. Zhadin, M. N., O. N. Deryugina, and T. M. Pisachenko, "Influence of combined DC and AC magnetic fields on rat behaviour," *Bioelectromagnetics*, Vol. 20, 377–386, 1999.
4. Lisi, A., A. Foletti, M. Ledda, E. Rosola, L. Giuliani, E. D'Emilia, and S. Grimaldi, "Extremely low frequency 7 Hz 100 μT electromagnetic radiation promotes differentiation in human epithelial cell line HaCaT," *Electromagnetic Biology and Medicine*, Vol. 25, No. 4, 269–290, 2006.
5. Gerardi, G., A. de Ninno, M. Prosdocimi, V. Ferrari, F. Barbaro, S. Mazzariol, D. Bernardini, and G. Talpo, "Effects of electromagnetic fields of low frequency and low intensity on rats metabolism," *Biomagnetic Research and Technology*, Vol. 6, No. 3, 2008.
6. Zhadin, M., "Combined action of static and alternating magnetic fields on ion motion in a macromolecule: Theoretical aspects," *Bioelectromagnetics*, Vol. 19, 279–292, 1998.
7. Zhadin, M. and F. Barnes, "Frequency and amplitude windows in the combined action of DC and low frequency AC magnetic fields on ion thermal motion in a macromolecule: Theoretical analysis," *Bioelectromagnetics*, Vol. 26, 323–330, 2005.
8. Zhadin, M. and L. Giuliani, "Some problems in modern bioelectromagnetics," *Electromagn. Biol. Med.*, Vol. 25, No. 4, 227–43, 2006.

9. Giuliani, L., S. Grimaldi, A. Lisi, E. D'Emilia, N. Bobkova, and M. Zhadin, "Action of combined magnetic fields on aqueous solution of glutamic acid: The further development of investigations," *Biomagn. Res. Technol.*, Vol. 6, No. 1, 2008.

10. Nieuwkoop, P. and J. Faber, "Normal table of Xenopus laevis," Amsterdam, North Holland, 1956.

11. Severini, M., A. D. Dattilo, and A. de Gaetano, "Sublethal effect of a sinusoidal magnetic field on the Xenopus laevis (Daudin) tadpoles," *Int. J. Biometeorol.*, Vol. 48, 91–97, 2003.

12. Learch, A., R. J. Reiter, K. A. Hovwes, K. O. Nonaka, and K. A. Stokkan, "Evidence that extremely low frequency Ca (2+) cyclotron resonance depresses pineal melatonin in vitro," *Neurosci. Lett.*, Vol. 124, 213–215, 1991.

13. Muehsam, D. J. and A. A. Pilla, "Weak field modulation of ion dynamics in a potential well: mechanistic and thermal noise considerations," *Bioelectrochem. Bioenerg.*, Vol. 28, 355–365, 1994.

Electromagnetic Mapping of Urban Areas: The Example of Monselice (Italy)

C. Giliberti[1], F. Boella[2], A. Bedini[1], R. Palomba[1], and L. Giuliani[2]

[1]Institute for Prevention and Work Safety (ISPESL), Rome, Italy
[2]Institute for Prevention and Work Safety (ISPESL), Venice, Italy

Abstract— In this work, the theoretical evaluation of the electromagnetic field (*emf*) produced by radio base stations (*rbs*) in the city of Monselice, sited in the northern part of Italy is presented. An area of $16\,\text{km}^2$, characterized by 11 *rbs* sites has been selected. A census of the *rbs* sites has been carried out, collecting: the location of the sites, the technical data of their antennas, the shape of the ground, the position of all the buildings (*Gauss-Boaga* coordinates) in the area and their heights. Two different evaluations of the *emf* in this area are presented. The first one, representing the buildings by their barycentre placed at the height of each building, calculates in these points the electric field levels using the classical far-field equation, assuming the *rbs* working at the maximum power declared. Another theoretical evaluation of the *emf* has been carried out by the application of a calculation code working with the *ray tracing* method. It provides an output where a map of the electric field produced by the *rbs* on the surfaces of the buildings in an area around a electromagnetic sites is shown, assuming the *rbs* working at the maximum power.

1. INTRODUCTION

In the last years, the number of the electromagnetic field (*emf*) sources in the frequency range of the microwaves has increased, principally in the urban areas, due to the proliferation of radio-base stations (*rbs*) for mobile communications. It has produced concern among the public about the potential health risks of long time exposition to the *emf* emitted from the *rbs*, in the working and living environments. This leads to the necessity of continuous monitoring and prediction of the *emf* strength. At the international level, several organizations have developed guidelines to protect the general public from the *emf* emitted from the *rbs* antennas. In Italy, the issue of public exposure to sources with frequencies between $100\,\text{kHz}$ and $300\,\text{GHz}$ is regulated by one decree promulgated in 2003 [1], in terms of three levels: (i) *limits*, levels that haven't to be exceeded in any circumstances for the protection from short terms effects; (ii) *attention levels*, that have not to be exceeded into gambling areas, schools and buildings where people stay for more than 4 hours, as a precaution from the potential risks on health due to long time exposition; (iii) *quality targets*, levels to achieve in a long period in order to minimize people exposure. In Table 1, the values related to the upper three levels, defined in terms of effective electric and magnetic fields and power density, are presented. Moreover, the decree determines how the measurements have to be performed by averaging the effective electric and magnetic field on 6 minutes and on an area equivalent to the vertical section of the human body. In this work, we present an example of the electromagnetic mapping of an urban area, performed in the territory of the town of Monselice, sited in the northern part of Italy. Here, the theoretical evaluation of the distribution of the *emf* generated by the *rbs*, working in the urban territory, has been carried out by calculation programs used in the *Laboratory of Radiation and Ultrasounds Pollution* of ISPESL.

Table 1: Exposure limits, attention levels, quality target fixed by the Italian law [1].

	Exposure limits ($3\,\text{MHz}$–$3\,\text{GHz}$)	**Attention levels and Quality targets**
E_{eff}	$20\,\text{V/m}$	$6\,\text{V/m}$ ($0.1\,\text{MHz}$–$300\,\text{GHz}$)
H_{eff}	$0.05\,\text{A/m}$	$0.016\,\text{A/m}$ ($0.1\,\text{MHz}$–$300\,\text{GHz}$)
Power density	$1\,\text{W/m}^2$	$0.10\,\text{W/m}^2$ ($3\,\text{MHz}$–$300\,\text{GHz}$)

2. METHODS

An area of $16\,\mathrm{km}^2$ in the territory of Monselice has been selected, according with the following criteria: the availability of a detailed and up-to-date vector cartography, high number of buildings (18.294) and presence of *rbs* for mobile communications. In particular, about the urban environment, some specific data have been acquired as the shape of the ground and its altitude above sea level, the position of all the buildings defined as polygons which vertex are expressed in the *Gauss-Boaga* coordinates, the height of all the buildings above the sea level. In the selected area, a census of the *rbs* has been performed, finding 11 sites, all located on pylons, which correspond to 66 emitting sources, 9 working in the UMTS technology, 2 characterized by several *rbs* coexisting at the same site and they were georef erred. In order to make a theoretical evaluation of the people exposure levels to the *emf* produced by the *rbs*, the following technical data of their antennas have been collected: type of antenna, its gain and radiation pattern, vertical tilt, frequency band, power to the connector of the antenna, its position expressed in *Gauss-Boaga* coordinates, height above the terrain, orientation respect to the geographical North. Two different evaluations have been performed. In the first one, we applied the classical equation of the electromagnetic field intensity in the far-field region [2]. We calculated the electric field levels by using the following far field equation:

$$E\,(\mathrm{V/m}) = \sqrt{30 \cdot [G_{\max} - Att(\theta; \phi)] \cdot P}/r \tag{1}$$

where $Att(\theta, \phi)$ is the attenuation respect to the maximum gain $G_{\max}$ of the antenna as a function of vertical and horizontal angles, r the distance from the *emf* source, P is the power at the antenna connector. Representing all the buildings in the selected area by the barycentre of their polygons, the calculation of the electric field levels produced by the *rbs* under examination has been carried out in one point for each building, placed at its top. We supposed cautiously the *rbs* working at the maximum power declared by the company and all channels active [3]. In order to evaluate the global *emf* due to the *rbs*, an overall calculation was made of the emissions of all 66 systems, considering in every point the sum of each *rbs* contribution. The electric field was calculated using the digital terrain model (DTM) on a grid of points with a $50\,\mathrm{m}$ step. The theoretical model based on far-field propagation is weak because of many approximations: it gives good results only in the far field zone and in a free space transmission approximation, which occurs when no elements of the propagation environment, like walls, corners, ground, can be encountered. In these conditions, the far-field model is precautionary, i.e., the results obtained are an over-estimate evaluation of people exposure to the electromagnetic radiation produced by the *rbs*. In an open country, where there are no obstacles, unless the reflection of the ground, the free-space formula can be useful to calculate the electric field levels. Instead, in an urban environment, it underestimates the electric field levels due to the presence of the ground, buildings and some other objects around the transmitting antenna which cause reflections, transmissions, diffractions, diffuse scattering. A careful assessment of the exposure of urban population to the *emf* generated by the *rbs*, requires the use of algorithms that take into account the interferences in the propagation of the field. This is an important factor for the accuracy of the simulations, because especially digital systems are more sensitive to channel degradation in form of multipath distortion and fading. A more rigorous approach is based on the *ray tracing* method, which allows the simulation of the propagation of the electromagnetic waves between the transmitting antenna and the reception point, by taking into account the influence of all reflection and diffraction phenomena during the propagation, on the basis of the geometrical optics theory. The total received electric field at a point is the sum of the electric fields of each multipath component that illuminates the receiver. To implement *ray tracing* simulations, the knowledge of both the environmental geometry (digital terrain model) and the three-dimensional geometry of the city, i.e., shape and location of each building, is necessary. This approach has the advantage of taking 3D environments into account, and is theoretically more precise, increasing the accuracy of the prediction of the *emf* levels, in the neighborhood of a specific electromagnetic site. Although it is possible to model complex urban environment, using this kind of method, it is however difficult to get all the input data needed to take into account the geometrical and electrical features of the obstacles present within a certain urban area of propagation. The inaccuracies in the topographical and morphological data of the urban scene may influence in any case the accuracy of the results calculated by this approach. Imprecision in the building database, lack of information about material properties (medium, thickness, structure, roughness, etc) can occur, having a strongly negative impact on the quality of the field predictions obtained by this approach. Then, for the calculation of the *emf* in the city of Monselice, a second simulation of the electric

field levels has been performed, using a calculation code which works with the *ray tracing* method. Each building has been schematized in terms of a parallelepiped, and the *ray tracing* procedure has been implemented to compute the *emf* everywhere outside, also in the streets and squares of the city. The output provides a false colour 3D map or 2D representation of the electric field radiated by the *rbs* antennas on the surfaces of the buildings in a specific area around the electromagnetic site, assuming the *rbs* included in the area working at the maximum power.

3. RESULTS

Figure 1(a) shows the plan of the selected area $(16\,km^2)$ in the town of Monselice that included the buildings and the *rbs*, all georef erred, together with a zoom of the sector of the map where the *rbs* are located. The electric field levels, estimated using the far field equation, in the selected area for the Town of Monselice are shown in Figure 1(b). By the analysis of the map of the *emf* strength obtained at the top of each building, it is possible to identify potential critical urban areas for people exposure in relation to the *rbs* locations. The data obtained allow to compare the theoretical electric fields levels with those fixed by the Italian law. It is clear that, in this representation, mostly of the urban territory is exposed to electric field levels lower than $1\,V/m$. Areas characterized by the presence of several *rbs* coexisting at the same site, show electric field levels up to $3.0\,V/m$. The statistical distribution of the electric field levels in the selected area is showed in Figure 2. The statistics has been performed for n. 4 classes of the electric field levels: the first referred to results of calculated electric field levels lower than $1.0\,V/m$; the last class referred to results of calculated electric field levels higher than $3.0\,V/m$ but lower than $6\,V/m$. Most of the estimated electric field levels are in the range $E < 1.0\,V/m$ (98.63%); the class $1.0 \leq E \leq 2.0\,V/m$ includes the 1.35% of the whole electric field values; the third class includes only 0.03% of the values and the last class $E \geq 3.0\,V/m$ doesn't include any value. Thus, it can be concluded that, supposing cautiously that all *rbs* channels are active and working at the maximum power, the population is exposed to electric fields levels lower than the cautionary level of the electric field of $6\,V/m$, better lower than its half, according with the Italian law.
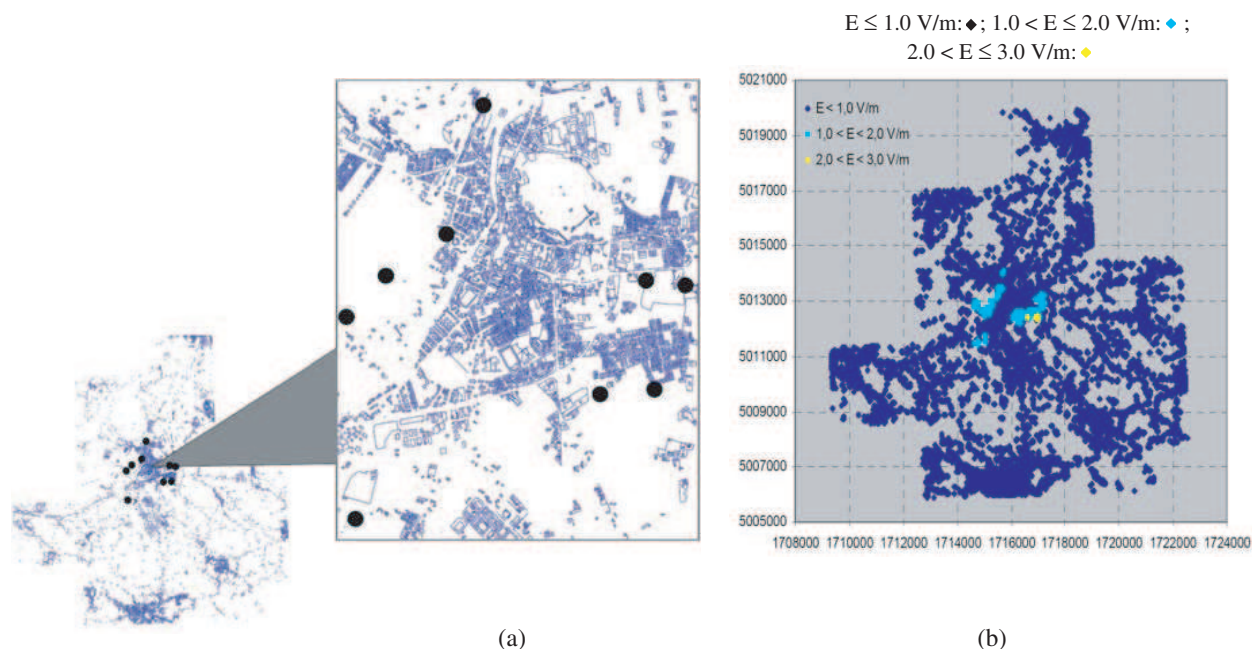
Figure 1: (a) Territory of the town of Monselice with buildings and radio base stations (•) and a zoom of the area where the *rbs* are located; (b) Estimation of the electric field levels, using the far field equation, with different colors in the selected area.

This result is typical for a town in Italy and it seems a good consequence of the Italian standards concerning electromagnetic safety. Because the evaluation method of *ray tracing* is very conservative, including the overlay of all the *rbs* working at the maximum level — that is not a realistic condition — we can consider the exposure of people in Monselice close the quality target suggested by the Salzburg Resolution [4] equal to $1\,mW/m^2$. Two examples of the results obtained using the

ray tracing algorithm, are shown in Figures 3(a) and (b). Figure 3(a) shows the 3D distribution of the electric field levels calculated in an square area including the whole region under examination and containing all the *rbs*. Figure 3(b) shows a snapshoot of an area $700\,\text{m} \times 700\,\text{m}$ containing 2 *rbs* distant $350\,\text{m}$ one from the other, one of them is a co-site.

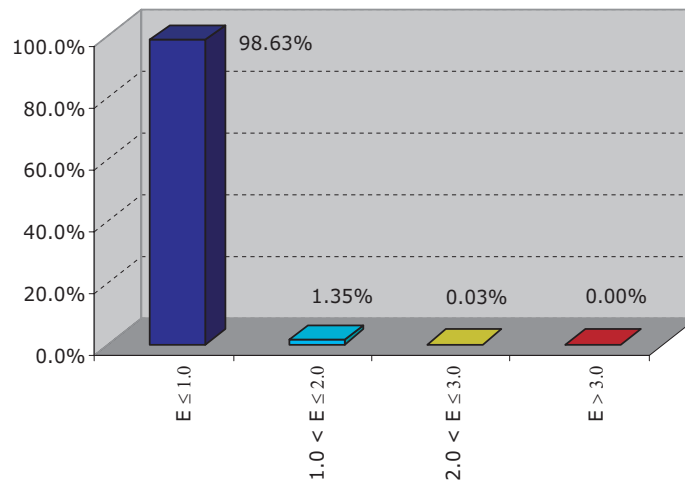Figure 2: Statistical distribution of the electric field levels calculated by using the far field equation.
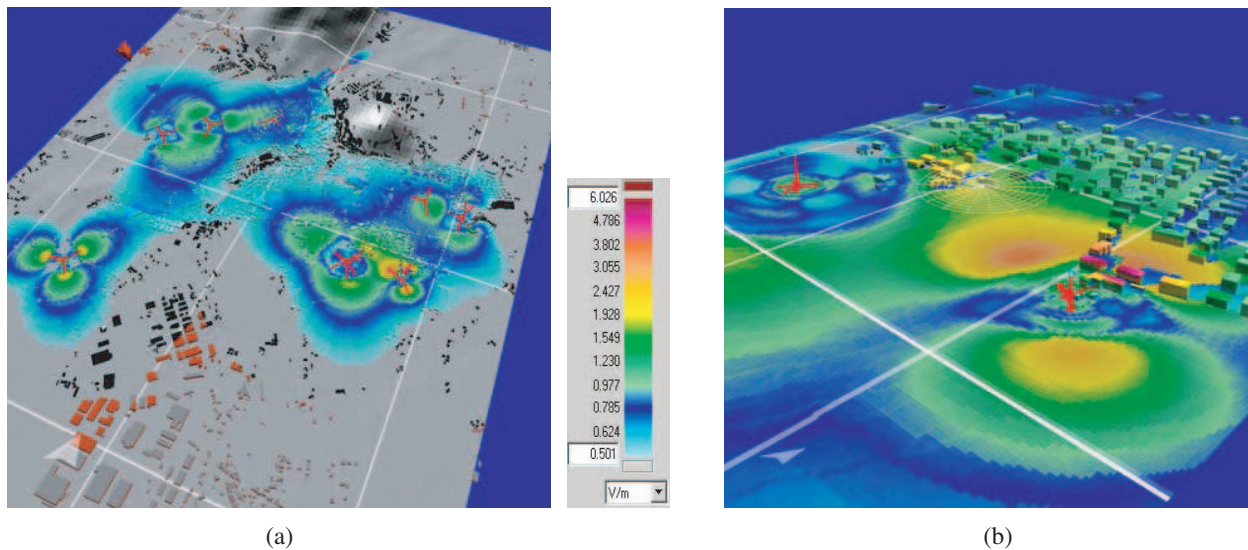
Figure 3: Results of the *ray tracing* algorithm in Monselice: (a) Distribution of the electric field levels on the buildings around all the *rbs*; (b) Distribution of the electric field levels on the buildings around 2 *rbs*.

4. CONCLUSIONS

An area in the town of Monselice has been selected to evaluate the total electromagnetic field produced by *rbs*. Two theoretical evaluations of the *emf* has been implemented to verify people exposure to the emitted fields. The first one in the barycentre of the buildings at the top of them, assuming all the base stations working at the maximum power, by using the far field equation. Another more detailed analysis, carried out by using the *ray tracing* algorithm, has been performed to evaluate the *emf* in detail for people living in the neighborhood of a *rbs*. The results allow to create a map of the electromagnetic impact produced by the *rbs* and the statistical distribution of the estimated electric field levels, as a tool to evaluate people exposure to the *emf* in a complex urban environment. Moreover, it can be useful for the future when new *rbs* have to be added in order to increase the overall network's capacity. The results of both the simulations carry out electric field levels lower than the exposure *limits* ($20\,\text{V/m}$), the *attention levels* and the *quality targets* ($6\,\text{V/m}$) fixed by the Italian law.

REFERENCES

1. Italian DPCM, "Exposure limits, attention levels and quality targets for protection of people exposure to electric, magnetic and electromagnetic fields produced with frequency between 100 kHz and 300 GHz," G.U. 28/08/2003, No. 199, July 2003.

2. Standard CEI 211-7, "Guide for the measurement and the evaluation of electromagnetic fields in the range 10 kHz–300 GHz, with reference to the Human exposure," 2001.

3. Giuliani, L., A. Bedini, C. Giliberti, and R. Palomba, "Electric field environmental levels in the Italian cities: A comparing analysis concerning the maximum levels detected on the top and on the faces of 100.000 buildings in Pisa downtown and in Rome downtown," *Proceedings of the 4th International EMF Conference on Electromagnetic Fields and Biological Effects*, 35, Kunming, China, September 2005.

4. *International Conference on Cell Tower Siting Linking Science & Public Health Salzburg*, June 7–8, 2000. www.salzburg.gv.at/celltower_e

Charge Moment Tensor and the Rotation Equation of a Charged Rigid Body in a Uniform Magnetic Field

Guo-Quan Zhou, Cao Guan, and Si-Lei Zhang

Department of Physics, Wuhan University, Wuhan 430072, China

Abstract— Based on a new concept, i.e., charge moment tensor, and Euler's equation in classical mechanics, the complete dynamic and kinetic equations of the fixed-point rotation for a charged rigid body under a uniform external magnetic field have been derived, and its equivalence to the Lagrange dynamic equations in another paper is emphasized.

1. PREFACE

A rotational charged body has magnetic moment [1–3] and must be subject to a moment of force in an external magnetic field. In view of electromagnetism, it is of theoretical importance and extensive application background to investigate the electrodynamics of a rotational charged body in a external electromagnetic field [1–7]. The mathematical formulation of the dynamic theory about a general charged particle or a continuous charged medium has been well established [8, 9]. References [1–3] introduces a concept of magnetic-moment quadric, deduces and numerates some rules and examples about computing the magnetic moment of a rotational charged body. Meanwhile, the conditions of zero magnetic moment for an arbitrary rotational charged body have been given explicitly in reference [2]. A natural method of introducing the new concept of charge moment tensor has been proposed in references [6], making it possible to construct a more explicit dynamic and kinetic theory for a rotational charged body. As is well known, movement of a rigid body can be viewed as superposition of movement of its center of mass and the rotation around the center, and the latter is only the theme of the present paper. In order to maintain the charge distribution to be constant with respect to the rigid body itself in the course of its movement, we take a charged rigid body as a reference to study its dynamical equation, put our research object under limitation of constant charge distribution (e.g., some kinds of charged dielectric media), slow rotation and no gravitation so that the damping effect of electromagnetic radiation generated from acceleration of its movement and the relativistic effects caused by rotation can all be ignorable.

2. REVIEW OF SOME FUNDAMENTAL CONCEPTS AND FORMULAE

Starting from following formula of magnetic moment for a moving charged body or a point-charge system [8]

$$\vec{P}_m = \frac{1}{2} \sum_i Q_i \left(\vec{r}_i \times \vec{v}_i \right), \tag{1}$$

where $\vec{r}_i$ is the position vectors of the point charge Q_i measured from the origin O in the body coordinate frame $O\text{-}XYZ$, $\vec{v}_i$ is the velocity of point charge Q_i at $\vec{r}_i$, reference [1–3] has introduced a 3-dimension and 2-rank symmetric **charge moment tensor** $\tilde{T}(O)$ to calculate the **magnetic moment** generated by a rigid charged body rotating about a fixed point O with an angular velocity $\vec{\omega}$ (in a fixed reference system).

$$\vec{P}_m(O) = \frac{1}{2}\tilde{T}(O) \cdot \vec{\omega} \tag{2}$$

For the case of discrete point-charge distribution, the tensor element is

$$T_{\alpha\beta}(O) = \sum_i Q_i \left[r_i^2 \delta_{\alpha\beta} - x_{i\alpha}x_{i\beta} \right], \quad (\alpha \text{ and } \beta = 1,\, 2,\, 3) \tag{3}$$

here $\vec{r}_i = (x_{i1},\, x_{i2},\, x_{i3}) = (x_i,\, y_i,\, z_i)$. For the case of continuous charge distribution

$$\widetilde{T}(O) \equiv \int_v \left(r^2 - \vec{r}\vec{r} \right) \rho_e\left(\vec{r}\right) d^3\vec{r} \tag{4}$$

i.e.,

$$\tilde{T}(O) = \begin{pmatrix} T_{xx} & T_{xy} & T_{xz} \\ T_{yx} & T_{yy} & T_{yz} \\ T_{zx} & T_{zy} & T_{zz} \end{pmatrix} = \begin{pmatrix} T_{11} & T_{12} & T_{13} \\ T_{21} & T_{22} & T_{23} \\ T_{31} & T_{32} & T_{33} \end{pmatrix} \tag{5}$$

with its tensor element given in a more explicit form

$$T_{\alpha\beta}(O) = \int_v \rho_e(x_1, x_2, x_3) \left[r^2 \delta_{\alpha\beta} - x_\alpha x_\beta \right] dx_1 dx_2 dx_3 \tag{6}$$

here $\vec{r} = (x_1, x_2, x_3) = (x, y, z)$. And $\delta_{\alpha\beta}$ is a Kronecker notation.

Tensor $\tilde{T}(O)$ is apparently determined only by the spatial distribution of the charge system unless the change of its moving state affects the distribution of charge. Unlike the magnetic moment (2), charge moment tensor $\tilde{T}(O)$ is independent of the movement of this charged body, just like its inertial tensor which is independent of the movement of this rigid body.

In a new Cartesian coordinate system $O\text{-}XYZ$ spanned with the three **principal axes** [6], tensor $\tilde{T}(O)$ can be expressed in a diagonal form

$$\tilde{T}(O) = \text{diag}(T_1, T_2, T_3) \tag{7}$$

And for the case of fixed point rotation O the magnetic moment is

$$\vec{P}_m(O) = \frac{1}{2} \left(T_1 \omega_x \vec{i} + T_2 \omega_y \vec{j} + T_3 \omega_z \vec{k} \right) \tag{8}$$

(Here $\vec{i}$, $\vec{j}$, $\vec{k}$ are the unit vectors of axes X, Y, Z, respectively).

3. DYNAMIC EQUATIONS OF ROTATIONAL CHARGED RIGID BODY UNDER A UNIFORM MAGNETIC FIELD AND A TIME-DEPENDENT TORQUE

According to formula (8), the moment of force generated by the uniform magnetic field (with respect to the center of mass O in the fixed coordinate frame $O\text{-}\xi\eta\zeta$) is

$$\overrightarrow{M} = M_x \vec{i} + M_y \vec{j} + M_z \vec{k} = \overrightarrow{P}_m \times \vec{B} = \frac{1}{2} \left[\tilde{T}(O) \cdot \vec{\omega} \right] \times \vec{B} \tag{9}$$

Note that $\vec{\omega}$ is the angular velocity of the moving charged body with respect to fixed coordinate frame $O\text{-}\xi\eta\zeta$, but expressed in the body Cartesian coordinate system $O\text{-}XYZ$ spanned with the principal axes of inertia tensor. The uniform magnetic induction $\vec{B}$ is also supposed to be along with the axis $O\zeta$ of coordinate frame $O\text{-}\xi\eta\zeta$ in a fixed reference system, and φ, θ, ψ respectively stand for the angles of precession, nutation, and rotation, shown as Fig. 1.

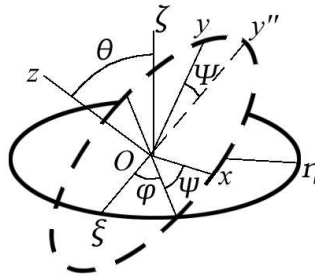Figure 1: Euler's angles for a rotational rigid body around its center of mass.

Then using formula (9), the dynamic equations of the rotational charged rigid body are Euler's equations (in the fixed coordinate frame $O\text{-}\xi\eta\zeta$).

$$\tilde{J} \cdot \frac{d\vec{\omega}}{dt} + \vec{\omega} \times \left(\tilde{J}\vec{\omega} \right) = \frac{1}{2} \left[\tilde{T}(O) \cdot \vec{\omega} \right] \times \vec{B} \tag{10}$$

or

$$
\begin{cases}
J_x\dot{\omega}_x - (J_y - J_z)\omega_y\omega_z = \frac{1}{2}[(T_{21}B_z - T_{31}B_y)\omega_x + (T_{22}B_z - T_{32}B_y)\omega_y + (T_{23}B_z - T_{33}B_y)\omega_z] \\
J_y\dot{\omega}_y - (J_z - J_x)\omega_z\omega_x = \frac{1}{2}[(T_{31}B_x - T_{11}B_z)\omega_x + (T_{32}B_x - T_{12}B_z)\omega_y + (T_{33}B_x - T_{13}B_z)\omega_z] \\
J_z\dot{\omega}_z - (J_x - J_y)\omega_x\omega_y = \frac{1}{2}[(T_{11}B_y - T_{21}B_x)\omega_x + (T_{12}B_y - T_{22}B_x)\omega_y + (T_{13}B_y - T_{23}B_x)\omega_z]
\end{cases}
\tag{11}
$$

here $T_{ij} = T_{ji}$, $(i, j = 1, 2, 3)$ and $\tilde{J}(O) = \mathrm{diag}\,(J_x, J_y, J_z)$, is the principal-axes inertia tensor of the rigid body with respect to point O. Note that although $\tilde{J}$ is diagonal in the principal-axes coordinate system, generally the charge moment tensor $\tilde{T}$ isn't definitely of a diagonal form at the same time, but still expressed as formula (5). It is due to a fact that the principal axes of the inertia moment tensor of the rigid body aren't generally coincident with that of the charge moment tensor.

Equations (11)–(13) are the complete equation groups which are effective for an arbitrary rotational charged rigid body with an constant charge distribution and under a uniform magnetic field.

It is worthy of mentioning that Equations (11)–(13) are completely equivalent to the Lagrange version of dynamic equations proposed in another paper [6], only if we make use of Euler's kinetic equations

$$
\begin{cases}
\omega_x = \dot{\varphi}\sin\theta\sin\psi + \dot{\theta}\cos\psi \\
\omega_y = \dot{\varphi}\sin\theta\cos\psi - \dot{\theta}\sin\psi \\
\omega_z = \dot{\varphi}\cos\theta + \dot{\psi}
\end{cases}
\tag{12}
$$

and combine with following expression of the magnetic field

$$
\vec{B} = B_x\vec{i} + B_y\vec{j} + B_z\vec{k} = B\,(\sin\theta\cos\psi \;\; \sin\theta\sin\psi \;\; \cos\theta)
\tag{13}
$$

By the way, the right hand side of Equation (11) can be rewritten in a matrix form

$$
\tilde{J} \cdot \frac{d}{dt}\vec{\omega} + \vec{\omega} \times \left(\tilde{J} \cdot \vec{\omega}\right) = \frac{1}{2}\tilde{\Lambda} \cdot \vec{\omega}
\tag{14}
$$

with

$$
\tilde{\Lambda} = \begin{pmatrix}
T_{21}B_z - T_{31}B_y & T_{22}B_z - T_{32}B_y & T_{23}B_z - T_{33}B_y \\
T_{31}B_x - T_{11}B_z & T_{32}B_x - T_{12}B_z & T_{33}B_x - T_{13}B_z \\
T_{11}B_y - T_{21}B_x & T_{12}B_y - T_{22}B_x & T_{13}B_y - T_{23}B_x
\end{pmatrix}
\tag{15}
$$

It is easy to find that matrix $\tilde{\Lambda}$ has a zero determinant, i.e.,

$$
\det\left(\tilde{\Lambda}\right) = 0
\tag{16}
$$

Generally it is difficult to find a strict analytic solution to the nonlinear Equations (14)–(15). Limited to space, but simple conclusions can be drawn for some symmetric cases. For instance, a charged body with symmetry

$$
J_x = J_y = J_z \equiv J, \quad T_1 = T_2 = T_3 \equiv T,
\tag{17}
$$

Equation (10) can be reduced to simple vector form

$$
J\frac{d\vec{\omega}}{dt} + \vec{\omega} \times (J\vec{\omega}) = \frac{1}{2}T\vec{\omega} \times \vec{B},
\tag{18}
$$

or

$$
\frac{d}{dt}\vec{\omega} = \frac{T}{2J}\vec{\omega} \times \vec{B} = \vec{\Omega} \times \vec{\omega},
\tag{19}
$$

$$
\vec{\Omega} = -\frac{T}{2J}\vec{B}
\tag{20}
$$

This rightly satisfies the sufficient and necessary condition for a vector to make a regular precession given in reference [10]. Therefore the angular momentum $\vec{J}$ will rotate with a precession angular velocity $\vec{\Omega}$. This is in fact equivalent to Larmor precession which depicts the movement of a particle with magnetic moment in a uniform magnetic field. The different point is the rotational charged medium is of an arbitrary shape and distribution of charge and mass but with symmetry of (17).

4. CONCLUDING REMARKS

Research on a charged rigid body in an electromagnetic field is an important and valuable pursuit involved in many disciplines which provide the foundation of its application in many engineering and technology fields. It is worthy of mention that, even for a rotational rigid body under the background without electromagnetic field, there are only several examples such as Euler-Poinsot case, Lagrange-Poisson case, Kovalevskaya case that can be strictly solved. Using Euler's theory in classical mechanics and a new concept, i.e., charge moment tensor, we successfully derived the dynamical and kinetic equations of a rotational charged rigid body with a constant charge distribution in a uniform magnetic field. Its equivalence to the Lagrange version of dynamic equations proposed in another paper is stressed. It is worthy of mentioning that a tiny classical charged particle rotating in a steady magnetic field $\vec{B}(\vec{r})$ (i.e., a time-independent but space-dependent magnetic field) must approximately satisfy Equations (11)–(13), because within a sufficient small space the steady magnetic field can be treated approximately as a uniform magnetic field.

REFERENCES

1. Zhou, G.-Q., *Progress In Electromagnetics Research*, PIER 68, 156–160, New York, 2007.
2. Zhou, G.-Q., et al., *Progress In Electromagnetics Research*, PIER 70, 211–223, New York, 2007.
3. Zhou, G.-Q., *PIERS Proceedings*, 89–93, Beijing, China, March 26–30, 2007.
4. Krasheninnikov, S. I., V. I. Shevchenko, et al., *Physics Letter A*, Vol. 361, 133–135, 2007.
5. Kroh, H. J., et al., *Phys. Rev. E*, Vol. 62, No. 5, 7309–7314, 2000.
6. Zhou, G.-Q., *PIERS Proceedings*, Beijing, China, 2009, (in progress).
7. Dolinsky, Yu. and T. Elperin, *Phys. Rev. E*, Vol. 75, 026611, 2007.
8. Jackson, J. D., *Classical Electrodynamics*, John Wiley & Sons, Inc., New York, 1962.
9. Liu, J.-P., *Electrodynamics [M]*, Higher Education Press, Beijing, 2004, (Ch).
10. Zhou, G.-Q., *Physics and Engineering*, Vol. 11, No. 1, 22–25, 2001, (Ch).

Natural Introduction of Charge Moment Tensor and the Lagrangian of a Rotational Charged Rigid Body

Guo-Quan Zhou, **Si-Lei Zhang**, and **Cao Guan**

Department of Physics, Wuhan University, Wuhan 430072, China

Abstract— A natural method of introducing a new concept, i.e., charge moment tensor, has been found. Its application in the Lagrange dynamic equations of a rotational charged rigid body under a uniform magnetic field has been derived for the case of fixed-point rotation, and the corresponding invariants have also been recognized. Meanwhile, some simple conclusions about a special symmetric case have been drawn.

1. INTRODUCTION

Any rotational charged body has a definite magnetic moment, and is subject to a moment of force imposed by an external magnetic field [1–3]. Computing the magnetic moment $\vec{P}_m$ of a rotational charged body is only the first step to study its dynamic and kinetic behaviors in electromagnetic fields. In view of electromagnetism, it is very important to derive a dynamic equation for a rotational charged body under a given electromagnetic field [4–6]. For a general charged particle or a continuous charged medium, the mathematical formulation of its dynamic behavior has been established and well known [7–10]. Based on a strict and delicate analogue relation, references [1–3] have introduced the concept of magnetic-moment quadric, deduced a series of rules and given some examples about calculating the magnetic moment of a rotational charged body. Meanwhile, the conditions of zero magnetic moment for an arbitrary rotational charged body have been formulated explicitly in reference [2]. Nevertheless, a natural method of introducing the new concept of charge moment tensor has been proposed in the present paper, making it possible to construct an explicit Lagrange dynamic theory and kinetic equations for a rotational charged body.

Generally speaking, movement of a rigid body can be viewed as superposition of movement of its center of mass and the rotation around the center, and the latter is just the theme of the present paper. We take a charged rigid body as an instance in the present paper, and put our research object under limitation of slow rotation, constant charge distribution, and no gravitation so that the electromagnetic induction, the relativistic effects caused by rotation can all be ignorable.

2. NATURAL INTRODUCTION OF CHARGE MOMENT TENSOR AND THE MAGNETIC MOMENT FOR A ROTATIONAL CHARGED BODY

A localized steady-state conductive current $\vec{J}$ will generate a **magnetic moment** [8–10]

$$\vec{P}_m = \frac{1}{2} \int \vec{r}\,' \times \vec{J}\left(\vec{r}\,'\right) d^3 \vec{r}\,' \tag{1}$$

For a point-charge system or a dielectric rigid body with continuous charge distribution rotating around a fixed point O in the rigid body with an angular velocity $\vec{\omega}$, we can also give an expression of $\vec{P}_m$ with [10]

$$\vec{P}_m = \frac{1}{2} \sum_i Q_i \left(\vec{r}_i' \times \vec{v}_i'\right) \quad \text{(For a point-charge system)} \tag{2}$$

Here $\vec{v}_i' \left(= \vec{\omega} \times \vec{r}_i'\right)$ is the velocity of point charge Q_i with respect to the fixed point O. $\vec{r}\,'$ is the position vector of point charge Q_i in the body coordinate system $O\text{-}X'Y'Z'$. $\vec{r}_i' = (x_{i1}', x_{i2}', x_{i3}') = (x_i', y_i', z_i')$. Then from (2)

$$\vec{P}_m = \frac{1}{2} \sum_i Q_i \left[\vec{r}_i' \times \left(\vec{\omega} \times \vec{r}_i'\right)\right] = \frac{1}{2} \sum_i \left[Q_i \left(r_i'^2 - \vec{r}_i'\vec{r}_i'\right)\right] \vec{\omega} \tag{3}$$

Hence from (2), a new concept — **charge moment tensor** $\tilde{T}(O)$ with respect to the fixed point O can be defined as

$$T_{\alpha\beta}(O) = \sum_i Q_i \left[r_i'^2 \delta_{\alpha\beta} - x_{i\alpha}' x_{i\beta}'\right], \quad (\alpha \text{ and } \beta = 1, 2, 3) \tag{4}$$

or

$$
\tilde{T}(O) =
\begin{pmatrix}
\sum_i Q_i \left(y_i'^2 + z_i'^2 \right) & -\sum_i Q_i x_i' y_i' & -\sum_i Q_i x_i' z_i' \\
-\sum_i Q_i x_i' y_i' & \sum_i Q_i \left(z_i'^2 + x_i'^2 \right) & -\sum_i Q_i y_i' z_i' \\
-\sum_i Q_i x_i' z_i' & -\sum_i Q_i y_i' z_i' & \sum_i Q_i \left(x_i'^2 + y_i'^2 \right)
\end{pmatrix}
\tag{5}
$$

For the case of continuous charge distribution,

$$
\tilde{T}(O) \equiv \int_V \left(r'^2 - \vec{r}\,'\vec{r}\,' \right) \rho_e \left(\vec{r}\,' \right) d^3 \vec{r}\,'
\tag{6}
$$

i.e.,

$$
\tilde{T}(O) =
\begin{pmatrix}
T_{xx} & T_{xy} & T_{xz} \\
T_{yx} & T_{yy} & T_{yz} \\
T_{zx} & T_{zy} & T_{zz}
\end{pmatrix}
=
\begin{pmatrix}
T_{11} & T_{12} & T_{13} \\
T_{21} & T_{22} & T_{23} \\
T_{31} & T_{32} & T_{33}
\end{pmatrix}
\tag{7}
$$

with its tensor element given in a more explicit form

$$
T_{\alpha\beta}(O) = \int_v \rho_e \left(x_1', \, x_2', \, x_3' \right) \left[r'^2 \delta_{\alpha\beta} - x_\alpha' x_\beta' \right] dx_1' dx_2' dx_3'
\tag{8}
$$

Here $\vec{r}\,' = (x_1', \, x_2', \, x_3') = (x', \, y', \, z')$, $r'^2 = x_1'^2 + x_2'^2 + x_3'^2$, and $\delta_{\alpha\beta}$ is a Kronecker notation, $\rho_e(\vec{r}\,')$ is the volume density of charge. Apparently tensor $\tilde{T}(O)$ is decided only by the spatial distribution of the charge system unless the change of its moving state affects the distribution of charge.

Thus according to (1)–(6), the **magnetic moment** with respect to the fixed point O in a fixed reference system $(O\text{-}\xi\eta\zeta)$ is

$$
\vec{P}_m(O) = \frac{1}{2} \tilde{T}(O) \cdot \vec{\omega}
\tag{9}
$$

Hence we have introduced a 3-dimension and 2-rank symmetric **charge moment tensor** $\tilde{T}$ in a natural method. We find $\tilde{T}(O)$ naturally emerging in expression of the magnetic moment $\vec{P}_m(O)$ in (9), and apparently different from the existing concept of electric quadruple moment [9], i.e.,

$$
\tilde{D}_{ij} = \int_v \left(3 x_i' x_j' - r'^2 \delta_{ij} \right) \rho \left(\vec{r}\,' \right) dV', \quad (i, \, j = 1, \, 2, \, 3)
\tag{10}
$$

which had been introduced long before in the theory of electric multi-pole expansion of electric potential for a charge system. However, it is easy to find a relation between them which can be expressed as

$$
\tilde{T}(O) = -\frac{1}{3} \tilde{D}(O) + \frac{2}{3} r'^2 I
\tag{11}
$$

Here I is a 3×3 identity matrix.

Suppose the direction cosine of an arbitrary fixed axis is $\vec{l} = (\cos\theta_1, \, \cos\theta_2, \, \cos\theta_3)$, then the so-called **scalar charge moment** T_l with respect to this fixed axis (which passes point O) is

$$
\begin{aligned}
T_l \left(O, \, \vec{l} \right) = \vec{l} \cdot \tilde{T} \cdot \vec{l} ={} & T_{11} \cos^2\theta_1 + T_{22} \cos^2\theta_2 + T_{33} \cos^2\theta_3 \\
& + 2\,T_{12} \cos\theta_1 \cos\theta_2 + 2\,T_{23} \cos\theta_2 \cos\theta_3 + 2\,T_{31} \cos\theta_3 \cos\theta_1
\end{aligned}
\tag{12}
$$

It can be immediately deduced that a rotational charged body with an angular velocity of $\vec{\omega}$ with respect to the same axis $(O, \, \vec{l})$ passing through point O and along with the direction of $\vec{l}$, must has a **scalar charge moment** (given $\vec{\omega} = \omega \vec{l}$).

$$
T_l = \frac{\vec{\omega}}{\omega} \cdot \tilde{T} \cdot \frac{\vec{\omega}}{\omega}
\tag{13}
$$

And the **magnetic moment** with respect to the fixed axis $(O, \vec{l})$ is

$$\vec{P}_m\left(O, \vec{l}\right) = \frac{1}{2}T_l\vec{\omega} = \frac{1}{2}\left(\frac{\vec{\omega}}{\omega} \cdot \tilde{T}(O) \cdot \frac{\vec{\omega}}{\omega}\right)\vec{\omega} = \frac{1}{2}l_i\tilde{T}_{ij}l_j\vec{\omega} \tag{14}$$

Here the repeated indices represent summation from 1 to 3 according to Einstein's convention.

In a new Cartesian coordinate system $O\text{-}X'Y'Z'$ (in body reference system), which is rigidly linked with the charged body and spanned with the three **principal axes**, charge moment tensor $\tilde{T}(O)$ has a definite meaning that is independent of the movement of this charged body and can be expressed in a diagonal form

$$\tilde{T}(O) = \begin{pmatrix} T_1 & 0 & 0 \\ 0 & T_2 & 0 \\ 0 & 0 & T_3 \end{pmatrix} \tag{15}$$

Then according to Equation (14) or (15), in the principal-axes coordinate system, the magnetic moment with respect to the same fixed axis $(O, \vec{l})$ is

$$\vec{P}_m\left(O, \vec{l}\right) = \frac{1}{2}\left(T_1 \cos^2\theta_1 + T_2 \cos^2\theta_2 + T_3 \cos^2\theta_3\right)\vec{\omega} \tag{16}$$

On the other hand, according to formula (9), in the principal-axes coordinates system, the magnetic moment with respect to fixed point O is

$$\vec{P}_m(O) = \frac{1}{2}\left(T_1\omega_x\vec{i} + T_2\omega_y\vec{j} + T_3\omega_z\vec{k}\right) \tag{17}$$

Here $\vec{i}$, $\vec{j}$, $\vec{k}$ are the unit vectors of axes X, Y, Z, respectively.

3. THE LAGRANGIAN OF ROTATIONAL CHARGED DIELECTRIC RIGID BODY IN AN UNIFORM MAGNETIC FIELD

Lagrange's dynamic theory can be used to depict the above rotation system. Suppose ω_x, ω_y, ω_z are respectively the three components of the angular velocity expressed in the Cartesian coordinate frame $O\text{-}X'Y'Z'$ (also the principal-axis coordinate system of its inertia tensor), also suppose the direction of external uniform magnetic field is along the axis $O\zeta$ of coordinate frame $O\text{-}\xi\eta\zeta$ in a fixed reference system, and φ, θ, ψ respectively stand for the angles of precession, nutationand rotation, shown as Fig. 1.
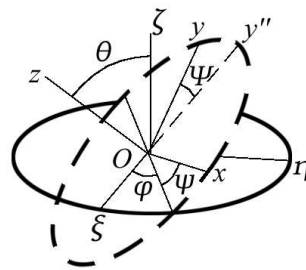

Figure 1: Euler's angles describing the movement of a rigid body around its center of mass.

Then the Euler's kinetic equation is

$$\begin{pmatrix} \omega_x \\ \omega_y \\ \omega_z \end{pmatrix} = \begin{pmatrix} \sin\theta\sin\psi & \cos\psi & 0 \\ \sin\theta\cos\psi & -\sin\psi & 0 \\ \cos\theta & 0 & 1 \end{pmatrix} \begin{pmatrix} \dot{\varphi} \\ \dot{\theta} \\ \dot{\psi} \end{pmatrix} \equiv \tilde{M}\begin{pmatrix} \dot{\varphi} \\ \dot{\theta} \\ \dot{\psi} \end{pmatrix} \tag{18}$$

Here

$$\tilde{M} = \begin{pmatrix} \sin\theta\sin\psi & \cos\psi & 0 \\ \sin\theta\cos\psi & -\sin\psi & 0 \\ \cos\theta & 0 & 1 \end{pmatrix} \tag{19}$$

We select the three Euler's angles φ, θ, ψ as the generalized coordinates of the systemthen the rotation kinetic energy of this system is

$$E_k\left(\varphi,\,\theta,\,\psi;\,\dot\varphi,\,\dot\theta,\,\dot\psi\right) = \frac{1}{2}\left(\omega_x\,\omega_y\,\omega_z\right)\tilde I\left(\omega_x\,\omega_y\,\omega_z\right)^T = \frac{1}{2}\left(\dot\varphi\,\dot\theta\,\dot\psi\right)M^T\tilde I\,M\left(\dot\varphi\,\dot\theta\,\dot\psi\right)^T \tag{20}$$

Here the superscript "T" represents transposition of a matrix, $\tilde I$ is the principal-axis inertia tensor, i.e., $\tilde I(O) = \mathrm{diag}(I_x, I_y, I_z)$, and M are given by (19). On the other hand, the uniform magnetic field $\vec B$ along with direction $O\zeta$ can be expressed in terms of Euler's angles φ, θ, ψ and the value of $\vec B$

$$\vec B = B\sin\theta\cos\psi\,\vec i + B\sin\theta\sin\psi\,\vec j + B\cos\theta\,\vec k = B\left(\sin\theta\cos\psi\ \sin\theta\sin\psi\ \cos\theta\right) \tag{21}$$

Then according to (9) and (21), the potential energy of a rotational charged dielectric rigid body in a uniform magnetic field is

$$V_m = -\vec P_m\cdot\vec B = -\vec B\cdot\vec P_m = -\frac{B}{2}\left(\sin\theta\cos\psi\ \sin\theta\sin\psi\ \cos\theta\right)\cdot\left\{\tilde T\cdot\left[M\left(\dot\varphi\,\dot\theta\,\dot\psi\right)^T\right]\right\} \tag{22}$$

Thus the Lagrangian of this system is

$$L(\varphi,\,\theta,\,\psi;\,\dot\varphi,\,\dot\theta,\,\dot\psi) = E_k - V_m = \frac{1}{2}\left(\dot\varphi\,\dot\theta\,\dot\psi\right)M^T\tilde I\,M\left(\dot\varphi\,\dot\theta\,\dot\psi\right)^T$$
$$+\frac{B}{2}\left(\sin\theta\cos\psi\ \sin\theta\sin\psi\ \cos\theta\right)\cdot\left\{\tilde T\cdot\left[M\left(\dot\varphi\,\dot\theta\,\dot\psi\right)^T\right]\right\} \tag{23}$$

Note that although $\tilde I$ is diagonal in the principal-axes coordinate system, generally the charge moment tensor $\tilde T$ isn't definitely of a diagonal form at the same time, but still expressed as formula (7). Then the Lagrange dynamic equations of the conservative system are

$$\frac{d}{dt}\left(\frac{\partial L}{\partial\dot\varphi}\right) - \frac{\partial L}{\partial\varphi} = 0 \tag{24}$$

$$\frac{d}{dt}\left(\frac{\partial L}{\partial\dot\theta}\right) - \frac{\partial L}{\partial\theta} = 0 \tag{25}$$

$$\frac{d}{dt}\left(\frac{\partial L}{\partial\dot\psi}\right) - \frac{\partial L}{\partial\psi} = 0 \tag{26}$$

The above equations determine the dynamic behaviors of this rotation system. It is easy to recognize immediately that φ and t are ignorable variables (i.e., the cyclic coordinates) of the system, the corresponding generalized momentum $P_\varphi = \frac{\partial L}{\partial\dot\varphi}$ and energy are invariants (i.e., the integrals of motion).

4. SOME SIMPLE CONCLUSION ABOUT A SYMMETRIC CASE

When the concerned dielectric rigid body is of a 4-degree symmetric axis about the distribution of its mass and charge, then the center of mass and center of charge are just the same point, the origin O of body reference system. The principal axes of inertia moment tensor $\tilde I$ and those of the charge moment tensor $\tilde T$ are therefore also collinear and define the above body Cartesian coordinate system, in which both $\tilde I$ and $\tilde T$ are diagonal and

$$I_x = I_y \neq I_z, \quad T_1 = T_2 \neq T_3 \tag{27}$$

According to formula (17)–(19), the magnetic moment corresponding to angular velocity $\vec\omega$ is

$$\vec P_m = \frac{1}{2}\left(T_1\omega_x\vec i + T_2\omega_y\vec j + T_3\omega_z\vec k\right)$$
$$= \frac{1}{2}\left[T_1\left(\dot\varphi\sin\theta\sin\psi + \dot\theta\cos\psi\right)\vec i + T_2\left(\dot\varphi\sin\theta\cos\psi - \dot\theta\sin\psi\right)\vec j + T_3\left(\dot\varphi\cos\theta + \dot\psi\right)\vec k\right] \tag{28}$$

then according to (19), (20) and (27), we have

$$E_k = \frac{I_x}{2}\left(\dot\theta^2 + \dot\varphi^2 \sin^2\theta\right) + \frac{I_z}{2}\left(\dot\psi + \dot\varphi\cos\theta\right)^2 \tag{29}$$

and according to (21), (27) and (28), we have

$$V_m = -\vec{P}_m \cdot \vec{B} = -\frac{B}{2}\left[T_1\left(\dot\varphi\sin^2\theta\sin 2\psi + \dot\theta\sin\theta\cos 2\psi\right) + T_3\left(\dot\varphi\cos^2\theta + \dot\psi\cos\theta\right)\right] \tag{30}$$

At last we attain the Lagrangian of the above rotational rigid body with a 4-degree symmetric axis, that is

$$\begin{aligned}
L&\left(\varphi,\theta,\psi;\dot\varphi,\dot\theta,\dot\psi,t\right)\\
&= E_k - V_m = \frac{I_x}{2}\left(\dot\theta^2 + \dot\varphi^2\sin^2\theta\right) + \frac{I_z}{2}\left(\dot\psi + \dot\varphi\cos\theta\right)^2\\
&\quad + \frac{B}{2}\left[\left(T_1\sin^2\theta\sin 2\psi + T_3\cos^2\theta\right)\dot\varphi + \left(T_1\sin\theta\cos 2\psi\right)\dot\theta + \left(T_3\cos\theta\right)\dot\psi\right]
\end{aligned} \tag{31}$$

We can immediately recognize that variables t and φ are the cyclic coordinates (i.e., the so-called ignorable variables) of this system. According to the Lagrange dynamic Equations (24)–(26), the energy of this system and the generalized momentum $P_\varphi = \frac{\partial L}{\partial \dot\varphi}$ are invariants (i.e., the integrals of motion). Substituting expression (31) into Lagrange Equations (24)–(26), we attain the following dynamic equations which determine the movement of the rigid body

$$\left(I_x\sin^2\theta + I_z\cos^2\theta + I_z\cos\theta\right)\dot\varphi + \frac{1}{2}BT_1\sin^2\theta\sin 2\psi + \frac{1}{2}BT_3\cos^2\theta = const. \tag{32}$$

$$\begin{aligned}
&I_x\ddot\theta + \frac{1}{2}\left[(I_z - I_x)\sin 2\theta\right]\dot\varphi^2 + (I_z\sin\theta)\dot\varphi\dot\psi + \frac{1}{2}(BT_3\sin 2\theta)\dot\varphi\\
&+ \left(-BT_1\sin\theta\sin 2\psi + \frac{1}{2}BT_3\sin\theta\right)\dot\psi - \frac{1}{2}BT_1\sin 2\theta\sin 2\psi = 0
\end{aligned} \tag{33}$$

$$\begin{aligned}
&I_z\ddot\psi + (I_z\cos\theta)\ddot\varphi - (I_z\sin\theta)\dot\theta\dot\varphi + \left(BT_1\sin\theta\sin 2\psi - \frac{1}{2}BT_3\sin\theta\right)\dot\theta\\
&- (BT_1\sin^2\theta\cos 2\psi)\dot\varphi = 0
\end{aligned} \tag{34}$$

Equation (32) is obviously integrable and corresponds to the integral of motion of this system.

5. CONCLUDING REMARKS

Research on a charged rigid body in an electromagnetic field is an important and valuable pursuit involved in many disciplines [2–7] which provide the foundation of its application in many engineering and technology fields. It should be noticed that the expression of magnetic moment for the case of fixed-point rotation, (9), is different from that for a fixed-axis rotation, (14), just like the angular moment of a rigid body about a fixed-point rotation is different from that about a case of fixed-axis rotation.

Making use of the new concept of charge moment tensor related to magnetic moment of a rotational charged body and Lagrange dynamic theory in analytic mechanics, we successfully derived the Lagrangian of a rotational charged dielectric rigid body in a uniform magnetic field, giving concrete and simple conclusions for a symmetric case. In another paper, we have discussed in detail the dynamics and stability problem of a concrete model.

ACKNOWLEDGMENT

REFERENCES

1. Zhou, G.-Q., *Progress In Electromagnetics Research*, PIER 68, 156–160, New York, 2007.
2. Zhou, G.-Q., et al., *Progress In Electromagnetics Research*, PIER 70, 211–223, New York, 2007.

3. Zhou, G.-Q., *PIERS Proceedings*, 89–93, Beijing, China, March 26–30, 2007.
4. Krasheninnikov, S. I., V. I. Shevchenko, et al., *Physics Letter A*, Vol. 361, 133–135, 2007.
5. Kroh, H. J., et al., *Phys. Rev. E*, Vol. 62, No. 5, 7309–7314, 2000.
6. Dolinsky, Yu. and T. Elperin, *Phys. Rev. E*, Vol. 75, 026611, 2007.
7. Jones, T. B., *Electromechanics of Particles*, Cambridge University Press, Cambridge, England, 1995.
8. Landau, L. D. and E. M. Lifshitz, *Electrodynamics of Continuous Media*, Pergamon Press, Oxford, 1984.
9. Liu, J.-P., *Electrodynamics [M]*, Higher Education Press, Beijing, 2004, (Ch).
10. Jackson, J. D., *Classical Electrodynamics*, John Wiley & Sons, Inc., New York, 1962.

Simplified Variational Principles for Barotropic Magnetohydrodynamics

A. Yahalom

Ariel University Center of Samaria, Ariel 40700, Israel

Abstract— Variational principles for magnetohydrodynamics were introduced by previous authors both in Lagrangian and Eulerian form. In a previous work Yahalom & Lynden-Bell introduced a simpler Eulerian variational principles from which all the relevant equations of magnetohydrodynamics can be derived. The variational principle were given in terms of six independent functions for non-stationary flows and three independent functions for stationary flows. This is less then the seven variables which appear in the standard equations of magnetohydrodynamics which are the magnetic field $\vec{B}$ the velocity field $\vec{v}$ and the density ρ. In this work I will attempt to improve on our previous results thus reducing the number of functions needed even further.

1. INTRODUCTION

Variational principles for magnetohydrodynamics were introduced by previous authors both in Lagrangian and Eulerian form. Sturrock [1] has discussed in his book a Lagrangian variational formalism for magnetohydrodynamics. Vladimirov and Moffatt [2] in a series of papers have discussed an Eulerian variational principle for incompressible magnetohydrodynamics. However, their variational principle contained three more functions in addition to the seven variables which appear in the standard equations of magnetohydrodynamics which are the magnetic field $\vec{B}$ the velocity field $\vec{v}$ and the density ρ. Kats [3] has generalized Moffatt's work for compressible non barotropic flows but without reducing the number of functions and the computational load. Moreover, Kats have shown that the variables he suggested can be utilized to describe the motion of arbitrary discontinuity surfaces [4, 5]. Sakurai [6] has introduced a two function Eulerian variational principle for force-free magnetohydrodynamics and used it as a basis of a numerical scheme, his method is discussed in a book by Sturrock [1]. A method of solving the equations for those two variables was introduced by Yang, Sturrock & Antiochos [7]. In a recent work Yahalom & Lynden-Bell [8, 9] have combined the Lagrangian of Sturrock [1] with the Lagrangian of Sakurai [6] to obtain an **Eulerian** Lagrangian principle depending on only six functions. The vanishing of the variational derivatives of this Lagrangian entail all the equations needed to describe barotropic magnetohydrodynamics without any additional constraints. The equations obtained resemble the equations of Frenkel, Levich & Stilman [10] (see also [11]). Furthermore, it was shown that for stationary flows three functions will suffice in order to describe a Lagrangian principle for barotropic magnetohydrodynamics. The non-singlevaluedness of the functions appearing in the reduced representation of barotropic magnetohydrodynamics was discussed in particular with connection to the topological invariants of magnetic and cross helicities. It was shown how the conservation of cross helicity can be easily generated using the Noether theorem and the variables introduced in that paper. In the current paper I improve on the previous results and show that four functions are enough to describe a general non stationary barotropic magnetohydrodynamics, the idea is borrowed from [12] see also [13–15].

The plan of this paper is as follows: First we introduce the standard notations and equations of barotropic magnetohydrodynamics. Next we introduce the potential representation of the magnetic field $\vec{B}$ and the velocity field $\vec{v}$. This is followed by a review of the Eulerian variational principle developed by Yahalom & Lynden-Bell [8, 9]. After those introductory sections we will present the four function Eulerian variational principles for non-stationary magnetohydrodynamics.

2. THE STANDARD FORMULATION OF BAROTROPIC MAGNETOHYDRODYNAMICS

The standard set of equations solved for barotropic magnetohydrodynamics are given below:

$$\frac{\partial \vec{B}}{\partial t} = \vec{\nabla} \times \left(\vec{v} \times \vec{B} \right), \tag{1}$$

$$\vec{\nabla} \cdot \vec{B} = 0 \tag{2}$$

$$\frac{\partial \rho}{\partial t} + \vec{\nabla} \cdot (\rho \vec{v}) = 0, \tag{3}$$

$$\rho \frac{d\vec{v}}{dt} = \rho \left(\frac{\partial \vec{v}}{\partial t} + \left(\vec{v} \cdot \vec{\nabla} \right) \vec{v} \right) = -\vec{\nabla} p(\rho) + \frac{\left(\vec{\nabla} \times \vec{B} \right) \times \vec{B}}{4\pi}. \tag{4}$$

The following notations are utilized: $\frac{\partial}{\partial t}$ is the temporal derivative, $\frac{d}{dt}$ is the temporal material derivative and $\vec{\nabla}$ has its standard meaning in vector calculus. $\vec{B}$ is the magnetic field vector, $\vec{v}$ is the velocity field vector and ρ is the fluid density. Finally $p(\rho)$ is the pressure which we assume depends on the density alone (barotropic case). The justification for those equations and the conditions under which they apply can be found in standard books on magnetohydrodynamics (see for example [1]). Equation (1) describes the fact that the magnetic field lines are moving with the fluid elements ("frozen" magnetic field lines), Equation (2) describes the fact that the magnetic field is solenoidal, Equation (3) describes the conservation of mass and Equation (4) is the Euler equation for a fluid in which both pressure and Lorentz magnetic forces apply. The term:

$$\vec{J} = \frac{\vec{\nabla} \times \vec{B}}{4\pi}, \tag{5}$$

is the electric current density which is not connected to any mass flow. The number of independent variables for which one needs to solve is seven ($\vec{v}$, $\vec{B}$, ρ) and the number of Equations (1), (3), (4) is also seven. Notice that Equation (2) is a condition on the initial $\vec{B}$ field and is satisfied automatically for any other time due to Equation (1). Also notice that $p(\rho)$ is not a variable rather it is a given function of ρ.

3. POTENTIAL REPRESENTATION OF VECTOR QUANTITIES OF MAGNETOHYDRODYNAMICS

It was shown in [8] that $\vec{B}$ and $\vec{v}$ can be represented in terms of five scalar functions α, β, χ, η, ν. Following Sakurai [6] the magnetic field takes the following form:

$$\vec{B} = \vec{\nabla} \chi \times \vec{\nabla} \eta. \tag{6}$$

Hence $\vec{B}$ satisfies automatically Equation (2) and is orthogonal to both $\vec{\nabla}\chi$ and $\vec{\nabla}\eta$. A similar representation was suggested by Dungey [16] but not in the context of variational analysis. Moreover, the velocity $\vec{v}$ can be represented in the following form:

$$\vec{v} = \vec{\nabla}\nu + \alpha \vec{\nabla}\chi + \beta \vec{\nabla}\eta. \tag{7}$$

this representation is a generalization of the Clebsch representation for magnetohydrodynamics [17].

4. THE ACTION OF BAROTROPIC MAGNETOHYDRODYNAMICS

It was shown in [8] that the action of barotropic magnetohydrodynamics takes the form:

$$A \equiv \int \mathcal{L} d^3 x dt,$$

$$\mathcal{L} \equiv -\rho \left[\frac{\partial \nu}{\partial t} + \alpha \frac{\partial \chi}{\partial t} + \beta \frac{\partial \eta}{\partial t} + \varepsilon(\rho) + \frac{1}{2} \left(\vec{\nabla}\nu + \alpha \vec{\nabla}\chi + \beta \vec{\nabla}\eta \right)^2 \right] - \frac{1}{8\pi} \left(\vec{\nabla}\chi \times \vec{\nabla}\eta \right)^2, \tag{8}$$

in which $\varepsilon(\rho)$ is the specific internal energy. Taking the variational derivatives to zero for arbitrary variations leads to the following set of equations:

$$\frac{\partial \rho}{\partial t} + \vec{\nabla} \cdot (\rho \vec{v}) = 0 \tag{9}$$

$$\frac{d\chi}{dt} = 0, \tag{10}$$

$$\frac{d\eta}{dt} = 0, \tag{11}$$

$$\frac{d\nu}{dt} = \frac{1}{2}\vec{v}^2 - w, \tag{12}$$

in which w is the specific enthalpy.

$$\frac{d\alpha}{dt} = \frac{\vec{\nabla}\eta \cdot \vec{J}}{\rho}, \tag{13}$$

$$\frac{d\beta}{dt} = \frac{\vec{\nabla}\chi \cdot \vec{J}}{\rho}. \tag{14}$$

In all the above equations $\vec{v}$ is given by Equation (7). The mass conservation Equation (3) is readily obtained. Now one needs to show that also Equation (1) and Equation (4) are satisfied.

It can be easily shown that provided that $\vec{B}$ is in the form given in Equation (6), and Equation (10) and Equation (11) are satisfied, then Equation (1) are satisfied.

We shall now show that a velocity field given by Equation (7), such that the equations for α, β, χ, η, ν satisfy the corresponding Equations (9)–(14) must satisfy Euler's equations. Let us calculate the material derivative of $\vec{v}$:

$$\frac{d\vec{v}}{dt} = \frac{d\vec{\nabla}\nu}{dt} + \frac{d\alpha}{dt}\vec{\nabla}\chi + \alpha\frac{d\vec{\nabla}\chi}{dt} + \frac{d\beta}{dt}\vec{\nabla}\eta + \beta\frac{d\vec{\nabla}\eta}{dt}. \tag{15}$$

It can be easily shown that:

$$\frac{d\vec{\nabla}\nu}{dt} = \vec{\nabla}\frac{d\nu}{dt} - \vec{\nabla}v_k\frac{\partial\nu}{\partial x_k} = \vec{\nabla}\left(\frac{1}{2}\vec{v}^2 - w\right) - \vec{\nabla}v_k\frac{\partial\nu}{\partial x_k},$$

$$\frac{d\vec{\nabla}\eta}{dt} = \vec{\nabla}\frac{d\eta}{dt} - \vec{\nabla}v_k\frac{\partial\eta}{\partial x_k} = -\vec{\nabla}v_k\frac{\partial\eta}{\partial x_k},$$

$$\frac{d\vec{\nabla}\chi}{dt} = \vec{\nabla}\frac{d\chi}{dt} - \vec{\nabla}v_k\frac{\partial\chi}{\partial x_k} = -\vec{\nabla}v_k\frac{\partial\chi}{\partial x_k}. \tag{16}$$

In which k_x is a Cartesian coordinate and a summation convention is assumed. Equations (10)–(12) where used in the above derivation. Inserting the result from Equations (13), (14), (16) into Equation (15) yields:

$$\begin{aligned}
\frac{d\vec{v}}{dt} &= -\vec{\nabla}v_k\left(\frac{\partial\nu}{\partial x_k} + \alpha\frac{\partial\chi}{\partial x_k} + \beta\frac{\partial\eta}{\partial x_k}\right) + \vec{\nabla}\left(\frac{1}{2}\vec{v}^2 - w\right) \\
&\quad + \frac{1}{\rho}\left(\left(\vec{\nabla}\eta \cdot \vec{J}\right)\vec{\nabla}\chi - \left(\vec{\nabla}\chi \cdot \vec{J}\right)\vec{\nabla}\eta\right) \\
&= -\vec{\nabla}v_k v_k + \vec{\nabla}\left(\frac{1}{2}\vec{v}^2 - w\right) + \frac{1}{\rho}\vec{J}\times\left(\vec{\nabla}\chi \times \vec{\nabla}\eta\right) \\
&= -\frac{\vec{\nabla}\rho}{\rho} + \frac{1}{\rho}\vec{J}\times\vec{B}. \tag{17}
\end{aligned}$$

In which we have used both Equation (6) and Equation (7) in the above derivation. This of course proves that the barotropic Euler equations can be derived from the action given in Equation (8) and hence all the equations of barotropic magnetohydrodynamics can be derived from the above action without restricting the variations in any way except on the relevant boundaries and cuts. The reader should take into account that the topology of the magnetohydrodynamic flow is conserved, hence cuts must be introduced into the calculation as initial conditions.

5. A SIMPLER ACTION FOR BAROTROPIC MAGNETOHYDRODYNAMICS

Can we obtain a further reduction of barotropic magnetohydrodynamics? Can we formulate magnetohydrodynamics with less than the six functions α, β, χ, η, ν, ρ? The answer is yes, in fact four functions χ, η, ν, ρ will suffice. To see this we may write the two Equations (10), (11) as equations for α, β that is:

$$\begin{aligned}
\frac{d\chi}{dt} &= \frac{\partial\chi}{\partial t} + \vec{v}\cdot\vec{\nabla}\chi = \frac{\partial\chi}{\partial t} + \left(\vec{\nabla}\nu + \alpha\vec{\nabla}\chi + \beta\vec{\nabla}\eta\right)\cdot\vec{\nabla}\chi = 0, \\
\frac{d\eta}{dt} &= \frac{\partial\eta}{\partial t} + \vec{v}\cdot\vec{\nabla}\eta = \frac{\partial\eta}{\partial t} + \left(\vec{\nabla}\nu + \alpha\vec{\nabla}\chi + \beta\vec{\nabla}\eta\right)\cdot\vec{\nabla}\eta = 0, \tag{18}
\end{aligned}$$

in which we have used Equation (7). Solving for α, β we obtain:

$$\alpha[\chi, \eta, \nu] = \frac{\left(\vec{\nabla}\eta\right)^2 \left(\frac{\partial \chi}{\partial t} + \vec{\nabla}\nu \cdot \vec{\nabla}\chi\right) - \left(\vec{\nabla}\eta \cdot \vec{\nabla}\chi\right)\left(\frac{\partial \eta}{\partial t} + \vec{\nabla}\nu \cdot \vec{\nabla}\eta\right)}{\left(\vec{\nabla}\eta \cdot \vec{\nabla}\chi\right)^2 - \left(\vec{\nabla}\eta\right)^2 \left(\vec{\nabla}\chi\right)^2}$$

$$\beta[\chi, \eta, \nu] = \frac{\left(\vec{\nabla}\chi\right)^2 \left(\frac{\partial \eta}{\partial t} + \vec{\nabla}\nu \cdot \vec{\nabla}\eta\right) - \left(\vec{\nabla}\eta \cdot \vec{\nabla}\chi\right)\left(\frac{\partial \eta}{\partial t} + \vec{\nabla}\nu \cdot \vec{\nabla}\chi\right)}{\left(\vec{\nabla}\eta \cdot \vec{\nabla}\chi\right)^2 - \left(\vec{\nabla}\eta\right)^2 \left(\vec{\nabla}\chi\right)^2} \tag{19}$$

Hence α and β are not free variables any more, but depend on χ, η, ν. Moreover, the velocity $\vec{v}$ now depends on the same three variables χ, η, ν:

$$\vec{v} = \vec{\nabla}\nu + \alpha[\chi, \eta, \nu]\vec{\nabla}\chi + \beta[\chi, \eta, \nu]\vec{\nabla}\eta. \tag{20}$$

Since $\vec{v}$ is given now by Equation (20) it follows that the two Equations (10), (11) are satisfied identically and need not be derived from a variational principle. Finally The above expressions should be substituted in Equation (8) to obtain a Lagrangian density $\mathcal{L}$ in terms of χ, η, ν, ρ.

$$\mathcal{L} \equiv -\rho \left[\frac{\partial \nu}{\partial t} + \alpha[\chi, \eta, \nu]\frac{\partial \chi}{\partial t} + \beta[\chi, \eta, \nu]\frac{\partial \eta}{\partial t}\right.$$
$$\left. + \varepsilon(\rho) + \frac{1}{2}\left(\vec{\nabla}\nu + \alpha[\chi, \eta, \nu]\vec{\nabla}\chi + \beta[\chi, \eta, \nu]\vec{\nabla}\eta\right)^2\right] - \frac{1}{8\pi}\left(\vec{\nabla}\chi \times \vec{\nabla}\eta\right)^2, \tag{21}$$

Taking the variational derivatives to zero for arbitrary variations leads to the following set of equations:

$$\frac{\partial \rho}{\partial t} + \vec{\nabla} \cdot (\rho\vec{v}) = 0, \tag{22}$$

$$\frac{d\nu}{dt} = \frac{1}{2}\vec{v}^2 - w, \tag{23}$$

$$\frac{d\alpha[\chi, \eta, \nu]}{dt} = \frac{\vec{\nabla}\eta \cdot \vec{J}}{\rho}, \tag{24}$$

$$\frac{d\beta[\chi, \eta, \nu]}{dt} = \frac{\vec{\nabla}\chi \cdot \vec{J}}{\rho}. \tag{25}$$

Those equations should be solved for χ, η, ν, ρ.

6. CONCLUSION

We have shown that barotropic magnetohydrodynamics can be represented in terms of four scalar functions χ, η, ν, ρ instead of the seven quantities which are the magnetic field $\vec{B}$ the velocity field $\vec{v}$ and the density ρ. Some algebraic manipulations may result in a simpler expressions both for the Lagrangian and the equations of motion than can be obtained by brute force substitution this is left for future endeavors.

Anticipated applications include stability analysis and the description of numerical schemes using the described variational principles exceed the scope of this paper.

It was shown by the author [18] that variational principles can be used directly for numer- ical analysis (simulation) without the need to refer to the fluid equations. This mathematical construction may lead to better algorithms for simulating fluid dynamics in terms of the needed computer memory and CPU time. This approach was applied to potential flows in a series of papers [19–21]. Moreover, it was implemented in a user friendly software package FLUIDEX (which can be down loaded from the web site www.fluidex-cfd.com). A variational formalism of magnetohydrodynamics should have the same application.

As for stability analysis I suspect that for achieving this we will need to add additional constants of motion constraints to the action as was done by [22], hopefully this will be discussed in a future paper.

REFERENCES

1. Sturrock, P. A., *Plasma Physics*, Cambridge University Press, Cambridge, 1994.
2. Vladimirov, V. A. and H. K. Moffatt, "On general transformations and variational principles for the magnetohydrodynamics of ideal fluids. Part 1. fundamental principles," *J. Fluid. Mech.*, Vol. 283, 125–139, 1995.
3. Kats, A. V., "Variational principle in canonical variables, Weber transformation, and complete set of the local integrals of motion for dissipation-free magnetohydrodynamics," (Los Alamos Archives — physics-0212023), *JETP Lett.*, Vol. 77, 657, 2003.
4. Kats, A. V. and V. M. Kontorovich, "Hamiltonian description of the motion of discontinuity surfaces," *Low Temp. Phys.*, Vol. 23, 89, 1997.
5. Kats, A. V., "Variational principle and canonical variables in hydrodynamics with discontinuities," *Physica D*, Vol. 459, 152–153, 2001.
6. Sakurai, T., "A new approach to the force-free field and its application to the magnetic field of solar active regions," *Pub. Ast. Soc. Japan*, Vol. 31, 209, 1979.
7. Yang, W. H., P. A. Sturrock, and S. Antiochos, "Force-free magnetic fields: The magneto-frictional method," *Ap. J.*, Vol. 309, 383, 1986.
8. Yahalom, A. and D. Lynden-Bell, "Simplified variational principles for barotropic magnetohydrodynamics," (Los-Alamos Archives — physics/0603128), *Journal of Fluid Mechanics*, Vol. 607, 235–265, 2008.
9. Yahalom, A., "Using magnetic fields to optimize material flow: A variational approach to magnetohydrodynamics," *Proceedings of the Israeli-Russian Bi-National Workshop*, Jerusalem, Israel, June 2007.
10. Frenkel, A., E. Levich, and L. Stilman, "Hamiltonian description of ideal MHD revealing new invariants of motion," *Phys. Lett. A*, Vol. 88, 461, 1982.
11. Zakharov, V. E. and E. A. Kuznetsov, "Hamiltonian formalism for nonlinear waves," *Usp. Fiz. Nauk*, Vol. 40, 1087, 1997.
12. Yahalom, A. and D. Lynden-Bell, "Simplified variational principles for barotropic fluid dynamics," (Los-Alamos Archives — physics/0603162), submitted to *Journal of Fluid Mechanics*.
13. Yahalom, A., "CFD methods derived from simplified variational principles," *Proceedings of the AIAA Conference*, Reno, USA, January 2007.
14. Yahalom, A., "A finite element approach derived from the simplified variational principle," *Proceedings of the 9th ASME Engineering Systems Design and Analysis Conference (ESDA 2008)*, Haifa, Israel, July 2008.
15. Yahalom, A., "Simplified variational principles for stationary barotropic fluid dynamics," *Proceedings of the Fifth International Conference on Mathematical Modeling of Metal Technologies (MMT 2008)*, Ariel, Israel, September 2008.
16. Dungey, J. W., *Cosmic Electrodynamics*, Cambridge University Press, Cambridge, 1958.
17. Lamb, H., *Hydrodynamics*, 248, Dover Publications, 1945.
18. Yahalom, A., "Method and system for numerical simulation of fluid flow," US patent 6,516,292, 2003.
19. Yahalom, A. and G. A. Pinhasi, "Simulating fluid dynamics using a variational principle," *Proceedings of the AIAA Conference*, Reno, USA, January 2003.
20. Yahalom A., G. A. Pinhasi, and M. Kopylenko, "A numerical model based on variational principle for airfoil and wing aerodynamics," *Proceedings of the AIAA Conference*, Reno, USA, January 2005.
21. Ophir, D., A. Yahalom, G. A. Pinhasi, and M. Kopylenko, "A combined variational & multi-grid approach for fluid simulation," *Proceedings of the International Conference on Adaptive Modelling and Simulation (ADMOS 2005)*, 295–304, Barcelona, Spain, September 2005.
22. Yahalom A., J. Katz, and K. Inagaki, "Energy principles for self-gravitating barotropic flows-part two-the stability of maclaurin discs," *Mon. Not. R. Astron. Soc.*, Vol. 268, 506–516, 1994.

Semi-analytical Approach for a Specific Microstructured Fiber

Kiyotoshi Yasumoto

Department of Computer Science and Communication Engineering
Kyushu University, Fukuoka 819-0395, Japan

Abstract— A semi-analytical approach for a specific microstructured fiber, which is formed by layered cylindrical arrays of circular rods in a homogeneous background medium, is presented. The M circular rods are symmetrically distributed on each of the N-concentric circular cylindrical surfaces The method uses the T-matrix of a circular rod in isolation, the reflection and transmission matrices for a cylindrical array, and the generalized reflection and transmission matrices for a cylindrically layered structure.

1. INTRODUCTION

Photonic crystal fibers, with a core of a higher average index than the microstractured claddings, are now finding applications in diverse areas such as fiber-optic communications, fiber lasers, nonlinear photonic devices, highly sensitive sensors, and so on [1]. The modal properties of photonic crystal fibers have been extensively investigated using the finite element method [2], the multipole method [3], the finite difference frequency domain method [4, 5]. These numerical methods can be versatilely applied to various microstructured configurations but are computationally intensive. Approximate analytical methods using the effective index model [6] or a variational principle [7] have been also proposed to investigate the fundamental modal properties of photonic crystal fibers.

In this paper, we shall present a semi-analytical approach for the scalar field in a specific microstructured fiber which consists of layered cylindrical arrays of M circular rods symmetrically distributed on each of N-layered concentric circular cylindrical surfaces. The method uses the T-matrix of a circular rod in isolation, the reflection and transmission matrixes for a cylindrical array, and the generalized reflection and transmission matrices for a cylindrically layered structure [8]. Through this approach, the analytical model [9] developed for layered planar arrays of circular rods is extended to the layered cylindrical arrays.

2. GEOMETRY OF THE PROBLEM

The specific microstructured fiber considered here is formed by N-layered cylindrical arrays of circular rods located in a homogeneous background medium with material constants ε_c and μ_c as shown in Fig. 1. The M circular rods are symmetrically distributed on each of the N concentric circular cylindrical surfaces with radii d_ν ($\nu = 1, 2, 3, \ldots, N$). Fig. 1 shows a typical example with $M = 6$. The M circular rods should be identical along one ring but those on different rings need not be necessarily identical. The cylindrical surface with radius d_ν is labeled as the ν-th layer. The radius and material parameters of the circular rods distributed on the ν-th layer are denoted by r_ν, ε_ν, and μ_ν, respectively. The radii d_ν and r_ν must satisfy the condition $d_{\nu+1} - d_\nu > r_{\nu+1} + r_\nu$ so that the consecutive layers do not interpenetrate each other. The concentric homogeneous region within $d_\nu + r_\nu < \rho < d_{\nu+1} - r_{\nu+1}$ is labeled as the (ν)-th region.

3. FIELD EXPRESSIONS

A scalar wave analysis is employed using the cylindrical wave expansion. For simplicity, we assume the case where $M = 6$. The general case with arbitrary M can be dealt with in the same way. From the symmetry of the structure, the field is not changed under the rotation by an angle of $\pi/3$ with respect to the global origin O. Taking into account this symmetric properties, the field in the (ν)-th region can be expressed as follows:

$$\varphi^{(\nu)}(\rho,\, \varphi) = \sum_{n=-\infty}^{\infty} \left[b_n^{(\nu)} J_n(\kappa\rho) e^{in\varphi} + c_n^{(\nu)} Y_n(\kappa\rho) e^{in\varphi} \right] \sum_{j=1}^{6} (e)^{-in(j-1)\pi/3} \tag{1}$$

where $\kappa = \sqrt{n_c^2 k^2 - \beta^2}$, $J_n(\kappa\rho)$ and $Y_n(\kappa\rho)$ are the Bessel and Neumann functions of the m-th order, $\{b_n^{(\nu)}\}$ are the amplitudes of the cylindrical waves scattered from the outer circular rods on
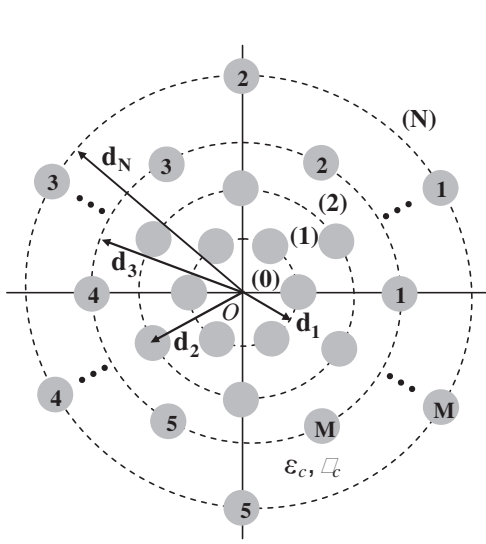
Figure 1: N-layered cylindrical arrays formed by M circular rods symmetrically distributed on each of concentric circular cylindrical surfaces with radii d_ν $(\nu = 1, 2, 3, \ldots, N)$.
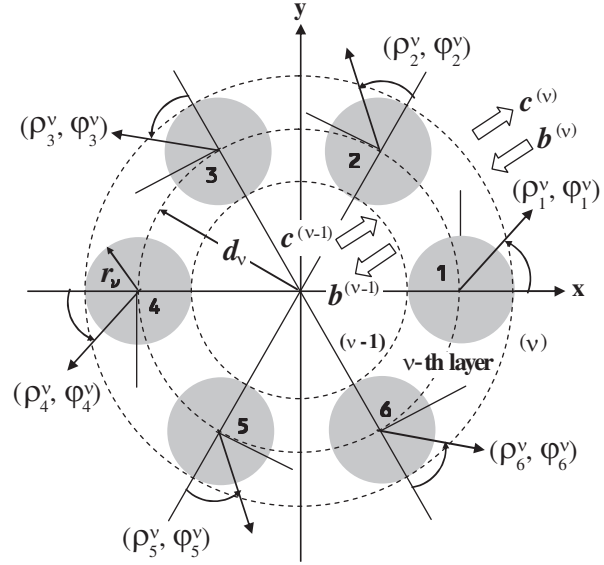
Figure 2: Schematic view of the scattering process by the circular rods on the ν-th layer and the six local coordinates $\rho_j^\nu = r_\nu$ $(j = 1, 2, 3, \ldots, 6)$ fixed to each of the rods.

the $(\nu + 1)$-th layer, $\{c_n^{(\nu)}\}$ are those scattered from the inner circular rods on the ν-th layer, and β is the propagation constant. Equation (1) is rewritten in the matrix form as follows:

$$\varphi^{(\nu)}(\rho, \varphi) = \tilde{\boldsymbol{\Phi}}^{\mathrm{T}} \cdot \boldsymbol{b}^{(\nu)} + \tilde{\boldsymbol{\Psi}}^{\mathrm{T}} \cdot \boldsymbol{c}^{(\nu)} \tag{2}$$

with

$$\tilde{\boldsymbol{\Phi}}^{\mathrm{T}} = \tilde{\boldsymbol{\Phi}}^{\mathrm{T}} \cdot \boldsymbol{\sigma}, \quad \tilde{\boldsymbol{\Psi}}^{\mathrm{T}} = \tilde{\boldsymbol{\Psi}}^{\mathrm{T}} \cdot \boldsymbol{\sigma}; \quad \boldsymbol{\Phi} = \left[J_m(\kappa\rho) \mathrm{e}^{im\varphi} \right], \quad \boldsymbol{\Psi} = \left[Y_m(\kappa\rho) \mathrm{e}^{im\varphi} \right] \tag{3}$$

$$\boldsymbol{\sigma} = [\sigma_n \delta_{nn'}], \quad \sigma_n = 1 + (-1)^n + 2\cos(n\pi/3) + 2\cos(2n\pi/3) \tag{4}$$

$$\boldsymbol{b}^{(\nu)} = [b_m^{(\nu)}], \quad \boldsymbol{c}^{(\nu)} = [c_m^{(\nu)}] \tag{5}$$

where the vector quantities are defined as the column vectors and the superscript T denote the transpose of the indicated vectors.

4. REFLECTION AND TRANSMISSION MATRICES

4.1. Incidence of the Field $\tilde{\boldsymbol{\Phi}}^{\mathrm{T}} \cdot \boldsymbol{b}^{(\nu)}$

The scattering process characterizing the reflection and transmission by the circular rods on the ν-th layer and the six local cylindrical coordinate systems fixed to each of the rods are schematically illustrated in Fig. 2. Let us consider that the field $\tilde{\boldsymbol{\Phi}}^{\mathrm{T}} \cdot \boldsymbol{b}^{(\nu)}$ is incident from the (ν)-th region on the ν-th layer of the arrays and is scattered. The scattered field in the (ν)-th region with $\rho_j^\nu > r_\nu$ $(j = 1, 2, 3, \ldots, 6)$ are expressed as follows:

$$\Psi^{s(\nu)} = \sum_{j=1}^{6} \sum_{m=-\infty}^{\infty} a_m^{(\nu)} Y_m(\kappa\rho_j^\nu) \mathrm{e}^{im\varphi_j^\nu} \tag{6}$$

where $(\rho_j^\nu, \varphi_j^\nu)$ $(j = 1, 2, 3, \ldots, 6)$ are the local cylindrical coordinate systems whose origins are located at the centers of each circular rod as shown in Fig. 2 and $\{a_m^{(\nu)}\}$ denote the unknown scattering amplitudes. It should be noted that $\{a_m^{(\nu)}\}$ take the same values for all the rods because of the symmetry of the structure. Equation (6) can be rewritten in the matrix form as follows:

$$\Psi^{s(\nu)} = \left(\sum_{j=1}^{6} \boldsymbol{\Psi}_j^{\mathrm{T}} \right) \cdot \boldsymbol{a}^{(\nu)}; \quad \boldsymbol{\Psi}_j^{(\nu)} = \left[Y_m(\kappa\rho_j^\nu) \mathrm{e}^{im\varphi_j^\nu} \right], \quad \boldsymbol{a}^{(\nu)} = \left[a_m^{(\nu)} \right]. \tag{7}$$

The scattered field (7) must satisfy the boundary conditions on the surfaces $\rho_j^\nu = r_\nu$ ($j = 1, 2, 3, \ldots,$ 6) of each circular rod under the presence of the incident field $\tilde{\boldsymbol{\Phi}}^{\mathrm{T}} \cdot \boldsymbol{b}^{(\nu)}$. Since the structure and the incident field are not changed under the rotation by $\pi/3$ with respect to the global origin O, we can consider the boundary condition only on the $\sharp 1$ rod. Note that if this boundary condition on $\sharp 1$ rod was satisfied, the boundary conditions on all other rods are automatically satisfied.

In order to apply the boundary condition on the $\sharp 1$ rod, the scattered fields based on the local coordinates $\rho_j^\nu = r_\nu$ ($j = 2, 3, \ldots, 6$) are transformed into those expressed in terms of the local coordinate (ρ_1^ν, φ_1^ν). This transformation is easily performed using the Graf's addition theorem for the cylindrical functions. After straightforward manipulations, we have the following relations:

$$\Psi^{s(\nu)} = \boldsymbol{\Psi}_1^{(\nu)\mathrm{T}} \cdot \boldsymbol{a}^{(\nu)} + \boldsymbol{\Phi}_1^{(\nu)\mathrm{T}} \cdot \sum_{j=2}^{6} \mathbf{K}_j^{(\nu)} \cdot \boldsymbol{a}^{(\nu)}; \quad \mathbf{K}_j^{(\nu)} = \left[K_{j,\,mn}^{(\nu)} \right] \tag{8}$$

where

$$\begin{aligned} K_{2,\,mn}^{(\nu)} &= Y_{m-n}(\kappa d_\nu)(-1)^m \mathrm{e}^{i(m+n)\pi/3}, \\ K_{3,\,mn}^{(\nu)} &= Y_{m-n}(\sqrt{3}\kappa d_\nu)(-1)^m \mathrm{e}^{i(m+n)\pi/6}, \\ K_{4,\,mn}^{(\nu)} &= Y_{m-n}(2\kappa d_\nu)(-1)^m, \\ K_{5,\,mn}^{(\nu)} &= Y_{m-n}(\sqrt{3}\kappa d_\nu)(-1)^m \mathrm{e}^{-i(m+n)\pi/6}, \\ K_{6,\,mn}^{(\nu)} &= Y_{m-n}(\kappa d_\nu)(-1)^m \mathrm{e}^{-i(m+n)\pi/3}, \end{aligned} \tag{9}$$

As the second step of the analysis, the incident field $\tilde{\boldsymbol{\Phi}}^{\mathrm{T}} \cdot \boldsymbol{b}^{(\nu)}$ given in the global coordinate system (ρ, φ) is transformed into the local coordinate system (ρ_1^ν, φ_1^ν) using the Graf's addition theorem. Then we have

$$\tilde{\boldsymbol{\Phi}}^{\mathrm{T}} \cdot \boldsymbol{b}^{(\nu)} = \boldsymbol{\Phi}_1^{(\nu)\mathrm{T}} \cdot \boldsymbol{\alpha}^{(\nu)} \cdot \boldsymbol{b}^{(\nu)} \tag{10}$$

where

$$\boldsymbol{\Phi}_1^{(\nu)\mathrm{T}} = \left[J_m(\kappa \rho_1^\nu) \mathrm{e}^{im\varphi_1^\nu} \right]; \quad \boldsymbol{\alpha}^{(\nu)} = \left[\alpha_{mn}^{(\nu)} \right], \quad \alpha_{mn}^{(\nu)} = (-1)^{m-n} \sigma_n J_{m-n}(\kappa d_\nu). \tag{11}$$

Using Equations (8) and (10), the total field around the $\sharp 1$ rod may be expressed in the following form:

$$\Psi(\rho_1^\nu,\,\varphi_1^\nu) = \boldsymbol{\Phi}_1^{(\nu)\mathrm{T}} \cdot \left(\mathbf{K}^{(\nu)} \cdot \boldsymbol{a}^{(\nu)} + \boldsymbol{\alpha}^{(\nu)} \cdot \boldsymbol{b}^{(\nu)} \right) + \boldsymbol{\Psi}_1^{(\nu)\mathrm{T}} \cdot \boldsymbol{a}^{(\nu)}; \quad \mathbf{K}^{(\nu)} = \sum_{j=2}^{6} \mathbf{K}_j^{(\nu)}. \tag{12}$$

In Equation (12), the first term may be viewed as the incident field impinging on the $\sharp 1$ rod, whereas the second term is the scattered field from the same cylinder. This argument leads to a relationship between $\boldsymbol{b}^{(\nu)}$ and $\boldsymbol{a}^{(\nu)}$ as follows:

$$\boldsymbol{a}^{(\nu)} = \mathbf{T}^{(\nu)} \cdot \left(\mathbf{K}^{(\nu)} \cdot \boldsymbol{a}^{(\nu)} + \boldsymbol{\alpha}^{(\nu)} \cdot \boldsymbol{b}^{(\nu)} \right) \tag{13}$$

where $\mathbf{T}^{(\nu)}$ is the T-matrix of the circular rod of the ν-th layer in isolation, whose close form expression is given in the standard text book [8]. From Equation (13) we have

$$\boldsymbol{a}^{(\nu)} = \bar{\mathbf{T}}_+^{(\nu)} \cdot \boldsymbol{b}^{(\nu)}; \quad \bar{\mathbf{T}}_+^{(\nu)} = \left(\mathbf{I} - \mathbf{T}^{(\nu)} \mathbf{K}^{(\nu)} \right)^{-1} \mathbf{T}^{(\nu)} \boldsymbol{\alpha}^{(\nu)} \tag{14}$$

where $\bar{\mathbf{T}}_+^{(\nu)}$ may be regarded as an aggregate T-matrix of the six circular rods symmetrically distributed on the ν-th layer.

Using Equation (14) in Equation (7), the scattered field is expressed in terms of the amplitude vector $\boldsymbol{b}^{(\nu)}$ of the incident field. However, the expression is still based on the local coordinate systems $\rho_j^\nu = r_\nu$ ($j = 1, 2, 3, \ldots, 6$). As the third step to obtain the reflection and transmission matrices, Equation (7) is transformed into the expression based on the global coordinate system

(ρ, φ) by making use of the Graf's addition theorem. The resulting expressions are different in the (ν)-th region for $\rho > d_\nu + r_\nu$ and the $(\nu - 1)$-th region for $\rho < d_\nu - r_\nu$. When $\rho > d_\nu + r_\nu$, we have

$$\Psi^{s(\nu)}(\rho, \varphi) = \tilde{\boldsymbol{\Psi}}^{\mathrm{T}} \cdot \boldsymbol{\chi}^{(\nu)} \cdot \boldsymbol{a}^{(\nu)}; \quad \boldsymbol{\chi}^{(\nu)} = \left[\chi_{mn}^{(\nu)} \right], \quad \chi_{mn}^{(\nu)} = J_{m-n}(\kappa d_\nu). \tag{15}$$

For the incident field $\tilde{\boldsymbol{\Phi}}^{\mathrm{T}} \cdot \boldsymbol{b}^{(\nu)}$ form the (ν)-th region, Equation (15) yields the reflected field into the same region. Using Equation (14) in Equation (15), the reflected field into the (ν)-th region may be expressed as follows:

$$\Psi^{s(\nu)} = \tilde{\boldsymbol{\Psi}}^{\mathrm{T}} \cdot \mathbf{R}_{\nu, \nu-1} \cdot \boldsymbol{b}^{(\nu)}; \quad \mathbf{R}_{\nu, \nu-1} = \boldsymbol{\chi}^{(\nu)} \bar{\mathbf{T}}_{+}^{(\nu)}. \tag{16}$$

From the comparison of Equation (16) with Equation (2), it follows that $\mathbf{R}_{\nu, \nu-1}$ gives the reflection matrix of the ν-th layer, which defines the reflection from the $(\nu - 1)$-th region to the (ν)-th region by the circular rods on the ν-th layer. When $\rho < d_\nu - r_\nu$, on the other hand, the scattered field (7) is expressed in global coordinate system (ρ, φ) as follows:

$$\Psi^{s(\nu)} = \tilde{\boldsymbol{\Phi}}^{\mathrm{T}} \cdot \boldsymbol{\eta}^{(\nu)} \cdot \boldsymbol{a}^{(\nu)}; \quad \boldsymbol{\eta}^{(\nu)} = \left[\eta_{mn}^{(\nu)} \right], \quad \eta_{mn}^{(\nu)} = Y_{m-n}(\kappa d_\nu). \tag{17}$$

Substituting Equation (14) into Equation (17), the scattered field in the $(\nu - 1)$-region is obtained as

$$\Psi^{s(\nu-1)} = \tilde{\boldsymbol{\Phi}}^{\mathrm{T}} \cdot \mathbf{F}_{\nu-1, \nu} \cdot \boldsymbol{b}^{(\nu)}; \quad \mathbf{F}_{\nu-1, \nu} = \boldsymbol{\eta}^{(\nu)} \bar{\mathbf{T}}_{+}^{(\nu)}. \tag{18}$$

From the comparison of Equation (18) with Equation (2), it follows that $\mathbf{F}_{\nu-1, \nu}$ gives the transmission matrix of the ν-th layer, which defines the transmission from the (ν)-th region to the $(\nu - 1)$-th region through the circular rods on the ν-th layer.

4.2. Incidence of the Field $\tilde{\boldsymbol{\Psi}}^{\mathrm{T}} \cdot \boldsymbol{c}^{(\nu-1)}$

Let us consider that the field $\tilde{\boldsymbol{\Psi}}^{\mathrm{T}} \cdot \boldsymbol{c}^{(\nu-1)}$ is incident from the $(\nu - 1)$-th region on the ν-th layer of the circular rods and scattered. Following the same analytical procedure as described in **4.1**, the transmitted field $\Psi^{s(\nu)}$ into the (ν)-th region with $\rho > d_\nu + r_\nu$ and the reflected field $\Psi^{s(\nu-1)}$ into the $(\nu - 1)$-th region with $\rho < d_\nu - r_\nu$ are obtained as follows:

$$\Psi^{s(\nu)} = \tilde{\boldsymbol{\Psi}}^{\mathrm{T}} \cdot \mathbf{F}_{\nu, \nu-1} \cdot \boldsymbol{c}^{(\nu-1)}; \quad\quad\quad \mathbf{F}_{\nu, \nu-1} = \boldsymbol{\gamma}^{(\nu)} \bar{\mathbf{T}}_{-}^{(\nu)} \tag{19}$$

$$\Psi^{s(\nu-1)} = \tilde{\boldsymbol{\Phi}}^{\mathrm{T}} \cdot \mathbf{R}_{\nu-1, \nu} \cdot \boldsymbol{c}^{(\nu-1)}; \quad\quad\quad \mathbf{R}_{\nu-1, \nu} = \boldsymbol{\eta}^{(\nu)} \bar{\mathbf{T}}_{-}^{(\nu)} \tag{20}$$

with

$$\bar{\mathbf{T}}_{-}^{(\nu)} = \left(\mathbf{I} - \mathbf{T}^{(\nu)} \mathbf{K}^{(\nu)} \right)^{-1} \mathbf{T}^{(\nu)} \boldsymbol{\gamma}^{(\nu)}; \quad \boldsymbol{\gamma}^{(\nu)} = \left[\gamma_{mn}^{(\nu)} \right], \quad \gamma_{mn}^{(\nu)} = (-1)^{m-n} \sigma_n Y_{m-n}(\kappa d_\nu) \tag{21}$$

where $\mathbf{F}_{\nu, \nu-1}$ defines the transmission matrix from the $(\nu - 1)$-th region to the (ν)-th region through the ν-th layer of cylindrical array and $\mathbf{R}_{\nu-1, \nu}$ defines the reflection matrix from the $(\nu - 1)$-th region to the $(\nu - 1)$-th region.

5. GENERALIZED REFLECTION AND TRANSMISSION MATRICES

If the positions of the 6 cylinders on the ν-th layer are shifted counterclockwise by an angle of θ_ν with respect to the global coordinate $x\text{-}O\text{-}y$. the reflection and transmission matrices are slightly modified as

$$\hat{\mathbf{R}}_{\nu, \nu-1} = \boldsymbol{\theta}_\nu \mathbf{R}_{\nu, \nu-1} \boldsymbol{\theta}_\nu^{-1}, \quad \hat{\mathbf{R}}_{\nu-1, \nu} = \boldsymbol{\theta}_\nu \mathbf{R}_{\nu-1, \nu} \boldsymbol{\theta}_\nu^{-1} \tag{22}$$

$$\hat{\mathbf{F}}_{\nu-1, \nu} = \boldsymbol{\theta}_\nu \mathbf{R}_{\nu-1, \nu} \boldsymbol{\theta}_\nu^{-1}, \quad \hat{\mathbf{F}}_{\nu, \nu-1} = \boldsymbol{\theta}_\nu \mathbf{R}_{\nu, \nu-1} \boldsymbol{\theta}_\nu^{-1} \tag{23}$$

where $\boldsymbol{\theta}_\nu = [\mathrm{e}^{-im\theta_\nu} \delta_{mm'}]$ is a diagonal matrix. The generalized reflection and transmission matrices of the N-layered system as shown in Fig. 1 can be obtained by concatenating the reflection and transmission matrices for each layer of the cylindrical arrays. This calculation is performed using $\hat{\mathbf{R}}_{\nu, \nu-1}$, $\hat{\mathbf{R}}_{\nu-1, \nu}$, $\hat{\mathbf{F}}_{\nu-1, \nu}$, and $\hat{\mathbf{F}}_{\nu, \nu-1}$ given by Equations (22) and (23). Taking into account the scattering process as schematically shown in Fig. 3, the total field in the (ν)-th region is expressed as follows:

$$\Psi^{(\nu)} = \tilde{\boldsymbol{\Psi}}^{\mathrm{T}} \cdot \boldsymbol{c}^{(\nu)} + \tilde{\boldsymbol{\Phi}}^{\mathrm{T}} \cdot \boldsymbol{b}^{(\nu)} = \left(\tilde{\boldsymbol{\Psi}}^{\mathrm{T}} + \tilde{\boldsymbol{\Phi}}^{\mathrm{T}} \cdot \bar{\bar{\mathbf{R}}}_{\nu, \nu+1} \right) \cdot \boldsymbol{c}^{(\nu)} \tag{24}$$

where $\bar{\bar{\mathbf{R}}}_{\nu,\nu+1}$ represents the generalized reflection matrix viewed from the (ν)-th region to all of outer regions. The recursive relation for the generalized reflection matrix for the N-layered structure is obtained as

$$\bar{\bar{\mathbf{R}}}_{\nu,\nu+1} = \hat{\mathbf{R}}_{\nu,\nu+1} + \hat{\mathbf{F}}_{\nu,\nu+1}\bar{\bar{\mathbf{R}}}_{\nu+1,\nu+2}\left(\mathbf{I} - \hat{\mathbf{R}}_{\nu+1,\nu}\bar{\bar{\mathbf{R}}}_{\nu+1,\nu+2}\right)^{-1}\hat{\mathbf{F}}_{\nu+1,\nu}. \tag{25}$$

Equation (25) is recursively used to calculate the generalized reflection matrices $\bar{\bar{\mathbf{R}}}_{N-2,N-1}$ to $\bar{\bar{\mathbf{R}}}_{12}$, starting from $\bar{\bar{\mathbf{R}}}_{N-1,N} = \hat{\mathbf{R}}_{N-1,N}$. It should be noted that the $\tilde{\mathbf{\Psi}}$-field does not exist in the innermost region (0) and the $\tilde{\mathbf{\Phi}}$-field does not exist in the outermost region (N).
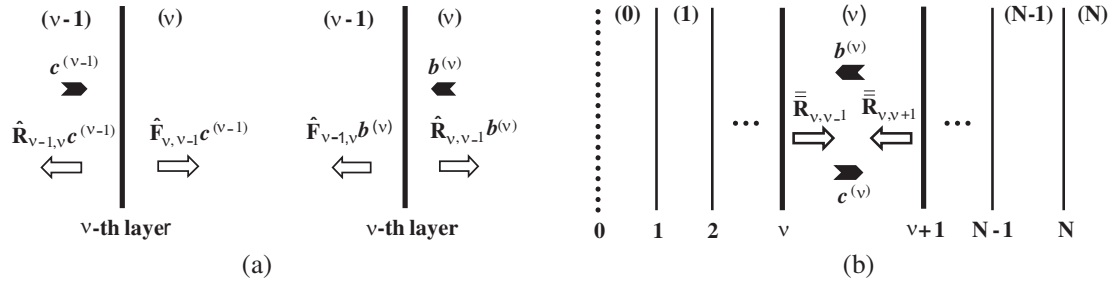
Figure 3: Scattering process in layered cylindrical arrays: (a) two scattering process in a single layer array and (b) generalized reflection matrix in N-layered arrays.

6. MODAL FIELDS AND PROPAGATION CONSTANTS

In the region (1) of the N-layered system as shown in Fig. 1, we have the following relation:

$$\mathbf{b}^{(1)} = \bar{\bar{\mathbf{R}}}_{12} \cdot \mathbf{c}^{(1)}, \quad \mathbf{c}^{(1)} = \hat{\mathbf{R}}_{10} \cdot \mathbf{b}^{(1)}. \tag{26}$$

Equation (27) leads to

$$\left(\mathbf{I} - \bar{\bar{\mathbf{R}}}_{12}\hat{\mathbf{R}}_{10}\right) \cdot \mathbf{b}^{(1)} = 0 \tag{27}$$

where $\bar{\bar{\mathbf{R}}}_{12}$ is calculated using the recursive relation (25). Equation (28) yields the dispersion equation for the mode propagation constant β as follows:

$$|\mathbf{I} - \bar{\bar{\mathbf{R}}}_{12}\hat{\mathbf{R}}_{10}| = 0. \tag{28}$$

The solutions to Equation (29) is used in Equaiton (28) to determine the amplitude vector $\mathbf{b}^{(1)}$ characterizing the mode fields. Using the solutions of $\mathbf{b}^{(1)}$ in Equation (27), $\mathbf{c}^{(1)}$ is obtained. The other amplitude vectors $\mathbf{b}^{(\nu)}$ and $\mathbf{c}^{(\nu)}$ can be recursively calculated. The mode field distribution in each of (ν)-th region can be obtained by substituting the calculated amplitude vectors $\mathbf{b}^{(\nu)}$ and $\mathbf{c}^{(\nu)}$ into Equation (24).

7. CONCLUDING REMARKS

We have presented a semi-analytical approach for a specific microstructured fiber which is formed by layered cylindrical arrays of M circular rods symmetrically distributed on each of N-layered concentric circular cylindrical surfaces. The method uses the T-matrix of a circular rod in isolation, the reflection and transmission matrixes for a cylindrical array, and the generalized reflection and transmission matrices for a layered cylindrical structure. Although the formulation was presented for the scalar field, its extension to the vector fields is straightforward. In this case, we must introduce two scalar fields representing E_z and H_z fields. The T-matrix of a circular rod, the reflection and transmission matrixes, and the generalized reflection and transmission matrices are defined in terms of the cylindrical harmonics of both E_z and H_z fields as the basis. Then the size of matrices to be solved becomes four times larger than that of the scalar field case.

REFERENCES

1. Russell, P. St. J., "Photonic-crystal fibers," *J. Lightwave Technol.*, Vol. 24, 4729–4749, 2006.
2. Brechet, F., J. Marcou, D. Pagnoux, and P. Roy, "Complete analysis of the characteristics of propagation into photonic crystal fibers by the finite element method," *Opt. Fiber Technol.*, Vol. 6, 181–191, 2000.
3. White, T. P., B. T. Kuhlmey, R. C. McPhedran, D. Maystre, G. Renversez, C. Martijin de Sterke, and L. C. Botten, "Multipole method for micro-structured optical fibers, I. Formulation," *J. Opt. Soc. Am. B*, Vol. 19, 2322–2330, 2002.
4. Zhu, Z. and T. G. Brown, "Full vectorial finite difference analysis of microstructured optical fibers," *Opt. Express*, Vol. 10, 853–864, 2002.
5. Yu, C. P. and H. C. Chang, "Applications of the finite difference frequency domain mode solution method to photonic crystal structures," *Electromagnetic Theory and Applications for Photonic Crystals*, Ed. K. Yasumoto, CRC Press, New York, 351–400, 2005.
6. Knight, J. C., T. A. Birks, P. St. J. Russell, and J. P. Sandro, "Properties of photonic crystal fiber and the effective index method," *J. Opt. Soc. Am. A*, Vol. 15, 748–752, 1998.
7. Sharma, A. and H. Chauhan, "Variational analysis of index-guiding microstructured fibers," *Digest of the 4th Research Forum of Japan-Indo Collaboration Project on Infrastructural Communication Technologies Supporting Fully Ubiquitous Information Society*, 52–56, Tokyo, Japan, July 2008.
8. Chew, W. C., *Waves and Fields in Inhomogeneous Media*, Van Nostrand Reinhold, New York, 1990.
9. Yasumoto, K. and H. Jia, "Modeling of photonic crystals by layered periodic arrays of cylinders," *Electromagnetic Theory and Applications for Photonic Crystals*, Ed. K. Yasumoto, CRC Press, New York, 123–190, 2005.

An Analytical Solution for the Logarithmic Singularity Associated with MoM Applied to Dielectrics and MFIE and Its Optimal Evaluation with Polynomial Quadratures

Thierry Gilles[1], **Marc Piette**[1], **and Christophe Craeye**[2]

[1]Ecole Royale Militaire, Laboratoire d' Electromagnétisme Appliqué (LEMA)
Avenue de la Renaissance 30, Bruxelles 1000, Belgium
[2]Université catholique de Louvain, Laboratoire TELE
Place du Levant 2, Louvain-la-Neuve 1348, Belgium

Abstract— Two complete analytical solutions are presented for the double integral with $1/R^3$ singularity occurring in electromagnetic problems involving the MFIE-f and MFIE-nxf. These analytical solutions are used to assess the accuracy obtained with high efficiency polynomial quadratures in the evaluation of the singular outer integral. It is shown that a 16 nodes gaussian quadrature integration can provide the required accuracy.

1. INTRODUCTION

Using the MFIE to solve for the equivalent surface currents around the closed surface S of metallic or dielectric bodies requires the evaluation of the integral expression (1).

$$Z_{mn} = \iint_{S_m} \vec{w}_m\left(\vec{r}\right) \cdot \left(\frac{1}{2}\vec{n}_m\left(\vec{r}\right) \times \vec{f}_n\left(\vec{r}\right) + \iint_{S_n} \vec{f}_n\left(\vec{r}'\right) \times \vec{\nabla}'G\left|\vec{r} - \vec{r}'\right| \cdot dS'\right) dS \qquad (1)$$

Remembering that $|\vec{r} - \vec{r}'| = \left|\vec{R}\right| = R$, the gradient of the free space Green function is given by:

$$\vec{\nabla}'G(R) = \vec{\nabla}'\frac{e^{-jkR}}{4\pi R} = (jkR + 1)\frac{e^{-jkR}}{4\pi R^3}\vec{R} = \left[\frac{1}{4\pi R^3} + \frac{k^2}{8\pi R} - j\frac{k^3}{12\pi} - \frac{k^4 R}{32\pi} + \ldots\right]\vec{R} \qquad (2)$$

The weighting function $\vec{w}_m$ will be $\vec{f}_m$ or $\vec{n}_m \times \vec{f}_m$, where $\vec{n}_m$ is the unit vector normal to S_m. We will consider RWG functions $\vec{f}_m$ and $\vec{f}_n$ defined on the adjacent flat triangle pairs S_m and $S_n \subseteq S$ [1]. Consequently in (1) the integral on S_m and S_n is a sum of integrals on the triangles T_m^+, T_m^- and T_n^+, T_n^- : $Z_{mn} = Z_{mn}^{++} + Z_{mn}^{+-} + Z_{mn}^{-+} + Z_{mn}^{--}$. The expressions of the RWG basis functions on the triangles T_n^+ and T_n^- are given by (3), where $A_n^\pm$ is the area of the triangle $T_n^\pm$ and L_n is the length of the edge common to T_n^+ and T_n^-.

$$\vec{f}_n^\pm\left(\vec{r}'\right) = \pm\frac{L_n}{2A_n^\pm}\left(\vec{r}' - \vec{p}_n^\pm\right) = \pm C_n^\pm\left(-\vec{R} + \vec{r} - \vec{p}_n^\pm\right) \qquad (3)$$

The functions $\vec{f}_m^-$ on T_m^- and $\vec{f}_n^+$ on T_n^+ are illustrated on Fig. 1. From here on we will concentrate on one such integral on triangles. When $T_m^\pm$ and $T_n^\pm$ share common points, R can go to 0, making the inner integrand in (1) infinite by virtue of the $1/R^3$ and $1/R$ terms revealed in (2). For self terms situations, like $T_n^- = T_m^-$, the improper integral on S_n reduces to its principal value: the nXf term in (1):

$$Z_{mn}^{--} = \iint_{T_m^-} \vec{w}_m\left(\vec{r}\right) \cdot \left(\frac{1}{2}\vec{n}_m\left(\vec{r}\right) \times \vec{f}_n^-\left(\vec{r}\right)\right) dS \qquad (4)$$

If $T_m^\pm \neq T_n^\pm$, the nXf term in (1) is identically 0 and only the double integral on S_m and S_n remains. For coplanar triangles, like T_m^+ and T_n^-, the three vectors involved in the dot and cross product in (1) lead to $Z_{mn}^{+-} = 0$.
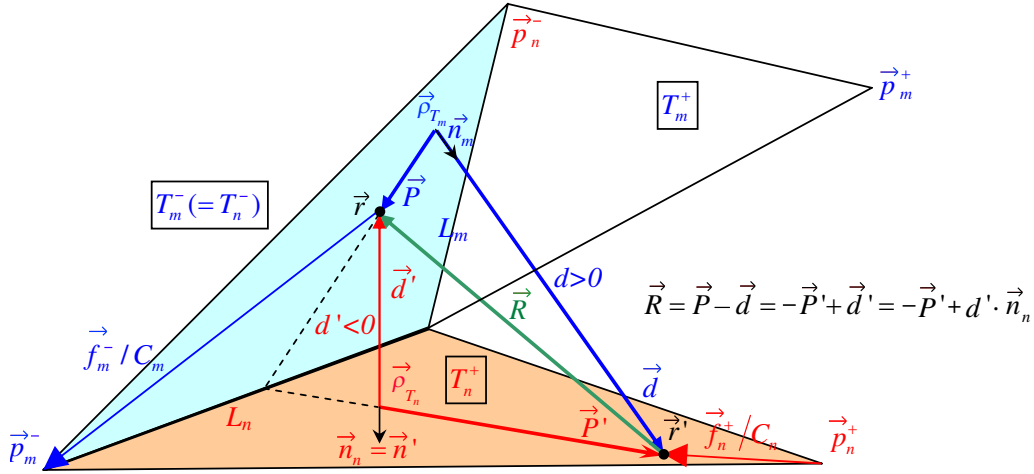
Figure 1: Vectors involved in the two nested surface integrals.

2. EXTRACTION OF THE $1/R$ AND $1/R^3$ SINGULARITIES AND THE REMAINING LOGARITHMIC SINGULARITY

If the triangles share a common edge (T_m^- and T_n^+) or a common vertex (T_m^+ and T_n^+) without being coplanar as in Fig. 1, the extraction of both the R^{-3} and R^{-1} singularities [2] decomposes (1) into the sum of three integrals:

$$\iint_{T_m^\pm} \vec{w}_m^\pm(\vec{r}) \cdot \left(\iint_{T_n^+} \left[\vec{f}_n^+(\vec{r}') \times \vec{R} \left(\frac{jkR+1}{4\pi R^3} e^{-jkR} - \frac{1}{4\pi R^3} - \frac{k^2}{8\pi R} \right) \right] \cdot dS' \right) dS \tag{5}$$

$$\iint_{T_m^\pm} \vec{w}_m^\pm(\vec{r}) \cdot \left(\iint_{T_n^+} \left[\vec{f}_n^+(\vec{r}') \times \vec{R} \left(\frac{k^2}{8\pi R} \right) \right] \cdot dS' \right) dS \tag{6}$$

$$\iint_{T_m^\pm} \vec{w}_m^\pm(\vec{r}) \cdot \left(\iint_{T_n^+} \left[\vec{f}_n^+(\vec{r}') \times \vec{R} \left(\frac{1}{4\pi R^3} \right) \right] \cdot dS' \right) dS \tag{7}$$

Integral (3) can be evaluated numerically with standard polynomial quadratures: the integrands are bounded everywhere on S_n then on S_m. Evaluation of (6) and (7), having singular integrands on S_n, can be performed as follows: analytical closed form solution for the inner integral, then numerical evaluation of the outer integral. For integral (6), containing the R^{-1} singularity, this scheme works perfectly [3]. We now observe from (2) that the contribution of (6) to the real part of (1) becomes dominant as soon as $1/(4\pi R^3) > k^2/8\pi R$, i.e., $R < \lambda/5$. This is always the case for the adjacent triangles we are dealing with: accuracy of the MoM dictates that triangle sides should never exceed $\lambda/10$. It is therefore important to evaluate (7) with enough accuracy.

Using (3) and the fact $\vec{R} \times \vec{R} = \vec{0}$, Equation (7) can be rewritten as:

$$\pm C_n \iint_{T_m^\pm} \vec{w}_m^\pm(\vec{r}) \cdot (\vec{r} - \vec{p}_n^+) \times \left(\iint_{T_n^+} \frac{\vec{R}}{4\pi R^3} \cdot dS' \right) dS \tag{8}$$

The inner vector integral of (8) can be further decomposed into a tangential component lying in the triangle T_n^+ and a normal component directed along $\vec{n}'$:

$$\iint_{T_n^+} \frac{\vec{R}}{4\pi R^3} \cdot dS' = -\iint_{T_n^+} \frac{\vec{P}'}{4\pi R^3} \cdot dS' + \iint_{T_n^+} \frac{\vec{d}'}{4\pi R^3} \cdot dS' = (s) + (n) \tag{9}$$

The analytical solution of (n) can be shown [4] to be a vector directed along $\vec{n}'$ towards $\vec{r}$ of length $\Omega(\vec{r})/4\pi$, the normalized solid angle from which the triangle T_n^+ is seen from the point $\vec{r}$. Its value is bounded between -0.5 and $+0.5$. The analytical solution of (s) on the contrary [2], [4] is not bounded everywhere on T_m:

$$\iint_{T_n^+} \frac{-\vec{P}'}{4\pi R^3} \cdot dS' = \frac{1}{4\pi} \sum_i \vec{m}_i' \int_{\partial_i T_n^+} \frac{dl'}{R} = \frac{1}{4\pi} \sum_i \vec{m}_i' \cdot \ln \left[\frac{R_i'^+(\vec{r}) + l_i'^+(\vec{r})}{R_i'^-(\vec{r}) + l_i'^-(\vec{r})} \right] \tag{10}$$

The unit vector $\vec{m}'_i$ is normal to the edge $\partial_i T^+_n$ pointing outwards T^+_n, in the plane of T^+_n. The vector $\vec{l}'_i = \vec{n}' \times \vec{m}'_i$. The *signed values* l'^-_i and l'^+_i are the coordinates of the i'^- and i'^+ vertices at both ends of the edge $\partial_i T^+_n$, the negative and the positive vertex being determined with respect to the orientation of the unit vector $\vec{l}'_i$. The *positive values* $R'^-_i (R'^+_i)$ are the distances between $\vec{r}$ and $i'^-(i'^+)$.

If $\vec{r}$ is located on the common edge L_n then (10) becomes infinite as $R'^-_i(\vec{r}) + l'^-_i(\vec{r}) = 0$. The corresponding outer integral in (8) possesses at its turn a singular integrand. A very elegant solution to avoid this logarithmic singularity has been proposed in [5], but it introduces some programming complexity: the order of integration on T_m and T_n must be inverted and line integrals do appear. A few other integration schemes are available for singular integrands, but they are far more complex to implement [6]. As an alternative we chose to investigate the possibility to use the high efficiency polynomial quadratures having only inner nodes described in [7] and more recently in [8]. To assess the ability or not for these quadratures to evaluate correctly the logarithmic singularity we derived two analytical solutions for a canonical case.

3. ANALYTICAL SOLUTION

We present the analytical solution for the tangential component of (9) in the canonical situation depicted on Fig. 2 and for both weighting function $\vec{w}_m = \vec{f}_m$ and $\vec{n}_m \times \vec{f}_m$. Straightforward vector calculus shows that the normal component of (9) is identically zero in this canonical case, for both $\vec{w}_m$. Therefore, (9) becomes:

$$I = (C_{mn}/4\pi) \cdot \sum_i \iint_{T_m} \vec{w} \cdot \left[(\vec{r} - \vec{p}') \times \vec{m}'_i\right] \cdot Q'_i \cdot dS \tag{11}$$

with $C_{mn} = \pm \frac{L_m L_n}{4 A_m A_n} = \pm\sqrt{2}$, $\vec{w} = (\vec{r} - \vec{p})$ or $\vec{n} \times (\vec{r} - \vec{p})$ and $Q'_i = \ln\left[\frac{R'^+_i(\vec{r}) + l'^+_i(\vec{r})}{R'^-_i(\vec{r}) + l'^-_i(\vec{r})}\right]$.

After computation of the vector cross and dot products, (11) further reduces to the sum of only two integrals on edges $\partial_1 T_n$ and $\partial_2 T_n$, the integral on $\partial_3 T_n$ being identically zero:

$$I = \sqrt{2}/4\pi \left\{ \iint_{T_m} P(x,y) \cdot Q'_1(\vec{r}) dS - (\sqrt{2}/2) \cdot \iint_{T_m} P(x,y) \cdot Q'_2(\vec{r}) dS \right\} = \sqrt{2}/4\pi \{I_1 - I_2\} \tag{12}$$

with $P^f(x,y) = -x$ and $P^{nxf}(x,y) = x^2 + y^2 - y$, according to the choice of the weighting function $\vec{w}_m$.
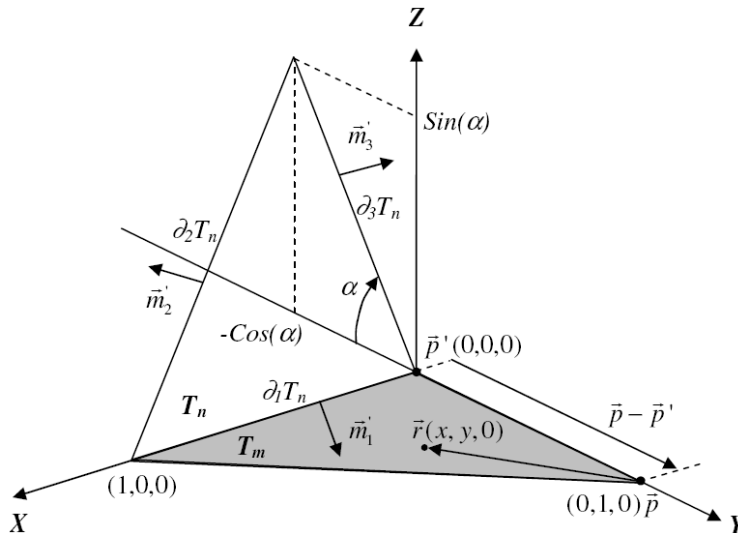
Figure 2: Geometry of the canonical case solved analytically for $\alpha = 90°$.

The integrals I_1 on $\partial_1 T_n$ and I_2 on $\partial_2 T_n$ become:

$$I_1 = \left\{ \int_0^1 \int_0^{1-y} P(x,y) \cdot \ln \left[\sqrt{(1-x)^2 + y^2} + (1-x) \right] dxdy \right.$$
$$\left. - \int_0^1 \int_0^{1-x} P(x,y) \cdot \ln \left[\sqrt{x^2 + y^2} - x \right] dydx \right\} = I_1^+ - I_1^- \tag{13}$$

$$I_2 = \frac{1}{\sqrt{2}} \left\{ \begin{array}{l} \int_0^1 \int_0^{1-y} P(x,y) \cdot \ln \left[\sqrt{x^2 + y^2 + 2y\cos\alpha + 1} + (x + y\cos\alpha + 1) \big/ \sqrt{2} \right] dxdy \\ - \int_0^1 \int_0^{1-x} P(x,y) \cdot \ln \left[\sqrt{(1-x)^2 + y^2} + (x + y\cos\alpha - 1) \big/ \sqrt{2} \right] dxdy \end{array} \right\}$$
$$= I_2^+ - I_2^- \tag{14}$$

Regarding I_2, an analytical solution has been derived for I_2^- only and in the case $\alpha = 90°$. As I_2^+ remains bounded everywhere on T_m, it can be evaluated very accurately with numerical methods, as shown in Table 2.

Table 1: Analytical expressions for I_1^-, I_1^+ and I_2^-.

	$\vec{w}_m = \vec{f}_m$	$\vec{w}_m = \vec{n}_m \times \vec{f}_m$
I_1^-	$\left[11 + 9\sqrt{2}\ln\left(\sqrt{2}+1\right) \right]/36$	$\left[-2 - \sqrt{2}\ln\left(\sqrt{2}+1\right) \right]/16$
I_1^+	$\left[11 - 12\ln\left(\sqrt{2}+1\right) \right]/36$	$\left[2 - 3\sqrt{2} + \ln\left(\sqrt{2}+1\right) \right]/24$
I_2^-	$\left[11 + 3\sqrt{2}\left(\ln(\sqrt{2}+1) - \pi/2\right) + 3\ln 2 \right]/(36\sqrt{2})$	$\left[1 + \ln(\sqrt{2}-1) + \sqrt{2}\left(\pi/8 - 1\right) \right]/(12\sqrt{2})$

All details of the lengthy computations can be found in [9] for $\vec{w}_m = \vec{f}_m$ or obtained from the first author for $\vec{w}_m = \vec{n}_m \times \vec{f}_m$.

4. ACCURACY OF THE NUMERICAL EVALUATION WITH HIGH EFFICIENCY POLYNOMIAL QUADRATURES

The singular integrands in (13) and (14) become infinite only on the edge $\partial_1 T_n$ with a smooth logarithmic behavior. One can hope to converge to the analytical solutions derived above using efficient polynomial quadratures having only inner nodes. The accuracy that can be obtained with these quadratures can be observed in the evaluation of I_2^+, the only regular integrand: it improves very quickly with increasing number of integration nodes. In the absence of analytical solution for I_2^+, the numerical solution obtained with 73 nodes is used as a reference to measure the relative error of the other cases, as shown in Table 2.

Let's examine now the the total terms I_f and I_{nxf} given by Equation (12) evaluated with the same quadratures.

The relative error is now improving much slower with the amount of quadrature nodes. Surprisingly enough, the 16 and 42 nodes quadratures outperform all the other choices for both $\vec{w}_m = \vec{f}_m$ and $\vec{w}_m = \vec{n}_m \times \vec{f}_m$, showing a relative error (well) below 0.5% with 16 nodes. Note also from Table 2 that 7 nodes are sufficient to obtain a similar accuracy with non singular integrals.
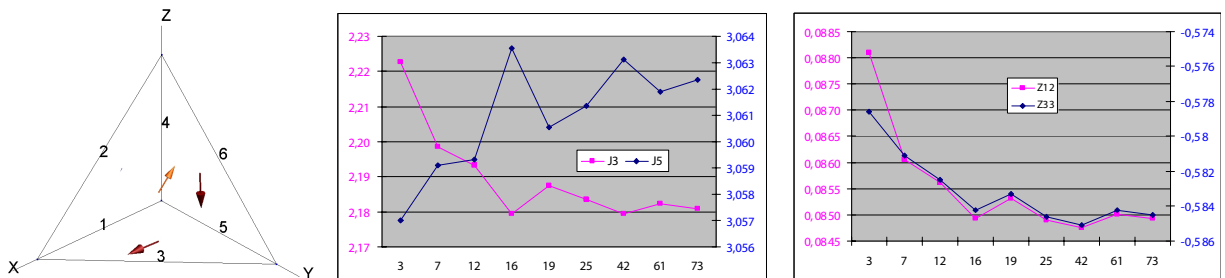
Figure 3: Numerical example.

As explained above, (5) and (6) are comparable to or smaller than (7). Still to obtain the overall relative error on $Z_{mn} = Z_{mn}^{++} + Z_{mn}^{+-} + Z_{mn}^{-+} + Z_{mn}^{--}$ it is still necessary to add to (11) the values of the three other contributors. In the numerical example presented below $Z_{12}^{++} = 0.01076$ and corresponds to our analytical example in the case $\vec{w}_m = \vec{n}_m \times \vec{f}_m$. The value of $Z_{12} = 0.0849$! This means that the relative error on Z_{12} is only 8 times smaller than the relative error on Z_{12}^{++}, emphasizing again the necessity of an accurate evaluation of the singular integral (7).

Table 2: Relative error on the regular term I_2^+.

# nodes	$I_{2,f}^+$: Numerical	|Relative error|	$I_{2,nxf}^+$: Numerical	|Relative error|
1	-0.08450337367004	$0.11e-0$	-0.028167791223347	$4.90e-0$
3	$-\mathbf{0.094}612293851424$	$1.37e-3$	$+\mathbf{0.007}012501289788$	$21.4e-3$
4	$-\mathbf{0.094}697637869101$	$2.28e-3$	$+0.006604208568921$	$78.4e-3$
6	$-\mathbf{0.09448}3384173796$	$10.3e-6$	$+\mathbf{0.007}157053742892$	$1.20e-3$
7	$-\mathbf{0.09447}8779228638$	$38.5e-6$	$+\mathbf{0.0071}7151008889$	$0.81e-3$
12	$-\mathbf{0.094482}452578854$	$0.42e-6$	$+\mathbf{0.007165}729119605$	$1.30e-6$
16	$-\mathbf{0.094482}394759082$	$0.20e-6$	$+\mathbf{0.007165}750921513$	$4.40e-6$
19	$-\mathbf{0.094482}408305059$	$54.9e-9$	$+\mathbf{0.007165}727125872$	$1.05e-6$
25	$-\mathbf{0.094482413}691372$	$2.09e-9$	$+\mathbf{0.007165719}331997$	$34.6e-9$
42	$-\mathbf{0.094482413496}551$	$28.7e-12$	$+\mathbf{0.00716571957}576$	$0.56e-9$
61	$-\mathbf{0.094482413493}793$	$0.47e-12$	$+\mathbf{0.007165719579}58$	$7.82e-12$
73	-0.094482413493837	Ref.	$+0.007165719579802$	Ref.

Table 3: Relative error on I.

# nodes	$I_f = -0.03505$		$I_{nxf} = 0.01074$	
	Numerical	Rel error	Numerical	Rel error
1	-0.01693	-0.52	-0.00564	-1.53
3	-0.02545	-0.27	$+0.00384$	-0.63
4	-0.02613	-0.25	$+0.00384$	-0.64
6	-0.02969	-0.15	$+0.00685$	-0.36
7	-0.03102	-0.12	$+0.00775$	-0.28
12	-0.03217	-0.082	$+0.00868$	-0.19
16	$\mathbf{-0.03517}$	$\mathbf{+0.0033}$	$\mathbf{+0.01074}$	$\mathbf{+0.0007}$
19	-0.03341	-0.047	$+0.00954$	-0.11
25	-0.03420	-0.024	$+0.01026$	-0.044
42	$\mathbf{-0.03510}$	$\mathbf{+0.0012}$	$\mathbf{+0.01088}$	$\mathbf{+0.0136}$
61	-0.03450	-0.016	$+0.01034$	-0.037
73	-0.03481	-0.007	$+0.01056$	-0.017

5. NUMERICAL EXAMPLE

The four faces metallic pyramid depicted on Fig. 3 is $1\,\mathrm{m} \times 1\,\mathrm{m} \times 1\,\mathrm{m}$ and illuminated by a $10\,\mathrm{MHz}$ plane wave polarized along X and travelling from $-Z$ to $+Z$. The electric currents in the middle of every four faces obtained with the MFIE$_{nxf}$ are depicted as well, showing a strong X-Z orientation, as expected. On Fig. 3, we also show the influence of the number of quadrature nodes used to evaluate every singular terms: firstly on Z_{12}, the interaction between the RWGs defined on edges 1 and 2, and secondly on the real part of J_3 and J_5, the coefficients of the RWGs defined on edge 3 and 5, contributing to the strongest electric currents. If accuracy below 1% is aimed at, then the best choice seems to be 16 (or 42) nodes. There is no gain to use 25, 61 or even 73 nodes!

6. CONCLUSION

The $1/R^3$ singularity arising in electromagnetic problems involving the MFIE needs careful treatment. The integration method presented in this paper as a simpler and more versatile alternative to [5] provides a less accurate estimation of the singular terms, but it has proved to have negligible effect on the overall accurracy, especially if the 16 nodes quadrature described in [6] is chosen.

REFERENCES

1. Rao, S. M., D. R. Wilton, and A. W. Glisson, "Electromagnetic scattering by surfaces of arbitrary shape," *IEEE Transactions on Antennas and Prop.*, Vol. 30, No. 3, 409–418, May 1982.
2. Hodges, R. E. and Y. Rahmat-Samii, "The evaluation of MFIE integrals with the use of vector triangle basis functions," *Microwave and Optical Technology Letters*, Vol. 14, No. 1, January 1997.
3. Wilton, D. R., S. M. Rao, A. W. Glisson, D. H. Schaubert, O. M. Al-Bundak, and C. M. Butler, "Potential integrals for uniform and linear source distribution on polygonal and polyhedral domains," *IEEE Transactions on Antennas and Prop.*, Vol. 32, No. 3, March 1984.
4. Graglia, R. D., "On the numerical integration of the linear shape functions times the 3-D Green's function or its gradient on a plane triangle," *IEEE Transactions on Antennas and Prop.*, Vol. 41, No. 10, 1448–1454, October 1993.
5. Ylä-Oijala, P. and M. Taskinen, "Calculation of CFIE impedance matrix elements with RWG and $n \times$ WG functions," *IEEE Transactions on Antennas and Prop.*, Vol. 51, No. 8, 1837–1846, August 2003.
6. Cools, R. and A. Haegemans, "CUBPACK: A package for automatic cubature; framework description," *ACM Trans. on Mathematical Software*, Vol. 29, No. 3, 287–296, September 2003.
7. Dunavant, D. A., "High degree efficient symmetrical Gaussian quadrature rules for the triangle," *International Journal for Numerical Methods in Engineering*, Vol. 21, 1129–1148, 1985.
8. Wandzura, S. and H. Xiao, "Symmetric quadrature rules on a triangle," *Computers and Mathematics with Applications*, Vol. 45, No. 12, 1829–1840, June 2003.
9. Gilles, T., M. Piette, and C. Craeye, "A partial analytical solution for the logarithmic singularity associated with MoM applied to dielectrics and its evaluation with polynomial quadratures," *Proc. ACES'07*, 2007.

Non-radiating Field Wave Scattering from Discontinuities in Planar Surface

Feng Chen, Huiling Zhao, and Wei Wan

Northwestern Polytechnical University, Xi'an, Shaanxi 710072, China

Abstract— In order to investigate how discontinuities affect non-radiating fields, one kind of non-radiating field wave — evanescent wave scattering by a conducting planar surface with groove is studied. Evanescent wave is generated by a half wavelength dipole antenna corresponding to its r^{-2} and r^{-3} terms in the near field. A numerical model is created via Frequency Difference Time Domain (FDTD) method computation. Re-radiation boundary condition is introduced in the process in order to improve the calculation efficiency. By comparing the far field antenna pattern with groove to without groove, the transformed propagating field from evanescent field can be obtained. The calculated results indicate that relative location and orientation between antenna and groove largely affect the transformed propagating part. Groove width and depth affection also discussed.

1. INTRODUCTION

Any sources can be divided into radiation and non-radiation sources. The former provide propagating wave which is known to contribute to the far-field monostatic or bistatic scattering, while the latter provide non-radiating field which is confined in a certain region and can not be detected outside the region [1]. One can obtain local information about an object by perturbation of the evanescent field [2]. This has been used a lot in near-field microscopy and near-field optics [3]. In microwave region, investigating the perturbation of evanescent field will help to have a better antenna arrangement, or help to detect objects buried underground [4], or improve the resolution in microwave imaging, etc.

In this paper, perturbation of evanescent field generated by a half wavelength dipole antenna is investigated via a modified FDTD. Re-radiation boundary condition (rRBC) which was first introduced into FDTD by R. E. Diaz [5] is used in the calculation process. Compared with Berenger's PML [6], rRBC is superior both in code writing and computational efficiency. Using this numerical model, perturbation affection of relative location and orientation between antenna and groove, groove width and depth is discussed.

2. RADIATION FIELD OF DIPOLE ANTENNA

It is well known that the radiation electric field components of a dipole antenna as function of spherical coordinates are:

$$
\begin{aligned}
E_r &= \mathrm{j}\frac{I\mathrm{d}l}{2\pi}\sqrt{\frac{\mu_0}{\varepsilon_0}}\cos\theta\left(\frac{1}{r^2}+\frac{1}{\mathrm{j}kr^3}\right)\mathrm{e}^{-\mathrm{j}kr} \\
E_\theta &= \mathrm{j}\frac{I\mathrm{d}l}{2\lambda}\sqrt{\frac{\mu_0}{\varepsilon_0}}\sin\theta\left(\frac{1}{r}+\frac{1}{\mathrm{j}kr^2}-\frac{1}{k^2r^3}\right)\mathrm{e}^{-\mathrm{j}kr} \\
E_\varphi &= 0
\end{aligned}
\tag{1}
$$

where the dipole is of length $\mathrm{d}l$ and current I, be placed coincident with the z axis and with its center at the origin. $k = \omega\sqrt{\varepsilon_0\mu_0}$.

It is apparent that only the $1/r$ terms present a nonzero contribution for the far field, which corresponds to a spherical wave with $1/r^2$ variation of the energy. The remaining $1/r^2$ and $1/r^3$ terms represent the evanescent waves which are confined in the vicinity of the dipole and cannot be detected in the far region. Evanescent waves can be detected only if they are perturbed and therefore are partially transformed into propagating waves. Possible approaches for achieving perturbation are by frustrating the evanescent waves with geometric or electromagnetic properties discontinuities.

3. DIPOLE RADIATION IN THE VICINITY OF A GROOVE

In order to investigate the part of propagating wave transformed from evanescent wave owing to discontinuity, a physical model which is illustrated in Fig. 1 is introduced. The half wavelength

dipole is supposed working at 10 GHz, and is located above a conducting planar surface with the orientation in either perpendicular (as shown in Fig. 1(a)) or parallel (as shown in Fig. 1(b)) to the surface. The distance between the dipole and the surface is h. The groove is just beside the dipole with width w and depth d.
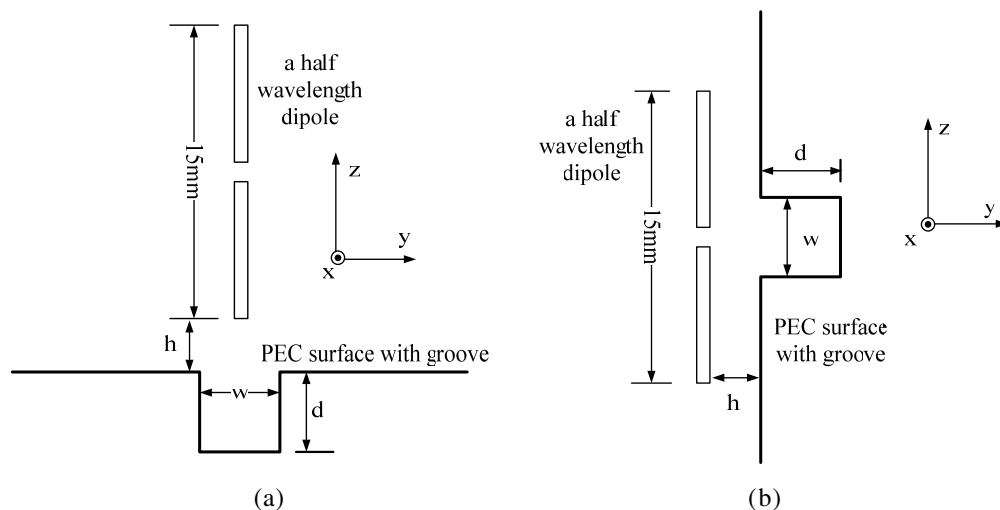
Figure 1: Schematic of a half wavelength dipole radiation in the vicinity of a perfect electric conducting surface with a groove. (a) dipole perpendicular to the surface, (b) dipole parallel to the surface.

A numerical model of Fig. 1 is created via Finite Difference Time Domain method (FDTD) computation. In the calculation process, one wavelength is divided into 36 cells.

4. THE APPLICATION OF RE-RADIATING BOUNDARY CONDITION IN FDTD

Because of the memory of the computer is limited, the process of the computation is confined in a certain region. In order to guarantee the correctness of the results obtained, the outgoing traveling waves are expected not to be reflected back into the computational domain.

The approach is to define planar boundaries inside the FDTD domain at which the discrete FDTD version of *Schelkunoff*'s equivalent currents are calculated. These currents are then flipped in sign, and used to radiate an exact negative copy of the field crossing the boundary as Fig. 2. The fields and currents in the FDTD space are discrete. In Fig. 2, the current $-J_{e(n+1,m)}$ which was located at the same position of $E_{(n+1,m)}$ could not be calculated accurately. Because the $J_{e(n+1,m)}$ is relative to $H_{(n+1,m)}$, which did not calculate in the FDTD space. Therefore the currents were obtained from the adjacent cell's electric or magnetic fields (E or H) as the Fig. 2 showed.
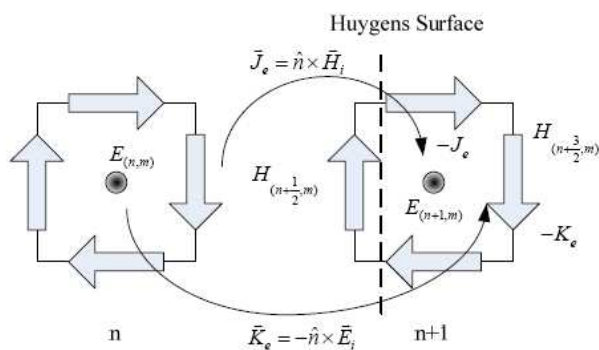
Figure 2: The teleportation recipe for creating an exact copy of an FDTD field in another FDTD space.
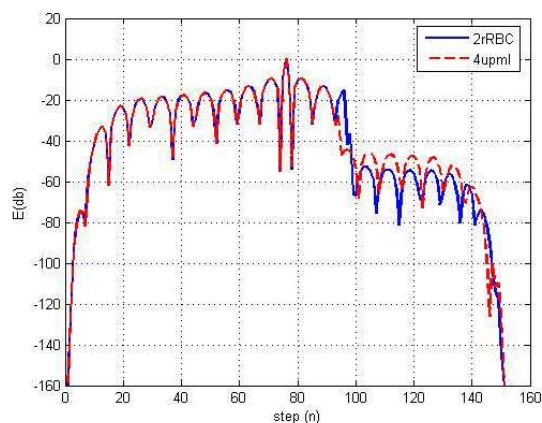
Figure 3: The attenuation of two wall rRBC and four wall UPML.

The Huygens termination which is the simplest possible termination for the Yee grid is located behind the rRBC. From Fig. 3, with the Huygens termination the field of the re-entering pulse was about $-37\,\mathrm{dB}$ below the original pulse. Comparing the two lines in Fig. 3, we see that the two wall rRBC get more attenuation than four walls UPML, moreover rRBC is simpler than UPML in code writing.

5. NUMERICAL EXPERIMENTS

For Fig. 1(a), set $d = 4\,\mathrm{mm}$ and $w = 4\,\mathrm{mm}$. Setting $h = 3.5\,\mathrm{mm}$ means the groove is just in the nearest field of the dipole. Far field antenna pattern with groove and without groove are calculated. Numerical far field patterns in decibel as a function of θ are shown in Fig. 4 with angle $\varphi = 0°$. It is demonstrated that groove perturbation is negligible when the dipole is perpendicular to the surface.

For Fig. 1(b), all parameters are set identical to Fig. 5. Numerical far field patterns in decibel as a function of θ are shown in Fig. 4 with angle $\varphi = 0°$. Comparing these two lines, we find that two new peaks are appeared at $\theta = 50°$ and $\theta = 130°$ because of the groove. The beam of the wave with groove is obviously wider than the beam without groove. It illustrates that the energy of the evanescent wave is partially transformed into the energy of propagating wave.
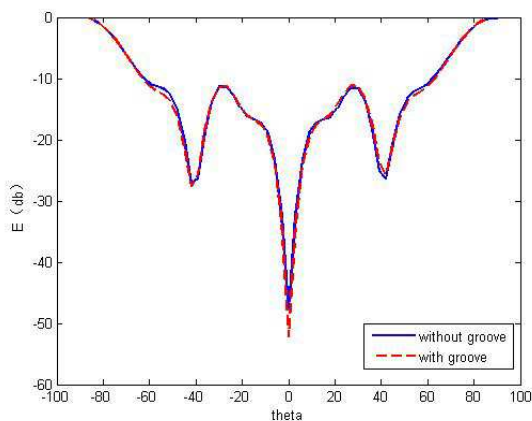
Figure 4: Far field pattern for Fig. 1(a) with different groove width, $\varphi = 0°$.
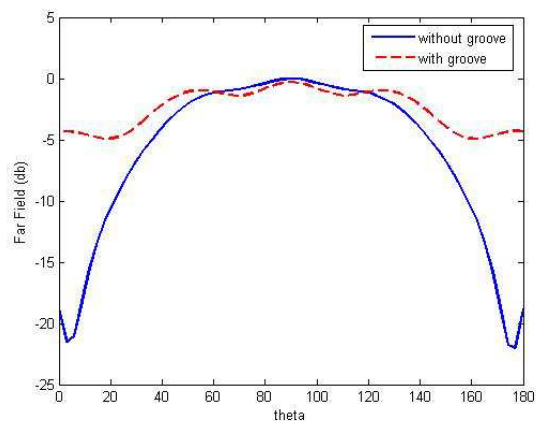
Figure 5: Far field pattern for Fig. 1(a) with different groove width, $\varphi = 90°$.

Figure 4 and Fig. 5 demonstrate that it is observable that part of the evanescent wave transforms into propagating wave when the dipole is parallel to the surface with groove. Therefore in the next section, we will study affections of different parameters based on the model as shown in Fig. 1(b).
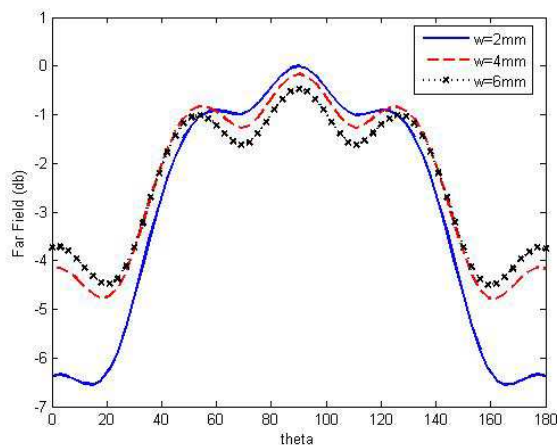
Figure 6: Far field pattern for Fig. 1(b) with different groove width.

The groove was set with the different width of 2 mm, 4 mm and 6 mm. Other parameters are $d = 4$ mm and $h = 3.5$ mm. As can be seen from Fig. 6, the side lobe of far field pattern increase with width of the groove and gradually come to saturate when w is larger than 4 mm. In the meantime, the main lobe decrease a little bit. The resulting beams become wider with increase width of the groove.

Given $w = 4$ mm and $h = 3.5$ mm, the far field pattern as function of θ and φ with different groove depth are depicted in Fig. 7 and Fig. 8. The depth of the groove was set with 4 mm, 6 mm and 8 mm. As can be seen from Fig. 7, the far field amplitude for $d = 6$ mm is larger than $d = 4$ mm and $d = 8$ mm and vibrate much than the other two. It illustrated that the part of propagating power transformed from evanescent wave affected by the groove's depth, and the affection is not monotony like the groove's width. Fig. 8 shows that the far field amplitudes as a function of φ don't change too much, but vibration increase with increase of groove's width.
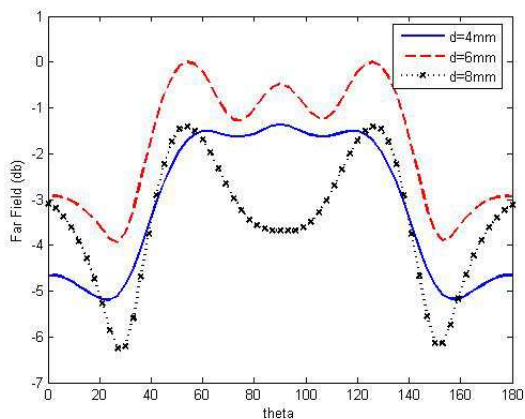
Figure 7: Far field pattern for Fig. 1(b) with different groove width, $\varphi = 120°$.
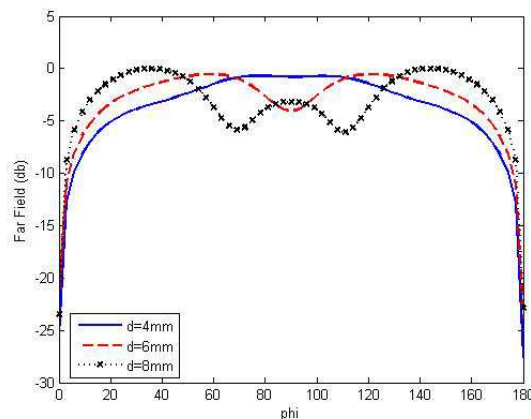
Figure 8: Far field pattern for Fig. 1(b) with different groove width, $\theta = 90°$.

6. CONCLUSIONS

Far field pattern of a half wavelength dipole antenna in the vicinity of conducting surface with groove is calculated by FDTD. Re-radiation boundary condition is introduced in the process. By comparing the far field antenna pattern with groove to without groove, the transformed propagating field from evanescent field is obtained. Numerical results show that the transformed part is observable when the dipole is parallel to the surface with groove, while it is negligible when the dipole is perpendicular to the surface; the affection of groove's width is monotony, while groove's depth is not. The conclusions can be advantageously used in overall arrangements of antennas on aircrafts, electromagnetic compatibility and microwave imaging.

ACKNOWLEDGMENT

REFERENCES

1. De Fornel, F., *Evanescent Waves: From Newtonian Optics to Atomic Optics*, Springer-Verlag Berlin and Heidelberg GmbH & Co. K, 2001.
2. Schultz, J. W., E. J. Hopkins, and E. J. Kuster, "Near-field probe measurements of microwave scattering from discontinuities in planar surface," *IEEE Trans. on Antennas and Propagation*, Vol. 51, No. 9, 2361–2368, 2003.
3. Courjon, D., *Near-field Microscopy and Near-field Optics*, Imperial College Press, 2003.
4. Smith, G. S. and L. E. R. Petersson, "On the use of evanescent electromagnetic waves in the detection and identification of objects buried in lossy soil," *IEEE Trans. on Antennas and Propagation*, Vol. 48, No. 9, 1295–1300, 2000.
5. Diaz, R. E., "A simple stackable re-radiating boundary condition (rRBC) for FDTD," *IEEE Antennas Propagation Magazine*, Vol. 46, No. 1, 2004.

6. Berenger, J. P., "A perfectly matched layer for the absorption of electromagnetic waves," *J. Comp. Phys.*, Vol. 114, 185–200, 1994.

Relativistic High Harmonics Generation in Underdense Plasma Produced by a Super Intense Femtosecond Laser Pulse

F. Abbasi[1] and K. Salimi[2]

[1]Vali-Asr University of Rafsanjan, Iran
[2]Sharif University of Technology of Tehran, Iran

Abstract— A high intensity laser incident on a vacuum-plasma interface, insert an Intensive electromagnetic force on electrons and charged particles. Relativistic charged particle movements lead to the high order harmonics generation of the incident wave. Efficiency of high harmonics increases with the intensity laser incident, So that the non-relativistic velocities of the particles vary to the relativistic velocities. Efficiency of high harmonics increases with the intensity laser incident. In previous works that has done in this field the researcher have reported-odd harmonics generated in direction of propagation of laser incident and even harmonics generated in normal direction of propagation of laser incident but in experimental results we can observe all harmonics in direction of propagation. The set of equations that are presented in other papers had been solved for SHG and THG while we have been presenting a set of equations and numerical analytic program do for any harmonics.

1. INTRODUCTION

With the advent of high power lasers it has become possible to study the interaction of free electrons in extremely high laser fields. Such lasers based on the principle of chirp pulse amplification [1]. At these ultrahigh intensities electrons quiver with velocities close to the velocity of light. In this limit, the effect of lights magnetic field on electron motion should become comparable to that of its electric field, and the electron mass should increase because of the relativistic correction. The primary quantity of interest is the normalized field strength $a_\circ$ given by $a_\circ = eE/m\omega c \approx 10^{-9}\sqrt{I(\mathrm{W/cm}^2\lambda(\mu\mathrm{m}))}$ for values of $a_\circ < 1$ the electron motion is linear. The nonlinear regime is accessed when $a_\circ$ approaches unity, which corresponds to an intensity $'10^{18}\mathrm{W/cm}^2$. The ultra relativistic limit corresponds to $a_\circ \gg 1$. In this paper, we will be primarily interested in the case $a_\circ \approx 1$. It can be shown that in this case the electron moves in the well-known figure-eight orbit. In this paper we study High harmonics generation from free electrons in plasma irradiated by short intense laser pulse. Using "charge conservation", "momentum conservation" and Maxwell equations, we will obtain a set of equations for harmonics.

2. HARMONICS GENERATION

Consider a vacuum-plasma interface at $z = 0$ with $z > 0$ as vacuum and $z < 0$ uniform plasma of density $n_\circ$.

A laser pulse perpendicular on a vacuum-plasma interface is incident on the interface (cf. Fig. 1).

$$\vec{E}_\circ = E_\circ e^{-(t-\tau/(\tau/2))^2} \tag{1}$$

where τ is in order of 10^{-15}.
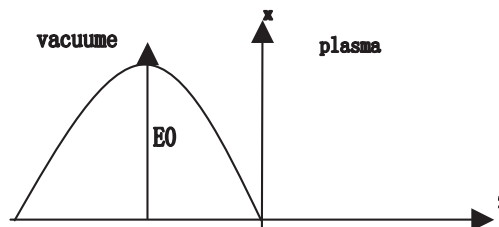
Figure 1: Schematic of incidence of a laser pulse perpendicular on a vacuum-plasma interface.

The equations governing electron momentum and energy are

$$\frac{d\vec{p}}{dt} = -e\vec{E} - \frac{e}{c}\vec{V} \times \vec{B} \tag{2}$$

$$\frac{d\gamma}{dt} = \frac{1}{m_\circ c^2}\vec{V} \cdot \vec{E} \tag{3}$$

where c, e, $m_\circ$, and γ are velocity of light electronic charge, rest mass and time averaged value of relativistic factor, respectively.

Using Eqs. (2) and (3) we can write

$$\frac{\partial \vec{V}}{\partial t} = \frac{-1}{m_\circ \gamma}\left[e\vec{E} + \frac{e}{c}\vec{V} \times \vec{B} + \frac{1}{c^2}\left(\vec{V} \cdot \vec{E}\right)\vec{V}\right] - \vec{V} \cdot \nabla\vec{V} \tag{4}$$

Using $\vec{J} = -ne\vec{V}$, current density, and $\rho = -ne$, electron density, in equation of continuity we get

$$\frac{\partial n}{\partial t} + \vec{\nabla} \cdot n\vec{V} = \circ \tag{5}$$

Using Maxwell's equations, we can write

$$\nabla^2 \vec{E} - \frac{1}{c^2}\frac{\partial^2 \vec{E}}{\partial t^2} = \frac{1}{c^2}\frac{\partial}{\partial t}(n\vec{V}) - 4\pi e\vec{\nabla}\frac{\partial n}{\partial t} \tag{6}$$

We assume all of harmonics are produced as this process occurred, so we can consider electric field, magnetic field, velocity and density as a furrier series

$$\vec{E}(z,t) = \sum_{n=-\infty}^{+\infty} \vec{E}_n(z,t)e^{i(n\omega_\circ t - k_n z)} + c \cdot c \tag{7}$$

$$\vec{B}(z,t) = \sum_{n=-\infty}^{+\infty} \vec{B}_n(z,t)e^{i(n\omega_\circ t - k_n z)} + c \cdot c \tag{8}$$

$$\vec{V}(z,t) = \sum_{n=-\infty}^{+\infty} \vec{V}_n(z,t)e^{i(n\omega_\circ t - k_n z)} + c \cdot c \tag{9}$$

$$n(z,t) = \sum_{m=-\infty}^{+\infty} n_m(z,t)e^{i(m\omega_\circ t - k_m z)} + c \cdot c \tag{10}$$

Attention, Negative index shows reflection wave and wave number is $k_n = n\omega_\circ\sqrt{1 - \omega_p^2/n^2\omega_\circ^2}\Big/c$ where ω_p is plasma frequency and $\omega_\circ$ is frequency of laser incident.

Amplitude of fields is depend on space and time so it seems, we can't separate harmonics like single frequency state, we solve this problem by getting furrier transform from Eqs. (7)–(10) and see, if we assume that overlapping bandwidth of SVA is very negligible, $\Delta\omega \ll \omega_\circ$, we can separate harmonics from each other (cf. Fig. 2).
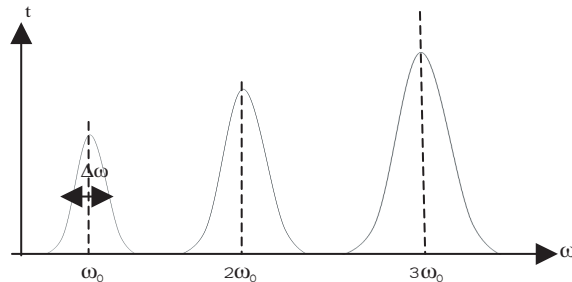
Figure 2: Schematic of harmonic's spectra.

Finally, using Eqs. (7)–(10) in Eqs. (4)–(6) we obtain sex coupled equations.

Two equations for electric field in direction of x and z, two equations for velocity in direction of x and z, one for density and one for magnetic field that obtain from Faraday's law. We solve these equations for two state, $n = 0$ and $n \neq 0$.

1. Zeroth harmonic ($n = 0$)

By replacing n as zero in equations we get excellent results about Plasmon waves and drift velocity that confirm previous work in this field. These results hoped us that our equations and numerical analytic program are powerful tools to computing harmonic. We don't discuss about this topics here.

2. High harmonic ($n \neq 0$)

If $n \neq 0$ in equations then we achieve to high harmonics by solve the equations in this situation. For abbreviating here we only represent density equation. Wave equation, Velocity equation, electric and magnetic field equation follow such process.

$$
\sum_m \left(\frac{\partial n_m(z,t)}{\partial t} + im\omega_\circ n_m(z,t) e^{i(m\omega_\circ t - k_m z)} \right) + \left(\frac{\partial n_m^*(z,t)}{\partial t} + im\omega_\circ n_m^*(z,t) e^{-i(m\omega_\circ t + k_m z)} \right)
$$

$$
= -\sum_m \sum_p \left(n_m(z,t) \left(\frac{\partial \vec{V} z_p(z,t)}{\partial z} - ik_p \omega_\circ \vec{V} z_p(z,t) \right) \right) e^{i((m+p)\omega_\circ t - (k_m + k_p)z)}
$$

$$
+ n_m^*(z,t) \left(\frac{\partial \vec{V} z_p(z,t)}{\partial z} - ik_p \omega_\circ \vec{V} z_p(z,t) \right) e^{i((-m+p)\omega_\circ t - (-k_m + k_p)z)} + \ldots \tag{11}
$$

For ease we simplify the equations by some variation in variables, as you can see in follows

$$
\frac{\partial n_m(z,t)}{\partial t} + im\omega_\circ n_m(z,t) e^{i(m\omega_\circ t - k_m z)} + \left(\frac{\partial n_m^*(z,t)}{\partial t} + im\omega_\circ n_m^*(z,t) e^{-i(l\omega_\circ t + k_l z)} \right)
$$

$$
= -\sum_p \left(n_{m-p}(z,t) \left(\frac{\partial \vec{V} z_p(z,t)}{\partial z} - ik_p \omega_\circ \vec{V} z_p(z,t) \right) \right) e^{i(m\omega_\circ t - (k_{m-p} + k_p)z)} + \leftarrow l + p = m,\ l = m - p
$$

$$
n_{-m+p}^*(z,t) \left(\frac{\partial \vec{V} z_p(z,t)}{\partial z} - ik_p \omega_\circ \vec{V} z_p(z,t) \right) e^{i(m\omega_\circ t - (-k_{m-p} + k_p)z)} + \leftarrow -l + p = m,\ l = -m + p \tag{12}
$$

where $L_{m'} = 2\pi/k_{m'}$ and $T_{m'} = 2\pi/\omega_\circ m'$.
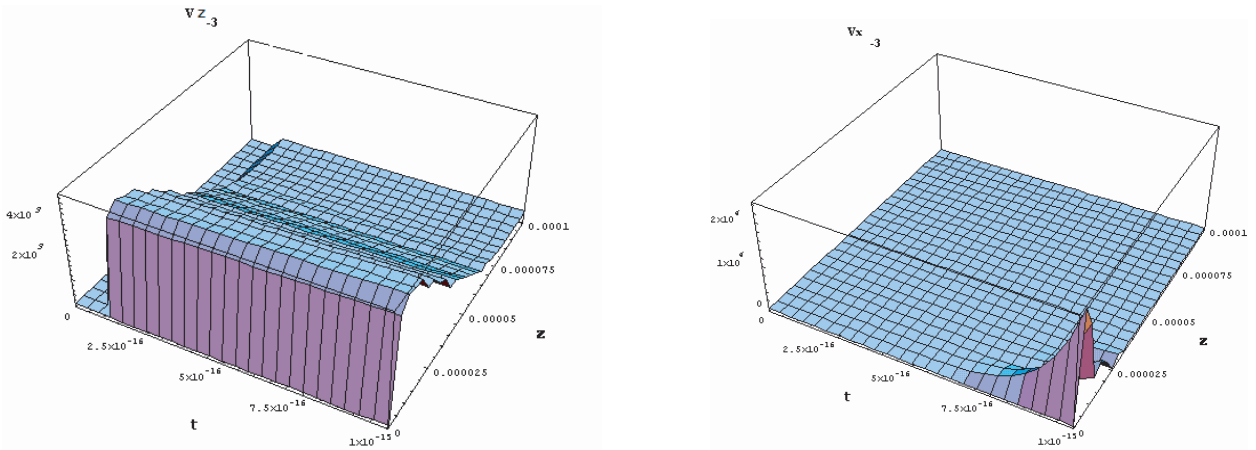
Figure 3: Reflected component of velocity of third harmonic in direction of propagation of laser incident, z, and its field, x.
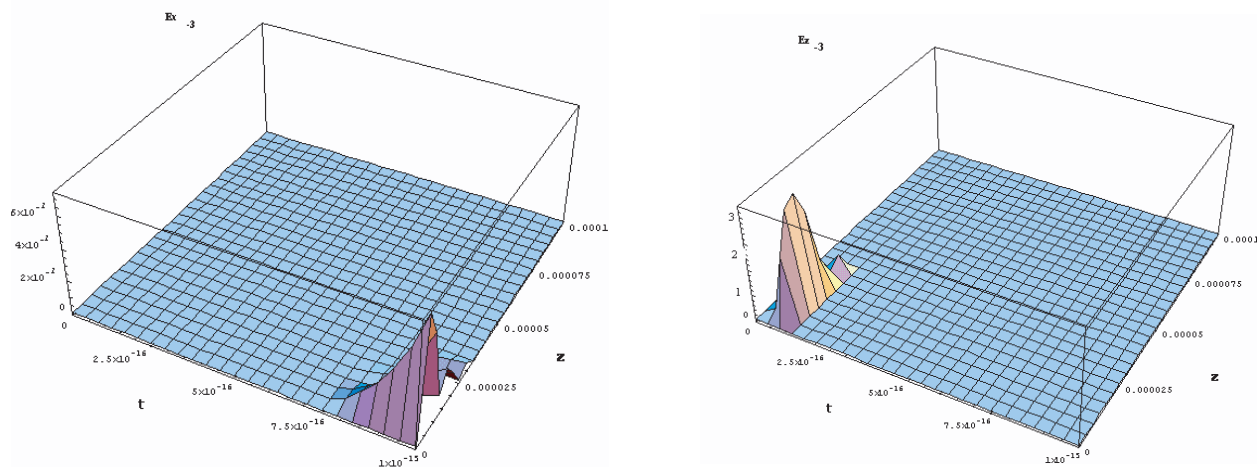
Figure 4: Reflected component of electric field of third harmonic in direction of propagation of laser incident, z, and its field, x.
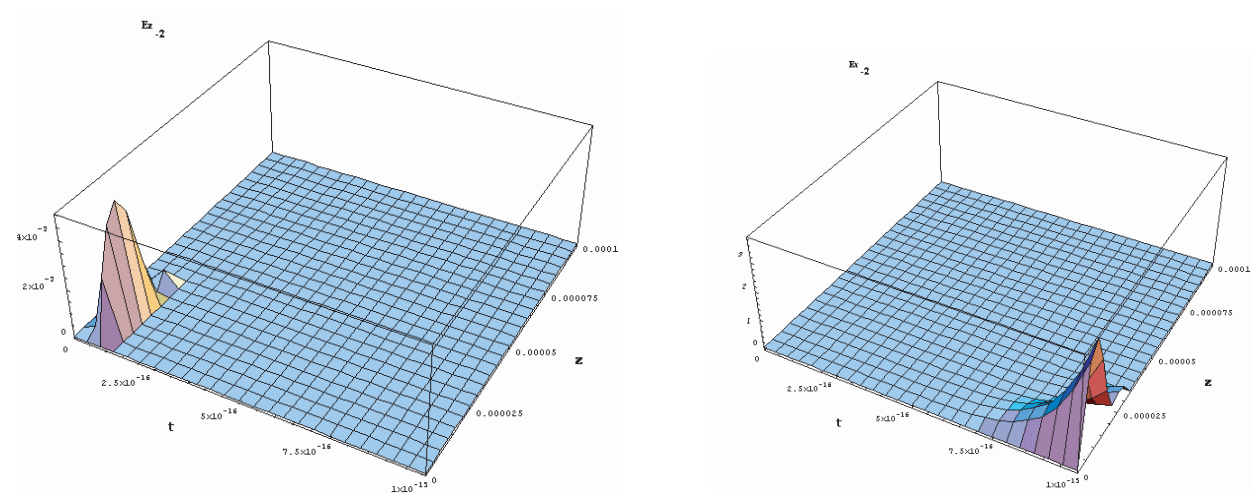
Figure 5: Reflected component of electric field of second harmonic in direction of propagation of laser incident, z, and its field, x.

3. CONCLUSIONS

Solving sex coupled equations velocity, density, electric and magnetic field for each harmonics gives interesting result. We plot variation of density, velocity, electric field and magnetic field (in two directions, propagation of laser incident and normal to it) of high harmonics as a function of time and space. One of considerable results in this paper is harmonics generation in direction of propagation of laser incident and normal to it (for abbreviating here we only represent result of third harmonic).

Because the primary electric field is in direction of x, we expect velocity in this direction be more than in direction of z, as Fig. 3 shows, maximum intensity of reflected component of electric field in direction of x is 2×10^4 m/s and in direction of z is 4×10^3 m/s. This process continues for other harmonics but in higher harmonic the intensity decrease, because of decreasing of harmonics influence. Fig. 4 shows reflected component of electric field of third harmonic in direction of propagation of laser incident, z, and maximum intensity in this direction is 2.5 StaV/cm and in direction of x is 6×10^{-2} StaV/cm. Fig. 5 shows reflected component of electric field of second harmonic in direction of propagation of laser incident, z, and maximum intensity in this direction is 4×10^{-2} StaV/cm and in direction of x is 3 StaV/cm. In previous works that has done in this field the researcher have reported-odd harmonics generated in direction of propagation of laser incident and even harmonics generated in normal direction of propagation of laser incident [2] but in experimental results we can see all harmonics in direction of propagation [3]. In this paper

we consider $\vec{V} \cdot \nabla \vec{V}$ term in velocity equation (it means plasma is considered as a fluid) and see all of harmonics in both of direction, but comparison between Figs. 4 and 5 get interesting result (comparison between intensity of 2th and 3th, the intensity of odd harmonics in direction of laser incident propagation is more than even harmonics in this direction but in direction of laser's field (normal direction) intensity of even harmonics is more. We did our comparison until 16th harmonic. We can say by considering plasma as a fluid, all harmonics has been seen in two direction but intensity of odd harmonics is more in direction of propagation of laser incident, this idea confirms for even harmonics in normal direction of propagation of laser incident.

REFERENCES

1. Lin, H., L. M. Chen, and J. C. Kieffer, "Harmonic generation by an intense laser pulses in underdense plasma," *Phys. Rev. E*, Vol. 65, 036414, 2002.
2. Esarey, E., et al., "Nonlinear analysis of relativistic harmonic generation by intense lasers in plasma," *IEEE Trans. Plasma Sci.*, Vol. 21, 95, 1993.
3. Banerjee, S. and A. R. Valenzuela, "High harmonic generation in relativistic laser — plasma interaction," *Physics of Plasmas*, Vol. 9, 5, 2003.

High Harmonic Generation in Magnetic Underdense Plasma

K. Salimi[1] and F. Abbasi[2]

[1]Sharif University of Technology of Tehran, Iran
[2]Vali-Asr University of Rafsanjan, Iran

Abstract— A high intensity laser normal incident (10^{20} W/cm^2) on a vacuum-plasma interface produces high harmonics in reflected components. Efficiency of high harmonics increases with the intensity laser incident. So the non-relativistic velocities of the particles vary to the relativistic velocities. Consequently, electrons in such high fields are predicted to quiver nonlinearly, moving in figure eight patterns, rather than in straight lines, and thus to radiate photons at harmonics of the frequency of the incident laser light. To meet the challenge of high power, short wavelength coherent radiation generation, it is quite to investigate the conditions under which harmonics generation efficiency can be maximized. We insert a magnetic field on plasma to increase the harmonics generation efficiency.

1. INTRODUCTION

With the advent of high power lasers it has become possible to study the interaction of free electrons in extremely high laser fields. Such lasers based on the principle of chirp pulse amplification [1]. At these ultrahigh intensities electrons quiver with velocities close to the velocity of light. In this limit, the effect of lights magnetic field on electron motion should become comparable to that of its electric field, and the electron mass should increase because of the relativistic correction. It can be shown that in this case the electron moves in the well-known figure-eight orbit and radiate photons in frequency of laser incident. In this paper we study high harmonics generation by a normal incident, relativistically intense laser pulse on vacuum-**magnetic** plasma. The equations of the "charge conservation" and the "momentum conservation" and Maxwell equations are written for the electromagnetic fields. Then the high order harmonics equations are derived, seven coupled equations. We plot variation of efficiency of high harmonics as a function of time and space. To meet the challenge of high power, short wavelength coherent radiation generation, it is quite to investigate the conditions under which harmonics generation efficiency can be maximized [2]. We insert a magnetic field on plasma to increase the harmonics generation efficiency. Comparison between efficiency of high harmonics in underdense plasma and in magnetic underdense plasma shows, magnetic field can increases efficiency, considerably. One of the work we do in this paper is considering γ, relativistic factor, as a function of time and space such as other variables, velocity, density, electric and magnetic field (in other paper γ has been considered constant or as a function of laser intensity).

2. HARMONICS GENERATION

Consider a vacuum-plasma interface at $z = 0$ with $z > 0$ as vacuum and $z < 0$ uniform plasma of density n_o. A laser pulse perpendicular on a vacuum-plasma interface is incident on the interface (cf. Fig. 1).

$$\vec{E}_o = E_o e^{-(t-\tau/(\tau/2))^2} \tag{1}$$

where τ at order of 10^{-15}.
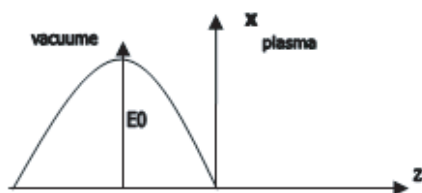
Figure 1: Schematic of incidence of a laser pulse perpendicular on a vacuum-plasma interface.
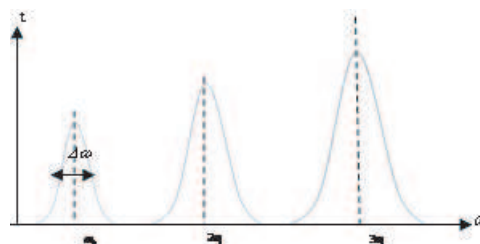

Figure 2: Schematic of harmonic's spectra.

The equations governing electron momentum and energy are

$$\frac{d\vec{p}}{dt} = -e\vec{E} - \frac{e}{c}\vec{V} \times \vec{B} \tag{2}$$

$$\frac{d\gamma}{dt} = \frac{1}{m_o c^2}\vec{V} \cdot \vec{E} \tag{3}$$

where c, e, m_o, and γ are velocity of light electronic charge, rest mass and time averaged value of relativistic factor, respectively.

Using Eqs. (2) and (3) we can write

$$\frac{\partial \vec{V}}{\partial t} = \frac{-1}{m_o \gamma}\left[e\vec{E} + \frac{e}{c}\vec{V} \times \vec{B} + \frac{1}{c^2}\left(\vec{V} \cdot \vec{E} \right)\vec{V} \right] - \vec{V} \cdot \nabla \vec{V} \tag{4}$$

Using $\vec{J} = -ne\vec{V}$, current density, and $\rho = -ne$, electron density, in equation of continuity we get

$$\frac{\partial n}{\partial t} + \vec{\nabla} \cdot n\vec{V} = o \tag{5}$$

Using Maxwell's equations, we can write

$$\nabla^2 \vec{E} - \frac{1}{c^2}\frac{\partial^2 \vec{E}}{\partial t^2} = \frac{1}{c^2}\frac{\partial}{\partial t}\left(n\vec{V} \right) - 4\pi e\vec{\nabla}\frac{\partial n}{\partial t} \tag{6}$$

We assume all of harmonics are produced as this process occurred, so we can consider electric field, magnetic field, velocity and density as a furrier series

$$\vec{E}(z,t) = \sum_{n=-\infty}^{+\infty} \vec{E}_n(z,t)e^{i(n\omega_o t - k_n z)} + c.c \tag{7}$$

$$\vec{B}(z,t) = \sum_{n=-\infty}^{+\infty} \vec{B}_n(z,t)e^{i(n\omega_o t - k_n z)} + c.c \tag{8}$$

$$\vec{V}(z,t) = \sum_{n=-\infty}^{+\infty} \vec{V}_n(z,t)e^{i(n\omega_o t - k_n z)} + c.c \tag{9}$$

$$n(z,t) = \sum_{n=-\infty}^{+\infty} n_m(z,t)e^{i(m\omega_o t - k_m z)} + c.c \tag{10}$$

We consider γ, relativistic factor, as a function of time and space such as other variables. In other papers γ was estimated in this way [3]:

$$\gamma = \left(1 - V^2/c^2 \right)^{-1/2} = \left(1 + \frac{1}{2}\frac{V^2}{C^2}\cos^2\omega t + \dots \right) \tag{11}$$

In relativistic region $V = \alpha C$ where $0 < \alpha < 1$ thus $\langle \gamma \rangle \approx 1 + \alpha^2/2$ for example if $\alpha = 0.7$ then $\gamma = 1.33$ but we consider γ as a "function" of time and space such as other variables.

$$\gamma(z,t) = \sum_{m=-\infty}^{+\infty} \gamma_m(z,t)e^{i(m\omega_o t - k_m z)} + c.c \tag{12}$$

Attention, negative index shows reflection wave and wave number is $k_n = n\omega_o\sqrt{1 - \omega_p^2/n^2\omega_o^2}/c$, where ω_p is plasma frequency and ω_o is frequency of laser incident.

Because of ponderomotive force in plasma, velocity and electric field has components in both of direction, propagation and normal on it.

$$\vec{V} = (V_x, o, V_z) \tag{13}$$

$$\vec{E} = (E_x, o, E_z) \tag{14}$$

$$\vec{B} = (o, B_y, o) \tag{15}$$

amplitude of fields is depend on space and time so it seems, we can't separate harmonics like single frequency state, we solve this problem by getting furrier transform from Eqs. (7)–(10) and see, if we assume that overlapping bandwidth of SVA is very negligible, $\Delta\omega \ll \omega_o$, we can separate harmonics from each other (cf. Fig. 2).

Finally, Using Eqs. (7)–(10) in Eqs. (4)–(6) we obtain seven coupled equations.

Two equations for electric field in direction of x and z, two equations for velocity in direction of x and z, one for density and one for magnetic field that obtain from Faraday's law. We solve these equations for two state, $n = 0$ and $n \neq 0$.

1. Zeroth harmonic ($n = 0$)

By replacing n as zero in equations we get excellent results about Plasmon waves and drift velocity that confirm previous work in these fields. These results hoped us that our equations and numerical analytic program are powerful tools to computing harmonic. We don't discuss about this topics here. For non magnetic plasma we consider $B_o = 0$ in $t = 0$, $z = 0$ but in magnetic plasma we consider it about 10^5 T.

2. High harmonic($n \neq 0$)

If $n \neq 0$ in equations then we achieve to high harmonics by solve the equations in this situation. for abbreviating here we only represent magnetic field equation. Wave equation, Velocity equation, electric and magnetic field equation follow such process.

$$\sum_m \left(\left(\frac{\partial Ex_m(z,t)}{\partial z} - ik_m Ex_m(z,t) \right) + \frac{1}{c}\left(\frac{\partial By_m(z,t)}{\partial t} + im\omega_o By_m(z,t) \right) \right) e^{i(m\omega_o t - k_m z)}$$

$$+ \left(\left(\frac{\partial Ex_m^*(z,t)}{\partial z} + ik_m Ex_m^*(z,t) \right) + \frac{1}{c}\left(\frac{\partial By_m^*(z,t)}{\partial t} - im\omega_o By_m^*(z,t) \right) \right) e^{i(m\omega_o t - k_m z)} = o \ (16)$$

We integrate from Eq. (11) over time and space interval

$$\left(\left(\frac{\partial Ex_m(z,t)}{\partial z} - ik_m Ex_m(z,t) \right) + \frac{1}{c}\left(\frac{\partial By_m(z,t)}{\partial t} + im\omega_o By_m(z,t) \right) \right) = o \qquad (17)$$
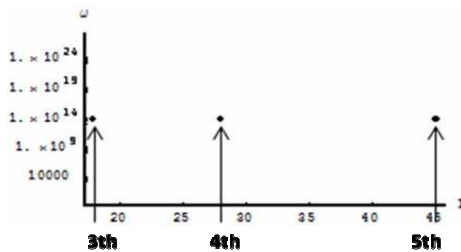
Figure 3: Intensity of 3th, 4th and 5th I (a.u.) in term of $\omega_o = 4.8 \times 10^{13}$ in non magnetic plasma.
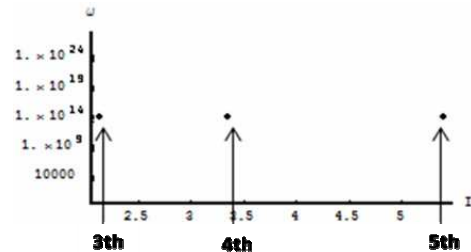
Figure 4: Intensity of 3th, 4th and 5th I (a.u.) in term of $\omega_o = 4.8 \times 10^{13}$ in magnetic plasma.

3. CONCLUSIONS

We solved seven coupled equations velocity, density, electric and magnetic field for each harmonics in magnetic plasma and non-magnetic plasma and compared their results.

Comparison between Fig. 3 and Fig. 4 shows by insert a magnetic field on plasma efficiency of 3th, 4th and 5th harmonics intensity increases about 9 times. We do our comparison until 20th and notice magnetic field can increases efficiency of harmonics.

REFERENCES

1. Lin, H., L. M. Chen, and J. C. Kieffer, "Harmonic generation by an intense laser pulses in underdense plasma," *Phys. Rev. E*, Vol. 65, 036414, 2002.
2. Chen, S. Y., et al., "Observation of phase matched relativistic harmonic generation," *Physical Review Letters*, Vol. 84, No. 24, 1996.
3. Parashar, J. and A. K. Sharma, "Second harmonic by an obliquely incident laser on a vacuum plasma interface," *Europhys. Lett.*, Vol. 41, 389, 1998.

Applications of Silicon-based Photonic Crystal

Huihui Zhang, **Huajun Shen**, **Jingtao Zhou**, and **Xinyu Liu**

Institute of Microelectronics of Chinese Academy of Sciences, China

Abstract— Silicon photonic crystals provide an exciting new tool for the manipulation of photons in semiconductor industry. In this article, photonic crystal theory and applications of silicon-based photonic crystal are presented. Photonic bandgap is calculated and analysed, which are meaningful to the research of silicon-based photonic crystal devices.

1. INTRODUCTION

Silicon photonics has recently attracted intense interest in light of potential as cost effective opto-electronic solutions for applications in the fields of optical interconnects, telecommunications, and optical sensors [1, 2]. Any technological development in either silicon or associated microelectronics industry can provide an impetus in the advancement of silicon based integrated optics. As a good example, the rapid advances and breakthroughs in silicon-on-insulator (SOI) technology make it possible to build waveguide-based photonic microstructures on SOI substrate by conventional processing techniques compatible with silicon microelectronics manufacturing [3].

2. PHOTONIC CRYSTAL THEORY AND APPLICATIONS OF SILICON-BASED PHOTONIC CRYSTAL

Photonic crystals, also known as photonic bandgap material, can mold the flow of light in a controlled fashion. They are periodic arrays of dielectric materials that open up band gaps for electromagnetic waves, that is, frequency ranges where photon propagation is forbidden. It has been demonstrated both theoretically and experimentally that line defects introduces into a photonic crystal can guide light within the band gap. PBG waveguides have many advantages over traditional dielectric waveguides. For instance, they can guide light in air, not only in dielectric, thus decreasing material losses at optical frequencies. Bends in photonic crystal waveguides can also carry electromagnetic waves around sharp bends with high efficiency [4].

Silicon photonics is still a booming research area. From optical prospective, silicon is an excellent dielectric medium at 1.55 µm wavelength region. The index is high, ranging from 3.4–3.6 depending on the growth process. Silica is also transparent at this wavelength, but with lower index around 1.45–1.5 depending on the doping. Silicon and silica can be combined easily for index guiding. The fabrication process is mostly compatible with CMOS technology. Low-loss waveguides and other planar devices have been successfully realized on the SOI platform [5, 6]. One big driving force is the need to replace electronic interconnects in today's microprocessors, which has become the bottleneck that limits the operating speed of microelectronic devices. Experts project that optical interconnects will be used to connect computer boards in five years, while the use of optical interconnects within the chip is being investigated and will possibly be realized in 10–15 years [7, 8].

3. COMPUTATION OF THE PHOTONIC BANDGAP

In source-free material, the Maxwell equations can be written as

$$\nabla \times H = \varepsilon_0 \varepsilon(r) \frac{\partial H(r, t)}{\partial t} \tag{1}$$

$$\nabla \times E = -\mu_0 \mu(r) \frac{\partial E(r, t)}{\partial t} \tag{2}$$

For the frequency ω, we can have photonic Eigen Equation as

$$\left[\nabla \times \frac{1}{\varepsilon(r)} \nabla \times \right] H(r) = \frac{\omega^2}{c_2} H(r) \tag{3}$$

The result of solving the Equation (3) is the band structure.

Finite-Difference Time-Domain method is a powerful tool in solving electromagnetic problems. This method was proposed by Yee in 1966 [9] and further developed by Taflove in the 1970s [10]. It

has been widely used to study electromagnetic wave propagation in different structures for optical device simulations, antenna design, and etc.

Yee suggested a convenient way to discretize Maxwell equations both in time and in space. FDTD updates the field components using the values from the previous time step and one must specify an initial field distribution to trigger the updating. Commonly used source excitations include plane waves, point Gaussian pulses and waveguide eigen-mode excitations.

Special care must be taken at the boundary of the finite computational domain. The boundary can be reflecting, such as perfect electric conductor and perfect magnetic conductor, or absorbing. Commonly used absorbing boundary conditions include first order Mur and perfectly matched layer.

We calculate the photonic bandgaps by FDTD. The results are show in the Fig. 1 and Fig. 2. From the Fig. 1 and Fig. 2, we see that the band structure for TE and TM modes are completely different. There are photonic bandgaps for one polarization but not for the other polarization. Inside the gap, no extended states are permitted, and incident light is reflected. The result provides some useful insights into the appearance of bandgaps, which are meaningful to the research of silicon-based photonic crystal devices.
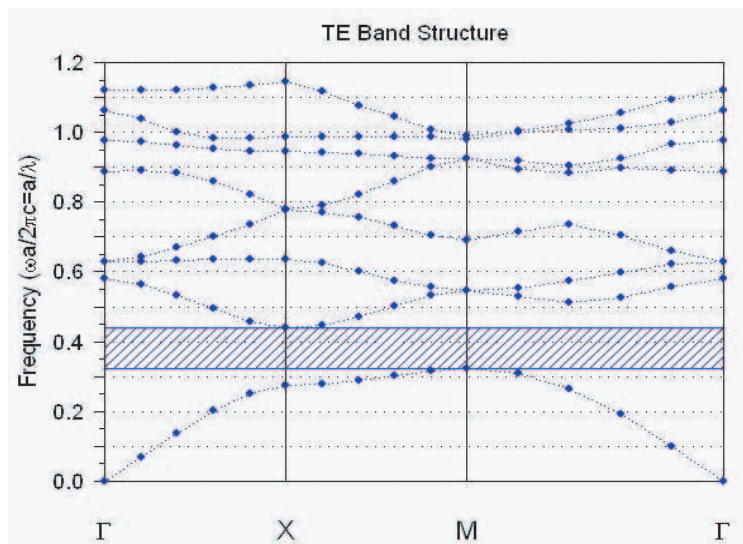
Figure 1: The photonic band structure for TE.
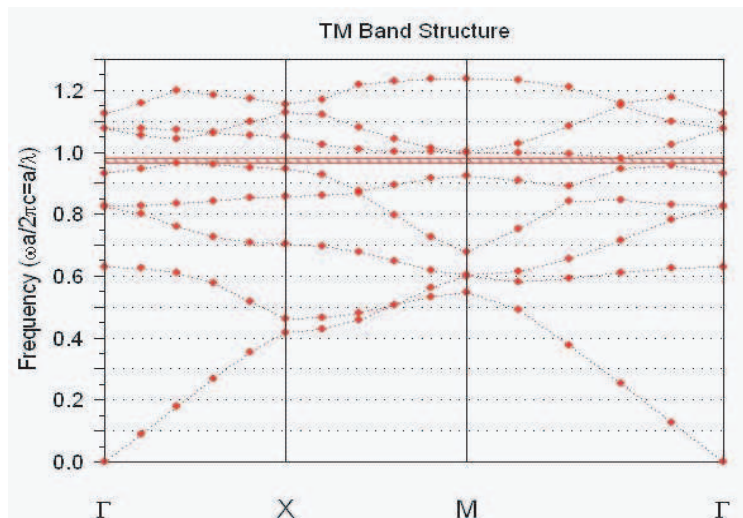
Figure 2: The photonic band structure for TM.

4. CONCLUSIONS

Photonic crystals, in which the refractive index changes periodically, provide an exciting new tool for the manipulation of photons and have received keen interests from a variety of fields. In this paper, we would like to review the applications of photonic crystals by focusing on silicon-based photonic crystals and calculated the photonic bandgaps by FDTD, which are meaningful to the research of silicon-based photonic crystal devices.

REFERENCES

1. Clemens, J. T., "Silicon microelectronics technology," *Bell Labs Technical Journal*, Vol. 2, No. 4, 76–102, 1997.
2. Koch, T. L., "Opportunities and challenges in silicon photonics," *IEEE LEOS, Annual Meeting Conference*, (IEEE Cat. No. 06CH37736C), 2, 2006.
3. Roelkens, G., D. Van Thourhout, and R. Baets, "Laser emission and photo detection in an InP/InGaAsP layer integrated on and coupled to an SOI waveguide circuit," *Opt. Express*, Vol. 14, 8154–8159, 2006.
4. Yablonovitch, E., "Photonic band structure," *J. Opt. Soc. Am. B*, Vol. 10, 283–295, 1993.
5. Pavesi, L., "Will silicon be the photonic material of the third millennium?," *J. Phys.: Condens. Matter*, Vol. 15, 1169–1196, 2003.
6. Vlasov, Y. and S. McNab, "Losses in single-mode silicon-on-insulator strip waveguides and bends," *Opt. Express*, Vol. 12, 1622–1631, 2004.
7. McNab, S. J., N. Moll, and Yu. A. Vlasov, "Ultra-low loss photonic integrated circuit with membrane-type photonic crystal waveguides," *Opt. Express*, Vol. 11, 2927–2939, 2003.
8. Ziyang, Z., "Silicon-based photonic devices: Design, fabrication and characterization," Doctoral Thesis, Royal Institute of Technology, 2008.
9. Yee, K. S., "Numerical solution of initial boundary value problems involving Maxwell's equations in isotropic media," *IEEE Trans. Antennas and Propagation*, Vol. 14, 302, 1966.
10. Taflove, A., *Computational Electrodynamics: The Finite-Difference Time-Domain Method*, second edition, Artech House, Boston, MA, 2000.

Focusing Properties of Radially Polarized Beam with Radial Cosine Phase Wavefront

X. Gao[1,2]**, J. Wang**[1]**, L. Sun**[1,3]**, and S. Zhuang**[2]

[1]Electronics and Information College, Hangzhou Dianzi University
Hangzhou 310018, China
[2]University of Shanghai for Science and Technology, Shanghai 200093, China
[3]Key Laboratory of RF Circuit & System (Hangzhou Dianzi University)
Ministry of Education, China

Abstract— The focusing properties of radially polarized beam with radial cosine wavefront phase are investigated. For radially polarized beam without any wavefront phase, focus pattern is ring for low numerical aperture, while only one intensity peak for high numerical aperture due to stronger longitudinal field component in focal region. When the radially polarized beam with radial cosine wavefront phase is focused, focal pattern differs with frequency parameter in cosine function. For high numerical aperture, focal shift occurs, and focal patterns also evolve considerably, for instance, from only one peak to two or multiple peaks. Focal shift value fluctuates for low frequency parameter, drops sharply, and then comes back slightly. Simultaneously, Peak intensity ratio of radially polarized component to longitudinal polarized component in focal region decreases slowly, and then increases very quickly.

1. INTRODUCTION

As a kind of the vector beam, radially polarized beam has gained much interest recently due to its applications such as particle-trapping, optical data storage, laser machining and lithography [1]. The presence of high intense longitudinal electric field in focal region of the laser beam can also enhance nonlinear effects [2], and can also be used for laser particle acceleration without a plasma wave. Focusing properties of radially polarized beam is worth investigating and may be used in many optical systems [3]. The intensity distributions near the focal point for radially polarized laser beams including higher-order transverse modes are also calculated based on vector diffraction theory [4], which illustrates that the strong longitudinal component forms a sharper spot at the focal point under a high-NA focusing condition. In addition, the intensity distributions of a tightly focused radially polarized beam that has a double-ring-shaped transverse mode pattern were calculated based on vector diffraction theory [5] to show that the distribution of the longitudinally component near the focus varied drastically with the degree of truncation of the incident beam by a pupil. Many researchers have paid attention to the focusing properties of radially polarized beam with uniform wavefront distribution in high numerical aperture system. In fact, the wavefront distribution can affect the focal properties remarkably. In this paper, focusing properties of the radially polarized beam with radial cosine wavefront phase are investigated in detail. Section 2 indicates the principle of the focusing system, and the results and discussions are shown in Section 3. The conclusions are summarized in Section 4.

2. PRINCIPE OF THE FOCUSING SYSTEM

When the radially polarized beam is focused, there are two kinds of fields in focal region, radilly polarized component and longitudinally polarized component, and using the same analysis method as that in Reference 3, the electric field in focal region can be written as

$$\vec{E}(r, \varphi, z) = E_r \vec{e}_r + E_z \vec{e}_z \tag{1}$$

where $\vec{e}_r$ and $\vec{e}_z$ are the unit vectors in the radially and propagating directions, respectively. E_r and E_z are amplitudes of the two orthogonal components and can be expressed as

$$E_r(r, z) = A \int_0^\alpha \cos^{1/2}(\theta) \cdot P(\theta) \sin(2\theta) \cdot J_1(kr \sin \theta) \exp(ikz \cos \theta) \, d\theta \tag{2}$$

$$E_z(r, z) = 2iA \int_0^\alpha \cos^{1/2}(\theta) \cdot P(\theta) \sin^2(\theta) \cdot J_0(kr \sin \theta) \exp(ikz \cos \theta) \, d\theta \tag{3}$$

where r and z are the radially and axial coordinates of observation point in focal region, respectively. k is wave number and $P(\theta)$ is the pupil apodization function. In addition, $\alpha = a \sin(NA)$, NA is the numerical aperture of the focusing optical system. The intensity in focal region is proportional to the square modulus of the Equation (1) with incident radially polarized beam.

In the system investigated in this paper, the wavefront distribution is radial cosine distribution, and can be written as

$$\varphi = \pi \cdot \cos\left(\pi \cdot C \cdot r\right) = \pi \cdot \cos\left[\pi \cdot C \cdot \tan\left(\theta\right)/\tan\left(\alpha\right)\right] \tag{4}$$

where C is frequency parameter in cosine part of the wavefront phase distribution, and denotes the radial change frequency of the phase. r is the normalized radial coordinate in focal region. The motive to choose this kind of radial cosine wavefront is that it is very simple and easy to carry out. The electric field in focal region can be written in the same form as Equation (1), however the two orthogonal components E_{rm} and E_{zm} are different and should be expressed as

$$E_{rm}\left(r, z\right) = A \int_0^\alpha \cos^{1/2}\left(\theta\right) \cdot \exp\left(i\varphi\right) \cdot P\left(\theta\right) \sin\left(2\theta\right) \cdot J_1\left(kr \sin\theta\right) \exp\left(ikz \cos\theta\right) d\theta \tag{5}$$

$$E_{zm}\left(r, z\right) = 2iA \int_0^\alpha \cos^{1/2}\left(\theta\right) \cdot \exp\left(i\varphi\right) \cdot P\left(\theta\right) \sin^2\left(\theta\right) \cdot J_0\left(kr \sin\theta\right) \exp\left(ikz \cos\theta\right) d\theta \tag{6}$$

The radial polarized component and longitudinal polarized component can be calculated according to Equation (5) and Equation (6), respectively. In this article, the focusing properties of the radially polarized beam without any wavefront modulation is calculated firstly, then the radial cosine wavefront modulation is added to investigate the focusing properties of the radial cosine wavefront radially polarized beam. Without loss of generality, transverse intensity distribution of the incident beam is uniform.

3. RESULTS AND DISCUSSIONS

Firstly, the focusing properties of radially polarized beam without any wavefront phase modulation are calculated for low numerical aperture $NA = 0.5$. Total intensity distribution is not one intensity peak, focal pattern is a intensity ring, which shows that radially polarized beam can not accomplish tighten focusing for low numerical aperture. In order to understand the cause of this phenomenon, radially polarized component and longitudinal polarized component in focal region are also calculated. It should be noted that all intensity distributions in this paper are all normalized by maximum intensity value. Radially polarized component turns on ring focal pattern, while axial polarized component is only one intensity peak. It can be seen that the peak value of radially polarized component is stronger than that of axial polarized component, which denotes that for low numerical aperture, the radially polarized component domains the total intensity distribution in focal region. In order to understand the focusing properties of the beam deeply, focusing properties under condition of high numerical aperture are investigated. There is only one intensity peak. Therefore, the numerical aperture is very important parameter in focusing process of the radially polarized beam, and can affect focal pattern considerably. When the radially polarized is used as incident beam, the numerical aperture should be taken into consideration. Radially polarized component is ring shape, while axial polarized component is one intensity peak. However, the intensity scale is different, for high numerical aperture, the longitudinal polarized component is stronger than radially polarized component, and affects the total intensity distribution in focal region. The intensity ratio of the radially polarized component to longitudinal polarized component play an important role in the total intensity pattern in focal region.

The dependence of the ratio on the numerical aperture is calculated and illustrated in Figure 1. From the figure it can be seen that the ratio increases with increasing numerical aperture, which denotes that with increasing numerical aperture, the longitudinal polarized component takes more and more part in total intensity distribution in focal region, and domains the focal pattern more considerably.

Above all, the wavefront of the radially polarized beam is uniform, now the focal intensity distribution of radially polarized beam with radial cosine wavefront phase is investigated in detail. Total intensity distributions in focal region for high numerical aperture $NA = 0.9$ with increasing frequency parameter C. It can be seen from calculation that for small frequency C there is one intensity peak, and with increasing frequency parameter C, the intensity peak shifts along in axial direction towards optical aperture. Increase the frequency parameter C, focal intensity peak
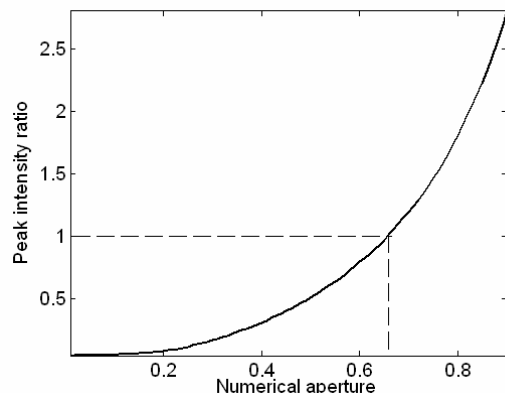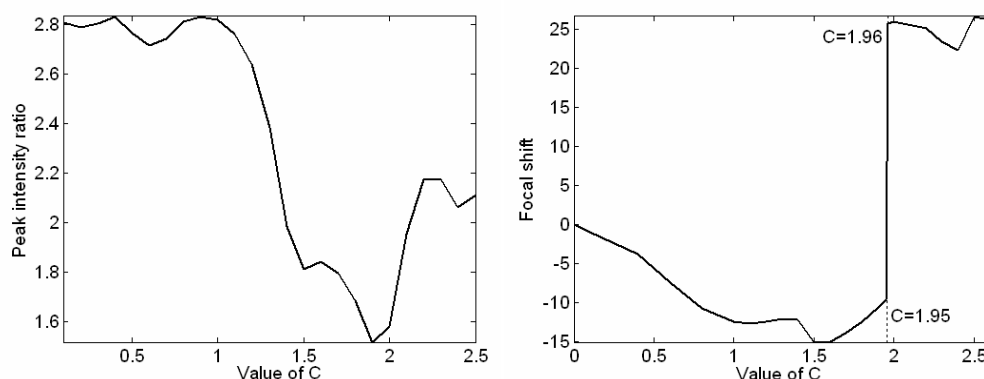
Figure 1: Peak intensity ratio of radially polarized component to axial polarized component in focal region with increasing numerical aperture *NA*.

continue to shift along optical axis, and simultaneously, several small intensity peaks come into being in the far side of the maximum peak from optical aperture, and become stronger and stronger. With increasing frequency parameter C, these several intensity peaks begin overlapping in axial direction, and form one long focal intensity line with intensity swipe along optical axis in the far side of the maximum intensity peak from optical aperture. In addition, the intensity value of intensity line decreases with increasing axial coordinate in wrap line. Increase frequency parameter C continuously, the value of the intensity line become stronger, and its shape also changes very considerably, evolves to triangle shape with smooth intensity fluctuation. In the same changing process, the maximum intensity peak also become asymmetrical in axial direction, its slope side near optical aperture shrinks with increasing frequency parameter C. When frequency parameter C increases to $C = 2.0$, novel focal pattern comes into being, the former maximum intensity peak evolves very considerably, one intensity peak splits into two intensity peaks, and the new intensity peak near optical aperture broadens in transverse direction, while the other new intensity peak is relative narrow transversely, and these two intensity peaks also overlap closely. Simultaneously, the intensity line also changes sharply, its value of sides in axial direction shrink, so its shape becomes sharper triangle, in addition, its intensity increases to exceed that of other intensity peaks, which show that focal switch occurs.

The axial intensity distribution can be plotted to show the changing process more clearly, Figure 2 illustrates several axial intensity distributions lines, in which focal shift and focal switch occur simultaneously. Frequency parameter C can affect the focal pattern very considerably, and some novel focal intensity distributions may occur, so, by altering frequency parameter C, desirable focal pattern may be obtained. In optical trapping system, it is usually deemed that the forces exerted on the particles in light field include two kinds of forces, one is the gradient force, which is proportional to the intensity gradient; the other is the scattering force, which is proportional to
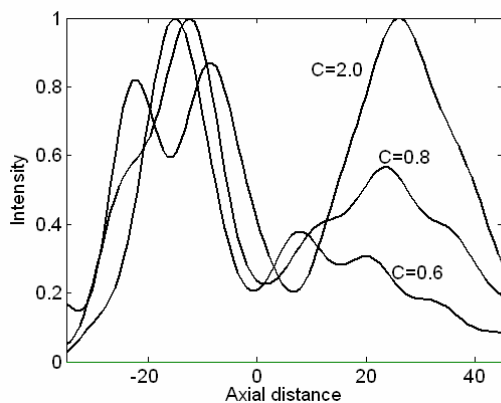
Figure 2: Axial intensity distributions for $NA = 0.9$ with different C.

the optical intensity. Therefore, the tunable focal shift predicts that the position of optical trap may be controllable. Relative intensity value of the raidally polarized component and longitudinal polarized component can affect the total intensity distribution considerably.

Therefore, peak intensity ratio of radially polarized component to axial polarized component in focal region with increasing value of frequency parameter C for $NA = 0.9$ is calculated and shown in Figure 3(a). It can be seen that the longitudinal polarized component is always stronger than radially polarized component, while the peak intensity ratio fluctuates for small frequency parameter C. Then when frequency parameter C increases to about 1, the peak intensity ratio decreases sharply, and increases back slightly when frequency parameter C is about 1.5, then decreases continuously. With frequency parameter C approaches to about 1.85, the peak intensity ratio decreases to the lowest value, comes back to increases quickly. With increasing frequency parameter C, the peak intensity ratio also fluctuates. The frequency parameter C is very important parameter that can affect the peak intensity ratio in focal region.

With increasing frequency parameter C, focal pattern and the peak intensity ratio both evolve considerably. Focal shift also occurs with changing focal pattern. Dependence of Focal shift on increasing value of C for $NA = 0.9$ is calculated and illustrated in Figure 3(b). Focal shift means the motivation of the focal peak whose intensity value is the strongest. It can be seen that the focal shift decreases smoothly with increasing frequency parameter C firstly, and reaches its minimum value when frequency parameter C is about 1.5. Then focal shift increases slowly. It should be noted that the focal shift decreases means that focal peak shifts towards to optical aperture of the focusing system. However, when frequency parameter C increases to 1.95, focal switch happens, so the focal shift becomes positive and fluctuates with increasing frequency parameter C.

Figure 3: (a) Peak intensity ratio of radially polarized component to axial polarized component in focal region with increasing value of C; (b) Dependence of focal shift on increasing value of C for $NA = 0.9$.

4. CONCLUSIONS

The focusing of radially polarized beam with radial cosine wavefront phase distribution is investigated. When the radially polarized beam with radial cosine wavefront phase is focused, focal pattern differs with different frequency parameter in cosine function. For high numerical aperture, focal shifts occur, and focal pattern evolves considerably, focus splits from only one peak into two or multiple peaks. Focal shift value also fluctuates for low frequency parameter, drops sharply, and then comes back slightly. Simultaneously, peak intensity ratio of radially polarized component to longitudinal polarized component decreases slowly, then increases very quickly.

REFERENCES

1. Phual, P. B. and W. J. Lai, "Simple coherent polarization manipulation scheme for generating high power radially polarized beam," *Opt. Express*, Vol. 15, 14251–14256, 2007.

2. Hayazawa, N., Y. Saito, and S. Kawata, "Detection and characterization of longitudinal field for tipenhanced Raman spectroscopy," *Appl. Phys. Lett.*, Vol. 85, 6239–6241, 2004.
3. Dorn, R., S. Quabis, and G. Leuchs, "Sharper focus for a radially polarized light beam," *Phys. Review Lett.*, Vol. 91, 233901, 2003.
4. Kozawa, Y. and S. Sato, "Sharper focal spot formed by higher-order radially polarized laser beams," *J. Opt. Soc. Am. A*, Vol. 24, 1793–1798, 2007.
5. Kozawa, Y. and S. Sato, "Focusing property of a double-ring-shaped radially polarized beam," *Opt. Lett.*, Vol. 31, 820–822, 2006.

Investigation of Slow Wave Structure with Metal PBG Structures

Xi Gao, Ziqiang Yang, Limei Qi, Zongjun Shi, Feng Lan, and Zheng Liang

Institute of High energy Electronics, University of Electronic Science and Technology of China
No. 4, Section 2, North Jianshe Road, Chengdu 610054, China

Abstract— The dispersion curves of TM modes of two-dimensional (2D) photonic band gap (PBG) structures formed by triangular arrays of metal posts are calculated using Finite-Difference Time-Domain (FDTD) method, and the global frequency band gap of TM modes of the PBG structures with different values of the ration of the post radius (r) to the post spacing (a) are obtained from the calculated dispersion curves. According to the global frequency band gap, a PBG cavity supporting TM_{01}-like mode is designed. Furthermore a Ka band slow wave system with PBG structure is constructed and the electromagnetic characteristic and impedance of which are analyzed.

1. INTRODUCTION

Vacuum electron devices are important sources of high power microwave for use in radar, communication etc. It is attractive to extend its operation frequency to millimeter wave range, which would open up many new applications. However, when the frequency increases to millimeter-wave range, the output power must be confined because of the too small dimension. Though overmoded structure can alleviate the problem, mode competition is another issue to be solved.

Recently, many theoretic and experimental investigations of photonic band gap (PBG) structures have demonstrated that they can effectively depress the unwanted modes in vacuum electron devices such as accelerator [1], gyrotron [2] and Cherenkov oscillator [3].

In this paper, we firstly analyze the dispersion curve and global frequency band gap of TM mode in metal PBG with triangular lattice, and then investigate the electromagnetic characteristic and impedance in Ka band slow wave system (SWS) consisting of PBG structure.

2. THE GLOBAL FREQUENCY BAND GAP OF TM MODE

2.1. The Basic Theory

Figure 1 shows the two-dimensional metal PBG structure with triangular lattice, in which the radius of rods is r and lattice constant is a.
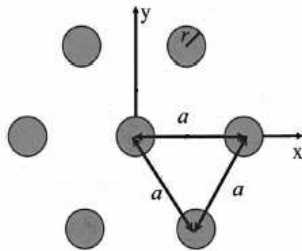
Figure 1: Scheme of metal PBG structure with triangular lattice.
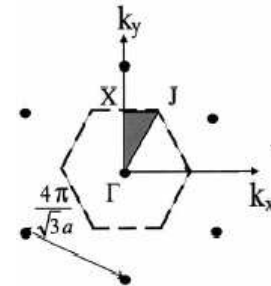
Figure 2: Reciprocal lattices and Brillouin zones for triangular lattice.

We only consider the TM mode of PBG structure consisting of perfect metal rods, the discrete equation based on the Maxwell equations can be expressed as following:

$$\mu \frac{H_y^{n+\frac{1}{2}}(i,j) - H_y^{n-\frac{1}{2}}(i,j)}{\Delta t} = \frac{E_z^n(i+1,j) - E_z^n(i,j)}{\Delta x} - jk_x \frac{E_z^n(i+1,j) + E_z^n(i,j)}{2} \tag{1}$$

$$\mu \frac{H_x^{n+\frac{1}{2}}(i,j) - H_x^{n-\frac{1}{2}}(i,j)}{\Delta t} = -\frac{E_z^n(i,j+1) - E_z^n(i+1,j)}{\Delta y} + jk_y \frac{E_z^n(i,j+1) + E_z^n(i+1,j)}{2} \tag{2}$$

$$\varepsilon \frac{E_z^{n+1}(i,j) - E_z^n(i,j)}{\Delta t} = \frac{H_y^{n+\frac{1}{2}}(i,j) - H_y^{n+\frac{1}{2}}(i-1,j)}{\Delta x} - \frac{H_x^{n+\frac{1}{2}}(i-1,j) - H_x^{n+\frac{1}{2}}(i,j-1)}{\Delta y}$$

$$-jk_x \frac{H_y^{n+\frac{1}{2}}(i,j) + H_y^{n+\frac{1}{2}}(i-1,j)}{2} + jk_y \frac{H_x^{n+\frac{1}{2}}(i-1,j) + H_x^{n+\frac{1}{2}}(i,j-1)}{2} \quad (3)$$

The periodic boundary condition can be written:

$$E_z(1,j) = E_z(N,j)e^{(i(a/2)k_y + i(\sqrt{3}a/2)k_x)}$$
$$E_z(j,1) = E_z(j,N)e^{ik_x a} \quad (4)$$

The dispersive relation can be obtained by solving the Equations (1)–(3) on the periodic boundary condition (4). In Equation (4), the N denotes the number of mesh.

2.2. Simulation and Result

Figure 4 shows the dispersion characteristics for the TM modes as the wave vector $k_\perp$ varies from the center of the Brillouin zone (Γ point in Fig. 2), to the nearest edge of the Brillouin zone (X point in Fig. 2), and to the far edge of the Brillouin zone (J point in Fig. 2). For $r/a = 0.2$, the first and the second mode are intersecting as shown in Fig. 4, which means no band gap appears between them. However, there is a cutoff frequency that is zeroth-order band gap.

To determine the global band gaps of TM modes, we calculate the dispersion curves of the PBG structures with different rations r/a. Fig. 4 shows the TM global frequency band gaps as functions of r/a, which is in good agreement with the global frequency band gaps obtained using coordinate-space, finite-difference code [4]. In fact there are any other band gaps, but here we only take into account the firt two band gaps. This figure shows that the zeroth-order band gap begins from the zero frequency and another band gap appeares when the ration $r/a > 0.2$.
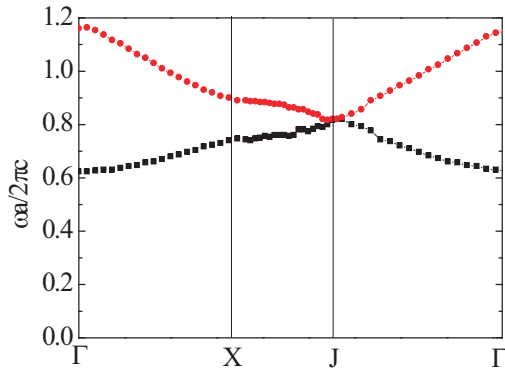
Figure 3: The dispersion curve of two lowest TM modes.
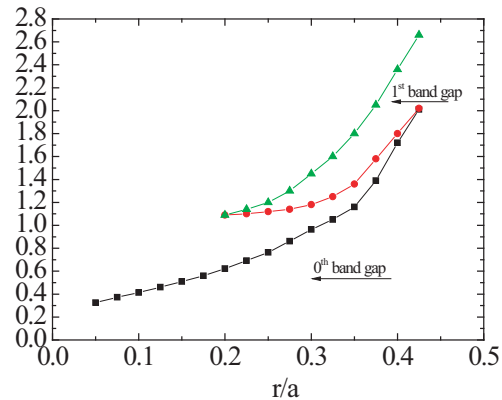
Figure 4: Plots of global frequency band gap for TM mode.

3. THE CHARACTERISTIC OF KA BAND SLOW WAVE SYSTEM WITH PBG STRUCTURES

According to Fig. 4, with the help of High Frequency Simulator (HFSS), a PBG cavity having a defect formed by removing seven rods from the center of the lattice is designed. The parameters of lattice constant and the radius of rods are 3.8 mm and 0.5 mm respectively. Among the TM_{0n}-like modes, only TM_{01}-like mode can be supported by the cavity [5]. Using the PBG structure, we have constructed a SWS whose physical mode is shown in Fig. 5. The SWS parameters are: the thickness of metal plate $d = 2$ mm, the length of period $z_0 = 3$ mm and the radius of center opening of the metal plate $r_1 = 5.8$ mm. The SWS has mode selectivity because of the exiting of PBG structure. It is hopeful to solve the mode competition in millimeter band Cherenkov device.

To learn about the electric field characteristic of the TM_{01}-like mode in the SWS, we simulate the electric field of the axial modes. Fig. 6 shows the electric field patterns of the π-mode of

the TM_{01}-like mode in the SWS. The electric field mainly centers the surface of the SWS, which implies the electric field is mostly occupied by slow wave. At the same time, there are six peak values because of the hexagonal boundary of the defect. The poor azimuthal symmetry of the electric field will make the coupling impedance have a poor azimuthal symmetry. Fig. 7 shows the coupling impedance as functions of $r(x)$ and $r(y)$. The $r(x)$ and $r(y)$ respectively denote the location in x direction and y direction in defect. The coupling impedance have a good azimuthal symmetry in the center of defect. However, at the surface of the SWS, the coupling impedance in oy axis is much higher than that in ox axis, which means the coupling impedance has poor azimuthal symmetry. The poor impedance would affect the efficiency of bea-wave interaction. As a result, we should choose appropriate location of electronic beam to improve the efficiency of the device.
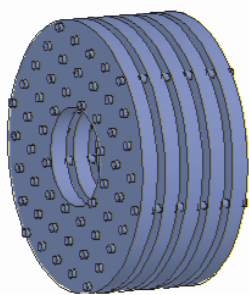
Figure 5: The physical mode of SWS.
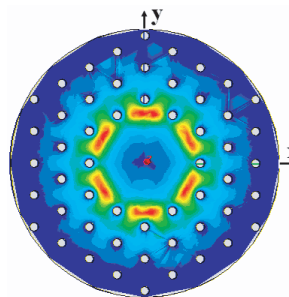
Figure 6: The electric field patterns in the π point of dispersion curve of TM_{01}-like mode in SWS.
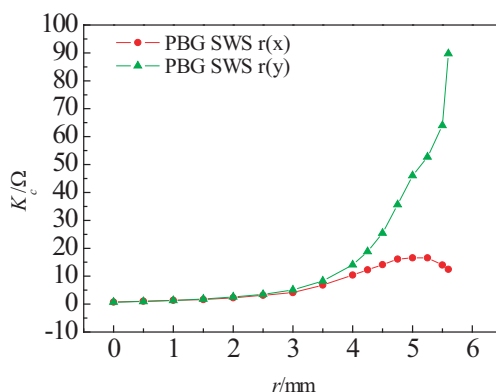
Figure 7: Coupling impedance in PBG SWS.

4. CONCLUSION

The global frequency band gap of TM modes of the PBG structures formed by triangular arrays of metal posts are calculated using FDTD method. According to the global band gap, we design a PBG cavity and SWS consisting of the PBG structure. Due to the existing of PBG structure, the SWS has mode selectivity, which is helpful to solve the mode competition. On the other hand, the characteristic of electric field and copuling impedance of the SWS has been investigated.

REFERENCES

1. Smirnova, E. I., A. S. Kesar, et al., *Phys. Rev. Lett.*, Vol. 95, 074801, 2005.
2. Sirigiri, J. R., K. E. Kreischer, et al., *Phys. Review Lett.*, Vol. 86, 5628, 2001.
3. Liu, X., H. Lei, et al., *Optics Communications*, Vol. 281, No. 1, 102–107, 2008.
4. Smirmova, E. I., C. Chen, M. A. Shapiro, J. R. Sirigiri, et al., *Journal of Applied Physics*, Vol. 91, 0021, 2002.
5. Gao, X., Z. Yang, et al., *Nuclear Instruments and Methods in Physics Research A*, Vol. 592, 292–296, 2008.

Transmission Characteristics of Electromagnetic Waves in Plasma Photonic Crystal by a Novel FDTD Method

Limei Qi, **Ziqiang Yang**, **Xi Gao**, **Feng Lan**, and **Zongjun Shi**

Institute of High Energy Electronic, University of Electronic Science and Technology of China
Chengdu, Sichuan 610054, China

Abstract— Plasma photonic crystal (PC) has been attracted much attention due to their new particular characteristics in which electromagnetic waves with frequency below plasma frequency can propagate through it. In this paper, we analyze the transmission characteristics of electromagnetic waves for two types of plasma PC-the one with plasma rods arranged in vacuum periodically and an antiparallel one for the second type. A novel Finite-difference time-domain (FDTD) formulation for plasma is derived, the high accuracy and efficiency is conformed by comparing the reflection and transmittance coefficients of electromagnetic waves through a collision plasma with Z transform method.

1. INTRODUCTION

Photonic crystal (PC) has been attracted much attention since the initial predictions of Yablonovitch [1] and John [2]. This active research area has been extended to plasma PC which is expected to obtain many new particular characteristics than conventional one [3–6]. It is well known that electromagnetic waves with frequency below plasma frequency cannot propagate through a bulk plasma, while vacuum components are introduced periodically, it is possible for electromagnetic waves to be guided below the plasma frequency. Generally, there are two types of 2D plasma PC [7].The first type (type-1) is a 2D PC in which plasma rods are arranged in vacuum periodically, while the second one (type-2) is an antiparallel structure composed of air holes in a bulk plasma. In this paper, we investigate the dispersion characteristics of TE mode for type-1 and type-2 plasma, the analysis is based on a novel Finite-difference time-domain (FDTD) formulation. Their transmission curves in the Γ-X direction are also calculated using CST Microwave Stdio, a 3D EM simulation software based on Finite Integration, which is in agreement with the dispersion curves calculated by the novel FDTD method.

2. THEORETICAL MODEL AND NUMERICAL METHOD

Figure 1(a) and (b) show the schematic structures of two types of 2D plasma PC with square lattice. We assume the radius of the circular rods and lattice constant are a and R respectively, the relative dielectric function for circular rods and background are ε_a and ε_b, respectively. In this paper, we utilize the frequency-dependent dielectric function for the unmagnetized collision plasma that meets the Drude formula [8]:

$$\varepsilon_r(\omega) = 1 + \frac{\omega_p^2}{\omega \left(j v_c - \omega \right)} \tag{1}$$

where ω is the electromagnetic wave frequency, $\omega_p = (e^2 n_e / \varepsilon_0 m)^{1/2}$ is the electron plasma frequency with an electron density n_e, and v_c is the collision frequency.

Maxwell equations that describe wave propagation in plasma are:

$$\frac{\partial H}{\partial t} = -\frac{1}{\mu_0} \nabla \times E \tag{2}$$

$$\frac{\partial D}{\partial t} = \nabla \times H \tag{3}$$

$$D = \varepsilon_0 \varepsilon_r E = \varepsilon_0 E + P \tag{4}$$

where $P = \varepsilon_0 \frac{\omega_p^2}{\omega(j v_c - \omega)} E$

We substitute Eq. (4) to Eq. (3) and obtain:

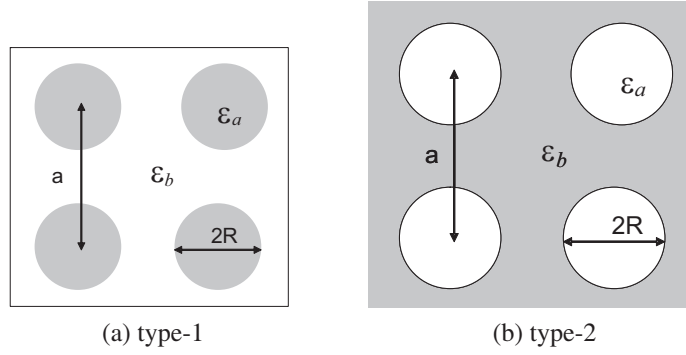$$\frac{\partial E}{\partial t} = \frac{1}{\varepsilon_0} \left[\nabla \times H - P_t \right] \tag{5}$$

Figure 1: Schematic structures of 2-D square lattice plasma PC (a) type-1 with circular plasma rods immersed in dielectric background and (b) type-2 with circular dielectric rods in bulk plasma. The gray area represents plasma.

where

$$P_t = \frac{\partial P}{\partial t} = \varepsilon_0 \frac{\omega_p^2}{(v_c + j\omega)} E \tag{6}$$

Multiply Eq. (3) by $e^{v_c t}$ and do time derivative on the two side yields

$$\frac{\partial P_t}{\partial t} = -v_c P_t + \varepsilon_0 \omega_p^2 E \tag{7}$$

Then, the Maxwell equations for propagating in plasma are:

$$\begin{aligned}
\frac{\partial H}{\partial t} &= -\frac{1}{\mu_0} \nabla \times E \\
\frac{\partial E}{\partial t} &= \frac{1}{\varepsilon_0} \left[\nabla \times H - \frac{\partial P}{\partial t} \right] \\
\frac{\partial P_t}{\partial t} &= -v_c P_t + \varepsilon_0 \omega_p^2 E
\end{aligned} \tag{8}$$

In a two-dimensional case, the fields can be decoupled into two transversely polarized modes, namely, the TE mode and the TM mode. As the standard FDTD method, the E field is defined at integer time steps and H field at half integer time steps. Then, the following FDTD time stepping formula are the spatial and time discretization of Eq. (8) for the TE mode:

$$\begin{aligned}
H_z^{n+\frac{1}{2}}\left(i+\frac{1}{2}, j+\frac{1}{2}\right) &= H_z^{n-\frac{1}{2}}\left(i+\frac{1}{2}, j+\frac{1}{2}\right) + \frac{dt}{\mu_0 dy}\left[E_x^n\left(i+\frac{1}{2}, j+1\right) - E_x^n\left(i+\frac{1}{2}, j\right)\right] \\
&\quad - \frac{dt}{\mu_0 dx}\left[E_y^n(i+1, j+1) - E_y^n(i+1, j)\right] \\
E_x^{n+1}\left(i+\frac{1}{2}, j\right) &= E_x^n\left(i+\frac{1}{2}, j\right) + \frac{dt}{\varepsilon_0 dy}\left[H_z^{n+\frac{1}{2}}\left(i+\frac{1}{2}, j+\frac{1}{2}\right) - H_z^{n+\frac{1}{2}}\left(i+\frac{1}{2}, j-\frac{1}{2}\right)\right] \\
&\quad - \frac{dt}{\varepsilon_0}P_{tx}^{n+\frac{1}{2}}\left(i+\frac{1}{2}, j\right) \\
P_{tx}^{n+\frac{1}{2}}\left(i+\frac{1}{2}, j\right) &= \frac{1 - v_c t/2}{1 + v_c t/2}P_{tx}^{n-\frac{1}{2}}\left(i+\frac{1}{2}, j\right) + \frac{\varepsilon_0 \omega_p^2 t}{1 + v_c t/2}E_x^n\left(i+\frac{1}{2}, j\right) \\
E_y^{n+1}\left(i, j+\frac{1}{2}\right) &= E_y^n\left(i, j+\frac{1}{2}\right) - \frac{dt}{\varepsilon_0 dx}\left[H_z^{n+\frac{1}{2}}\left(i+\frac{1}{2}, j+\frac{1}{2}\right) - H_z^{n+\frac{1}{2}}\left(i-\frac{1}{2}, j+\frac{1}{2}\right)\right] \\
&\quad - \frac{dt}{\varepsilon_0}P_{ty}^{n+\frac{1}{2}}\left(i, j+\frac{1}{2}\right)
\end{aligned} \tag{9}$$

$$P_{ty}^{n+\frac{1}{2}}\left(i, j+\frac{1}{2}\right) = \frac{1 - v_c t/2}{1 + v_c t/2}P_{ty}^{n-\frac{1}{2}}\left(i, j+\frac{1}{2}\right) + \frac{\varepsilon_0 \omega_p^2 t}{1 + v_c t/2}E_y^n\left(i, j+\frac{1}{2}\right)$$

In order to establish the accuracy of the FDTD method for plasma, a comparison with the Z transform [9] for the reflection and transmittance coefficients will be made by considering a one-dimensional plasma slab. The wave is normally incident on the 1.5 cm thick plasma slab which has a plasma frequency of 28.7 GHz ($\omega_p/2\pi$) and a collision frequency v_c of 20 GHz, the one-dimensional problem space consists of 800 spatial cells each 75 μm thick, with the plasma slab occupying cells 300 through 500. The time step is 0.125 ps. Fig. 2 gives the refection and transmittance coefficients for the two methods, red dash line and black solid line are the results for the Z transform and the new FDTD method, respectively. It can be seen that the two simulation results coincide with each other. These figures exhibit that the new FDTD algorithm are very accurate. From Fig. 2, we can also see that there is a cutoff frequency below the plasma frequency 28.7 GHz where electromagnetic wave can't propagate through the bulk plasma.
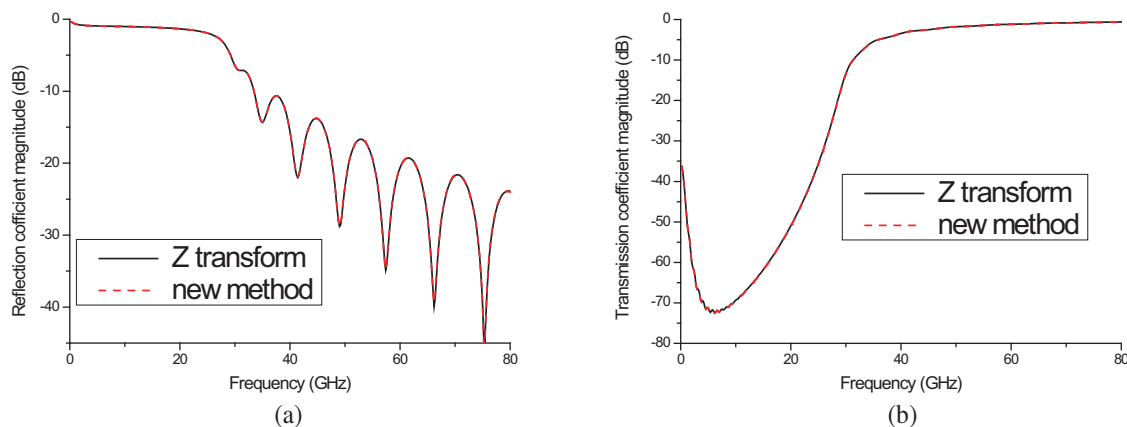
Figure 2: (a) Reflection and (b) transmission coefficients for one-dimensional plasma slab by two methods, the red dash line and black solid line denote the results by the new method derived above and the Z transform method, respectively.

3. DISPERSION CHARACTERISTICS OF TE MODE FOR TWO TYPES OF PLASMA PC

In this following, we apply the new FDTD algorithm derived above to calculate the dispersion curves in the Γ-X direction for the two types of plasma PC of Fig. 1, the transmittance curves for them are also presented which are simulated by Computer Simulation Technology (CST) [10], only TE mode is considered for simplicity. The main parameters of the simulation are summarized in Table 1. Note that ε_b and ε_a for type-1 and type-2 plasma PC are all assumed to 1.

Table 1: Main parameters for simulation.

Lattice	$a = 3\,\text{mm}$
Filling factor of circle rod	$f = 0.5$
Plasma frequency	$\omega_p = 2\pi \times 28.7\,\text{GHz}$
Collision frequency	$v_c = 20\,\text{GHz}$

Figure 3(a) shows the dispersion curves of TE mode in the Γ-X direction for type-1 plasma PC, we can see that there is a PBG between 17 and 23 GHz. There is also a band gap in the transmittance simulated by the CST in Fig. 3(b). If we define frequencies under -30 dB can't propagate through the plasma PC, then, the band gap varies from 17 to 23 GHz, which is in agreement with that in Fig. 3(a). Fig. 4 (a) gives the dispersion curves of TE mode in the Γ-X direction for type-2 plasma PC, there are two band gaps with one varies for 0 to 15 GHz and another varies from 24.1 to 30.2 GHz, they are all in accordance with what are simulated by the CST.
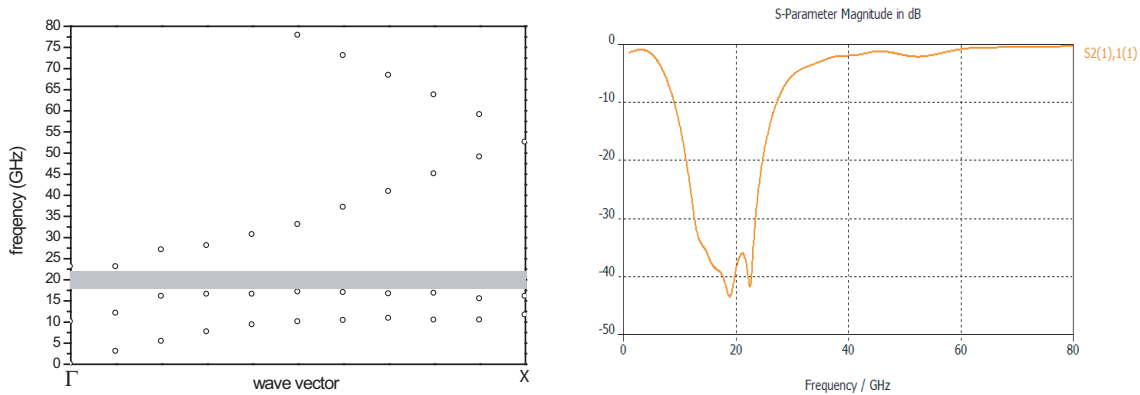
Figure 3: (a) Band diagram using the new FDTD method and (b) the transmittance simulated by CST of the TE mode for type-1 plasma PC in Γ-X direction.
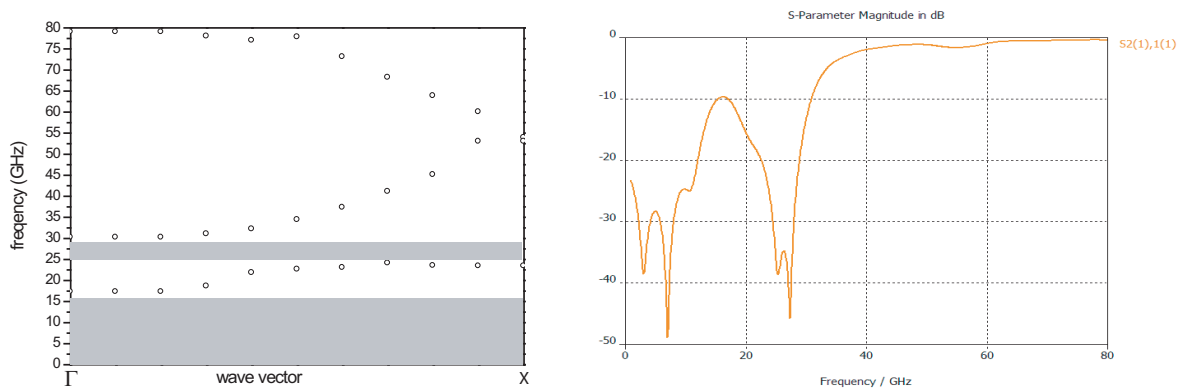

Figure 4: (a) Band diagram using the new FDTD method and (b) the transmittance simulated by CST of the TE mode for type-2 plasma PC in Γ-X direction.

4. CONCLUSION

In conclusion, a novel FDTD method for calculating unmagnetized collision plasma is derived, the accuracy of the method is examined by the Z transform method. The dispersion curves for two types of plasma PC in the Γ-X direction is obtained based on the novel FDTD method, which are in agreement with the transmission curves simulated by CST.

REFERENCES

1. Yablonovitch, E., "Inhibited spontaneous emission in solid-state physics and electronics," *Phys. Rev. Lett.*, Vol. 58, 2059–2062, 1987.
2. John, S., "Strong localization of photons in certain disordered dielectric superlattices," *Phys. Rev. Lett.*, Vol. 58, 2486–2489, 1987.
3. Liu, S., W. Hong, and N. Yuan, "Finite-difference time-domain analysis of unmagnetized plasma photonic crystals," *Int. J. Inf. Millimeter Waves*, Vol. 27, No. 3, 403–423, 2006.
4. Sakai, O., T. sakaguchi, Y. Ito, and K Tachibana, "Interaction and control of millimetre-waves with microplasma arrays," *Plasma Phys. Control. Fusion*, Vol. 47, B617–B627, 2005.
5. Sakai, O., T. Sakaguchi, and K. Tachibana, "Verification of a plasma photonic crystal for microwaves of millimeter wavelength range using two-dimensional array of columnar microplasmas," *Appl. Phys. Lett.*, Vol. 87, 241505–1–3, 2005.
6. Sakai, O., T. Sakaguchi, and K. Tachibana, "Plasma photonic crystals in two-dimensional arrays of microplasmas," *Contrib. Plasma Phys.*, Vol. 47, No. 1–2, 96–102, 2007.

7. Sakai, O. and K. Tachibana, "Properties of electromagnetic wave propagation emerging in 2-D periodic plasma structures," *IEEE Transactions on Plasma Science*, Vol. 35, No. 5, 1267–1273, 2007.

8. Luebbers, R. J., F. Humsberger, and K. S. Kunz, "A frequency-dependent finite-difference time-domain formulation for transient propagation in plasma," *IEEE Transactions on Plasma Science*, Vol. 35, No. 5, 29–34, 2007.

9. Sullivan, D. M., "Frequency-dependent FDTD methods using z transforms," *IEEE Trans. Antennas Propag.*, Vol. 40, 1223–1230, 1992.

10. CST Microwave Studio (Version 5.0), CST Computer Simulation Technology, 2006.

3D FDTD Method Analysis of Light-beam Scattering from a RAD-MSR Disk Models

Di Yang, **Akira Yokoyama**, **and Toshitaka Kojima**

Graduate School of Electronics, Kansai University

3-3-35 Yamate-cho, Suita-shi, Osaka 564-8680, Japan

Abstract— Recently, because of the increase of computer information handled by computers, higher density storage devices are expected. The magnetically super resolution (MSR) is one of the high density versions for improving the conventional magneto-optical (MO) disk. The rear aperture detection (RAD) is proposed to increase the capacity by ten times or more. The center aperture detection (CAD) is also proposed for advanced storage magneto-optical (ASMO) disks. Moreover, narrower focused beam can be realized by using blue laser light, so that the track pitch can be much more reduced. Therefore, narrower track pitches give rise to the increase of the crosstalk between adjacent tracks.

In the present paper, we try to apply the three-dimensional finite-difference time-domain (FDTD) method to the analysis of the light-beam scattering and the characteristic of detected signal from a rear aperture detection-magnetic super resolution (RAD-MSR) disk model and examine the influences of the groove depth on the crosstalk characteristics.

1. INTRODUCTION

The magneto-optical disks are used as rewritable type media of information. However, the optical diffraction limit prevents the possibility for increasing the storage capacity. In order to break such an optical diffraction limit, the magnetically-induced super resolution (MSR) method [1] has been proposed. For MSR, several different kinds of methods have also reported such as Front Aperture Detection (FAD), Rear Aperture Detection (RAD), and Center Aperture Detection (CAD) [2]. We have already analyzed the signal detection characteristics of MO disks with CAD method [3].

In the present paper, we try to analyze the scattering of light from a RAD-MSR disk model using blue laser and high NA object lens by FDTD method [4].

2. BASIC THEORY

2.1. FDTD Method

In a MO medium, the Maxwell's equations in the time domain are expressed as

$$\left. \begin{array}{l} \mu_0 \frac{\partial}{\partial t} \mathbf{H} = -\nabla \times \mathbf{E} \\ \hat{\varepsilon} \frac{\partial}{\partial t} \mathbf{E} = \hat{\sigma} \mathbf{E} + \nabla \times \mathbf{E} \end{array} \right\} \tag{1}$$

where the permittivity and the conductivity are assumed to take tensor forms, and the permeability to equal the one in free space. The finite difference formulation in time domain of Eq. (1) is the same as the one for the conventional FDTD method.

The permittivity of the medium is given by the tensor with opposite sign pure imaginary off-diagonal components as shown in Eq. (2):

$$\hat{\varepsilon} = \begin{bmatrix} \varepsilon & \varepsilon_{xy} & 0 \\ \varepsilon_{yx} & \varepsilon & 0 \\ 0 & 0 & \varepsilon \end{bmatrix} = \begin{bmatrix} \varepsilon & j\varepsilon_{xy} & 0 \\ -j\varepsilon_{xy} & \varepsilon & 0 \\ 0 & 0 & \varepsilon \end{bmatrix} \tag{2}$$

where the sign of the off-diagonal components is changed by reversing the direction of magnetization. Substituting Eq. (2) in Eq. (1), the FDTD update equation for MO medium can be obtained [5]. In order to calculate the update equation, we have to carry out calculations containing several complex quantities. Therefore, all electromagnetic field quantities should be defined as complex quantities.
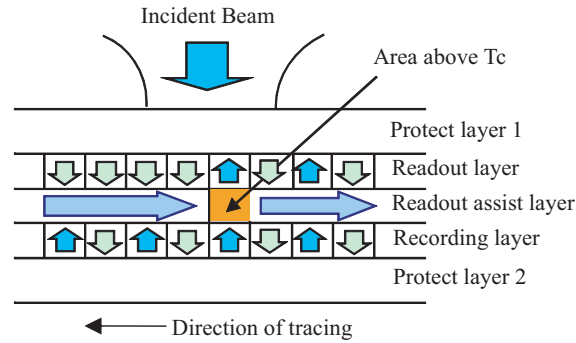
Figure 1: Cross section structure.

2.2. RAD-MSR Readout Principle

The RAD-MSR disk is composed of three exchange uniting layers, readout layer [GdFeCo] with week magnetic wall anti-magnetism, assistance readout layer [GdFe] with both relatively low Curie temperature and perfect in-plane magnetization characteristic in room temperature, recording layer [TbFeCo] with big magnetic wall anti-magnetism as shown in Fig. 1.

The each magnetic medium is heated by the illuminated light-beam, and its temperature distribution becomes Gaussian. Because the disk rotates at high speed, the rear side from the center of the beam spot becomes high temperature. Therefore, in the illuminated spot, there are two different kind of magnetized regions, i.e., the mask (reading impossible) region where the initialization magnetic field still exists due to low temperature and the aperture (reading possible) region where initialization magnetic field vanishes due to high temperature. As the result, it is possible to readout electively the readout the small magnetic district below optical resolution.

The readout layer is magnetized in one direction by the initialization magnetic field in low temperature area, and the readout assistance layer is heated by light-beam until it becomes Curie temperature. As a result, the readout assistance layer loses its magnetism, and because the magnetic coercive force of readout layer is decreased, the magnetic field of the recording layer is transcribed on readout layer. That is, it is possible to detect the record mark.

3. MODEL FOR ANALYSIS

In order to analyze the models, let us consider the three dimensional RAD-MSR disk model which has five layered structure with Land/Groove as shown in Fig. 2. The disk model is assumed to be moved in the x direction. In order to make recorded marks, the LD-pulse luminescence magnetic modulation method is assumed to be used. In this analysis, we consider the case where the recoded and non-recorded marks are alternately allocated. Therefore, the magnetized area has the shape as shown in Fig. 3, when it is seen from the surface of the disk. The upward magnetization corresponds to the recorded state and the downward one does to the non-recorded state. In this figure, the bit length is assumed to be 240 nm and the bit radius to be 120 nm.
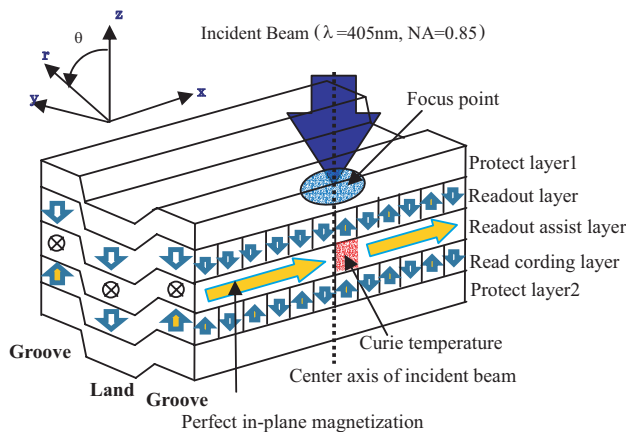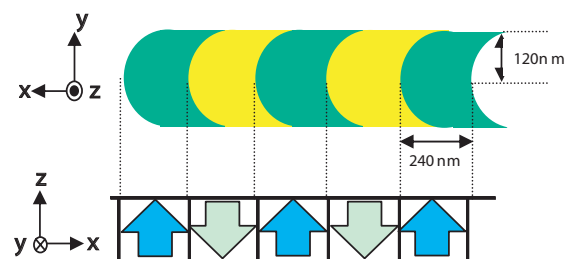

Figure 2: Three-Dimensional RAS-MSR Disk Model.

Figure 3: Bit mark shape.

The thicknesses of protective layer 1, readout layer, readout assist layer, recording layer, and protect layer 2 are assumed to be 50 nm, 20 nm, 30 nm, 40 nm, and 40 nm, respectively. Moreover, the depth of substrate is assumed to be 40 nm, the width of land to be 265 nm, the width of groove to be 265 nm, the tilt width between land and groove to be 40 nm and the adjacent mark radii smaller than about 240 nm. The medium constant of each level is shown in Table 1. The values of the non-diagonal permittivity can be estimated by the fact that in general the polarized angle of the detected light from MO medium is about 0.3 degree. We cannot obtain the exact values at the present time, however, the values used in the present analysis are chosen so that the polarized angles become about 0.3 degree. In Table 1, ε_0 is the permittivity of free space.

Table 1: Medium constant of each level.

		Permittivity [F/m]	
		ε	ε_{xy}
PC substrate		$2.5\varepsilon_0$	0.0
Protect layer 1		$4.28\varepsilon_0$	0.0
Readout layer	In-plane	$2.0\varepsilon_0$	$0.1\varepsilon_0$
	Non-rec.	$2.0\varepsilon_0$	$0.1\varepsilon_0$
	Rec.	$2.0\varepsilon_0$	$-0.1\varepsilon_0$
Readout assist layer	In-plane	$2.5\varepsilon_0$	$-0.1\varepsilon_0$
	Non-mag.	$2.5\varepsilon_0$	0.0
Recording layer	Non-rec.	$2.0\varepsilon_0$	$0.1\varepsilon_0$
	Rec.	$2.0\varepsilon_0$	$-0.1\varepsilon_0$
Protect layer 2		$4.28\varepsilon_0$	0.0

In the present FDTD analysis, we use cubic cells with 3 nm edges, and the size of the computation region is taken as 331 cells in both x and y directions and 201 cells in z direction. The incident light is assumed to be a Gaussian beam with the beam radius or spot size 150 nm and with the x-directed electric field, where 405 nm is the wave length of the incident light in free space.

The source distribution for exciting Gaussian electromagnetic fields with given parameters is assumed be located at the position from the surface of readout layer by the distance 112 cells [9].

It is well known that the crosstalk is greatly decreased when the depth of the track is about $\lambda/6n$ derived from scalar theory. However, the narrower track pitch such as blue laser disk structure can produce much more cross talk. Therefore, in the present paper, we try to analyze the dependence of the crosstalk characteristics on the groove depth h around $\lambda/6n$. Fig. 4 shows four different cases with or without adjacent marks for recorded or non-recorded case for the present analysis.
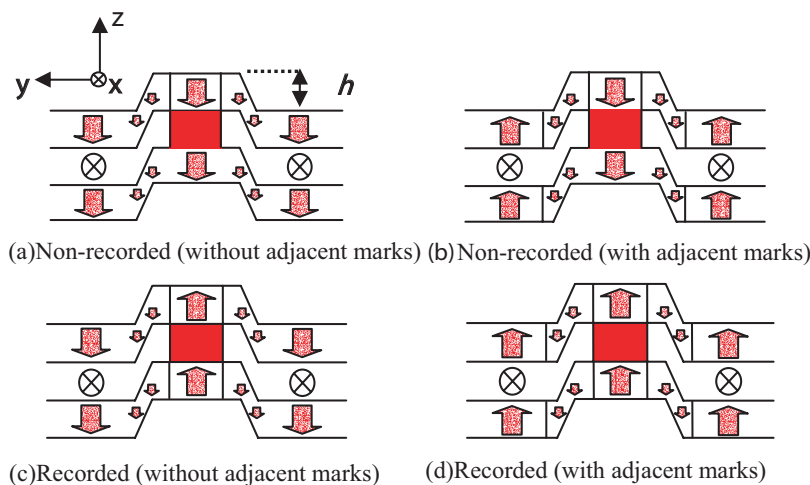

(a)Non-recorded (without adjacent marks) (b)Non-recorded (with adjacent marks)

(c)Recorded (without adjacent marks)   (d)Recorded (with adjacent marks)

Figure 4: States of recording

4. RESULTS AND DISCUSSIONS

Figure 5(a) and Fig. 5(b) shows the main-polarized (x-directed) and cross-polarized (y-directed) components of the far-zone scattered electric fields in x-z plane for the cases where the groove depth are 10 nm, 30 nm, 50 nm and 70 nm, respectively. On the other hand, Fig. 6(a) and Fig. 6(b) correspond to the main-polarized and cross polarized components in y-z plane. In MO disks, the direction of vertical magnetization of bit region dominates the direction of cross-polarized component of diffracted electric field. In those figures, the scattering patterns are normalized by the maximum field amplitude scattered from a perfectly conducting plane. The diffraction pattern of the main-polarized component depends on the groove depth of course, however, it dose not depend on the recorded or non-recorded state as shown in Fig. 5(a) and Fig. 6(a). On the other hand, Fig. 5(b) and Fig. 6(b) indicates that the cross-polarized component depends on the states where the recoded signal exists or not. We can observe the difference of the strength of the cross-

(a) main-polarized component   (b)cross-polarized component
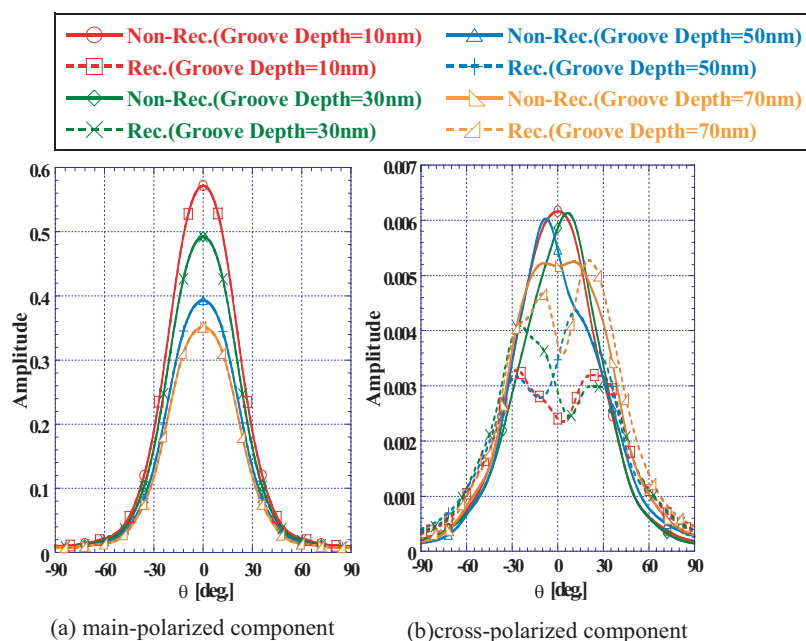
Figure 5: Far field in x-z plane.

(a) main-polarized component   (b)cross-polarized component
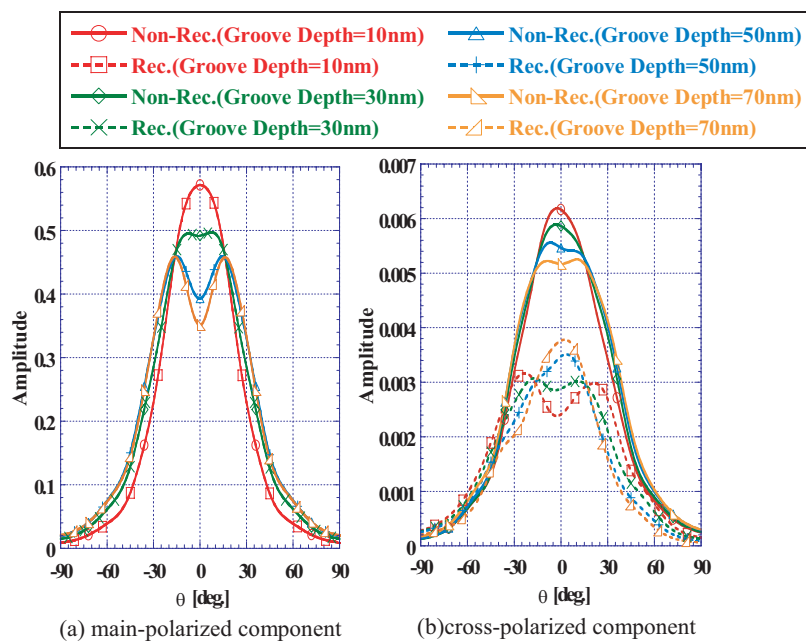
Figure 6: Far field in y-z plane.

polarized field between recorded and non-recoded states. In MO disks, the phase angle between main-polarized and cross-polarized components is also an important factor for the detection of signals [10]. The phase angles between main-polarized and cross-polarized components collected by the object lens with a given NA are shown in Fig. 7. From this figure, we can observe that the phase differences in the direction of optical axis for the non- recorded states take almost constant value 180 degrees for the change of the groove depth.

On the other hand, the phase differences for the recorded states are varied by the groove depth change, i.e., they become zero degree for the cases where the depth becomes 60 nm or more, however, for other cases, they deviate from 0 degree. That is, we have better readout characteristics for the cases of 60 nm or more groove depth more than other cases. The optimum value of groove depth $\lambda/6n = 42, 72$ nm is predicted by the scalar theory. However, the optimum value based on the present analysis is greater than the scalar one. For the case of 50 nm groove depth for which the worst case is indicated in Fig. 7, we show how the phase characteristic depends on the recoding state of adjacent marks in Fig. 8. From this figure, the influence of the adjacent marks on the phase characteristic is not observed for this analysis.
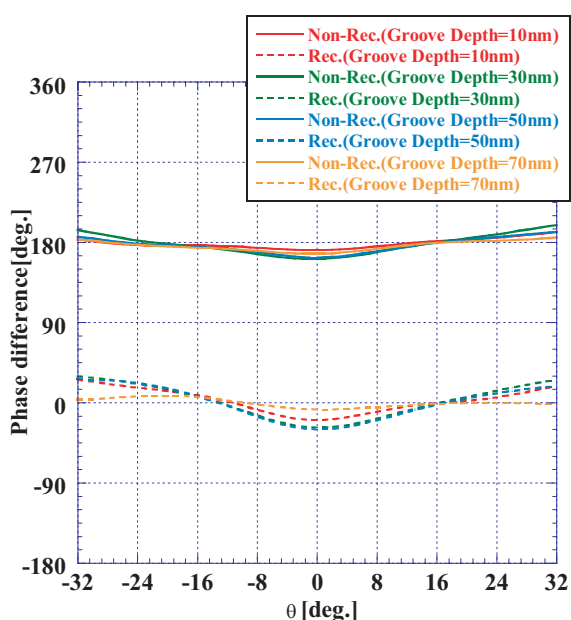
Figure 7: Three-dimensional RAS-MSR disk model.
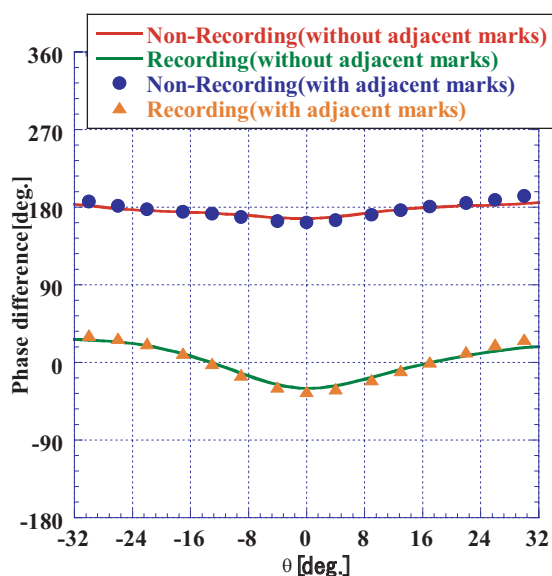
Figure 8: Bit mark shape.

5. CONCLUSION

In the present paper, we have applied the three-dimensional FDTD method to the analysis of the light-beam scattering and the characteristic of detected signal from a RAD-MSR disk model and examined the influences of the groove depth on the crosstalk characteristics. The results obtained here indicate that the diffraction pattern of the main-polarized component depends on the groove depth of course, however, it dose not depend on the recorded or unrecorded state. On the other hand, the cross-polarized component depends on the states where the recoded signal exists or not. It has been also shown that the phase difference in direction of optical axis for the non-recorded states does not depend on the change of groove depth. On the other hand, the phase differences for the recorded states are varied by the groove-depth change, i.e., they become zero degree for the cases where the depth becomes 60 nm or more. However, for other cases, they deviate from zero degree. That is, we have better readout characteristics for the cases of 60 nm or more groove depth than other cases. It ha been shown that the optimum value of groove depth in this analysis is grater than the well-known value $\lambda/6n = 42, 72$ nm obtained from scalar theory.

REFERENCES

1. Shinoda, M., A. Nakaoki, M. Kanno, and M. Kaneko, "High-density magneto-optical disk using land/groove recording and magnetically induced super-resolution by rear aperture detection," *The Magnetics Society of Japan*, Vol. 21, No.4–2, 329–332, Oct. 1997.

2. Kaneko, M., "Prospects of magneto-optical disks using magnetically induces super-resolution," *The Magnetics Society of Japan*, Vol. 23, No. 10, 1999–2004, July 1999.

3. Miyake, M. and T. Kojima, "Three dimensional numerical analysis of light-beam scattering from magneto-static CAD-MSR disk," *IEICE Technical Report*, E-2, C-7-10, 48, 2004-3.

4. Uno, T., *Finite Difference Time Domain Method for Electromagnetic Field and Antenna Analyses*, Corona Publ. Co. Ltd., 1998.

5. Kojima, T., T. Sasai, I. Kobayashi, and Y. He, "(FD)^{2}TD analysis of light-beam scattering from MO disks with land/groove recording structures," *IEICE Trans. Electron*, Vol. 85-C, No. 10, 1776–1783, Oct. 2002.

6. Takahashi, S., T. Hamaguchi, T. Hisamitsu, M. Takuma, and A. Yamada, "A mobile storage device with the magneto-optical disk of a 50 mm diameter and 730 MB capacity," *IEEE Trans. Consum. Electron*, Vol. 48, No. 3, 589–595, Aug. 2002

7. Zhang, Y., H. Xia, X. Wang, D. Shen, F. Gan, and Z. Li, "Transition from in-plane to perpendicular magnetization in GdFeCo/AlN/TbFeCo magnetostatic coupling films," *J. Mater. Sci.*, Vol. 39, No. 6, 2233–2236, Mar. 2004

8. Imai, S., H. Awano, and N. Ota, "High recording density magneto-optical recording methods using magnetic domain expansion readout techniques," *IEICE Trans. Electron, Electron*, Vol. J84-C, No. 3, 169–175, Mar. 2001.

9. He, Y., T. Kojima, T. Uno, and S. Adachi, "FDTD analysis of three-dimensional light-beam scattering from the magneto-optical disk structure," *IEICE Trans. Electron*, Vol. 81-C, No. 12, 1881–1888, Dec. 1998

10. Kobayashi, I., T. Kojima, S.-I. Fukai, and Y. He, "Numerical analysis of light-beam diffraction from magneto-optical disk medium by FDTD method," *IEICE Trans. Electron*, Vol. 84-C, No. 9, 1189–1196, Sep. 2001.

Application of Laser Plasma Source with a Gas-puff Target in Calibration of Extreme Ultraviolet Detectors

J. Mikolajczyk and R. Rakowski

Institute of Optoelectronics, Military University of Technology
2 Kaliskiego Str., 00-908 Warsaw, Poland

Abstract— The paper presents a laser plasma source with a gas puff target as a metrology tool for EUV technology. The investigations of the source are described. The spectrum emitted from the source and the conversion efficiency (CE) was measured. The results give an opportunity to design a procedure for a calibration of detectors for extreme ultraviolet. The special laboratory setup was developed based on the procedure. The setup is characterized by very low outlay and good metrology features as well. Compared to currently used systems, this setup can be applied in small factories and laboratories producing for instance EUV detectors.

1. INTRODUCTION

Extreme Ultra Violet (EUV) is radiation laying in the wavelength range from 5 nm to 40 nm [1]. The range corresponds to the level of photon energy from 250 eV to 30 eV. Nowadys EUV radiation is applied to many technologies and science fields. The radiation spectral span is very useful for material technologies. For a short time, EUV radiation has been also used in micro- and nano-machining of organic polymers. This technology is based on the disruption of the polymer structure by photons. The use of EUV radiation is a new trend in a new generation projection lithography. The EUV lithography makes it possible a mass production of nanoelectronics (chips, memories). In the nearest future the sizes of electronics structures will be less than 32 nm. EUV lithography is characterized by higher efficiency in comparison with other modern technologies (for example electron, ion or x-ray lithography). In the paper, the results of the characterization of the EUV laser-plasma source with the gas puff target are presented. The source has been designed at the Institute of Optoelectronics [2].

2. LASER PLASMA SOURCE WITH GAS PUFF TARGET

The EUV radiation can be generated during some kinds of physics processes (e.g., recombination or deexcitation in highly charged ions interior as well as electrons bremsstrahlung.

Nowadays synchrotron is the most composite source with good radiation parameters. However, many applications would benefit from table-top sources having high power peak and repetition rate. Compact sources provide better accessibility for application researches as well as lower costs. Such sources include for example laser plasmas, in which radiation is generated in high temperature plasma containing highly excited ion stages. The debris-free compact sources can be applied to metrology and diagnostics of EUV technology elements.

In the described source the gas puff target is irradiated with radiation generated by Nd : YAG laser. The radiation parameters (irradiance of the order of $0.4 \cdot 10^{10}$ W/cm^2) and gas density are sufficient for hot plasma creation. The main elements of the source are a Nd : YAG laser and a vacuum chamber with equipment. In the chamber the electromagnetic valves setup with positioning system was mounted. The setup serves a production of a gas target made up of two areas of different gases. The gas target with two streams is created by outflow of working gas (for example xenon, krypton, argon) in the midst of buffering light gas (helium, hydrogen) in concentric manner. Details of the valves system is described elsewhere [3]. The main task of buffering gas relies on maintaining high density of the working gas. The double-stream approach provides high density of the gas target.

3. INVESTIGATION TOOLS

During investigations of the source different kinds of measurements and diagnostics tools were used. For the spectrum analysis, a transmission gratings spectrograph was applied. The transmission grating was mounted in the pinhole providing spectrum measurements as well as spatial analysis. The image of the source was observed by pinhole camera with Mo/Si multilayer mirror. The picture was recorded by special CCD cameras operating at the EUV spectral range. The received

spectrums also make it possible to determine energetic features of the source. However the energy efficiency was calculated basing on signals from the calibrated silicon photodiodes. The scheme of the investigation setup is shown in Fig. 1.
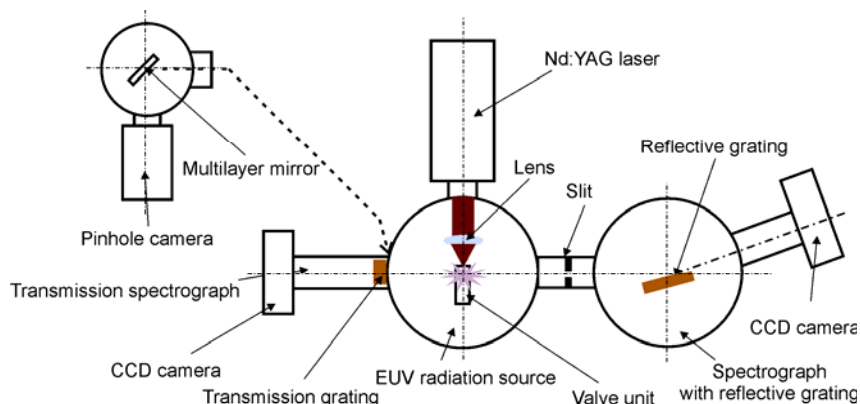

Figure 1: Experimental setup with investigation tools.

4. INVESTIGATION OF RADIATION SOURCE

During the first part of research the influence of the composition of the gas target as well as the time delay between the synchronization signal for gas nozzles opening and Nd : YAG laser pulse (Δt_{Xe}, He, H, Ar) on EUV radiation intensity were investigated. The nozzle time delay results directly in density profile of the working gas in the target. The preliminary results showed that for Xe working gas the time delay of $800\,\mu s$ is the most optimal for the maximum source intensity. The comparison of the registered EUV source intensity at wavelength of $13.5\,nm$ for different time delays and for selected buffering gases is presented in Fig. 2.

The results show that the lowest radiation intensity in the EUV range was measured in the Xe/Ar gas puff target case. Deep analysis of the time delay influence on EUV intensity for Xe/He and Xe/H targets show that the maximum source intensity is observed for time delays in the range from $300\,\mu s$ to $400\,\mu s$. The highest intensity at $13.5\,nm$ wavelength range was obtained for Xe/H target.

The determined optimal values of the time delays were selected for measurements of the EUV radiation energy at $13.5\,nm$ using AXUV 100 series calibrated photodiodes. In Fig. 3, the radiation energy versus time delay for Xe/He gas puff target is presented. The optimum value of the time delay $\Delta t_{He} = 350\,\mu s$ was found.

The investigations of influence of the laser focal spot position on the gas target were performed for established conditions of target creation: $t_{Xe} = 800\,\mu s$ and $t_{He} = 350\,\mu s$. The position of the focal spot was controlled in three directions: H — height, Δy — width, and Δx — depth. The
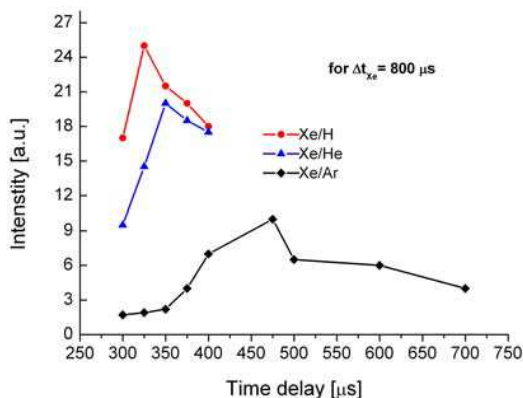
Figure 2: The relative intensity of the EUV radiation source vs. time delay of nozzle opening for some composition of gas target.
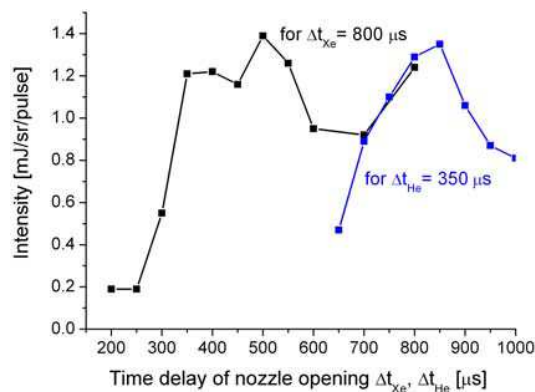
Figure 3: Pulse energy of the EUV at $13.5\,nm$ source vs. time for Xe/He gas puff target.

investigation results are presented in Fig. 4. The maximum energy pulses of EUV radiation were observed for $H = 1\,\mathrm{mm}$ (distance from the nozzles exit) and $\Delta x = 1\,\mathrm{mm}$ (defocusing).

The absolute measurements of the EUV source energy at 13.5 nm were made using the calibrated photodiodes. Additionally, calculations of the pulse energy for various laser focal positions, based on the spectral investigations, were also made. The obtained results are shown in Fig. 5. The maximum value of pulse energy at $13.5 \pm 0.5\,\mathrm{nm}$ was $0.79 \pm 0.15\,\mathrm{mJ/sr/pulse}$ corresponding to the source efficiency of $0.88\%/2\pi$ (BW = 7.4%). The optimal position of the laser focal spot in regard to the gas puff target corresponds to following values of optimization parameters: $H = 1\,\mathrm{mm}$, $\Delta x = 1\,\mathrm{mm}$ and $\Delta y = 600\,\mu\mathrm{m}$.
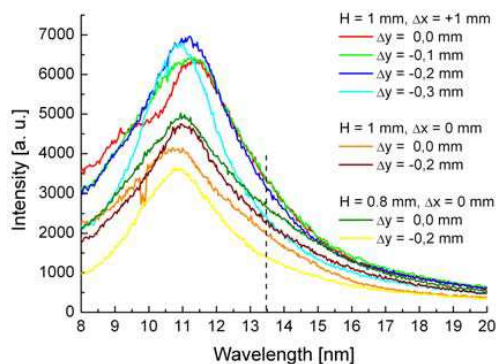
Figure 4: EUV source spectrum depending on position of the laser focal spot on gas target [4].
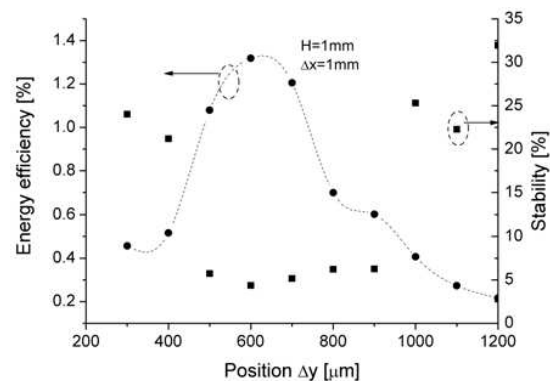
Figure 5: EUV source CE and stability vs. Δy position of laser focal spot on gas target.

The influence investigations of the gas pressure in the valves on EUV intensity were carried out for Xe/He gas puff target (for optimal parameters of the time delays and the position of the laser focal spot on the target as well). The measurements were made using calibrated photodiodes. In Fig. 6, the measurements results of the mean pulse energy for different values of the gases pressures are presented.

Analysis of the characteristics shows that there is neither significant nor straightforward dependence of pulse energy on helium pressure in the valve. The maximum pulse intensity value was $1.32 \pm 0.11\,\mathrm{mJ/sr}$ per pulse for pressures: $P_{Xe} = 1.2\,\mathrm{MPa}$ and $P_{He} = 0.3\,\mathrm{MPa}$ and is the maximum intensity attained during the source investigations. The present data corresponds to conversion efficiency of 1.91% (for BW = 7%) or 0.36% (for BW = 2%).

5. CALIBRATION PROCEDURE

The presented results show that the conditions of plasma generation in the source fundamentally determine the metrology parameters of the laboratory setup for detectors calibration. The operation conditions of the source must be a compromise between high efficiency and a good stability. For the selected conditions, the radiation energy of the source is of $1\,\mathrm{mJ/sr/pulse}$ and stability of 5%.
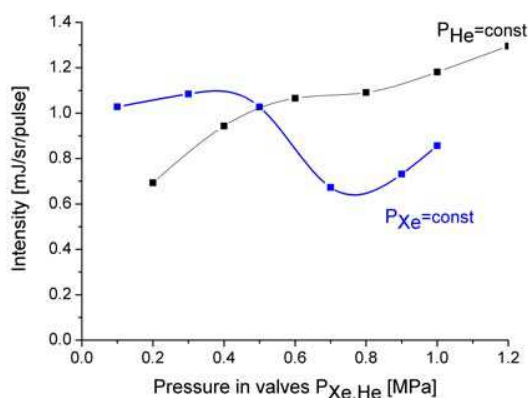

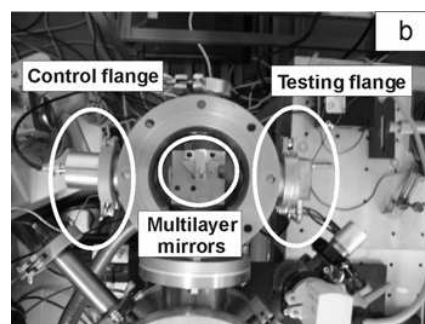Figure 6: EUV source pulse intensity at 13.5 nm vs. pressure of the gases in valves.

Figure 7: The view of the calibration setup.

The measured stability of the source radiation results in accuracy of the calibration procedure. For this reason, a special testing procedure was prepared. The procedure is based on responsivities comparison of the tested detector with the model one. The calibration setup uses a special optical element that acts as *beam splitter* consisted of two multilayer mirrors. The view of the setup is presented in Fig. 7. The diagnostic beam is separated into two chamber flanges. At the same time, the one part of radiation irradiates the tested detector and the second one is directed to the model calibrated detector. Based on the measured signals from the both detectors, the responsivity of the tested detector is calculated.

In the calibration method, the influence of the source stability on the calibration procedure is minimised. Metrology analysis of the testing procedure and used instruments makes it possible to determine the accuracy of the calibration process. The uncertainty of the responsivity measurements at $13.5 \, \text{nm} \pm 7.4\%$ was of 7.3%.

6. CONCLUSIONS

The paper presents results of the investigation of the laser plasma source with the gas puff target. The investigations give an opportunity to determine optimal parameters of the source operation. The results showed that the efficiency and stability depend on conditions of plasma generation. The conditions relate to changes of time delays between opening time delays of valves nozzles and Nd : YAG laser pulse, energy of the laser pulse, pressures of the gases in the valves, and the position of the Nd : YAG laser focal spot on the target. Optimum operation parameters of the EUV source were determined. Maximum value of the measured energy was $1.32 \pm 0.11 \, \text{mJ/sr/pulse}$. The value is equivalent to conversion efficiency of 1.91% (BW $= 7\%$) or 0.36% (BW $= 2\%$). The further work in the direction of commercialization of the calibration setup should put emphasis on increasing of the EUV source intensity by rise the energy of Nd : YAG laser pulses and their duration and frequency as well.

REFERENCES

1. Attwood, D., "Soft X-rays and extreme ultraviolet radiation: Principles and applications," Cambridge University Press, Cambridge, 2000.
2. Rakowski, R., A. Bartnik, H. Fiedorowicz, R. Jarocki, J. Kostecki, J. Krzywiński, J. Mikołajczyk, L. Ryć, M. Szczurek, and P. Wachulak, "Spectral and spatial measurements of a laser-produced plasma EUV source for 13.5 nm based on a double-stream Xe/He gas puff target," *Proc. SPIE*, Vol. 5958, 706–716, 2005.
3. Fiedorowicz, H., A. Bartnik, R. Jarocki, R. Rakowski, and M. Szczurek, "Enhanced X-ray emission in the 1-KeV range from a laser-irradiated gas puff target produced using the double-nozzle setup," *Appl. Phys. B*, Vol. 70, 305–308, 2000.
4. Fiedorowicz, H., A. Bartnik, R. Jarocki, J. Kostecki, J. Krzywiński, J. Mikołajczyk, R. Rakowski, A. Szczurek, and M. Szczurek, "Compact laser plasma EUV source based on a gas puff target for metrology applications," *J. Alloys Comp.*, Vol. 401, 99–103, 2005.

Electromagnetic Modes in Hybrid Periodic-non-periodic Dielectric Porous Silicon Multilayers

José Escorcia-García[1] and Miguel E. Mora-Ramos[2]

[1]Centro de Investigación en Ingeniería y Ciencias Aplicadas
Universidad Autónoma del Estado de Morelos
Ave. Universidad 1001, Cuernavaca 62209, México
[2]Facultad de Ciencias, Universidad Autónoma del Estado de Morelos
Ave. Universidad 1001, Cuernavaca 62209, México

Abstract— In this work, we study the main features of the spectra of electromagnetic modes propagating in porous Si layered systems. We consider the case of the combination of periodic (Bragg-like) and quasiregular layered components, taking into a quasiregular-periodic-quasiregular geometry. The non-periodic sequences used to simulate the quasiregular regions are of the Fibonacci type. Normal incidence transfer matrix formalism is used to calculate the electromagnetic modes as well as the electric field amplitudes corresponding to each of them. The existence of a selectively localized behavior of some optical modes in the structures is particularly discussed.

1. INTRODUCTION

The use of quasiregular dielectric heterostructures as a source for the design and fabrication of one-dimensional (1D) systems with original optical and mechanical properties has been a subject of study in recent years [1–7]. Within this context, the design of hybrid periodic-quasiperiodic systems is among the proposals for the obtention of 1D quasicrystals. For instance, the selective spatial localization of atom displacements has been studied in one-dimensional hybrid quasi-regular/periodic atomic chains [5, 6]. In the case of dielectric multilayers, the hybrid systems are said to show complementary optical responses [3]. On the other hand, by combining two Fibonacci quasi-periodic structures and a periodic structure to form a heterostructure, a broad omnidirectional reflection band is obtained [8].

The study of the properties of the electromagnetic field associated to transverse electrical modes propagating through hybrid periodic-quasiregular dielectric heterostructures is the subject of the present article. In this work we provide a theoretical analysis of the optical propagation in hybrid periodic/Fibonacci dielectric multilayers designed with the values of refractive indices typical of the porous silicon (PS). Periodic parts of the structures are represented by $\lambda/4$ Bragg mirrors. Fibonacci generations of A and B layers of the same widths of Bragg ones are the corresponding quasi-regular constituents in the systems. The geometrical configurations considered are of the types Bragg-Fibonacci-Bragg (BM-FN-BM), and Fibonacci-Bragg-Fibonacci(FN-BM-FN). In this sense, we show the properties of selective localization of the electric field intensity for certain specific light modes within the porous silicon dielectric multilayers.

2. MODEL SYSTEMS AND SIMULATION TOOL

Hybrid structures here studied are designed using Bragg reflectors fulfilling the $\lambda_0/4$ condition. In our particular case we have chosen $\lambda_0 = 800\,\text{nm}$, and the corresponding refractive indices are $n_A = 1.8$ and $n_B = 1.2$. Consequently, the layer widths are $d_A = \lambda_0/4n_A = 111.11\,\text{nm}$, and $d_B = \lambda_0/4n_B = 166.67\,\text{nm}$.

The theoretical simulation is made using the transfer matrix formalism. This tool is derived for one-dimensional problems that can be resolved via the solution of a master equation which ultimately reduces to a linear system of first order ordinary differential equations [9]. Here, the analysis is made in the case of the 1D Maxwell equation for the TE modes propagating in a dielectric structure. Information about the implementation of this approach to investigate light propagation in dielectric structures can be obtained from several different sources in the literature. To refer only to some of the more recently published ones we mention those of of Refs. [10, 11]. For the sake of simplicity, in our particular case normal incidence is assumed, although oblique one is straightforward.

3. RESULTS AND DISCUSSION

The intensity (squared amplitude of the field) of TE modes in hybrid BM-FN-BM porous silicon dielectric heterostructures is shown in Figure 1. The Bragg substructures are eighth-period mirrors while the central part is a fourth order Fibonacci sequence. Four different values of the wavelength are used to illustrate corresponding oscillation behaviors. It is seen that some modes exhibit what it might be called a selective confinement within the structure. This feature is present in several forms; but there are two main ones. One of them corresponds to the localization of the amplitude of the oscillation within the quasi-regular -central- substructure (Figure 1(c))). The value of the wavelength of this particular mode is $\lambda = 843.93$ nm. The second form shows the field intensity confined to one of the -outermost- periodic substructures, for $\lambda = 689.19$ nm (Figure 1(d))). These two kinds of oscillation patterns were also theoretically predicted for phonon modes associated with the vibration of hybrid Fibonacci-Periodic chains of atoms [5, 6]. However, in our case we are detecting them in dielectric systems for a *considerably smaller* number of active layers.

On the other hand, less spectacular confinement properties can be noticed. For instance, there is a suggested stationary pattern in Figure 1(a)) ($\lambda = 420.47$ nm). In addition, sharp peaks of the field intensity are located only centered at positions that correspond to the middle of the A-layers in the structure (Figure 1(b)), $\lambda = 400$ nm). In this case, it is clearly seen that there are two sharp double-peaks located within the Fibonacci part of the hybrid structure. The position of these double-peaks coincide with those of the two AA defect-like layers introduced by the presence of the quasi-regular structure.

It is worth mentioning at this point that the four wavelengths above considered belong to stationary electromagnetic modes in the structure. That is, they correspond to oscillations with
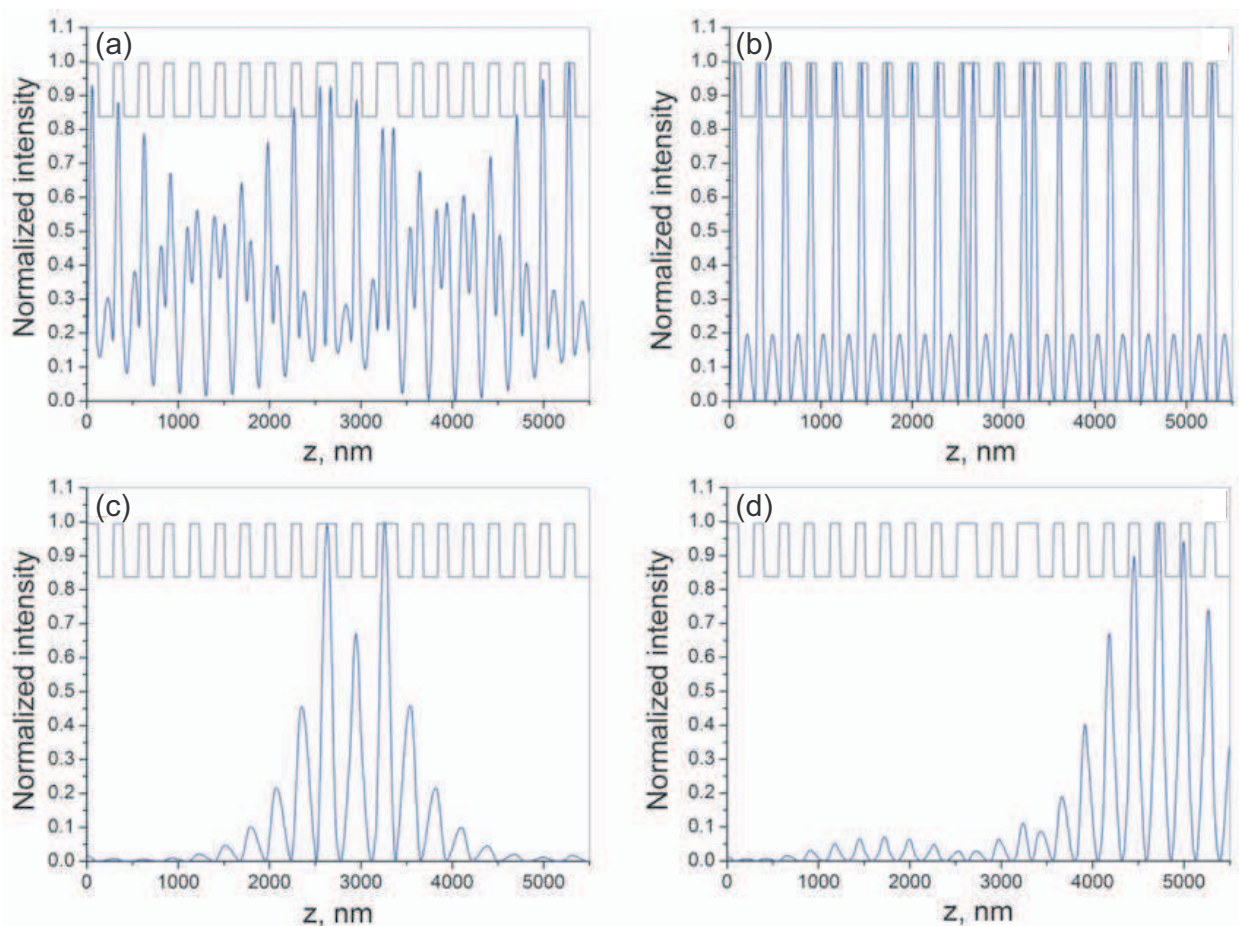

Figure 1: Electric field normalized intensities of TE modes in 8BM-4FN-8BM hybrid porous silicon dielectric heterostructure as functions of the position. The corresponding values of the wavelength are: (a) $\lambda = 420.47$ nm, (b) $\lambda = 400$ nm, (c) $\lambda = 843.932$ nm, and (d) $\lambda = 689.19$ nm. The layer profile, according to the values of the refractive indices is superimposed for illustration.

zero field intensity on both ends of the system. The mode with $\lambda = 400\,\text{nm}$ is, at the same time, stationary for each of the Bragg substructures.

Figure 2 shows the results for the normalized field intensities of TE modes that propagate through hybrid 4FN-8BM-4FN porous silicon heterostructures. This is the geometry complementary to the one previously investigated. In this case we again see the two main selective mode localizations above discussed. In Figure 2(a)) sharply defined intensity peaks centered at the A layers of the structure -with double-peaks located in the AA defect-like of Fibonacci substructures- are obtained for the mode of $\lambda = 400\,\text{nm}$, that is stationary for both the Bragg parts and the entire structure. Figure 2(b)) shows a side-located within a Fibonacci substructure field intensity for a mode of $\lambda = 800\,\text{nm}$. This mode is such that its amplitude becomes zero for at both ends of the complete structure, at both ends of the central Bragg substructure, and is also stationary for both Fibonacci substructures. Curiously this wavelength coincides with λ_0, that determines the widths of the A and B layers via the $\lambda_0/4$ condition.

Figures 2(c) and 2(d) represent modes with selective localization at the central Bragg substructure. The mode whose field intensity depicted in 2(c) has $\lambda = 683.95\,\text{nm}$. Figure 2(d) corresponds to a mode for which $\lambda = 963.49\,\text{nm}$. Besides the difference in shape of the central higher peaks in both figures, it is interesting to notice that in case (c) they are centered at A layers while in case (d) those peaks are centered at B layers. Both modes are stationary for the whole structure.
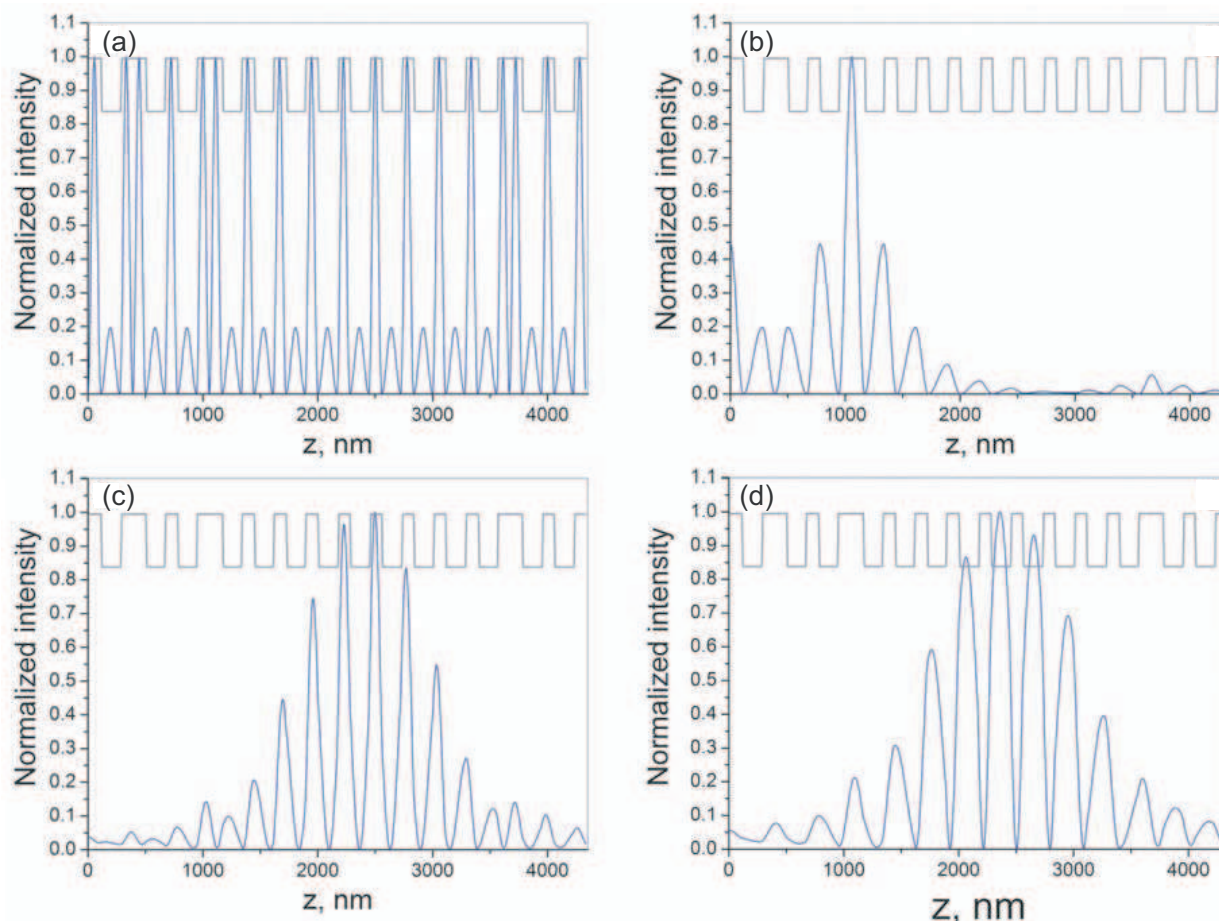

Figure 2: Electric field normalized intensities of TE modes in 4FN-8BM-4FN hybrid porous silicon dielectric heterostructure as functions of the position. The corresponding values of the wavelength are: (a) $\lambda = 400\,\text{nm}$, (b) $\lambda = 800\,\text{nm}$, (c) $\lambda = 683.95\,\text{nm}$, and (d) $\lambda = 963.49\,\text{nm}$. The layer profile, according to the values of the refractive indices is superimposed for illustration.

4. CONCLUSIONS

In this work we have studied the properties of the amplitude of stationary TE oscillations associated to the propagation of light throughout hybrid Periodic-Fibonacci porous silicon dielectric

multilayers. It is shown that several of these wavelengths correspond to modes with selective spatial localization. Confinement of the field intensity is found to occur almost completely whether at the quasi-periodic Fibonacci substructure or at the periodic Bragg ones, for different values of λ. This fact could be of utmost interest if it can be proved that such a property may contribute to electric field confinement in hybrid-designed microcavities. In these systems, a laser field is confined in the microcavity, together with certain stationary eigenmodes of the system. The possibility of some kind of resonance between both fields is certainly very much appealing.

Noteworthy, the results has been obtained for system with a rather small number of layers. Undoubtedly, increasing the orders of both types of substructures will lead to more accurately defined localization patterns. But this could become inconvenient for some photonic applications. The many different designs that can be derived using hybrid geometries for dielectric multilayers open the scope for ulterior investigations. It could be interesting to explore the use of another quasiregular sequences to fabricate the hybrid heterostructures. We can mention, for instance, the Thue-Morse, the Period-Doubling, and the Rudin-Shapiro. Work along this line is already in progress.

ACKNOWLEDGMENT

REFERENCES

1. Macia, E., "Optical engineering with fibonacci dielectric multilayers," *Appl. Phys. Lett.*, Vol. 73, No. 23, 3330–3332, 1998.
2. Yang, X., Y. Liu, and X. Fu, "Transmission properties of light through the fibonacci-class multilayers," *Phys. Rev. B*, Vol. 59, No. 7, 4545–4548, 1999.
3. Macia, E., "Exploiting quasiperiodic order in design of optical devices," *Phys. Rev. B*, Vol. 63, 205421–1–8, 2001.
4. Jiang, X., Y. Zhang, and S. Feng, "Photonic band gaps and localization in the Thue Morse structures," *Appl. Phys. Lett.*, Vol. 86, 201110–1–3, 2005.
5. Montalbán, A., V. R. Velasco, J. Tutor, and F. J. Fernández-Velicia, "Phonon confinement in one-dimensional hybrid periodic/quasiregular structures," *Phys. Rev. B*, Vol. 70, 132301–1–4, 2004.
6. Montalbán, A., V. R. Velasco, J. Tutor, and F. J. Fernández-Velicia, "Selective spatial localization of the atom displacements in one-dimensional hybrid quasi-regular (Thue Morse and Rudin Shapiro)/periodic structures," *Surf. Sci.*, Vol. 601, 2538–2547, 2007.
7. Agarwal, V. and M. E. Mora-Ramos, "Optical characterization of polytype fibonacci and Thue Morse quasiregular dielectric structures made of porous silicon multilayers," *J. Phys. D: Appl. Phys.*, Vol. 40, 3203–3211, 2007.
8. Wen, D. J., H. Peng, and W. H. Zhou, "Broad omnidirectional reflection band forming using the combination of fibonacci quasi-periodic and periodic one-dimensional photonic crystals," *Chinese Phys. Lett.*, Vol. 20, 1963–1965, 2003.
9. Mora, M. E., R. Pérez, and Ch. Sommers, "Transfer matrix in one-dimensional problems," *J. Physique*, Vol. 46, 1021–1026, 1985.
10. Carretero, L., M. Perez-Molina, P. Acebal, S. Blaya, and A. Fimia, "Matrix method for the study of wave propagation in one-dimensional general media," *Opt. Express*, Vol. 14, No. 23, 11385–11391, 2006.
11. Kumar, N. and S. P. Ojha, "Photonic crystals as infrared broadband reflectors with different angles of incidence: A comparative study," *Progress In Electromagnetics Research*, PIER 80, 431–445, 2008.

Study on the Influence of the Incidence Direction on the Photonic Band Gap in Porous Si-based Dielectric Heterostructures

José Escorcia-García[1] and Miguel E. Mora-Ramos[2]

[1]Centro de Investigación en Ingeniería y Ciencias Aplicadas
Universidad Autónoma del Estado de Morelos
Ave. Universidad 1001, Cuernavaca 62209, México
[2]Facultad de Ciencias, Universidad Autónoma del Estado de Morelos
Ave. Universidad 1001, Cuernavaca 62209, México

Abstract— The effect of the angle of incidence upon the omnidirectional reflectance of an electromagnetic wave that propagates throughout $\lambda/4$ multilayered dielectric porous-silicon-based heterostructures is theoretically studied. The transfer matrix formalism is used to perform simulations of light propagation for different angles of incidence. Several distinct arrays for the dielectric profiles are considered. They include periodic, quasiregular and hybrid quasiregular-periodic layer sequences. The same study is extended to deal with non-quarter-lambda stacking rugate and Gaussian structures. All structures have a total thickness of around 15.8 m approximately, with refractive indices of 1.2 and 2.5 for the constituent layers. The results show the advantage of the porous-silicon hybrid structure to generate enhanced omnidirectional reflectance up to 60°.

1. INTRODUCTION

The capability of creating layered structures endowed with diverse properties has attracted great attention to study the optical properties of the photonic crystals (PC) [1, 2]. A one-dimensional PC-say, for instance, a Bragg mirror (BM)-consists of a periodic arrangement of different materials with a period of the order of the optical wavelength, which forbid the propagation of light in specific wavelength ranges [3–5]. These ranges are called photonic bandgaps (PBGs) and are angle dependent, due to the differences in the periodicity experienced by light propagating at non-normal incidences [6]. The ability to reflect the radiation in a particular range of frequencies, for all possible angles of incidence and whatever polarization, is denominated omnidirectional reflection (ODR) [7–11]. In 1998 Fink et al. demonstrated the first theoretical and experimental omnidirectional mirror (OM) using one dimensional PCs [7]. Later Chigrin et al. described the effect at optical frequencies (604.3–638.4 nm) using 19 layers of $Na_3AlF_6/ZnSe$ [11]. Since then many materials have been used to construct these systems. One of them is silicon, which has interesting properties for the fabrication of photonic devices in the near-infrared as well as it is compatible with silicon-based microelectronics. This has already investigated in combination with SiO_2 to produce omnidirectional mirrors.

Another way to produce an omnidirectional mirror consists of the modulation of the porosity inside of a bulk silicon substrate by HF electrochemical etching, denominated porous silicon (PS), which produces a periodic variation of the refractive index as is typical in the case of multilayer systems as Bragg mirrors (BM). In spite that one-dimensional porous silicon PCs, like BM, are easy and feasible to fabricate at any frequency, these do not have a wide omnidirectional range. Therefore, different procedures have been considered to enlarge the omnidirectional range of PS mirrors, such as (a) by increasing the refractive index contrast, (b) by considering structures with variable period or variable number of layers [12], and (c) by constructing a sequence of two or more periodic structures with an omnidirectional gap higher than the individual omnidirectional gaps. Besides, in recent years the possibility of obtaining enhanced PBGs and ODR from multiple and hybrid structures has been put forward [13, 14].

In this work we report the theoretical omnidirectional reflectance of four different quarter-wave stack structures such as periodic Bragg mirror (BM), quasi-regular Thue-Morse (TM) and Fibonacci (FN), as well as a hybrid BM-FN-BM structure. In addition, a Gaussian structure (GS) was generated and simulated to compare its ODR with the structures mentioned above. The results show that the hybrid structure exhibits a wide photonic bandgap, even larger than the GS structure, enhancing the omnidirectional reflection until an incident angle of 60°, after of which the ODR band divides in multiple ODR sub-bands.

2. MODEL SYSTEMS AND SIMULATION TOOL

The heterostructures here studied are built from two different porous silicon layers with refractive indices $n_A = 2.5$ and $n_B = 1.2$. These layers are designed to satisfy the $\lambda/4$ condition and are stacked following the substitution rules for the construction of a periodic structure called Bragg mirror ($A \rightarrow AB$, $B \rightarrow AB$), a quasi-regular TM ($A \rightarrow AB$, $B \rightarrow BA$), a quasi-periodic FN ($A \rightarrow AB$, $B \rightarrow A$), as well as a hybrid Fibonacci structure. The hybrid structure is built of a *sandwich-like* combination of two Bragg and one FN multilayered structures; that is, a Bragg-Fibonacci-Bragg (BM-FN-BM) geometry. In our particular case we have chosen $\lambda = 800$ nm. Therefore, the corresponding layer widths will be $d_A = \lambda/4n_A = 80$ nm, and $d_B = \lambda/4n_B = 166.67$ nm. With the aim to compare the optical response of the distinct structures we have also simulated a multilayered system that does not satisfy the $\lambda/4$ condition. In this case it is a Gaussian heterostructure, whose type has proven to show interesting properties such as a wide omnidirectional reflectance band [15, 16]. The refractive index is smoothly and progressively varied following a Gaussian profile between $n_{\max} = 2.5$ and $n_{\min} = 1.2$. In order to have a good basis for a comparison of the increment/reduction of the omnidirectional reflectance, all structures were calculated for a total physical thickness of 15.8 µm approximately.

The theoretical simulation is made using the transfer matrix formalism. This tool is derived for one-dimensional problems that can be resolved via the solution of a master equation which ultimately reduces to a linear system of first order ordinary differential equations [18]. The analysis is made in the case of the 1D Maxwell equation for the transverse electric modes propagating in the structure, which has piecewise constant dielectric functions. In this case, it is necessary to use the variant suitable to deal with oblique angles of incidence [17].

3. RESULTS AND DISCUSSION

In Figure 1(a) we show the reflectivity of one periodic structure for two arbitrary values of incidence angle at 0° and 60°. As can be observed, the reflectance spectrum shows a wide photonic bandgap of $5700\,\mathrm{cm}^{-1}$ (for normal incidence) centered at $12500\,\mathrm{cm}^{-1}$ (800 nm) and multiple sidelobes out the PBG, which is blue-shifted and its width is reduced to a value of $4004\,\mathrm{cm}^{-1}$ at incidence angle of 60. Nevertheless, the ODR range where the reflectance is maximum corresponds to $2036\,\mathrm{cm}^{-1}$ at 60°. These are usual optical properties of the periodic structures which have been reported for different authors, and recently theoretically discussed by Kumar et al. [17]. On the other hand, Figure 1(b) shows the optical reflectance of quasi-regular Thue-Morse structure of 7th order, which consists of 128 layers following the substitutional rule mentioned above. In view that TM structure is considered as a kind of an intermediate between periodic and quasi-periodic systems, it is reasonable to expect multiple narrow PBGs in the whole spectrum at normal incidence, as can be observed in the Figure 1(b). The reflectivity spectrum shows two major photonic bangaps of 2135 and $2205\,\mathrm{cm}^{-1}$ centered at 8120 and $16915\,\mathrm{cm}^{-1}$, respectively. Increasing the incidence angle the PBGs
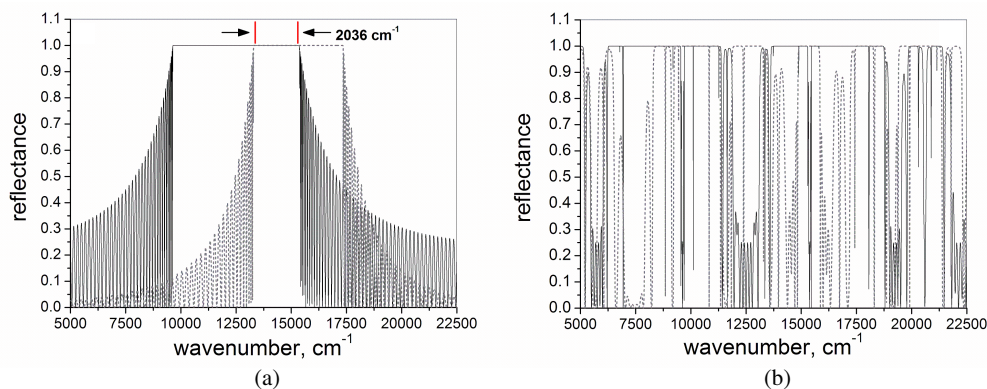

Figure 1: Reflectance spectra calculated for periodic and quasi-periodic Thue-Morse structures. (a) Period structure was simulated with 64 periods AB having refractive indices of $n_A = 2.5$ and $n_B = 1.2$ with thicknesses of $d_A = 80$ nm and $d_B = 166.67$ nm, respectively. (b) Quasi-periodic Thue-Morse structure was simulated with 128 layers corresponding to 7th order generation with the same refractive indices and thicknesses as corresponding to the BM structure. Solid line displays the reflectance spectra at normal incidence (0) while the dashed line displays the reflectance spectra at 60°.

decrease and shift to the higher wavenumber side, giving a reduction in the ODR which disappears after 50° (see, Figure 3(b)) due to there is no matching between the narrow PBGs appearing at this incidence angle with respect to the PBGs at normal incidence. Therefore, at 60° (Figure 1(b)) only very small photonic bandgaps are observed.

In Figure 2(a) it is shown the reflectivity spectrum of a 10th order quasi-periodic Fibonacci structure containing 140 layers. The four missing layers were removed in order to obtain a total thickness of 15.8 µm. However all remaining layers were disposed following the substitutional rule of Fibonacci construction. Figure 2(b) shows the outcome of the reflectivity spectrum calculation for the hybrid BM-FN-BM structure. Two periodic structures of 17.5 periods together with an 8th order FN structure are the components of the hybrid structure. The major PGBs presented in both the FN and hybrid BM-FN-BM structures decrease and blue-shift with increasing the incidence angle, as was discussed for the two previously considered structures. However, some important aspects can be pointed out from these two structures. Firstly, the FN structure (Figure 3(a)) shows only two narrow PBGs with ODR of 582 and $142 \, \text{cm}^{-1}$ centered at 10583 and $17170 \, \text{cm}^{-1}$, respectively. In spite that the ODR band of the periodic structure ($2726 \, \text{cm}^{-1}$ for 17.5 periods) does not match with the ODR bands of the FN structure, the combination of both as a hybrid structure gives a broad ODR band of $5831 \, \text{cm}^{-1}$ shown in the part b) of Figure 2. Secondly, the right side of the ODR band in the hybrid structure remains almost constant with an increase in the incidence angle and only the left side is blue-shifted. This effect results from the significantly different dielectric contrast associated to the "sandwich-like" geometrical distribution of FN and BM structures, since it does not seem to be observed in the individual structures. However, a more carefully study must be carried out later on.

Owing to understand the enhancement of the ODR due to the hybrid BM-FN-BM structure, we simulated a Gaussian structure which has been demonstrated to have a broad ODR band. The structure was generated to obtain a PBG centered at $12500 \, \text{cm}^{-1}$ (800 nm), in order to compare it with the previously quarter-wave stack structures, by repeating a substructure of width $D = 226 \, \text{nm}$, where its refractive index is given by the envelope of a Gaussian profile. The whole structure is composed of 70 cycles with a total thickness of 15.8 µm. The reflectivity spectrum exhibits a broad PBG of $4327 \, \text{cm}^{-1}$ at normal incidence which decreases to $1772 \, \text{cm}^{-1}$ at incidence angle of 60. What comes out of this comparison is that until now the hybrid structure BM-FN-BM seems to have a better broad ODR band (5831 cm) than the other structures at least to an incidence angle of 60°.

Figure 3(b) shows the change of the ODR with an increase in the incidence angle for all structures mentioned in this work. As can be seen, the quasi-periodic FN and TM structures have the smaller ODR bands, with respect to the other structures, which disappear at angle of incidence of 50° and 60°, respectively. On the other hand, the hybrid BM-FN-BM structure have the largest ODR ($5831 \, \text{cm}^{-1}$) band until an incidence angle of 60°, after of which the ODR band divide into two
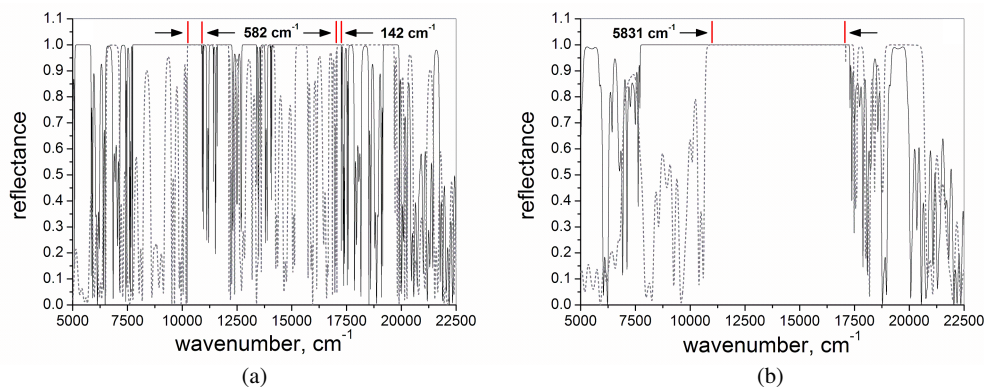

Figure 2: Reflectance spectra calculated for quasi-periodic Fibonacci and Hybrid BM-FN-BM structures. (a) 10th order FN structure simulated with 140 layers following the substitutional rule of Fibonacci, and (b) hybrid BM-FN-BM structure simulated with a 8th order FN structure sandwiched between two BM consisting of 17.5 periods. The refractive indices and thicknesses used for layers A and B are the same as corresponding Figure 1. Solid line represents the reflectance spectra at normal incidence (0°) and dashed line represents the reflectance spectra at 60°.
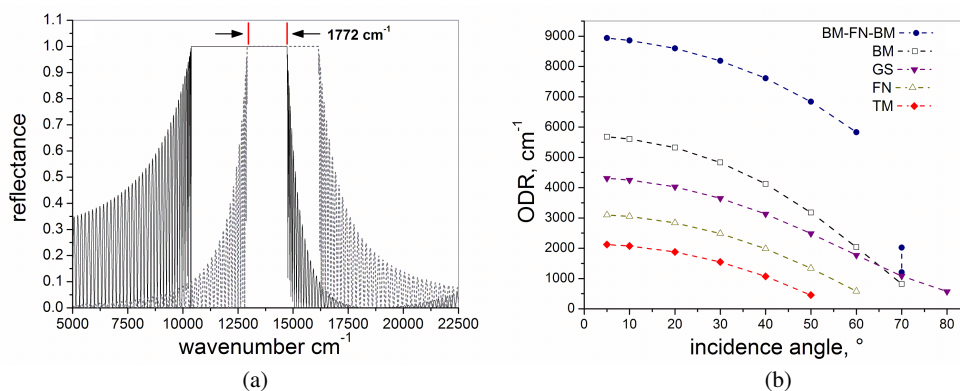
Figure 3: (a) Reflectance spectra calculated for the Gaussian structure which consists of a repetition of 70 substructures with a thickness $D = 226$ nm each ones. The refractive index of the substructure follows a Gaussian profile between the values of $n_{max} = 2.5$ and $n_{min} = 1.2$. Solid line represents the reflectance spectra at normal incidence (0°) and dashed line at 60°. (b) The graph shows the decrease of the ODR band of the different structures with an increase in the incidence angle.

ODR sub-bands of 1208 and 2019 cm^{-1} (two blue circles joined with a dashed line) for an angle of incidence of 70°. Beyond this angle, the two sub-bands again divide by two to form four ODR sub-bands and the process of division continue with increasing the incidence angle. It is worth to note that although the Gaussian structure has not a large ODR band, compared with the hybrid structure, this can retain the ODR behavior for almost all incidence angles. Finally, depending on the application of interest we can use a hybrid structure to obtain a broad PBG with a wide ODR band, like reflectors, to obtain a good reflectance until a certain critical angle of incidence, or we can use a Gaussian structure to obtain a whole ODR band at any incidence angle.

4. CONCLUSIONS

We have theoretically investigated in this article the effect of the variation of the angle of incidence of the electromagnetic waves that propagate across porous silicon dielectric multilayers. Several geometrical distributions for the arrangement of layers in the heterostructures are considered, including periodic, Thue-Morse, Fibonacci and Gaussian profiles. These preliminary studies show that the fabrication of porous-silicon-based Periodic/Fibonacci hybrid can lead to reflectors with wide omnidirectional photonic bandgaps.

ACKNOWLEDGMENT

REFERENCES

1. Yeh, P., *Optical Waves in Layered Media*, John Wiley & Sons, New York, 1988.
2. Auerbach, S. M., K. A. Carrado, and P. K. Dutta, *Handbook of Layered Materials*, Marcel Dekker Inc., New York, 2004.
3. Yablonovitch, E., "Inhibited spontaneous emission in solid-state physics and electronics," *Phys. Rev. Lett.*, Vol. 58, 2059–2062, 1987.
4. John, S., "Strong localization of photons in certain disordered dielectric superlattices," *Phys. Rev. Lett.*, Vol. 58, 2486-2489, 1987.
5. Winn, J. N., *Photonic Crystals: Molding the Flow of Ligth*, Princeton University Press, Princeton, NJ, 1995.
6. Johnson, S. G. and J. D. Joannopoulos, "Introduction to photonic crystals: Bloch's theorem, band diagrams and gaps (but no defects)," *Photonic Crystal Tutorial*, 1–16, 2003, http://ab-initio.mit.edu/photons/tutorial/.
7. Winn, J. N., Y. Fink, S. Fan, and J. D. Joannopoulos, "Omnidirectional reflection from a one-dimensional photonic crystal," *Opt. Lett.*, Vol. 23, 1573–1575, 1998.
8. Fink, Y., J. N. Winn, S. Fan, C. Chen, J. Michel, J. D. Joannopoulos, and E. L. Thomas, "A dielectric omnidirectional reflector," *Science*, Vol. 282, 1679–1782, 1998.

9. Bruyant, A., G. Lrondel, P. J. Reece, and M. Gal, "All-silicon omnidirectional mirrors based on one-dimensional photonic crystals," *Appl. Phys. Lett.*, Vol. 82, 3227, 2003.

10. Dal Negro, L., M. Stolfi, Y. Yi, J. Michel, X. Duan, L. C. Kimerling, J. LeBlanc, and J. Haavisto, "Photon band gap properties and omnidirectional reflectance in Si/SiO2 ThueMorse quasicrystals," *Appl. Phys. Lett.*, Vol. 84, No. 25, 5186–5188, 2004.

11. Chigrin, D. N., A. V. Lavrinenko, D. A. Yarotsky, and S. V. Gaponenko, "Observation of total omnidirectional reflection from a one-dimensional dielectric lattice," *Appl. Phys. A: Mater. Sci. Process.*, Vol. 68, 25–28, 1999.

12. Agarwal, V., J. Escorcia-Garcia, and M. E. Mora-Ramos, "Optical properties of delta polytype quasiregular dielectric structures made of porous silicon," *Phys. Stat. Sol. (a)*, Vol. 204, No. 5, 1367–1371, 2007.

13. Zhang, C., F. Qiao, and J. Wan, "Enlargement of nontransmission frequency range in photonic crystals by using multiple heterostructures," *J. Appl. Phys.*, Vol. 87, 3174, 2000.

14. Wen, D. J., H. Peng, and W. H. Zhou, "Broad omnidirectional reflection band forming using the combination of fibonacci quasi-periodic and periodic one-dimensional photonic crystals," *Chinese Phys. Lett.*, Vol. 20, 1963–1965, 2003.

15. Arriaga, J. and X. I. Saldaña, "Band structure and reflectivity of omnidirectional Si-based mirrors with a Gaussian profile refractive index," *J. Appl. Phys.*, Vol. 100, 044911-1-4, 2006.

16. Arriaga, J., "Omni-directional gap of 1-D photonic crystals based on porous silicon with a Gaussian profile refractive index," *Phys. Stat. Sol. (c)*, Vol. 2, 534–536, 2007.

17. Kumar, N. and S. P. Ojha, "Photonic crystals as infrared broadband reflectors with different angles of incidence: A comparative study," *Progress In Electromagnetics Research*, PIER 80, 431–445, 2008.

18. Mora, M. E., R. Pérez, and Ch. Sommers, "Transfer matrix in one-dimensional problems," *J. Physique*, Vol. 46, 1021–1026, 1985.

Improved Property in Inverted Bottom-emission Organic Light-emitting Diodes Using 8-Hydroxyquinolinolatolithium Layer

J. F. Li[1, 2]**, W. L. Chang**[2]**, and F. J. Zhang**[1]

[1]School of Physical Science and Technology, Lanzhou University, Lanzhou 730000, China
[2]School of Mathematics, Physics & Software Engineering
Lanzhou Jiaotong University, Lanzhou 730070, China

Abstract— We demonstrate inverted bottom-emission organic light-emitting diodes (IBOLEDs) using 8-Hydroxyquinolinolatolithium (Liq) as an electron injection layer and an indium-tin-oxide coated glass substrate directly as cathode. The performances of devices with different thickness of Liq were investigated. Experiment results show that the efficiency of device with 1-nm-thick Liq is four times higher than that without Liq. The turn-on voltage of devices decreased from 20 to 9 V as the 1-nm-thick Liq was employed. Liq itself is an organic material which has a very similar electronic structure to Alq_3. Therefore the energy level mismatch would be minimal and made the number of injected electrons and holes balance, and it significantly improves the device properties by inserting Liq electron injection layer between the emitting layer and cathode. At the same time, we also demonstrate IBOLEDs using LiF as an electron injection layer and an indium-tin-oxide coated glass substrate directly as cathode. We found that the device using Liq as an electron injection layer is less sensitive to the Liq thickness than using LiF in efficiency. This property of Liq would be very important in the mass production. The difference may be attributed to the fact that Liq is an organic semiconductor and LiF an insulator, it can only be used when deposited as an ultra-thin layer. Our experimental results support the assumption that free lithium released from lithium quinolate is responsible for the improved device performance, and this release is more effective than that observed in devices with LiF. The results prove that Liq layer is also suitable for electron injection in IBOLEDs with an indium-tin-oxide coated glass substrate directly as cathode. This IBOLEDs can be integrated readily with the n-channel of the α-Si TFT backplane, which is proved to be useful in manufacturing Active-matrix organic light emitting device with high-power efficiency and long device stability for future large-size OLEDs display applications.

1. INTRODUCTION

In recent years, organic light-emitting devices (OLEDs) have attracted considerable interest due to their promising applications in flat-panel displays by replacing cathode ray tubes (CRTs) or liquid crystal displays (LCDs). They have various advantageous features such as self-emission, high luminous efficiency, full-colour capability,wide viewing angle, high contrast, low power consumption, low weight, potentially large area colour displays and flexibility.

Transparent or surface-emitting OLEDs are of considerable interest for many display applications as they can easily be integrated with either Si or organic thin film transistor driver electronics for active-matrix displays [1, 2]. For display drivers employing n-channel field effect transistors, it is desirable that the bottom contact of the OLEDs is the cathode. This requires that OLEDs have an inverted structure with a cathode as the bottom contact [3, 4]. The inverted OLEDs enable a direct connection between the bottom cathode and the n-channel field effect transistors drain line, which results in a decrease in driving voltage andan improvement of stability. Several researchers usually have opted for Al as bottom cathode and have tried to sputter transparent indium tin oxide (ITO) as anode on organic layers to fabricate inverted top-emission OLEDs (ITOLEDs) [5–7]. However, the sputter deposition of ITO is known to induce radiation damage to the organic layer [8]. This problem can only partially be overcome by using protective buffer layer, such as PTCDA and CuPc, et al. Other authors have used a semitransparent film of Au (10–20 nm), NiO, indium zinc oxide, or Ag/TeO_2, as the top anode of ITOLEDs [9–11]. However, the variation of electroluminescence (EL) spectra at different viewing angles caused by microcavity effect induced by the two opposite reflective metal/semitransparent metal electrodes somehow limits the advantage of this approach. Taking the above-mentioned problem into consideration, this study focused on inverted bottom-emission OLEDs (IBOLEDs). Therefore, the bottom electrodes were formed on ITO, which was used as the transparent current carrier.

At the same time, Enhancement and optimization of charge injection and transport and carrier balance are very important issues in achieving highly bright and efficient devices. In the past years,

great efforts have been made to improve and balance carrier injection into the emitting layer to achieve high-efficiency devices [12–15]. To enhance electron injection, considerable research has been carried out with various electron injection layers (EILs) of salts and metal oxides. Recently, it has been reported that several research groups have improved OLEDs with 8-hydroquinolatolithium (Liq) as an EIL [16–18]. Liq has attracted attention on account of its superior evaporation property and insensitivity to thickness control compared with other insulator EIL. Moreover, Liq itself is an organic material which has a very similar electronic structure to Alq_3, the most common electron transport material. Therefore the energy level mismatch would be minimal and would contribute to an improvement in device performance.

From all things considered, in this study, we recently succeeded in fabricating novel IBOLEDs with the structure of $ITO/Liq/Alq_3/TPD/MoO_3/Al$. Here, Liq was electron injection layer, ITO was the cathode, Al was the anode and MoO_3 was hole injection layer. We will demonstrate that this device structure makes the number of injected electrons and holes balance, and it significantly improves the device properties by inserting Liq electron injection layer between the emitting layer and cathode. It is generally believed that the IBOLEDs developed in this work can be integrated with α-Si TFT process that would considerably accelerate the commercialization of large-size Active-matrix organic light emitting device.

2. EXPERIMENTS

In our experiments, the device structure with $ITO/Liq/Alq_3/NPB/MoO_3/Al$ was fabricated. The control devices with the structures of $ITO/LiF/Alq_3/NPB/MoO_3/Al$ and $ITO/Alq_3/NPB/MoO_3/Al$ were also prepared for comparison. The devices structures are shown in Fig. 1. The thickness of either Liq or LiF was varied in the range of 0.5–2.0 nm. Indium tin oxide (ITO) coated glass with a nominal surface resistance of $20\,\Omega/sq$ was used as the substrate for IBOLEDs. ITO substrates were cleaned by ultrasonication in acetone and alcohol separately. After being rinsed in hot and cold de-ionized water for several times, the substrate was dried in an infrared oven. For thermal deposition of the organic and metal layers, the operating vacuum was $1.2 \times 10^{-3}\,Pa$. The aluminum cathodes were depositioned through a shadow mask to form devices with an area of $0.16\,cm^2$. The electrical characteristics of The IBOLEDs were measured with a keithley 2400 source meter.

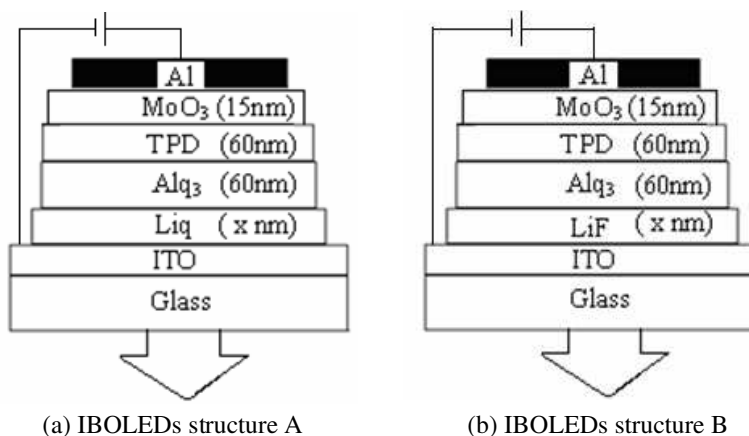(a) IBOLEDs structure A   (b) IBOLEDs structure B

Figure 1: Structure of devices of different election injection layer.

3. RESULTS AND DISCUSSION

Figure 2 and Fig. 3 show the curve of current density-voltage (J-V) of the devices with various Liq and LiF thickness while fixing thickness of all the other layers, respectively. From the figures, it can be seen that both devices have the obvious rectification characteristic. When the driving voltage is less than the turn on voltage of the device, the current density of the device is very small. However, when the driving voltage is higher than the turn on voltage of the device, the current density promptly increases with the rising of the driving voltage. It can be also seen that the performances of the devices using Liq or LiF as an injection layer are nearly identical. What is more, they are far better than the device with an only ITO cathode. As the thickness of Liq or LiF layer increases, the current density-voltage curves does not shift to higher continuously, but

shift to lower when the thickness of LiF or Liq is higher than 1.0 m. It might be attributed to the following two reasons.
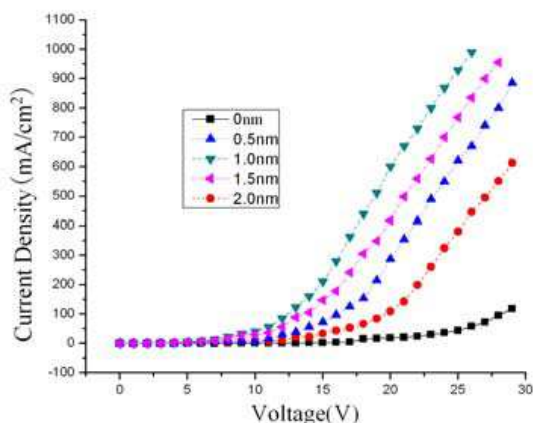

Figure 2: J-V curve of devices with different thicknesses of Liq.
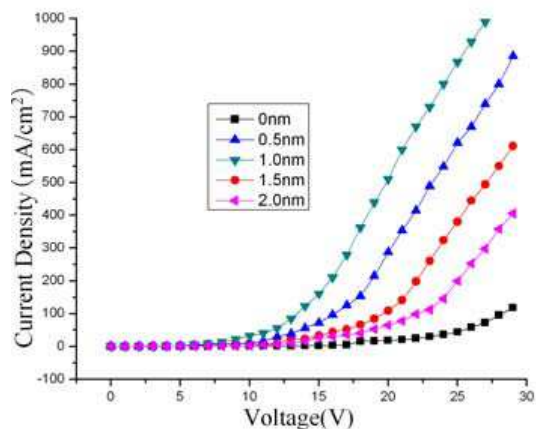

Figure 3: J-V curve of devices with different thicknesses of LiF.

On the one hand, Cho et al. [18] measured the photoelectron emission and found that the energy band of Alq$_3$ was bent downward by more than $0.56\,\mathrm{eV}$ when Alq$_3$ surface is in contact with Liq, thus lowering the electronic barrier height. When Liq or LiF was inserted, this cause electron injection to increase at a given driving voltage compared with the structure without Liq or LiF. That is to say, using Li ion can improve the electron injecting efficiency. Therefore, when the thickness is less than 1.0 nm, current will be higher as the thickness gains.

On the other hand, Tak and Bässler [19] found that current and quantum efficiency (QE) of OLEDs may depend on the thickness (L_e) of an organic layer between the cathode and the emitting layer and current decreases with the increased L_e. As a result, we deduce that the insertion of EIL in OLEDs may lead to the accumulation of positive charges at the internal interface increase the electric field inside the cathodic compartment while the electric field acting at the hole injectioning contact is screened accordingly. This causes hole injection (holes are considered to be the majority carriers), and the total current to decrease at a give external field. As L_e increases the hole as well as the electron density stored at the interface per unit area decreases.

From above two aspects consideredwhen the thickness of EIL is less than 1.0 nm, the former plays a crucial role, current increases with the increase of the thickness. However, when the thickness of EIL is more than 1.0 nm, The latter plays a crucial role, current decreases with the increase of the thickness.

Figure 4 and Fig. 5 show the cruve of brightness-voltage (B-V) for device with various Liq and LiF under fixed thickness of other layer, respectively. Considerably higher brightness was observed in the device with Liq or LiF EIL compared with that without it. We believe it is due to the increased injected electrons, which is caused by the EIL, that results in more balanced charge carriers injected and more carrier recombination at the emitting zone. Therefore, the property of the devices with EIL is improved. For example, at a current density of $100\,\mathrm{mA/cm^2}$, the devices using Liq $(1.0\,\mathrm{nm})$/ITO, LiF $(1.0\,\mathrm{nm})$/ITO and Al cathodes require driving voltage of $10.7\,\mathrm{V}$, $11.4\,\mathrm{V}$, $27\,\mathrm{V}$, and have luminance of $309\,\mathrm{cd/m^2}$, $314\,\mathrm{cd/m^2}$, $77\,\mathrm{cd/m^2}$, respectively.

Figure 6 shows the variations of efficiencies at a current density of $60\,\mathrm{mA/cm^2}$ for Liq/ITO and LiF/ITO devices with different thicknesses of Liq and LiF. As the thickness of Liq or LiF layer increases, the efficiencies are increase first and decrease later in both cases. For instance, when the thickness of Liq or LiF increases to 1.0 nm from 0 nm. The efficiencies ascend to 3.2 and $3.1\,\mathrm{cd/A}$ from 0.6 and $0.6\,\mathrm{cd/A}$ respectively,but when the thickness of Liq or LiF increases to 2.0 nm from 1.0 nm. The efficiencies drop to 2.5 and $0.9\,\mathrm{cd/A}$ from 3.2 and $3.1\,\mathrm{cd/A}$, respectively. These tendencies of dependence of the EL efficiency on the thickness of injection layer in the two devices are similar, but the variation of efficiency of Liq device vs thickness of injection layer is smaller than that of LiF device. This means that the device performance by using Liq as an injection layer is less sensitive to Liq thickness than LiF as an injection layer. This property of Liq would be very important in the mass production. The difference may be attributed to the fact that Liq is an organic semiconductor and LiF an insulator.
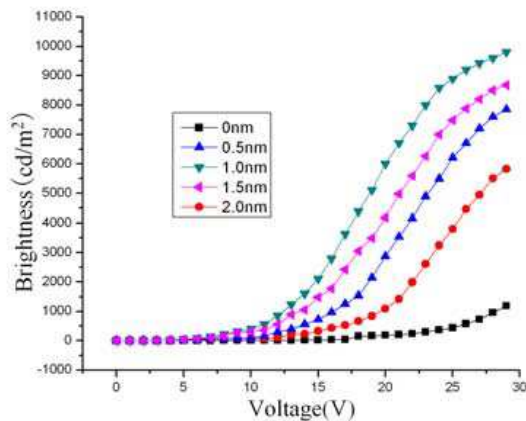
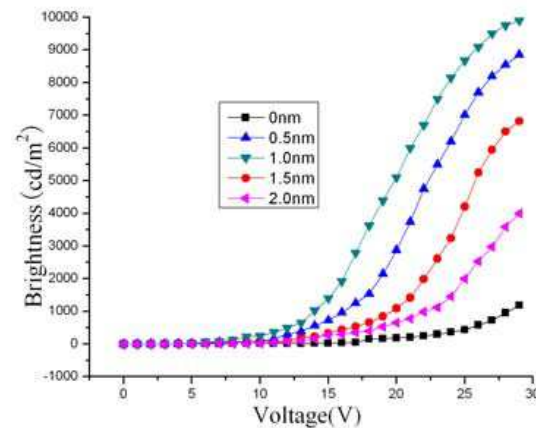Figure 4: B-V curve of devices with different thicknesses of Liq.

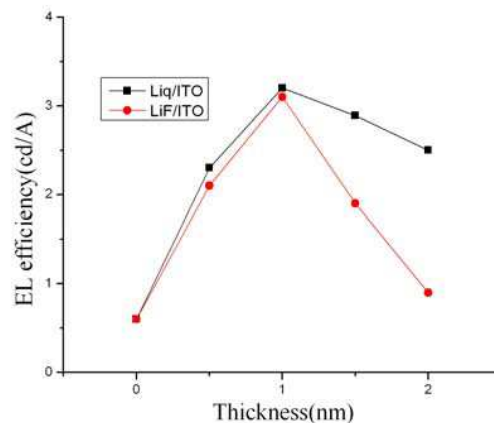Figure 5: B-V curve of devices with different thicknesses of LiF.

Figure 6: Variations of elefficiencies at current density of $100\,\mathrm{mA/cm^2}$ for devices with different thicknesses of Liq and LiF, respectively.

4. CONCLUSIONS

In summary, we have succeeded in fabricating the IBOLEDs of high efficiency by inserting an electron injection layer using Liq or LiF between the emitting layer and cathode. The thickness of Liq and LiF influences the curve of J-V, B-V and EL η-V by testing and analysing. The result demonstrates that the thickness of Liq or LiF influences the performance of the IBOLEDs. In considering the electrical and optical properties, Liq layers with a thickness of 1.0 nm are excellent obtaining high-performance devices. And, the performance of the device with Liq as an EIL is less sensitive to Liq thickness than that with LiF as an EIL. Such a structure with optimal thickness of 1 nm Liq or LiF not only improved brightness and EL efficiencies, but also decreased turn-on voltage. What's more, this IBOLEDs can be integrated readily with the n-channel of the α-Si TFT backplane, which is proved to be useful in manufacturing Active-matrix organic light emitting device with high-power efficiency and long device stability for future large-size OLEDs display applications.

ACKNOWLEDGMENT

REFERENCES

1. Hayashi, S., T. Koyama, and Y. Taniguchi, *Appl. Phys. Lett.*, Vol. 78, 3343, 2001.

2. Kang, M. H., J. H. Hur, Y. D. Nam, E. H. Lee, S. H. Kim, and J. Jang, *J. Non-Crystalline Solids*, Vol. 354, 2523, 2008.

3. Bulovi, V., P. Tian, P. E. Burrows, M. R. Gokhale, and S. R. Forrest, *Appl. Phys. Lett.*, Vol. 70, 2954, 1997.

4. Zhou, X., M. Pfeiffer, J. S. Huang, J. Blochwitz-Nimoth, D. S. Qin, A. Werner, J. Drechsel, B. Maennig, and K. Leo, *Appl. Phys. Lett.*, Vol. 81, 922, 2002.

5. Choi, H. W., Y. Kim, W. K. Kim, and J. L. Lee, *Appl. Phys. Lett.*, Vol. 81, 082102, 2005.

6. Chen, C. W., C. L. Lin, and C. C. Wu, *Appl. Phys. Lett.*, Vol. 85, 2469, 2004.

7. Meng, Y. L., W. F. Xie, N. Zhang, S. F. Chen, J. Li, W. Hu, Y. Zhao, J. Y. Hou, and S. Y. Liu, *Microelectronics J.*, Vol. 39, 723, 2008.

8. Liao, L. S., L. Shung, W. C. Chan, X. M. Ding, T. K. Sham, I. Bello, C. S. Lee, and S. T. Lee, *Appl. Phys. Lett.*, Vol. 75, 1619, 1999.

9. Hou, L., F. Huang, W. Zeng, J. B. Peng, and Y. Cao, *Appl. Phys. Lett.*, Vol. 87, 153509, 2005.

10. Choi, H. W., S. Y. Kim, W. K. Kim, and J. L. Lee, *Appl. Phys. Lett.*, Vol. 87, 082102, 2005.

11. Chen, S. F., R. L. Song, J. Wang, Z. Y. Zhao, Z. H. Jie, Y. Zhao, B. F. Quan, W. Huang, and S. Y. Liu, *J. Luminescence*, Vol. 128, 1143, 2008.

12. Xiong, Y., W. Xu, C. Li, B. Liang, L. Zhao, J. B. Peng, Y. Cao, and J. Wang, *Organic Electronics*, Vol. 9, 533, 2008.

13. Yang, L. Y., X. Z. Chen, H. Xu, D. Q. Ye, H. Tian, and S. G. Yin, *Appl. Surf. Sci.*, Vol. 254, 5055, 2008.

14. Kim, D. E., W. S. Kim, B. S. Kim, B. J. Lee, and Y. S. Kwon, *Thin Solid Films*, Vol. 516, 3637, 2008.

15. Wang, F. C., S. Liu, and C. L. Zhang, *Microelectronics J.*, Vol. 38, 259, 2007.

16. Zheng, X. Y., Y. Z. Wu, R. G. Sun, W. Q. Zhu, X. Y. Jiang, Z. L. Zhang, and S. H. Xu, *Thin Solid Films*, Vol. 478, 252, 2005.

17. Kim, S. H. and J. Jang, *Appl. Phys. Lett.*, Vol. 91, 103501, 2007.

18. Cho, K., S. W. Cho, P. E. Jeon, H. Lee, C. Whang, K. Jeong, S. J. Kang, and Y. Yi, *Appl. Phys. Lett.*, Vol. 92, 093304, 2008.

19. Tak, Y. H. and H. Bassler, *J. Appl. Phys.*, Vol. 81, 6963, 1997.

Analysis of the Injection Layer of Liq in Inverted OLEDs Using Atomic Force Microscopy and X-ray Photoelectron Spectroscopy

J. F. Li[1,2], **W. L. Chang**[2], **and F. J. Zhang**[1]

[1]School of Physical Science and Technology
Lanzhou University, Lanzhou 730000, China
[2]School of Mathematics, Physics & Software Engineering
Lanzhou Jiaotong University, Lanzhou 730070, China

Abstract— A comprehensive understanding of the electronic states of the surface and interface is meaningful for organic light-emitting devices (OLEDs). 8-Hydroxyquinolinolatolithium (Liq)/ indium-tin-oxide (ITO) thin film are analyzed using X-ray photoelectron spectroscopy (XPS). Atomic force microscopy (AFM) is also applied to investigate the morphology of Liq/ITO film. The above-mentioned ITO is directly employed as cathode and Liq as electron injecting layer in inverted OLEDs. AFM observation indicated that the surface is complanate, the Liq growth is uniform and defects cover basically the surface of ITO. Furthermore, the number of pinholes is small. And what is more, the analysis of the sample surface and interface further verifies this result by using XPS. XPS results show, the core-levels of Li 1s, C 1s, N 1s, O 1s, In 3d5/2, and Sn 3d5/2, spectra slightly shift towards lower binding energy with the increase of the sputtering time, which may be caused by the effect of oxygen, indium and tin in ITO diffusing into Liq layer. At the same time, Liq is found to have the ability of restraining the diffusion of chemical constituents from ITO to the electron transport layer, which is beneficial to the improvement of the performance and useful lifetime of the inverted OLEDs. Besides these, the single feature of the Li 1s peak becomes two peaks, indicating there is the interaction of Li atoms with ITO. This reaction has caused a chemical change in Liq, which also might be an important reason that Liq layer can enhance the injection of electron. Our experimental results support the assumption that free lithium released from Liq. These results may explain that Liq is very effective to be used as an electron injection layer for inverted bottom-emission organic light-emitting diodes.

1. INTRODUCTION

In recent years, organic light-emitting devices (OLEDs) have attracted considerable interest due to their promising applications in flat-panel displays by replacing cathode ray tubes (CRTs) or liquid crystal displays (LCDs). They have various advantageous features such as self-emission, high luminous efficiency, full-color capability, wide viewing angle, high contrast, low power consumption, low-weight, potentially large area color displays and flexibility. Enhancement and optimization of charge injection and transport and carrier balance are very important issues in achieving high bright and efficient devices. In the past years, great efforts have been made to improve and balance carrier injection into the emitting layer to achieve high efficiency devices [1–4]. For example, selecting fluorescence material with high efficiency, multi-layer structure and interface modification of cathodeand anode, etc. Inverted OLEDs are of considerable interest for many display applications as they can easily be integrated with either traditional amorphous silicon thin film transistor (a-Si TFT) or organic thin transistor driver electronics for active-matrix displays. For display drivers employing n-channel field effect transistors, it is desirable that the OLEDs have an inverted structure with a cathode as the bottom contact [5, 6]. The inverted OLEDs enable a direct connection between the bottom cathode and the n-channel field effect transistors drain line, which results in a decrease in driving voltage and improved stability. However, due to the difficulty or shortcoming forming a transparent electrode onto an organic layer, the bottom electrodes were formed on indium-tin-oxide (ITO) which was used as the transparent current carrier. In addition, 8-Hydroxyquinolinolatolithium (Liq), instead of LiF, was widely used to enhance the injection of electrons in the OLEDs industry on account of its superior evaporation property and insensitivity to thickness control [7–9]. According to the study of the inverted transparent OLEDs with the ITO bottom contact directly as the cathode [6, 10], the electron-injection potential barrier is decreased because of the influence of dipole. That is to say, using Li ion can improve the electron injecting efficiency. Prior to this work, we have reported an inverted device with the structure of ITO/Liq/Alq3/NPB/MoO3/Al,compared with the device without Liq, the performance of device is improved. This paper reports the influence of Liq in inverted OLEDs using atomic force microscopy (AFM) and x-ray photoemission spectroscopy (XPS).

2. EXPERIMENT

The substrate is an ITO coated glass. It was cleaned by ultrasonication in acetone and alcohol separately. After being rinsed in hot and cold de-ionized water for several times, the substrate was dried in an infrared oven. In a vacuum better that 5×10^{-4} Pa, Liq was evaporated and deposited on the surface of the ITO coated glass substrate. The substrate temperatureis is 50°C. The thickness of Liq film was about 200 nm.

The surface morphology of the Liq/ITO was observed by a Topometrix Explorer atomic force microscopy (AFM) with high resolution, and it was scanned in two modes of the topographic and lateral force contact. The scanning area of the AFM image was $8.0 \times 8.0 \, \mu m^2$, and the height in the direction vertical to the surface was shown by grey scale. The weaker the grey scale, the larger the undulated height of microscopic outline in Z direction.

The x-ray photoemission spectroscopy (XPS) data were collected by an ESCALAB-220IXL x-ray photoemission spectroscopy with a base vacuum better than 1×10^{-8} Pa. Mg $K\alpha$ radiation ($h\nu = 1253.6 \, eV$) used as x-ray source was operated at 300 W. In order to investigate the electron state of the interface, the Liq/ITO sample was sputtered by argon ion beam with 3.0 KeV kinetic energy for 20 minutes in a vacuum chamber of 3×10^{-7} Pa. The sputtering area was $0.75 \times 0.75 \, cm^2$ and the ion beam density was $1.0 \, \mu A/0.75 \times 0.75 \, cm^2$. Then the XPS results were treated with scienta 300 data system and related software.

3. RESULTS AND DISCUSSION

3.1. The Effect of Defects in the Surface of ITO Film on Quality of Transport Materials

The contact between crystal grains of ITO is quite tight, so dislocations are usually formed on grain boundaries [11]. Moreover, the surface atoms are more active than bulk atoms and the activation energy of forming point defect is small [12], thus the concentration of point defects such as the In vacancies in the surface is much higher than in the bulk [13]. The uneven distribution of defects in ITO has great effect on film quality of the transport material. Because the binding ability of transport material with defects is stronger than with perfect surface, the deposited material will first combines with them and crystal nucleus are formed [14]. The uneven distribution of defects determines the uneven formation of crystal nucleus, therefore the transport layer deposition on ITO has defects and pinholes, and the film quality is poor. All these immediately result in many effects: (1) The interfacial resistance of ITO and transport layer, and the working voltage of the device becomes higher. (2) Oxygen atoms diffuse from ITO into transport layer, causing the degeneration of the transport material, forming luminescence quenching centers, and leading to the low efficiency of carriers injection and bad long-term stability of the device.

3.2. Analysis of the Surface of Liq Injecting Layer Deposited on ITO Using AFM

Figure 1 shows the surface morphology of Liq/ITO by AFM. From this figure, we can see that Liq molecules form an island-like structure, and the distribution of these island is uniform, so the surface of Liq is complanate. Though the growth of Liq big-area islands appears on some places, it covers basically the defects on ITO and the number of pinholes is small.
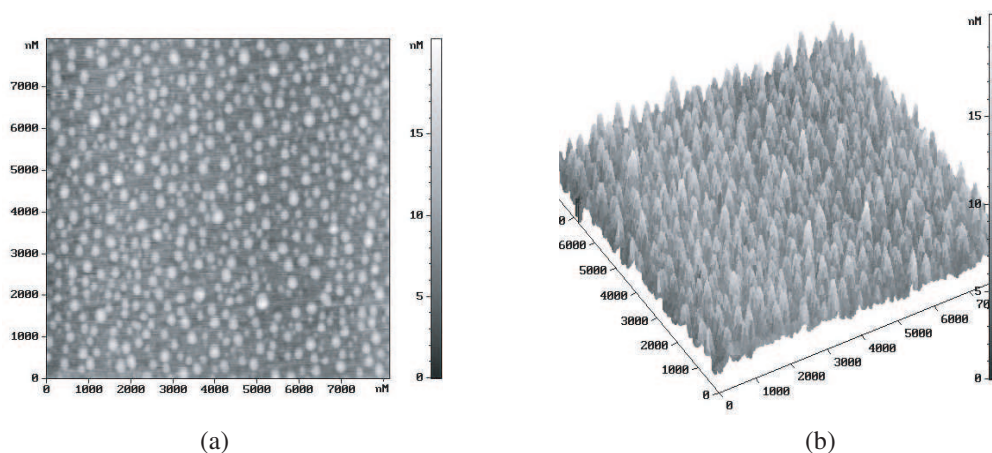

(a)　　　　　　　　　　　　　　　　　　　(b)

Figure 1: AFM micrographs of Liq/ITO surface, (a) the lateral force mode, (b) the topographic mode.

3.3. Analysis of the Surface and Interface of Liq/ITO Using XPS

The whole XPS scanning spectrum of the Liq/ITO surface is shown in Fig. 2, and its peaks correspond to the electron states of Li 1s, C 1s, N 1s and O 1s. The facts that In 3d and Sn 3d peaks are extremely weak indicate ITO film is completely covered by Liq layer with almost no cracks.

The Li 1s fine XPS spectrum of the sample is given in Fig. 3. In this figure, the peak of Li 1s spectrum is located at 55.4 eV, corresponding to the binding energy of Li$^+$. The results demonstrate that the Li 1s spectrum peak gradually become weaker as the sputtering time increases, indicating that the Liq layer gradually becomes thinner and the Li atoms decrease. As the sputtering time increases, the Li core-level has about a 0.2 eV shift to higher binding energy, reflecting the energy-level bending in Li at Liq/ITO interface. Furthermore, the single feature of the Li 1s peak becomes two peaks. New peak or broadening are observed in Li 1s spectrum, indicating there is the interaction of Li atoms with ITO.
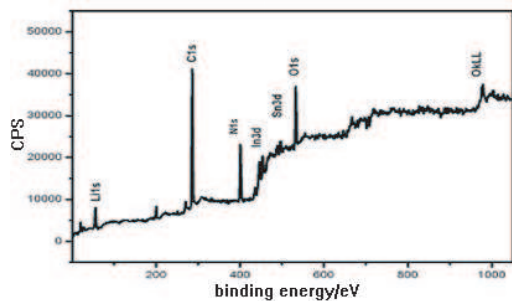
Figure 2: XPS whole scan spectra of Liq/ITO surface.
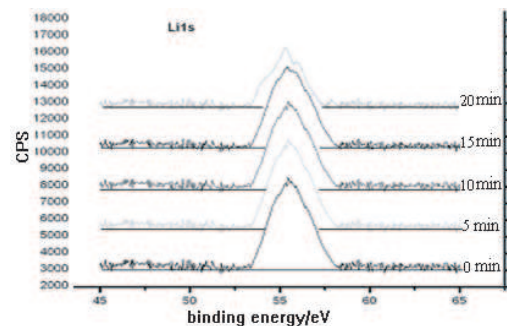
Figure 3: The evolution of the XPS fine spectra of Li 1s of the sample as the sputtering time increases.

In Fig. 4, we also can find that there are three peaks in the C 1s spectrum, with the main peak locating at 284.7 eV corresponding to the binding energy of carbon in C-C and C-H bonds of the quinolate rings in the Liq molecule [15, 16]. There are two components at 286.0 and 287.4 eV, which can be attributed to the C-O bonds (286.1 eV) and C-N=C bonds (287.0 eV). The evolution behavior of the Cls peak area differs from the Li 1s, with the increase of the time, the C 1s peak area first increases gradually and then reduces slowly. This is because the ITO-coated glass substrates were cleaned ultrasonically in the organic solvent, and there was considerable carbon contamination remaining on the ITO film surface. In general, if the carbon contamination on the ITO film surface is only considered the number of C atoms should decrease continuously as the depth increases. So we have to consider the carbon contamination on the ITO film surface. Cleaning procedure can only partly diminish and not completely decrease the carbon contamination. At the same time, according to different binding energies of C atoms, we can distinguish between carbon that migrates from the ITO into the Liq and the carbon already found in the Liq. The number of C atoms diffused from the ITO surface into Liq increases gradually with increment of C 1s peak area. At the same time, the carbon contamination was removed from the Liq and ITO by argon ions sputtering, termed as the selective sputtering effect of argon ions [17], so the C 1s peak area does not increase continuously.
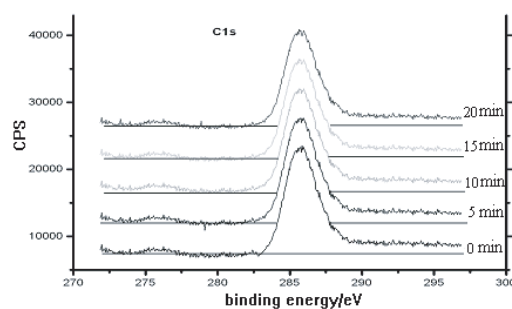

Figure 4: The evolution of the XPS fine spectra of C 1s of the sample as the sputtering time increases.
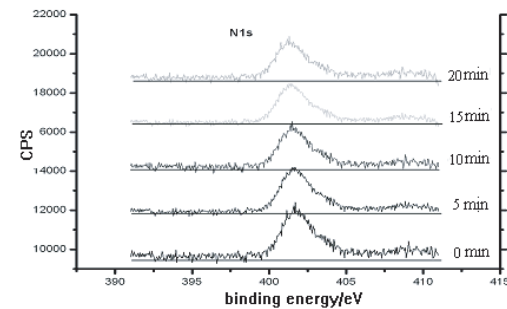
Figure 5: The evolution of the XPS fine spectra of N 1s of the sample as the sputtering time increases.

From Fig. 5, we can find the fine spectrum of N 1s is comprised of only one component. The core-level of N 1s locates at 401.6 eV corresponding to the binding energy of nitrogen in C-N bonds of the quinolate rings in the Liq [18]. It is similar to the Li 1s spectrum that the N 1s spectrum also becomes weaker with the increasing sputtering time. However, the N 1s spectrum gradually becomes more irregular as the sputtering time increases, which may be resulted from the N atoms interaction with O, In and Sn atoms diffused into the Liq.

Figure 6 show the evolution of the XPS fine spectrum of O 1s of the sample as the sputtering time increases. The main peak at 533.6 eV corresponds to the binding energy of oxygen in C-O bonds, while the other peak locates at about 534.1 eV, which may be caused by the absorbed O_2 and H_2O. As the Liq layer becomes thinner, the absorbed O_2 and H_2O reduce, so the O 1s peak area decreases drastically first. But as sputtering time increases, more and more O atoms in the ITO film are excited, which results in substantial increases of the O 1s peak area when the sputtering time is ≥ 10 min. The O 1s peak slightly shifts to lower binding energy because of the transmission of more secondary electrons of the O atoms in ITO, and O atom in In_2O_3 and SnO_2 with binding energies of 529.8 and 530.1 eV, respectively, which are lower than that in Liq molecules. The fact demonstrates that the addition of Liq can restrain the diffusion of chemical constituents from ITO to electron transport layer in multi-structure inverted OLEDs

Figures 7 and 8 show the evolution of the XPS fine spectra of In 3d and Sn 3d of the sample as the sputtering time increases. The peak of In 3d and Sn 3d are both weak for the surface, which further accounts for the covering effect of Liq to the defects on ITO surface. The peak at 447.1 eV corresponds to the binding energy of indium in In-O bonds in In_2O_3.
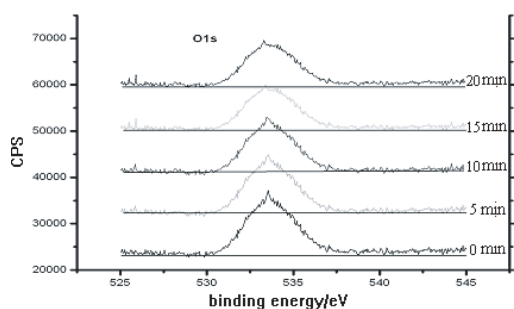

Figure 6: The evolution of the XPS fine spectra of O 1s of the sample as the sputtering time increases.
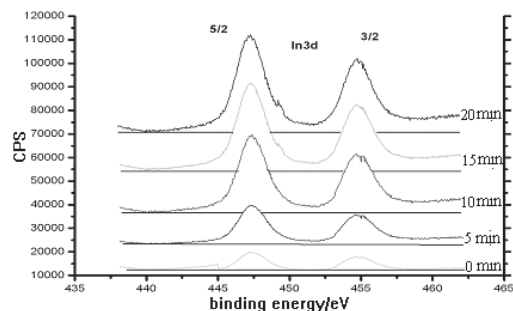
Figure 7: The evolution of the XPS fine spectra of In 3d of the sample as the sputtering time increases.

In the Sn 3d spectrum (Fig. 8), the peak of Sn 3d5/2 is located at 488.6 eV corresponds to the binding energy of tin in Sn-O bonds in SnO_2. In the process of argon ions sputtering, the signal of In 3d secondary electrons stronger and stronger because the Liq layer become thinner and thinner, and increasing In 3d secondary electrons are excited. The In indium 3d5/2 peak locates at about 447.1 eV, corresponding to the binding energy of In atoms in In_2O_3. As sputtering time increases, the In 3d spectrum has no significant difference in binding energy and particularly in the shape of peak, which implies that the ITO structure is not significantly modified by argon ions sputtering and ITO film has stable property. The peak of Sn 3d is relatively weak, The Sn 3d5/2 peak locates at about 488.8 eV corresponding to the binding energy of Sn atoms in SnO_2 [19]. As sputtering time
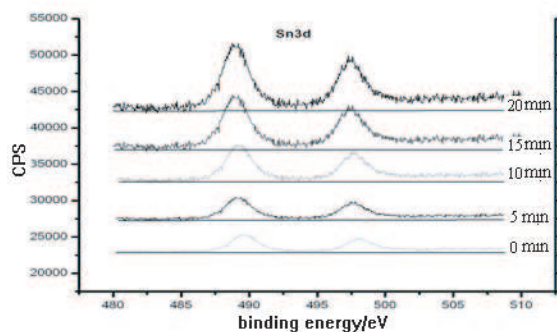

Figure 8: The evolution of the XPS fine spectra of Sn 3d of the sample as the sputtering time increases.

increases, the Sn 3d spectrum also has no significant difference in binding energy and particularly in the shape of peak. However, the excitation of Sn atoms is much weaker than that of In, so the peak of Sn 3d is much lower than that of In 3d. At the same time, the selective sputtering effect of argon ions make the O that exist in ITO film decrease gradually, in which the interaction of O atoms with Li, C and N become stronger, and the interaction of O atoms with In and Sn atoms gradually is declining, with the result of the In_2O_3 and SnO_2 turning into suboxides or metal states In and Sn [20], so that the binding energy of In and Sn atoms decreases.

4. CONCLUSIONS

In summary, we have investigation that the surface and interface electron states of the Liq/ITO sample with the utilization of AFM and XPS technology. For the surface of the Liq/ITO thin film, AFM results suggest that the surface is complanate, the Liq growth is uniform and defects cover basically the surface of ITO, and the number of pinholes is small. And these can also be testified from the In and Sn peaks are extremely weak in the whole XPS scanning spectrum of the Liq/ITO surface. Through the evolution of the XPS whole scanning spectrum recorded at the surface of the sample as the sputtering time increases, the peak area of C atoms increases first and then decreases slowly because of the carbon contamination. At the interface, N interacts with O, In and Sn respectively. Furthermore, the single feature of the Li 1s peak becomes two peaks, indicating there is the interaction of Li atoms with ITO. These reactions have caused a chemical change in Liq, which might be an important reason that Liq layer can enhance the injection of electron. Besides these, the layer of Liq is found to behave as an obstacle to the diffusion of O atoms from ITO film. So the addition of Liq injection layer can restrain the diffusion of chemical constituents from ITO to electron transport layer, decreasing the number of luminescence quenching centers, so the carriers injection efficiency and long-term stability of the devices are improved, which benefits the improvement of the performance and useful life time of devices.

REFERENCES

1. Chu, T. Y., J. F. Chen, S. Y. Chen, C. J. Chen, and C. H. Chen, *Appl. Phys. Lett.*, Vol. 89, 053503, 2006.
2. Guo, T. F. , F. S. Yang, and Z. J. Tsai, *Appl. Phys. Lett.*, Vol. 88, 113501, 2006.
3. Uchida, T., T. Mimura, M. Ohtsuka, T. Otomo, M. Ide, A. Shida, and Y. Sawada, *Thin Solid Films*, Vol. 496, 75, 2006.
4. Wang, H. F., L. D. Wang, and Z. X. Wu, *Appl. Phys. Lett.*, Vol. 88, 131113, 2006.
5. Bulovi, V., P. Tian, P. E. Burrows, M. R. Gokhale, and S. R. Forrest, *Appl. Phys. Lett.*, Vol. 70, 2954, 1997.
6. Zhou, X., M. Pfeiffer, J. S. Huang, J. Blochwitz-Nimoth, D. S. Qin, A. Werner, J. Drechsel, B. Maennig, and K. Leo, *Appl. Phys. Lett.*, Vol. 81, 922, 2002.
7. Zheng, X. Y., Y. Z. Wu, R. G. Sun, W. Q. Zhu, X. Y. Jiang, Z. L. Zhang, and S. H. Xu, *Thin Solid Films*, Vol. 478, 252, 2005.
8. Liu, Z. G., O. V. Salata, and M. Nigel, *Synth. Met.*, Vol. 128, 214, 2002.
9. Qu, B., Z. J. Chen, F. Xu, H. Y. Cao, Z. H. Lan, Z. Y. Wang, and Q. H. Gong, *Organic Electronics*, Vol. 8, 529, 2007.
10. Lee, Y. J., J. Y. Kim, S. N. Kwon, C. K. Min, Y. Yi, J. W. Kim, B. K. Koo, and M. P. Hong, *Organic Electronics*, Vol. 9, 407, 2008.
11. Taga, N., H. Odaka, Y. Shigesato, I. Yasui, M. Kamei, and T. E. Haynes, *J. Appl. Phys.*, Vol. 80, 978, 1996.
12. Yun, Z. Z., E. X. Wang, and L. X. Wan, *Surface and Interface Physics*, 40, University of Electronic Science and Technology of China Press, Chengdu, Chinese, 1993.
13. Wu, C. C., C. I. Wu, J. C. Sturm, and A. Kahn, *Appl. Phys. Lett.*, Vol. 70, 1348, 1997.
14. Wu, Z. Q. and B. Wang, *Film Growth*, 179, Science Press, Beijing, Chinese, 2001.

15. Le, Q. T., F. M. Avendano, E. W. Forsythe, L. Yan, C. W. Tang, and Y. Gao, *J. Vac. Sci. Tech. A*, Vol. 17, 2314, 1999.

16. Watts, J. F. and J. E. Castle, *J. Mater. Sci.*, Vol. 19, 2259, 1984.

17. Guo, Y. C. and Z. X. Wang, *The Physics of Amorphous State*, 249, Science Press, Beijing, Chinese, 1984.

18. Marsh, J., L. Minel, and M. G. Barthes-Labrousse, *Appl. Surf. Sci.*, Vol. 133, 270, 1998.

19. Ou, G. P., Z. Song, Y. Y. Wu, X. Q. Chen, and F. J. Zhang, *Chin. Phys.*, Vol. 15, 1296, 2006.

20. Liu, L. M. and Y. Q. Xiong, *Acta Physica Sinica*, Vol. 49, 1883, 2000.

Low Cost 1×2 Acrylic-based Plastic Optical Fiber Coupler with Hollow Taper Waveguide

Abang Annuar Ehsan[1], **Sahbudin Shaari**[1], **and Mohd Kamil Abd. Rahman**[2]

[1]Institute of Microengineering and Nanoelectronics (IMEN), Universiti Kebangsaan Malaysia
43600 UKM, Bangi, Selangor, Malaysia
[2]Faculty of Applied Science, Universiti Teknologi MARA
40450 Shah Alam, Selangor, Malaysia

Abstract— A 1×2 Plastic optical fiber (POF) Y-coupler has been designed and fabricated using a simple acrylic (PMMA) mold insert. The device is composed of three segments: an input POF fiber, an intermediate hollow taper waveguide and output POF fibers. The acrylic mold insert has been fabricated using EGX-400 desktop engraver machine with a spindle speed of 15 K rpm and feed rate of 5 mm/sec. The engraved regions which is a form of U-groove allows 1 mm core step index PMMA POF fibers to be slotted into the mold insert. The short POF fibers at the input and output ends are slotted inside the mold insert before the interfaces of the taper waveguide. A top acrylic plate is then placed on top of the fabricated device and sealed. The final device has been tested for both splitter and combiner operations for an effective power of 1 mW. The device has an insertion loss of 10.48 dB. In the splitter operation, the device has a splitting ratio of $52 : 48$. In the combiner operation, the combined power is -11.15 dB for input power of -11.90 dB and -12.05 dB.

1. INTRODUCTION

Plastic optical Fiber (POF) is a well known medium for short distance communication application and it is finally making a way into the optical fiber market. It does not require any expensive or special tool, no special training and no long technical procedures to operate. POF is basically an optical fiber with large-core size with multimode characteristics, low cost, and robust characteristics. In addition to short distance communication, POF is also being used in signaling, lighting and decoration system. Other niche application of POF are in the automotive, entertainment, and sensor industries [1]. In all of these applications, it is necessary to split or combine the optical signals using passive optical components.

Among the passive components for POF applications, optical coupler plays an important role that is borne out by the availability of a complete line of products. There have been many techniques of assembling POF couplers. These techniques include (i) twisting and fusion (ii) side polishing (iii) chemical etching (iv) cutting and gluing (v) thermal deformation (vi) molding (vii) biconical body and (viii) reflective body [2].

The 1×2 POF coupler which has been fabricated here may be an alternative to that of the optical 1×2 POF coupler which was fabricated by IMM (*Institut für Mikrotechnik Mainz*) in Germany. The insertion loss of the device by IMM is about 6 dB [3]. The fabrication technique requires several additional steps including laser machining (excimer laser) for PMMA resist patterning and injection molding for moulding. A similar device with circular cross section have also been fabricated by Takezawa et al. [4] which showed low excess loss (1.91 dB). Nevertheless, the device requires the use of injection molding tool which can increase the cost of making these devices. Hollow waveguides on the other hand are waveguides where the inner section is hollowed. They have been previously used in laser light delivery system for medical application [5, 6] where the radiation wavelengths used are greater than 2 μm [6]. These devices are also being used for photonics integrated circuits where temperature insensitivity is required [7, 8].

A 1×2 POF coupler has been designed using a simple acrylic-based mold insert. The POF coupler device is composed of three sections: an input POF fiber, an intermediate hollow taper waveguide and output POF fibers. Finally, based on the CAD design, mold insert of the device is fabricated using a desktop engraver on an acrylic block. POF cable of 1 mm core size is inserted at the input and output branches of the coupler. The POF coupler here is part of the passive components that are being designed and fabricated to be used in a new portable optical access-card system [9, 10]. This 1×2 POF coupler will be one part of the optical code generating device where the other part will be the 1×2 asymmetric couplers. By using low-cost arcylic material which can be easily obtained in large bulk sheet and low-cost desktop engraver system, we are able

to fabricate POF coupler with very minimum cost. The design and fabrication processes shown in this paper illustrate the potential of low-cost acrylic material and a simple engraving technique for producing POF coupler. Nevertheless, some modifications are required in order to improve the optical performance of the devices which will be illustrated also along in this paper.

2. POF COUPLER DESIGN

The 1×2 coupler is the simplest coupler design where the input optical power is split into two. The basic coupler design will utilize a simple 1×2 Y-coupler which is shown in Fig. 1. In this coupler design, the splitting angle is set large at an angle of 53°, as shown in this figure.
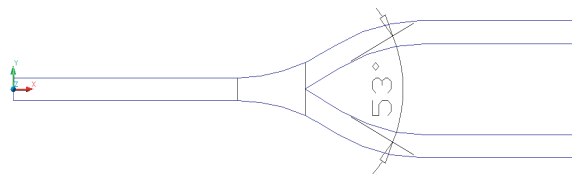
Figure 1: CAD design of 1×2 POF Y-coupler with large splitting angle.

The input and output waveguides are constructed using POF fibers which are slotted into a Y-shaped mold insert, shown in Fig. 2. The POF fibers are slotted until the fibers are positioned just before the taper waveguide region as shown in this figure.
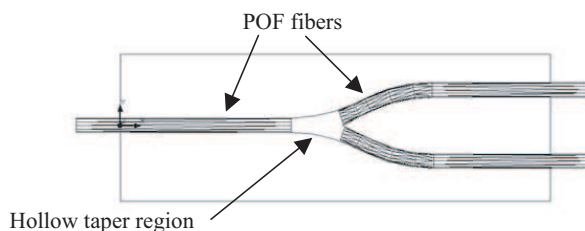
Figure 2: 1×2 POF Y-coupler block layout.

The slot width of the mold insert has been set at $1\,\mathrm{mm}$ which allow the POF fiber to fit in firmly. The POF fibers used are standard SI POF with NA of 0.5, core size of $980\,\mu\mathrm{m}$, refractive indices of the core and cladding are 1.49 and 1.42 respectively. Due to the hollow structure of the taper waveguide region, non-sequential ray tracing will not give a good result of the device optical characteristics based simply on the acrylic material itself. However, the optical characteristics of the hollow taper waveguide region can be modified by simply filling this space with low-cost UV curable glue, normally used for connecting fibers and are easily available. The ray tracing results for the UV-glue filled taper waveguide region will be shown briefly to illustrate how the simple optical device can be constructed and ray traced easily. Fig. 3 shows the device construction of the 1×2 POF coupler with the UV-glue filled taper waveguide region and the ray tracing results for this device is shown in Fig. 4.
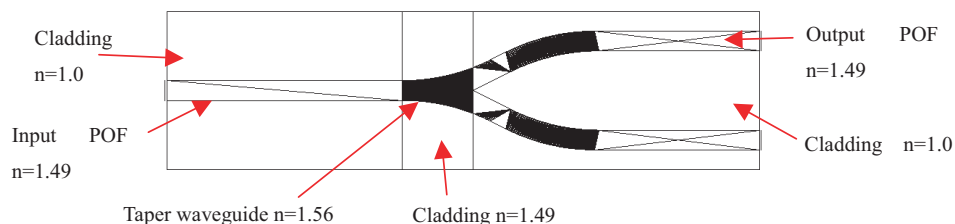

Figure 3: 1×2 POF Y-coupler block layout with UV-glue filled taper waveguide region.

The output power for the POF couplers have been obtained from the ray tracing plot. The output signal measured at the output ports of the 1×2 POF coupler is $0.24\,\mathrm{mW}$ and $0.25\,\mathrm{mW}$. The insertion loss of this device is about $6\,\mathrm{dB}$ whereas the excess loss of this device is about $3\,\mathrm{dB}$.

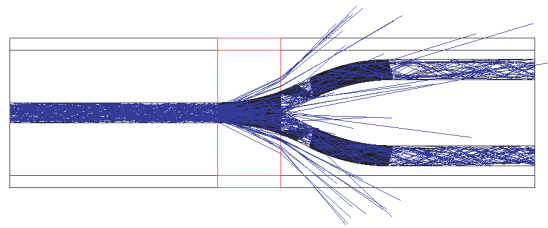Figure 4: 1×2 POF Y-coupler ray tracing diagram.

3. POF COUPLER FABRICATION AND MEASUREMENT

In this project, a rigid mold insert is designed and fabricated using a micro engraving tool. We have used acrylic material as the main substrate and cladding region for the taper waveguide. The RI of the acrylic material used is about 1.49. The waveguide design is then engraved onto the acrylic substrate using EGX-400 desktop engraver tool.

The fabrication start with the acrylic sample positioned onto the workpiece of the machine. The machine parameters are configured using a CAD/CAM machining software. Milling tool size of 0.5 mm is used and spindle speed of 15,000 rpm and feed rate of 5 mm/sec have been utilized. After the mold insert has been fabricated, short SI POF fibers (10 cm) are inserted into the engraved slots (input and output ports) until the fibers are positioned just before the taper waveguide region. Fig. 5 illustrates the steps taken in the fabrication of the 1×2 POF coupler.

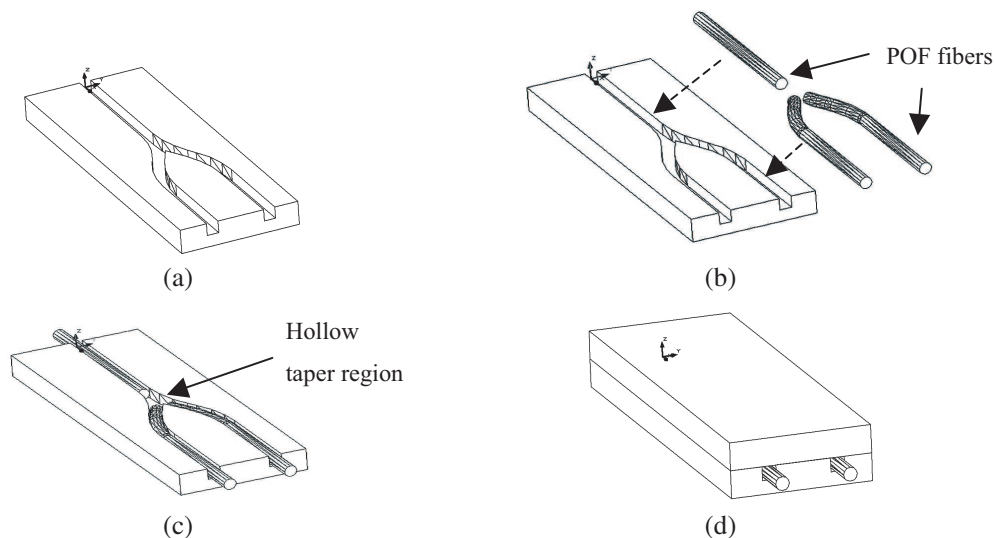Figure 5: 1×2 POF Y-coupler fabrication step, (a) acrylic mold inert with engraved U-grooves, (b) POF fibers insertion, (c) POF fibers alignment, (d) enclosed POF coupler.

The insertion and excess loss of this device has been tested using a light emitting diode (LED) at a wavelength of 650 nm using Advanced Fiber Solution FF-OS417 and optical meter OM210. The effective input power P_{in} is 0 dBm. The output power detected at both output ports are $P_1 = -10.1$ dB and $P_2 = -10.48$ dB. The insertion loss of this device is about 10.48 dB. The effective tap-off ratio or the splitting ratio is 52 : 48. The high loss is expected due to the hollow structure of this device. Similarly in the combiner operation, the device exhibit high loss as expected due to the hollow taper waveguide region. The output power detected for each input port individually are $P_{\text{out (1)}} = -11.90$ dB and $P_{\text{out (2)}} = -12.05$ dB. The output power detected when both input ports are activated are $P_{\text{out (combine)}} = -11.15$ dB. These values correspond to the expected result for a combiner where the combined output power will be halved.

The fabricated devices are shown in Fig. 6. The acrylic-based mold insert for 1×2 POF couplers are shown in Fig. 6(a) and a close up view in Fig. 6(b). The connected 1×2 POF coupler is shown in Fig. 6(c).
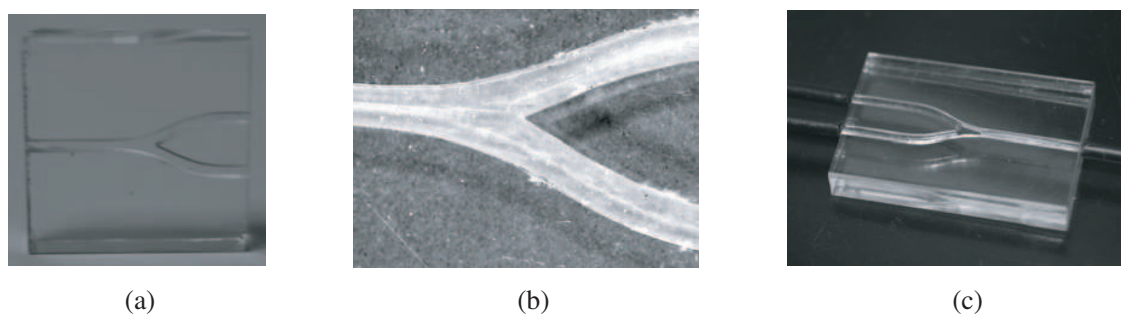
Figure 6: Fabricated 1 × 2 POF coupler, (a) Y-Coupler mold insert, (b) close view of the taper region, (c) Y-coupler with POF fibers.

4. CONCLUSIONS

Low cost 1 × 2 POF coupler with hollow taper waveguide has been designed and fabricated. This device is part of our initial work on an optical code generating device for a portable optical access-card system. The POF coupler has been fabricated using cheap acrylic material and fabricated using a desktop engraving system. The device structure is composed of input POF fiber, middle hollow taper waveguide and output POF fibers where the hollow structure can be modified by filling this area with cheap UV curable glue. The insertion loss of the hollow structure device is still high at 10.48 dB but the device has been shown to work in both splitter and combiner operation.

ACKNOWLEDGMENT

REFERENCES

1. Kawase, L. R. and H. S. Nalwa, *Passive Optical Fiber Devices — Polymer Optical Fibers*, American Scientific Publishers, California, 2004.
2. Ziemann, O., J. Krauser, P. E. Zamzow, and W. Daum, *Passive Components for Optical Fiber — POF Handbook*, 2nd Edition, Springer, Berlin, 2008.
3. Klotzbuecher, T., T. Braune, D. Dadic, M. Sprzagala, and A. Koch, "Fabrication of optical 1 × 2 POF couplers using the laser-LIGA technique," *Proc. SPIE Laser Micromachining for Optoelectronic Device Fabrication*, Vol. 4941, 121–132, Brugge, Belgium, October 2003.
4. Takezawa, Y., S. Akasaka, S. Ohara, T. Ishibashi, H. Asano, and N. Taketani, "Low excess losses in a Y-branching plastic optical waveguide formed through injection molding," *Appl. Opt.*, Vol. 33, No. 12, 2307–2312, 1994.
5. Hongo, A., T. Koike, and T. Suzuki, "Infrared hollow fibers for medical applications," *Hitachi Cable Review*, Vol. 23, 1–5, 2004.
6. Verdaasdonk, R. M. and C. F. P. Swol, "Laser light delivery systems for medical applications," *Phys. Med. Biol.*, Vol. 42, 869–894, 1997.
7. Miura, T., F. Koyama, Y. Aoki, A. Matsutani, and K. Iga, "Hollow optical waveguide for temperature-insensitive photonic integrated circuit," *Jpn. J. Appl. Phys.*, Vol. 40, Part 2, No. 7A, L688–L690, 2001.
8. Miura, T., F. Koyama, and A. Matsutani, "Modeling and fabrication of hollow optical waveguide for photonic integrated circuits," *Jpn. J. Appl. Phys.*, Vol. 41, Part 1, No. 7B, L4785–L4789, 2002.
9. Ehsan, A. A., S. Shaari, and M. K. A. Rahman, "Portable optical security card system," *Malaysia Patent*, File No. PI 20071163, July 2007.
10. Ehsan, A. A., S. Shaari, M. K. A. Rahman, and K. M. R. Kee Zainal Abidin, "Optical code generating device using 1 × N asymmetric hollow waveguide couplers," *Acta Photonica Sinica*, Vol. 37, No. 5, 849–854, 2008.

Analysis of a New Measurement for Electromagnetic Field with Polarization Imformation of Fiber Grating

Yang Su, **Hui Peng**, and **Yuquan Li**

Institute of Communications Engineering

PLA University of Science and Technology, Nanjing, Jiang Su, China

Abstract— In this paper a new magnetic field measurement using polarization imformation of fiber grating including polarization dependent loss (PDL)and different group delay (DGD) is proposed. Through the formula derivation in certain condition, the linear relationship between the peak value of DGD or PDL and magnetic field in measurement range is gained. The simulations and experiments validate this method.

1. INTRODUCTION

Fiber grating is sensitive to the stress, temperature and other environmental factors. It has caused much attention because of its advantages and it has been used widely. There are many papers about measurements of electromagnetic field [1–4]. [1–3] reported the method using magnetostrictive materials. This kind of method has cross-sensitive effect and needs special compensation, what's more it can't measure pulsed electromagnetic field. [4] proposed a direct measurement using magnetic birefringence. But this method is not suitble for weak electromagnetic field because the Verdet constant of fiber is very small. In this paper a new magnetic field measurement using polarization imformation of fiber grating including polarization dependent loss (PDL)and different group delay (DGD) and the simulations and experiments validate this method.

2. THEORETICAL ANALYSIS

For silica, the change in index induced by a magnetic field applied to a fiber is given by

$$n_L - n_R = \frac{VB\lambda}{\pi} \tag{1}$$

where the subscripts L and R represent the index for right and left circularly polarized light at FBG. At a wavelength of $\sim 1.3\,\mu\text{m}$, the Verdet constant is $\sim 8 \times 10^{-5}\,\text{rad/Gm}$. B is the magnetic field value.

$T_L(\lambda)$ and $T_R(\lambda)$ present the transmission power coefficients of the left and the right circularly polarized light at FBG respectively. That is derived in [5],

$$T_{L(R)}(\lambda) = \left| t_{L(R)}(\lambda) \right|^2 = \frac{\alpha_{L(R)}^2}{\sigma_{L(R)}^2 \sinh^2(\alpha_{L(R)}L) + \alpha_{L(R)}^2 \cosh^2(\alpha_{L(R)}L)} \tag{2}$$

where $\alpha_{L(R)} = \sqrt{\kappa^2 - \sigma_{L(R)}^2}$, $\kappa = \pi\nu\delta n/\lambda$, $\sigma_{L(R)} = 2\pi n_{neff}(\frac{1}{\lambda} - \frac{1}{\lambda_{B,L(R)}}) + \frac{2\pi}{\lambda}\delta n$, n_{neff} is the mean effective refractive index of the fiber. σ is the "dc" self-coupling coefficient and κ is the "AC" coupling coefficient. δn is the index modulation of the FBG and ν is the contrast of the interference pattern. L is the grating length. λ_B is the Bragg wavelength,define as $\lambda_B = 2n_{eff}\Lambda$ where Λ is the grating period.

PDL is defined as the maximum change in the transmitted power when the input state of polarization is varied over all polarization states. For FBG,

$$PDL(\lambda) = \left| 10\log_{10}\left(T_L(\lambda)/T_R(\lambda) \right) \right|_{\text{(dB)}} \tag{3}$$

We derived the simple expression of PDL and under the condition of $\sigma_y^2/k^2 \gg 1$, the equation of (3) can approximately given by

$$PDL(\lambda) = 80Bk\frac{n_{eff}V\lambda\Lambda}{(\ln 10)\lambda_B^2 \sigma_L \sigma_R}_{\text{(dB)}} \tag{4}$$

DGD is defined as the difference of group delay of the two polarized modes [6–9]. For FBG the group delay is

$$\tau = \frac{n_{eff}}{c} \frac{\frac{\kappa^2}{\alpha\sigma^2}\sinh(\alpha L)\cosh(\alpha L) - L}{\frac{\kappa^2}{\sigma^2}\cosh^2(\alpha L) - 1} \tag{5}$$

So the DGD of FBG is the difference of the two group delay, that is $\Delta\tau = |\tau_L - \tau_R|$, with Eq. (5), we can get

$$\Delta\tau = |\tau_L - \tau_R| = \left| \frac{n_{eff,L}}{c} \frac{\frac{\kappa^2}{\alpha_L\sigma_L^2}\sinh(\alpha_L L)\cosh(\alpha_L L) - L}{\frac{\kappa^2}{\sigma_L^2}\cosh^2(\alpha_L L) - 1} - \frac{n_{eff,R}}{c} \frac{\frac{\kappa^2}{\alpha_R\sigma_R^2}\sinh(\alpha_R L)\cosh(\alpha_R L) - L}{\frac{\kappa^2}{\sigma_R^2}\cosh^2(\alpha_R L) - 1} \right| \tag{6}$$

On the condition of $\sigma_y^2/k^2 \gg 1$, Eq. (6) can be simplified as

$$\Delta\tau = B\frac{6n_{eff}^2 V\Lambda}{c\lambda_B\sigma_L\sigma_R} \tag{7}$$

In the measure range of magnetic field, σ_L, σ_R are constants approximately. Under those approximate conditions, the linearity between peak value of PDL or DGD and the magnetic field have been find from Eqs. (4) and (7), respectively.

3. SIMULATION ANALYSIS

We design a FBG with 1.455 of n_{eff}, 535 nm of Λ, 40 mm of L and 5×10^{-5} of δn. According to the given data and Eqs. (5) and (8), the simulation results can be get to systematically analyze the wavelength evolution of PDL and DGD.

In this section, we used previous analytical relations to analyse the impact of grating parameters on the wavelength evolution of PDL and DGD. Fig. 1 to Fig. 3 (fo PDL) and Fig. 4 to Fig. 6 (for DGD) represent the wavelength dependency of PDL and DGD as a function of the magnetic field B, the grating length L and the grating modulation index δn, respectively. For all simulation results we chosen $n_{eff} = 1.455$ and $\Lambda = 535$ nm.
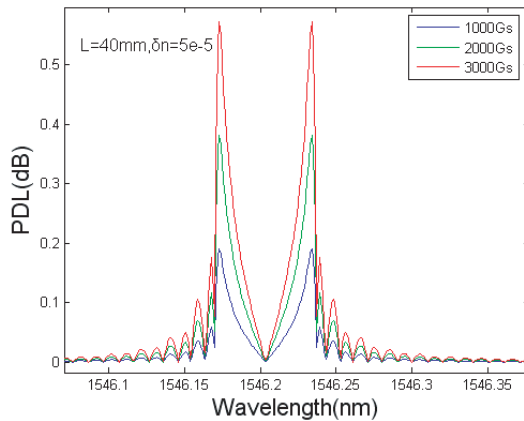

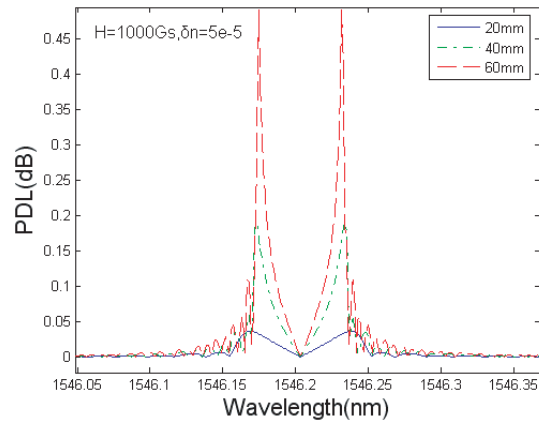Figure 1: PDL versus wavelength at different magnetic field.

Figure 2: PDL versus wavelength at different grating length.

As expected, the increase of B leads to a general increase of PDL and DGD amplitude. Moreover, the magnetic field does not change the shape of the spectrum. The modifications of L and δn have the same effects on the PDL and DGD spectra. For high values of L and δn, DGD and PDL present a greater variation at the limits of the main transmission band. The increase of L and δn leads to very high values of DGD and PDL. So we can design gratings with different length or index modulation to meet the requirements.

Further research find that PDL and DGD are not always have linear relationship with magnetic filed. That is consistent with theoretical analysis. The linearity will tend to saturation when B exceed the measurement range. Fig. 7 shows the PDL and DGD peak versus magnetic field at fiber
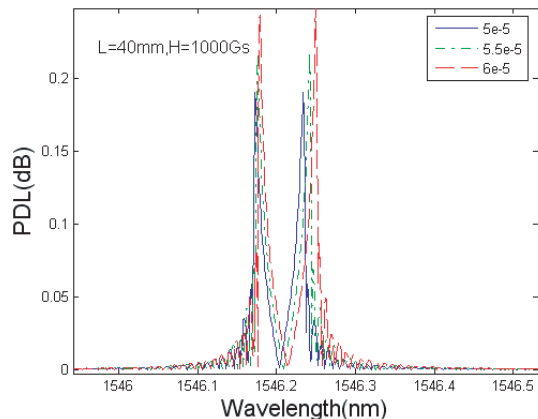
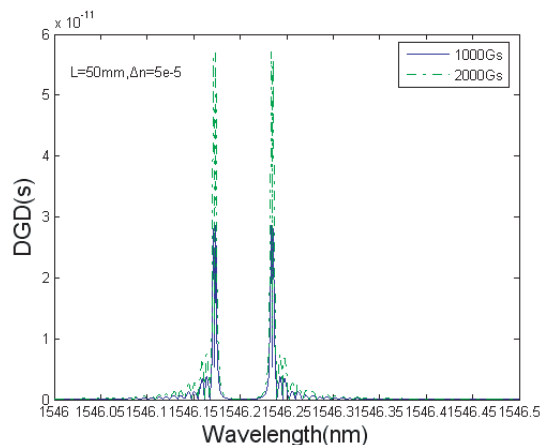Figure 3: PDL versus wavelength at different modulation depth.

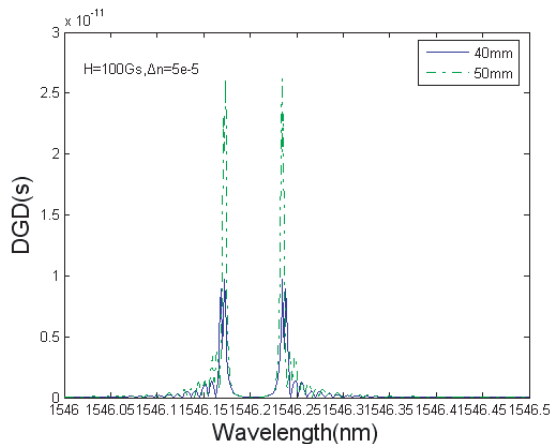Figure 4: DGD versus wavelength at different magnetic field.

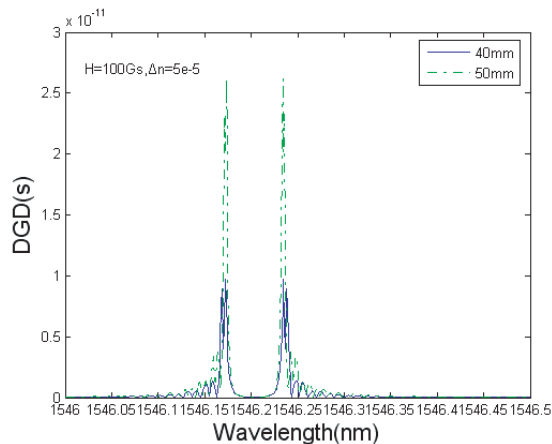Figure 5: DGD versus wavelength at different grating length.

Figure 6: DGD versus wavelength at different modulation depth.

length 40 mm and 50 mm (for PDL) and 50 mm and 60 mm (for DGD). From these figures we can see that the saturated PDL are 30 dB and 35 dB respectively and the saturated DGD are 700 ps and 1300 ps respectively. Thus we can determine the measurement range given designed parameters.
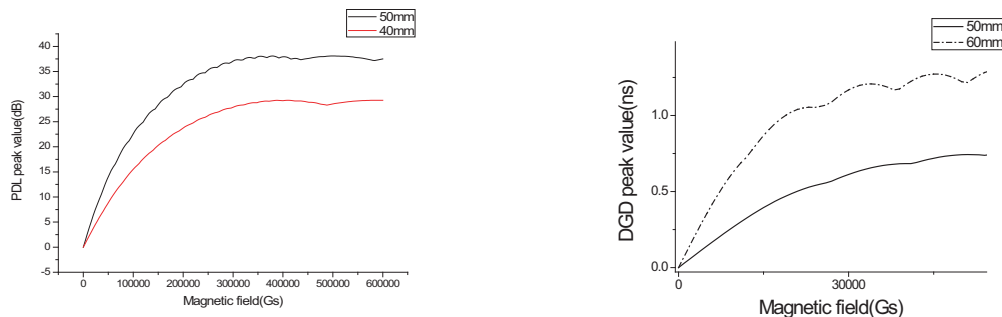

Figure 7: PDL and DGD peak versus magnetic field at different length of fiber grating.

4. EXPERIMENTS

The FBG used in the experiments was fabricated by written into a hydrogen-loaded standard single mode fibre using the phase mask method with a cw frequency-doubled Argon laser. The parameters are: $n_{eff} = 1.455$, $\Lambda = 535$ nm, $\delta n = 2.4 \times 10^{-5}$, $\lambda_B = 1547.54$ nm. Fig. 8 and Fig. 10 depict the PDL and DGD evolutions of the grating at different magnetic field. There are two clear

peak in PDL and DGD. Fig. 9 and Fig. 11 show the difference between the experimental results and simulational results in which the linear relationship of experimental data is shown.. The two curves are parallel approximately and the gap is about 0.3 dB and 13 ps for PDL and DGD respectively which are due to the intrinsic PDL and DGD. The fluctuation of experiment curve is come from two reasons: one is the vibrancy of fiber or grating, the other is that the fiber used to connect grating and OVA is common fiber but not polarization maintaining fiber.
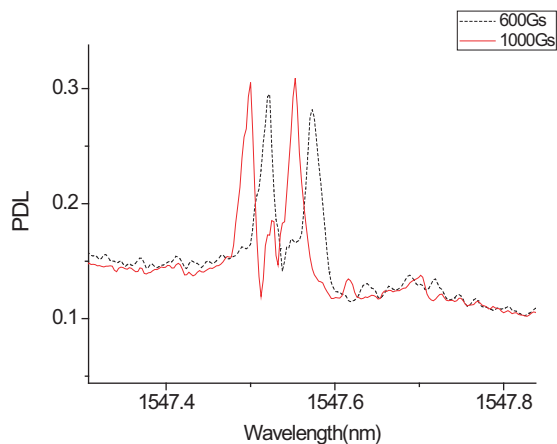

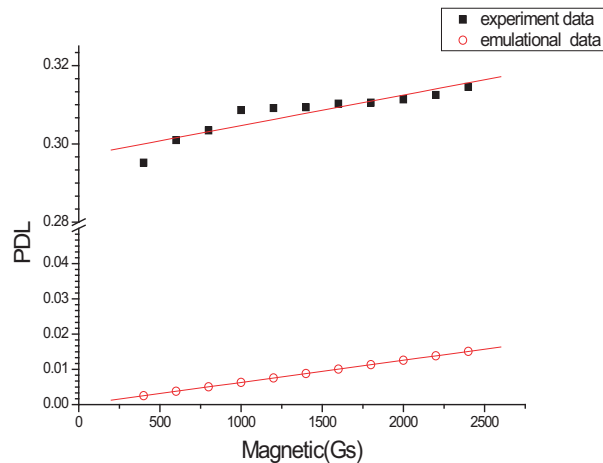Figure 8: The PDL with magnetic field.

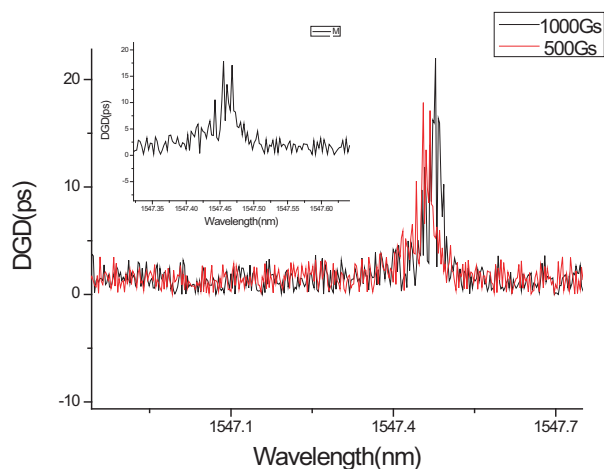Figure 9: Applied magnetic field versus PDL peak.

Figure 10: The DGD spectrum with magnetic field.

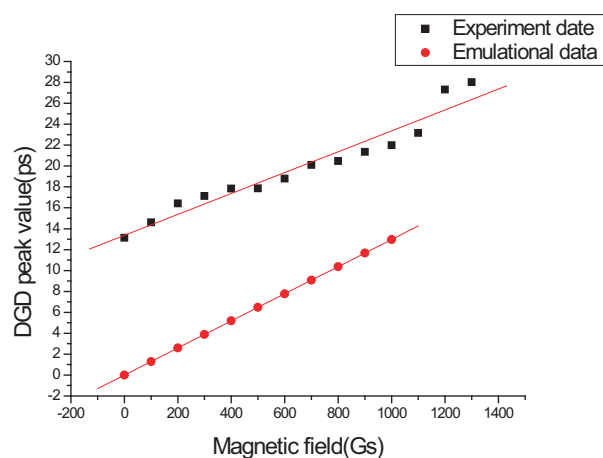
Figure 11: Applied magnetic field versus DGD peak.

In PDL experiments the sensitivity of this sensor is 6.3×10^{-6} dB/Gs when the PDL resolution of OVA is 10^{-5} dB and the minimum value of magnetic field that can be measure is 2 Gs. Using the same OVA in DGD experiment the minimal magnetic field which can be measured is about 0.001 Gs. The simulations and experiments validate this method.

5. CONCLUSIONS

A novel, simple method to measure magnetic field directly with PDL and DGD of FBG is reported. The simulations show the linear relationship between the peak value of polarization information and magnetic field in the measurement range. The effect of grating length and index modulation coefficient to PDL and DGD are researched as well as the measuring range. Simulations and experiments validate this method.

REFERENCES

1. Wang, L. and R. Zhu, "Sensing scheme for magnetic field with fiber bragg grating," *[J] Laser & Infrared*, Vol. 29, No. 4, 238–242, 1999.
2. He, W., W. Shi, and A. Ye, "Realization of long period fiber grating based on magnetic field sending scheme," *[J] Optical Technique*, Vol. 27, No. 6, 545–546, 2001.
3. Zhang, H. and Y. Li, "Magnetic field sensor based on fiber bragg grating," *[J] Journal of PLA University of Science and Technology*, Vol. 5, No. 2, 33–35, 2004.
4. Kersey, A. D. and M. J. Marrone, "Fiber Bragg grating high-magnetic-field probe," *[A] Proc. SPIC, Tenth International Conference on Optical Fiber Sensors*, Vol. 2360, No. 9, 53–56, 1994.
5. Erdogan, T., "Fiber grating spectra," *J. of Lightwave Technol.*, Vol. 15, 1277–1294, 1997.
6. Bette, S., C. Caucheteur, et al., "Spectral characterization of differential group delay in fiber Bragg grating written into Hi-Bi optical fiber," *[C] ECCO 2005 Proceedings*, Vol. 3, paper we4, 131.
7. Bette, S., C. Caucheteur, M. Wuilpart, and P. Megret, "Theoretical and experimental study of differential group delay and polarization dependent loss of study of Bragg gratings written in birefringent fiber," *[J]. Opt. Commun.*, Vol. 269, 331–337, 2007.
8. Lu, P., D. Grobnic, and S. J. Mihailov, "Characterization of the birefringence in fiber Bragg gratings fabricated with an ultrafast-infrared laser," *[J] J. Lightwave. Technol.*, Vol. 25, No. 3, 779–786, 2007.
9. Kaminow, I. P. and T. Li, *Optical Fiber Telecommunication [M]*, Beijng University of Ports and Telecommunication Press, 2006.

Optoelectronic Sensor for NO$_x$ Detection

J. Wojtas[1], Z. Bielecki[1], J. Mikolajczyk[1], M. Nowakowski[1],
T. Stacewicz[2], and A. Czyzewski[3]

[1]Institute of Optoelectronics, Military University of Technology
2 Kaliskiego Str., 00-908 Warsaw, Poland
[2]Institute of Experimental Physics, Warsaw University
69 Hoza Str., 00-681 Warsaw, Poland
[3]Institute of Applied Optics, 18 Kamionkowska Str., 03-805 Warsaw, Poland

Abstract— The paper presents opportunities of Cavity Enhanced Absorption Spectroscopy (CEAS) technique application in nitrogen oxides (NO$_x$) detection. In this method the absorbing gas concentration is determined by decay time measurement of the light pulse trapped in an optical cavity. Measurements are not sensitive to fluctuation of both laser power and photodetector sensitivity. CEAS technique is a modification of Cavity Ring Down Spectroscopy (CRDS) technique. It is based on off-axis arrangement of an optical cavity. NO$_x$ detection is carried out in the visible and infrared range. The signal is registered with a developed low noise photoreceiver. Features of the presented sensor show that it is possible to build a portable trace gases sensor. Its sensitivity could be comparable with that of chemical detectors. Such a system has several advantages: relatively low price, small size and weight, and possibility of detection of other gases.

1. INTRODUCTION

Spectroscopic measurements based on the light absorption belong to the most common methods of matter investigation. Direct absorption spectroscopy is a simple, non-invasive, in situ technique for obtaining information about different species. From an absorption spectrum, quantitative absolute concentrations can be extracted. However, direct absorption spectroscopy suffers from a low sensitivity that limits its extension into several research fields. This low sensitivity results from the fact that a small light attenuation must be measured.

Several experimental schemes can improve the sensitivity, increasing the absorption path length (multipassing, in a White cell or a Herriott cell), and combining direct absorption spectroscopy with a modulation technique. In 1988 O'Keefe and Deacon developed pulsed absorption technique: cavity ring-down spectroscopy — CRDS [1]. In the last decade many various experimental schemes of CRD spectroscopy were elaborated.

Recently, Engeln et al. presented modification of CRDS technique, called Cavity Enhanced Absorption Spectroscopy (CEAS) [2]. It is based on off-axis arrangement of the optical cavity. In this configuration, the light is repeatedly reflected by the mirrors, however, the reflection points are spatially separated (Fig. 1). There are some advantages of this setup. The light passes the resonator many times before the beams overlap. Due to that, either the dense mode structure of low finesse occurs or the mode structure does not establish at all. Avoiding the light interference, it provide eliminating sharp resonances of the cavity, so the problems connected with their coincidence with laser modes and sharp absorption lines do not occur. In these conditions, all wavelengths and phase information of the electric field can be neglected, leading to description of optical intensity only.
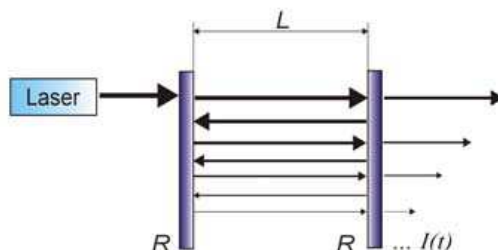

Figure 1: Idea of CEAS method (R — mirrors refraction coefficient, $I(t)$ — light intensity, L — resonator length).

Moreover, the off-axis design eliminates optical feedback from the cavity to the light source (which is especially important for diode lasers). Then in these configurations the light is many times reflected by the mirrors and it fills the whole volume of the cavity. At least in comparison with ordinary CDRS, the integrating spectroscopy with off-axis cavity adjusting is much less sensitive for the cavity misalignment caused, e.g., by the refractive index fluctuations due to turbulences or small mechanical instabilities.

Nitrogen oxides are ones of the most important factors of atmosphere quality. At present, NO_x are commonly detected by using the methods based on chemiluminescences. Their sensitivities reaches single ppb, while e.g., common ambient NO_2 concentration is about 20 ppb. However for many applications, especially in medicine and explosives materials detections, such precision is not sufficient. Moreover the price of such detectors is rather high. Recent development of GaN and InGaN laser diodes working in blue-violet spectral region, where high absorption of NO_x occurs, provides opportunity to construct fully optoelectronic detector. Due to that CEAS technique can be applied to NO_x monitoring.

2. ANALYSIS

In CEAS method, the pulse of the laser light is injected into optical cavity (resonator) equipped with spherical and high reflectance mirrors. The pulse yields to multiple reflections in the resonator. After each reflection, part of the laser light leaves resonator because of lack of 100% mirrors reflectivity. The part of light outgoing from cavity is registered by a photodetector, the most frequently by the photomultiplier tube (PMT). The electric signal from the PMT can be observed and archived e.g., by the digital oscilloscope (Fig. 2).
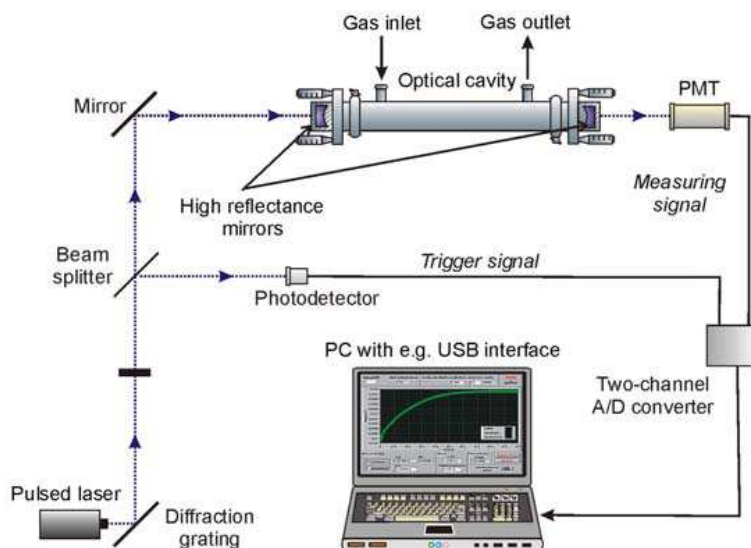

Figure 2: Typical experimental setup.

The amplitude of this signal exponentially decreases

$$I(t) = I_0 e^{\frac{[(1-R)+\alpha L]c}{L}t} = I_0 e^{-\frac{t}{\tau}}, \tag{1}$$

where I_0 is the initial intensity, c denotes the light speed, α is the absorption coefficient. Speed of the decay intensity $I(t)$ of the pulse of the laser light is dependent on mirrors reflectivity coefficient R, resonator length L, diffraction losses, and extinction, that is absorption and scattering of a light in absorber filled cavity.

The cavity losses are inversely proportional to decay time of exponential signal in the cavity τ, and the maximum intensity in the cavity is directly proportional to τ. Engeln et al. are shown that time-integrated intensity of the light leaking out of the cavity is linearly proportional to the cavity decay time τ. Therefore, by measuring of radiation decay time constant τ, determination of the absorption coefficient is possible [3],

$$\tau = \frac{L}{c \cdot [(1-R) + \alpha L]}. \tag{2}$$

The decay time τ is measured once when the cavity is empty ($\alpha = 0$), and next when the cavity is filled with the absorber ($\alpha > 0$). By comparison of decay times for these two cases, a value of the absorber concentration N can be found

$$N = \frac{\alpha}{\sigma} = \frac{1}{\sigma \cdot c} \left(\frac{1}{\tau} - \frac{1}{\tau_0} \right), \tag{3}$$

where σ denotes the absorption cross section, while τ_0 and τ are the time constants of the exponential decay of the output signal for empty resonator and for the resonator filled with the absorber, respectively.

Assuming that relative precision of τ determination is equal to

$$F = \frac{\tau_0 - \tau}{\tau_0}, \tag{4}$$

detectable concentration limit N_L can be described by the formula

$$N_L = \frac{F}{c\sigma\tau_0}. \tag{5}$$

3. EXPERIMENTS

In the researches we used the experimental scheme presented in Fig. 2. The resonator consisted of two mirrors (Los Gatos) which reflectivities R reached value better than 0.99992 at the wavelength of interest. The distance between the mirrors was 60 cm. During investigation 200 mW pulsed diode laser (TopGaN) working at 414 nm, and dye laser with rhodamine as lasing medium and Nd : YAG laser as a pumped source were used. The diode generated pulses of radiation which FWHM duration time was about 50 ns and the repetition rate was 1 KHz, and ca. 10 Hz in the case of dye laser. The laser radiation was directed into the cavity using the diffraction grating and the mirror. The use of the diffraction grating eliminated the broadband fluorescence of the diode, which affected the output signal. The cavity was also connected with the gas mixing system (two mass flow controllers: β-ERG) supplied from bottle with gas mixture and source of pure nitrogen. Intensity leaking the resonator through the rear mirror was measured by a photomultiplier connected with computer through A/C transient digitizer and USB interface. After averaging of the signal over 100000 pulses, the precision of the decay time determination about $F = 0.1\%$ was achieved (Fig. 3). It corresponds with the NO_2 detection limit few hundreds of ppt (10^{-12}).

In the case of nitrogen dioxide detection we used optical system, which wavelength was well matched to the NO_2 absorption spectrum (Fig. 4). As a light source pulsed blue diode laser (414 nm) was applied. The value of NO_2 absorption cross section σ around this wavelength exhibits several minima and maxima, but varying around value of $6 \times 10^{-19}\,cm^2$ [4].

The measurement with a good detection limit requires also good filtration of the investigated air, which is necessary to avoid the light scattering in the aerosol particles as well as the dust deposition on the mirror surfaces. Thanks to optimization of optical system and signal processing system we achieved detection limit better than 0.5 ppb (for $\sigma = 6 \times 10^{-19}\,cm^{-2}$) [5]. After averaging the signal

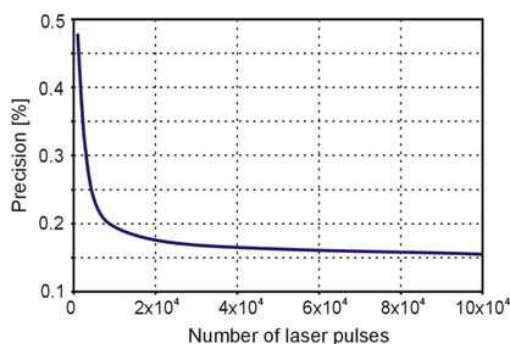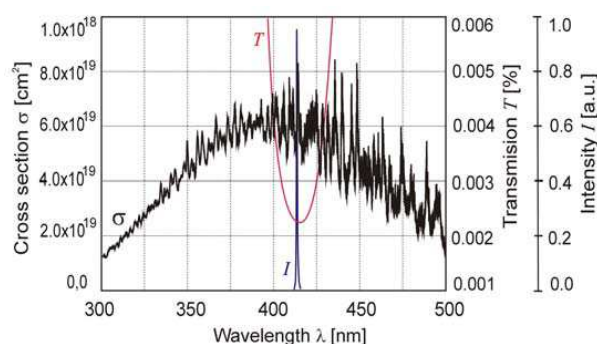Figure 3: Precision of decay time determination as a function of a pulses number.

Figure 4: Dependence NO_2 absorption cross section σ, mirrors transmission T, and laser intensity I on wavelength λ.

of over 2048 pulses, about $F = 1\%$ precision of the decay time determination was obtained, and after averaging of the signal of over 10000 laser pulses, precision about $F = 0.2\%$ [6].

Our sensor was also used to demonstrate of nitrate (NO_3) absorption spectrum measurements. In this case a dye laser working in the 629 nm–676 nm range was applied. We achieved outcomes, which we are comparable with NO_3 reference spectrum (Fig. 5) [7].

In the frame of our further work we will apply our sensor to nitric oxide (NO) detection. The NO absorption cross section is presented in Fig. 6 [8]. There, QCL laser (e.g., Alpes laser model # sb1770DN) and photoreceiver with detector optimized for wavelength of interest (ca. 5.25 µm) will be used. Such detectors with thermoelectric coolers are available from Vigo Systems (e.g., PVI-2TE-5 type). These detectors are produced using mercury cadmium telluride (MCT) epitaxial techniques.
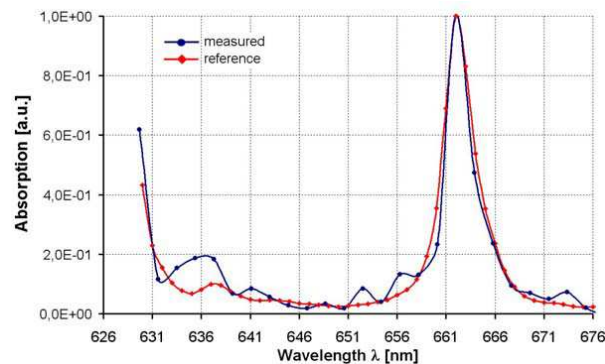

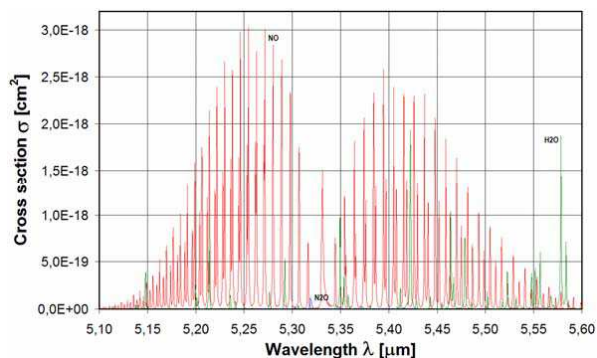Figure 5: Measured and reference NO_3 absorption spectrum.

Figure 6: Dependence NO absorption cross section σ on wavelength λ.

4. CONCLUSIONS

The paper presents spectroscopic technique, CEAS, which was applied to construction of optoelectronic NO_x detection system. The resonator quality was determined by measuring the time of the radiation imprisonment, and therefore is not sensitive for fluctuation of both the laser power and the photodetector sensitivity. The features of constructed detection system show that it is possible to build NO_2 detector, the sensitivity of which could be comparable with that of chemical detectors. Such a kind of system has several advantages for example: relatively low price, small size and weight, it might be also applied to other gas detection.

ACKNOWLEDGMENT

REFERENCES

1. O'Keefe, A. and D. A. Deacon, "Cavity ringdown optical spectrometr for absorption measurements using pulsed laser sources," *Rev. Sci. Instrum.*, Vol. 59, No. 12, 2544–2551, 1988.
2. Engeln, R., G. Berden, R. Peeters, and G. Meier, "Cavity enhanced absorption and cavity enhanced magnetic rotation spectroscopy," *Review of Scientific Instruments*, Vol. 69, No. 11, 3763–3769, 1998.
3. Kasyutich, V. L., C. E. Canosa-Mas, C. Pfrang, S. Vaughan, and R. P. Wayne, "Off-axis continuous — Wave cavity-enhanced absorption spectroscopy of narrow-band and broadband absorbers using red diode lasers," *Appl. Phys. B*, Vol. 75, 755–761, 2002.
4. Merienne, M. F., A. Jenouvrier, and B. Coquart, "The NO_2 absorption spectrum. I: Absorption cross-sections at ambient temperature in the 300–500 nm region," *J. Atmos. Chem.*, Vol. 20, No. 3, 281–297, 1995.
5. Wojtas, J. and Z. Bielecki, "Signal processing system in cavity enhanced spectroscopy," *Opto-Electron. Rev.*, Vol. 16, No. 4, 44–51, 2008.
6. Bielecki, Z., W. Kolosowski, G. Różański, and J. Wojtas, "Nitrogen dioxide detection using optoelectronic sensor," *Computational Methods and Experimental Measurements*, 809–818, WIT Press, 2007.

7. Marinelli, W. J., D. M. Svanson, and H. S. Johnson, "Absorption cross sections and line shape for the NO_3 (0–0) band," *J. Chem. Phys.*, Vol. 76, 2864, 1982.
8. http://www.epa.gov/ttn/emc/ftir/aedcdat1.html.

Continuum Electronic Bound States in Rectangular Quantum Wells and Barriers

E. A. Carrillo-Delgado, **I. Rodríguez-Vargas, and S. J. Vlaev**

Unidad Académica de Física, Universidad Autónoma de Zacatecas
Calzada Solidaridad Esquina Con Paseo La Bufa S/N, Zacatecas, Zacatecas 98060, México

Abstract— We present numerical calculations that support the existence of electronic states confined in the continuous part of the spectrum in single rectangular quantum wells and barriers. We study the conditions necessary for the creation of these states. We find strong energetic and spatial localization of quasi-bound states at high energies in the conduction band. The results can be used in the design of optoelectronic devices that operate on the basis of continuum bound states.

1. INTRODUCTION

The quantum mechanics predicts the existence of quasi-bound states in the continuous part of the spectrum for electronic confinement of exotic potentials [1–3]. Experimentally, these states have been demonstrated in 1992 [4]. These states, also known as continuum bound states or above barrier states, have properties — strong energetic and spatial localization — similar to those of the discrete energy levels. Optical transitions involving electronic states of this type have been found recently in several complex quantum systems [6–8]. The development of new spectroscopies, such as those that work with temporal resolution, opens way to study the quasi-bound states from the experimental standpoint [9, 10]. The aim of this work is to begin systematic, detailed and profound studies about the conditions that generate quasi-bound states. So it would be possible to design optoelectronic devices that operate through optical transitions between these states.

2. MODEL

Earlier, we have been carried out works where we study the quasi-bound states in quantum wells with different potential profiles [11–15]. These studies show that the quasi-bound states exist not only for exotic potentials, but also for typical confinement potentials. In the present paper, the systems under study are a rectangular quantum well $Al_xGa_{1-x}As/GaAs/Al_xGa_{1-x}As$ and a rectangular quantum barrier $GaAs/Al_xGa_{1-x}/GaAs$. In Fig. 1, we show (a) the density of states of the bulk materials $GaAs$ and $Al_xGa_{1-x}As$, and (b) the schematic representation of the formation of the $GaAs/Al_xGa_{1-x}As$ quantum well. The methodology of the study relies on solving the Schrödinger equation within the tight-binding model [16] in terms of the Green functions. The electronic structure calculations are performed within the lines of the spin-dependent sp^3s^* orbital basis and the Surface Green Function Matching method (SGFM). We calculate numerically the density of electronic states (DOS) in the center of the two-dimensional Brillouin zone, around the interval of interest, from -15 to $+15$ eV. We found the energy and spatial distributions of the quasi-bound states.

3. RESULTS AND DISCUSSION

In Fig. 1(a), we present the DOS versus energy for the continuum part of the energy spectrum in the case of a rectangular quantum well with a thickness of 5 ML and potential depth of 282 meV that corresponds to an Aluminum concentration of 0.3. It is possible to see the existence of a state above the barrier at an energy of 4.915 eV. In Fig. 1(b), we show the spatial distribution of the mentioned energy state finding a strong localization that resemblances to a rather large state linked to the discrete spectrum part. At first sight, the electronic state above the barrier seems a bound state, so in order to investigate a little bit more about the nature of this kind of states we calculate the spatial distribution for the above barrier state of Fig. 1 as well as the spatial distribution of the firsts state confined within the discrete spectrum part for the same parameters used in Fig. 1.

To determine the degree of localization of a bound state or quasi-bound state we analyzed its spatial distribution in discrete scale where the unit is one atomic layer (Figs. 2 and 3). In Figs. 1–3 the monolayer is a discrete unit that contains two different atomic layers, one of cation and one of anion. We can see a bound state in the discrete spectrum part as a Bloch state of constant spectral
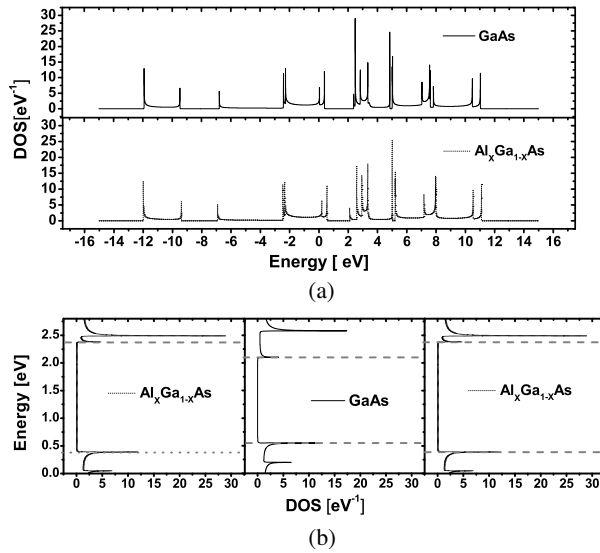
Figure 1: (a) Density of states for bulk $GaAs$ and $Al_xGa_{1-x}As$; (b) Representative sketch of the formation of a well through the band gap discontinuities of the materials.
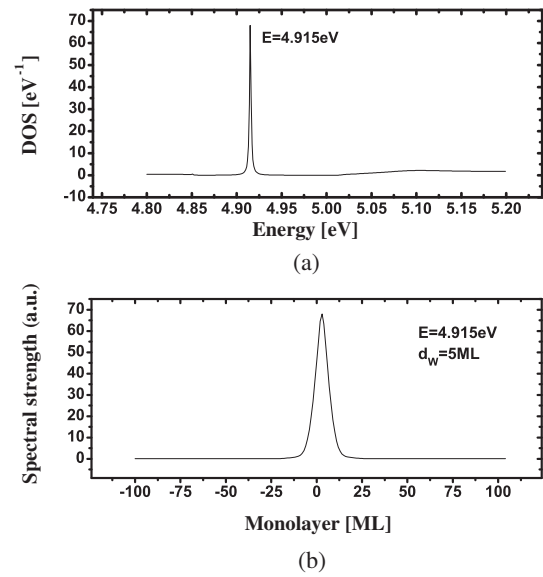

Figure 2: (a) Density of states versus energy above the barrier of a $GaAs/Al_xGa_{1-x}As$ quantum well and (b) spatial distribution of the above barrier state with energy 4.915 eV. The well width and potential depth are 5 ML and 277 meV, respectively. The energy origin is at the valence band of $Al_xGa_{1-x}As$ when $x = 1$.
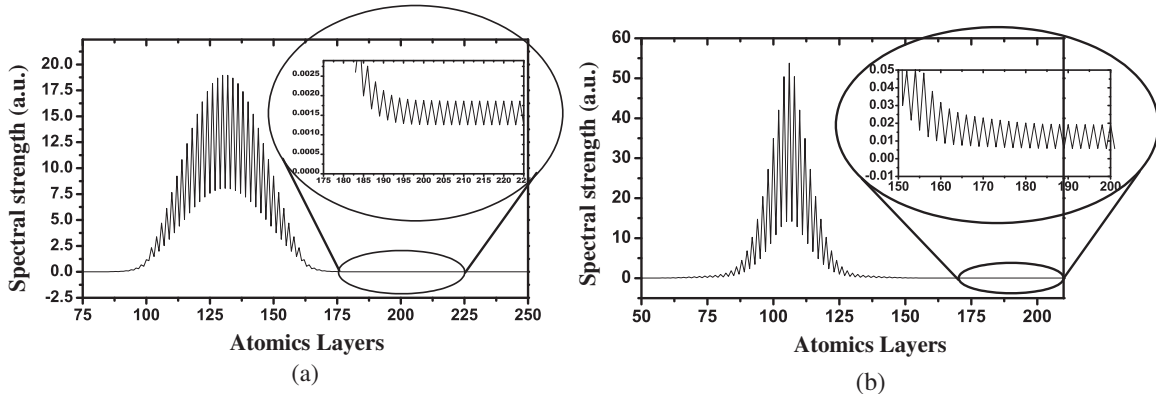

Figure 3: Spatial distribution at atomic scale for (a) the first bound state of the discrete spectrum and (b) the bound state in the continuum for the quantum well of Fig. 1.

strength which oscillates at the atomic scale with a monolayer period, Fig. 3(a). The amplitude of these oscillations changes when we change the imaginary part of the energy in the numerical calculation. In other words, the probability of finding the bound state outside the well tends to zero. The curve in monolayer scale is the envelope of the curve at atomic scale. If the state is bound in the continuum we observe the same behavior (Fig. 3). However, the magnitude of the oscillations is still within the numerical error of the calculation.

In the process of building a barrier or well, as usual, we look at the main gap, but if we consider higher energies we see pseudo-gaps in which other confinement effects can occur (see Fig. 1). The confinement effects in the pseudo-gaps can be radically different from these effects in the main gaps. As an example we consider a potential barrier (in the main gap) formed by $GaAs/Al_xGa_{1-x}As/GaAs$ with the same parameters (well width and potential depth) as in Fig. 1. If we look at the energy interval of 3 to 5 eV it is possible to observe the formation of a "pseudo-well" due to the "pseudo-band gap" discontinuities between $GaAs$ and $Al_xGa_{1-x}As$, Fig. 4. So, a state would be within a "pseudo-well" and would be quasi-bound, see Figs. 2 and 3. We can understand a quasi-bound state as a Bloch state that was confined some time in the well. The state then escapes because the density of states in the pseudo-gap is different from zero. We have found other energy

intervals within "pseudo-wells" that could confine, better or worse, energy states. This could be an explanation of the quasi-bound states observed in single quantum barriers [17, 18]. Although, further studies are needed to understand the exact mechanism that originates the quasi-bound states in single quantum wells and barriers.
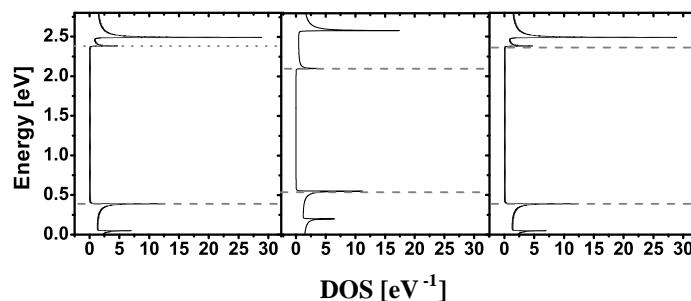

Figure 4: $GaAs/Al_xGa_{1-x}/GaAs$ quantum barrier (at the main gap) forming a "pseudo-well" in the energy interval of 3 to 5 eV. The parameters and energy origin are the same as in Fig. 1.

4. CONCLUSION

We found a way to design quantum wells that generate quasi-bound states for electrons. The procedure is based on the wave nature of the electron. The results will facilitate the search for systems that contain embedded quantum wells between two superlattices where Capasso states appear with spatial localization in the well region and with strong energy localization over the barrier. Optical transitions between quasi-bound states and between bound and quasi-bound states could be of practical interest in different applications of quantum wells.

REFERENCES

1. Bastard, G., "Quantum-size effects in the continuum states of semiconductor quantum wells," *Phys. Rev. B*, Vol. 30, No. 6, 3547–3549, 1984.
2. Weber, T. A. and D. L. Pursey, "Continuum bound states," *Phys. Rev. A*, Vol. 50, No. 6, 4478–4487, 1994.
3. Pursey, D. L. and T. A. Weber, "Bound quantum states with no classical turning points," *Phys. Rev. A*, Vol. 52, No. 5, 4255–4258, 1993.
4. Capasso, F., C. Sirtori, J. Faist, D. L. Sivco, S.-N. G. Chu, and A. Y. Cho, "Observation of an electronic bound states above a potential well," *Nature*, Vol. 358, No. 6387, 565–567, 1992.
5. Rosu, H. C. and J. L. Moran-Lopez, "Stationary states in a potential well," *Quant-ph/0702181v1*, 2007.
6. Bulgakov, E. N., I. Rotter, and A. F. Sadreev, "Comment on 'bonud states eigenenrgy outside and inside the continuum for unstable multilevel systems'," *Phys. Rev. A*, Vol. 75, No. 6, 067401, 2007.
7. Nakamura, H., N. Hatano, S. Garmon, and T. Petrosky, "Quasibound states in the continuum in a two chanel quantum wire with an adatom," *Phys. Rev. Lett.*, Vol. 99, No. 21, 210404, 2007.
8. Voo, K.-K. and C. S. Chu, "Localized states in the continuum in low-dimensional system," *Phys. Rev. B*, Vol. 74, No. 15, 155306, 2006.
9. Levy, M., R. Beserman, R. Kapon, A. Sa'ra, V. Thierry-Mieg, and R. Planel, "Energy-level localization in Bragg-confined asymmetric coupled quantum wells studied by electric field modulation spectroscopy," *Phys. Rev. B*, Vol. 63, No. 7, 075312, 2001.
10. Imam, N., E. N. Glytsis, and T. K. Gaylord, "The quasibound state model for self-consistent characteristics of semiconductor intersubband devices," *Superlattices Microstruct.*, Vol. 29, No. 1, 411–425, 2001.

11. Vlaev, S. J. and V. M. Gonzáles-Robles, "Mean lifetimes of quasi-bound electronic states in single rectangular quantum wells," *Phys. Stat. Sol. (c)*, Vol. 2, No. 10, 3653–3656, 2005.

12. Vlaev, S. J., I. Rodríguez-Vargas, and L. M. Gaggero Sager, "Resonant states in n-type δ-doped *GaAs* quantum wells," *Phys. Stat. Sol. (c)*, Vol. 2, No. 10, 3649–3652, 2005.

13. Vlaev, S. J., I. Rodríguez-Vargas, and L. M. Gaggero-Sager, "Mean life times of quasi-bound states in δ-doped *GaAs* quantum wells," *Microelectron. J.*, Vol. 36, No. 3–6, 347–349, 2005.

14. Jelev-Vlaev, S., J. Madrigal-Melchor, V. M. González-Robles, and D. A. Contreras Solorio, "Quasi-bound electronic states in parabolic *GaAs/AlGaAs* quantum wells and barriers," *Microelectron. J.*, Vol. 39, No. 3–4, 442–446, 2008.

15. Pichardo, X. A., V. M. González-Robles, and S. J. Vlaev, "Mean lifetimes of quasi-bound electronic states in rectangular *GaAs/AlGaAs* barriers," *Microelectron. J.*, Vol. 39, No. 3–4, 414–417, 2008.

16. Vlaev, S., V. R. Velasco, and F. García-Moliner, "Electronic states in graded-composition heterostructures," *Phys. Rev. B*, Vol. 49, No. 16, 11222–11229, 1994.

17. Martelli, F., M. Capizzi, A. Frova, A. Polimeni, F. Sarto, M. R. Bruni, and M. G. Simeone, "Exciton confinement in *GaAs* quantum barriers," *Phys. Rev. B*, Vol. 48, No. 3, 1643–1646, 1993.

18. Luo, H., N. Dai, F. C. Zhang, N. Samarth, M. Dobrowolska, and J. K. Furdyna, "Observation of quasibound states in semiconductor single quantum barriers," *Phys. Rev. Lett.*, Vol. 70, No. 9, 1307–1310, 1993.

Scanning Tunneling Microscope Studies of Co Growth on the Ru(0001) Surface

H. J. Zhang[1], **Y. F. Xu**[1], **X.-S. Wang**[2], **H. F. Wu**[1], **H. Y. Li**[1], **S. N. Bao**[1], **and P. He**[1]

[1]Department of Physics, Zhejiang University, Hangzhou 310027, China
[2]Department of Physics, National University of Singapore
Lower Kent Ridge Road, Singapore 119260, Singapore

Abstract— Co growth on the Ru(0001) surface from submonolayer to multilayer at room temperature and with different annealing temperature treatment were studied by using scanning tunneling microscope (STM). At room temperature, the Co forms a 2-D wetting layer at the first layer and followed with grow in the 3-D clusters mode from the second layer. In multilayer with different annealing temperature treatment case, 3-D Co clusters changed into 3-D islands and their height increased with the annealing temperature and then decreased at even higher annealing temperature. In about one monolayer case, the individual Co 2-D islands coalesced together to form Co wetting layers and the Co layer diffused away from the edges of the Ru steps with their shape changed from uniform to compact as the annealing temperature increased, no 3-D Co islands were observed.

1. INTRODUCTION

Investigations of the magnetic properties of magnetic thin films on nonmagnetic surfaces have been attracted much of interest since they involve the viewpoint of fundamental issues and technological applications such as magnetoelectronics and high-density magnetic storage devices [1–3]. As a first step, understanding of the growth mechanism and formation of magnetic nanostructures will promote to have a better view on the relation between the nanostructures and the magnetic properties of magnetic thin films [4, 5]. Nanostructures of magnetic materials by self-assembly are of great interests to create new functional materials approach to ultrahigh-density storage media. Co magnetic nanodots grow on the Ru(0001) surface, as a typical and interesting self-assembled epitaxial magnetic structures, has been studied by atomic force microscopy (AFM), magnetic force microscopy (MFM), low energy electron microscopy (LEEM), and photoemission electron microscopy (PEEM) [3, 6–10]. This system has been under intense scrutiny for the last several years and its magnetic properties have been mapped very precisely, however the detailed understanding of the growth mechanism of Co on Ru(0001) is still limited.

In this paper, we report on our recent investigations of Co growth on the Ru(0001) surface by using scanning tunneling microscopy (STM). The results showed clearly the structural and morphological evolutions upon Co coverage of the film and annealing of the film at different temperatures.

2. EXPERIMENTAL

The experiments were performed in a multifunctional ultrahigh-vacuum (UHV) VT-SPM system (Omicron) with a base pressure better than 2×10^{-10} mbar. The system has been described in details elsewhere [11–13]. In brief, it consists of a fast entry lock for sample and tip loading, a preparation chamber, an analysis chamber, and a STM/AFM chamber. The system is equipped with a few of resistive-heating and electron-beam-heating evaporators, an electron-bombardment sample heater, an argon-ion sputter gun, a low-energy electron diffraction (LEED) optics and ultraviolet photoemission spectroscopy (UPS) and X-ray photoemission spectroscopy (XPS).

The cleaning of the Ru(0001) surface was achieved by several cycles of argon-ion sputtering and e-beam heat annealing (> 1200 K). The sample cleanliness was verified by LEED, STM and XPS measurements. Co was deposited from pure Co coil, which was cleaned thoroughly with preheating. The deposition rate was about 0.2 ML/min. The sample was kept at room temperature during the growth. All the STM measurements were taken with constant current mode at room temperature.

3. RESULTS AND DISCUSSION

3.1. Co Film Growth at Room Temperature

Figure 1 shows the typical STM images collected on Co films deposited on the Ru(0001) surface at different coverage. For a Co film at a coverage of about 0.1 ML, the STM image (Fig. 1(a))

showed that single-atomic 2-D Co islands, with an upward triangular shape, randomly distributed on the Ru terraces. As the coverage increased, for example, to 0.7 ML (Fig. 2(b)), larger and more irregular 2-D Co islands were formed on the Ru terraces because of Co islands coalesce, and some new Co islands (clusters) started to form on the top of the first Co atomic layer (wetting layer). Further deposition of Co results in 3-D Co clusters growth on the top of Co wetting layer. Fig. 1(c) shows a typical STM image of about 1.5 ML of Co on Ru(0001), the Co clusters are formed on the top of the Co wetting layer, but the density of the clusters is still lower. For Co film at a coverage of 3.2 ML (Fig. 1(d)). The amount of the Co clusters increased, and the size of the clusters becomes smaller, giving rise to more rough surface.

The results showed that, at the present growth conditions, the growth of Co on Ru(0001) in submonolayer regime is in the single atomic-layer growth mode. Thermodynamically, this is understandable considering the surface and interface energies in film growth [11, 14]. A smaller surface free energy of the overlayer and a strong overlayer-substrate binding lead to the first atomic layer coating the whole surface (wetting layer) to provide optimum energy reduction. The surface free energy of Co is $2.709 \, \mathrm{Jm}^{-2}$, which is smaller than the Ru substrate surface free energy of $3.4 \, \mathrm{Jm}^{-2}$ [15]. On the other hand, diffusion and nucleation kinetics of adatoms play an important role in determining the morphology and 2D island shape of the overlayer. For example, formation of fractal islands is typical for the overlayer in the diffusion limited aggregation (DLA) [16, 17] growth in which diffusion of individual atom on both substrate and island terraces is activated whereas atomic migration along island edge is prohibited. If edge-diffusion is also highly activated, the island shape should be compact. More interestingly, as shown in Fig. 1(a), at the lower coverage limit, the Co overlayer grows into the 2-D triangular islands with the edges running along the equivalent [1000] direction, reflecting the threefold symmetry of the Ru(0001) substrate, and formation of these triangular islands indicates the diffusion anisotropy of Co adatoms across the corners on the Ru(0001) substrate, which results in the triangular growth mode [19, 20]. Because of the mismatch between the Co and Ru (about 8%, the lattice constant: $2.5 \, \text{Å}$ for Co while $2.71 \, \text{Å}$ for Ru), the Co film has to via misfit dislocation to release the strain to remain the smooth of the film. In this case, a Stranski-Krastanov (SK) mode with one wetting layers and subsequent 3-D clusters growth occurred.
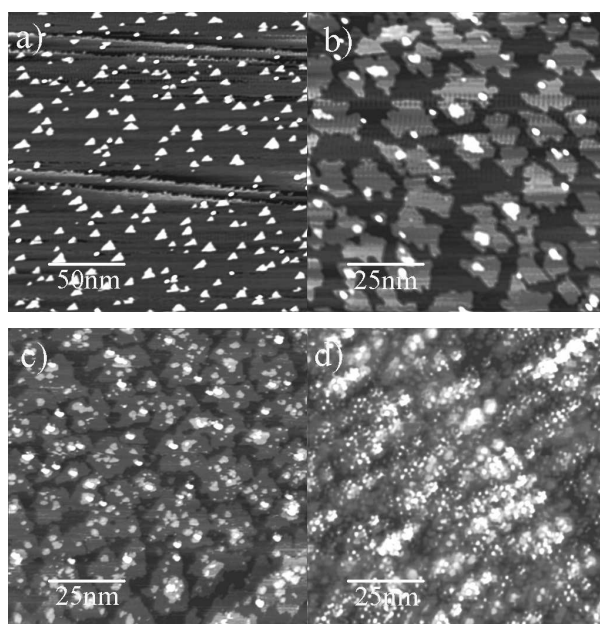
Figure 1: STM images of Co deposited on Ru(0001) surface at the coverage of (a) 0.1 ml ($200 \times 200 \, \mathrm{nm}^2$, $V_{\mathrm{gap}} = -0.475 \, \mathrm{V}$, $I = 4.112 \, \mathrm{nA}$), (b) 0.7 ml ($100 \times 100 \, \mathrm{nm}^2$, $V_{\mathrm{gap}} = -0.526 \, \mathrm{V}$, $I = 0.804 \, \mathrm{nA}$), (c) 1.5 ml ($100 \times 100 \, \mathrm{nm}^2$, $V_{\mathrm{gap}} = 1.423 \, \mathrm{V}$, $I = 0.643 \, \mathrm{nA}$), (d) 3.2 ml ($100 \times 100 \, \mathrm{nm}^2$, $V_{\mathrm{gap}} = -0.072 \, \mathrm{V}$, $I = 4.426 \, \mathrm{nA}$).

After deposition of 3.2 ML Co on Ru(0001) at room temperature, the sample was then be annealed at different temperatures. Fig. 2(a) shows a typical STM image after the sample was annealed at 200°C for 30 min, 3-D interconnected Co islands with flat tops and characteristic shape holes in the islands were observed. The typical height of those islands is about 0.25–1 nm.

Further annealing the sample at 300°C for 30 min leads to significantly thicker, and well-shaped 3-D interconnected islands (see Fig. 2(b)). The holes in the islands grew larger, since some Co atoms diffuse and cooperated into form these thicker 3-D islands (typical height: 1.2 nm). The atomic structure on the topmost surface of those Co island shows good coincidence to bulk Co(0001) (see Fig. 2(g)). After the sample was then annealed at 400°C for 30 min, those 3-D interconnected islands were separated to higher divided 3-D islands and the thickness of these islands increased to about 2.5 nm (Fig. 2(c)). When the annealing temperature was increased even higher, for example, to 500°C, some islands stop growing higher (marked as A in Fig. 2(d)), while the thicknesses of some other islands decreased (marked as B in Fig. 2(d)), indicating desorption of some Co atoms

Figure 2: STM images of Co deposited on Ru(0001) surface at the coverage of 5.1 ml with annealing treatment at the temperature of (a) 200°C for 30 min ($500 \times 500 \, \text{nm}^2$, $V_{\text{gap}} = -0.207 \, \text{V}$, $I = 1.144 \, \text{nA}$), (b) 300°C for 30 min ($1000 \times 1000 \, \text{nm}^2$, $V_{\text{gap}} = -0.429 \, \text{V}$, $I = 1.159 \, \text{nA}$), (c) 400°C for 30 min ($1000 \times 1000 \, \text{nm}^2$, $V_{\text{gap}} = -0.224 \, \text{V}$, $I = 1.144 \, \text{nA}$), (d) 500°C for 30 min ($1000 \times 1000 \, \text{nm}^2$, $V_{\text{gap}} = -0.358 \, \text{V}$, $I = 0.504 \, \text{nA}$), (e) 600°C for 30 min ($1000 \times 1000 \, \text{nm}^2$, $V_{\text{gap}} = -0.156 \, \text{V}$, $I = 1.670 \, \text{nA}$), (f) 700°C for 30 min ($1000 \times 1000 \, \text{nm}^2$, $V_{\text{gap}} = -0.152 \, \text{V}$, $I = 1.886 \, \text{nA}$), (g) atomic structures of the Co islands ($10 \times 10 \, \text{nm}^2$, $V_{\text{gap}} = -0.002 \, \text{V}$, $I = 6.973 \, \text{nA}$).

at this temperature. Further increase the annealing temperature up to 600°C and 700°C results in decrease in the height of Co islands (as shown in Figs. 2(e) and (f)) and change in the shape of those islands from sharp to compact.

At room temperature, a Stranski-Krastanov (SK) mode with one Co wetting layers and subsequent 3-D Co clusters growth on Ru surface occurred, this growth behavior provide the smallest surface energy of Co/Ru system. Meanwhile, annealing the sample provide a additional kinetic energy for the system to overcome the energy barrier and drive away from the local energy minimum at room temperature and develop towards a broader energy landscape. At high annealing temperature, the system could be trapped in another growth behavior to get energy minimum,
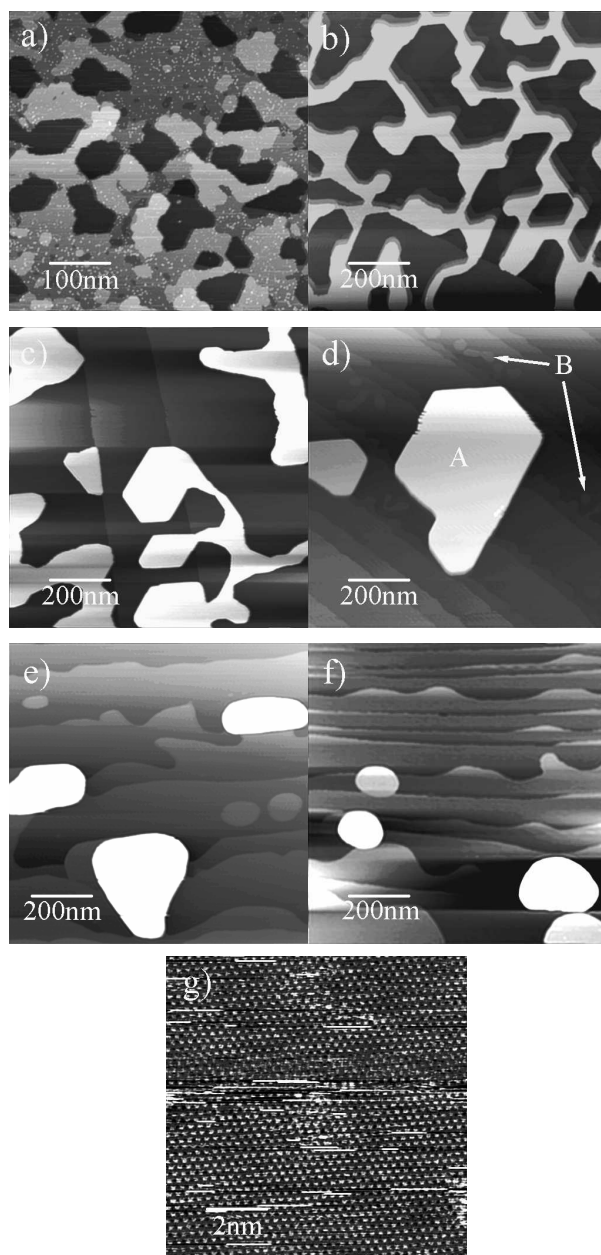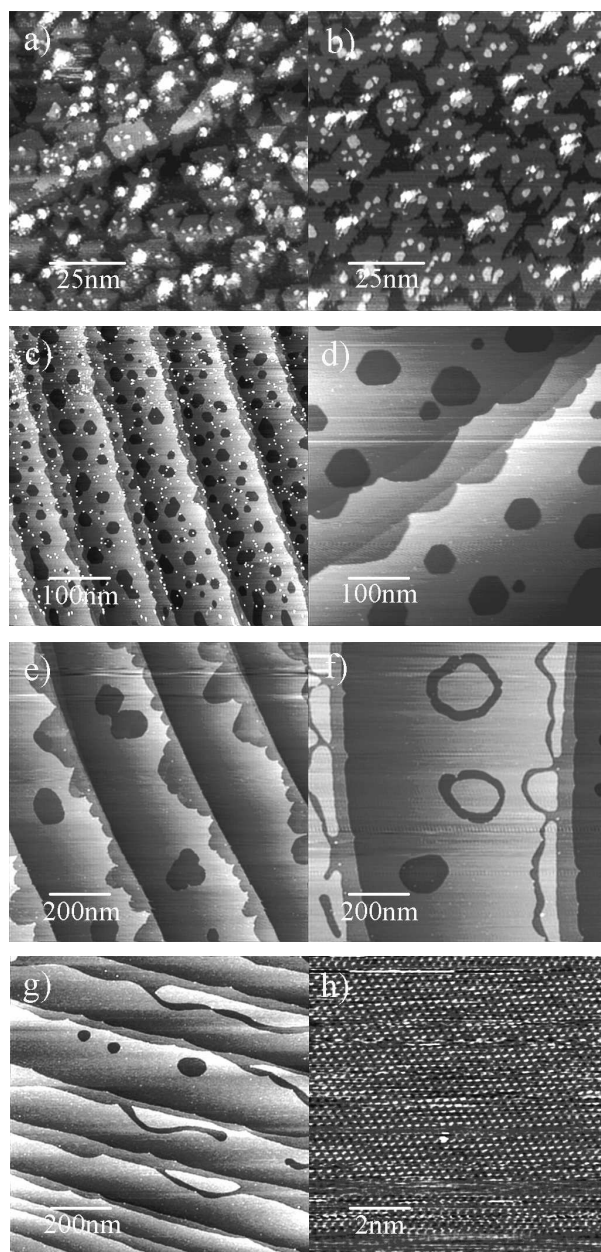

Figure 3: STM images of Co deposited on Ru(0001) surface at the coverage of about 1 ml with annealing treatment at the temperature of (a) R.T. ($100 \times 100\,\text{nm}^2$, $V_{\text{gap}} = 1.423\,\text{V}$, $I = 0.630\,\text{nA}$), (b) 100°C for 30 min ($100 \times 100\,\text{nm}^2$, $V_{\text{gap}} = 1.423\,\text{V}$, $I = 0.872\,\text{nA}$), (c) 200°C for 30 min ($500 \times 500\,\text{nm}^2$, $V_{\text{gap}} = 1.162\,\text{V}$, $I = 0.837\,\text{nA}$), (d) 300°C for 30 min ($500 \times 500\,\text{nm}^2$, $V_{\text{gap}} = -0.029\,\text{V}$, $I = 1.490\,\text{nA}$), (e) 400°C for 30 min ($1000 \times 1000\,\text{nm}^2$, $V_{\text{gap}} = 1.367\,\text{V}$, $I = 0.756\,\text{nA}$), (f) 500°C for 30 min ($1000 \times 1000\,\text{nm}^2$, $V_{\text{gap}} = 1.028\,\text{V}$, $I = 1.068\,\text{nA}$), (g) 600°C for 30 min ($1000 \times 1000\,\text{nm}^2$, $V_{\text{gap}} = -0.743\,\text{V}$, $I = 1.026\,\text{nA}$), (h) atomic structures of the Co wetting layer ($10 \times 10\,\text{nm}^2$, $V_{\text{gap}} = -0.002\,\text{V}$, $I = 37.626\,\text{nA}$).

such as 3-D islands growth behavior for this case.

The growth behavior of multilayer Co on Ru(0001) at room temperature and followed with annealing procedures shows that 3-D Co islands growth occurred only when the system was annealed to a given temperature, that's the same reason why all the Co nanodots of Co/Ru(0001) system were obtained as the substrate temperature was hold at about 350°C during Co depositions [3, 6–10].

Figure 3(a) shows a STM image of about 1 ML Co deposited on the Ru(0001) surface, small Co dots were observed on the Co wetting layer, and the shape of those individual 2-D Co islands (wetting layer) were not compact. When the sample was annealed at 100°C for 30 min, little had changed in the morphology (shown in Fig. 3(b)). However, with the sample annealed at 200°C for 30 min, the surface morphology was changed a lot, as shown in Fig. 3(c). Those individual 2-D wetting Co islands diffused together with holes left inside the Co wetting layer. Those holes tends to be straight along the six-fold [0001] direction of the Ru(0001) substrate. Fig. 3(h) shows the atomic structure of Co wetting layer, unlike the structure of Co island (Fig. 2(g)), the unite cell is a little ???(?? nm to 0.25 nm), which maybe due to mismatch between Co and Ru. The formation of Co wetting layer and uniform shape holes (vacancy islands) is mainly attributed to a stress-driven mechanism. Annealing the sample provide enough diffusing energy for Co atoms to overcome the diffusion barrier. Those vacancy islands are immerged together and became larger as the sample was annealed at 300°C (shown in Fig. 3(d)). The size of the vacancy islands are further increased as the sample was post-annealed at 400°C as shown in Fig. 3(e), and these vacancy islands became a little compact. The compacting of the vacancy islands more clear as the annealing temperatures increased to 500°C and 600°C (see Figs. 3(f) and (g)). Another interesting phenomena is that when the annealing temperature was increased to 300°C and higher, the borders of the Co wetting layer run away from the Ru steps. As discussed above, the formation of fractal islands is typical for diffusion limited aggregation (DLA) [21] growth in which diffusion of an individual atom on both substrate and island terraces is activated whereas atomic migration along an island edge is prohibited. If edge diffusion is also highly activated, the island shape should be compact. In the present case of Co growth on Ru(0001), the shape of the vacancy islands are uniform for the film grown at room temperature, and those islands are compact with the sample be annealed at a temperature of 400°C and higher, indicating that the diffusivity of Co atoms on Ru(0001) is fairly low at room temperature, and highly activated at a temperature of 400°C and higher. The relatively low diffusivity of Co atom at RT is also evidenced by the random distributed small triangle Co islands on the Ru surface when the coverage was very low (see Fig. 1(a)). In general, because of the more coordinate numbers at the Ru steps, the adsorption energy for Co atoms at the Ru steps could be larger than that for Co atoms on the Ru terrenes. Meanwhile, the diffusion barrier of Co atoms is fairly high at RT. Only when the sample was annealed at enough high temperature, Co atoms have enough kinetic energy to overcome the barrier to diffuse away from the edge of the Ru steps and form compact islands. It is also the reason for formation of the well-shaped 3-D crystallites islands at low annealing temperature, and those islands become compact ones at high annealing temperature, in the case of multilayer Co on Ru(0001) (see Fig. 2 and discussions above).

To have surface free energy minimum, 3-D Co islands grew on the bare Ru(0001) is unacceptable. In fact, though the sample at this coverage was annealed to even higher temperature till the Co wetting layer was desorbed, no 3-D Co islands were observed in our measurement. This result also provide the evidence for the conclusion of multiplayer Co deposited onto Ru(0001) and be annealed case, which will formed 3-D islands that grew on the Co wetting layer over the Ru surface instead of on the bare Ru surface.

4. CONCLUSION

We have carried out STM measurements of Co growth on the Ru(0001) surface from submonolayer to multilayer. The results show clearly Co growth on Ru(0001) exhibits a Stranski-Krastanov mode. The Co forms a 2-D wetting layer at the first layer and starts to grow in the 3-D clusters mode from the second layer. The growth behavior can be understood in terms of optimum energy reduction for Co coating the whole substrate surface with smaller free surface energy.

We also investigated the morphology of multilayer and about one monolayer Co on the Ru(0001) surface with different annealing temperature treatment by STM. For multilayer case, 3-D Co islands would formed on the Co wetting layer, the height of those islands increased with the annealing temperature and then decreased because of the Co atoms diffusing into the vacuum at even higher annealing temperature. It is annealing that provides an additional kinetic energy that drives the Co/Ru to a new SK growth behavior (3-D islands grew on wetting layer) to get energy minimum.

For about one monolayer case, as the annealing temperature increased, the individual Co 2-D islands coalesced together to form Co wetting layer, the Co layer diffused away from the edges of the Ru steps and their shape changed from uniform to compact, no 3-D Co islands formed at even higher annealing temperature. With higher kinetic energy at high annealing temperature, the Co atoms will then have higher diffusivity to form compact shape, overcome the barrier and diffused away from the edges of Ru steps. No 3-D Co islands formed on bare Ru surface because of request of the surface free energy minimum.

ACKNOWLEDGMENT

REFERENCES

1. Pietzsch, O., A. Kubetzka, M. Bode, and A. Wiesendanger, *Science*, Vol. 292, 2053, 2001.
2. Heinze, S., M. Bode, A. Kubetzka, et al., *Science*, Vol. 288, 1805, 2000.
3. El Gabaly, F., S. Gallego, et al., *Phys. Rev. Lett.*, Vol. 96, 147202, 2006.
4. Millelsen, A., L. Ouattara, and E. Lundgren, *Surf. Sci.*, Vol. 557, 109–118, 2004.
5. Valvidares, S. M., T. Schroeder, O. Robach, et al., *Phys. Rev. B*, Vol. 70, 224413, 2004.
6. Cheng, R., J. Pearson, H. F. Ding, et al., *Phys. Rev. B*, Vol. 69, 184409, 2004.
7. Yu, C., J. Pearson, and D. Li, *J. Appl. Phys.*, Vol. 91, 6955, 2002.
8. Ding, H. F., A. K. Schmid, D. J. Keavney, D. Li, et al., *Phys. Rev. B*, Vol. 72, 035413, 2005.
9. Yu, C., D. Li, J. Pearson, and S. D. Bader, *Appl. Phys. Lett.*, Vol. 78, 1228, 2001.
10. Li, D., C. Yu, J. Pearson, and S. D. Bader, *Phys. Rev. B*, Vol. 66, 020404(R), 2002.
11. Zhang, H. J., B. Lu, X.-S. Wang, F. Hu, H. Y. Li, S. N. Bao, and P. He, *Phys. Rev. B*, Vol. 70, 235415, 2004.
12. Lu, B., H. J. Zhang, Y. S. Tao, H. Huang, H. Y. Li, S. N. Bao, P. He, and Q. Chen, *Appl. Phys. Lett.*, Vol. 86, 061915, 2005.
13. Zhang, H. J., B. Lu, H. Y. Li, S. N. Bao, and P. He, *Surf. Sci.*, Vol. 556, 63, 2004.
14. Himpsel, F. J., J. E. Ortega, G. J. Mankey, and R. F. Willis, *Adv. Phys.*, Vol. 47, 511, 1998.
15. Bauer, E. and J. H. van der Merwe, *Phys. Rev. B*, Vol. 33, 3657, 1986.
16. Brune, H., *Surf. Sci. Rep.*, Vol. 31, 121, 1998.
17. Meyer zu Heringdorf, F. J., M. C. Reuter, and R. M. Tromp, *Nature*, Vol. 412, 517, London, 2001.
18. Voigtländer, B., *Surf. Sci. Rep.*, Vol. 43, 127, 2001. (and references therein)
19. Ogura, S., K. Fukutani, M. Matsumoto, T. Okano, et al., *Phys. Rev. B*, Vol. 73, 125442, 2006.
20. Ovesson, S., A. Bogicevic, and B. I. Lundqvist, *Phys. Rev. Lett.*, Vol. 83, 2608, 1999.
21. Brune, H., *Surf. Sci. Rep.*, Vol. 31, 121, 1998.

Childhood Leukemia Risk Due to High Voltage Transmission Line in Tehran — Iran

Navid Khaledi and Nima Khaledi

Science and Research Campus, Young Researchers Club of Islamic Azad University
Tehran, Iran

Abstract— Up to the best of our knowledge, the first report on the relationship between childhood cancer and electromagnetic field emitted from power lines dates back to 1979. In our research, a group of 202 children suffering from leukemia has been studied (as case group). Map of Tehran was divided to 921600 square regions using AUTOCAD software. Using random number generator 4000 square regions were selected of which 86 were located 100 meters or less from the power line (as simulated control group), corresponding to $0.2\,\mu\text{T}$. Out of 202 children 7 were living in these selected area. Statistical analysis shows that Odds Ratio is equal to 1.63 (95% CI $= 0.8 - 3.6$) that shows a causal relationship between electromagnetic field and childhood leukemia.

1. INTRODUCTION

Wertheimer and Leeper [1] were of the pioneer that researched about the effect of electromagnetic fields on the occurrence to childhood leukemia. After that, other researchers like Savitz [2] and M. Feychting [3] in different countries such as US, Sweden and Denmark surveyed this topic. All named researcher showed that being in front of the magnetic field of power lines increase risk of childhood leukemia. Also some more effects reported for magnetic fields, that we can mention nervous system tumors for example. But nervous system tumors, was not subject of this research.

Two prevalent type of leukemia is Acute Lymphoblastic Leukemia (ALL) and Acute Myelogenous Leukemia (AML). Percent of suffering from ALL is 78% and from AML is 19% [4].

We enrolled randomly 202 children with acute lymphoblastic leukemia (ALL) who were under 9 years of age, in Tehran as case group. Mathematical simulation has been applied for control group, too. So, this research based on case-control study.

2. MATERIALS AND METHODS

The average of magnetic field in 100 meters, for power lines, is about $0.2\,\mu\text{T}$ [5].

In case group, those children their houses was in distance of up to 100 meters from 230 kV and 400 kV cables, were considered "exposed case group". As described above, mathematical simulation for control group has been used. In the way that, map of Tehran was divided to (921600 =)960 × 960 squares by using AutoCad software and with this software earmarked a number for every square, and generated random number between 0 and 921600, then we selected 4000 first numbers (squares) as control group, if this number showed residential point. This 4000 numbers was our control group. In this 4000 squares, those numbers (squares) was in 100 meters region, named "exposed control group". In fact, this squares, shown children's habitat. Dwelling place of children can be expanded to their population. This election and expand is true, because number of children suffering from leukemia is too smaller than healthy children. Since afoul to leukemia in children is 3 in 100,000 per year [6], so with excellent approximation all children of a city can be assumed healthy. Notice, showing 92,1600 squares on letter sheet or in this article is impossible, because showing this number of squares in bounded size of this paper, redound to a black picture. Thus, only for presentation this method, showed just very lesser number of squares in Figure 1. But in Figure 2, an arbitrary region of Tehran is selected. And in this case squares size is real.

We should not forget effect of exposure from internal sources in the house. But this effect equal for every peoples, thus can neglect that.

3. STATISTICAL CALCULATION

Relation existence between power lines magnetic field and childhood leukemia, done by statistical calculations. This association calculated by Odds Ratio (OR) and the random variability was assessed by 95% confidence intervals (95% CI). Being little number of leukemia patients was one of reasons that we chose OR.

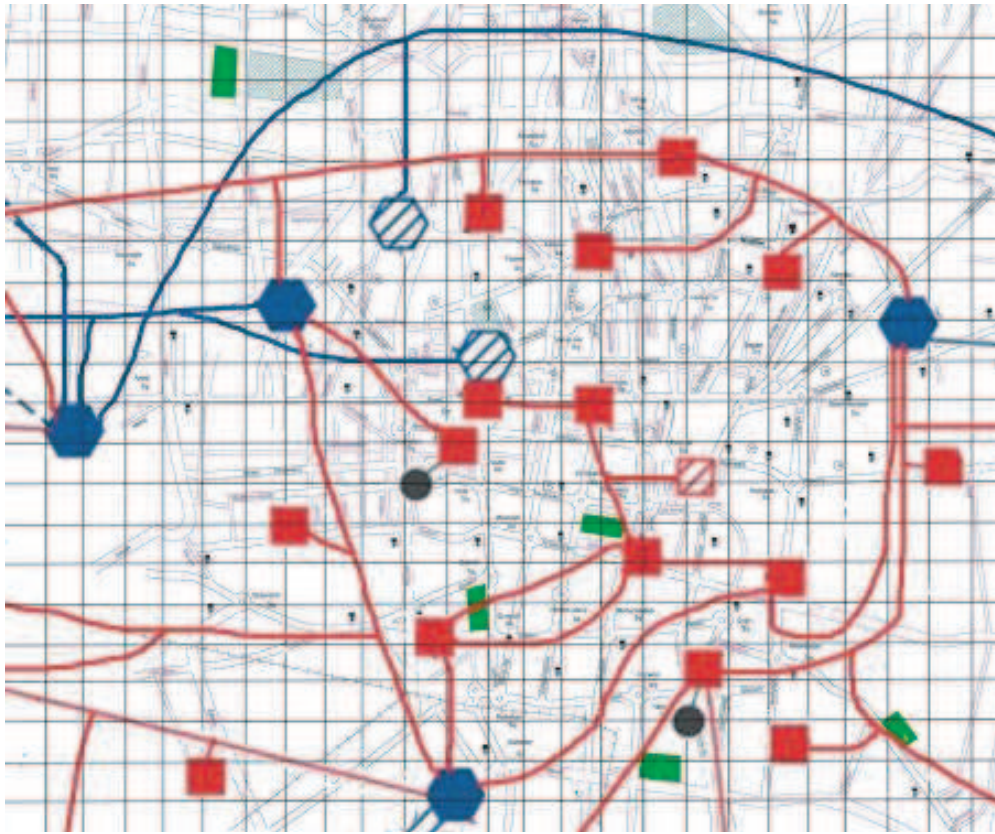The calculations indicated in Table 2.

Figure 1: The divided map of Tehran (squares size is not real). Blue lines indicate 230 kV power lines. Red lines indicate 400 kV power lines.

Figure 2: 230 kV power lines transition, in arbitrary region of Tehran (squares size is real). Gray shadow shows the 100 meters border in per side of cable.

Table 1: Exposed and unexposed case and control group.

	All population	Exposed No.	Exposed (%)	Confidence Interval (95% CI)	Unexposed No.
Case group	202	7	3.46	1.52–7.3	195
Control group	4000	86	2.15	1.73–2.66	3914

Table 2: Calculated Odds Ratio and confidence interval.

	Value
OR	1.63
Confidence Interval (95% CI)	0.8–3.6

4. CONCLUSIONS

By using content of Table 1 Odds Ratio was calculated. As shown, this value equal to 1.63 (95% CI 0.8–3.6) which is greater than 1. Hence, can deduced, magnetic field of power lines can be influence on the increase of leukemia risk. This result had accordance on other researches done by Savitz, Martha, or Feychting and other researchers. The difference was only on OR value. They acquired OR respectively: 1.93, 1.53, 2.49 [7]. This difference, arise from various conditions.

REFERENCES

1. Wertheimer, N. and E. Leeper, "Electrical wiring configurations and childhood cancer," *Am. J. Epidemiol*, Vol. 109, 273–284, 1979.
2. Savitz, D. A., H. Wachtel, F. A. Barnes, E. M. John, and J. G. Tvrdik, "Case-control study of childhood cancer and exposure to 60-Hz magnetic fields," *Am. J. Epidemiol*, Vol. 128, 21–38, 1988.
3. Feychting, M., G. Schulgen, J. H. Olsen, and A. Ahlboml, "Magnetic fields and childhood cancer — A pooled analysis of two scandinavian studies," *European Journal of Cancer*, Vol. 31A, No. 12, 20335–2039, 1995.
4. www.envirohealthpolicy.net, Children, Cancer, and the Environment.
5. www.wapa.gov, Electric and Magnetic Fields FACTS, Western Area Power Administration.
6. Barnes, F. S. and B. Greenebaum, *Handbook of Biological Effects of Electromagnetic Fields*, CRC Press, 2007.
7. Wartenberg, D., "Residential EMF exposure and childhood Leukemia: Meta-analysis and population attributable risk," *Bioelectromagnetics Supplement*, Vol. 5, S86–S104, 2001.

Electromagnetic Pulse Alter Permeability of the Blood-brain Barrier in Rats

Guirong Ding, Xiaowu Wang, Kangchu Li, Yongchun Zhou,
Lianbo Qiu, and GuoZheng Guo

Department of Radiation Medicine, School of Public Health
Fourth Military Medical University, Xi'an 710032, China

Abstract— The effect of electromagnetic pulse (EMP) exposure on blood-brain barrier (BBB) permeability in rat brain after whole-body exposed or sham exposed to EMP at 200 kV/m for 400 pulses (1 Hz) was investigated. At 1, 3 and 6 h after EMP exposure, disruption of BBB integrity in rat frontal cerebral cortex was detected by transmission electron microscopy and immunohistochemistry using lanthanum nitrate and endogenous albumin as vascular tracers respectively. The results showed that in control rat brain, lanthanum nitrate tracer was limited to the capillary lumen, no lanthanum nitrate and albumin tracer extravasation was found. After EMP exposure, lanthanum nitrate ions reached the tight junction, basal lamina and the pericapillary tissue. Similarly, albumin immunopositive staining was also found in the pericapillary tissue. The changes of BBB permeability were transient, the leakage of BBB was found at 1 h, and reach the peak at 3 h, then began to recover at 6 h after EMP exposure. These results suggest that exposure to EMP at 200 kV/m for 400 pulses (1 Hz) could increase the permeability of BBB in rat frontal cerebral cortex and this change is recoverable.

1. INTRODUCTION

With the increasing use of modern techniques including electromagnetic applicationspossible health risks to the human body and, in particular, the brain being exposure to electromagnetic fields has already become a public concern. It was reported that radiofrequency field exposure from mobile telephones resulted in a significantly increased risk for brain tumors [1], but this view has not been confirmed by laboratory studies. It is well known that blood-brain barrier (BBB) plays an important role in maintaining the homeostasis of brain microenvironment, which is essential for the normal function of brain. A variety of pathological conditions can adversely affect the BBB and lead to its disruption in humans and laboratory animals. Usually, the disturbances of the BBB permeability were assessed by observing the extravasation of external tracers such as Evans Blue and lanthanum nitrate or of internal serum constituents such as albumin. In this study we used both endogenous albumin and lanthanum nitrate to assess the changes in BBB permeability in rats after electromagnetic pulses (EMP) exposure.

2. MATERIALS AND METHODS

2.1. Animals and EMP Exposure

Sprague-Dawley rats, male, weighing 200–250 g, were obtained from Animal Center of the Fourth Military Medical University (Xi'an, China). The rats were kept separately in a specific pathogen-free environment with free access to sterile laboratory pellets and water. The animals were sham or whole-body exposed to 1 Hz EMP at 200 kV/m for 400 pulses. During exposure, the rats were awake and not restrained the exposure chamber. The exposure conditions produced a rise in rat rectal temperature less than 0.2°C.

2.2. Albumin Immunohistochemistry

At 1, 3 and 6 h after EMP exposure, five animals from each group were anesthetized with 40 mg/kg sodium pentobarbital, i.p. The heart was exposed and the left ventricles were perfused with 0.9% saline, followed by perfusion with 200 ml fixative (4% paraformaldehyde in phosphate-buffered saline, pH 7.4) for 15 min. After the perfusion, brains were immersed in the fixative and kept for more than 24 h, then coronal slices were embedded in paraffin and 4 μm sections were cut. The accurate histological detection of any extravasated endogenous albumin was performed using goat anti-rat albumin (Bethyl Laboratories, Inc) as the primary antibody and 2-step plus poly-HRP anti goat IgG detectionsystem (ZSGB-Bio). The sections were counterstained with hematoxylin to enhance the nuclear staining. The efficacy of the vascular tracer was confirmed with a positive control group exposed to adrenaline known to increase vascular permeability in the brain. For

negative controls, adjacent sections were processed with the same steps with the exception of the primary antibodies. Pictures were taken from the sections by means of a digital camera attached to Nikon light microscope.

2.3. TEM Study of Blood-brain Barrier Permeability

Transmission electronic microscopic (TEM) studies were conducted at the Electronic Microscope Center of the Fourth Military Medical University using JEM-100SX electronic microscope (Hitachi, Tokyo, Japan). At 1, 3 and 6 h after EMP exposure, four animals from each group were anesthetized with 40 mg/kg sodium pentobarbital, i.p. The heart was exposed and the left ventricles were perfused with 0.9% saline, followed by perfusion with the fixative consisting of one part 4% lanthanum nitrate and two parts 6% glutaraldehyde-0.1 M sodium cacodylate (pH 7.40–7.50) for 2 h. At the end of brain perfusion, the frontal cerebral cortex were isolated and cut into 1 mm^3 pieces. The isolated tissues were immersed in 4% glutaraldehyde for 2 h, and then washed in two changes of PBS. The tissues were immersed in 1% osmium tetroxide for 2 h, and then washed with PBS for 5 min. After being embedded, the specimens were heated at 60°C for 48 h. The sections were dyed with acetic acid uranium and lead, and then observed under TEM.

3. RESULTS

3.1. Effect of EMP on Permeability of BBB Using Albumin Tracer

In the sham exposure rats, no blood vessels showing albumin leakage in the frontal lobe of rat cortex, at 1 h after 200 kV EMP exposure for 400 pulses, a little extravasated serum albumin was found in a few capillaries, the albumin leakage of BBB became evident at 3 h (Fig. 1).
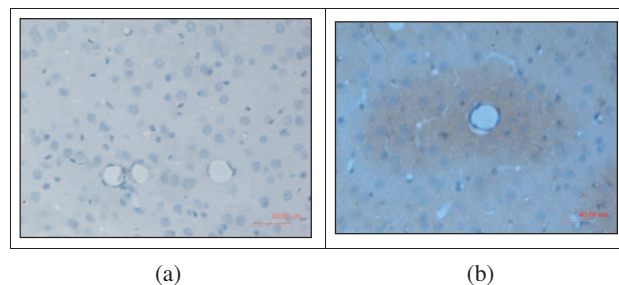

(a) (b)

Figure 1: Extravasated serum albumin in the frontal lobe of rat cortex at 3 h after EMP exposure (200 kV, 400 pulses). (a) Sham exposure; (b) EMP exposure; Bar = 40 µm.

3.2. BBB Permeability after EMP Exposure by TEM

Lanthanum nitrate has been proven lacking the ability to penetrate the BBB and thus widely used as a marker to examine the integrity of BBB by TEM [2, 3]. As shown in Fig. 2, in sham exposure rat brain, the lanthanum stains were exclusively located in cerebral capillary. EMP exposure resulted in the leakage of capillary lanthanum stain to the surrounding of cerebral capillaries. Lanthanum stains could be found in the tight junction and basal lamina at 1h after EMP exposure (200 kV, 400 pulses), which invaded into the parenchyma area at 3 h after EMP exposure, then the extravasation of lanthanum nitrate decreased at 6 h after EMP exposure.

Sham exposure   1h after EMP exposure   3h after EMP exposure

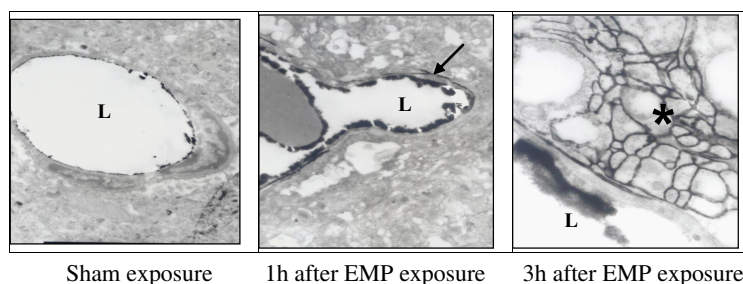Figure 2: Electron micrographs of representative frontal lobe cortex microvessels from sham exposure rats showing lanthanum nitrate circumscribed at the luminal (L) space, no lanthanum tracer is reaching the basal lamina. At 1 h after EMP exposure (200 kV, 400 pulses), the extracellular tracer appears in base membranes (arrow), and invaded into the parenchyma area at 1 h after EMP exposure (asterisk).

4. DISCUSSION

BBB is a specialized structure responsible for the maintenance of the neuronal microenvironment, which protects the brain from foreign toxic substances but allows passage of the molecules that are necessary for metabolism. A wide variety of toxic conditions such as anoxia, hypertension and ionizing radiation could increase the permeability of BBB. Since Frey et al. [4] reported that 1.2 GHz CW exposure induced a significant increase in BBB permeability, many studies have been performed, but the results were controversial. Most of the researchers believe that the permeability change is associated with an increase in temperature induced by electromagnetic field. In recent years, the effect of nonthermal radio frequency exposure on BBB permeability has also been investigated, both positive and negative findings were reported [5, 6]. Salford group using more than 1800 Fisher rats proved that sub thermal power levels from both pulse modulated and continuous RF fields have the potency to significantly open the BBB for the animals' own albumin (but not fibrinogen) to pass out into the brain and to accumulate in the neurons and glial cells surrounding the capillaries [7]. But their results could not be replicated by other laboratories [8]. One study exposing of Rats to a 1436 MHz TDMA Field at a high SAR (2000 mW/kg) also reported no significant albumin leakage [9]. Recently, Grafström et al. investigated in a rat model the effects of repeated exposures under a long period (55 weeks) to 900 MHz GSM radiation in order to mimic the real life situation, with often life-long exposure to the electromagnetic fields emitted by mobile phones, but no significant alteration of any these histopathological parameters was found [10].

In this study, we investigated the BBB permeability after EMP exposure using lanthanum nitrate and endogenous albumin as vascular tracers. The results showed that EMP exposure (200 kV, 400 pulses) increased the BBB permeability. Moreover, we investigated the time course (1, 3 and 6 h) of BBB opening induced EMP exposure. It was found that the BBB permeability increased at 1 h after EMP exposure and reach the peak at 3 h, then began to recover at 6 h. These results indicate that EMP exposure under this condition could transiently alter the permeability of BBB in rat.

ACKNOWLEDGMENT

REFERENCES

1. Hansson, M. K., L. Hardell, M. Kundi, and M.-O. Mattsson, "Mobile telephones and cancer: Is there really no evidence of an association?," *Int. J. Mol. Med.*, Vol. 12, 67–72, 2003.
2. Bradbury, M. W. and R. Deane, "Permeability of the blood–brain barrier to lead," *Neurotoxicology*, Vol. 14, 131–136, 1993.
3. Le Sueur, L. P., C. B. Collares-Buzato, and M. A. Cruz-Hffling, "Mechanisms involved in the blood-brain barrier increased permeability induced by Phoneutria nigriventer spider venom in rats," *Brain Research*, Vol. 1027, 38–47, 2004.
4. Frey, A. H., S. R. Feld, and B. Frey, "Neural function and behaviour: Defining the relationship," *Ann. NY Acad. Sci.*, Vol. 247, 433–439, 1975.
5. Hossmann, K. A. and D. M. Hermann, "Effects of electromagnetic radiation of mobile phones on the central nervous system," *Bioelectromagnetics*, Vol. 24, 49–62, 2003.
6. D'Andrea, J. A., C. K. Chou, S. A. Johnston, and E. R. Adair, "Microwave effects on the nervous system," *Bioelectromagnetics Supplement*, Vol. 6, S107–S147, 2003.
7. Persson, B. R. R., J. Eberhardt, L. Malmgren, M. B. Persson, A. Brun, and L. G. Salford, "Effects of microwaves from GSM mobile phones on the blood-brain barrier and neurons in rat brain," *PIERS Online*, Vol. 1, No. 6, 638–641, 2005.
8. Johnston, S. A., "Behavioral and cognitive effects of mw electromagnetic field exposures," *PIERS Online*, Vol. 3, No. 5, 751–757, 2007.
9. Tsurita, G., H. Nagawa, S. Ueno, S. Watanabe, and M. Taki, "Biological and morphological effects on the brain after exposure of rats to a 1436 MHz TDMA field," *Bioelectromagnetics*, Vol. 21, 364–371, 2004.
10. Grafströma, G., H. Nittbyb, A. Brunc, L. Malmgrend, B. R. R. Perssona, L. G. Salfordb, and J. Eberhardta, "Histopathological examinations of rat brains after long-term exposure to GSM-900 mobile phone radiation," *Brain Research Bulletin*, Vol. 77, 257–263, 2008.

The Research on the Harm of Biological Effect of Mobile Phone Radiation to Human Body

Yang Li and Guizhen Lu

Information Engineering School, Communication University of China
Beijing 100024, China

Abstract— This paper presents recent situations about the biological effect of mobile phone radiation, and enumerates some relative investigations and experiments. The former theoretic research has been reviewed, and then it indicates that classical theory may be not suitable to explain microcosmic phenomena and the methods should be ameliorated. The viewpoint that the interaction between the DNA molecule and adscititious electromagnetic wave can be analyzed with the quantum theory in the microcosmic domain namely in the nucleus has also been given. It is proposed that one reason of the electromagnetic biological effect is due to that the DNA molecule is affected by adscititious electromagnetic waves and then molecular energy level structure changes. The formula derivation of the quantum theory is listed and the explanation of its quantum theory effects is put forward. Finally, the paper points out that the results of action between microwave radiation and DNA molecule is probably belong to a kind of biological effect which is long-time and slow-effect.

1. INTRODUCTION

As early as in 1975, when the mobile communication was still at the beginning in the Europe and North America, some environmentalists predicted that the human beings would face the serious problems about electromagnetic pollution in the 21st century. After many years, the prediction gradually became the truth along with the development of mobile communication technology and popularization of personal cell phones.

In 1982, the U.S government made a new standard of radiofrequency radiation. Although the new standard was also established based on the thermal effect, it had difference from the former one for it had more experimental data from the animals and its main characteristic was adopting the conception of dosimetry. It still used field intensity and power density, but its standard was calibrated by dose rate, namely specific absorption rate (SAR, which unit is W/Kg or mW/g) [1]. From then on, the SAR has been employed to measure the thermal effect of handsets and gradually accepted by the whole world. There have been numerous papers which take FDTD as their primary method to study the SAR and a lot of progress in experiments has been obtained since 1992. So far many countries have pushed electromagnetic radiation standards according to the SAR value.

From the research papers in recent 10 years it can be concluded that thermal effects are relatively simple and more popular to investigate. Almost all the papers of the IEEE start with the SAR and use different electromagnetic calculational methods (but the most commonly used method is FDTD) to obtain the theoretical calculation or computer simulation results about the SAR values in the human head under different mobile phone radiation condition. The calculation and simulation results make us know how the energy from mobile phone radiation distribute in the head. However, it is very hard to validate the results in the experiments and the majority of the experiments are just simulation ones with the phantoms or human body models. There are so many cases that are correlated with the health if the mobile phone users use their phones for a long time and it is difficult to explain with thermal effects. Therefore, the thermal effects and SAR actually can't open out the biological harm to the human body and the brain tissue. Therefore, the research of non-thermal effects especially biological effects with the characteristic of window effects [2] is considered to be a hotspot about mobile phone radiation.

2. THE EXAMPLES OF BIOLOGICAL EFFECTS

The biological effect of the mobile phone radiation is that a human being has physiological changes evidently when he is under the radiation of his mobile phone but the temperature of his body doesn't change anything clearly.

2.1. The Research of Epidemic

There was an investigation in Sweden, which indicated that the mobile phones of analog format could be more hurtful to the users than the ones of GSM from the aspects of attention and memory [3]. Another investigation in Sweden was taken by Harrell and his workmates, which pointed out that the users would have more chances to suffer from the neuroma when they were using the mobile phone of analog format [4]. Szmigielski also had a research in Poland, in which the soldiers who were often irradiated by the RF were checked up and at last they were found to have 6 times of probability of getting lymphoma and leukemia [5]. The literature [6] had a lot of tests from the swatch of some people aged between 18~50 in Chengdu China, which presented that the mobile phone radiation would cause syndrome of nervous system.

2.2. The Animal Experiments in Microwave Frequency Band

The frequency band of electromagnetic wave from the mobile phone belongs to microwave band, so plenty of animal experiments are done as analogs under microwave radiation. Salford and his assistants put the rats to the exposure of electromagnetic field produced by mobile phones, and the SAR values were respectively $2\,\text{mW/Kg}$, $20\,\text{mW/Kg}$, and $200\,\text{mW/Kg}$. Afterward, they found that blood brain barrier permeability increased under the condition of non-thermal [7]. The report [8] gave us results of experiments about the damage produced by mobile phone radiation to the rats, and told us that the radiation could reduce the activity of SOD and the content of NO in blood serum and inducing apoptosis of hepatocyte.

In addition, some studies on the rodents show that RF fields can influence the DNA molecules directly. When the rats were put into the 2.45 GHz EM field for 2 hours everyday, the researchers discovered gene rearrangement in brain tissues or experimental cells after 120, 150 and 200 days [9]. Lai and Singh notified that single-stranded DNA and double-stranded DNA of some animals' brain cells were obviously destroyed after 2 hours when the animal were exposed in the EM field of 2.45 GHz pulse wave or continuous wave [10, 11].

3. THE REVIEW OF FORMER THEORIES ABOUT BIOLOGICAL EFFECTS

At present, there are some old theories which were put forward before 1990s, such as coherent electric vibrations theory, cyclotron resonance theory, ion channels of biomembrane theory, free radical theory and so on [12]. But these theories and hypotheses have their limitations respectively, only being able to explain partial phenomena, and some of them are oppugned by K. R. Foste, who thinks that all these theories need to be improved further [13]. In recent years, there is a new theory named "adaptive resonance theory", which tries to explain the biological effects from the viewpoint of quantum theory and considers the interaction between the microwave and the cell membrane [14]. As we all know that the quantum theory accords with all laws of movement, especially the problems in the microcosmic domain in which classical mechanics and classical electromagnetics are not able to resolve the phenomena. Adaptive resonance theory tries to explain the biological effects with the assumption that the EM radiation can tamper with the original membrane construction. It supposes that permeability of membranes to particles will be affected and place a premium on the biological effects when the external EM filed acts on the membranes to interfere the electric potential difference between both sides of them, with the status of resting, keeping the potential of 50~100 mV from inside to outside of the membrane.

Besides the cell membrane, the affect to the nucleus and DNA should also be considered. Blank and Reba Goodman has pointed out that microwave has the chance to change the DNA molecule, because the frequency of the EM fields radiated from the mobile phones are very high and there are charges shuttling on the DNA double helix, and the interaction between the microwave and charges will disturb the genetic material, namely genes [15]. Of course, their explanations barge up against difficulties, as Robert. K concludes and gets his conclusions that due to the ingoing electromagnetic wave energy is too weak even far less than the energy of particle vibration, and then he think that the parlance about the direct interaction between the EM fields and DNA molecules is hard to come into existence. However, the order of magnitude of DNA molecule is $10^{-8}\,\text{m}$, and it is not a macroscopic object, so the classic theory is apparently not suitable. It naturally takes trouble when we use the classic electromagnetics to explain the microcosmic phenomena for the order of magnitude of DNA molecules, but if we try to use quantum theory to solve this problem it is may promising.

4. THE INTERACTION BETWEEN ELECTROMAGNETIC WAVES AND DNA

If we can see the DNA molecule as a microcosmic quantum system and also take the external electromagnetic field as a tiny disturbing, the action from the microwave radiation to the DNA molecule can be ulteriorly studied with quantum theory.

It is supposed that the Hamilton functor of this system is H and it is time-independent, then it can be written as

$$H = H_{DNA} + H_{EM} \tag{1}$$

where H_{DNA} is the Hamilton functor of the DNA molecule and the H_{EM} is the Hamilton functor of external electromagnetic field as a tiny disturbing. If the eigenvalue E_{DNA} and eigenfunction ψ_{DNA} of H_{DNA} are both known, and the eigenvalue and eigenfunction of H are separately E_n and ψ_n, then

$$H\psi_n = E_n\psi_n \tag{2}$$

If there is not the tiny disturbing, the H is the H_{DNA}, E_n and ψ_n just are E_{DNA} and ψ_{DNA}. When the external electromagnetic field as a tiny disturbing is considered, the energy level will change from E_{DNA} to E_n, which means the energy level take a move and the wave function ψ_{DNA} can be turned into ψ_n. The energy level E_n corresponds with H, and can be inferred by the known discrete energy level E_{DNA} derived from H_{DNA}. Similarly, ψ_n can be get from eigenfunction ψ_{DNA}.

4.1. E_{DNA} Is Non-degenerate

In this situation, there is only one eigenfunction relevant to the eigenvalue H_{DNA}, namely $\psi_n^{(1)}$, and it is the zero order approximation of ψ_n. The $\psi_n^{(1)}$ satisfies the condition that

$$H^{(1)}\psi_n^{(1)} = E_n^{(1)}\psi_n^{(1)} \tag{3}$$

On the assumption that the ψ_{DNA} has been normalized, then it can be deduced that

$$\psi_{DNA} \cdot (H_{DNA} - E_{DNA})\psi_n^{(1)} = -\psi_{DNA} \cdot \left(H^{(1)} - E_n^{(1)}\right)\psi_{DNA} \tag{4}$$

It is can be noticed that the eigenvalue E_{DNA} of H_{DNA} must be real number, therefore the H_{DNA} is Hermitian operator. Make the spatial integral of the upper formula, and consider the orthonormalization of $\psi_n^{(1)}$, we can get the equation

$$E_n^{(1)*} = \oiiint \psi_{DNA}^* H_{EM} \cdot \psi_{DNA} d\tau \tag{5}$$

which means the second order correction of the energy namly $E_n^{(1)}$ equals to the mean value of E_{DNA} state. On the other hand, if E_{DNA} is marked as

$$E_{DNA} = E_n^{(0)} \tag{6}$$

and

$$E_{DNA} = E_n^{(0)} \tag{7}$$

then E_n can be written to be

$$E_n = E_{DNA} + \lambda E_n^{(1)} + \lambda E_n^{(2)} + \cdots \tag{8}$$

At the same time, $E_n^{(2)} = \sum_l' a_l^{(1)} H'_{nl} = \sum_m^p \frac{H'_{ln} H'_{nl}}{E_n^{(0)} - E_l^{(0)}} = \sum_m' \frac{|H'_{nl}|^2}{E_n^{(0)} - E_l^{(0)}}$, if it is put into the formula (8), and combined with formulas (5), (6), (7), the energy of the DNA molecule which is affected by the tiny disturbing can be presented as

$$E_n = E_n^{(0)} + H'_{nn} + \sum_m' \frac{|H'_{nm}|^2}{E_n^{(0)} - E_m^{(0)}} + \cdots \tag{9}$$

It can be educed with formulas (6) and (8) that

$$\psi_n = \psi_n^{(0)} + \lambda\psi_n^{(1)} + \lambda\psi_n^{(2)} + \cdots \tag{10}$$

and then take the $\psi_n^{(1)} = \sum_m' \frac{H'_{mn}}{E_n^{(0)} - E_m^{(0)}} \psi_m^{(0)}$ into the formula (10), it can obtain the wave function of this system

$$\psi_n = \psi_n^{(0)} + \sum_m' \frac{H'_{mn}}{E_n^{(0)} - E_m^{(0)}} \psi_m^{(0)} + \cdots \tag{11}$$

The condition of a tiny disturbing comes into existence given the series formulas (9) and (11) both are convergent. If we want to judge whether the series is convergent, the general term must be known first, but both of these two series are unknown. Therefore, we only require that some of the known terms ought to be much less than the foregoing terms. So it is concluded that

$$\left| \frac{H'_{mn}}{E_n^{(0)} - E_m^{(0)}} \psi_m^{(0)} \right| \ll 1, \quad \left(E_n^{(0)} \neq E_m^{(0)} \right) \tag{12}$$

As the expression of the formula (12) shows that if the condition has been satisfied, it not only lies on the matrix element H'_{mn}, but also rests with the distance $\left| E_n^{(0)} - E_m^{(0)} \right|$ between energy levels. When the formula (12) is satisfied, a more accurate result is commonly able to be got in case of having calculated the first order correction.

4.2. E_{DNA} Is Degenerate

If E_{DNA} is degenerate, there is formula (6) $E_{DNA} = E_n^{(0)}$, and it is supposed that eigenvalue $E_n^{(0)}$ belonged to H has κ eigenfunctions: ϕ_1, ϕ_2, $\cdots$, then it will be induced that

$$H\phi_i = E_n^{(0)}\psi_i, \quad i = 1, 2, \ldots, \kappa \tag{13}$$

In this case, it is necessary to choose zero order approximate wave function from these κ eigenfunctions, and make the equation $(H^{(0)} - E_n^{(0)})\psi_n^{(1)} = -(H^{(1)} - E_n^{(1)})\psi_n^{(0)}$ solvable. Based on this condition, it is able to zero order approximate wave function $\psi_n^{(0)}$ as a linear combination of κ eigenfunctions:

$$\psi_n^{(0)} = \sum_{i=1}^{\kappa} C_i^{(0)} \phi_i \tag{14}$$

In order to confirm the corresponding the zero order approximate wave function of the energy $E_{nj} = E_n^{(0)} + E_{nj}^{(1)}$, we can put the value of $E_{nj}^{(1)}$ into the equation $E_{nj} - E_n^{(0)} = \sum_{i=1}^{\kappa} (H'_{li} - E_n^{(1)}\delta_{li})$, then solve a set of $C_i^{(0)}$ using the condition $C_i^{(0)} = 0$, $l = 1, 2, \ldots, \kappa$, and finally get the result if only take the $C_i^{(0)}$ into formula (9).

Because the Hamilton functor of a DNA molecule system is complex, it is possible to obtain no precise result but an approximate result, and then solve this problem with the approximate one.

5. CONCLUSIONS

The research about the biological effect of mobile phone radiation is of interdisciplinary subject, and relates to microwave technology, biology, medicine and physics. Although there are many experiments and theories, there is not any important breakthrough yet. There is still bifurcation on the viewpoint, and the conclusions of the experiments are often poles apart. The causation is likely to be ascribed to inconsistent experimental conditions, and for the complexities of the organisms themselves, and then for the repeatability of experiments is not good enough due to difference among Individuals. Accordingly it makes the researchers of these experiments have totally different conclusions.

It is well-known that ionizing radiation for its powerful ray energy has the ability to interact with the DNA molecules directly and lead to chemical bonds fracture, which is how ionizing radiation can scathe the human body. That is to say, ionizing radiation has the characteristic of short-time and fast-effect to harm the human beings, so its biological effects are very visible. If electromagnetic radiation in the microwave frequency bands is like the ionizing radiation to affect the DNA, to result in rupture of the chemical bonds and bring on the DNA damage, according to the actual situations, its effects should be of long-time and slow-effect. Whether or no, if the assumption that

the electromagnetic wave really can make DNA molecules change in some condition, the mobile phone radiation causing cancer will make theory become reality based on the hypothesis about gene mutation inducing cancer [16]. Thus it can be seen that these problems are needed to have more deep studies from the microcosmic domain.

ACKNOWLEDGMENT

REFERENCES

1. American National Standards Institute (ANSI), "Recommended practice for the measurement of potentially hazardous electromagnetic fields — RF and microwave," ANSI/IEEE C95.3-1992. Copyright 1992, The Institute of Electrical and Electronics Engineers, Inc. (IEEE), New York, NY 10017. For copies contact the IEEE: 1-800-678-4333 or 1-908-981-1393

2. Ross Adey, W., "Biological Effects of Electromagnetic Fields," *Journal of Cellular Biochemistry [J]*, Vol. 51, 410–411, 1993.

3. Mild, K. H., et al., "Comparisons of symptoms experienced by users of analogue and digital mobile phones: A Swedish-Norwegian epidemiological study," Report for the National Institute for Working Life, 1998

4. Hardell, L., A. Hallquist, K. H. Mild, et al., "Cellular and cordless telephones and the risk for brain tumours," *Eur. J. Cancer. Prev.*, Vol. 11, No. 4, 377–386, 2002.

5. Szmigielski, S., "Cancer morbidity in subjects occupationally exposed to high frequency (radiofrequency and microwave) electromagnetic radiation," *Sci. Total Environ.*, Vol. 180, No. 1, 9–17, 1996.

6. Fu, D.-G., Y.-F. Long, and L.-Q. Zhao, "Study on the measurement of the microwave radiation of mobile phone and its effect on human health [J]," *Journal of Occupational Health and Damage*, Vol. 20, No. 2, 85–89, 2005.

7. Salford, L. G., A. E. Brun, J. L. Eberhardt, et al., "Nerve cell damage in mammalian brain after exposure to microwaves from GSM mobile phones," *Environ. Health Perspect.*, Vol. 111, No. 7, 881–883, 2003.

8. Ai, Z., S. Zhag, and J. Wei, "Primary study on the influence of electromagnetic radiation emitted by mobile phone on rats [J]," *Beijing Biomedical Engineering*, Vol. 24, No. 3, 211–213, 2005.

9. Sarkar, S., S. Ali, and J. Behari, "Effect of low power microwave on the mouse genome: A direct DNA analysis [J]," *Mutat. Res.*, Vol. 320, 141–147, 1994.

10. Lai, H. and N. P. Singh, "A cute low-intensity microwave exposure increases DNA single strand breaks in rat brain cells [J]," *Bioelectromagnetics*, Vol. 16, 207–210, 1995.

11. Lai, H. and N. P. Singh, "Single-and double-strand breaks in rat brain cells after acute exposure to radiofrequency electromagnetic radiation [J]," *Int. J. Radiat. Bio.*, Vol. 69, 513–521, 1996.

12. Liu, Y.-N., "Review on the investigation of the mechanism of the biological effects of the electromagnetic radiation [J]," *Basic Medical Sciences and Clinics*, Vol. 20, No. 1, 22–23, 2000.

13. Kenneth, R. F., "Electromagnetic field effects and mechanisms [J]," *IEEE Engineering in Medicine and Biology*, 50–56, July/August 1996.

14. Liu, Y.-C. and H.-M. You, "The quantum theory of the thermal effect of bio-microwave and its mechanism [J]," *Journal of Microwaves*, Vol. 21, No. 4, 67–70, 2005.

15. Blank, M. and R. Goodman, "Extremely low frequency electromagnetic fields do not interact directly with DNA [J]," *Bioelectromagnetic*, Vol. 19, 136–137, 1998.

16. Hahn, W. C. and R. A. Weinberg, "Modelling the molecular circuitry of cancer [J]," *Nat. Rev. Cancer*, Vol. 2, No. 5, 331–341, 2002.

Suppression of Static Magnetic Field in Diffusion Measurements of Heterogeneous Materials

Eva Gescheidtova[1] **and Karel Bartusek**[2]

[1]Faculty of Electrical Engineering and Communication, Brno University of Technology
Kolejni 2906/4, Brno 612 00, Czech Republic
[2]Institute of Scientific Instruments, Academy of Sciences of the Czech Republic v.v.i
Kralovopolska 147, Brno 612 00, Czech Republic

Abstract— The paper describes a magnetic resonance (MR) method for establishing the diffusion coefficients in heterogeneous materials. The pulsed field gradient stimulated-echo methods have a reduced coupling between the applied magnetic field gradient and a constant internal magnetic field gradient caused by different susceptibilities throughout the sample. When studying systems where it is necessary to keep the duration of the pulse sequence at a minimum or to study diffusion as a function of observation time, the spin-echo method should be chosen. The basic idea is to acquire the spin echo amplitude with pulsed field gradient of opposite signs and to subtract in a suitable way the NMR signals measured. The measuring method and the digital signal processing enable eliminating the effect of static magnetic field on the accuracy of measuring. The method proposed can be used to measure diffusion-weighted images of liquids found in porous materials, and in the development of new MR tomography measuring methods in the Institute of Scientific Instruments of the Academy of Sciences of the Czech Republic, v.v.i.

1. INTRODUCTION

Imaging based on nuclear magnetic resonance is one of important methods for the study of tissues and molecules. The knowledge of the diffusion and other motions of the nuclei of different substances in the porous material under examination can bring new diagnostic results. The MR method enables measuring the slow motion of nuclei and molecules. In heterogeneous systems, where relaxation time T_2 is shorter than T_1 and where diffusion coefficient D is small, the use of the Pulsed Field Gradient Spin Echo (PFG-SE) sequence may be advantageous [1]. More sophisticated methods that eliminate the effect of magnetic susceptibility of biological materials have been introduced [2–7]. They are based on producing a stimulated echo, for which the diffusion time can be extended even in materials with a short relaxation time T_2. These techniques eliminate the effect of the so-called cross terms related to the space-dependent gradient of the basic field of the MR system.

The proposed method employs the PFG-SE pulsed sequence for three magnitudes of diffusion gradient and enables calculating the diffusion constant of the material being measured. The above procedure for calculating the b-factor makes it possible to eliminate the effect of the heterogeneity of static magnetic field, which is due to the magnetic susceptibility of the material being measured.

2. METHOD

The principle of measuring in the current spin-echo pulse sequence consists in applying two diffusion gradients of length δ [8]. The first of them is located between two RF pulses and serves the spins being brought out of phase in a defined way while the other gradient is applied after the 180° pulse and serves to bring the spins into phase again, Fig. 1. For the whole period of measuring, a static gradient magnetic field G_0 is acting on the spins, which is due to the magnetic susceptibility of the material being measured. The effect of this field on the precision of measuring the diffusion coefficient should be minimized.

If due to the diffusion the spins move randomly, the MR signal attenuation M can be described by a simple exponential equation

$$M = M_0 e^{bD}, \tag{1}$$

where M_0 is the signal intensity without diffusion (e.g., measured by a sequence without both the diffusion gradients and the static gradient magnetic field G_0). The constant b (the so-called b-factor) gives the pulse sequence sensitivity to diffusion, and is given by the integral

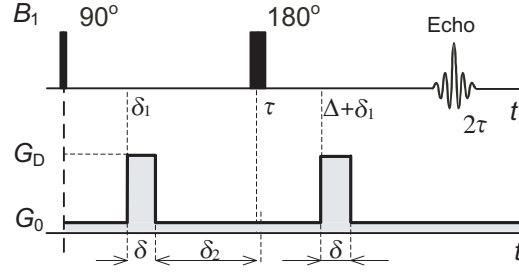$$b = -\gamma^2 \int_0^{2\tau} \left[\int_0^t G(t') dt' \right]^2 dt. \tag{2}$$

Figure 1: PFG-SE sequence.

Equation (2) is used to calculate the b-factor of pulse sequences of any effective gradient waveform. For the proposed technique [1] it can be derived that the drop in spin echo magnitude as expressed by the b-factor will be

$$b = -\gamma^2 \left[a_1 G_\mathrm{D}^2 - a_2 G_\mathrm{D} G_0 + a_3 G_0^2 \right], \tag{3}$$

where

$$a_1 = -\gamma^2 \delta^2 \left(\Delta - \frac{\delta}{3} \right), \quad a_2 = \gamma^2 \delta \left[(\delta_1^2 + \delta_2^2) + \delta(\delta_1 + \delta_2) + \frac{2\delta^2}{3} - 2\tau^2 \right], \quad a_3 = -\gamma^2 \frac{2}{3} \tau^3.$$

The effect of term (3) can be eliminated by measuring in the presence of gradient G_0 and in the presence of both gradients, G_0 and G_D.

After mathematical re-arrangement we obtain

$$b = -\gamma^2 \left\{ \delta^2 \left(\Delta - \frac{\delta}{3} \right) G_\mathrm{D}^2 - \delta \left[(\delta_1^2 + \delta_2^2) + \delta(\delta_1 + \delta_2) + \frac{2\delta^2}{3} - 2\tau^2 \right] G_\mathrm{D} G_0 \right\}. \tag{4}$$

For the ratio of the magnitudes of spin echoes measured with and without the diffusion gradient, $(G_\mathrm{D} = 0)$ (M_{G_D} and M_0), it holds

$$\ln \left(\frac{M_{G_\mathrm{D}}}{M_0} \right) = -\gamma^2 \left[a_1 G_\mathrm{D}^2 - a_2 G_\mathrm{D} G_0 \right] D. \tag{5}$$

By measuring the spin echo amplitudes M_{G_D}, M_{-G_D}, and M_0 and calculating according to relation (5) it is possible to calculate from three experiments the diffusion coefficients, according to the relation

$$D = \frac{\ln \left(\dfrac{M_{G_\mathrm{D}} M_{-G_\mathrm{D}}}{M_{G_\mathrm{D}=0}^2} \right)}{-2\gamma^2 \delta^2 \left(\Delta - \dfrac{\delta}{3} \right) G_\mathrm{D}^2}. \tag{6}$$

The accuracy of the measurement of diffusion coefficients depends on the inaccuracy of the diffusion gradient magnitudes, timing and determination of the spin echo magnitude. The timing error can be neglected in current tomography systems. The accuracy of determining the spin-echo magnitude greatly depends on the signal-to-noise ratio and on the drop in echo magnitude for the diffusion gradient used. The diffusion coefficient in heterogeneous materials calculated by relation (4) carries an error that is due to the cross term. In this case, the relative error due to the error in measuring the amplitude of NMR signal is given by the relation

$$\delta_\mathrm{D} = \frac{4\delta_\mathrm{M}}{\ln \left(\dfrac{M_{G_\mathrm{D}} M_{-G_\mathrm{D}}}{M_{G_\mathrm{D}=0}^2} \right)} \tag{7}$$

The error δ_M depends on the magnitude of signal-to-noise ratio in MR signal or in MR image.

3. EXPERIMENTAL VERIFICATION

Some experimental tests were made by measuring the diffusion coefficient of water both inside and outside of selected samples of porous materials of different properties. The change in the diffusion of water in porous materials was studied. The measuring method was experimentally tested on the MR tomograph 200 MHz/120 mm (4.7 T) in the ISI ASCR in Brno. The 6-interval sequence (PFG-SE), shown in Fig. 1, was used in the measurement. The error measured for the determination of spin echo magnitude for $G_D = 0$ and $G_0 = 0$ is $\delta_M = 1.8\%$.

When greater amplitudes of the two gradients are applied, the magnitude of spin echoes decreases to as little as one third, with the magnitude of noise remaining the same and with the error δ_M increasing. The non-suppressed effect of background field gradient will lead to a greater error of diffusion coefficient measurement than the error of spin echo determination is. For standard diffusion measurements with the spin or the stimulated echo one usually acquires several echo amplitudes as a function of the b-factor. This enables performing a fit or even a deconvolution of the data, and thus increasing the certainty of the results and gaining the distribution of diffusion coefficients. We believe that the method of three measurements provides for this kind of processing.

The samples were immersed in a beaker with deionized water and placed, together with the beaker, in the working space of tomograph. The diffusion coefficients were measured for the diffusion gradients $G_D = 0$ and ± 161 mT/m by the method of three measurement. Transverse slices, 3 mm thick, were measured in all samples. The images detected were 256×256 pixels. For each sample, the diffusion was determined in several different areas and the resultant value was determined as the arithmetic mean of these values.

The first sample to be measured was a 20×30 mm cylinder of a material used in industry for mechanical filters with diameter 0.5 mm pores. Fig. 2 gives the MR image of the sample, weighted by spin density and diffusion, with areas of diffusion evaluation marked out.
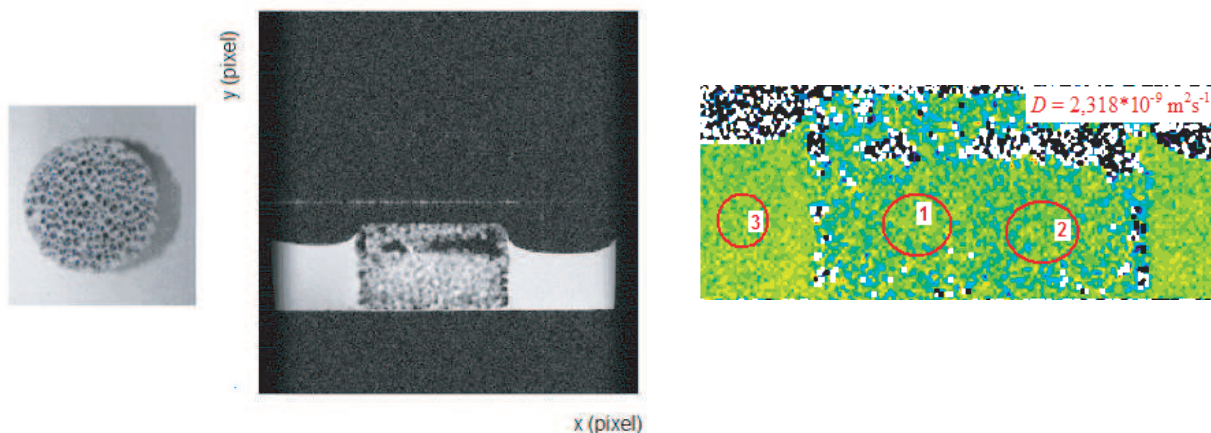

Figure 2: Measurement results for a sample of porous material, with 0.5 mm pores. (a) photograph of sample, (b) NMR image weighted by spin density, and (c) MR image weighted by diffusion.

After processing the values measured, the diffusion of water outside of the sample and at a temperature of 20.5°C is $D = 2.5 \cdot 10^{-9}$ m^{2}s^{-1}. The diffusion inside of the sample is $D = 2.3 \cdot 10^{-9}$ m^{2}s^{-1} [9]. The difference between these diffusions amounts to $0.182 \cdot 10^{-9}$ m^{2}s^{-1} and is proportional to the size of pores in the sample being measured. The measurement error, determined from the magnitude of standard noise deviation in the area of diffusion evaluation is $4.08 \cdot 10^{-10}$ m^{2}s^{-1}.

The second sample to be measured was a 20×40 mm cylinder of a material used in industry for mechanical filters with diameter 3.5 mm pores. Fig. 3 gives the photograph of the sample, its image weighted by spin density and its diffusion image with areas of measurement marked out.

After processing the values measured, the diffusion of water outside of the sample and at a temperature of 20.5°C is $D = 2.66 \cdot 10^{-9}$ m^{1}s^{-1}. The diffusion inside of the sample is $D = 2.5 \cdot 10^{-9}$ m^{2}s^{-1}. The change in the diffusion of water due to porous material is $0.16 \cdot 10^{-9}$ m^{2}s^{-1}. The measurement error is $3.22 \cdot 10^{-10}$ m^{2}s^{-1}.

The third sample to be measured was a white porous material used in catalysts of $35 \times 35 \times 20$ mm in dimensions. Fig. 4 gives the photograph of the sample, the MR image of water weighted by spin density, and the diffusion MR image with areas of measurement marked out.
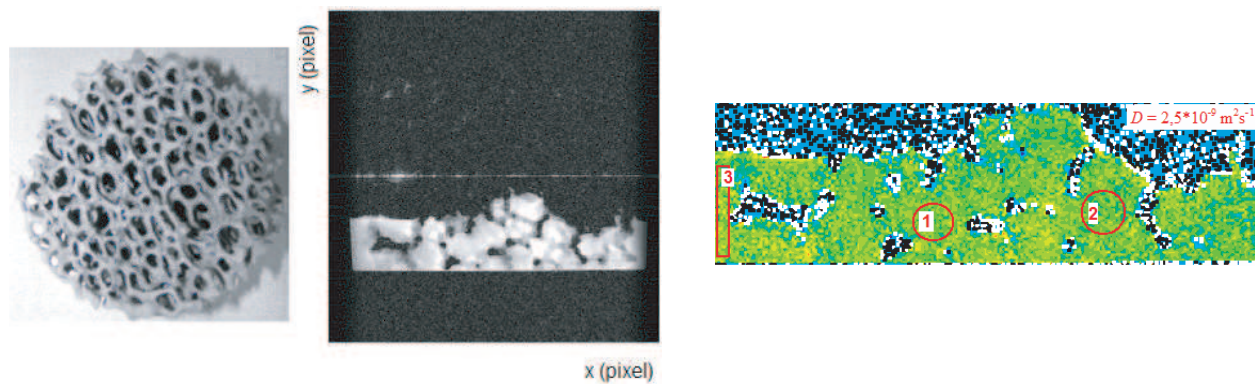
Figure 3: Measurement results for a sample of porous material with 3.5 mm pores. (a) photograph of sample, (b) MR image weighted by spin density, and (c) MR image weighted by diffusion.
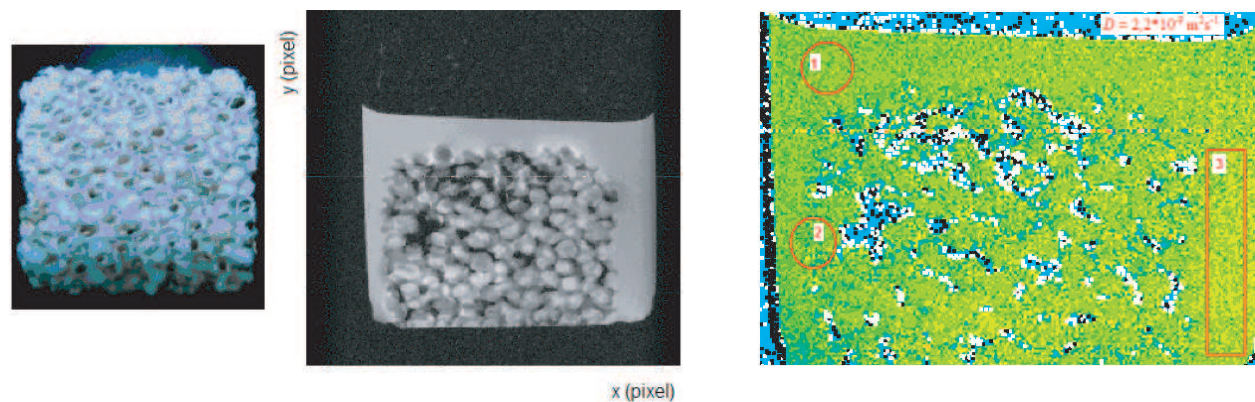

Figure 4: Measurement results for a sample of porous material with 1.5 mm pores. (a) photograph of the sample, (b) MR image weighted by spin density, and (c) MR image weighted by diffusion.

After processing the values measured, the diffusion of water outside of the sample and at a temperature of 20.5°C is $D = 2.44 \cdot 10^{-9}\,\mathrm{m^2s^{-1}}$. The diffusion inside of the sample is $D = 2.2 \cdot 10^{-9}\,\mathrm{m^2s^{-1}}$. The change in the diffusion of water in porous material is $0.16 \cdot 10^{-9}\,\mathrm{m^2s^{-1}}$ and the measurement error is $3.22 \cdot 10^{-10}\,\mathrm{m^2s^{-1}}$.

When measuring the diffusion map of thin slices, the noise in the image is pronounced and higher than in the measurement of the whole volume on an NMR spectrometer. Time averaging is often used to increase the signal-to-noise ratio. Gradient pulses in imaging sequences in all directions (readout, phase and slice selection) can affect the accuracy of diffusion measurement. The methods proposed reduce this effect. These methods can be applied in measurements on current MR tomography systems, which are in most cases furnished with the standard spin-echo method for diffusion measurement.

4. CONCLUSIONS

In the paper, the measurement of the diffusion coefficients of water in heterogeneous systems is described. It is characterized by a special method of measuring, digital image processing, and calculation of the diffusion coefficients. An advantage of the three measurement arrangement is the elimination of both the cross terms $G_D G_0$ and the term with G_0^2. The diffusion constant being measured depends on the time parameters of measurement, stability of the RF channel for nucleus excitation and MR signal reception, accuracy of the determination of spin echo magnitude, and on the magnitude of the diffusion gradient.

The technique will be made use of in the measurement of diffusion-weighted images of solids or gas found in porous materials, and in the development of new MR tomography measuring methods in the Institute of Scientific Instruments of the Academy of Sciences of the Czech Republic, v.v.i.

REFERENCES

1. Stejskal, E. O. and J. E. Tanner, "Spin diffusion measurements: Spin echoes in the presence of a time-dependent field gradient," *J. Chem. Phys.*, No. 42, 288, 1965.

2. Tanner, J. E., "Use of the stimulated echo in NMR diffusion studies," *J. Chem. Phys.*, Vol. 52, 2523–2526, 1970.

3. Cotts, R. M., M. J. R. Hoch, T. Sun, and J. T. Markert, "Pulsed field gradient stimulated echo methods for improved NMR diffusion measurements in heterogeneous systems," *J. Magn. Reson.*, Vol. 83, 252–266, 1989.

4. Sorland, H. G., B. Hafskjold, and O. Herstad, "A stimulated-echo method for diffusion measurements in heterogeneous media using pulsed field gradients," *J. Magn. Reson.*, Vol. 124, 172–176, 1997.

5. Sun, P. Z., J. G. Seland, and D. Coryb, "Background gradient suppression in pulsed gradient stimulated echo measurements," *J. Magn. Reson.*, Vol. 161, 168–173, 2003.

6. Galvosas, P., F. Stallmach, and J. Kärger, "Background gradient suppression in stimulated echo NMR diffusion studies using magnetic pulsed field gradient ratio," *J. Magn. Reson.*, Vol. 166, 164–173, 2004.

7. Sorland, H. G., D. Aksnes, and L. Gjerdaker, "A pulsed field gradient spin-echo method for diffusion measurements in the presence of internal gradients," *J. Magn. Reson.*, Vol. 137, 397–401, 1999.

8. Bartusek, K. and E. Gescheidtova, "MRI method of diffusion measurement in heterogeneous materials," *Measurement Science and Technology*, Vol. 19, 1–8, 2008.

9. Holz, M., S. R. Heil, and A. Sacco, "Temperature-dependent self-diffusion coefficients of water and six selected molecular liquids for calibration in accurate ^{1}H NMR PFG measurements," *Phys. Chem. Chem. Phys.*, Vol. 2, 4740–4742, 2000.

Compensating the Effect of Static Magnetic Field in MR Measurement of Diffusion

Karel Bartusek[1] and Eva Gescheidtova[2]

[1]Institute of Scientific Instruments, Academy of Sciences of the Czech Republic, v.v.i.
Kralovopolska 147, Brno 61200, Czech Republic
[2]Faculty of Electrical Engineering and Communication, Brno University of Technology
Kolejni 2906/4, Brno 61200, Czech Republic

Abstract— The paper describes a modified PFGSE MR method of measuring diffusion coefficients in heterogeneous materials. The principle of the proposed method consists in measuring the decrease in spin echo when applying diffusion gradients of different polarities. The detected images must be processed using special methods. The method greatly reduces the effect of static magnetic field gradient on the precision of measuring diffusion coefficients.

1. INTRODUCTION

When studying the properties of live tissues and also inanimate materials, one of the currently most important methods can be seen in imaging techniques based on the magnetic resonance (MR) principle. These methods allow measuring the very slow motion (diffusion) $10^{-10} \div 10^{-12}\,\mathrm{m^2/s}$ of atomic nuclei and molecules in substances examined. The knowledge of the motion of atomic nuclei in porous materials brings new diagnostic potentials. The very first method for diffusion measurement, the Pulsed Field Gradient Spin Echo (PFGSE), was described as early as 1965 [1]. It can only be used to measure diffusion in substances with sufficiently long relaxation times T_1 and T_2. The nuclei of substances encountered in porous materials have short relaxation times (units of milliseconds).

In the years 1987–2004, PFGSE methods of measuring diffusion were described [2–6] that do away with the interfering effect of magnetic susceptibility of examined substances, based on the appearance of simulated echo. Their advantage is that substances with short relaxation times T_2 can be measured but relaxation times T_1 must be longer than the time interval between two diffusion impulses. Measuring sequences were developed based on the spin echo and on the application of bipolar gradients [7], which were less dependent on the undesirable mutual influencing of gradients.

Our proposed method employs the PFGSE measuring sequence, in which three or four diffusion gradients of different polarities are generated [8]. Simple calculations can be used to compensate for the inhomogeneities of static magnetic field, which are due to the magnetic susceptibility of the substance being measured. Shaped impulses in the measuring sequence extend the diffusion measurement time, which is always limited by relaxation time T_1 of the substance under measurement. To be able to measure diffusion in substances with short relaxation times T_1, we must reduce the measuring time to a minimum while maintaining sufficient precision of the measurement.

2. METHOD

To measure the diffusion coefficients of atoms and molecules, the PFGSE measuring sequence is used, which is shown in Fig. 1. The regular sequence of spin echo is extended by two diffusion gradients. The first of them, applied between two RF impulses, puts the spins out of phase in a defined way. The second gradient, which brings the spins into phase again, follows after a 180° impulse. A static gradient G_0, which results from the magnetic properties of the substance being measured, is acting here during the whole measurement.

The drop in MR signal M_{G_D} due to diffusion can be described by the exponential function

$$M_{G_\mathrm{D}} = M_0 \mathrm{e}^{bD}, \tag{1}$$

where M_0 is the value of a signal measured without the application of diffusion gradients and G_D.

The constant b gives the sensitivity measuring sequence to diffusion and is given by the relation

$$b = -\gamma^2 \int\limits_0^{2\tau} \left[\int\limits_0^t G_\mathrm{D}(t')\mathrm{d}t' \right]^2 \mathrm{d}t. \tag{2}$$
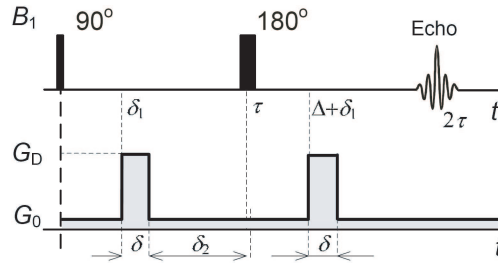
Figure 1: PFGSE MR technique for measuring diffusion in heterogeneous systems.

For the PFGSE method [1] the constant b is expressed by the relation

$$b = -\gamma^2 \left\{ \delta^2 \left(\Delta - \frac{\delta}{3} \right) G_D^2 - \delta \left[(\delta_1^2 + \delta_2^2) + \delta (\delta_1 + \delta_2) + \frac{2\delta^2}{3} - 2\tau^2 \right] G_D G_0 + \frac{2}{3} \tau^3 G_0^2 \right\}. \quad (3)$$

Substituting

$$a_1 = -\gamma^2 \delta^2 \left(\Delta - \frac{\delta}{3} \right), \quad a_2 = \gamma^2 \delta \left[(\delta_1^2 + \delta_2^2) + \delta (\delta_1 + \delta_2) + \frac{2\delta^2}{3} - 2\tau^2 \right],$$

relation (3) can be rewritten in the form

$$b = -\gamma^2 \left[a_1 G_D^2 - a_2 G_D G_0 + a_3 G_0^2 \right]. \quad (4)$$

The effect of the last term in Equations (3) and (4) can be eliminated by measurement in the presence of gradients G_0 and G_D, and by measurement for $G_D = 0$. The diffusion coefficient can be calculated from the drop in the magnitude of spin echo when measuring with M_{G_D}, and without the diffusion gradient $M_{G_D} = 0$ according to the relation

$$\ln \left(\frac{M_{G_D}}{M_{G_D=0}} \right) = -\gamma^2 \left[a_1 G_D^2 - a_2 G_D G_0 \right] D. \quad (5)$$

In a heterogeneous material the coefficient b, calculated from relation (5), carries an uncertainty due to the cross term. On the assumption that the timing error and the gradient level error are eliminated and only errors in determining the level of MR signal δ_M show up, the diffusion error in relative measure δ_D can be estimated according to

$$\delta_D = \frac{\Delta D}{D} = \frac{2\delta_M}{\ln \left(\frac{M_{G_D}}{M_{G_D=0}} \right)}. \quad (6)$$

Let us suppose that relative errors of determining the levels of spin echoes M_{G_D}, M_{-G_D} and $M_{G_D=0}$ are identical. To eliminate the cross term in Equation (5), three measurements can be performed: for positive, negative and zero diffusion gradients. Relation (5) can be rewritten quite simply to the form

$$\ln \left(\frac{M_{G_D} M_{-G_D}}{M_{G_D=0}^2} \right) = -2\gamma^2 a_1 G_D^2 D, \quad (7)$$

The diffusion coefficient can be established from the relation

$$D = \frac{\ln \left(\frac{M_{G_D} M_{-G_D}}{M_{G_D=0}^2} \right)}{-2\gamma^2 \delta^2 \left(\Delta - \frac{\delta}{3} \right) G_D^2}. \quad (8)$$

The relative error for three measurements is then

$$\delta_D = \frac{4\delta_M}{\ln \left(\frac{M_{G_D} M_{-G_D}}{M_{G_D=0}^2} \right)}. \quad (9)$$

If the positive and the negative gradient levels differ

$$-G_D = (1 + \xi)G_D,$$

where ξ is the relative error of negative gradient

$$\xi = \frac{\Delta G_D}{G_D},$$

there will be a systematic measuring error. For G_D and $-G_D$ relation (4) will change to

$$b_{+G_D} = -\gamma^2 \left[a_1 G_D^2 - a_2 G_D G_0 + a_3 G_0^2 \right], \tag{10}$$

$$b_{-G_D} = -\gamma^2 \left[a_1 (1 + \xi)^2 G_D^2 + a_2 (1 + \xi) G_D G_0 + a_3 G_0^2 \right]. \tag{11}$$

Relation (5) will change to

$$\ln \left(\frac{M_{G_D}}{M_{G_D=0}} \right) = -\gamma^2 \left[a_1 G_D^2 - a_2 G_D G_0 \right] D, \tag{12}$$

$$\ln \left(\frac{M_{-G_D}}{M_{G_D=0}} \right) = -\gamma^2 \left[a_1 (1 + \xi)^2 G_D^2 + a_2 (1 + \xi) G_D G_0 \right] D. \tag{13}$$

For three measurements (G_D, $-G_D$ and $G_D = 0$) the diffusion coefficient can be calculated according to the relation

$$\ln \left(\frac{M_{G_D} M_{-G_D}}{M_{G_D=0}^2} \right) = -2\gamma^2 \left(a_1 G_D^2 + a_1 G_D^2 \xi + \frac{a_2}{2} G_D G_0 \xi \right) D. \tag{14}$$

It can be seen from a comparison of relations (7) and (14) that the error of coefficient b is given by the sum of relative errors $a_1 G_D^2 \xi$, which are independent of gradient G_0 and error $a_2/2G_D G_0 \xi$. For low levels of the diffusion gradients applied the latter error can have a considerable effect.

Another method of eliminating the effect of gradient G_0 is based on four measurements, in which the diffusion gradients $2G_D$, $-2G_D$, and G_D, $-G_D$ are applied. In this case we obtain for the decreases in spin echo the relations

$$\ln \left(\frac{M_{2G_D}}{M_0} \right) + \ln \left(\frac{M_{-2G_D}}{M_0} \right) = -\gamma^2 \left[\left(a_1 G_D^2 (1 + (1 + \xi)^2) + 2a_2 G_D G_0 + 2a_3 G_0^2 \right) \right] D. \tag{15}$$

$$\ln \left(\frac{M_{G_D}}{M_0} \right) + \ln \left(\frac{M_{-G_D}}{M_0} \right) = -\gamma^2 \left[\left(4a_1 G_D^2 (1 + (1 + \xi)^2) + a_2 G_D G_0 + 2a_3 G_0^2 \right) \right] D. \tag{16}$$

The difference of relations (15) and (16) only depends on the parameters of time intervals and on the diffusion gradient. The effect of gradient G_0 and of the cross term is suppressed, as can be seen from the relation

$$\ln \left(\frac{M_{2G_D}}{M_0} \right) + \ln \left(\frac{M_{-2G_D}}{M_0} \right) - \ln \left(\frac{M_{G_D}}{M_0} \right) - \ln \left(\frac{M_{-G_D}}{M_0} \right) = -6\gamma^2 \left[a_1 G_D^2 + a_1 G_D^2 \xi + \frac{a_2}{6} G_D G_0 \xi \right] D. \tag{17}$$

For $\xi = 0$, the cross term will be eliminated, coefficient b will depend on the time interval chosen, on the accuracy of determining the magnitude of MR signal δ_M, and on gradient G_D. Relation (17) can be used for the calculation of the diffusion coefficient

$$D = \frac{\ln \left(\frac{M_{2G_D} M_{-2G_D}}{M_{G_D} M_{-G_D}} \right)}{-6\gamma^2 \delta^2 \left(\Delta - \frac{\delta}{3} \right) G_D^2}. \tag{18}$$

For four measurements according to (17) the error of coefficient b will drop to one third in comparison with three measurements.

$$\delta_D = \frac{4\delta_M}{\ln \left(\frac{M_{2G_D} M_{-2G_D}}{M_{G_D} M_{-G_D}} \right)}. \tag{19}$$

3. EXPERIMENTAL VERIFICATION

The proposed methods were verified experimentally by measuring diffusion in deionised water at temperatures of $20 \pm 0.2°$C. The measurements were carried out on an MR tomography 200 MHz / 120 mm (4.7 T) in the Institute of Scientific Instruments, Academy of Sciences of the Czech Republic in Brno. The relaxation times of the water measured were $T_1 = 2700$ ms and $T_2 = 380$ ms. The 6-interval PFGSE sequence was used in the measurement. The sequence parameters were set at $\delta = 5$ ms, $\Delta = 20$ ms. The diffusion gradients chosen were $G_D = \pm 2$ and ± 144 mT/m. The static gradient was measured in the range $G_0 = 0 \div 144$ mTm. The resultant waveforms of the dependence of diffusion coefficient on gradient G_0 are given in Fig. 2.
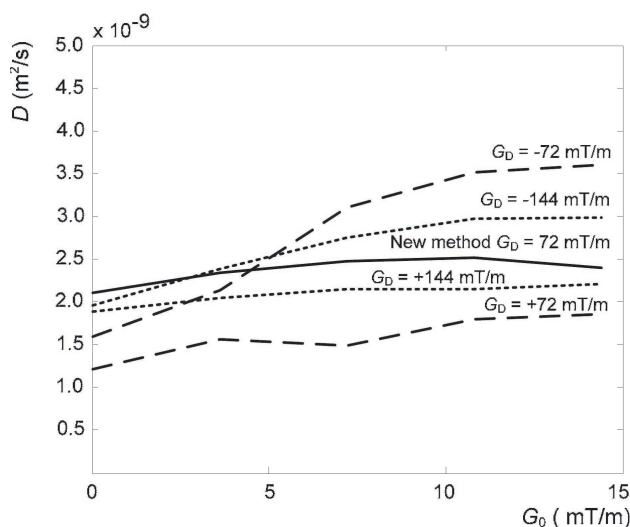

Figure 2: Results of measuring the diffusion of deionised water by both the PFGSE technique for the diffusion gradients $G_D \pm 72$ mT/m and ± 144 mT/m and the proposed four measurement method.

4. CONCLUSIONS

The method described in the paper has been proposed for measuring diffusion coefficients in heterogeneous systems. Its characteristic feature is a special measuring procedure and the calculation of coefficients. The advantage of conducting three of four measurements is the elimination of the influence of cross terms between the diffusion and the static gradients, and the elimination of the influence of the static gradient itself. The diffusion constants are dependent on the time parameters of the measuring sequence, the stability of the RF channel of tomograph for the excitation of nuclei, the accuracy of determining the spin echo magnitude, and on the level of the diffusion gradient.

The method will be used when measuring diffusion-weighted images of solids and gases that are present in porous materials.

REFERENCES

1. Stejskal, E. O. and J. E. Tanner, "Spin diffusion measurements: Spin echoes in the presence of a time-dependent field gradient," *J. Chem. Phys.*, No. 42, 288, 1965.
2. Tanner, J. E., "Use of the stimulatsd echo in NMR diffusion studies," *J. Chem. Phys.*, Vol. 52, No. 2523, 2523–2526, 1970.
3. Cotts, R. M., M. J. R. Hoch, T. Sun, and J. T. Markert, "Pulsed field gradient stimulated echo methods for improved NMR diffusion measurements in heterogeneous systems," *J. Magn. Reson.*, Vol. 83, 252–266, 1989.
4. Sorland, H. G., B. Hafskjold, and O. Herstad, "A stimulated-echo metod for diffusion measurements in heterogeneous media using pulsed field gradients," *J. Magn. Reson.*, Vol. 124, 172–176, 1997.

5. Sun, P. Z., J. G. Seland, and D. Coryb, "Background gradient suppression in pulsed gradient stimulated echo measurements," *J. Magn. Reson.*, Vol. 161, 168–173, 2003.

6. Galvosas, P., F. Stallmach, and J. Kärger, "Background gradient suppression in stimulated echo NMR diffusion studies using magnetic pulsed field gradient ratio," *J. Magn. Reson.*, Vol. 166, 164–173, 2004.

7. Sorland, H. G., D. Aksnes, and L. Gjerdaker, "A pulsed field gradient spin-echo method for diffusion measurements in the presence of internal gradients," *J. Magn. Reson.*, Vol. 137, 397–401, 1999.

8. Bartusek, K. and E. Gescheidtova, "MRI method of diffusion measurement in heterogeneous materials," *Measurement Science and Technology*, Vol. 19, 1–8, 2008.

9. Holz, M., S. R. Heil, and A. Sacco, "Temperature-dependent self-diffusion coefficients of water and six selected molecular liquids for calibration in accurate ^{1}H NMR PFG measurements," *Phys. Chem. Chem. Phys.*, Vol. 2, 4740–4742, 2000.

Wavelet Filtering and Level Set Segmentation of NMR Images for Monitoring the Development of Growing Cultures

J. Mikulka[1], E. Gescheidtova[1], and K. Bartusek[2]

[1]Department of Theoretical and Experimental Electrical Engineering
Brno University of Technology
Kolejni 4, Brno 61200, Czech Republic
[2]Institute of Scientific Instruments, Academy of Sciences of the Czech Republic
Kralovopolska 147, Brno 61264, Czech Republic

Abstract— The paper describes the pre-processing and subsequent segmentation of NMR images of growing tissue cultures. Images obtained by the NMR technique give three separately growing cultures. The aim of the work was to follow the speed of their development. Images obtained by means of the NMR device used are of very low resolution and contrast and there are no sharp edges between regions. Processing such images may prove to be quite difficult. A suitable algorithm was found, which consists of the pre-processing of the image and subsequent multiphase level set segmentation. The proposed method segments the image based on the intensity of the regions sought, and is suitable for working with NMR images in which there are no sharp edges. The method is described by partial differential equations that were transformed into corresponding difference equations solved numerically. Processing the detected images and measuring the sequence of NMR data give a graph of the growth development of the tissue cultures examined in comparison with manual measurement of their content.

1. INTRODUCTION

MRI is useful to obtain the number of hydrogen nuclei in biology tissue or to follow growing of cultures. There was provided examination by MR techniques [1] for rate of growth considering, rising of percentage of protons and cluster's shape of somatic germ. These measurements were part of research for hypothesis verification about increase percentage of water in process of tissue culture growth in case of cadmium contamination. In this case we put into tomograph operating area the measured tissue, choose the right slicing plane and measure MR image in this plane. The image is weighted by spin density and pixel intensity is equal to number of proton nucleus in chosen slice. MR image is a map of protons distribution in measured cluster of growing tissue culture [2].

The same technique was used for growth characterizing of early spruce germs contaminated by lead and zinc. There was computed intensity integral characterizing the number of protons in growing cluster and there were specified the changes of this value during the growth from MR images.

For measurement was used the spin-echo method because in contrast to gradient-echo technique the influence of the base magnetic field non-homogeneity is eliminated and images have better signal to noise ratio. The signal to noise ratio depends on the chosen width of slice. With thinner slices is the number of nucleus which generates signal smaller and the signal to noise ratio decreases. However the minimum width of slice is useful for tissue cultures imaging. The optimum width 2 mm was found. There was placed small flask filed by deionized water for tomograph parameters instability suppression during long-term measurement. Obtained intensities of each image were scaling according to intensity of water in the flask (Fig. 1).

For described experiments was used MR tomograph with horizontal magnet (magnetic field 4.7 T) and operating area with diameter of 120 mm. Active shield gradient coils generate the maximal gradient field 180 mT/m.

At the first the data were processed in MAREVISI software where was achieved the manual computation of cluster surface from diffusion image and intensity integral of clusters from images weighted by spin density. Further the images weighted by spin density were filtered by wavelet transformation and segmented by region level set method. From segmented clusters was computed their surface and intensity integral too. Both methods were compared.
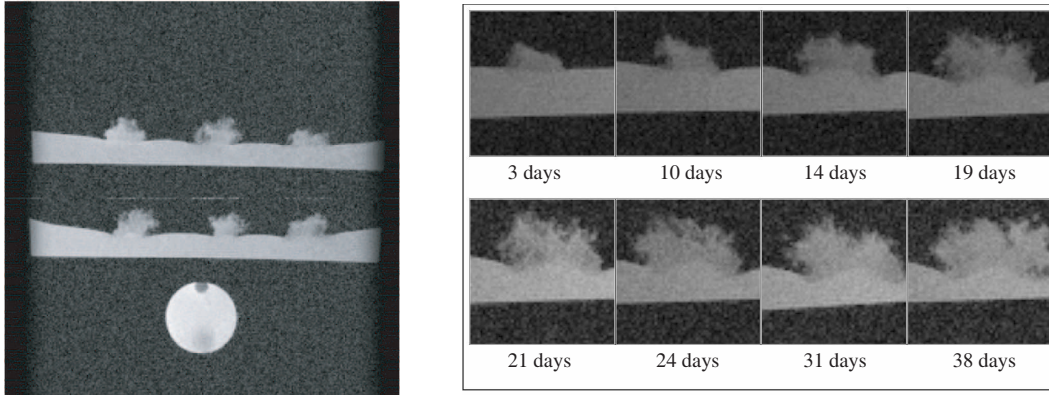
Figure 1: Example of obtained image with 6 clusters and small flask filed by water for checking and scaling the image, at the top are the clusters contaminated by Zn, at the bottom are the clusters contaminated by Pb, on the right is the example of one cluster growth which is contaminated by lead 1000 mg/l.

2. MEASUREMENT METHODS

The integral of image data could be established by two approaches. The first of them is sum of intensities in chosen part of image containing contaminated clusters divided by count of pixels

$$I_i = \frac{x_{\max} y_{\max}}{M \cdot N} \sum_1^M \sum_1^N s_i, \tag{1}$$

where I_i is intensity integral, $x_{\max} a y_{\max}$ are maximum dimensions of image in axis x and y.

The second approach utilizes properties of Fourier transformation and relation between MR image and interferential image which consist of obtained complex data. This relation could be described by following equation [3]:

$$s_i(k_x, k_y) = \int_{-\infty}^{\infty} \int_{-\infty}^{\infty} \rho_i(x, y) \cdot e^{-2\pi(k_x x + k_y y)} dx dy, \tag{2}$$

where k_x and k_y are axis in measured interferential image called spatial frequency, $\rho_i(x, y)$ is distribution of spin density in MR image. For $k_x = k_y = 0$ we obtain:

$$s_i(0,0) = \int_{-\infty}^{\infty} \int_{-\infty}^{\infty} \rho(x, y) dx dy = I_i. \tag{3}$$

Number of the protons nucleus in measured sample is proportional to integral I_i which is equal to intensity of interferential image in zero point, i.e., for $k_x = k_y = 0$. Integral of MR image after DFT could be computed by this equation:

$$I_i = \frac{x_{\max} y_{\max}}{M \cdot N} s_i(0,0). \tag{4}$$

The results of both methods are identical and the error is less than 1%. This approach is useful in case measurement of one tissue cluster.

For the results verification were the images filtered by means of wavelet transformation and consequently segmented by four-phase level set method, which is described by this equation:

$$F_4(\mathbf{c}, \mathbf{\Phi}) = \int_\Omega (u_0 - c_{11})^2 H(\Phi_1) H(\Phi_2) \, dx dy + \int_\Omega (u_0 - c_{10})^2 H(\Phi_1)(1 - H(\Phi_2)) \, dx dy$$

$$+ \int_\Omega (u_0 - c_{01})^2 (1 - H(\Phi_1)) H(\Phi_2) \, dx dy + \int_\Omega (u_0 - c_{00})^2 (1 - H(\Phi_1))(1 - H(\Phi_2)) \, dx dy$$

$$+ \nu \int_\Omega |\nabla H(\Phi_1)| + \nu \int_\Omega |\nabla H(\Phi_2)|, \tag{5}$$

In Fig. 2 is shown the example of processed image by described approach. The surface and intensity integral is then computed only from bounded clusters and due to the result is not devaluated by noise around clusters. The results are compared in the next chapter.

Figure 2: Example of the image processing, from the left: the original image, the wavelet transform filtered image and the segmented cluster by four-phase level set segmentation (green curve).

3. RESULTS

Relation between intensity of cluster (thereby relative number of protons) and time of growth is for various Zn and Pb contaminations shown in Fig. 3 and Fig. 4. Clearly, the proton concentration in cluster of tissue culture grows all the time independently on tissue culture growth capability. The capability of growth dramatically decreases after 14–20 days to minimum. Relation between number of protons in tissue culture with contamination Zn or Pb and level of concentration by this element is shown in Fig. 5 and Fig. 6. We can find a concentration in which the percentage of protons is the highest all the time of growing. With zinc contamination is the optimal concentration 250 mg/l and for lead is the concentration 50 mg/l. In diffusion images are the clusters more precisely bounded and the evaluation of cluster surface is more accurately. It does not reflect a concentration of proton nucleus and the results are different from intensity integral measurement. The cluster's surfaces were evaluated from images weighted by spin density by wavelet filtration method and consequential region four-phase level set segmentation.
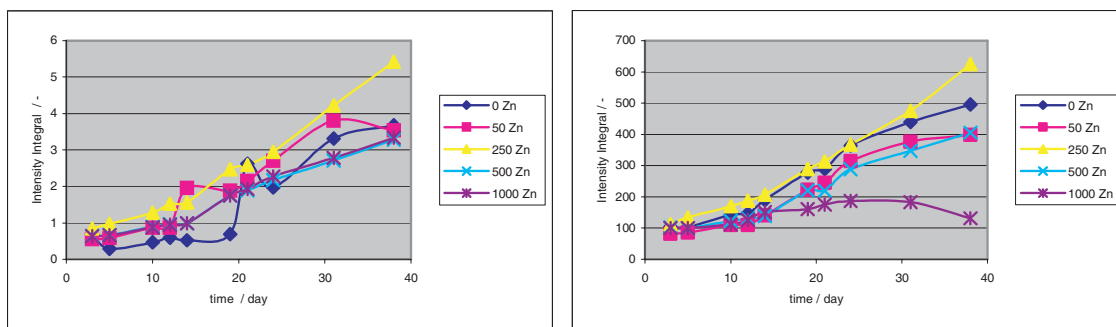

Figure 3: Measurement of intensity integral of clusters in the time for various Zn concentrations, on the top is the result of the manual method, on the bottom is the result of the segmented image processing.
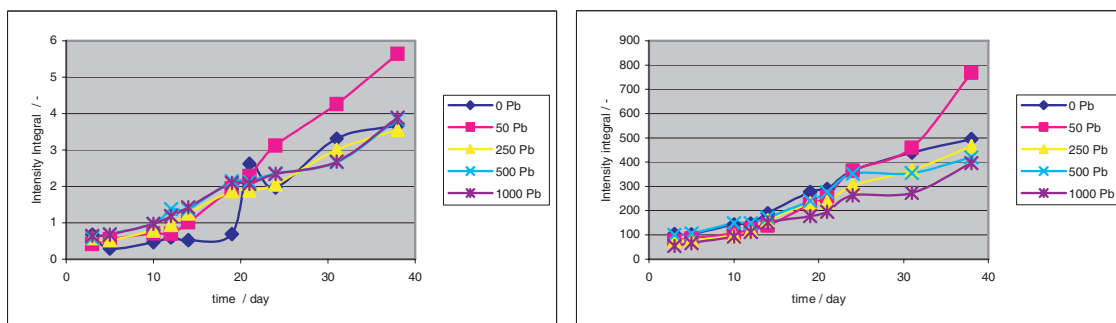

Figure 4: Measurement of intensity integral of clusters in the time for various Pb concentrations, on the top is the result of the manual method, on the bottom is the result of the segmented image processing.
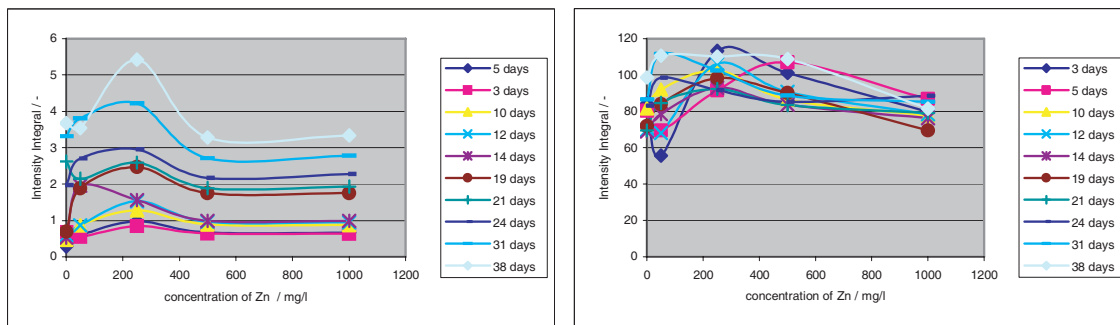
Figure 5: Measurement of intensity integral of clusters for various Zn concentrations, on the top is the result of the manual method, on the bottom is the result of the segmented image processing.
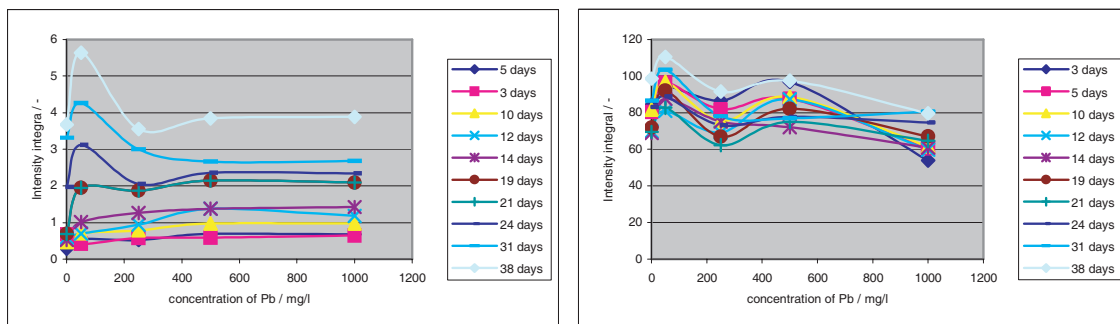

Figure 6: Measurement of intensity integral of clusters for various Pb concentrations, on the top is the result of the manual method, on the bottom is the result of the segmented image processing.

4. CONCLUSIONS

The MRI technique is useful for observing of the growth of the spruce germs and for verification of the hypothesis of increasing amount of water in the growing tissue cultures with various metal contaminations thereby their faster elutriation. The basic measurements and data processing by two different methods were taken. The aim of this work was the surface and the intensity integral measurement in time. Firstly the data were manually processed in the MAREVISI software by measuring of the cluster's surface in the diffusion images and then by the measuring of the intensity integral in the images weighted by the spin density. Further the images weighted by the spin density were processed by the wavelet transformation and segmented by the four-phase level set method and both monitored values were obtained in the Matlab. Both methods gives similar results thereby the measurement was verified.

ACKNOWLEDGMENT

REFERENCES

1. Supalkova, et al., "Multi-instrumental investigation of affecting of early somatic embryos of spruce by cadmium(II) and lead(II) ions," *Sensors*, Vol. 7, 743–759, 2007.
2. Callaghan, P. T., *Principles of Nuclear Magnetic Resonance Microscopy*, Clarendon Press, Oxford, 1991.
3. Liang, Z. P. and P. Lauterbur, *Principles of Magnetic Resonance Imaging*, IEEE Press, New York, 1999.
4. Vese, L. and F. Chan, "A multiphase level set framework for image segmentation using the Mumford and Shah model," *International Journal of Computer Vision*, Vol. 50, No. 3, 271–293, 2002. www.math.ucla.edu/ lvese/PAPERS/IJCV2002.pdf

Perimeter Measurement of Spruce Needles Profile Using MRI

J. Mikulka[1], E. Gescheidtova[1], and K. Bartušek[2]

[1]Dept. of Theoretical and Experimental Electrical Engineering, Brno University of Technology
Kolejni 4, Brno 612 00, Czech Republic
[2]Institute of Scientific Instruments, Academy of Sciences of the Czech Republic
Kralovopolska 147, Brno 612 64, Czech Republic

Abstract— The paper describes using of MRI methods to assess the perimeter of the profile of spruce needles. The aim of this work is to create of multi-instrumental equipment for research on heavy metal (cadmium and lead) influence on development of spruce needles cellular germ (somatic embryos). During the research were observed differences in germ growth with different concentration of cadmium. With a certain concentration of cadmium the perimeter of needle increases more than with other. It is due to more intensive water usage from cultivation medium and then attenuation of heavy metal concentration inside the needle. As one of the observational methods of the mentioned phenomenon, was chosen analysis of the NMR image susceptible to estimation of the needle growth by the perimeter of the needle profile. Slices of the spruce needles were observed on MR tomograph UPT AV CR with the induction of magnetic field 4.7 T. Concurrently a method in AF MZLU was applied by cutting the needles on hand microtome, the images of the slices were observed by a digital camera with 1600×1200 pixels resolution and by using a binocular magnifying glass. The aim of the article is to compare of experimental results observed by both mentioned methods.

1. INTRODUCTION

The perimeter and volume measurement can be important in taxonomy. The aim of research is the assessment of impact of heavy metals (cadmium and lead) on cellular germ development. The paper describes different approaches of the image processing for perimeter of the spruce needle crosscut measurement. There were measured the perimeters of 6 needles by four different methods. The result of the measurement is the perimeter of needle crosscut and it can be consequently useful to the volume computation by creation slice-by-slice three-dimensional model, which is the aim of the future work.

The slices of spruce needles were obtained by two ways. First of all the needles were analyzed by nuclear magnetic resonance (NMR) and obtained images were then processed. We can see the NMR images in Figure 1. The images were processed by manual tracing of a needle border and the perimeters of the needles were given by the length of the boundary. This is a time-consuming method, but it has good results. Then the NMR images were processed by semi-automatic method in ACC software. The second approach consist in manual slicing by a microtome and consequently taking a photo by Olympus digital camera with 1600×1200 pixels resolution using a binocular
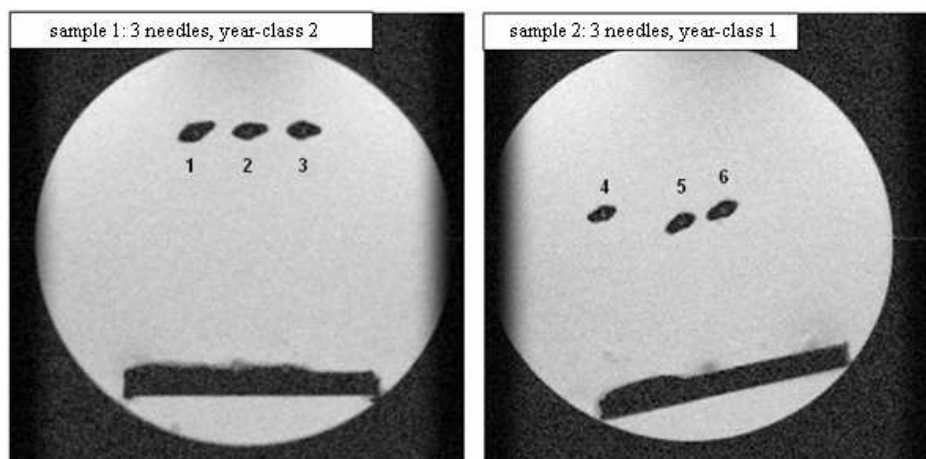

Figure 1: The samples of *Picea abies* needles, on the left are needles year-class 2, on the right are needles year-class 1.

magnifying glass as we can see in Figure 2. The three slices were made in the middle of the needles and the individual perimeters were averaged. The obtained images were processed automatically in GIMP software (edge detection, length of edge measurement).

Figure 2: The manual slicing of *Picea abies* needle, photographed by Olympus digital camera and by using a binocular magnifying glass.

The goal of the processing was the comparison of all results and verification of described methods. Therefore the reference method for segmentation of the NMR images was proposed. It is similar to manual tracing but the boundary of needle is established by isolines in Matlab. For a reason to specify an intensity level of the isoline was measured a reference image of a plastic tube filled with water with the inside diameter 4 mm. In this image, the suitable intensity level of the isoline was found. Then the perimeters of needles were measured on three levels around the reference level and the resultant perimeter was computed as their average.

2. PROPOSED METHOD

For correct evaluation of the perimeters of the needles it was necessary to find the mean value of intensity in the interface between the background and the needle. The experimental measurement was prepared. The plastic tube with known diameter filled with water was put into operating area of the mentioned tomograph. In the obtained image was found the suitable isoline for the correct perimeter measurement. The reference image and the found boundary are shown in the Figure 3. The results of the measurements in the reference image are summarized in Table 1.
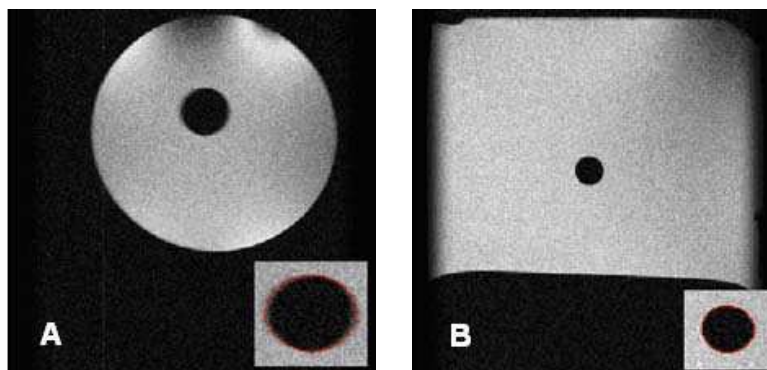

Figure 3: Reference images for suitable intensity assessment of pixels for isolines between background and object (plastic tube with inside diameter 4 mm).

As we can see in Table 1, in the reference image A the suitable intensity level was found 80 and in the reference image B (different resolution) level 120 in the full range 255. For the perimeter measurement of the needles was chosen mean value of these levels 100. The perimeters were computed from three isolines with pixel intensities 80, 100 and 120 and the resultant perimeter was given by their average. The example of the described measurement is shown in Table 2.

Table 1: Measured perimeters and corresponding tube inside diameters in reference images in relation to intensity of boundary-line, the real tube diameter was 4 mm.

Reference image A (50x50 mm, 256x256 pixels)			
intensity level (in the range 0-255)	measured perimeter O_m [mm]	corresponding diameter D_m [mm]	relative error D_m in relation to D [%]
80	12.50	3.98	0.50
100	12.85	4.09	-2.25
120	12.31	4.24	-6.00
Reference image B (30x30 mm, 256x256 pixels)			
intensity level (in the range 0-255)	measured perimeter O_m [mm]	corresponding diameter D_m [mm]	relative error D_m in relation to D [%]
80	12.18	3.88	3.00
100	12.35	3.93	1.75
120	12.54	3.99	0.25

Table 2: The perimeter measurement by three isolines and the resultant mean value of the perimeter.
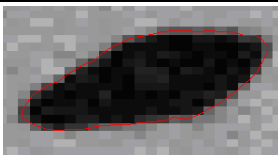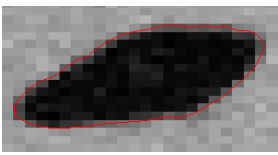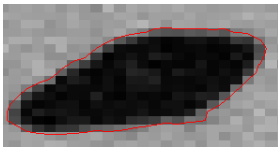
number of needle	intensity level	found boundary of needle	perimeter [mm]	mean value of the perimeters [mm]
1	80		3.1556	
1	100		3.2314	**3.2435**
1	120		3.3534	

Table 3: Comparison of measurement results obtained by 4 methods.

number of needle	method / the perimeter of needle [mm]			
	3 isolines in MR image	manual tracing in MR image	semi-automatic method by ACC SW in MR image	automatic measurement in photographed image (GIMP)
1	3.2435	3.246	3.266	3.320
2	2.9596	2.953	2.854	3.071
3	2.9085	2.904	2.908	3.027
4	2.5294	2.528	3.195	2.609
5	2.7971	2.799	2.903	2.992
6	2.8609	2.850	3.185	3.022

3. RESULTS

The results of measurements of the four described methods are compared in Tables 3 and 4. In the Table 3, we can see the perimeters of 6 needles obtained by the described methods and in the Table 4 there are shown errors of methods in relation to the proposed method which is taken as reference method.

Table 4: Comparison of relative errors of described methods in relation to "3 isolines" method.

measurement method	maximum relative error $\left|\delta\right|_{max}$ [%]	average relative error $\left|\delta\right|_{avg}$ [%]	median of relative error $\left|\delta\right|_{med}$ [%]
manual tracing in MR image	0.38	0.16	0.12
semi-automatic method by ACC SW in MR image	26.32	7.62	3.68
automatic measurement in photographed image (GIMP)	6.97	4.32	3.9

4. CONCLUSIONS

The growth of trees is dependent on the environmental impact. The paper compares some methods for perimeter of slice of spruce needle measurement as an instrument for monitoring of their development. There is noted the comparison of the perimeters obtained by the measurement in photographed image of manual sliced needle by the microtome and then by measurement in the MR image for verification. Both approaches give the similar results with 4% of average error. However, the semiautomatic processing method in ACC software gives the results with wide differences in individual measured values. This method is largely affected by random error.

REFERENCES

1. Aubert, G. and P. Kornprobst, *Mathematical Problems in Image Processing*, Springer, New York, 2006.
2. Vese, L. and F. Chan, "A multiphase level set framework for image segmentation using the mumford and shah model," www.math.ucla.edu/∼lvese/PAPERS/IJCV2002.pdf.
3. Chan, F. and J. Shen, "Image processing and analysis: Variational, PDE, wavelet and stochastic methods," *SIAM*, Philadelphia, 2005.

Characterization of Acetylcholine Hydrolysis under Continuous and Pulsed Microwaves Radiation Using Broadband Dielectric Measurement

C. Gilbert[1], **C. Pareige**[1], **A. Fourrier-Lamer**[1], **F. Maurel**[2], **and O. Meyer**[1]

[1]LGEP Supelec, CNRS UMR-8507, Univ. UPMC Paris 06, Univ. Paris Sud
11 rue Joliot Curie, F91192 Gif-sur-Yvette cedex, France
[2]ITODYS, CNRS, CNRS 7086, University of Paris 7, Bâtiment Lavoisier 15
rue Jean de Baïf, F75205 Paris cedex 13, France

Abstract— In this paper, we will describe the statement of our current advance in continuous and pulsed wave analysis on AchE activation. Acetylcholinesterase (AchE) is a major enzyme that catalyzes the hydrolysis of the neurotransmitter Acetylcholine into Choline and Acetic Acid, a reaction necessary to allow a cholinergic neuron to return to its resting state after activation. In a more general way, it controls nervous and neuromuscular impulses in mammalians species. We will try to determine how continuous waves (CW) or Pulsed Waves (PW) interact with this polarized entity. Dielectric relaxation determination in real time, will give us information about the synthesis output, and power density measurement, the energy activation threshold.

1. INTRODUCTION

In this paper, we will present the state of our works and the follow-up of a reaction of hydrolysis of acetylcholine in the presence of a catalyst, by broadband dielectric characterization during conventional thermal treatment and microwave treatment. The catalyst is an enzyme, acetylcholine esterase (AChE) [1, 2]. Acetylcholine is a neurotransmitter of neuromuscular junctions, a very often used exciter. The AChE of the central nervous system is involved in regulating the transmission of nerve impulses.

The experimental study will help in implementing various parameters: the power transmitted to the sample, the intensity of the electric field in the sample, the application duration of the intense field, the energy transmitted to the sample charges, and the relaxation activation energy of dipoles.

The study will particularly focuses on the early stages of the implementation of strong field (first seconds), step during which it will be assumed that the scope of power is directly linked to conductive entities instantly compared to the times involved in the experience and can then act as a catalyst for the reaction.

In a first step, the study of isolated molecules in the presence of an intense field will generalize previous studies carried out on non-biological molecules. Indeed, these studies have helped to evaluate the energy transmitted to the dipoles they carry. In a second step, we will achieve the study of the reaction follow-up itself.
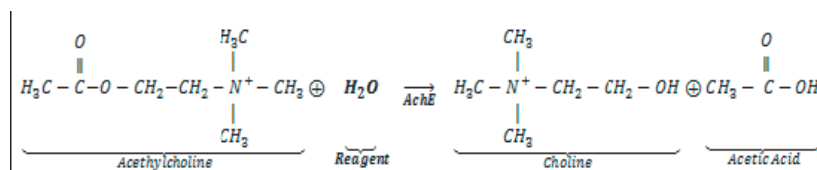

Figure 1: Hydrolysis reaction.

2. INSTRUMENTATION

The measuring bench under conventional and microwave thermal treatments [3] directly ensues, at the beginning, from experiences made on saponification [3–6]. The idea is to monitor under conventional heating the dielectric characteristics obtained by measuring admittance or reflectance coefficient of the cell placed at the end of a coaxial guide. For microwave treatment, a power wave at 2.45 GHz is applied for a fixed period (typically around 10 s) before switching electro-mechanically the cell on the impedance or network analyzer in order to measure the admittance.
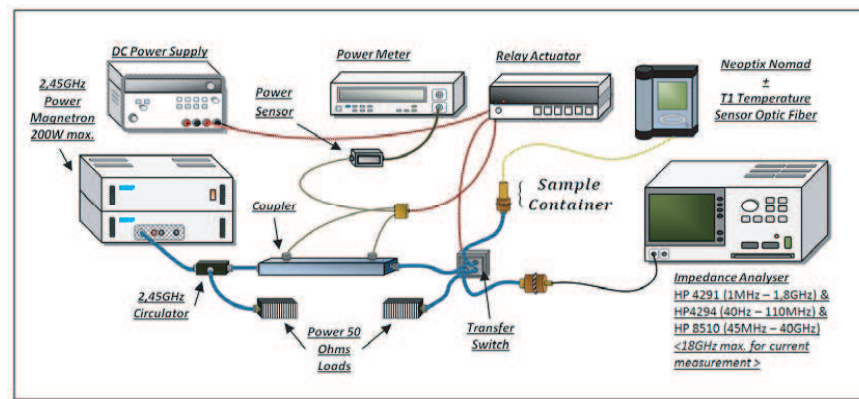
Figure 2: Instrumentation for dielectric characterization under MW irradiation.

During microwave treatment, we will essentially study the early stages of the treatment, crucial step in the evolution of the reaction for variable powers (1 to 10 Watts).

Dielectric characterization under microwave treatment is carried out using a cell with inhomogeneous filling [4, 5]. The measurement frequency band is 1 MHz–1.8 GHz. At room temperature, broadband characterization (100 Hz–18 GHz) is also done with a cell suitable for measuring liquids consisting of a cylindrical guide ended by a short circuit [7] and sealed by adding a dielectric coaxial top without loss (PTFE, PEEK . . .).
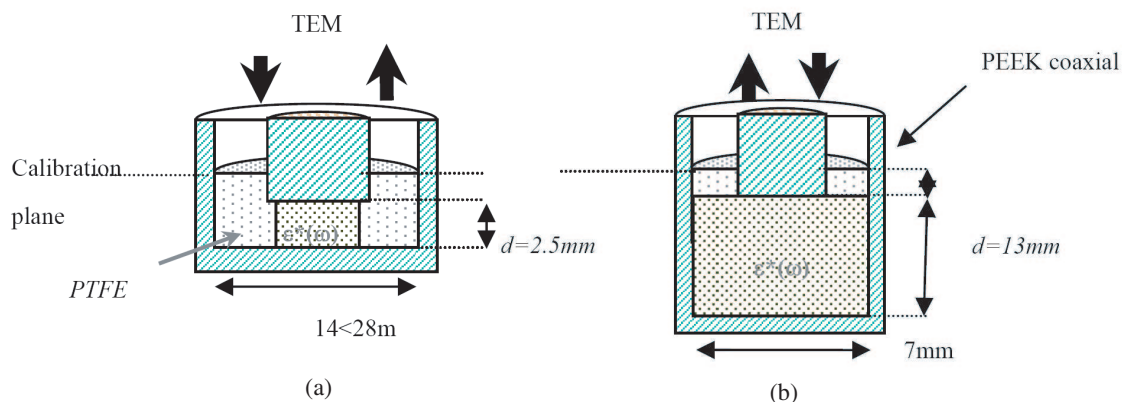

Figure 3: (a) Microwave heating cell. (b) Cell for broadband measurement of liquid.

3. FIRST RESULTS

The first measures concern basic products of the hydrolysis reaction, the molecule acetylcholine chloride and choline chloride in water at different concentrations.

The first measures (Figs. 3–4) show conductions and interface relaxation phenomena of type Maxwell-Wagner (MW) effects in low frequencies ($f < 10$ KHz). The significant conductivity of biological solutions generates significant interaction between electrodes and mobile charges which may mask the real part of epsilon by a polarization of the connection electrodes [8]. The relaxation of pure water is found at high frequencies (beyond 500 MHz for acetylcholine chloride). The evolution of conductivity for different concentrations of product in various solvents used (water, ethanol cf. Fig. 4, octanol cf. Fig. 3) shows that one of the first exploitable markers of reaction will be the conductivity marker of ions cl.

The concentration of the product also affects the relaxation of the dipole (s) although the intrinsic relaxation is hidden or "convoluted" with the one of solvent, conduction increasing with the concentration of molecules, ion cl$^-$ seems to be a first possible marker of reaction, relaxation remaining hidden until 1.8 GHz. The search for reaction markers has led us to test different solvents in order to try to observe (and monitor) a dipolar relaxation marker. Fig. 3, which represents the initial and final product dissolved in octanol clearly shows differentiated spectra allowing to identify

the beginning and the end of the reaction. The choice of solvent will be a decisive criterion for the quality of measures in fields carried out under power CW microwave fields.

On Figs. 5–6, we present an example of measures of broadband conductivity under microwave treatment at 2.5–5 W for the solvent (water) and mixtures. The response of materials allows checking the speed of temperature rise. It will be necessary to be able to observe the evolution of the reaction following the evolution of the permittivity and conductivity over time and temperature. After testing the treatment of the hydrolysis reaction under microwave fields CW at 2.45 GHz, we will adapt the bench in order to apply an impulsion field of high voltage to limit the effects of temperature while considering triggering the reaction. This instrumentation PW generator characteristics are 2 ns rise time, 100 ns fall time, maximum repeatability of 10 KHz and maximum voltage of 7 KV. The very quick peak of energy is supposed to polarize the enzyme, which could lead to inactivation or on the contrary to fasten the hydrolysis via the so called "Athermal Effect". That's what the study is about. The spectrum signal is equivalent to a spectrum UWB (PSD from DC to 3–4 GHz).

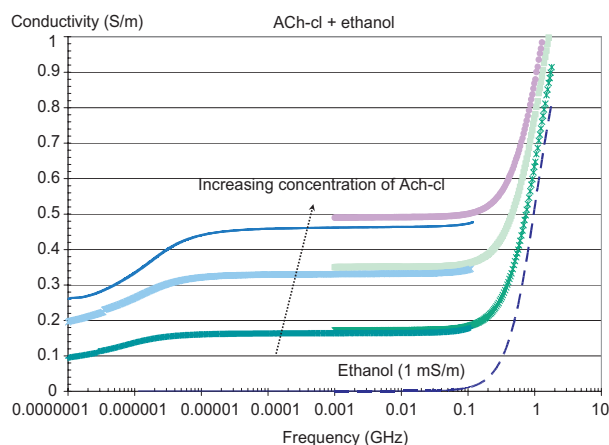

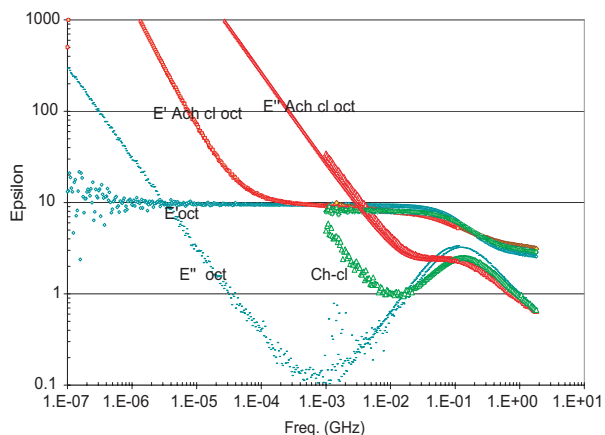Figure 4: Evolution of conductivity of Ach-l with ethanol.

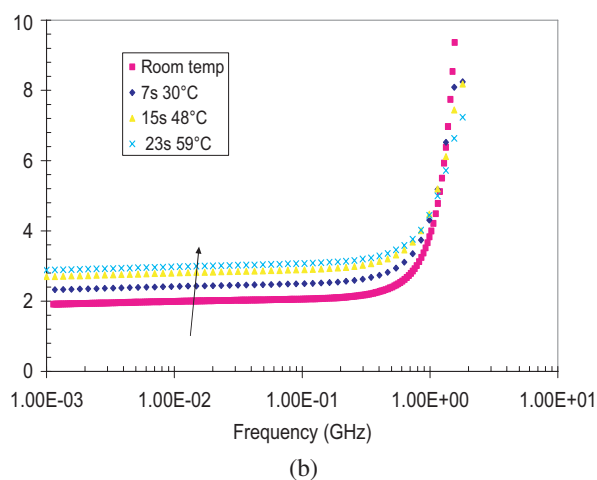Figure 5: Complex permittivity of octanol and mixtures ach-cl+octanol and ch-cl+octanol.
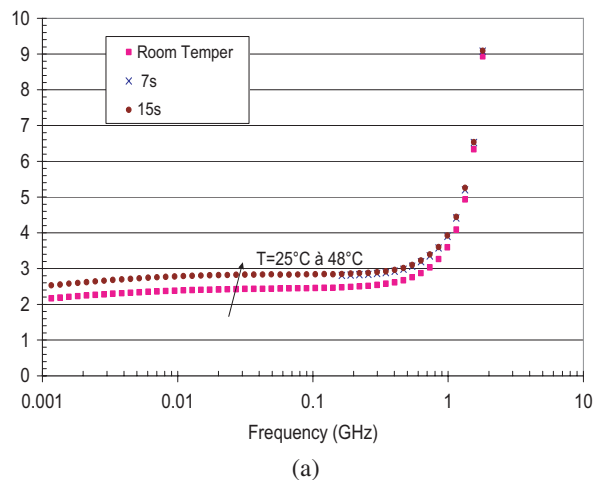
Figure 6: (a) Conductivity (S/m) of Achcl+water under microwave (2.5 W). (b) Conductivity (S/m) of Chcl+water under microwave (3 W).

4. DIELECTRIC MODELLING

Studying complex reactions relaxations process like enzymatic ones, it was necessary to introduce new software for dielectric modeling. In fact, a lot of algorithms try to optimize dielectric models represented in Argand diagram such as Cole-Cole [8], Cole-Davidson and Havriliak-Negami, but these last are quite useless for ultra complex materials including multiple relaxations (AchE). So we

choose to develop a visual approach in order to interact between physical model and dielectrics data (Fig. 9). Previous computational tools have been developed within the team, which only handle visual interaction of geometric optimization with classical Cole-Cole model. We actually have chosen a new approach that could manage each time it is necessary, either a robust optimization method based on classical geometric evaluation followed by the exact physical model corresponding [9] or manual evaluation of dielectrics data by the end user.

$$\underline{\varepsilon}(\omega) = \varepsilon_s + A \times (j\omega)^{-r}; \quad 1 \geq r \geq 0 \tag{1}$$

$$\underline{\varepsilon}(\omega) = \varepsilon_s + \frac{\Delta\varepsilon}{[1 + (j\omega\tau)^\alpha]^\beta} \tag{2}$$

with: Cole-Cole: $1 \geq \alpha \geq 0$ and $\beta = 1$, Cole-Davidson: $\alpha = 1$ and $1 \geq \beta \geq 0$ and Havriliak-Negami: $1 \geq \alpha \geq 0$ and $1 \geq \beta \geq 0$. These two steps can be performed on both low frequency conductivity, usually modeled by a first order polynomial (Eq. (1)), and relaxation representation, those based on Debye ones, previously quoted (Eq. (2)).
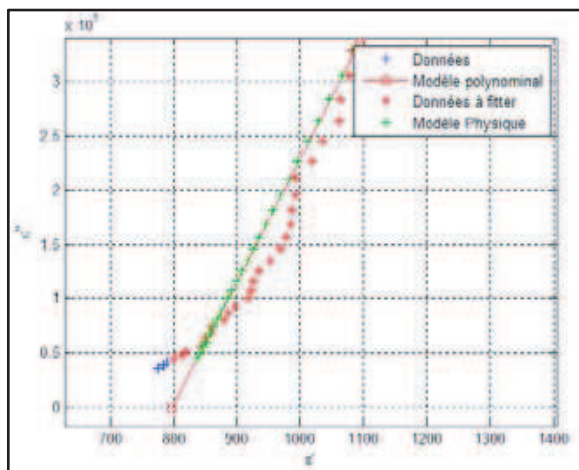

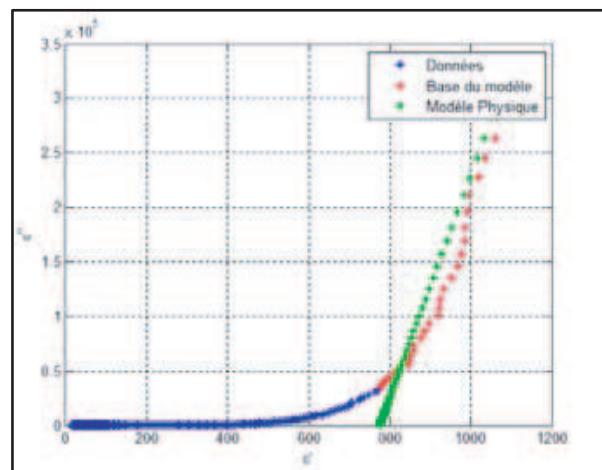Figure 7: Automatic computed decorrelation of low frequency conductivity.

Figure 8: Computer-aided decorrelation of low frequency conductivity.
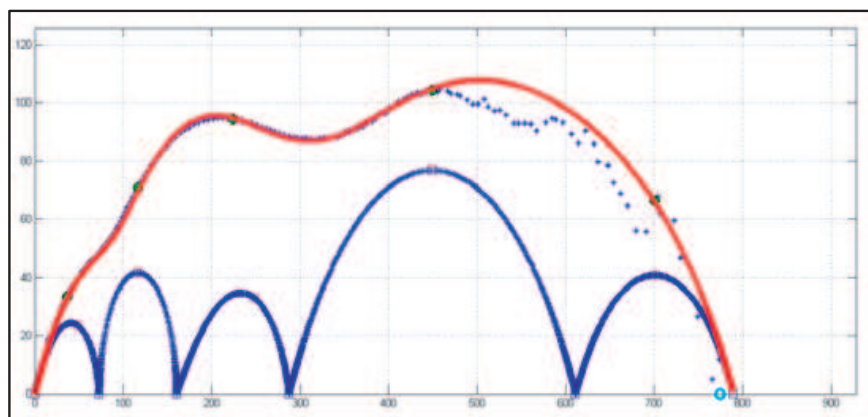
Figure 9: Computer-aided estimated relaxation model of $Li_{0.2}V_2O_5$ (ε_r'' vs ε_r').

Explaining the home-made software, Fig. 7 shows automatic selection points for automatic decorrelation computation of low frequency conductivity whereas Fig. 8 shows manual selection of base model first order polynomial. Integrated legends describe that blue and red dots represent complex permittivity data, red dots are those selected automatically by the algorithm. On Fig. 8, red line is traced by user itself, allowing manual selection of model parameters decorrelation, very useful for noisy dielectric measurement. Finally, when user decides to stop automatic or manual decorrelation step, the visual interaction process takes place (Fig. 9). Blue dots, are decorrelated dielectric data; blue lines, user fitted model data; and red line represents the sum of the various

dielectrics models at each frequency, the aim being to match red line (physical model), with blue dots (data). As it's showed above, graphical interaction lies on the various cursors, here, square ones and green ones, which by a user mouse displacement, will modify model parameters, which one (Eq. (2)) could be chosen within the software menu for each relaxation marker.

5. CONCLUSIONS

This paper describes the methodology used to try to observe the effect of a high-powered field on a biochemical reaction in the detection thresholds of power from which the reaction is modified or inhibited. The first concerns the treatment results achieved in CW on the reaction of hydrolysis of acetylcholine before interest in a sign of high intensity pulsed (PW). Today's work is about reinforcement of automatic decorrelation algorithm robustness in order to improve dielectrics data processing especially with Maxwell-Wagner effect. Further description will be providing soon on a complete article.

REFERENCES

1. Dvir, H., M. Harel, S. Bon, W. Q. Liu, M. Vidal, C. Garbay, J. L. Sussman, J. Massoulié, and I. Silman, "Structural insight into tetramerization of the synaptic form of acetylcholinesterase: Interaction of a polyproline II helix with four WWW motifs," *EMBO J.*, Vol. 23, 4394–4405, 2004.
2. Massoulié, J., "The origin of the molecular diversity and functional anchoring of cholinesterases," *Neuro Signals*, Vol. 11, 130–143, 2002.
3. Meyer, O., R. Weil, O. Dubrunfaut, and A. Fourrier-Lamer, "Caractérisation diélectrique large bande de molécules biologiques en milieu liquide confiné. Contribution à l'étude d'une réaction chimique biologique par caractérisation diélectrique large bande," *Proceeding of JCMM 2006*, Saint Etienne, France, April 2005.
4. Chevalier, S., "Nouvelle instrumentation appliquée à la chimie sous rayonnement micro-ondes. Aide à la compréhension d'une réaction de synthèse organique par caractérisation diélectrique sur une large bande de fréquences," PhD thesis, University of UPMC Paris 06, 2000.
5. Chevalier, S., O. Meyer, A. Fourrier-Lamer, A. Petit, A. Loupy, and F. Maurel, "New instrumentation for the comprehension of chemical reactions under microwave and classical heating with the aid of a wide frequency band dielectric spectroscopy," *Eur. Phys. J. AP*, Vol. 15, 223–229, 2001.
6. Meyer, O., S. Chevalier, R. Weil, A. Loupy, F. Maurel, and A. Fourrier-Lamer, "Chimie de synthèse: Paramètres diélectriques de systèmes isoles et de mélanges réactionnels Deuxième partie: Saponification d'un ester en présence d'un catalyseur," *Ann. Chim. Sci. Mat.*, Vol. 29, No. 4, 89–103, 2004.
7. Belhadj-Tahar, N. and A. Fourrier-Lamer, "Broad-band analysis of a coaxial discontinuity used for dielectric measurements," *IEEE Transactions on Microwave Theory and Technique*, Vol. 34, No. 3, 346–350, 1986.
8. Bishay, S. T., "Numerical methods for the calculation of the cole-cole parameters," *Egypt J. Sol.*, Vol. 23, No. 2, 2000.
9. Chelkowski, A., *Dielectrics Physics*, 117–122, Elsevier, 1980.
10. Badot, J. C., et al., "Submicro- and nanostructural effects on electrical properties of $Li_{0.2}V_2O_5$ thin films obtained by atomic layer deposition (ALD)," *Journal of Physics and Chemistry of Solids*, Vol. 67, 1270–1274, 2006.

Effect of Seed Pretreatment by Magnetic Fields on Seed Germination and Ontogeny Growth of Agricultural Plants

Ahmad Majd[1] and Azita Shabrangi[2]

[1]Islamic Azad University, North Branch, Tehran, Iran
[2]Physics Society, Plasma Physics Research Centre, Science and Research Campus
Islamic Azad University, Tehran, Iran

Abstract— Lentil belongs to Fabaceae family which has been cultivated since 8000 years ago. Nowadays different varieties of lentil are considered to be optimized because of its nutrient important and some medicinal properties. An experimental study of the influence of external magnetic field on the germination, ontogeny growth and anatomical structure were carried out. In this research, seeds of Lentil (*Lens culinaris L.*) were magnetically pretreated by different magnetic field intensities from 0.06 to 0.36 tesla (T) for different periods of time 5, 10, 20 minutes. Some seeds were plunged into the water during exposure to magnetic fields. Then seeds were placed in germinator and seed germination rate and seedling excretion rate were measured. Mean germination time showed a reduction for most of magnetic treatments therefore their rate of germination was increased. The range of greatest increase of germination were obtained from 0.18 T to 0.24 T. 15 days seedlings grown from pretreated seeds, which were plunged into the water during exposure to magnetic fields with 0/06 tesla intensity in 10, 20 minutes treatments, showed less and disorder growth in comparison to control. This decreased growth in 20 minutes treatment was more than 10 minutes treatment. On the other hand, 15 days seedlings grown from pretreated seeds in the same condition, but without water, showed more growth and leaf size increased too. Anatomical examination were carried out on 15 days seedlings, which were grown up from pretreated seeds in green house condition with natural light cycle 14-h light/10-hdarkness and 25§3±C daily night temperature. The results of experiments suggested that stele and xylem vessels develop and grow more than control and parenchyma cells are larger than control. The greatest difference was observed in leaf section. Air chambers and parenchyma cells were larger than control. These results suggested that some intensities of magnetic field improve significantly seed germination and growth of plants.

1. INTRODUCTION

Over many years, the effect of magnetic fields on plant life has been the subject of several studies. It has been reported that external magnetic fields influence both the activation of ions and polarization of dipoles in living cells. As early as 1930 Savostin reported 100% increase in the rate of elongation of seedlings under the influence of magnetic condition. Later Murphy [13] reported changes in seed germination Also, It was reported a strong magneto tropic affection on root development [2, 15]. Smith found that using different field combination one could separately alter the root mass, Leaf size and stems thickness [17]. In general the enhancement of growth under magnetic conditions appears to have been confirmed by many scientists [3, 7, 15]. Magnetic field were used widely as pretreatment for seeds to increase seed vigor, seedling growth and yield [1, 16]. However its physiological and mechanism are still poorly understood. In this study, we used Lens culinaris which is the most abundant species of Lens genus from Fabaceae family. We object to determine the optimal range of magnetic field intensities for increasing germination rate, growth and health of Lentil and generally finding the effect of magnetic field on plant in different aspects.

2. MATERIAL AND METHODS

2.1. Germination Test

Seeds of *Lens culinaris* cultivars (obtained from dry land agricultural research institute, IRAN) were selected for uniform size and shape. They were placed in the glass tube subjected to magnetic fields. Magnetic fields were generated by zeeman system with different magnetic induction ($B_1 = 0.06$ T, $B_2 = 0.12$ T, $B_3 = 0.18$ T, $B_4 = 0.24$, $B_5 = 0.30$ T, $B_6 = 0.36$ T).

In this experimental design three replicates ($n = 3$), with 20 seeds in each one were used. Thus groups of 50 seeds were subjected to each magnetic treatment, and analogous groups were used as control. Magnetic treatment was Provided, varying the exposure time (5, 10 and 20 minutes) and magnetic field induction (from B_1 to B_6). After pretreatment seeds were spread in moist filter

paper on Petri dishes and were placed in germinator. Some seeds were sowed in homogenous garden soil. The natural light cycle was 14-h Light/10h darkness and temperature $23 \pm 3°$C. The number of germinated seeds were registered 24h after pretreatment two times per day, and also seedling excretion rate was registered 48h after pretreatment. These parameters have been calculated using the seed calculator software for seed germination data analysis specifically developed by plant research international. The seed calculator program fits the accumulated germination data, using an equation which starts at zero value at time $t = 0$ (control)and ends at time 20 minutes. The software then calculates the germination parameters of the three replicates and mean germination data, including standard errors.

Figure 1: Set up of zeeman system.

2.2. Statistical Analyses

Seed calculator software analyzed the cumulative germination data, percentage of germinated seeds and time required for germination. A student t-test was done to find the significant differences between each magnetic treatment and control. Statistical analyses of the data of growth was performed with SPSS for windows software. The results were subjected to an analysis of variance (ANOVA) to detect differences between mean parameters of pretreated seeds with control.

3. RESULTS

3.1. Seed Germination and Seedling Emergence

Cumulative germination data and seedling data including standard error were calculated. Seed germination rate increased 33.7% ($P < 0.05$) in 5 minutes pretreatment by 0.18 T, which shows the most augmentation, and it decreased 16.7% ($P < 0.05$) by 0.06 T pretreatment. But in 10 minutes pretreatment by 0.18 T, seed germination rate increased 11.36% ($P < 0.05$). Beside that 0.24 T increased seed germination rate by 33.7% ($P < 0.05$) in 20 minutes pretreatment. These results showed that the best range of magnetic field intensities in order to augment seed germination rate are 0.18 T to 0.24 T. Fig. 1 illustrated the germination characteristics of the seed for various applied magnetic flux densities and exposure times at each fixed pretreatment time period of 5, 10 and 20 minutes. The percent germination of the seed is shown to have increased values of 1.5 times in 5 minutes pretreatment when the magnetic field intensity of 0.18 T was applied. The same augmentation was observed in 20 minutes pretreatment when magnetic field intensity of 0.24 T was applied. In 5 minutes pretreatment 0.18 T increased seedling emergence by 23% ($P < 0.05$) which shows the most augmentation in seedling emergence.

When immersed seeds in the water were pretreated by 0.06 T in different times (10, 20 minutes with a pause for 2 hours between them). Seedling after 15 days showed significant unarranged and
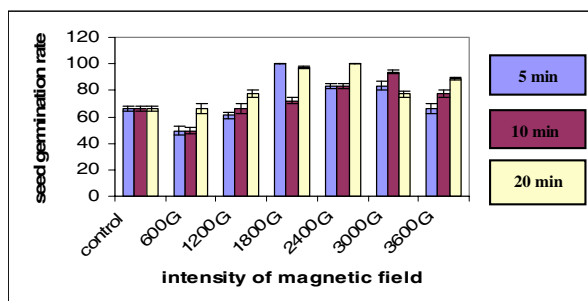

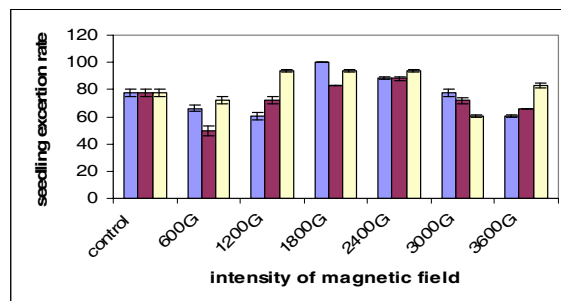Figure 2: Mean germination percentage after 24 hours.

Figure 3: Mean seedling exertion percentage after 48 hours.

less growth than control. But pretreated seeds by magnetic field without water in the test tube grew more than control, especially in 20 min treatment with a pause between treatment. (Figs. 3, 4), water temperature exposure to 0.06 T increased up to 4°C.

Figure 4: Seedlings yielding from pretreated seeds without water. They grew more by increasing exposing time.

Figure 5: Immersed seeds in the water pretreated by magnetic field (0.06 T) showed unarranged and less growth by increasing exposing time.

3.2. Anatomical Structure Observation

Thin section cut using a Mod, 1130 Biocat microtome were observed by Olympus microscope. Stem sections of the 15th days seedlings grown from seeds magnetically pretreated. These observations showed that stele and xylem vessels develop and grow more than control. Parenchyma cells are also larger than control. In root sections xylem vessels grew and developed more than control. Stele showed little development in comparison to control. The most significant alteration in structure was observed in leaf which has been illustrated in Fig. 5. Parenchyma cells (especially spongy parenchyma) looked larger. Air spaces seemed more volume and sub-stomata chambers were observed significantly larger than control.

4. DISCUSSION

As one of physical pre-sowing seed treatments that increased yield of cultivated plants, the feasibility of a magnetic flux density field treatment on biological objects had been discussed for more than a century. Our results showed that magnetic fields treatment can change and mostly enhance seed germination rate and seedling emergence rate which was consistent with many previous studies [10, 13, 20]. The authors found that suitable MF-pretreatment (0.18 T) could speed up seedling development and increase biomass. Similar result were also reported in cauliflower, tomato and cucumber [21]. In general the rate of germination of pretreated seed was higher than untreated seed. Carbonell found that magnetic treatment produced a biostimulation of the germination. Florez observed an increase for the initial growth stages and an early sprouting of rice seeds exposed to 125 and 250 mT stationary magnetic field [18].

The mechanisms are not well known yet, but several theories have been proposed, including biochemical changes or altered enzyme activities by Phirke et al. (1996). Garcia and Arza [9] carried out an experiment study on water absorption by lettuce seeds previously treated in a stationary magnetic field of 1 to 10 mT. They reported an increase in water uptake rate due to the applied magnetic field, which may be the explanation for the increase in the germination seed of treated lettuce seeds. It seems changes in intracellular levels of ca^{2+} and in other ionic current density across cellular membrane (Lyle et al., 1991) cause alteration in osmotic pressure and changes in capacity of cellular tissues to absorb water [9]. By analyzing the changes in ca^{2+} distribution and contents in cells of pea flax, lentil, onion and radish seedlings exposed to weak magnetic field, it was concluded that such a stress has resulted in serious disturbances at the cellular level. Magnetic fields cause effects related to interference with cytoplasm ion currents or ion distribution [20]. Therefore potential sensing component could be ca^{2+} ions. The increase of ca^{2+} level is fully consistent with assumption of the parametrical resonance model (Ledney 1996). It is believed that primary link in the chain of events triggered by weak magnetic field action in a biological system is the ca^{2+} ions connected with ca^{2+} — binding site of the proteins [4, 5]. We also observed seedlings growth from treated plunged seeds in the water that showed unarranged and less growth than control. On the other hand seedlings grown from pretreated seeds without water in the same condition showed more

growth by increasing the exposure time (there was a pause between times of treatment). Considering that these plants have ferritin cells, and each ferritin cell has 4500 Fe atoms, it is obvious that they have an outstanding role in the plants growth. As the last spin magnetic moment of the Fe atom posed to an external magnetic field, the composition of them creates an oscillator in the system. Then we have a moment of force on ferritin cells. This oscillator exerts its energy, then damps and finally locates in the field direction. The relaxed energy increased the internal temperature, as a result it is situated in a proper temperature for growing. This phenomenon occurs in the initial minutes of applying the magnetic field. So it depends on the number of times of locating the plant in magnetic field (Vaezzadeh M. et al., 2005). Different growth rate in different growth condition (such as immersed seeds in water) suggested that response to magnetic treatment would be different. Therefore, the response depends not only on the magnetic induction and its gradient (Wittkind et al., 1990), but also on the physiological state of experimental organism as proposed by Mcleod et al. [19]. As a result we need to concentrate on defining the environmental conditions accompanying the response to magnetism.

Anatomical structure observation showed that stele and xylem vessels develop and grow more than control. This may be attributed to peroxidase enzyme augmentation which causes more lignifying and it speeds up making secondary structure. Parenchyma cells are larger than control in both root and shoot (including stem and leaf). Belyauskays in 2004 reported that magnetic field effect on G2 Phase of cell cycle in lentil and flax.

In fact magnetic fields causes G2 phase to become longer and cells division decrease. Air pores and sub-stomata chamber in leaf are more and larger than control. It suggests that gas exchange would be easier and more accelerated than control. Spongy parenchyma cells are the most effective cells under stress and different environmental factors, because their cell walls are thinner than others.

In conclusion, the magnetic field pre-treatment enhanced seed germination rate and seedling emergence percentage. Also it has positive effect on lentil seedlings, such as stimulating seedling growth and development.

REFERENCES

1. Ahmet, E., "Effects of magnetic fields on yield and growth in strawberry," *Camarosa. J. Hort. Sci. Biotec.*, Vol. 78, 145–147, 2003.
2. Audus, L. J., "Magnetotropism: A new plant growth response," *Nature*, Vol. 185, 132–134, 1960.
3. Bathnagar, D. and A. Deb, "Some aspects of pregermination exposure of wheat seeds to magnetic field I. Germination and early growth," *Seed Res.*, Vol. 5, 129–137, 1977.
4. Belyavskaya, N. A., "Biological effects due to week magnetic field on plants," *Advancesin Space Research*, Vol. 34, 1566–1574, 2004.
5. Belyavskaya, N. A., "Ultrastructure, and calcium balance in meristem cells of pea roots exposed to extremely low magnetic fields," *Advances Space Research*, Vol. 28, No. 4, 645–650, 2001.
6. Dayal, S. and R. P. Singh, "Effects of seed exposure to magnetic field on the height of tomato plants," *Indian J., Agric. Sci.*, Vol. 59, 483–486, 1986.
7. Debeaujon, I., "Gibb requarirment for Arabidobsis seed germination is determind both by testa caractorestic and embryonic Absisic acid," *Plant Physiol.*, Vol. 122, 415–424, 2000.
8. Florez, M., et al., "Exposure of maize seeds to stationary magnetic fields: Effects on germination and early growth," *Environmental and Experimental Botany*, 2005.
9. Garcia, F. and L. I., Arze, "Influence of a stationary magnetic field on water relations in lettuce seeds. Part I: Theoretical considerations," *Bioelectromagnetics*, Vol. 22, No. 8, 589–595, 2001.
10. Martines, E., M. V. Carbonell, and M. Florez, "Magnetic biostimulation of initial growth stages of wheat," *Electromagn. Biol. Med.*, Vol. 21, No. 1, 43–53, 2002.
11. Mericle, R. P., et al., "Magnetic fields and ionizing radiation: Effects and interactions during germination and early seeding development," *Radiation Botany*, Vol. 6, No. 2, 11966, 111–127, 2004.
12. Moon, J. D. and H. S. Chung, "Acceleration of germination of tomato seed by applying Ac electrical magnetic fields," 2004.
13. Murphy, J. D., "The influence of magnetic field on seed germination," *Am. J. Bot.*, Vol. 29, Suppl. 15, 1942.
14. Negishi, Y., et al., "Growth of pea epicotyl in low magnetic field implication for space research," 1999.

15. Penuelas, J., et al., "Diamagnetic susceptibility and root growth responses to magnetic fields in lens culinaris,glycine soja, and triticum aestivum," *Electromagnetic Biology and Medicine*, Vol. 23, No. 2, 97–112, 2004.
16. Pietruszweski, S., "Effects of magnetic seed treatment on yields of wheat," *Seed Sci. Techol.*, Vol. 21, 621–626, 1993.
17. Pittman, U. J., "Effects of magnetic seed treatment on yields of barley, wheat and oats on Suthern Alberta," *Can. J. Plant Sci.*, Vol. 57, 37–45, 1977.
18. Savostin, P. W., "Magnetic growth relations in plants," *Planta*, Vol. 12, 327, 1930.
19. Smith, S. D., B. R. Mcleod, and A. R. Liboff, "Biological systems in transition sensitivity to extremely low-frequence fields," *Electro. Magnetobiol.*, Vol. 11, 29–42, 1992.
20. Walleczeh, J. and I. Budinger, "Pulsed magnetic field. Effects on calcium signaling in lymphocytes," *Febs. Lett.*, Vol. 314, 351–355, 1992.
21. Yinan, Y., et al., "Effect of seed pretreatment by magnetic field on the sensitivity of cucumber (Cucumis Sativus) seedlings to ultraviolet-β radiation," 2004.

Effect of Magnetic Fields on Growth and Antioxidant Systems in Agricultural Plants

Azita Shabrangi[1] and Ahmad Majd[2]

[1]Physics Society, Plasma Physics Research Centre, Science and Research Campus
Islamic Azad University, Tehran, Iran
[2]Islamic Azad University, North Branch, Tehran, Iran

Abstract— Magnetic fields are considered as an environmental factor that has significant effects on function and growth of plants. In this research, seeds of Lentil (*Lens culinaris L.*, which contains significantly Fe^{2+} as a ferromagnetic element) were magnetically pretreated by different magnetic field intensities from 0.06 to 0.36 tesla (T) by using Zeeman system for different periods of time 5, 10 and 20 minutes. Seedlings growth data were measured in green house condition with natural light cycle 14-h light/10-h darkness and $25 \pm 3°$C daily and night temperature. Activity changes assay of Ascorbate peroxidase (APX) and Superoxide Dismutase (SOD) were carried out by spectrophotometer in 15 days seedlings.

The greatest root growth in 3 days seedlings was observed in seedlings which were grown up from pretreated seeds by 0/3 tesla magnetic field intensity in 20 minutes pretreatment. The greatest shoot growth was also seen in 0/24 tesla magnetic field intensity in 20 minutes pretreatment. The results of experiments suggested that in 15 days seedlings, the greatest growth and biomass was observed in 0.18 T. Root had more growth than shoot under effect of magnetic fields. Leaf size and stem thickness were increased too. These seedlings were more resistant to drought stress. Activity enzymes assay suggested that APX activity increased in both root and shoot by increasing magnetic field intensities and SOD activity also increased in root of pretreated plants. All the results suggested that pretreated plants by magnetic fields are more resistant against harmful environmental factors. Moreover growth data of seedlings changed in comparison with control and in some intensity of magnetic fields increased.

1. INTRODUCTION

The effects of magnetic field on living systems, particularly the effect on growth of plants have been the object of numerous researchers. The first studies were conducted by Savostin (1930) who reported 100% increase in the rate of elongation of seedlings under the influence of magnetic condition. Audus (1960) and Pittman (1965) reported a strong magneto tropic affection on root development. Smith, et al. (1993) found that using different field combination one could separately alter the root mass, leaf size and stems. In general the thickness roots seem more susceptible to magnetic field than shoots [10] enhancement of growth under magnetic conditions appears to have been confirmed by many scientists [4, 10, 18]. Magnetic field were used widely as pretreatment for seeds to increase seed vigor, seedling growth and yield [1, 16]. Previous studies by them indicated that suitable magnetic treatment increased the absorption and assimilation of nutrients [10], and ameliorated photosynthetic activities [11]. Akoyonoglou (1964) reported that the activity of carboxy dismutase was increased by exposure to magnetic field. Many studies found that MF-Pretreatment could alleviate the inhibitory effect of heat and stress enhanced its saline-alkali tolerance [19, 23], and delayed the senescence process [15]. However, its physiological and mechanism are still poorly understood. Magnetic treatment are assumed to enhance seed vigor by influencing the biochemical process that involve free radicals and by stimulating the activity of proteins and enzymes [14]. The vast majority of biological substances are proteins that contain metal ions, such as hemoglobin, cytochrome or ferritin, which can be paramagnetic [17]. In this research, we used Lentil (*Lens culinaris L*) contain significantly Fe as a ferromagnetic element. We object to find the range of magnetic field intensities which has positive effect on growth and health of Lentil. In general we aim to find the effect of magnetic field on plant cell in different aspects.

2. MATERIAL AND METHODS

2.1. Growth Test

Seeds of *Lens culinaris* cultivars (obtained from dry land agricultural research institute, Iran) were selected for uniform size and shape. They were placed in the glass tube exposed to magnetic fields. Static magnetic fields were generated by zeeman system (Fig. 1) with different magnetic induction

($B_1 = 0.06$ T, $B_2 = 0.12$ T, $B_3 = 0.18$ T, $B_4 = 0.24$, $B_5 = 0.30$ T, $B_6 = 0.36$ T) in steps 0/06 T. Magnetic treatment was Provided, varying the exposure time (5, 10 and 20 minutes). Glass tube contains seeds were placed between pole pieces which is made of soft iron with variable horizontal magnetic field strength (from B_1 to B_6). A DC power supply with continuously variable output current (up to 15 A) was used for the magnet. A digital tesla meter operating on the principle of Hall sensor monitored the field strength produced in the pole gap of 2.5 cm. Tesla meter in connection with B-Probe measured intensity of magnetic flux in the range of 0/01 mT to 2 T.

Having calculated the best fit, the software calculates growth parameters of the three replicates, including standard errors. After 3 days, ten such seedlings from each replicate were randomly taken for measuring root and shoot length in cm. The growth and physiological tests were carried out at the spring season. The seeds were sowed in homogenous garden soil after germination. This test was performed under a natural light cycle of 12-h light/12-h darkness, and temperature 25±3°C. Total fresh weight (root and shoot) were measured in the 15th days seedlings. Some of pretreated seeds, after disinfecting were cultured in MS solid culture medium.

Figure 1: Set up of zeeman system.

2.2. Activity Enzyme Assay

The assays of SOD and APX were performed on 15 days seedlings (root and shoot separately). Shoot and root (2 g of fresh weight) exhibiting no visible injury symptoms were homogenized in 10 ml of 100 mM potassium phosphate buffer (pH 7.5) containing 2 mM EDTA and 2% (w/v) soluble PVP-10.5 mM. AsA were added for measurement of APX activity. The slurry was centrifuged at 15000×g for 20 min. The supernatant was filtered (Millipore, Mitex 0.5 μm) and used for enzyme analysis. APX activity was determined by monitoring the decrease in A290 for 4 min in 3 ml of reaction mixture containing 100 mM potassium phosphate buffer (ph 7.5), 0.5 mM AsA, 0.4 mM H_2O_2 and shoot or root extract. Correction were made for the oxidation of AsA in the absence of H_2O_2. The SOD activity was measured by spectrophotometer as described by Beyer and Fridovich (1989). The reaction mixture contained 50 mM potassium phosphate buffer (pH 7.8), 9.9 mM methionine, 57 μm nitro blue tetrazolium (NBT) and 0.9 μm riboflavin and 0.025% (w/v) triton X-100 and appropriate amount of shoot or root extract. The A560 was recorded after a 10 min illumination period. In this assay 1 unite of SOD is defined as the amount required to inhibit the photo reduction of nitro blue tetrazolium by 50%. The specific activity of SOD was expressed as units mg^{-1} fresh weight of plant (Calatayud A. et al., 2003).

2.3. Statistical Analyses

Statistical analyses were conducted using SPSS for windows. After testing the normality of the data distribution, the variance analyses (ANOVA) was used to test the main effects of magnetic field pretreatment. A student test t-test was done to find the significant differences between each magnetic treatment and control. Means were compared to detect differences between parameters of pretreated seeds and plants grown from them with control.

3. RESULTS

3.1. Seedling Growth

Cumulative seedling data (shoot and root length, biomass, enzyme activity) including standard error were calculated In order to perform our experiment precisely. The most significant different growth was observed in seedlings grown from pretreated seeds by 0.18 T and 0.24 T magnetic intensities (Fig. 3).

Growth data measured on 3rd and 15th days after seeding allow us to corroborate the effect observed in the activity enzyme assays. The greatest root growth in 3 days seedlings was observed in seedlings which were grown up from pretreated seeds by 0/3 tesla magnetic field intensity in 20 minutes pretreatment (Fig. 7). In shoot, it was seen in 0/24 tesla magnetic field intensity in 20 minutes pretreatment Root had more growth than shoot under effect of magnetic field (Fig. 6).

Table 1: Effect of seed pretreatment by static magnetic field and its duration on growth characteristics of lentil.

Magnetic Fields (T)	Root length in 3 days seedlings (cm) $\pm$ mean standard error			shoot length in 3 days seedlings (cm) $\pm$ mean standard error		
	5 min	10 min	20 min	5 min	10 min	20 min
Control	1.73 ± 0.145	1.73 ± 0.145	1.73 ± 0.251	1.4 ± 0.208	1.4 ± 0.208	1.4 ± 0.208
0.06	$1.9 \pm 0.208^*$	$1.85 \pm 0.202^*$	$1.93 \pm 0.404^*$	$1.07 \pm 0.066^*$	$1.0 \pm 0.0^{**}$	$1.33 \pm 0.166^*$
0.12	$2.25 \pm 0.144^*$	$2.75 \pm 0.144^*$	$2.5 \pm 0.5^*$	$1.32 \pm 0.928^*$	$1.7 \pm 0.0^{**}$	$1.5 \pm 0.288^*$
0.18	$2.25 \pm 0.144^*$	$2.35 \pm 0.202^*$	$2.5 \pm 0.5^*$	$1.25 \pm 0.144^*$	$1.76 \pm 0.12^*$	$2 \pm 0.0^{**}$
0.24	$2.75 \pm 0.086^*$	$2.2 \pm 0.115^*$	$2.75 \pm 0.25^*$	$1.55 \pm 0.288^{**}$	$1.25 \pm 0.144^*$	$2.25 \pm 0.144^*$
0.30	$2.85 \pm 0.202^*$	$3 \pm 0.173^*$	$1.65 \pm 0.05^{**}$	$1.35 \pm 0.202^*$	$1.35 \pm 0.086^*$	$1.25 \pm 0.144^*$
0.36	$2.25 \pm 0.144^*$	$2.25 \pm 0.144^*$	$1.75 \pm 0.251^*$	$1.77 \pm 0.208^*$	$1.66 \pm 0.166^*$	$1.23 \pm 0.208^*$

Significant difference $^*P < 0.05$　　　Significant difference $^{**}P < 0.01$

Also these data allow us to distinguish significant differences between fresh weights of lentil seedlings exposed to a magnetic field for different time versus control. Total fresh weight (biomass) of plants measured on the 15th days after plotting (Fig. 4). The most increase in biomass was observed in 20 minutes treatment by 0.18 T which was 1.46 times more than control particularly in roots. The root characteristics of the seedlings showed significant increase in root length, root thickness and lateral roots.

In summary most of Lentil seedlings which have been grown from pretreated seeds by different magnetic fields induction values, were significantly higher and heavier than control (Figs. 2 and 3).
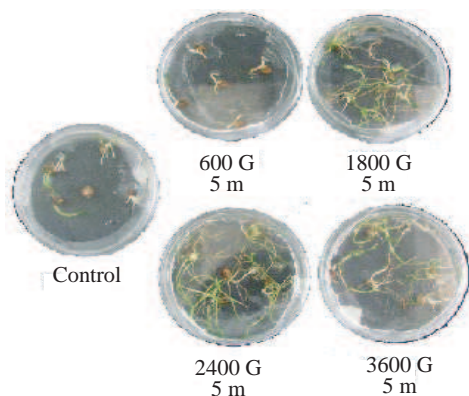

Figure 2: This figure illustrates that the most increased growth was provided by 0.18 T (in solid MS culture medium).

Figure 3: 3 weeks seedlings grown from pretreated seeds.

3.2. Activity Enzyme Results

Figure 5 illustrates APX activity in root and shoot. APX activity increased by augmenting intensity of magnetic field from 0.18 T to 0.36 T. SOD activity didn't show significant differences especially in shoot. In part of our experiment we observed that seedlings yielding from pretreated seeds by stronger magnetic fields are more resistant to drought and stress. That cooperated with increasing of APX activity.

Table 2: Effect of seed pretreatment by static Magnetic field and different exposure time on biomass (fresh weight) and APX activity in15 days seedling.

Magnetic Fields (T)	Biomass (gr) $\pm$ Mean standard error			APX activity in shoot	APX activity in root
	5 min	10 min	20 min	20 min	20 min
Control	0.26 ± 0.0028	0.26 ± 0.0028	0.26 ± 0.0028	0.92 ± 0.002	0.8 ± 0.042
0.06	$0.25 \pm 0.0098^*$	$0.33 \pm 0.0115^{**}$	$0.33 \pm 0.0034^{**}$	1.1 ± 0.378	$0.86 \pm 0.014^{**}$
0.12	$0.318 \pm 0.0011^{**}$	$0.32 \pm 0.0034^{**}$	$0.34 \pm 0.0017^{**}$	$0.95 \pm 0.005^{**}$	$1.24 \pm 0.032^*$
0.18	$0.34 \pm 0.0005^{**}$	$0.31 \pm 0.0046^{**}$	$0.38 \pm 0.0057^{**}$	$2.06 \pm 0.145^*$	$3.19 \pm 0.0.012^*$
0.24	$0.31 \pm 0.0046^{**}$	$0.30 \pm 0.0063^{**}$	$0.28 \pm 0.0057^{**}$	$2.26 \pm 0.145*$	$3.4 \pm 0.152^*$
0.30	$0.250 \pm 0.046^{**}$	$0.30 \pm 0.0057^*$	$0.27 \pm 0.0086^*$	$2.43 \pm 0.233^*$	$3.23 \pm 0.384^*$
0.36	$0.25 \pm 0.0005^{**}$	$0.20 \pm 0.0057^{**}$	$0.23 \pm 0.0046^{**}$	$2.86 \pm 0.202^*$	$3.62 \pm 0.273^*$

Significant difference $^*P < 0.0$ Significant difference $^{**}P < 0.01$
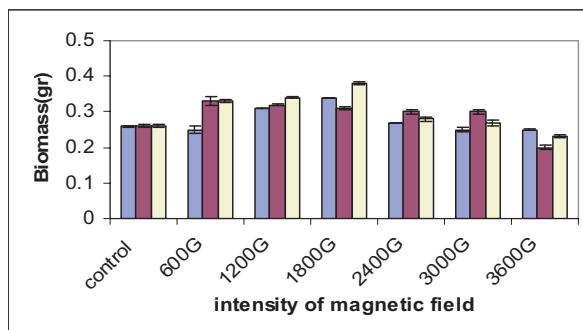

Figure 4: Effect of different magnetic field intensities in different Periods of exposure time on biomass (series1: 5 min, series2: 10 min, series3: 20 min).
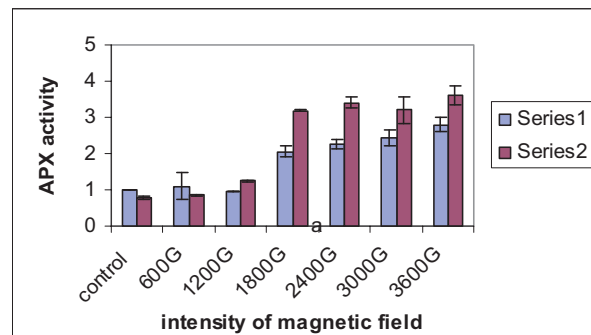

Figure 5: APX activity in root increase more than shoot (series1: shoot, series2: root).
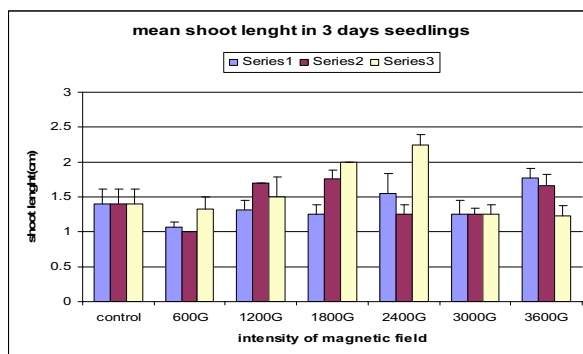

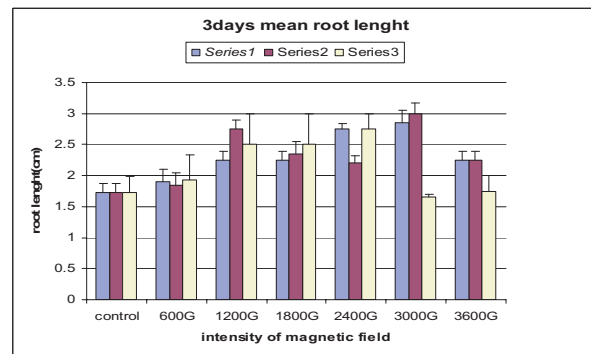Figure 6: Shoot length (cm) of 3 days seedlings (series1: 5 min, series2: 10 min, series3: 20 min).

Figure 7: Root length (cm) of 3 days seedling (series1: 5 min, series2: 10 min, series3: 20 min).

4. DISCUSSION

Magnetic fields are only one of several factors that effect on plant growth and development. Results obtained in this growth test allow us to conclude that magnetic treatment improves first stages of growth in higher plants. In general the seedlings from seeds magnetically pretreated grew taller and heavier than untreated controls. These seedlings showed greatly improved root characteristics. It is suggested that this technique may be profitably exploited as lentil is generally grown without irrigation and enhanced root growth will be useful in extracting moisture from deeper layers. The stimulatory effect of the application of different magnetic intensities on the growth data reported in

this paper is in agreement with that obtained by other researchers. Florez et al. (2004) observed an increase for the initial growth stages and an early sprouting of rice seeds exposed to 125 and 250 mT stationary magnetic field. Martinez et al. (2000, 2002) observed similar effects on wheat and barley seeds magnetically treated. The mechanisms are not well known yet, but several theories have been proposed, including biochemical changes or altered enzyme activities by Phirke et al. (1996). Lentil seedlings from magnetically pretreated seeds grew more than the untreated, and also biomass and root growth were significantly increased in most of intensities. This effect was accorded with other crop or horticultural species with magnetic field treatment, e.g., strawberry [1] wheat [16] and cucumber [24]. Biomass increasing needs metabolic changes particularly increasing protein synthesis. Magnetic field is known as an environmental factor which effects on gene expression. Therefore by augmentation of biological reactions like protein synthesis, biomass would increase too. Moreover transcriptional factors are under effect of magnetic field stimulation [23]. The effects of magnetic fields are superimposed on endogenous rhythms in some situation leading to inhibition, and in others to stimulation, while sometimes no effects had been reported. The interaction of magnetic field and exposure time indicated that certain combination of magnetic field and duration like 0.18 T and 0.24 T for 20 min were highly effective in enhancing growth characteristics. This observation suggests that there may be a resonance-like phenomena which increases the internal energy of the seed that occurs when there is an appropriate combination of magnetic field and exposure time [10]. Therefore it may be possible to get higher yield [22]. Also, it appears that there is a window at 0.06 T and 0.36 T for 5 min exposure where magnetic field negatively interacts and reduced the seedling traits. Belyauskays in 2004 reported that magnetic field effect on G2 Phase of cell cycle in lentil and flax. In fact magnetic fields causes G2 phase to become longer and cells division decrease.

Another parameter is activity enzyme assay. Stress enzyme like APX increased in seedling which was grown from pretreated seeds. But SOD doesn't show significant differences. These stress enzymes scavenge free radicals. They have antioxidant mechanism. APX Scavenges $OH^{\circ-}$ and SOD also scavenges $O_2^{\circ-}$. In fact stress enzymes decrease oxidative stress. Some studies have suggested that magnetic field exposure could be due to both the increase in the concentration [9] and oscillating of free radicals [21]. Magnetic fields are known to effect radical pair recombination and they may increase the concentration of oxygen free radicals in living cells. Increasing the concentration of free radicals creates oxidative stress, enhances stress response and some biological reactions, such as DNA damage occurs under this concentration.

At present, we hope to attract the attention of the scientific community to study this interesting phenomenon. Many tests in collaboration with engineers, chemists, physicists and biologists are necessary in order to establish the proper mechanism of action.

REFERENCES

1. Ahmet, E., "Effects of magnetic fields on yield and growth in strawberry," *Camarosa. J. Hort. Sci. Biotec.*, Vol. 78, 145–147, 2003.
2. Akoyunoglou, G., "Effect of magnetic field on carboxydismutase," *Nature*, Vol. 4931, 452–454, 1964.
3. Audus, L. J., "Magnetotropism: A new plant growth response," *Nature*, Vol. 185, 132–134, 1960.
4. Bathnagar, D. and A. Deb, "Some aspects of pregermination exposure of wheat seeds to magnetic field. I. Germination and early growth," *Seed Res.*, Vol. 5, 129–137, 1977.
5. Belyavskaya, N. A., "Biological effects due to week magnetic field on plants," *Advancesin Space Research*, Vol. 34, 1566–1574, 2004.
6. Belyavskaya, N. A., "Ultrastructure, and calcium balance in meristem cells of pea roots exposed to extremely low magnetic fields," *Advances Space Research*, Vol. 28, No. 4, 645–650, 2001.
7. Calatayud, A., et al., "Effect of 2-month ozone exposure in spinach leaves on photosynthesis, antioxidant systems and lipid peroxidation," *Plant Physiology and Biochemistry*, Vol. 41, 839–845, 2003.
8. Florez, M., et al., "Exposure of maize seeds to stationary magnetic fields: Effects on germination and early growth," *Environmental and Experimental Botany*, 2006, 2005.
9. Jajte, J. M., "Programmed cell death as a biological function of electromagnetic fields at a frequency of (50/60 Hz)," *Medycyna Pracy.*, Vol. 51, 383–389, 2000.
10. Kavi, P. S., "The effect of non-homogeneous gradient magnetic field susceptibility values in situ ragi seed material," *Mysore J. Agric. Sci.*, Vol. 17, 121–123, 1983.

11. Lebedev, I. S. and L. T. Litvinenko, "After effect of a permanent magnetic field on photochemical activity of chloroplast," *Sovient Plant Physiol.*, Vol. 24, 394–395, 1977.

12. Lednev, V. V., "Bioeffects of weak combind,static and alternating magnetic fields," *Biofizika*, 224–232, 1996 (in Russian).

13. Martines, E., M. V. Carbonell, and M. Florez, "Magnetic biostimulation of initial growth stages of wheat," *Electromagn. Biol. Med.*, Vol. 21, No. 1, 43–53, 2002.

14. Murry, L. E., "Plant growth response in electrostatic field," *Nature*, Vol. 207, 1177–1178, 1965.

15. Piacentini, M. P., D. Fraternale, and E. Piatti, "Senescence delay and change of antioxidant enzyme levels in Cucumis sativus Letiolated seedlings by ELF magnetic fields," *Plant Sci.*, Vol. 161, 45–53, 2001.

16. Pietruszweski, S., "Effects of magnetic seed treatment on yields of wheat," *Seed Sci. Techol.*, Vol. 21, 621–626, 1993.

17. Piruzyan, L. A., A. A. Kuznetsov, and V. M. Chikov, "About the magnetic heterogeneity of biological systems," *Izvestiya Acad. Sci. USSR Ser. Biol.*, Vol. 5, 645–653, 1980.

18. Pittman, U. J., "Effects of magnetic seed treatment on yields of barley, wheat and oats on Suthern Alberta," *Can. J. Plant. Sci.*, Vol. 57, 37–45, 1977.

19. Romana, R. and J. Igor, "Weak magnetic field decreases heat stress in cress seedlings," *Electromagn. Biol. Med.*, Vol. 21, 69–80, 2002.

20. Savostin, P. W., "Magnetic growth relations in plants," *Planta*, Vol. 12, 327, 1930.

21. Scaiano, J. C., F. L. Cozens, and N. Mohtat, "Development of a model and application of the radical pair mechanism to radicals in micelles," *Photochem. Photobiol.*, Vol. 62, 818–829, 1995.

22. Vashish, A., et al., "Exposure of seeds to static magnetic field enhances germination and early growth characteristics in chickpea," *Bioelectromagnetics*, Vol. 29, 571–578, 2008.

23. Xi, G., Z. D. Fu, and J. Ling, "Change of peroxidase activity in wheat seedlings induced by magnetic field and its responce under dehydration condition," *Acta Bot. Sinica*, Vol. 36, 113–118, 1994.

24. Yao, Y., et al., "Effect of seed pretreatment by magnetic field on the sensitivity of cucumber (Cucumis Sativus) seedlings to ultraviolet-β radiation," *Environ. Experi. Bot.*, 2004.

The Weak Combined Magnetic Fields Reduce the Brain β-Amyloid in an Animal Model of Sporadic Alzheimer's Disease

N. V. Bobkova, V. V. Novikov, N. I. Medvinskaya,
I. Yu. Aleksandrova, and E. E. Fesenko

Institute of Cell Biophysics, Russian Academy of Sciences, Pushchino 142290, Russia

Abstract— Subchronic effect of weak combined magnetic fields (MFs) on spatial memory and level of brain β-amyloid (βA) was studied in mice with ablation of the olfactory bulbs and control sham-operated (SO) animals. The bulbectomized (BE) mice show the main signs of Alzheimer's type degeneration such as memory impairment, the increase of the βA level in the brain, pathology in the acetylcholinergic system, and the loss of neurons in the brain structures responsible for memory [5–7, 9]. The combined MFs consisted of the constant component 42 μT and of the variable component 0.08 μT The variable field was the sum of two signals of frequencies of 4.38 and 4.88 Hz. Exposure to the MFs (4 hours for 10 days) induced the reduction of the βA level in the brain of the BE mice, but did not protected their memory from impairment. However, the same MFs improved the spatial memory in SO mice. The beneficial effect of the MFs in the SO animals was prolonged and was revealed for a month after exposure to the MFs. The results suggest that the MFs can be used to prevent the Alzheimer's disease in a group of risk as well as in other diseases involving amyloid protein deposition in different tissues.

1. INTRODUCTION

β-amyloid (βA) is a key pathogenic agent in Alzheimer's disease (AD). The abnormal amyloidogenesis, leading to βA protein deposition in the extracellular and perivascular spaces of the brain, is one of the main causes of neuron death in AD. Therefore, efforts of many researchers are focused on investigation of methods to prevent the βA deposition and to remove the senile plaques, formed by βA, from the brain. The efficiency of this approach was demonstrated in transgenic animals carrying the inserted human gene of βA precursor protein. The cleaning of their brain from amyloid plaques, caused by immunization against βA, was accompanied by recovery of spatial memory [1]. However, this method has a number of negative side effects in patients with AD. Therefore, the problem of removing of βA aggregates from the brain remains quite important.

Earlier we studied the mechanisms of the effect of weak combined magnetic fields (MFs) on properties of aqueous solutions of various biologically active ions and also proteins and peptides [2–4]. We used the low-frequency variable component with strength about 10 nT and constant component with strength comparable to the geomagnetic field. According to our proposed algorithm the frequencies of the variable component of the MF formally corresponded to the cyclotron frequencies of ionic forms of a number of amino acids at a ratio between the inductions of the constant and variable components of 500–3000. Such MFs have an extremely high biological activity; in particular, it was shown that its can accelerate the decomposition of the βA into soluble peptide fragments with a decreased neurotoxic effect and with less capability to form the insoluble aggregates.

In this work the effect of the weak combined MFs was studied *in vivo* in bulbectomized (BE) mice. Previously we showed that ablation of olfactory bulbs induced the behavioral, morphological, immunological, and biochemical signs similar to AD in mice, rats, and guinea pigs [5–9]. BE animals demonstrated pronounced impairment of the spatial memory, an increase in the βA level in the brain, pathology in the acetylcholinergic system, and the loss of neurons in the brain structures responsible for memory. Therefore, BE animals are a valid model of sporadic AD.

2. METHODS

The experiments were carried out on 3-month-old male NMRI mice weighing 25 ± 0.6 g. Animals were allowed food and water *ad libitum* and housed in groups of eight in standard laboratory cages under 12 h : 12 h light-dark conditions (light from 8.00 AM) at 21–23°C. Bulbectomy was performed under Nembutal anesthesia (40 mg/kg, ip) using a 0.5% Novocain solution for local anesthesia in scalping. The olfactory bulbs were removed bilaterally by aspiration through a rounded needle attached to a water pump. Single burr hole of 2 mm diameter was drilled over the olfactory bulbs, using a stereotaxic coordinates (AP-2; L 0; H 3.5). The extent of the lesion was assessed both visually and histologically at the end of the experimental study. The control was sham-operated (SO) mice, subjected to the same procedures except the olfactory bulb ablation. The

BE and SO animals were exposed to the weak combined MFs five weeks after bulbectomy. A setup for generating a MF consisted of two pairs of coaxial Helmhollz coils oriented along the geomagnetic field vector. A direct current was supplied to one of the pairs of coils to generate a constant component of MF with induction of $42\,\mu\text{T}$. An alternating current signal produced by a programmable sinusoidal current generator was fed to other pair of coils to create a variable component of MF with induction of amplitude of $80\,\text{nT}$. The current signal was the sum of two signals with frequencies of 4.38 and $4.88\,\text{Hz}$, which correspond to the cyclotron frequencies of lysine and aspartic acid, respectively. In this case, the magnetic induction vectors of the constant and variable components of the field were aligned. The MFs were measured with a Mag-03 MS 100 threeaxial MF sensor (Bartington Instruments Ltd, United Kingdom). The animals were exposed to MF in 4-h sessions for 10 days. The experiments were carried out in the presence of the natural and technogenic magnetic backgrounds with an induction of 50-Hz component of 20–$40\,\text{nT}$. The SO and BE animals without exposure to the weak combined MFs were groups of active controls. They were under activity of natural geomagnetic field with an induction of $-40 - 42\,\mu\text{T}$ and at the same magnetic noise level as for the test groups.

After exposure to the MF, the mice were trained in a Morris water maze for 5 days (four trials per day). Experiments were performed in a test room with extra-maze cues to facilitate spatial learning. A circular swimming tank (80 cm diameter and 40 cm wall height with an escape platform of 5 cm-diameter) was filled to depth of 30 cm with water at $23°\text{C}$ and rendered opaque by adding powdered milk. The tank was mentally divided into four sectors: The escape platform was located in the middle of the third quadrant during training. It was submerged to a depth of 0.5 cm so as to be invisible to a swimming animal during the whole period of training. Latency to reach the invisible platform was then determined. If the animals failed to locate the platform within test period for 60 s, they were placed on the platform for 10 s. Spatial memory was tested on the following day after completion of training in the absence of the hidden platform. During the test period (60 sec), occupancy time spent in each sector was recorded. To reveal the possible aftereffect of the MF, in a month, the animals were trained again in the water maze where the escape platform was placed into another sector. Procedure of training and testing of memory were repeated. After behavioral experiments the mice were decapitated under anesthesia. The neocortex and the hippocampus were removed, and the β-amyloid level was determined in extracts of these brain structures using a modified DOT analysis described earlier [5]. In this method, a nitrocellulose membrane was pretreated for 1 min with 40% ovalbumin in phosphate buffer and then for 10 min with 2.5% glutar aldehyde, samples were applied to the membrane, and the membrane was kept for 1 h in 4% ovalbumin in phosphate buffer with 0.1% NaN_3. Statistical analysis of the spatial memory training and testing was carried out with ANOVA using the ANOVA statistical package "Statistica 6.0". The p values were reported for repeated measures. The preference for platform target sector in comparison to other indifferent sectors was assessed by *post hoc* analysis using a multiple-range LSD test. The statistical significance of the difference of βA level was evaluated using two-tailed Student's test. All data were expressed as mean $\pm$ sem. All animal experiments were performed in accordance with the guidance of the National Institutes of Health for Care and Use of Laboratory Animals, NIH Publications No. 8023, revised 1978.

3. RESULTS AND DISCUSSION

The data in Table 1 show that the latencies to reach the escape platform were not significantly different in animals of different groups in each day of training; however, the average latency in the SO animals were significantly lower than in the BE mice. It indicates the decreased ability to study spatial skills in the BE animals. The exposure to the MF decreased the average latency in the SO animals only. The data suggest that the MF does not affect the learning rate in the BE mice and that the SO animals have an increased sensitivity to the MF. One month after exposure to the MF the SO animals demonstrated an increased latency on the first day of retraining. The reason for this could be the high level of spatial memory, which allows these mice to remember, where the escape platform was located at the first training and makes difficult to find its new location. This effect of the MF was not revealed in BE mice.

The results of the factor analysis are presented in Table 2 demonstrate not significant factor of sector preference for both groups of BE and BE exposed to MF (BE+MF). This indicates that these mice have no preference for any sector of the water maze. The SO animals exposed to the same MF demonstrated a significant increase in the factor of sector preference. It was due to the recognition of the sector, where escape platform is located during training, as the results of the Post

Table 1: Effect of the weak combined MF on latency (sec) to find the escape platform in BE and SO mice during days of training and repeated training (one month after first training).

Groups of animals		Days of Training					
		1	2	3	4	5	Average of latency, c
T R A I N I N G	BE	46.8 ±4.1	29.9 ±6.0	16.7 ±4.4	17.1 ±2.5	17.0 ±5.3	25.5** ±2.3
	BE+ MF	36.3 ±5.2	30.8 ±5.0	19.1 ±4.1	22.5 ±4.1	12.0 ±3.2	24.1 * ±2.2
	SO	37.4 ±7.1	19.4 ±5.5	11.7 ±2.2	7.5 ±2.1	7.3 ±1.9	16.7 ±2.3
	SO+ MF	21.4** ±6.4	11.8 ±4.0	11.3 ±3.0	7.8 ±1.5	9.2 ±1.8	12.3* ±1.8
R E T R A I N I N G	BE	16.3 ±4.4	12.1 ±2.3	12.8** ±1.8	12.1 ±3.0	14.2 ±1.9	13.5 ±1.3
	BE+ MF	19.1 ±4.7	14.2 ±3.9	11.5** ±1.9	14.1* ±2.4	13.1 ±2.7	14.4 * ±1.5
	SO	9.4 ±2.5	7.3 ±1.3	4.9 ±0.9	8.8 ±2.1	9.2 ±1.9	7,9 ±1.9
	SO+ MF	29.1** ±7.8	8.3 ±1.3	9.7** ±1.4	6.8 ±0.9	7.8 ±1.7	12.3 ±2.5

The significance of the differences is indicated with respect to SO animals: $*p < 0.05$; $**p < 0.01$ and $***p < 0.001$.

hoc analysis revealed (Fig. 1). After retraining period, animals of all groups showed reliable means of the factor of sector preference (Table 2). However, results of the *post hoc* analysis, presented in Fig. 2, showed the significance preference of sector, in which platform was located during retraining period only in groups of SO animals, especially in SO mice, exposed to the MF. Both groups of BE mice (BE and BE+MF) demonstrated the loss of spatial memory (Fig. 2).
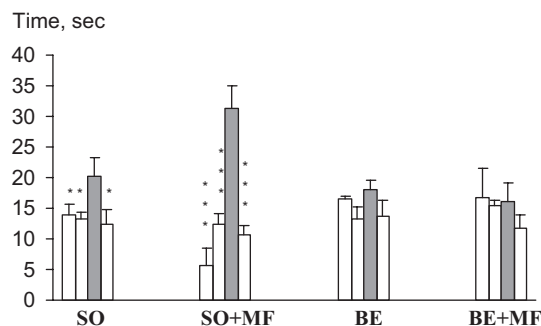

Figure 1: Effect of the weak MFs on the spatial memory of BE and SO mice. The ordinate is the time spent in each sector of a Morris water maze. The hatched bin represents the time in sector in which escape platform was located during training: The empty bins denote time in indifferent sectors of the water maze. The significance of differences is indicated between sector in which escape platform was located during training and other sectors. $*p < 0.05$, $**p < 0.01$ and $***p < 0.001$. The other notations are as in Table 1.

Thus, the behavioral study revealed that the BE mice did not remember the sectors, in which the saving platform was located during training and retraining periods. It supports our previous data on the impairment of the spatial memory in BE animals [5, 9]. The subchronic exposure to the weak MFs did not affect spatial memory of these animals. However, the MFs improved the memory in SO mice. The beneficial effect of the MF on the memory of these animals persisted for a month after exposure to the MF.

Table 3 presents the absolute values of βA level in the extracts of the neocortex and the hippocampus in different groups of experimental animals. The sensitive DOT analysis revealed that
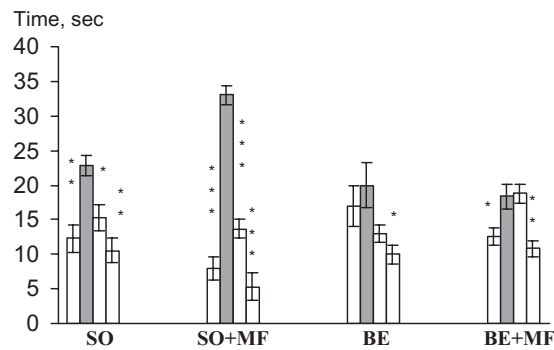
Figure 2: Aftereffect of the weak MF on the spatial memory in SO and BE mice retrained one month after first training. The notation is as in Fig. 1.

Table 2: The means of Factor of the recognizing of the Morris water maze sectors by time spent there in BE and SO mice exposed to the weak MF.

Groups of animals	Mean of the Factor Training period		Mean of the Factor Retraining period (one month after first testing))	
	F	p	F	p
SO	$F(3,12) = 3.73$	$0.042*$	$F(3,12) = 7.73$	$0.009**$
SO+MF	$F(3,12) = 30.18$	$0.000\ldots***$	$F(3,12) = 61.07$	$0.000\ldots***$
BE	$F(3,12) = 2.18$	0.14	$F(3,12) = 4.35$	$0.026*$
BE+MF	$F(3,16) = 0.64$	0.6	$F(3,16) = 11.9$	$0.003**$

Significance of Factor: * -$p < 0.05$; ** - $p < 0.01$; *** - $p < 0.001$.

the βA level in the extracts of the BE animals was more than five times higher ($p < 0.001$) in comparison to SO mice. The exposure to the MF induced the reliably decrease the βA level almost threefold ($p < 0.01$), but it was higher then in SO mice ($p < 0.05$).

Table 3: The level of the brain βA in BE and SO mice exposed to the weak MF.

Groups of animals	The level of βA (ng/g)
SO	5.03 ± 0.36
SO+MF	5.21 ± 0.37
BE	$34.12 \pm 4.17***$
BE+MF	$10.91 \pm 2.17^{*,\,\#\#}$

The significance of differences from the group of SO mice: $^*p < 0.05$ and $^{***}p < 0.001$. The significance of differences from the group of BE mice: $^{\#\#}p < 0.01$.

Thus, we revealed the reduction of the βA level in the brain of BE mice after exposure to the weak MFs. As already noted, we failed to detect the improving of their spatial memory. The absence of the positive effect of the weak MFs on spatial memory of BE mice can be explained by different causes. 1) Insufficient reduction the βA level in the brain. Its deposits are known to impair the nerve impulse transmission and. thereby, the memory. 2) The massive neuronal death in the cortex and the hippocampus of the BE mice, which was previously detected in these animals [6]. Therefore, we suggest that exposure to MFs should be applied prior to the loss of neurons on earlier stage of the neurodegeneration. Weak combined MFs can be an efficient way to prevent the development of AD. Note that there are different points of view on the effect of MF on the neurodegenerative processes. Some researchers consider the exposure to MF as a potential risk factor for neurodegenerative diseases [10], whereas others deny it [11]. Furthermore, there is evidence of a beneficial effect of MF on the cognitive processes and the visual memory in patients with AD [12, 13]. The MF using opens new possibilities of treating this severe disease.

Another way to increase the MF efficiency is the variation of its parameters. However, MFs have a broad effect on biological systems. Such MFs inhibit malignant tumor growth in experimental animals [14] due to stimulation of the tumor necrosis factor production [15]. It decreases the protein protection of DNA molecules against the action of DNase I in the mouse brain tissue and in aqueous solutions [16, 17], changes the microenvironment of protein macromolecules in aqueous solutions [18], and abruptly accelerate the spontaneous hydrolysis of proteins and peptides to form peptide fragments [4]. Our investigation gave interesting results, showing the significant improvement of the spatial memory in the SO animals under the action of the MF. This beneficial effect persisted in SO animals in a month. A lot of researchers suggest that the nervous system is very sensitive to weak MFs [19]. There is evidence that MFs, selectively activating the limbic structures of the brain, increase the resistance of animals to emotional stress [20]. Since the training in a water maze induces the stress in animals, in our experiments the MF may protect SO animals from development of the stress, which affected the rate and quality of their learning of the spatial skills. Thus, the data suggest that MFs can be applied for preventive purposes in a group of risk of AD.

REFERENCES

1. Solomon, B., *J. Mol. Neurosd.*, Vol. 20, No. 3, 283, 2003.
2. Novikov, V. V. and M. N. Zhadin, *Biofizika*, Vol. 39, No. 45, 1994.
3. Novikov, V. V., *Biofizika*, Vol. 43, 588, 1998.
4. Novikov, V. V. and E. E. Fesenko, *Biofizika*, Vol. 46, 235, 2001.
5. Aleksandrova, Yu., V. V. Kuvielikin, A. Kashparov, N. Medvinskaya, I. V. Ncsterova, S. M. Lunin, A. N. Samokhin, and N. V. Bobkova, *Binkhimiya*, Vol. 69, 218, 2004.
6. Bobkova, N. V., I. V. Nesterova, E. Dana, R. Dana, I. Yu. Aleksandrova, N. I. Medvinskaya, and A. N. Samokhin, *Morfologiya*, Vol. 123, No. 3, 27, 2003.
7. Bobkova, N. V., I. V. Nesterova, and V. I. Nesterov, *Bull. Eksp. Biol. Med.*, Vol. 131, 507, 2001.
8. Novoselova, E. G., N. V. Bobkova, O. A. Sinotova, V. B. Ogai, O. V. Glushkova, N. I. Medvinskaya, and A. N. Samokhin, *Dokl. Akad. Nauk*, Vol. 393, 559, 2003.
9. Bobkova, N. V., N. I. Medvinskaya, I. V. Nesterova, I. Y. Aleksandrova, A. N. Samokhin, Y. G. Gershovich, P. M. Gershovich, and V. A. Yashin, "Possible role of olfactory system in Alzheimer's disease genesis," *New Trends in Alzheimer's and Parkinson Disorders ADPD 2005*, 91–95, Edit. A. Fisher, I. Hanin, M. Memo, F. Stocchi, Medimond, 2005.
10. Hakansson, N., P. Guswvson, C. Johansen, and B. Flodems, *Epidemiology*, Vol. 14, No. 4, 420, 2003.
11. Noonan, C. W., J. S. Reif, and J. B. Burch, *J. Oeeup. Environ. Med.*, Vol. 44, No. 8, 769, 2002; *Biophysics*, Vol. 50, Suppl. 1, S7, 2005.
12. Sandyk, R., *Int. J. Neurosci.*, Vol. 81, No. 3–4, 199, 1995.
13. Sandyk, R., *Int. J. Neurosci.*, Vol. 76, No. 3–1, 185, 1994.
14. Novikov, V. V., N. I. Novikova, and A. K. Kachan, *Biofizika*, Vol. 41, 934, 1996.
15. Novoselova, E. G., V. B. Ogai, O. V. Sorokina, V. V. Novikov, and E. E. Fesenko, *Biofizika*, Vol. 46, 131, 2001.
16. Novikov, V. V., Yu. P. Shvetsov, E. E. Fesenko, and N. I. Novikova, *Biofizika*, Vol. 42, 733, 1997.
17. Fesenko, E. E., V. V. Novikov, and Yu. P. Shvetsov, *Biofizika*, Vol. 42, 742, 1997.
18. Fesenko, E. E., V. V. Novikov, V. V. Kuvichkin, and E. V. Yablokova, *Biofizika*, Vol. 45, 232, 2000.
19. Lyskov, E. B., J. Julilainen, V. Jousmaki, J. Punanen, S. Medvedcv, and O. Hanninen, *Bioelektromagnetics*, Vol. 14, No. 2, 87, 1993.
20. Gorbunova, A. V., N. V. Petrova, V. V. Ponugalova, et al., *Izv. Akad. Nauk SSSR. Ser. Biol.*, No. 5, 774, 1981.

Weak Combined Magnetic Field Accelerates Hydrolysis of βAmyloid-Protein *in vitro*

E. E. Fesenko, **V. V. Novikov**, **and N. V. Bobkova**

Institute of Cell Biophysics, Russian Academy of Sciences
Pushchino, Moscow Region 142290, Russia

Abstract— Previously, we determined that weak combined magnetic fields substantially accelerate the spontaneous hydrolysis of some proteins and peptides into fragments in solutions. Here we have shown that a weak combined variable magnetic field of $0.05\,\mu\text{T}$ with frequencies 3.58–4.88 Hz and constant magnetic field of $42\,\mu\text{T}$ accelerate the hydrolytic decomposition of β-amyloid in solution. The region of the molecule that is most sensitive to the weak magnetic field was determined. This region is located between residues Asp7 and Ser8. In this region the hydrolysis of β-amyloid under the action of the magnetic field takes place. It is known that β-amyloid is the key neurotoxic protein in the brain of patients with the Alzheimer's disease, accompanied by loss of memory and death. At present one of the main elements of the current strategy of AD treatment involves the active modification of the structural-functional characteristics of protein and peptide molecules participating in the pathological process. Therefore our results can form the basis for new approaches to treatment the diseases related to the accumulation of pathological proteins in different pathologies, including the Alzheimer's disease.

1. INTRODUCTION

It is known that β-amyloid (βA) is the key neurotoxic protein in the brain of patients with the Alzheimer's disease (AD), which is the most frequent cause of senile dementia accompanied by loss of memory and death. It is the product of proteolysis of the large amyloid precursor protein. βA is accumulated into oligomeric and fibrillar structures, which together with amyloid plaques cause neurodegeneration in the brain. At present one of the main elements of the current strategy of AD treatment involves active modification of the structural-functional characteristics of protein and peptide molecules participating in the pathological process [5–8]. Previously, we determined that weak combined magnetic fields substantially accelerate the spontaneous hydrolysis of some proteins and peptides into fragments in solutions [1–3] and in the animal brain [4]. These results can form the basis for new approaches to treatment the diseases related to the accumulation of pathological proteins in different pathologies, including AD. βA as well as a number of other proteins has to be sensitive to the action of weak magnetic fields of certain frequencies and amplitudes [3]. The aim of this investigation is to determine the optimal parameters of magnetic fields accelerating the decomposition (hydrolysis) of βA *in vitro*, and to find the regions of the molecule of βA that are sensitive to the action of the magnetic fields.

2. METHODS

Aqueous solutions of βA (Sigma, USA) were treated in sterile polyethylene cells; the preparing procedure was described in detail before [3]. The setup for exposure to magnetic field consisted of two coaxial coils for generating a constant magnetic field of strength B_{cf} and a variable magnetic field of strength B_{vf}; a programmable generator of sinusoidal electrical signals, which formed total multi-frequency or single-frequency signals to be sent to the coil generating the variable magnetic field; a direct current source, from which the current was fed to the coil generating the constant magnetic field; and a Permalloy magnetic shield for shielding from external magnetic fields with a shielding factor about 1000. In the experiments, B_{cf} was $42\,\mu\text{T}$ and B_{vf} (amplitude) was $0.05\,\mu\text{T}$. The non uniformity of the fields in the experimental zone was below 0.5%. The strength of the fields were monitored by direct measurements with a Mag-03 MS 100 fluxgate magnetometer (Bartington, UK). A total multifrequency variable magnetic field is used. Its frequencies formally corresponded to the cyclotron frequencies of ionic forms of free molecules of tyrosine, arginine, histidine, glutamic acid, lysine, and aspartic acid as calculated by the standard expression

$$\nu_c = \frac{q B_{\text{cf}}}{2\pi m},$$

where q and m are the charge and mass of an amino acid ion, respectively.

In the experiments, βA (30 µg/ml) was exposed to the magnetic field for 12 h at temperature 20–22°C. The solutions of βA were prepared using sterile double-distilled water or high-purity deionized water with a resistivity of 18 M'Ω cm, which was obtained on an E-pure 3 Module system (Barnstead/Thermolyne, USA). 0.01 M NaCl was added in water. The degree of hydrolysis of the protein was determined after separation of the hydrolysis products by high-performance liquid chromatography on LKB-Pharmacia chromatograph with an RP-318 C18 column 250 × 4.6 mm in size (Bio-Rad, USA) in a gradient of acetonitrile (Fluka, Switzerland). 1 ml of a sample is analyzed. The optical density of the eluate was measured at a length of wave 226 nm with a Uvicord SD-2158 UV detector. Amino acid analysis of the protein and its fragments of hydrolysis was performed with a Biotronic LS-3000 instrument (Germany) after complete hydrolysis of peptide bonds in 5.7 M HCl for 48 h at 110°C in evacuated ampoules.

The N-terminal residues in the fragments obtained by the protein hydrolysis and their sequences were determined by the dansyl chloride method. Some experimental results were represented as the coefficient of protein hydrolysis stimulation, which was calculated as the ratio of the degree of hydrolysis induced by magnetic field to the degree of spontaneous hydrolysis.

3. RESULTS AND DISCUSSION

High-performance liquid chromatography of the initial samples of βA shows a single individual peak at the 29th minute of elution (Fig. 1(a)), which corresponds to the emergence of the peak of βA in 52% acetonitrile. Each of the chromatograms of reference samples of the protein exposed in aqueous solution for 12 h contains several minor peaks (Fig. 1(b)), which precede the protein peak. These minor peaks are likely to be due to the spontaneous hydrolysis of the protein in aqueous solution, which results in decomposition of $6.6 \pm 0.4\%$ of the initial concentration of studied protein (Fig. 1(b)). In each of the chromatograms of test samples of protein solutions exposed for 12 h to a weak combined magnetic field with $B_{cf} = 42$ µT, $B_{vf} = 0.05$ µT, and the frequency range of the multifrequency component of 3.58–4.88 Hz under the conditions of cyclotron resonance for ions of a number of amino acids, there emerge two additional high-amplitude peaks corresponding to the eluate with a high optical density (Fig. 1(c)). In this case, the amplitude of the peak of the initial, no hydrolyzed protein is substantially (by $27 \pm 3\%$) lower (Figs. 1(b), 1(c)). Amino acid analysis
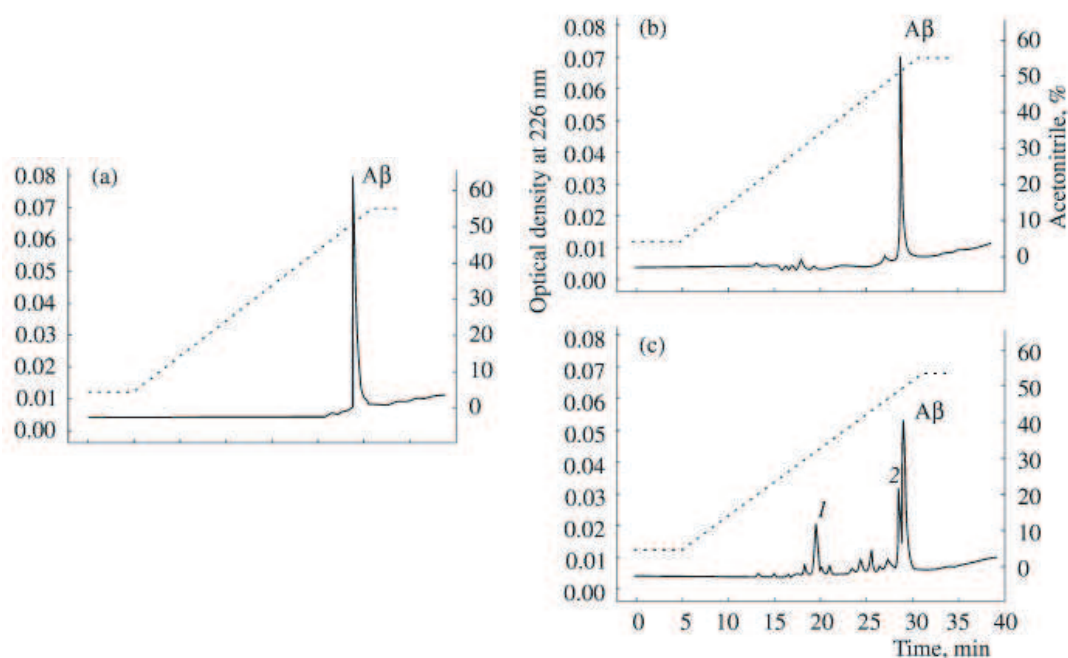

Figure 1: Elution profiles in high-performance liquid chromatography of 30 µg/ml βA after exposure to a weak combined magnetic field for 12-h. ($B_{cf} = 42$ µT, $B_{vf} = 0.05$ µT, the frequency range 3.58–4.88 Hz): (a) the initial peptide, (b) a reference sample after 12-h-exposure, and (c) a test sample. The numbers at the peaks refer to the hydrolysis products — (1) DAEFRHD and (2) SGYEVHHQKLVFFAEDVGSNKGAI-IGLMVGGVV.

and sequencing showed that the eluates corresponding to the additional peaks contained fragments of the initial protein molecule (Fig. 1). The data presented suggested considerable (by a factor of four) acceleration of the protein decomposition (hydrolysis) in the weak magnetic field tuned to the cyclotron resonance of ions of amino acids. The determination of amino acid sequence revealed that the region of the βA molecule that is most sensitive to weak magnetic fields was located between residues Asp7 and Ser8. In this region the βA is undertaken by hydrolysis under the action of the magnetic field. It is known that the disturbs the integrity of the region 4–11 responsible for activating the classical complement cascade, which leads to brain cell lysis and inflammation due to activation of microglia [5]. It is shown that any disturbance of the integrity of βA induces the decrease of its toxicity and ability to form fibrils. Although separate fragments of this protein are still capable to aggregating, the formation rate and stability of such fibrilar structures depend on amino acid sequence length [6–8]. In our case the peptide bond hydrolysis takes place primarily between residues 7 and 8. So we think that pathological activity of these more short fragments is lower than the activity of the βA. This method of acceleration of hydrolysis of βA can decrease its neurotoxicity and improve the state of patients. The data presented can be used to develop methods for remote correction of the state of patients with AD and other amyloidoses.

REFERENCES

1. Novikov, V. V., Yu. P. Shvetsov, and E. E. Fesenko, *Biofizika*, Vol. 42, No. 3, 746–50, 1997.
2. Shvetsov, Yu. P., V. V. Novikov, E. E. Fesenko, A. P. Chernov, and V. A. Ivanov, *Biofizika*, Vol. 43, No. 6, 977–80, 1998.
3. Novikov, V. V. and E. E. Fesenko, *Biofizika*, Vol. 46, No. 2, 235–41, 2001.
4. Novikov, V. V., Yu. P. Shvetsov, E. E. Fesenko, and N. I. Novikova, *Biofizika*, Vol. 42, No. 3, 733–7, 1997.
5. Valazzquez, P., D. H. Cribbs, T. L. Poulos, and A. J. Tenner, *Nat. Med.*, Vol. 3, No. 1, 77–9, 1997.
6. Castano, E. M., J. Ghiso, F. Prelli, P. D. Gorevic, A. Migheli, and B. Frangione, *Biochem. Biophys. Res. Commun.*, Vol. 141, No. 2, 782–9, 1986.
7. El-Agnaf, O. M., D. J. Guthrie, D. M. Walsh, and G. B. Irvine, *Eur. J. Biochem.*, Vol. 256, No. 3, 560–9, 1998.
8. Festy, F., L. Lins, G. Peranzi, J. N. Octave, R. Brasseur, and A. Thomas, *Biochim. Biophys. Acta*, Vol. 1546, No. 2, 356–64, 2001.

Electromagnetic Wave Absorption in K Band and V Band with Carbon Microcoils

Kuan-Ting Lin[1], **Jian-Yu Hsieh**[1], **Tao Wang**[1], **Cheng-Hung Li**[2],
Neng-Kai Chang[2], **Shey-Shi Lu**[1], **Shuo-Hung Chang**[2], and **Ying-Jay Yang**[1]

[1]Graduate Institute of Electronics Engineering, National Taiwan University, Taiwan, R.O.C.
[2]Department of Mechanica Engineering, National Taiwan University, Taiwan, R.O.C.

Abstract— In this paper, an electromagnetic wave absorption component consisting of carbon microcoils is realized. An electromagnetic wave absorber operating in K band and V band is implemented by carbon microcoils which are enwrapped in PDMS. Samples containing carbon fibers and carbon microcoils with different lengths were used as contrasts in the absorption experiment. The measured absorptions of the carbon microcoils are 15 dB (97%) at 26 GHz and 20 dB (99%) at the region from 64 to 70 GHz. The experimental results show that the carbon microcoils are superior in electromagnetic wave absorption and may be considered as a useful tool in future EMI/EMC applications.

1. INTRODUCTION

With the dramatic development of wireless communication technology in recent years, the safety of radiated electromagnetic (EM) wave becomes a more and more controversial issue. Regardless of the debate that whether radio signals are harmful to human bodies, relevant works on the prevention from EM wave exposure have been kept on going.

In general, the parameter adopted to evaluate the safety of a wireless device is addressed by specific absorption rate (SAR), which is the ratio (W/Kg) of absorbed EM wave power (W) to human weight (Kg). When this value is greater than 4 W/Kg, the body temperature would raise appreciably. The SAR specification of cell phones is under 1.6 W/Kg. In industry, copper-plating process is used to screen the EM wave of the cell phone and thus the electromagnetic compatibility (EMC) problem is solved. However such process would use a huge amount of chemicals, seriously polluting the environment. On the contrary, the process for the production of carbon microcoils is cleaner, where only acetylene and catalyzer (manganese and zinc) are used.

The absorption ratio of commercial products such EM wave absorbing clothes, curtain, and paint are generally above 20 dB (that is, 99%). In this paper, comparable absorption ratios in the range of millimeter-wave by using carbon microcoils are achieved.

2. EXPERIMENT

The experiment setup is depicted in Fig. 1, where a transmitter and a receiver were setup to determine the EM wave absorption rate of carbon-microcoils. On the transmitter side, a signal generator (SG) is connected to a rectangular horn antenna, which is directed to the other horn antenna on the receiver side. The receiving horn would collect the transmitted power and send it to the spectrum analyzer (SA) for power detection [1]. Owing to the narrower beamwidth of the horn antenna, the alignment during the whole experiment was much simplified and the cross-section
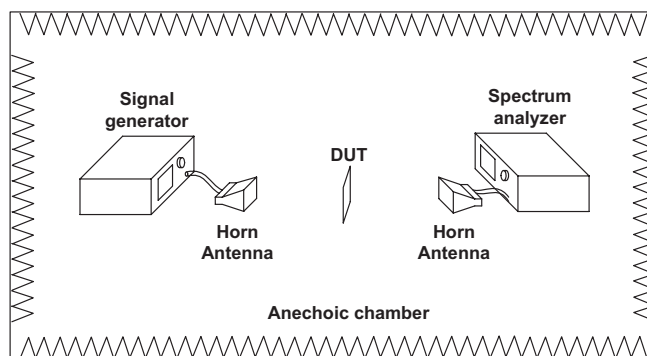

Figure 1: Measurement setup.

area of the device under test (DUT) was also greatly reduced. This experiment was performed in an anechoic chamber to minimize the effects of signal reflections and unwanted interferences.

The powders of carbon microcoils were doped in the liquid of polydimethyl siloxane (PDMS) as DUT. The structure of the DUT is shown in Fig. 2(a). After the PDMS was jellified from liquid to a soft cushion, a transparent film full of carbon-microcoils was formed and ready to be tested. The picture of the DUT is shown in Fig. 2(b), where the length, width, and thickness are 4 cm, 3 cm, and 3 mm, respectively. Note that the whole DUT were composed of four 1 cm × 1 cm dies and two 2 cm × 2 cm dies, due to the limitation (2 cm × 2 cm) of our processing capability.
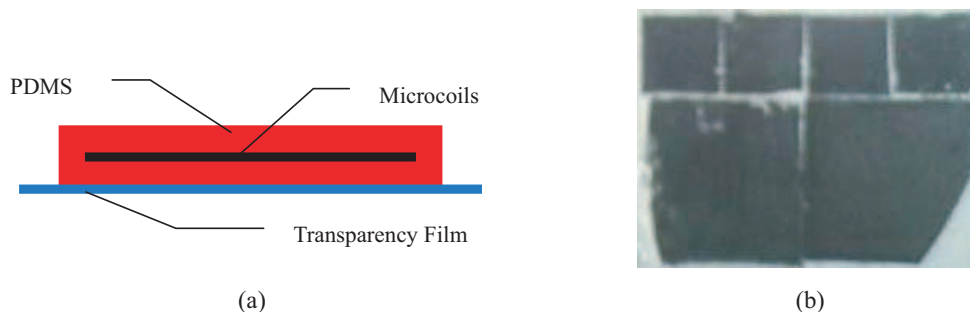
Figure 2: (a) The structure of the carbon-microcoils, (b) photograph of the carbon-microcoils.

Prior researches on EM wave absorption of carbon microcoils absorbers were mainly focused on the frequency range from 20 GHz to 40 GHz [2–4]. However, considering the future trend of WLAN applications (60 GHz) and automobile radar application (77 GHz) [5, 6], it is meaningful to explore the practical usages of carbon microcoils in higher frequency band. In this manuscript, the frequency bands of interest include not only the K band (from 18 GHz to 26.5 GHz) but also the V band (from 50 GHz to 75 GHz).

In this experiment, a signal with a constant power was emitted from the transmitter horn antenna, passing through the DUT and then received by the receiver horn. The difference of power levels (in dBm) detected by SA before and after inserting DUT was defined as the power absorption ratio.

3. EXPERIMENT RESULTS AND DISCUSSION

The EM wave absorption rate of the PDMS film with and without microcoils dopants are shown in Fig. 3, where an intrinsic PDMS layer was adopted as calibrator to exclude the contribution caused by PDMS and extract the real portion of the absorption rate contributed by carbon-microcoils. The difference between PDMS and micro-coils is smaller than 6 dB from 18 GHz to 24 GHz. Nevertheless the absorption by micro-coils becomes more dominant as the frequency is beyond 24 GHz. Moreover, the absorption power of micro-coils is PDMS Microcoils Transparency Film 15 dB larger than that of PDMS at 26 GHz. The measured results in units of both dB and percentage are summarized in Table 1. The EM wave absorption rate reaches 97% at 26 GHz which is comparable to commercial products nowadays.

Table 1: Electromagnetic wave absorption rates of carbon microcoils in K band.

Frequency	PDMS		Microcoils	
(GHz)	dB	%	dB	%
18	2.2	39.74	0.8	16.82
20	0	0.00	5.8	73.70
22	1.4	27.56	4.3	62.85
24	1.9	35.43	4.1	61.10
26	2.4	42.46	15.3	97.05

Furthermore, microcoils with different lengths were measured for comparisons. By manipulating the time of growth, we were able to control the length of these coils. Two samples with the same

size ($2\,\mathrm{cm} \times 2\,\mathrm{cm}$) but different coil lengths were tested, where one of them was grown for 5 minutes and the other was grown for 15 minutes. The measured results are shown in Fig. 4. It is observed that both DUTs seem to show a similar trend in terms of absorption response. Both absorption curves roughly exhibit a frequency independent characteristic with longer coils possessing better absorption rates. Such results might be explained by the fact that longer coils were distributed more intensely in the PDMS, and hence more energy was absorbed in them accordingly.
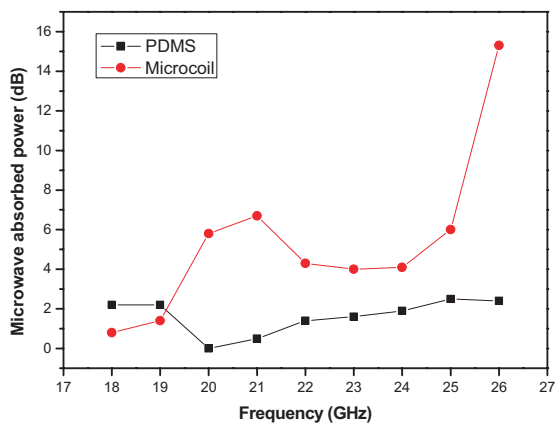
Figure 3: Electromagnetic wave absorption rate in K band.
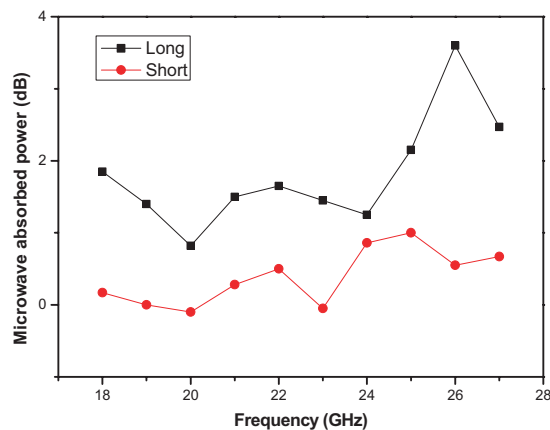
Figure 4: Electromagnetic wave absorption rate of microcoils with different length in K band.

The measured EM absorption rates of microcoils with different length percentage are shown in Table 2. Compared with the limited absorption rate of short coils ($< 20\%$), the long coils are more efficient. Although long coils possess a better performance in absorption than short coils, their absorption rates still do not exceed 60%. The lower absorption rate of this experiment may be attributed to the size of DUT in this experiment: the area of the samples for length comparison is $2\,\mathrm{cm} \times 2\,\mathrm{cm}$ while that of the samples of the former experiment is $4\,\mathrm{cm} \times 3\,\mathrm{cm}$. It means that the EM wave absorption power is proportional to the sample area. In addition, the absorption power can be raised by stacking the samples.

Table 2: Electromagnetic wave absorbed percentage with different microcoils' length in K band.

Frequency (GHz)	Long (dB)	Long (%)	Short (dB)	Short (%)
18	1.85	34.69	0.17	3.84
20	0.82	17.21	−0.1	−2.33
22	1.65	31.61	0.5	10.87
24	1.25	25.01	0.86	17.96
26	3.6	56.35	0.55	11.90

For further investigation, we extended the measurement frequency range to V band. In addition, samples with carbon fibers were also tested for contrast experiment, which were mixed with PDMS shown as in Fig. 5(a). The length, width and thickness of this sample are $7.5\,\mathrm{cm}$, $6.2\,\mathrm{cm}$ and $1.2\,\mathrm{cm}$, respectively. To calibrate the effects caused by intrinsic PDMS, a pure PDMS with the same dimensions was prepared. Fig. 5(b) shows the measured results. The ability of microcoils in power absorption is evidenced by the experimental results in V band frequency range, especially from $62\,\mathrm{GHz}$ to $72\,\mathrm{GHz}$, where the absorption rates are greater than $15\,\mathrm{dB}$. The peak value is $26.6\,\mathrm{dB}$ at $68\,\mathrm{GHz}$, corresponding to 99.8% absorption. On the contrary the absorption rate of carbon fibers is relatively small, which is below $10\,\mathrm{dB}$ over the band of interest and is close to the measurement results of the pure PDMS sample. The measured data are shown in Table 3.
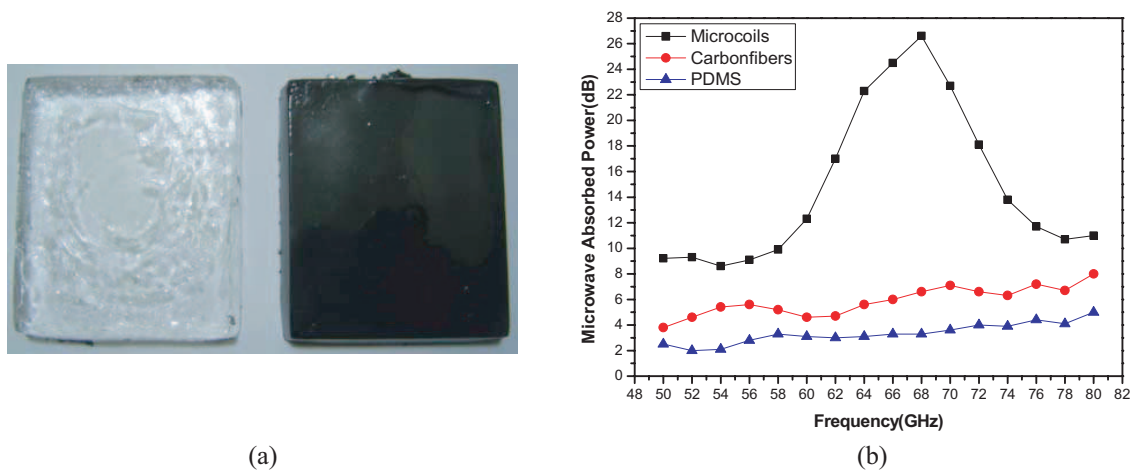
(a)   (b)

Figure 5: (a) Photographs of Pure PDMS and carbon fibers, (b) electromagnetic wave absorbed in V band.

Table 3: Electromagnetic wave absorbed percentage in V band.

Frequency (GHz)	Microcoils		Carbon fibers		Pure PDMS	
	dB	%	dB	%	dB	%
50	9.2	88.0	3.8	58.3	2.5	43.8
54	8.6	86.2	5.4	71.2	2.1	38.3
58	9.9	89.8	5.2	69.8	3.3	53.2
60	12.3	94.1	4.6	65.3	3.1	51.0
64	22.3	99.4	5.6	72.5	3.1	51.0
68	26.6	99.8	6.6	78.1	3.3	53.2
72	18.1	98.5	6.6	78.1	4	60.2
76	11.7	93.2	7.2	80.9	4.4	63.7
80	11	92.1	8	84.2	5	68.4

4. CONCLUSIONS

A new structure for millimeter wave absorber is proposed, which can achieve a 99% power absorption in frequency range from 64 to 70 GHz. The absorption rate of microcoils is apparently more promising in V band than in the K band and the longer coils show better absorption rates than shorter coils. It is also found that the absorbed power of carbon fibers sample is limited in V band. The experimental results reveal that the microcoil is very promising as an efficient absorbing material for the future EMC application in 60 GHz radio system. In addition, the fabrication of microcoil is more environment friendly compared with process of copper plating.

REFERENCES

1. Trautnitz, F.-W., "EMC absorbers through the years with respect to the new site VSWR validation procedure in the frequency range from 1 to 18 GHz — A practical approach," *IEEE Symposium of EMC*, Qingdao, China, 2007.

2. Saib, A., L. Bednarz, R. Daussin, C. Bailly, X. Lou, J.-M. Thomassin, C. Pagnoulle, C. Detrembleur, R. Jérôme, and I. Huynen, "Carbon nanotube composites for broadband microwave

absorbing materials," *IEEE Trans. Microw. Theory Tech.*, Vol. 54, No. 6, 2745–2754, June 2006.

3. Bregar, V. B., "Advantages of ferromagnetic nanoparticle composites in microwave absorbers," *IEEE Trans. Magn.*, Vol. 40, No. 3, 1679–1684, May 2004.

4. Motojima, S., Y. Noda, S. Hoshiya, and Y. Hishikawa, "Electromagnetic wave absorption properties of carbon microcoils in 12–110 GHz region," *J. Applied Physics*, Vol. 94, No. 4, 2325–2330, Aug. 2003.

5. Razavi, B., "A 60-GHz CMOS receiver front-end," *IEEE J. Solid State Circuits*, Vol. 41, No. 1, 17–22, Jan. 2006.

6. Gresham, I., N. Jain, T. Budka, A. Alexanian, N. Kinayman, B. Ziegner, S. Brown, and P. Staecker, "A compact manufacturable 76–77-GHz radar module for commercial ACC applications," *IEEE Trans. Microw. Theory Tech.*, Vol. 49, No. 1, 44–58, Jan. 2001.

Computer Simulation of Emission Spectra in Plasma Generated by an Alternating Electric Field

E. V. Koryukina

Tomsk State University, Lenin avenue 36, Tomsk 634050, Russia

Abstract— In the present work a method for calculation of emission spectra of atoms and ions in an alternating circular polarized electric field is proposed. The electric field of such polarization can be produced by a high-frequency discharge and under laser excitation. This theoretical method was realized in special software written in FORTRAN. Using this software, the dependences of shifts and splitting of spectral lines, transition probabilities and lifetimes on the electric field strength and frequency were investigated for the He, Ne, Ar and Kr atoms. Based on the simulation results, some interesting regularities were revealed.

1. INTRODUCTION

An electric field is always present in plasma either as an external field maintaining the discharge or an internal one inside the plasma micro-field formed by charged particles. The presence of this field leads not only to the Stark effect as such, but also to the fact that other atomic characteristics such as transition probabilities, and lifetimes show a certain dependence on changes in the parameters of the electric field. Of special interest is the investigation of the Stark effect and other characteristics of rare-gas atoms in the electric field since these gases are widely used for plasma processing.

The spectra of atoms subjected to an alternating electric field are determined from the non-stationary Schrödinger equation. The methods of solution of this equation depend on the type of field polarization. In this paper, we consider the dynamic Stark effect for the case of a circular polarized field. Electric fields of such polarization may be observed in a high-frequency discharge in electrodeless lamps [1] and under laser excitation [2]. In a circular polarized electric field, the solution of the Schrödinger equation is significantly simplified because of separation of spatial and time variables. Due to this separation, the non-stationary Schrödinger equation is reduced to the stationary one within the rotating-wave approximation [3]. The stationary Schrödinger equation can be solved within the stationary perturbation theory, but this theory is applicable only under a number of limitations. In fact, perturbation theory can be used only in the case where the electric field strength is relatively small and the perturbation induced by the electric field is smaller than the distance between neighboring energy levels. In addition, in the framework of this theory, resonance and non-resonance perturbation must be calculated by different methods. Finally, the excitation of an atom by low-frequency or high-frequency electric fields must be also calculated using different methods [4].

In the present work, a theoretical method suggested in [5] was applied to solution of the stationary Schrödinger equation. This method is free from limitations inherent in the perturbation theory and suitable in a wide range of frequency and strength of the electric field. Further, the wave functions and energies determined by suggested method are used for calculation of the transition probabilities and lifetimes of atoms in the electric field. These results are topical in plasma physics, because the data are necessary for understanding of the processes taking place in plasma and for diagnostics purposes.

2. CALCULATION METHOD

In a circular polarized electric field, the non-stationary Schrödinger equation is written as

$$i\frac{\partial \psi_n(\vec{r},t)}{\partial t} = (\widehat{H}_0(\vec{r}) - eF(x\cos\omega t \pm y\sin\omega t))\psi_n(\vec{r},t), \tag{1}$$

where ψ_n is the wave function of the n-th state of the system, $\widehat{H}_0(\vec{r})$ is the unperturbed Hamiltonian, and the operator $-eF(x\cos\omega t \pm y\sin\omega t)$ describes perturbation induced by the interaction of an atom with a circular polarized field of frequency ω and strength F. To go to the stationary Schrödinger equation, let us use the rotating-wave approximation [3].

In order to go to a rotating coordinate system rotating around the Z-axis with the frequency ω, let us introduce a wave function in this coordinate system

$$\varphi(\vec{r}, t) = \exp(i\omega t \widehat{J}_z)\psi(\vec{r}, t), \tag{2}$$

where $\widehat{J}_z$ is the z-component of the total angular momentum operator. After substitution of the wave function (2) in Eq. (1), we get

$$i\frac{\partial\varphi(\vec{r}, t)}{\partial t} = \widehat{Q}\varphi(\vec{r}, t), \quad \widehat{Q} = (\widehat{H}_0 - \omega\widehat{J}_z \pm F\widehat{D}_x). \tag{3}$$

As seen from Eq. (3), the operator $\widehat{Q}$ is time-independent. Hence, in the rotating-wave approximation, it is possible to go from the non-stationary Schrödinger Eq. (1) to the stationary one, and we get

$$\widehat{Q}\varphi(\vec{r}) = \varepsilon\varphi(\vec{r}), \tag{4}$$

where

$$\varphi(\vec{r}, t) = \exp(-i\varepsilon t)\varphi(\vec{r}), \tag{5}$$

$\widehat{Q}$ is the operator of energy of an atom in the electric field, and ε and $\varphi(\vec{r}, t)$ are the energy and wave function of the atom in the electric field in the rotating coordinate system.

It was shown in [5] that the wave functions and energies of the atom, being solutions to the Schrödinger Eq. (4), can be found from diagonalization of the energy matrix $\widehat{Q}$ with elements

$$Q_{mn} = E_n^{(0)}\delta_{mn} - \omega\langle\varphi_m^{(0)}(\vec{r})\left|\widehat{J}_z\right|\varphi_n^{(0)}(\vec{r})\rangle \pm F\langle\varphi_m^{(0)}|D_x|\varphi_n^{(0)}\rangle, \tag{6}$$

where $\varphi_n^{(0)}$ and $E_n^{(0)}$ are the wave function and energy of the n-th state of an atom in the absence of external electric field, F and ω are the strength and frequency of the external electric field, and D_x is the x-component of the dipole transition operator. Upon diagonalization of the energy matrix with elements (6), we get the energies ε_n and wave functions as

$$\varphi_n(\vec{r}, t) = e^{-i\varepsilon_n t}\sum_k C_{nk}\varphi_k^{(0)}(r) \tag{7}$$

for the n states of the atom in the external electric field in the rotating coordinate system. The coefficients C_{nk} in the wave function (7) depend on the frequency and strength of the external electric field. To find the average energies of the atom in the initial coordinate system, it is necessary to perform averaging over the oscillation period. Upon averaging, the average energy of the system in the electric field in the initial coordinate system is written in the following form

$$\bar{E}_n = \langle\psi_n(\vec{r}, t)|H(\vec{r}, t)|\psi_n(\vec{r}, t)\rangle = \varepsilon_n + \omega\langle\varphi_n(\vec{r})\left|\widehat{J}_z\right|\varphi_n(\vec{r})\rangle. \tag{8}$$

As seen from Eq. (8), $\bar{E}_n$ is time-independent. The matrix elements of the D_x operator are calculated as follows:

$$\begin{aligned}
\langle\varphi_m^{(0)}|D_x|\varphi_n^{(0)}\rangle &= \langle\gamma J M|D_x|\gamma'J'M'\rangle \\
&= \frac{(-1)^{J-M}}{\sqrt{2}}\left[\begin{pmatrix} J & 1 & J' \\ -M & -1 & M' \end{pmatrix} - \begin{pmatrix} J & 1 & J' \\ -M & 1 & M' \end{pmatrix}\right]\langle\gamma J\|D\|\gamma'J'\rangle
\end{aligned} \tag{9}$$

the reduced matrix elements $\langle\gamma J\|D\|\gamma'J'\rangle$ are calculated depending on a coupling scheme [5].

The wave functions and energies derived from diagonalization of the energy matrix are used for the calculation of the probabilities of spontaneous atomic transitions in the electric field. In the dipole approximation, the total transition probability of a radiation polarized with respect to the $\mathbf{e}_q$ direction and averaged over all possible orientations in the vector $\mathbf{D}$ space is calculated using the formula

$$A_{nm} = \frac{4\omega^3}{3\hbar c^3}\sum_q|\langle\Psi_n|D_q|\Psi_m\rangle|^2, \tag{10}$$

where D_q are the cyclic components of the dipole-moment vector $\mathbf{D}$. The wave functions Ψ_n are determined from the diagonalization of the energy matrix with the matrix elements (6). On substituting the wave functions Ψ_n and Ψ_m to Eq. (10) and using the Wigner-Eckart theorem, the expression for the probability of the $JM \rightarrow J'M'$ transition between magnetic energy sublevels becomes [5]

$$A(JM \rightarrow J'M') = \frac{4\omega_{JM,J'M'}^3}{3\hbar c^3}|D_{JM,J'M'}|^2,$$

$$D_{JM,J'M'} = \sum_q \sum_{ij} C_i^{(JM)*} C_j^{(J'M')}(-1)^{J_i-M_i} \cdot \begin{pmatrix} J_i & 1 & J_j \\ -M_i & q & M_j \end{pmatrix} \cdot \langle \gamma_i J_i \| D \| \gamma_j J_j \rangle, \quad (11)$$

where $C_i^{(JM)}$ and $C_j^{(J'M')}$ are the expansion coefficients from Eq. (7) and $\omega_{JM, J'M'}$ is the frequency of the $JM \rightarrow J'M'$ transition. The probabilities of the $J \rightarrow J'$ transitions between energy levels and the J-state lifetime τ_J of an atom in the electric field are calculated using the formulas

$$A(J \rightarrow J') = \frac{1}{2J+1} \sum_{MM'} A(JM \rightarrow J'M'), \quad \tau_J = \frac{1}{\sum\limits_{J'} A(J \rightarrow J')}. \quad (12)$$

As seen from the above formulas, our theoretical method is free from limitations inherent in the perturbation theory and allows us to simulate emission spectra of any atoms and ions in a wide range of electric field strengths and frequencies.

This theoretical method was realized in special software written in FORTRAN. Input data for software are the unperturbed energy level positions, the frequency ω and strength F of the electric field. Output data obtained at sequential passing of the software blocks are following: wave functions of an atom, spectral-line shifts and splitting (the Stark effect), transition probabilities, and Stark-level lifetimes in the electric field.

3. RESULTS AND DISCUSSION

In the present work, an electric fields of strength up to $10\,\mathrm{KV/cm}$ and with different frequencies, namely, $\omega = 100\,\mathrm{MHz}$, $\omega = 241.813 \cdot 10^5\,\mathrm{MHz}$ and $\omega = 283.005 \cdot 10^6\,\mathrm{MHz}$ were considered. The electric fields of such frequencies are produced by real excitation sources, $\omega = 100\,\mathrm{MHz}$ is the electric field frequency in a high-frequency discharge in electrodeless lamps [1], $\omega = 241.813 \cdot 10^5\,\mathrm{MHz}$ is the frequency of CO_2-laser and $\omega = 283.005 \cdot 10^6\,\mathrm{MHz}$ is the frequency of Nd-laser [2]. Only spectral lines in the visible spectral region were examined, but other spectral regions also can be studied with no limitations. The calculations were performed with the LS coupling scheme for the He atom, and the JL coupling scheme for the rest rare-gas atoms. In calculations of the He, Ne and Ar spectra the ns-, np-, nd- and nf-states with the principal quantum number n up to 10 were taken into account (for the Kr atom, the same states were taken into account, but with n up to 13).

The simulation has allowed us to find a number of regularities in the emission spectra of rare-gas atoms in the electric field. Firstly, the direction of the spectral-line shift is changed to the opposite one for the spectral lines as the nuclear charge of the rare-gas atom is increased. As an illustration, Fig. 1 shows the behavior of spectral lines of the Ne, Ar and Kr atom in the electric field. For all spectral lines of rare-gas atoms, the dependence of the spectral line shift is quadratic with respect to the electric field strength. As a rule, the higher the energy level from which the transition occurs, the greater the shift and splitting of the corresponding spectral line. All exceptions from these rules have an explanation with strong interaction of energy levels in the electric field. It is obvious, the energy level interactions increase with the electric field strength.

Secondly, our calculations showed that an increase in the frequency of the electric field leads to a decrease in the shift and splitting of the Stark levels. In particular, for the $9f[3/2]_1 - 4d[1/2]_0$ spectral line of the Kr atom at $F = 10\,\mathrm{KV/cm}$ the values of the energy shift are 4, 0.8, and $-0.16\,\mathrm{cm}^{-1}$ and splitting magnitudes are 2.5, 1.9, and $0.15\,\mathrm{cm}^{-1}$ for the frequencies. $\omega = 100$, $241.813 \cdot 10^5$, and $283.005 \cdot 10^6\,\mathrm{MHz}$, correspondingly. Our calculations have shown that the reason for this decrease in shifts and splitting of spectral lines with growth of the electric field frequency is a decrease in the energy level interactions.

Thirdly, the calculation results demonstrated that, as a rule, the transition probabilities decrease with an increase in the electric field strength, but sometimes this regularity is broken because of the energy level interactions. The interaction of the Stark levels increasing with the growth of
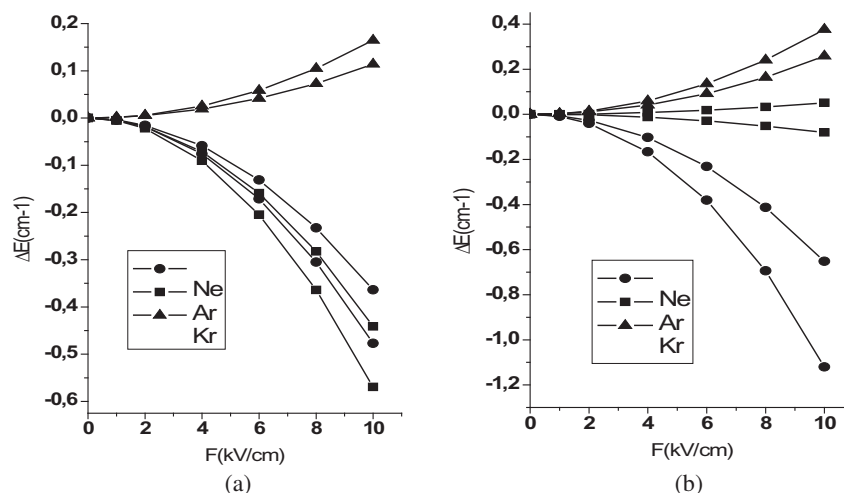
Figure 1: The Stark effect for spectral lines of rare-gas atoms ($\omega = 100$ MHz): (a) $ns[3/2]_1 - n'p[1/2]_0$ (Ne, Ar, Kr : n = 8, 9, 10; $n' = 3, 4, 5$) and (b) $nd[3/2]_1 - n'p[1/2]_0$, (Ne, Ar, Kr : n = 7, 7, 9; $n' = 3, 4, 5$).

the electric field strength leads to anomalies in the behavior of spectral lines and an appearance of forbidden lines. Moreover, obtained results showed that the Stark level interactions lead to an anisotropy of the transition probabilities (see Fig. 2).
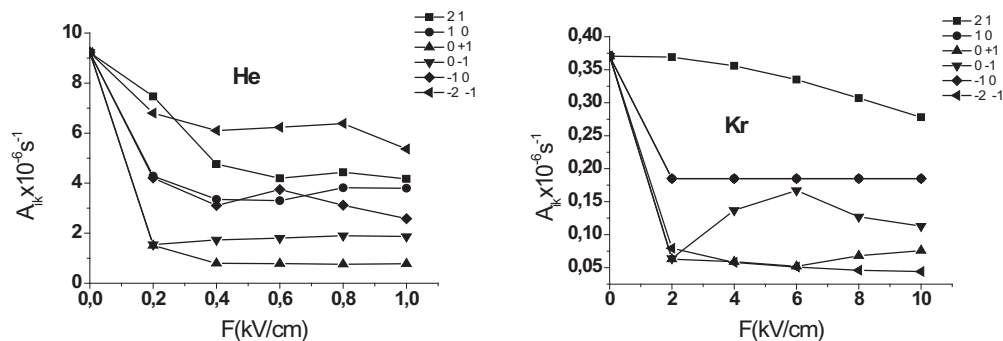

Figure 2: Transition probabilities for the $5^3D_2 - 2^3P_1$ of the He atom and $9s[3/2]_2 - 5p[1/2]_1$ spectral line of the Kr atom ($\omega = 100$ MHz).

It was found, that the transition probabilities and lifetimes have a polynomial dependence on the electric field strength, and the bigger the electric field frequency is, the bigger a degree of polynomial is.

4. CONCLUSIONS

Theoretical results obtained within the computer simulation allow us to explain the processes taking place in plasma. In particular, based on the calculation data, one can determine the electric field strength inside a discharge, clarify a mechanism of filling of the excited levels and reasons for anomalies in the behavior of spectral lines. Further, calculated probabilities and lifetimes can be used as input data in other theoretical calculations, for example, at a solution of the population density balance equations and calculation of spectral line intensities. Moreover, the simulation procedure can be useful for a prediction of new device properties.

ACKNOWLEDGMENT

REFERENCES

1. Revalde, G. and A. Skudra, "Optimization of mercury vapour pressure for high-frequency electrodeless light sources," *J. Phys. D: Appl. Phys.*, Vol. 31, 3343–3348, 1998.
2. Prohorov, A. M., *A Handbook of Lasers*, Vol. 1, Soviet Radio, Moscow, 1978.

3. Bunkin, F. V. and A. M. Prohorov, "Excitation and ionization of atoms in a strong radiation field," *Zh. Eksp. Teor. Fiz.*, Vol. 46, No. 3, 1091–1097, 1964 (in Russian).

4. Delone, N. B. and V. P. Krainov, *Atoms in Strong Light Fields*, Atompress, Moscow, 1984.

5. Koryukina, E. V., "Modelling of the dynamic Stark effect and calculation of the transition probabilities for an Ar atom," *J. Phys. D: Appl. Phys.*, Vol. 38, 3296–3303, 2005.

Terahertz Science and Technology and Applications

B. Zhu[1], **Y. Chen**[2], **K. Deng**[2], **W. Hu**[2], and **Z. S. Yao**[3]

[1]Center of Information and Networks, Chengdu University, China
[2]Institute of Astronautics and Aeronautics
University of Electronic Science and Technology of China, China
[3]National Key Laboratory of Space Microwave Technology, China

Abstract— In the past two decades, with the rapid development of the small-scale semiconductor technology, ultra-fast laser technology, as well as ultra-fast photonics technology, terahertz (THz for short) science and technology has shown great potential application. THz radiation, as a new kind of coherent light source, shows great scientific value and a wide range of applications in the field of basic researches such as physical chemistry, information and biology, etc., as well as in the field of technology researches, such as the materials, national security and medical technology, etc. The article summarizes the applications of THz technology in the field of basic research and civilian technology comprehensively, and focusing on its applications in security communication, anti-stealth radar, chemical and biological agent detection and the fields of national defense and military.

1. INTRODUCTION

THz radiation is a general designation of a particular band of electromagnetic radiation. Generally, THz wave denotes the electromagnetic wave with frequency between 0.1 THz and 10 THz. In some specific cases, THz wave denotes the radiation between 0.3 THz and 3 THz. Until the mid-80s of the last century, we knew little about the electromagnetic properties of this band and which formed the "terahertz gap" between far infrared and millimeter-wave. The THz radiation has been studied extensively since the emerged of the technology of the pulse THz based the ultra-fast optoelectronics. Over the past two decades, with the rapid development of low-scale semiconductor technology, ultra-fast laser technology, as well as ultra-fast photonics technology, THz science and technology has shown great potential applications. As a new type of coherent light source, THz radiation is of great scientific value and broad application prospects in physical chemistry, information and basic research in the field of biology, as well as materials, national security, medical and other technical fields. In this paper, the characteristics of the THz radiation is introduced, moreover, the applications of THz technology, based on THz technology in the military, national defense areas are introduced.

2. THE CHARACTERISTICS OF THz WAVE

The reason why THz wave was studied extensively, not only because it is a kind of electromagnetic radiation which is not familiar to human beings, more importantly, because it has many unique characteristics and broad application prospects.

Terahertz light resides between the microwave and mid-infrared regions of the electromagnetic spectrum. In the field of electronics, THz radiation is called millimeter wave or sub-millimeter-wave; in the field of optics, it is known as far-infrared ray. From the view of energy, the energy of THz band locates between electronic and photonic.

2.1. Wave-particle Duality

First of all, THz radiation is the electromagnetic wave, so it has all the characteristics of electromagnetic waves. THz wave has particle nature and wave nature, such as interference and diffraction.

2.2. Penetrability

THz radiation has good penetrability on a lot of dielectric material and non-polar liquids. Therefore THz wave can be used to perspective imaging for a lot of non-transparent objects. The penetrability of THz wave makes it as the supplement of X-ray imaging and ultrasound imaging for security checks or quality control in nondestructive testing.

THz-wave imaging technologies, including the two-dimensional imaging, time-of-flight imaging, compound aperture imaging, computer-assisted tomography, as well as near-field imaging.

2.3. Security

THz radiation another notable feature is its security. Compared to X-ray with kilo-eV photon energy, the energy of THz radiation is only mill-electron volt. Its energy is lower than the energy of different types of chemical bond, so it will not cause harmful ionizing reaction. This is critical to the practical applications such as the security check of travelers, inspection of other biological samples, etc.

2.4. The Resolving Power of Spectrum

Although the THz radiation photon energy is relatively low, the band still contains a wealth of spectral information. Many organic molecules has strong absorption and dispersion characteristics in the THz band, the THz spectroscopy of material contains a wealth of physical and chemical information, which making them the unique characteristics, like fingerprints. Therefore, THz spectral imaging technology is not only able to differentiate objects morphology, but also identify the composition of objects.

2.5. Other Characteristics

Compared with the microwave, THz radiation has a higher frequency and bandwidth, as the communications carrier that can carry more information. Therefore THz wave has great potential applications in the short-distance high-capacity wireless communications. In imaging applications, THz wave has a higher spatial resolution, and therefore the image has more depth of field while maintaining the same spatial resolution.

3. THz APPLICATION OF SCIENCE AND TECHNOLOGY

The unique nature of THz radiation make it has broad and important application in the field of astrophysics, plasma physics and engineering, materials science and engineering, biomedical engineering, environmental science and engineering, spectroscopy and imaging technology, information science and technology, etc.

3.1. The Application THz Technology in Biomedicine

Since many biological macromolecules and DNA molecular rotation and vibration locate in the THz-band level generally, the organisms has a unique response to THz wave; therefore, THz radiation can be used for disease diagnosis, organisms detection and imaging, as shown in Fig. 1.
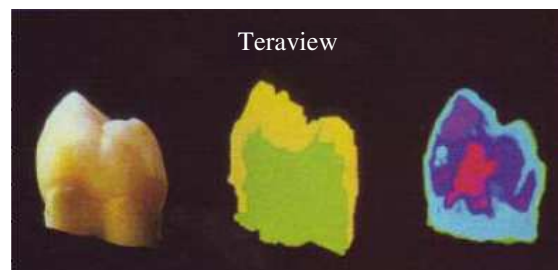
Figure 1: THz tomography of human teeth [1].

Computer-aided tomography technology is the three-dimensional imaging technique, which is developed and applied in the field of X-ray at first. THz wave can also be applied to computer-assisted tomography. X-ray tomographic imaging of objects can only reflect the distribution of absorption rate, while the THz tomography record the time waveform information of entire THz pulse. Therefore, according to different requirements can select a different physical detection, such as the electric field strength, peak time and even the spectral characteristics of the material. THz tomography can get not only the absorption rate distribution of objects, but also can get the three-dimensional distribution of the refractive index of objects and materials.

THz-wave imaging has several inherent limitations: (1) it is not able to penetrate the metal. Metal surface is almost 100 percent reflection index of the THz radiation, THz wave therefore is not able to detect metal objects container. (2) water has a strong absorption on the THz wave.

3.2. Safety Monitoring and Quality Control

THz radiation can also be used for detecting pollutants, biological and chemical detection, and therefore can be used to monitor the process of food preservation and food processing. The characteristics of THz wave, penetrating objects and security, can be used for non-contact, non-injury to

Figure 2: Detection of hidden metal weapons by THz wave.

detect specific substances, such as hidden explosives, drugs, weapons, etc [2] (as shown in Fig. 2). As a result of the strong capacity of penetration and low energy of THz electromagnetic waves (completely harmless to humans), THz imaging can completely replace the X-ray examination, CT scan, and be used in the material non-destructive monitoring and vital security sector and chemical and biological weapons inspection.

3.3. Nondestructive Testing

The safety and penetrable properties of THz wave can be used for nondestructive testing of building. The penetrability of THz wave can be measured from THz time-domain spectroscopy. Foam is the materials used Space shuttle commonly; the crash of the US space shuttle in 2003, "Columbia" is caused by the degumming of foam isolation in external fuel tank layer. Foam has very low absorption and refractive index on the THz wave, so THz waves can penetrate a few inches thick foam, and to detect the buried defects. THz imaging has been selected as the one of four type of future technology of NASA to detect the defects in space shuttle (the other three technologies for X-ray imaging, ultrasound imaging and laser imaging).

3.4. Astronomy and Atmospheric Research

THz is a very important radio astronomy band to ultra-high spatial resolution of the universe; therefore, we can use THz technology to carry study of the interstellar formation and the space research. A large number of atmospheric molecules such as water, carbon monoxide, nitrogen, oxygen can be detected in the THz band, which can be use to atmospheric environmental protection and the monitoring of the ozone layer.

3.5. Short Distance Wireless Communications and Networking

THz band has high frequency, wide bandwidth and more channel than the microwave, which is suitable for in local area networks and broadband mobile communications. 10 Gbps wireless transmission speeds can be obtained by THz communication, which is a few hundred or even thousands of times faster than current Ultra-Wideband technology, and is the future hope for large-capacity multimedia wireless communications. Some experts predict that in the near future THz wireless network will replace the wireless LAN or Bluetooth technology, become the major short-range wireless communications technology.

3.6. Military Applications

THz technology has three main applications in the military field: THz communications, THz non-destructive detection and anti-stealth THz ultra-wideband radar.

3.6.1. Secure Communication

In outer space, the transmission of THz is lossless, so we can achieve long-range space communications with very little power. At the same time, compared with the current space optical communication, THz wave has wider beam width, so it is easier to pointing in the long-distance space communication. And antenna system can achieve small and flat, and is particularly suited for secure communications between the stars and satellites.

3.6.2. Anti-stealth THz Ultra-wideband Radar

THz radar can emit tens of thousands of species frequency as well as pico-second and nanosecond pulse at GW level; it has many advantages and capabilities that ordinary radar does not have. THz radar has a broad application prospects in the military and national security.

THz radar launch THz pulse contains a wealth of frequency, which enable stealth aircraft to lose the role of narrow-band radar absorbing coating. Furthermore, THz radar has strong anti-stealth ability to shape stealthy and material stealthy.

Figures 3 and 4 show the radar imaging of military trailers and T72 tanks model in portable THz radar research projects which funded by US Army National Ground Intelligence Center [2].

Figure 3: THz radar imaging of military targets.
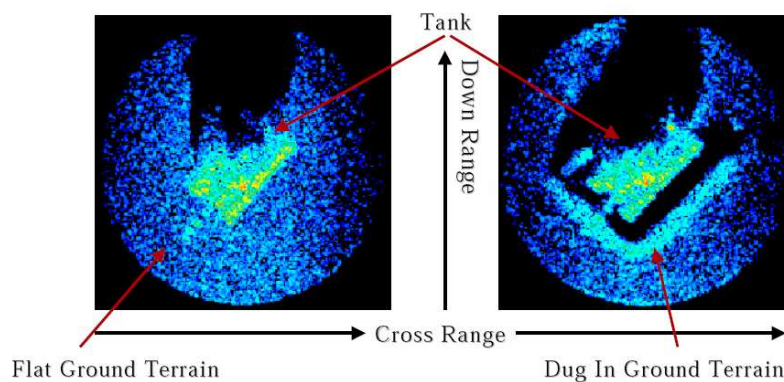
Figure 4: THz radar imaging of hidden military targets.

3.6.3. Chemical and Biological Agent Detection

THz pulse spectrum is very sensitive to molecules and the constitutes of their surrounding environment. Therefore, in all weather conditions, as well as smoke and dust environment, THz technology can be used in chemical detection of the air in the battlefield, and can identify of the type of the chemical and biological agents.

4. CONCLUSIONS

Nearly two decades, THz technology have made some progress and development in both basic research and applied research [3–6]. A comprehensive summary of the current THz technology in the field of basic research, technology research and civilian applications is given. And the paper is focused on the explanation of THz technology in the defense and the military field.

The prospects of THz technology are broad and attractive, and there is a long way to run to achieve the following goals, namely high power generation and high sensitive detection of THz radiation.

REFERENCES

1. Shur, M., "Terahertz technology: Devices and applications," *Proceedings of ESSCIRC*, 13–21, Grenoble, France, 2005.
2. Goyette, T. M., A. Gatesman, T. M. Horgan, et al., "THz compact range radar systems," Pennsylvania, June 13, 2003.

3. Murrill, S. R., B. Redman, and R. L. Espinolac, "Advanced terahertz imaging system performance model for concealed weapon identification," *Proc. SPIE*, Vol. 6549, 654902, 2007.

4. Semenov, A., H. Richter, U. Böttger, et al., "Imaging terahertz radar for security applications," *Proc. SPIE, Terahertz for Military and Security Applications VI*, Vol. 6949, 694902, 2008.

5. Hirata, A., T. Nagatsuma, T. Kosugi, et al., "10-Gbit/s wireless communications technology using sub-terahertz waves," *Proc. SPIE, Terahertz Physics, Devices, and Systems II*, Vol. 6772, 67720B, 2007.

6. Langdon, R. M., V. Handerek, P. Harrison, et al., "Military applications of terahertz imaging," *1st EMRS DTC Technical Conference*, A1, Edinburgh, 2004.

Influence of Shielding in Asymmetric Planar Structures for MMICs Applications

A. Khodja[1], C. Boularak[1], R. Touhami[1], H. Baudrand[2], and M. C. E. Yagoub[3]

[1]Instrumentation Laboratory, Faculty of Electronics and Informatics
U.S.T.H.B University, Algiers, Algeria
[2]ENSEEIHT, 2 rue Charles Camichel 31071, Toulouse Cedex 7, France
[3]SITE, University of Ottawa, 800 King Edward, Ottawa, Ontario, K1N 6N5, Canada

Abstract— An efficient full-wave numerical method is proposed for describe with respect to the dispersion parameters the influence of shielding in unilateral asymmetric structures which can support two different propagation modes defined by C-mode and π-mode. The EM operators formalism is used in order to simplify the resolution of the boundary problems leading to the Galerkin's procedure which permits to find propagation characteristics. The obtained results have been validated with a good precision compared with those available in the international literature.

1. INTRODUCTION

Asymmetric planar transmission lines are widely used for many applications in monolithic microwave integrated circuits (MMIC's) devices for communication systems, such as directional couplers, filters or impedance matching networks. Asymmetric structures can provide additional advantages compared with the symmetric ones because of their impedance transform nature and circuit design flexibility.

The propagation constants and coupling characteristics are described in terms of respectively even and odd modes for the symmetrical lines [1] and of C- and π-modes for the asymmetrical lines [2].

Design and characterization of planar structures are useful in the development of integrated circuits. For this, several numerical methods are appeared to model suitably those transmission structures. The transverse resonance method, combined with the electromagnetism operator formalism, is used in order to efficiently study in hybrid mode the shielding effects of metallic boxed coupled microstrip and coplanar lines as shown in Fig. 1.
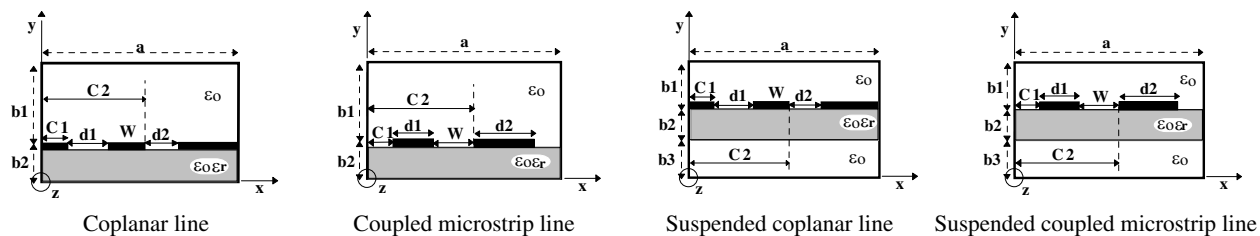
Figure 1: Cross sectional view of shielded unilateral asymmetric transmission lines.

In this paper, the dielectric substrate used to analyze shielded asymmetric planar structures is assumed to be homogeneous, isotropic, and lossless. Its upper face is partially metallized by two or three parallel uniform zero-thickness conducting strips along the direction of propagation (oz), as shown in Fig. 1.

2. TRANSVERSE RESONANCE METHOD FORMULATION

The mathematical process behind this integral method is the use of operators formalism in order to simplify the resolution of boundary problems. The purpose is the evaluation of the global admittance operator $\hat{Y}$ (or impedance operator $\hat{Z}$) to which the Galerkin's technique is applied [1, 2].

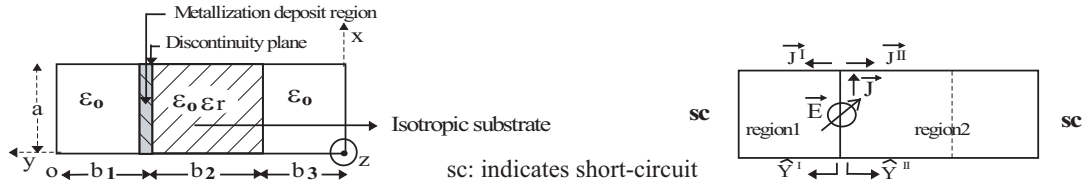Such process can be achieved through several steps described in the following sections [1, 2].

Figure 2: Equivalent network of the cross sectional view of unilateral structure with a rotation of $\pi/2$.

2.1. Equivalent Network Representation of Cross Section of Unilateral Structure

The equivalent circuit of an unilateral asymmetric line with negligible thickness, includes the presence of a fictitious electric source represented in Fig. 2 by a transverse electric field $\vec{E}$ across the slot due to the metallized interface delivering a surface current density source $\vec{J}$.

The admittance operators $\hat{Y}^I$ and $\hat{Y}^{II}$ (for region 1 and 2 respectively) are expressed on the discontinuity plane. In Fig. 2, oy is the direction of the fictitious propagation constant, while "sc" states for short-circuit.

2.2. Matrix Representation of the Boundary Conditions

The application of the boundary conditions on the interface (insulator-air or metal-air) requires that the transverse components of $\vec{E}$ and $\vec{J}$ in the xoz plane are respectively zero on the metal and outside the metal.

Let $\hat{Y}$ and $\hat{Z}$ be, respectively, the admittance and impedance operators associated to the analyzed line.

The Kirchoff's law yields to:

$$\vec{J} = (\hat{Y}^I + \hat{Y}^{II})\vec{E} = \hat{Y}\vec{E}, \quad \hat{Y} = \hat{Y}^I + \hat{Y}^{II} \tag{1}$$

where:

$$\vec{E} = \hat{Z}\vec{J} = \vec{0} \quad \text{on the metal} \tag{2}$$

$$\vec{J} = \hat{Y}\vec{E} = \vec{0} \quad \text{on the insulator} \tag{3}$$

2.3. Matrix Representation of $\hat{Z}$ And $\hat{Y}$ Operators

The matrix representation of the $\hat{Z}$ or $\hat{Y}$ operators requires involvement of a complete and orthogonal basis functions (f_n, $n = 0, \ldots, \infty$), and the calculation of the mode-admittances y_n^I and y_n^{II} of region 1 and 2 respectively. The matrix expressions of admittance and impedance operators are given by [1–3]:

$$\hat{Y} = \sum_{n=0}^{\infty} \left[|f_n\rangle \left(y_n^I + y_n^{II} \right) \langle f_n| \right]^{(e+h)} = \sum_{n=0}^{\infty} \left[|f_n\rangle\, y_n\, \langle f_n| \right]^{(e+h)} \tag{4}$$

$$\hat{Z} = \sum_{n=0}^{\infty} \left[|f_n\rangle \frac{1}{(y_n)} \langle f_n| \right]^{(e+h)} = \sum_{n=0}^{\infty} \left[|f_n\rangle\, z_n\, \langle f_n| \right]^{(e+h)} \tag{5}$$

$|f_n\rangle \langle f_n|$ represents the projection operator on the basis vectors $\{|f_n\rangle\}_{n=0,\infty}$, where the product of vector "bra" ($\langle f_n|$) with vector "cket" ($|g_n\rangle$) represents inner product of these two vectors.

"e" and "h" are respectively the TM_n and the TE_n mode along the transverse direction (oy).

2.4. Galerkin's Method

The application of Galerkin's method requires the decomposition of transverse electric field in the slots for coplanar line, or of transverse current density on the conductor strips for the coupled microstrip line, as a sum of trial functions [2] such as:

$$E_x = \sum_{p=1}^{kx} e_{px}\Phi_{px} \text{ and } E_z = \sum_{q=1}^{kz} e_{qz}\Phi_{qz} \tag{6}$$

$$J_x = \sum_{p=1}^{kx} e'_{px}\Phi'_{px} \text{ and } J_z = \sum_{q=1}^{kz} e'_{qz}\Phi'_{qz} \tag{7}$$

k_x and k_z are the number of trial functions by component respectively along ox and oz direction.

The electric field and the current density have to be zero respectively on the metallized strips and in the slots separating the conducting strips and they are given by:

$$|E\rangle^{(e+h)} = (\hat{Z}\,|J\rangle)^{(e+h)} = |0\rangle \quad \text{(on the metal)} \tag{8}$$

$$|J\rangle^{(e+h)} = (\hat{Y}\,|E\rangle)^{(e+h)} = |0\rangle \quad \text{(outside the metal)} \tag{9}$$

After applying the Galerkin's method to $\hat{Z}$ or $\hat{Y}$, a homogeneous system of the form "$LX = 0$" is obtained [1–3]. "L" is the dispersion matrix of $(k_x + k_z) * (k_x + k_z)$ dimension, whith $k_x = k_z = K$, where the elements are composed of mode admittances (for coplanar structure) or mode impedances (for coupled mirostrip structure) and inner products of basis functions with trial functions [3]. "X" is the vector containing the transverse current densities (or electric fields) coefficients (e_{px}, e_{qz}). Setting the determinant of L-matrix equal to zero, that will give the dispersion parameters.

3. CHOICE OF TRIAL FUNCTIONS

Trial functions have to respect several convergence criteria of this method [2] such as:

- Boundary conditions, proportionality conditions and metallic edge effects conditions.

Cosine trial functions taking into account the metallic edge effects are chosen for asymmetric lines such as:

3.1. Asymmetric Coplanar Line

C mode

$$\Phi_{mx}(x) = \begin{cases} \dfrac{\cos\left(\dfrac{(m-1)\pi(x-C1)}{d1}\right)}{\sqrt{\left(\dfrac{d1}{2}\right)^2 - \left(x - C1 - \dfrac{d1}{2}\right)^2}} & x \in [C1,\ C1 + d1] \\[4em] (-1)^m \dfrac{\cos\left(\dfrac{(m-1)\pi(x-C2)}{d2}\right)}{\sqrt{\left(\dfrac{d2}{2}\right)^2 - \left(x - C2 - \dfrac{d2}{2}\right)^2}} & x \in [C2,\ C2 + d2] \end{cases}$$

$$\Phi_{mz}(x) = \begin{cases} \sin\left(\dfrac{m\pi(x-C1)}{d1}\right) & x \in [C1,\ C1 + d1] \\[1.5em] (-1)^{m+1} \sin\left(\dfrac{m\pi(x-C2)}{d2}\right) & x \in [C2,\ C2 + d2] \end{cases}$$

π mode

$$\Phi_{mx}(x) = \begin{cases} \dfrac{\cos\left(\dfrac{(m-1)\pi(x-C1)}{d1}\right)}{\sqrt{\left(\dfrac{d1}{2}\right)^2 - \left(x - C1 - \dfrac{d1}{2}\right)^2}} & x \in [C1,\ C1 + d1] \\[4em] (-1)^{m+1} \dfrac{\cos\left(\dfrac{(m-1)\pi(x-C2)}{d2}\right)}{\sqrt{\left(\dfrac{d2}{2}\right)^2 - \left(x - C2 - \dfrac{d2}{2}\right)^2}} & x \in [C2,\ C2 + d2] \end{cases}$$

$$\Phi_{mz}(x) = \begin{cases} \sin\left(\dfrac{m\pi(x-C1)}{d1}\right) & x \in [C1,\ C1 + d1] \\[1.5em] (-1)^{m} \sin\left(\dfrac{m\pi(x-C2)}{d2}\right) & x \in [C2,\ C2 + d2] \end{cases}$$

3.2. Asymmetric Coupled Microstrip Line
C mode

$$\Phi_{mx}(x) = \begin{cases} \sin\left(\dfrac{m\pi(x-C1)}{d1}\right) & x \in [C1, \ C1+d1] \\[2mm] (-1)^m \sin\left(\dfrac{m\pi(x-C2)}{d2}\right) & x \in [C2, \ C2+d2] \end{cases}$$

$$\Phi_{mz}(x) = \begin{cases} \dfrac{\cos\left(\dfrac{(m-1)\pi(x-C1)}{d1}\right)}{\sqrt{\left(\dfrac{d1}{2}\right)^2 - \left(x-C1-\dfrac{d1}{2}\right)^2}} & x \in [C1, \ C1+d1] \\[6mm] (-1)^{m+1} \dfrac{\cos\left(\dfrac{(m-1)\pi(x-C2)}{d2}\right)}{\sqrt{\left(\dfrac{d2}{2}\right)^2 - \left(x-C2-\dfrac{d2}{2}\right)^2}} & x \in [C2, \ C2+d2] \end{cases}$$

π mode

$$\Phi_{mx}(x) = \begin{cases} \sin\left(\dfrac{m\pi(x-C1)}{d1}\right) & x \in [C1, \ C1+d1] \\[2mm] (-1)^{m+1} \sin\left(\dfrac{m\pi(x-C2)}{d2}\right) & x \in [C2, \ C2+d2] \end{cases}$$

$$\Phi_{mz}(x) = \begin{cases} \dfrac{\cos\left(\dfrac{(m-1)\pi(x-C1)}{d1}\right)}{\sqrt{\left(\dfrac{d1}{2}\right)^2 - \left(x-C1-\dfrac{d1}{2}\right)^2}} & x \in [C1, \ C1+d1] \\[6mm] (-1)^{m} \dfrac{\cos\left(\dfrac{(m-1)\pi(x-C2)}{d2}\right)}{\sqrt{\left(\dfrac{d2}{2}\right)^2 - \left(x-C2-\dfrac{d2}{2}\right)^2}} & x \in [C2, \ C2+d2] \end{cases}$$

4. NUMERICAL RESULTS

The developed computer program calculates the effective permittivity "ε_{eff}", phase constant "β" and wavelength "λ" of fundamental mode for C and π mode of shielded asymmetric coupled microstrip and coplanar lines, using trial functions of sinusoidal form which take into account the metallic edge effects, where the convergence of our results does not exceed four trial functions by component ($K \leq 4$) and 2000 modes according to the physical parameters of those asymmetrical planar lines.

(b2=0.254 mm, d1=0.08 mm, εr=2.22, C1=0.1 mm, w=0.45 mm, F=10 GHz)

(b2=0.125 mm, d1=0.1 mm, F=33 GHz, C1=0.1 mm, w=0.2 mm, εr=2.2)

(d1= d2=0.08 mm, b2=0.254 mm, C1=0.1 mm, εr=2.22, F=10 GHz)

(d1= d2=0.1 mm, b2=0.125 mm, C1=0.1 mm, εr=2.2, F=33 GHz)
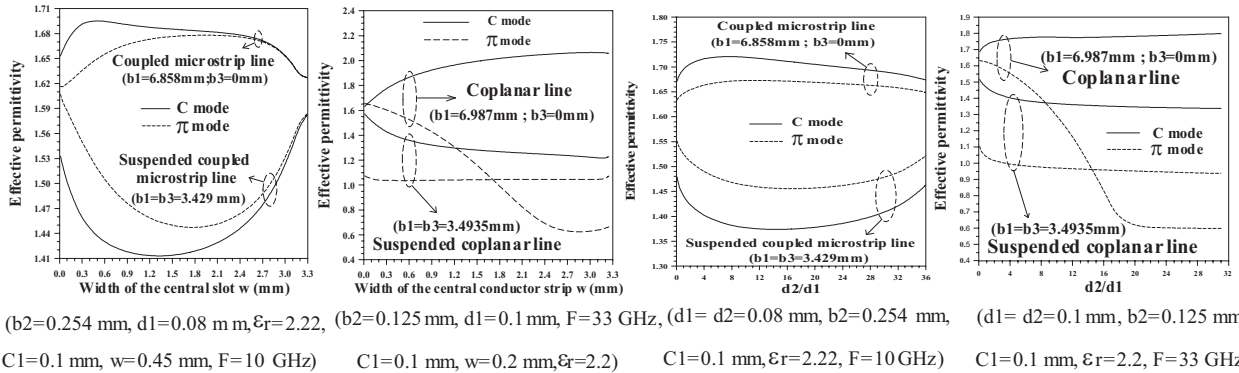
Figure 3: Variation of effective permittivity versus physical parameters.

Figure 3 shows the vertical metallic sides effect of shielding on the "ε_{eff}" of both C and π mode, when the width of slot(s) or metallic strips are varied. We deduce that shielding effect for coupled microstrip type structure is more important for wide slot(s) or wide conductor strips especially when the edges of metallic strips approach the vertical metallic sides. So the variation of "ε_{eff}" of C and π mode becomes more important. About asymmetric coplanar structure, when width of central conductor or slots varies, shielding effect is more important especially for π mode involving an important variation of "ε_{eff}".
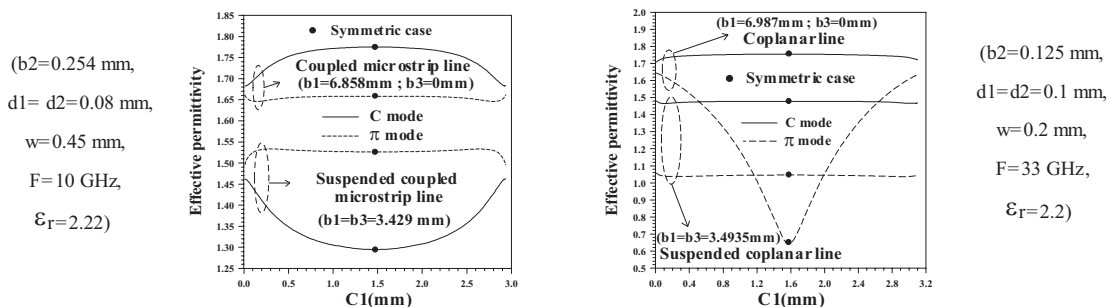
Figure 4: Evolution of effective permittivity versus C1.

According to the Figure 4, the influence of C1 on the "ε_{eff}" for asymmetric coupled microstrip type structure is more important for C-mode than for π-mode. Contrary to the shielded asymmetric coplanar line, the influence of C1 on the "ε_{eff}" is less important for C-mode than for π-mode. Moreover, by moving successively the substrate to the horizontal lower side of the shielding, the "ε_{eff}" increases more of C-mode and decreases more of π-mode respectively for asymmetric coupled microstrip and coplanar structures, especially for the symmetric case.
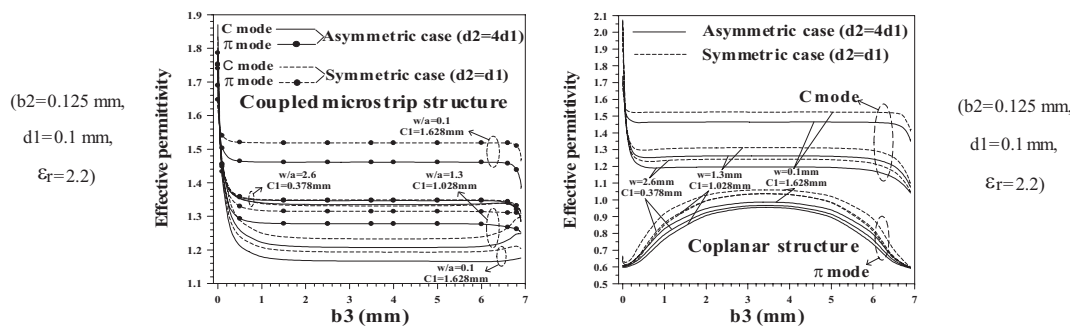
Figure 5: Evolution of effective permittivity versus $b3$.

Figure 5 shows the influence of horizontal metallic sides of shielding on "ε_{eff}" of both C and π mode for symmetric and asymmetric lines, by varying height "$b3$" for various values of central aperture for coupled microstrip structure or central metallic strip for coplanar structure. These curves indicate clearly the influence of the shielding on the "ε_{eff}" when the substrate is particularly near the lower horizontal conducting side. Moreover, for any value of "w" (see Figure 5) and when $b3$ varies between 1 mm and 6 mm, the horizontal metallic sides have no effect on "ε_{eff}", except for π mode of coplanar structure where "ε_{eff}" vary versus "$b3$".
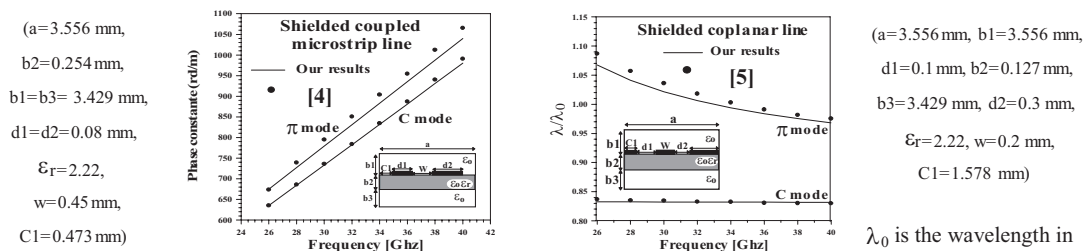
Figure 6: Comparisons between our results and those published.

According to the Figure 6, numerical obtained results by this integral method show a good agreement with those published in the literature [4, 5] where the maximum relative error does not exceed 1.96%.

5. CONCLUSIONS

Transverse resonance method combined with the mathematical operator formalism has been successfully used for the efficient full-wave mode analysis of shielding effect in asymmetric structures. The obtained results converge well with those available in the literature, due to the adequate choice of trial functions used in this method. This method can be applied easy on the metallic (or isolating) region for symmetric and asymmetric structures, by using operator $\hat{Z}$ (or $\hat{Y}$) to which the Galerkin procedure has been applied.

REFERENCES

1. Khodja, A., M. L. Tounsi, M. C. E. Yagoub, and R. Touhami, "Full-wave mode analysis of coupling effect in microwave planar transmission lines," *The Second IASTED International Conference on Antennas, Radar and Wave Propagation (ARP2005)*, 49–54, Banff, Alberta, Canada, July 2005.
2. Khodja, A., M. L. Tounsi, M. C. E. Yagoub, R. Touhami, K. Idinarene, and S. Gaoua, "Optimal choice of trial functions in the modeling of unilateral asymmetric microwave structure by integral method", *4th Mediterranean Microwave Symposium (MMS'2004)*, Marseille, France, June 2004.
3. Khodja, A, "Optimisation des fonctions d'Essai dans la modélisation de la ligne à ailettes unilatérale par la méthode de résonance transverse," Master Thesis, USTHB, Algiers, Algeria, April 2000.
4. Achkar, J., O. Picon, V. F. Hanna, and J. Citerne, "Analysis of symmetric and asymmetric coupled suspended striplines and some associated discontinuities", *20th EMC*, Budapest, Hungary, 1990.
5. Biswas, A. and V. K. Tripathi, "Analysis and design of asymmetric and multiple coupled finline couplers and filters," *IEEE MTTS*, Vol. 1, 403–406, 1990.

Electronic States in Mixed Cantor-like Potentials

D. S. Díaz-Guerrero, F. Montoya, and L. M. Gaggero-Sager

Facultad de Ciencias, Universidad Autónoma del Estado de Morelos

Ave. Universidad 1001, Cuernavaca, Morelos, México

Abstract— The transmittance is studied, using the transfer matrix method, for various multi-barrier systems. The calculations are made in the framework of effective mass theory. The transmittance is calculated for one system increasing the number of layers (generations). The systems are built by mixing a Cantor-like potential with a superlattice. Both cases, barriers and wells, for the Cantor-like potential, are considered to compare the variations between the known superlatice and the proposed mixed system. The resulting potential is as follows, first a superlattice, next a Cantor and finally another superlattice. Another interesting feature is to study the effect of the width and number of layers for the superlattices. The fractal dimension of the transmittance and the potential is calculated, using an image processing technique, to determine if some correlation exists between the fractality of the potential and the fractality of the transmittance.

1. INTRODUCTION

The study of a materials properties is of great importance due to the search of optimal devices, at least better than those exists today. For this the scientist, from a very methodological point of view, first look at the fundamental physical properties of such materials. One of the posibilities is the transmission coefficient, or transmittance, of an electromagnetic wave incident upon a quantum potential, tipically barriers or wells. This topic is covered in the college courses for a single rectangular barrier, nevertheless is very interesting to study some more complex systems. Among these, there is the so called superlattices, Figure 1, for wich the transmittance has been well characterized by their band structure [2, 3]. An even more irregular case is the Cantor-like potential [1, 5], witch is inspired in the Cantor set, in this system the height, width and distance of the barriers (or wells) are modified (Figure 2) just like int the construction of the Cantor set.

The knowledge of the properties of a given material gives the possibility of design devices more efficient and, in some cases, less expensive. For this reason, is important to increase the variety of those systems. Starting with the cited systems, the next logical step is mixing them, and this is the kind of systems that were chosen for this work, the mixed Cantor-like potentials.

2. METHODOLOGY

An mixed Cantor like potential is built using two superlattices and one Cantor-like potential. The mixing process is quite simple, in fact is just arranging the three systems in the following order, first a superlattice, next the Cantor potential and then the other superlattice, Figure 3. The
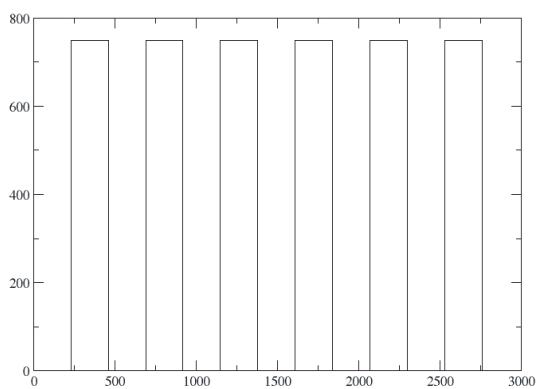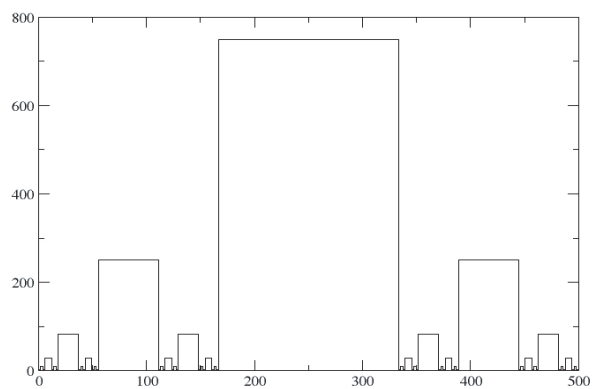

Figure 1: Superlattice potential, generation 6.

Figure 2: Cantor-like potential, generation 6.

transfer matrix method [2, 3] is used to calculate the transmittance of the previous systems. These calculations are made in the framework of effective mass theory. In this system, a given generation comprehend the same generation for the component systems, i.e., considere the generation 3 of the mixed Cantor-like potential, it has two superlattices and one Cantor-like potential of the third generation. It is worth to say that the superlattices increase their length, as the generation does, while the Cantor does not.

It is clear that the generation one corresponds to a superlattice of generation 3, which most have the characteristic band structure. This can be considered as an indicator to show that the method used to calculate de concatenated system is valid. This fact is important because of the scheme chosen to calculate the transmittance of the entire structure. It rests in the fact that it can be computed the transmittance of the first superlattice, keeping the resulting transmittance, and using it as input for the Cantor, and doing the same for the last superlattice. The parameters involved in this system are the height and width of the barriers and the distance between them. The parameters that are changed for study its effect on the transmittance are the width and distance. This parameter variation is applied to the superlattice systems. The key parameter for the Cantor potential is the length of the whole structure, in this case 750Å.

Since the Cantor-like potential is inspired on the Cantor set, which is a classic fractal, is reasonable to assume the potential is also fractal. One logical question is if any property of the potential such as the transmittance also show this feature. In order to go forward in this matter, an image processing technique is used to calculate the fractal dimension of the potential and of the transmittance.
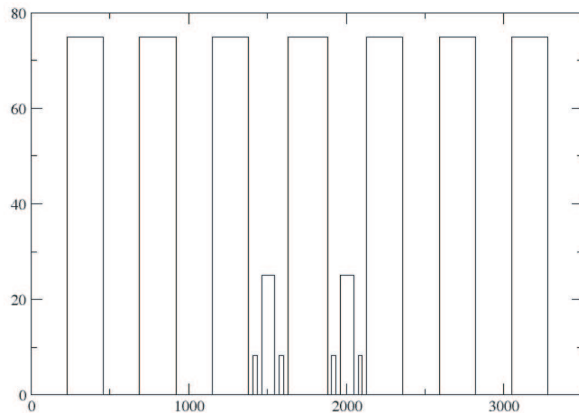
Figure 3: Mixed Cantor-like potential, generation 3.
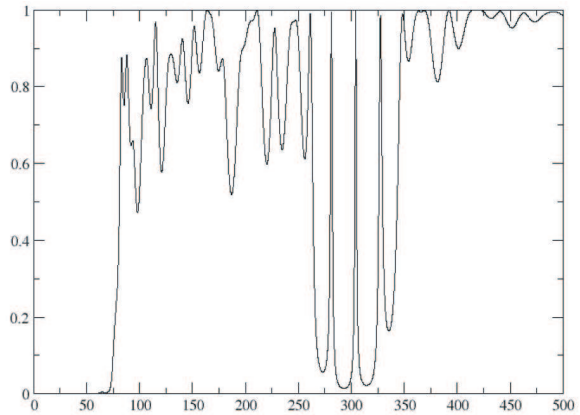
Figure 4: Transmittance for an width/distance of 23Å, generation 10.
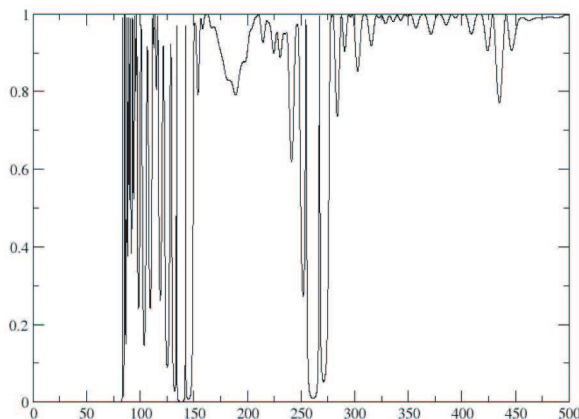
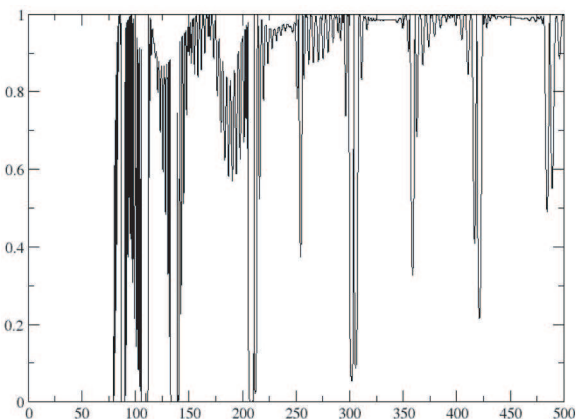Figure 5: Transmittance for an width/distance of 75Å, generation 10.

Figure 6: Transmittance for an width/distance of 230Å, generation 10.

3. RESULTS

The parameters used for the mixed Cantor-like potential are height 75Å; width and distance 23Å, 75Å and 230Å, the obtained transmittance seems very different, against the superlattice band structure, for the first two sets of parameters (Figures 4 and 5) but for the last one it seems to resemble the familiar band structure, although it has a more reach behavior, Figure 6. The most interesting feature for this results is that the set of maximum/minimum is no longer constant, fluctuations appears as the energy increases. Also, the number of local maximum and minimum is greater but without a regular amplitude behavior. This can be a consequence of adding smaller and closer barriers for the Cantor potential.

Figure 7 shows the calculated transmittance for a mixed Cantor-like potential in which the Cantor component is considered a well. As expected, the transmittance does not vary drastically. The main changes are again the maximum and minimum, in this case their fluctuation do not seems as cualitative periodic as in the barriers.

At last but not least, the fractal dimension is estimated. For this, an image processing technique developed by Frederic Moisy [6] is used. This tool implements the box counting method [7] for estimate the dimension. The nature of the potential and transmittance shapes considered in this paper make very hard to develop an accurate and reliable direct method for estimate the fractal dimension, this is why the Moisy's tool has been chosen.

The fractal dimension for the mixed Cantor like potential and for the corresponding transmit-
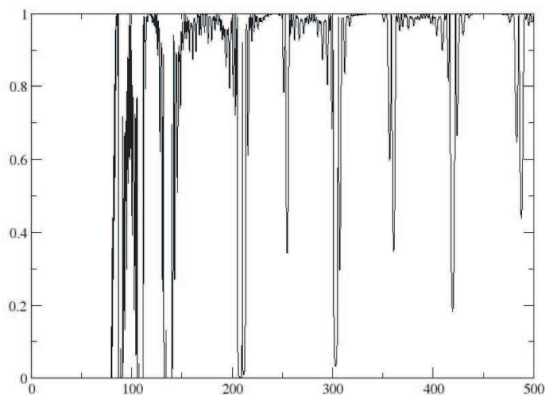
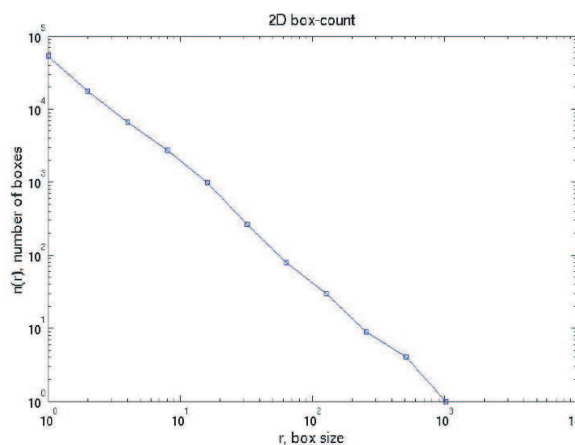Figure 7: Transmittance for an width/distance of 230Å, generation 10. Cantor well.

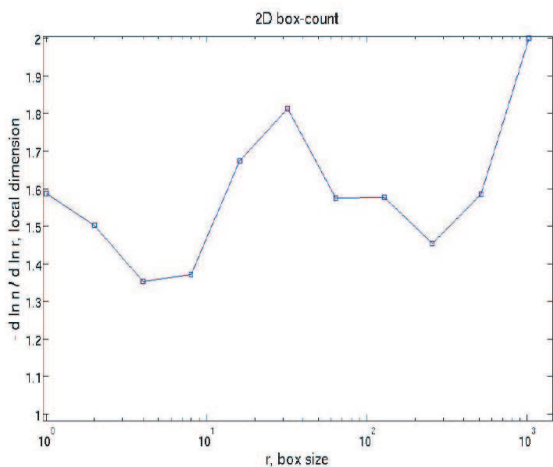Figure 8: Box counting power law test for the potential.

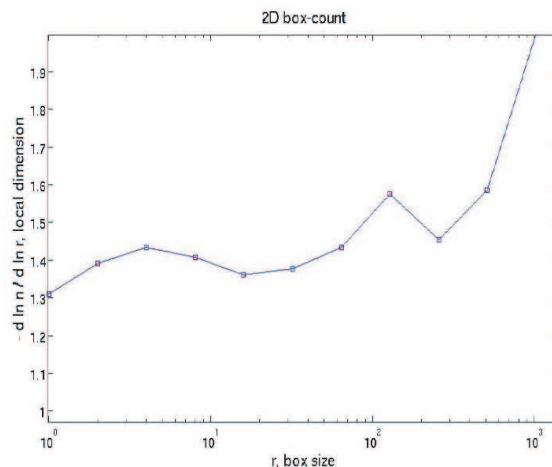Figure 9: Local exponent $D = -d\ln N/\ln R$ plot, for the mixed Cantor potential.

Figure 10: Local exponent $D = -d\ln N/\ln R$ plot, for the mixed Cantor's transmittance.

tance is calculated. For this estimation, the first feature to search for, is the power law, characteristic of fractal sets, Figure 8. Since the graph is not a straight line, this does not correspond to a fractal set, at least not for all values of the size of the boxes (R). Therefore, a region of the parameter R is search for. To do this the the local exponent $D = -d\ln N/\ln R$ is plotted (Figure 9), here N is the number of boxes needed to cover the set.

4. CONCLUSIONS AND PERSPECTIVES

This kind of systems modify the general behavior of the transmittance corresponding to the potential component systems. Also, the transmittance in function of the width of the barriers shows that the contribution of smaller barriers in the Cantor potential is reflected on the whole structure of maximum and minimum. Another interesting feature is the differences between the case in which the Cantor potential is composed of barriers and which is composed of wells. The well case seems to be more irregular perhaps due to mixing barriers and wells, however this can be improve the fractal dimension of the transmittance. Although the results for the fractal dimension are not conclusive, they allows to conjecture that the fractal dimension, of the potential and transmittance (Figure 10), is bounded in an non-integer range, from 1.3 to 1.8 for the potential and from 1.3 to 1.6 for the transmittance. Of course, in order to state such conclusion rigorously, a more direct approach for estimate the fractal dimension is needed. The obtained results suggests the possibility of characterize heterogeneous potential systems that resembles those presented here.

REFERENCES

1. Gaggero-Sager, L. M., E. R. Pujals, and O. Sotolongo-Costa, "Self-similarity in a Cantor-like semiconductor quantum well," *Phys. Stat. Sol. (B)*, Vol. 220, 167–169, 2000.
2. Griffiths, D. J. and C. A. Steinke, "Waves in locally periodic media," *Am. J. Phys.*, Vol. 69, No. 2, 137–154, 2001.
3. Pereyra, P. and E. Castillo, "Theory of finite periodic systems: General expressions and various simple and illustrative examples," *Phys. Rev. B*, Vol. 65, 205120, 2002.
4. Pérez-Álvarez, R. and F. García-Moliner, "The spectrum of quasiregular heterostructures," invited chapter in *Some Contemporary Problems of Condensed Matter Physics*, 1–37, Nova Science Publishers, ed. by S. Vlaev and M. Gaggero-Sager, 2000.
5. Díaz-Guerrero, D. S., F. Montoya, L. M. Gaggero-Sager, and R. Perez-Alvarez, "Transmittance and fractality in a Cantor-like multibarrier system," *Progress In Electromagnetics Research Letters*, Vol. 2, 149–155, 2008.
6. Moisy, F., http://www.mathworks.com/matlabcentral/fileexchange/13063.
7. Falconer, K., *Fractal Geometry: Mathematical Foundations and Applications*, Wiley Publisher.

Eigenvalues and Eigenfunctions in a Cantor-like Potential

L. M. Gaggero-Sager[1], **E. Pujals**[2], **and D. S. Díaz-Guerrero**[1]

[1]Facultad de Ciencias, Universidad Autónoma del Estado de Morelos
Ave. Universidad 1001, Cuernavaca, Morelos, México
[2]Instituto de Matemática Pura e Aplicada — IMPA
Dona Castorina 110, Rio de Janeiro, Brasil

Abstract— We study the so called Cantor-like potential, probably one of the closest potential we can imagine as selfsimilar. The numerical calculation was carried out for the effective mass equation miming a GaAs-AlGaAs heterostructure made by following a Cantor algorithm. We show that the first eigenfunctions exhibit in a great extend a selfsimilar aspect. Another main result is that a fractal dimension is found for the spectrum. This can be seen as a demonstration that this kind of potentials have this peculiarity. It is reasonable to think that other similar potential show this property.

1. INTRODUCTION

In a previous paper [1] some of us have studied the so called Cantor-like potential defined over a finite interval. Probably the apparent selfsimilarity of the probability density was the main result of Ref. [1]. Now we want to complete the description of the electronic wavefunctions and spectrum for this peculiar potential by reporting the first states and studying the dimension of the spectrum, i.e., the set of the eigenvalues.

The motivation for studying this kind of potentials comes out because it seems likely to find out that the transmittance reflects the selfsimilar property of the potential through its fractal dimension. In the other hand Lavrinenko et al. [2, 3] studied the propagation of classical waves of the optical Cantor filter. This system is not a self-similitary system, because the refractive indices are not scaled. The authors observed that the optical spectra has been shown spectral scalability In the las few years, a lot of experimental works, concerning the worth noting properties of porous silicon in chemical and biological sensing, have been reported. Moretti et al. [4] has compared the sensitivities of resonant optical biochemical sensor, based on both periodic and aperiodic porous silicon structures, such as Bragg and the Thue-Morse multilayer. They observed that the aperiodic multilayer is more sensitive than the periodic one. Find other similar systems in which the sensitive will be mayor is important for applications. Other authors has been studied systems inspired in the Cantor set but the differential operator that described those systems are not selfsimilar [17].

2. SEMICLASSICAL SOLUTION AND SELF-SIMILARITY

Observe that for the potential defined above the following properties are satisfied.

$$\text{if } 0 \le x \le 1/3 \qquad \text{then } V(x) = \frac{1}{3}V(3x) \tag{1}$$

$$\text{if } \frac{2}{3} \le x \le 1 \qquad \text{then } V(x) = \frac{1}{3}V(3x-2). \tag{2}$$

Now, let $E > \max[V(x)]$, be a eigenvalue of the continuous spectrum of the Schrödinger equation:

$$\frac{d^2 F(x)}{dx^2} + \frac{2m}{\hbar}(E - V(x))\, F(x) = 0. \tag{3}$$

For this eigenvalue, using semiclassical approximation, we get that the associated eigenfunction is [5–7]

$$F_E(x) = A_E(x)\, \exp\left[\frac{i}{\hbar}\, S_E(x)\right] \tag{4}$$

where

$$A_E(x) = \frac{C_1}{(2m\,(E - V(x)))^{1/4}} \tag{5}$$

$$S_E(x) = \int_0^x \sqrt{2m(E - V(x))}\, dx. \tag{6}$$

Using the properties of $V(x)$, observe that for any $x \in [0, 1/3]$

$$A_E(x) = \frac{C_1}{(2m(E - V(x)))^{1/4}} = \frac{C_1}{(2m(E - \frac{1}{3}V(3x))^{1/4}} = 3^{1/4}C_1 A_{3E}(3x). \tag{7}$$

This means that, up to a certain constant, the function A_E (of the eigenvalue E) in the interval $0 \leq x \leq 1/3$ is equal to the function A_{3E} (of the eigenvalue $3E$) in the interval $0 \leq x \leq 1$. On the other hand, for the function S_E, we have that for $x \in [0, 1/3]$

$$S_E = \frac{1}{\hbar} \int_0^x \sqrt{2m \left(E - \frac{1}{3}V(3x) \right)} \; dx. \tag{8}$$

Changing the integration variable x by $x' = 3x$, we have that for $x \in [0, 1/3]$

$$S_E(x) = \left(\frac{1}{3} \right)^{3/2} \int_0^{3x} \sqrt{2m(3E - V(x'))} \; dx' = \left(\frac{1}{3} \right)^{3/2} S_{3E}(3x). \tag{9}$$

So, for $x \in [0, 1/3]$

$$F_E(x) = C_1 \left(\frac{1}{3} \right)^{1/4} A_{3E}(3x) \cdot \exp \left[\frac{i}{\hbar} \left(\frac{1}{3} \right)^{3/2} S_{3E}(3x) \right]. \tag{10}$$

That is, the eigenfunction corresponding to the state E in the interval $[0, \frac{1}{3}]$ is self-similar to the eigenfunction corresponding to the state $3E$ in the interval $[0, 1]$. Arguing in the same way, and using the self-similarity of the potential in $[\frac{2}{3}, 1]$ we conclude also that the eigenfunction corresponding to the state E in the interval $[\frac{2}{3}, 1]$ is self-similar to the eigenfunction corresponding to the state $3E$ in the interval $[0, 1]$. Again, arguing in the same way we get that for any interval $f_{a_N}(I_0)$ (see previous section for definitions) the semiclassical approximation associated to the eigenvalue E over the interval $f_{a_N}(I_0)$ is self-similar over the interval $[0, 1]$ to the semiclassical approximation associated to the eigenvalue $3^N E$.

Since any value of E is an eigenvalue of the Schrödinger equation, then the self-similarity of the wave function is fulfilled for any value of E. This implies that for a quantum well with self-similar potential, it affects the wave functions in the whole continuous spectrum, not only the wave functions of the eigenvalues close to the well's limits, as would happen in a normal quantum well. This conclusion is general for any self-similar potential.

3. FORMAL SOLUTION AND SELF-SIMILARITY

We will now explain, in a little more rigorous and general manner, a theorem regarding the self-similarity of the wave functions of the continuous spectrum when the potential is a self-similar function.

Let us define the intervals $I_0 = [0, 1]$ and $J_0 = [\frac{1}{3}, \frac{2}{3}]$, and the functions $f_0(x) = \frac{1}{3}x$ and $f_1(x) = \frac{1}{3}x + \frac{2}{3}$, both of them defined in the basic interval $[0, 1]$ and having images in $[0, 1]$. In fact $f_0(I_0) = I_{(0)} = [0, \frac{1}{3}]$, $f_0(J_0) = J_{(0)} = [\frac{1}{9}, \frac{2}{9}]$, $f_1(I_0) = I_{(1)} = [\frac{2}{3}, 1]$, and $f_1(J_0) = J_{(1)} = [\frac{7}{9}, \frac{8}{9}]$. Similarly we define f_0 and f_1 (the same symbols as before) as the function which map linearly the interval $[a, b]$ into its first and third $1/3$ part respectively; then $f_0([a, b]) = [a, a + (b - a)/3]$ and $f_1([a, b]) = [b - (b - a)/3, b]$.

The intervals and functions just defined have a direct interpretation in terms of the standard Cantor construction. See Fig. 1. I_0 is the starting interval; J_0 is the central one third interval of I_0, typically *supressed*. On the other hand, function f_0 associates the whole starting interval I_0 with the left whole interval of the second Cantor generation ($I_{(0)}$) and the supressed interval J_0 with the supressed one in the next generation, left side ($J_{(0)}$); function f_1 associates the whole starting interval I_0 with the right whole interval of the second Cantor generation ($I_{(1)}$) and the supressed interval J_0 with the supressed one in the next generation, right side ($J_{(1)}$).

Renormalization for the Eigenfunctions and Eigenvalues: Let $E > 0$, $k > 0$ ($k = \hbar^2/(2m(x))$ where $m(x)$ is the position-dependent effective mass). In the sequel, we will note with $\Psi_{E,k}$, the solution of the problem

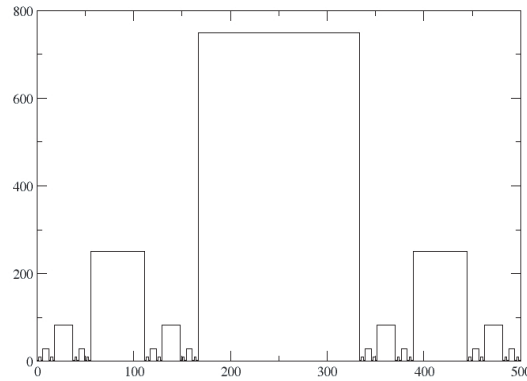$$k\Psi_{E,k}(x) + (E - V(x))\Psi_{E,k}(x) = 0 \tag{11}$$

Figure 1: Cantor like potential.

We want to study how the self-similarity of the potential V- and the mass $m(x)$- is reflected in the eigenfunctions and eigenvalues. More precisely we want to see if there exist some similarity between the eigenfunction restricted to the whole interval, and the same (or another) eigenfunction, when it is restricted to the interval $f_{a_N}(I_0)$. In others words, we want to see, if given E and $k > 0$, there exist $E' > 0$ and $k' > 0$ such that

$$\Psi_{E,k}(f_{a_N}^{-1}(x)) = \Psi_{E',k'}(x) \tag{12}$$

for any $x \in f_{a_N}(I_0)$. In this direction, we obtain the following Theorem which is a renormalization Theorem.

Theorem: *Let $E > 0$, $k > 0$ and the eigenfunction $\Psi_{E,k}$. Given $N > 0$ then, taking $s = 3^N$ we get that*

$$\Psi_{E,k}(f_{a_N}^{-1}(x)) = \Psi_{\frac{E}{s}, s^3 k}(x)$$

for any $x \in f_{a_N}(I_0)$.

Before to give the proof, observe that the Theorem is showing equivalently, that given $N > 0$ then

$$\Psi_{E,k}(f_{a_N}(x)) = \Psi_{sE, \frac{k}{s^3}}(x)$$

for any $x \in I_0$.

Now, let us give the proof.

Proof: We have that

$$k\Psi_{E,k}''(x) + (E - V(x))\Psi_{E,k}(x) = 0 \tag{13}$$

with $x \in [0, 1]$.

Taking the transformation $f_{a_N}^{-1} : f_{a_N}(I_0) \to I_0$, we get that for any $x \in f_{a_N}(I_0)$

$$k\Psi_{E,k}'' \circ f_{a_N}^{-1}(x) + (E - V \circ f_{a_N}^{-1}(x))\Psi_{E,k} \circ f_{a_N}^{-1}(x) = 0. \tag{14}$$

Using that $\Psi_{E,k}'' \circ f_{a_N}^{-1} = \frac{1}{3^{N^2}}(\Psi_{E,h} \circ f_{a_N}^{-1})''(x)$ and that $V(f_{a_N}^{-1}(x)) = 3^N V(x)$, noting $s = 3^N$ we get

$$\frac{1}{s^2}k(\Psi_{E,k} \circ f_{a_N}^{-1})''(x) + (E - sV(x))\Psi_{E,k} \circ f_{a_N}^{-1}(x) = 0 \tag{15}$$

for any $x \in f_{a_N}(I_0)$. This implies that $\Psi_{E,k} \circ f_{a_N}^{-1}$ is solution of

$$k'Y''(x) + (E' - V(x))Y(x) = 0, \tag{16}$$

where $k' = s^3 h$, and $E' = \frac{E}{s}$. And this means that

$$\Psi_{E,k}(f_{a_N}^{-1}(x)) = \Psi_{E',k'}(x) \tag{17}$$

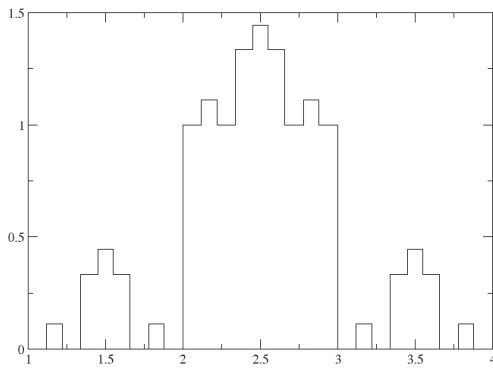for $x \in f_{a_N}(I_0)$. This finishes the proof.
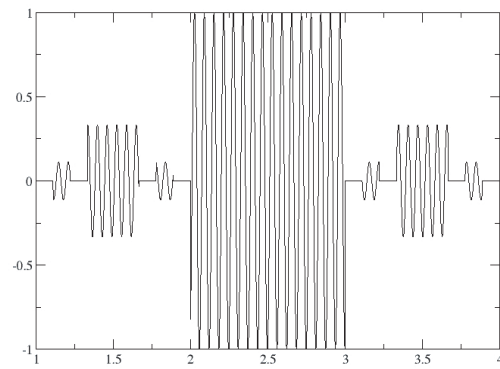
Figure 2: Another variety of the Cantor construction.

Figure 3: Cantor construction variety using an sinoidal function.

4. CONCLUSIONS

Firstly we have demonstrated that the wave functions exhibit a selfsimilarity property induced by the *symmetry* condition on the potential. We have given a proof in the framework of quasiclassical approximation. This is true in a variety of selfsimilarity quantum wells [11] (see for example Figures 2 and 3).

We have shown that in the case of a self-similar potential, regardless of the form that it may have, the eigenfunctions of the discrete levels are self-similar, in the whole spectrum. This is true for energy values, no matter how large it could be. This behavior of the self-similar quantum well is radically different from that known from a normal quantum well, which only affects the eigenfunctions of the levels closest to the well.

From a first sight, it could be suppoused that the system proposed is not different that the ones that appeared before in the literature. However, the system that we have considered are extremly differents from a topological point of view, since the the Hamiltonian proposed is self-similar [15, 16]. In particular recall that for the classical quantum well, the eigenfunctions show the presence of the quantum well for eigenvalues close to 0. However, in the case that we discuss, for any eigenvalues the associated eigenfunction "feels" the presence of the quantum well, despite how larger is the eigenvalue.

It is not difficult to extend these conclusions to other problems which theirs solution solve a wave equation (being classical or quantum [14]. For example, in a simple, classical, harmonic oscillator formed by a set of welded springs of different k's, such that $k(z)$ is self-similar, the amplitude of the oscillations will be self-similar in the interval T/3 with respect to interval T. There are some similar problems in classical mechanics (transverse waves on weighted strings where the linear mass density is a self-similarity function, for instance), in acoustics (sound propagation in a perfect fluid where the temperature is a self-similarity function) or electromagnetic waves (monochromatic electromagnetic propagating through a linear material where the permitivity is a self-similarity function) and others [13].

REFERENCES

1. Gaggero-Sager, L. M., E. R. Pujals, and O. Sotolongo-Costa, "Self-similarity in a Cantor-like semiconductor quantum well," *Phys. Stat. Sol. (b)*, Vol. 220, 167–169, 2000.
2. Zhukovsky, S. V., A. V. Lavrinenko, and S. V. Gaponenko, "Spectral scalability as a result of geometrical self-similarity in fractal multilayers," *Europhys. Lett.*, Vol. 66, No. 3, 455–461, 2004.
3. Lavrinenko, A. V., S. V. Zhukovsky, K. S. Sandomirski, and S. V. Gaponenko, "Propagatyion of classicla waves in non-periodic media: Scaling properties of an optical Cantor filter," *Phys. Rev. E*, Vol. 65, 036621, 2002.
4. Moretti, L., I. Rea, L. De Stefano, and I. Rendina, "Periodic versus aperiodic: Enhancing the sensitivity of porous silicon based optical sensors," *Applied Physics Letters*, Vol. 90, 191112, 2007.
5. Landau, L. D. and E. M. Lifschitz, *Mecanique Quantique*, editions Mir, Moscou, 1966.

6. Landau, L. D. and E. M. Lifschitz, *Quantum Mechanics, Nonrelativistic Theory*, Pergamon, New York, 1981.

7. Landau, L. D. and E. M. Lifschitz, *Mecánica Cuántica (teoría no-relativista)*, editorial Re-verté S. A., Barcelona, Buenos Aires, Mexico. 1967.

8. Pérez-Álvarez, R., F. García-Moliner, and V. R. Velasco, "Some elementary questions in the theory of quasiperiodic heterostructures," *J. of Phys.: Condens. Matter*, Vol. 13, 3689–3698, 2001.

9. Bastard, G., *Wave Mechanics Applied to Semiconductor Heterostructures*, Éditions de Physique, Paris, 1989.

10. Rasband, S. N., *Chaos Dynamics of Nonlinear Systems, Wiley Professional Paperback Series*, 1997.

11. Halsey, T. C., M. H. Jensen, L. P. Kadanoff, I. Procaccia, and B. I. Shraiman, "Fractal measures and their singularities: The characterization of strange sets," *Phys. Rev.*, Vol. A33, No. 2, 1141–1151, 1986.

12. Jitomirskaya, S. Y. and Y. Last, "Dimensional Hausdorff properties of singular continuous spectra," *Phys. Rev. Lett.*, Vol. 76, No. 11, 1765–1769, 1996.

13. Griffiths, D. J. and C. A. Steinke, "Waves in locally periodic media," *Am. J. Phys.*, Vol. 69, No. 2, 137–154, 2001.

14. R. Pérez-Álvarez, F. García-Moliner, C. Trallero-Giner, and V. R. Velasco, "Polar optical modes in Fibonacci heterostructures," *Journal of Raman Spectroscopy*, Vol. 31, No. 5, 421–425, 2000.

15. Simon, B., "Almost periodic Schrödinger operators: A review," *Adv. Appl. Math.*, Vol. 3, 463–490, 1982.

16. Simon, B., "Schrödinger operators in the twenty-first century," *Mathematical Physics*, 283–288, eds. A. Fokas, A. Grigoryan, T. Kibble, and B. Zegarlinski, Imperial College, London, 2000; Also *J. Math. Phys.*, Vol. 41, 3523–3555, 2000.

17. Agarwal, V., B. Alvarado-Tenorio, J. Escorcia-Garca, and L. M. Gaggero-Sager, "Cantor dielectric heterostructures made of nanostructured multilayers of porous silicon," *PIERS Online*, Vol. 4, No. 4, 451–454, 2008.

Relative Mobility and Relative Conductivity in ALD-FET (Atomic Layer Doped-field Effect Transistor) in GaAs

O. Oubram, L. M. Gaggero Sager, and D. S. Díaz-Guerrero

Facultad de Ciencias, Universidad Autónoma del Estado de Morelos
Av. Universidad 1001, Col. Chamilpa, CP 62209, Cuernavaca, Morelos, Mexico

Abstract— We calculate the relative mobility and relative conductivity between source and drain as function of gate voltage for Atomic Layer Doped-Field Effect Transistor (ALD-FET) in a GaAs matrix. The mobility is described via a relative quantity that was presented in [1]. That expression does not have empirical form, neither empirical parameter. Also a phenomenological expression of the conductivity is presented, which is derived from the mobility expression. The calculation this relative quantities was performed with a model for the ALD-FET that was shown in [2]. In the end, we report for the first time an analytical mobility of electronic relative ALD-FET. With these tools, it look that different behaviours of transport properties for ALD-FET.

1. INTRODUCTION

The system we are interested in is the ALD-FET in GaAs proposed by Y. Shiraki and collaborators [3]. They made a field effect transistor in which the channel is formed by growing an n-type Si delta-doped well and p-type delta doped barrier, these two wells are between the terminals of the source and the drain of a regular GaAs field effect transistor. The presence of this n-type quantum well produces a localized two-dimensional electronic gas (2DEG), which participates directly in the conduction channel, on the other hand, the presence of the p-type quantum well produces a gas, but of holes (2DHG), causing the 2DEG produced by the n-type delta-doped quantum well to be more confined. The use of this type of doping in semiconductor devices yields a great improvement in the performance of ultra high frequency optoelectronic devices [5]. The ALD-FET is also expected to exhibit a higher transconductance and high intrinsic transconductance [4, 6]. These FET's will also offer a very flat transconductance region, which is ideal for low distortion power amplification. Than a high electron mobility transistor due to the proximity of the delta channel to the gate [6].

This work will be the continuation of the preview study applied in δ-FET in [7, 8]. The present study is to analyze the change of the mobility and conductivity in the presence of p-type delta-doped barrier in different positions and densities, also to analyze the behavior the transport proieties in diferenties values of potential gate contact.

2. THEORETICAL BACKGROUND

The δ-doping technique allows one to obtain an extremely sharp doping profile and a high-density-doped layer. Potentials of this system is formed by a metal-semiconductor contact (Schottky barrier), followed by the n-type delta-doped quantum-well system and another of the p-type. The presence or not of a confined electronic gas depends on the parameters used in the construction of the system.

If there is electronic confinement, our model for describing the conduction band of the semiconductor in the ALD-FET system. The entire potential is mathematically presented by the following expression:

$$V(z) = \frac{2\pi e^2}{\epsilon_r} N_d (z + d - l)^2 \theta(l - z) + \left(-\frac{\alpha_n^2}{(\alpha_n|z| + z_{0n})^4} + \frac{\beta^2}{(\beta \cdot |z - d_p| + z_{0p})^4} \right) \theta(l_p - z) \quad (1)$$

where N_d is the background impurity density, ϵ_r is the electric permittivity constant of GaAs, and l is the screening distance for the electric field.

$\alpha_n = 2/(15\pi)$ and $z_{0n} = (\alpha_n^3/\pi N_{2de})^{1/5}$, is the distance at which the n-type delta-doped well is positioned, N_{2de} is the two-dimensional impurity density of the n-type delta-doped quantum-well. The p-type δ-doped quantum well centred at $z = d_p$, $m_{hh} = 0.51m_0$ is the mass of the heavy holes, $m_{lh} = 0.082m_0$ is the mass of the light holes for GaAs, $m_a = \left[1 + (m_{lh}/m_{hh})^{\frac{3}{2}} \right]^{\frac{2}{3}}$ with $\beta = 2 \cdot m_a^{\frac{3}{2}}/15 \cdot \pi$, $z_{p0} = (\beta^3/\pi P_{2d})^{1/5}$, P_{2d} is the impurities density of the p-type delta-doped quantum-well.

with l_p is the depletion region width, $V(l_p) = 0$,

where θ is the unit-step function.

The starting parameters for ALD-FET in GaAs are: $m^* = 0.067m_0$, $m_{hh} = 0.51m_0$, $m_{lh} = 0.082m_0$, $\epsilon_r = 12.5$, $n_{2D} = 7.5 \times 10^{12}\,\text{cm}^{-2}$, $p_{2D} = 5 \times 10^{12}\,\text{cm}^{-2}$, $p_{2D} = 10 \times 10^{12}\,\text{cm}^{-2}$, $p_{2D} = 5 \times 10^{13}\,\text{cm}^{-2}$.

Figure 1 shows the confining potential and the sub-band energies with their envelope wave functions $n_{2D} = 7.5 \times 10^{12}\,\text{cm}^{-2}$ and $p_{2D} = 5 \times 10^{13}\,\text{cm}^{-2}$, the background impurities is of $N_d = 10^{18}\,\text{cm}^{-3}$ at $T = 0\,\text{K}$. Here, n-type delta-doped quantum-well is located at $300\,\text{Å}$ from the interface and p-type delta doped barrier is located at $200\,\text{Å}$ from n-type delta well. The dashed curve represents the obtained confining potential profile and the solid curves represent the wave functions, potential profile, eigenvalues and eigenfunctions. Fig. 1 presents for $Vc = 500\,\text{MeV}$, eigenvalues $E_f - E_0 = 154.8\,\text{MeV}$, $E_f - E_1 = 56.94\,\text{MeV}$ and $E_f - E_2 = 11.88\,\text{MeV}$ with E_f (Fermi level) is taken to be at the bottom of conduction band.

In Table 1, we see the influence of the density of p-type delta-doped barrier on energy levels. The fundamental state does not feel the effects of the barrier, $E_f - E_0 = 154.8\,\text{MeV}$, E_0 is stable in the three different densities. En contrast superior levels feel the effect, the second level fell from $E_f - E_1 = 57.14\,\text{MeV}$ for $(5 \cdot 10^{12}\,\text{cm}^{-2})$ to $E_f - E_1 = 56.94\,\text{MeV}$ (for $5 \cdot 10^{13}\,\text{cm}^{-2}$), but the upper level decreases rapidly from $E_f - E_2 = 14.5\,\text{MeV}$ for $(5 \cdot 10^{12}\,\text{cm}^{-2})$ to $E_f - E_2 = 11.88\,\text{MeV}$ for $(5 \cdot 10^{13}\,\text{cm}^{-2})$. It is clear that the barrier affects more superior levels.

Based on the Thomas Fermi approximation to this ALD-FET, we study the electron transport properties of the system. This method also allows us to study the transport properties of the system. We only consider the ionized donor scattering mechanism, because it is the most important at low temperature. The Coulomb scattering potential due to the ionized impurities is considered as distributed randomly in the doped layer. Finally, we take the ratio of the mobility

$$\mu_{rel} = \frac{\mu^{np\delta,Vc\neq0}}{\mu^{n\delta,Vc=0}} = \frac{\iint_{IR^2} \rho_e^{n\delta,Vc=0}(z') \cdot \rho_{imp}^{n\delta,Vc=0}(z) \cdot |z - z'| \cdot dz \cdot dz'}{\iint_{IR^2} \rho_e^{np\delta,Vc\neq0}(z') \cdot \rho_{imp}^{np\delta,Vc\neq0}(z) \cdot |z - z'| \cdot dz \cdot dz'} \tag{2}$$

$\rho_e^{np\delta,Vc\neq0}(z') \left(\rho_e^{n\delta,Vc=0}(z')\right)$: The density of electrons of n-p delta doped (n delta doped) where
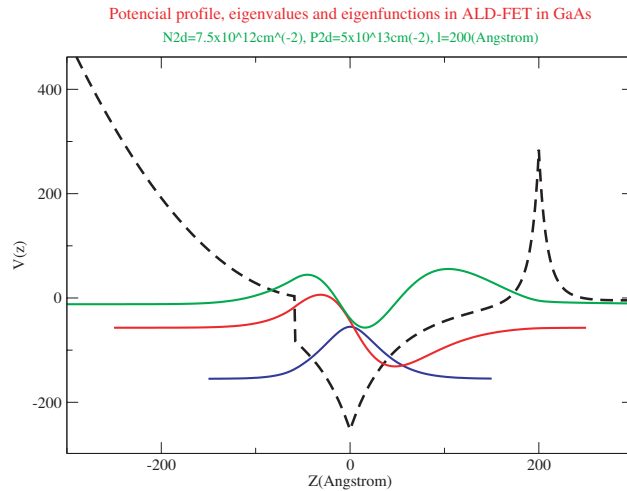

Figure 1: Conduction band, eigenvalues and eigenfunctiones, energies in MeV for $Vc = 500\,\text{MeV}$, $n_{2d} = 7.5 \cdot 10^{12}\,\text{cm}^{-2}$, $p_{2d} = 5 \cdot 10^{13}\,\text{cm}^{-2}$, $d_p = 200\,\text{Å}$.

Table 1: Energy levels (E_0, E_1, E_2) for different values of p-delta doped concentration, $d_p = 200\,\text{Å}$ and for $Vc = 500\,\text{MeV}$.

P_{2d} (cm^{-2})	$E_f - E_0$ (MeV)	$E_f - E_1$ (MeV)	$E_f - E_2$ (MeV)
$5 \cdot 10^{12}$	-154.8	-57.14	-14.5
$10 \cdot 10^{12}$	-154.8	-57.08	-13.68
$5 \cdot 10^{13}$	-154.8	-56.94	-11.88

the potential contact of the gate is $Vc \neq 0$ $(Vc = 0)$, respectively, with Vc is the potential contact of the gate.

$\rho_{imp}^{np\delta,Vc\neq0}(z)$ $\left(\rho_{imp}^{n\delta,Vc=0}(z)\right)$: The density of impurities of n-p delta doped (n delta doped) where the potential contact of the gate is $Vc \neq 0$ $(Vc = 0)$, respectively.

The former expression can be put in the following form:

$$\mu_{rel} = \frac{\mu^{np\delta,Vc\neq0,T=0}}{\mu^{n\delta,Vc=0,T=0}} = \frac{\sum_1^{ne} \int_{IR} \left|F_e^{n\delta,Vc=0}(z')\right|^2 \cdot \left(k_F^{n\delta,Vc=0} - E_i^{n\delta,Vc=0}\right) \cdot |z'| \cdot dz'}{\sum_1^{ne} \int_{IR} \left|F_e^{np\delta,Vc\neq0}(z')\right|^2 \cdot \left(k_F^{np\delta,Vc\neq0} - E_i^{np\delta,Vc\neq0}\right) \cdot |z'| \cdot dz'} \quad (3)$$

where $F_e^{np\delta,Vc\neq0}(z')$, $k_F^{np\delta,Vc\neq0}$ and $E_i^{np\delta,Vc\neq0}$, $(F_e^{n\delta,Vc=0}(z')$, $k_F^{Vc=0}$ and $E_i^{Vc=0})$ are the envelope function, the Fermi level and the ith level of n-p delta doped (n delta doped) where $Vc \neq 0$ $(Vc = 0)$ respectively, the former expression is valid for $T = 0\,\text{K}$. At the last, in first approximation, we present an analytical relative mobility quantity:

$V(lp) = 0$ and $V(L') = 0$, $L' > 0$

$$\rho_e(z)\,\alpha(E_f - V_n(z))^{3/2} \quad (4)$$

$$\mu_{rel} = \frac{\mu^{np\delta,Vc\neq0}}{\mu^{n\delta,Vc=0}} = \frac{\int_{lp}^{L'} \rho_e^{n\delta,Vc=0}(z) \cdot z \cdot dz}{\int_{lp}^{L'} \rho_e^{np\delta,Vc\neq0}(z) \cdot z \cdot dz} = \frac{\left(\left[\frac{5\cdot z-a}{(z-a)^5}\right]_{lp}^{L'}\right)^{n\delta,Vc=0}}{\left(\left[\frac{5\cdot z-a}{(z-a)^5}\right]_{lp}^{L'}\right)^{np\delta,Vc\neq0}} \quad (5)$$

with $a = \frac{z_{0n}}{\alpha_n}$ and $E_f = 0$ in GaAs.

3. RESULTS AND DISCUSSION

The Fig. 2 left contains the curve of relative mobility vs. Vc for $d_p = 600\,\text{Å}$ $(d_p = 600\,\text{Å})$. The mobility shows two different behaviors. The first is between $100\,\text{MeV}$ $(100\,\text{MeV})$ and $1150\,\text{MeV}$ $(1000\,\text{MeV})$ where we have the mobility ratio is rising from 1.07 (1.38) to 1.94 (3.1). The second is between $1150\,\text{MeV}$ (1000) and $1300\,\text{MeV}$ $(1300\,\text{MeV})$ where the mobility is rising also from 2.06 to 4.52. In the first interval, the mobility ratio creases mildly but in the second, it increases rapidly, we can see the potential contact affect more the mobility ratio when Vc superior $1150\,\text{MeV}$ $(1000\,\text{MeV})$. In the mobility ratio characteristic there are three regions, in other words there are two transitions, the first from $450\,\text{MeV}$ $(300\,\text{MeV})$ to $500\,\text{MeV}$ $(350\,\text{MeV})$ and the second from $1150\,\text{MeV}$ $(1000\,\text{MeV})$ to $1200\,\text{MeV}$ $(1050\,\text{MeV})$, respectively. The responsible of this transitions is
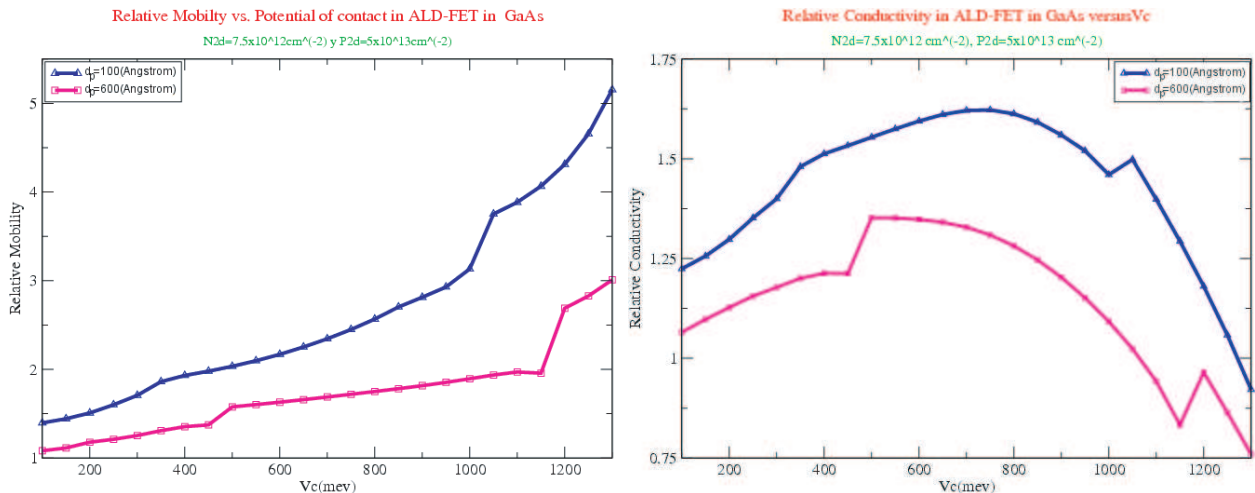

Figure 2: Relative mobility (left) and conductivity (right) as a function of potential of contact for two values of inter-well distance between the n-type well and the p-type barriers in ALD-FET in GaAs for $n_{2d} = 7.5 \cdot 10^{12}\,\text{cm}^{-2}$, $p_{2d} = 5 \cdot 10^{13}\,\text{cm}^{-2}$, $d_p = 100\,\text{Å}$ (Triangle up symbole), $d_p = 600\,\text{Å}$ (Square symbole).

the change in the number of state in δ-doped quantum well.

$$\sigma_{rel} = n_{rel} \cdot \mu_{rel} \tag{6}$$

$$n_{rel} = \frac{\sum_1^{ne} \left(k_F^{np\delta, Vc \neq 0} - E_i^{np\delta, Vc \neq 0} \right)}{\sum_1^{ne} \left(k_F^{n\delta, Vc = 0} - E_i^{n\delta, Vc = 0} \right)} \tag{7}$$

σ_{rel}: Relative conductivity, n_{rel}: Relative electronic density of the delta-doped quantum well, μ_{rel}: Relative mobility.

Relative conductivity vs. Vc characteristic shows fluctuation of conductivity ratio as a function of Vc, there are two zones type where $dp = 600\,\text{Å}$ ($dp = 100\,\text{Å}$), the first zone type is linear, it is in $[100\,\text{MeV}, 450\,\text{MeV}]$ ($[100\,\text{MeV}, 300\,\text{MeV}]$) and $[1200\,\text{MeV}, 1300\,\text{MeV}]$ ($[1050\,\text{MeV}, 1300\,\text{MeV}]$), the second zone type is parabolic, it is in $[500\,\text{MeV}, 1150\,\text{MeV}]$ ($[350\,\text{MeV}, 1050\,\text{MeV}]$), when $Vc \geq 500\,\text{MeV}$ ($Vc \geq 750\,\text{MeV}$) the Fig. 2 right shows that the conductivity decreases, the reason being that the conduction channel begins to close, due to the strong decrease of confined electrons in the delta-doped well, respectively.

The ALD-FET permits to have a negative differential resistance (NDR), NDR is seen in intervals $[500\,\text{MeV}, 1150\,\text{MeV}]$ ($[750\,\text{MeV}, 1000\,\text{MeV}]$) and in $[1200\,\text{MeV}, 1300\,\text{MeV}]$ ($[1050\,\text{MeV}, 1300\,\text{MeV}]$) for $dp = 600\,\text{Å}$ ($dp = 100\,\text{Å}$), in electronics we learn that an amplifier coupled with a properly designed positive feedback circuit can be made into an oscillator without input signal. We find the optimum $Vc = 500\,\text{MeV}$ ($Vc = 750\,\text{MeV}$) Contact potential to achieve the maximum conductivity, respectively,

At this part, the reference values are taken as function $d_p = +\infty$ (δ-FET case)

$$\mu_{rel} = \frac{\mu^{d_p, Vc = 500, T = 0}}{\mu^{d_p \neq +\infty, Vc = 500, T = 0}} \tag{8}$$

In the figure of mobility vs. d_p, and conductivity on vs. d_p, are having the same behavior, both decrease, but the mobility behaves in a manner little different than conductivity. In the first place decreases strongly from 1.41 at 2.15 between $50\,\text{Å}$ to $155\,\text{Å}$. In the second place, decreases slowly, from 1.31 to 1 between $160\,\text{Å}$ to $400\,\text{Å}$. The transition in the mobility and conductivity between $155\,\text{Å}$ and $160\,\text{Å}$ was affected at the change in the number of energy levels of the electronic structure where $d_p \geqslant 400\,\text{Å}$ we can consider that we have δ-FET not ALD-FET transistor, in other means, the p-type delta doped barrier does not have effect in the mobility and conductivity.
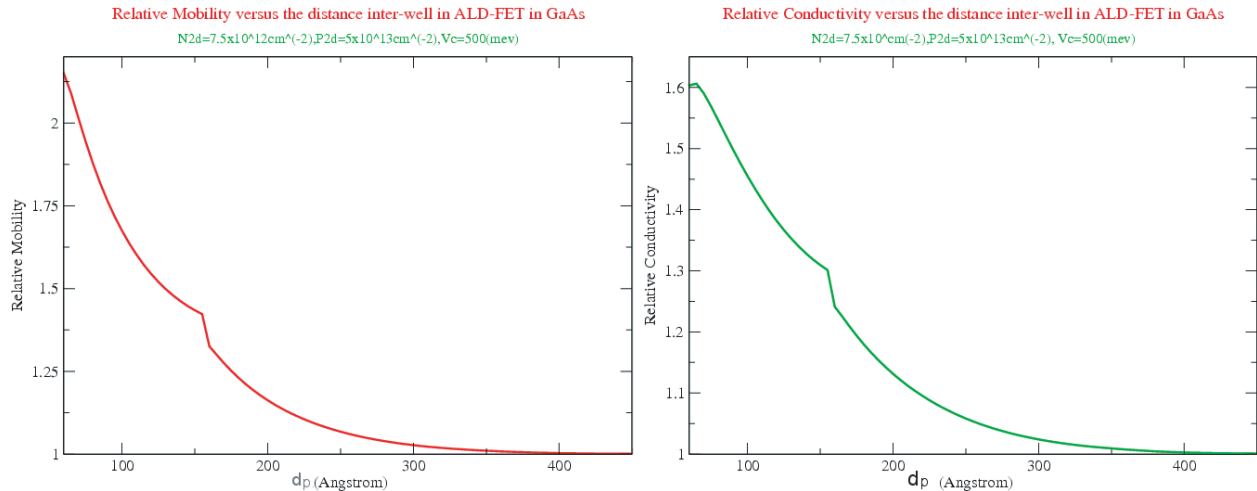

Figure 3: Relative mobility (left) and conductivity (right) versus the distance inter-well in ALD-FET in GaAs for $Vc = 500\,\text{MeV}$, $n_{2d} = 7.5 \cdot 10^{12}\,\text{cm}^{-2}$, $p_{2d} = 5 \cdot 10^{13}\,\text{cm}^{-2}$.

4. CONCLUSIONS

In summary, the results here reported could become of interest for future studies. The relative mobility expression can be a strong and easy way to study the range of parameters governing other electronic device and get the best choice of them.

REFERENCES

1. Rodriguez-Vargas, I., L. M. Gaggero-Sager, and V. R. Velasco, "Thomas-Fermi-Dirac theory of the hole gas of a double p-type delta-doped GaAs quantum wells," *Surf. Sci.*, Vol. 537, No. 1, 75–83, 2003.
2. Mora-Ramos, M. E. and L. M. Gaggero-Sager, "A simple model for atomic layer doped field-effect transistor (ALD-FET) electronic states," *Rev. Mex. Fís.*, Vol. 44, No. 3, 165–167, 1998.
3. Yamaguchi, K., Y. Shiraki, Y. Katayama, and Y. Murayamn, "A new short channel MOSFET with an atomic-layer-doped impurity-profile (ALD-MOSFET)," *J. Appl. Phys.*, Vol. 22, No. 22, 267–270, 1983.
4. Chenhsin, L., et al., "Charge control model of the double delta-doped quantum-well field-effect transistor," *IEEE Transactions on Electron Devices*, Vol. 41, No. 8, 1351–1356, 1994.
5. Kwok, K. N., "Characteristics of p- and n-channel poly-Si/Si1-xGex/Si sandwiched conductivitymodulated thin-film transistors," IEEE 0018-9383, 1996.
6. Nakajima, S., N. Kuwata, N. Shiga, K. Otobe, K. Matsuzaki, T. Sekiguchi, and H. Hayashi, "Characterization of double pulse-doped channel GaAs MESFETs," *IEEE Transactions on Electron Devices*, Vol. 14, No. 3, 146–148, 1993.
7. Oubram, O. and L. M. Gaggero-Sager, "Transport properties of delta doped field effect transisto," *PIERS Online*, Vol. 2, 81–7, 2008.
8. Gaggero-Sager, L. M. and R. Perez-Alvarez, "A simple model for delta-doped field-effect transistor electronic states," *J. Appl. Phys.*, Vol. 78, No. 7, 4566–4569, 1995.
9. Ioriatti, L., "Thomas-Fermi theory of δ-doped semiconductor structures: Exact analytical results in the high-density limit," *Phys. Rev. B*, Vol. 41, No. 12, 8340–8344, 1990.
10. Gaggero-Sager, L. M., R. Mora-Ramos, and D. A. Contreras-Solaris, "Thomas-Fermi approximation in p-type δ-doped qnantum wells of GaAs and Si," *Phys. Rev. B*, Vol. 57, No. 11, 6286–6289, 1998.

Design of a Novel Wideband Planar Inverted-F Antenna for Mobile Applications

Xingyu Zhang and Antti Salo

Adaptive Terminal Team, Nokia Research Center, Beijing 100176, China

Abstract— In order to meet the tendency of miniaturization, broadband, amalgamation of multi-systems for mobile communication terminals, a novel practical wideband internal planar inverted-F antenna (PIFA) is proposed in this paper. The presented antenna exhibits a very wide bandwidth ranging from 1.67 to 4.05 GHz with the definition of −10 dB return loss. The relative bandwidth is larger than those of the existing antennas with similar structures, and comes up to 83%, which makes the designed antenna cover the frequency bands of DCS1800, PCS1900, WCDMA, UMTS, WiBro, WLAN and DMB simultaneously. It is also found that the radiation patterns in free space, gain and efficiency of the proposed antenna satisfy the needs of wireless communication terminals. Moreover, the antenna with the optimized parameters was fabricated and measured. Good agreement between the measurement and simulation results can be observed.

1. INTRODUCTION

Nowadays, with the rapid development of wireless communication technologies, the quality and capability of communication systems have been improved a lot. Meanwhile, various kinds of mobile communication systems operating at different frequency bands have come out. Different antennas are often adopted in different mobile systems. Owing to this, the problem of integration and amalgamation for various communication systems appears. Besides, miniaturization of antennas for mobile portable terminals is still a major factor that should be taken into consideration. Hence, miniaturized antennas for multiple bands applications that can be easily integrated with carriers has been a hot topic in antenna design.

Planar inverted-F antenna (PIFA) with its advantages of compact structure, low profile, low manufacturing cost, easy fabrication and easy integration with portable devices is referred to as a preferable candidate for mobile terminals. A PIFA antenna with a tapered-type radiating patch operating at PCS band is reported in [1]. Its relative bandwidth reaches 17%. A T-shaped ground plane PIFA antenna working at UMTS band is designed in [2]. Its relative bandwidth comes to 17%. A PIFA antenna with a relative bandwidth of 21% that has a polygon radiating element and operates at PCS band is studied in [3]. A typical PIFA antenna with a conventional structure and a relative bandwidth of 15% is described in [4]. A T-shape slotted PIFA antenna for WCDMA application with a relative bandwidth of 38% is discussed in [5]. The antennas mentioned above are all applicable for a single-band mobile application. PIFA antennas for multi-system applications have also been reported a lot in the open literatures. A T- and S-shaped wideband PIFA for DCS/PCS/UMTS triple-band applications is designed in [6]. Its relative bandwidth comes up to 33% with the definition of −5 dB return loss. Also, there exist PIFA antennas with many separated radiating elements and feeding portions for multiple bands applications [7, 8]. However, the shortcoming of this kind of antenna is their large volume and complicated feeding structure. Therefore, it is desirable to design wideband PIFA antenna with single-layer and single-radiating patch for over three frequency bands mobile applications.

Based on the antenna design in [2], a more compact design of a practical wideband PIFA antenna is proposed in this paper. The simulated bandwidth for $S_{11} < -10$ dB ranges from 1.67 GHz to 4.05 GHz and the relative bandwidth reaches 83%, which indicates that the presented antenna can cover the frequency bands of DCS (1.71–1.88 GHZ), PCS (1.85–1.99 GHz), WCDMA (1.92–2.17 GHz), UMTS (1.92–2.17 GHz), WiBro (2.3–2.39 GHz), WLAN (2.4–2.484 GHz) and DMB (2.605–2.655 GHz) simultaneously. The antenna prototype was fabricated and measured. The experimental results agree well with the computed results. Other performances of the antenna also meet the demands of mobile terminals. It is demonstrated that the designed wideband PIFA antenna is an attractive candidate for mobile applications.

2. ANTENNA DESIGN

The configuration of the proposed wideband PIFA antenna is shown in Fig. 1. The ground plane with a size of 50 mm × 48 mm is cut off two rectangles that are symmetrical. The radiating patch

with a size of $22 \, \text{mm} \times 26 \, \text{mm}$ is just located on the top of the portion of the slotted ground plane. The antenna is shorted by a shorting plate and the profile is only $5 \, \text{mm}$ which is rather low. Also, air is chosen as the substrate between the radiating patch and the ground plane to improve the antenna efficiency. In the feeding part, the antenna is not directly fed by a $50 \, \Omega$ SMA coaxial cable. A trapezoidal plate with its thickness of $2 \, \text{mm}$ is adopted between the antenna patch and inner conductor of the $50 \, \Omega$ coaxial cable to broaden the impedance bandwidth of the antenna [9]. The radiating element, shorting plate and ground plane are all made by $0.2 \, \text{mm}$ thick metal plate.

The optimized design parameters for the proposed antenna are as following: $L = 50 \, \text{mm}$, $W = 48 \, \text{mm}$, $L_1 = 26 \, \text{mm}$, $W_1 = 22 \, \text{mm}$, $L_2 = 23 \, \text{mm}$, $W_2 = 10 \, \text{mm}$, $L_3 = 12 \, \text{mm}$, $W_3 = 12 \, \text{mm}$, $L_4 = 12 \, \text{mm}$, $W_4 = 3 \, \text{mm}$, $L_5 = 6 \, \text{mm}$, $L_6 = 2 \, \text{mm}$, $h = 4 \, \text{mm}$.

(a) Overall view   (b) Side view

(c) Top view
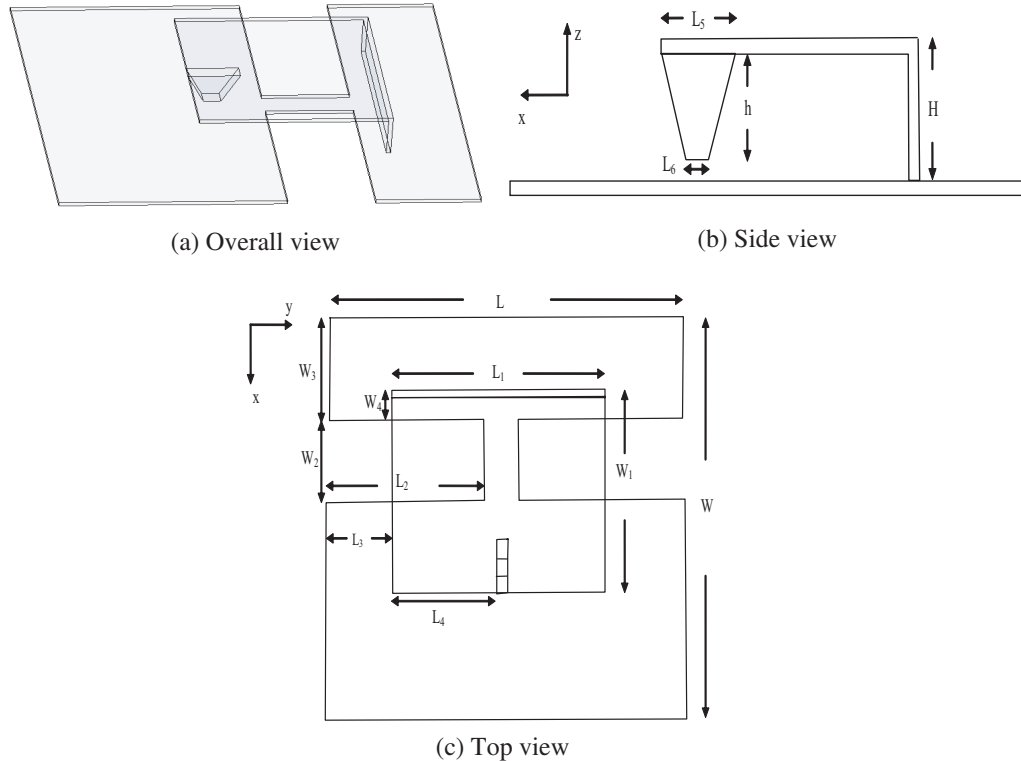
Figure 1: Geometry of the wideband PIFA antenna.

(a) Antenna return losses with different values of L_2 (b) Antenna return losses with different values of W_2
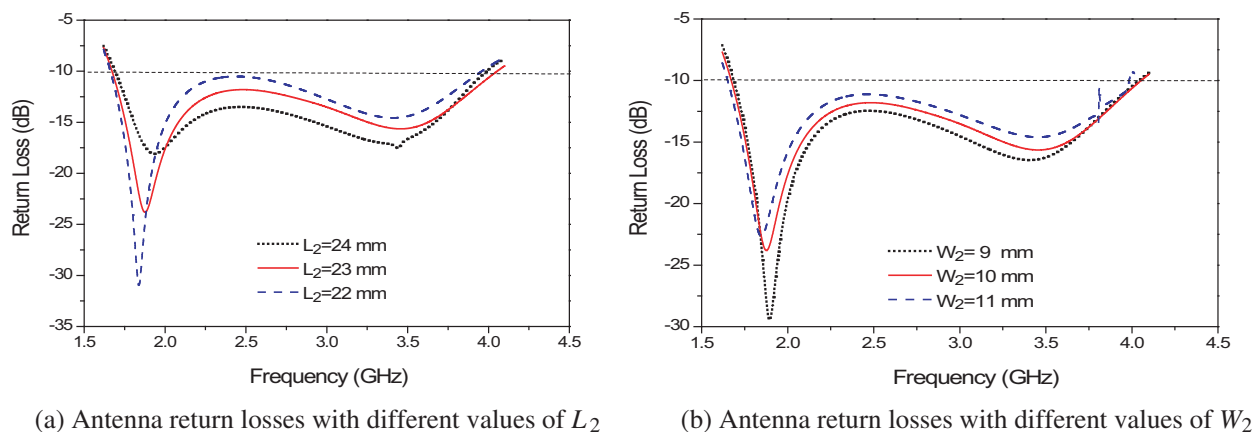
Figure 2: Effect of the slot size on ground plane on antenna property.

3. PARAMETRIC STUDIES

Figure 2 plots the return loss characteristics of the proposed antenna with variations of the slot size (i.e., L_2 and W_2) on the ground plane. It can be seen form Fig. 2 that the slot size on the ground plane mainly affects the impedance bandwidth and return loss values of the presented antenna.

The influence of the feeding structure on antenna performance is also studied. Fig. 3 depicts the return loss comparison of the proposed antenna and the antenna without the trapezoidal feeding plate. It can be concluded from Fig. 3 that the trapezoidal feeding plate has large impact on impedance bandwidth and resonant frequency of the studied antenna.

Effect of the antenna height on antenna performance is investigated too. Fig. 4 denotes the return losses of the antenna with various height. One can see from Fig. 4 that the antenna height mainly influences the bandwidth, resonant frequencies, and return loss values of the antenna. One can also see from Fig. 4 that the antenna bandwidth may still meet the bandwidth requirements when the antenna height is reduced to 4 mm, which indicates the validity of the proposed wideband antenna.

4. RESULTS AND ANALYSIS

The antenna with the optimized parameters was constructed and simulated by CST Microwave Studio. The simulated VSWR and return loss of the proposed antenna are exhibited as the solid lines in Fig. 5 and Fig. 6. It can be demonstrated from Figs. 5 and 6 that there are two resonant frequencies (i.e., 1.88 GHz and 3.48 GHz) for the presented antenna. Besides, the bandwidth defined by $S_{11} < -10$ dB is between 1.67 and 4.05 GHz. The relative bandwidth reaches 83% and the upper band of the bandwidth enters the frequency range of UWB (3.1–10.6 GHz), which indicates that the designed antenna can cover the bands of DCS, PCS, WCDMA, UMTS. WiBro, WLAN and DMB simultaneously. Such big bandwidth for single-layer and single-patch PIFA antennas is infrequent.
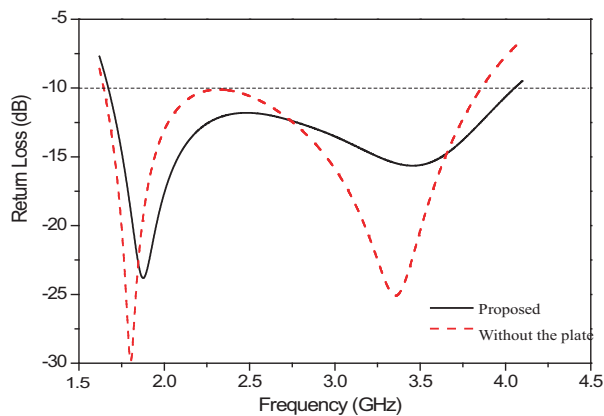
Figure 3: Influences of the trapezoidal feeding plate.
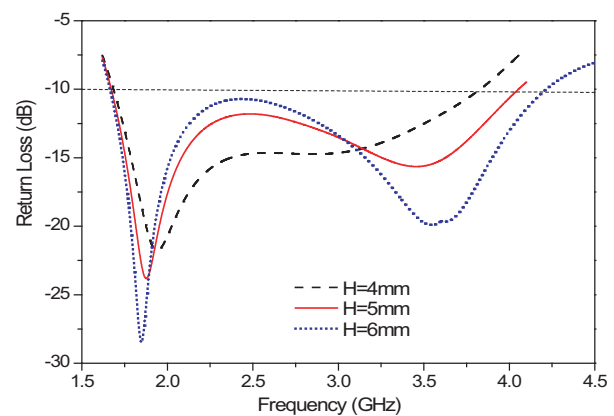
Figure 4: Effect of the antenna height.
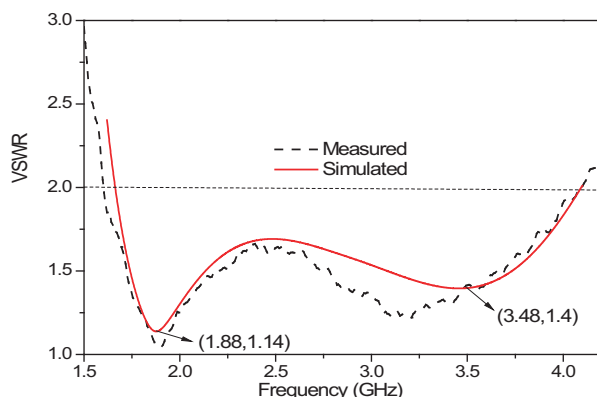
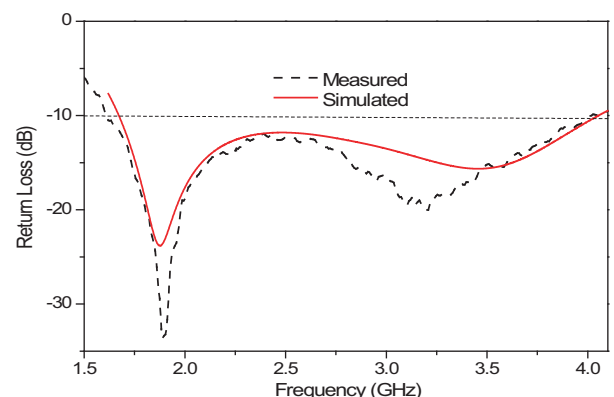Figure 5: Measured and simulated VSWR of the proposed antenna.

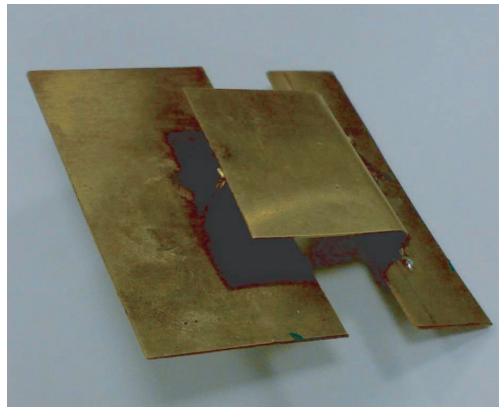Figure 6: Measured and simulated return losses of the proposed antenna.

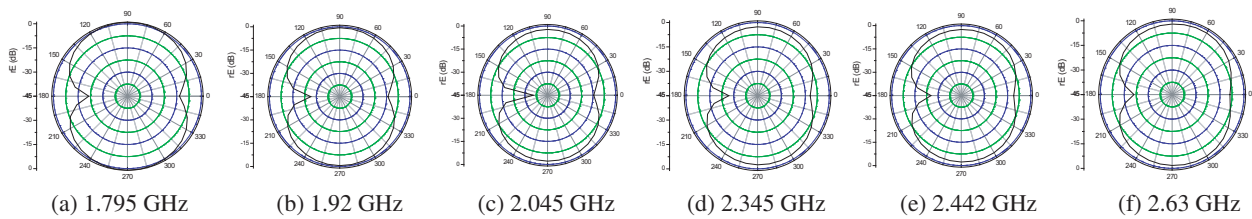Figure 7: Prototype of the fabricated antenna.

| (a) 1.795 GHz | (b) 1.92 GHz | (c) 2.045 GHz | (d) 2.345 GHz | (e) 2.442 GHz | (f) 2.63 GHz |

Figure 8: Radiation patterns of the proposed antenna at central frequencies in E-plane.

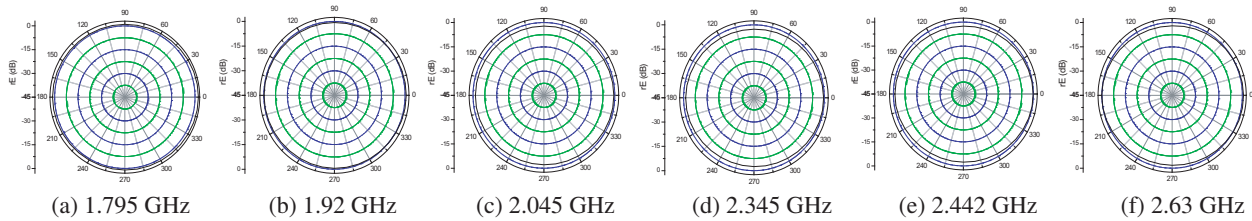| (a) 1.795 GHz | (b) 1.92 GHz | (c) 2.045 GHz | (d) 2.345 GHz | (e) 2.442 GHz | (f) 2.63 GHz |

Figure 9: Radiation patterns of the proposed antenna at central frequencies in H-plane.
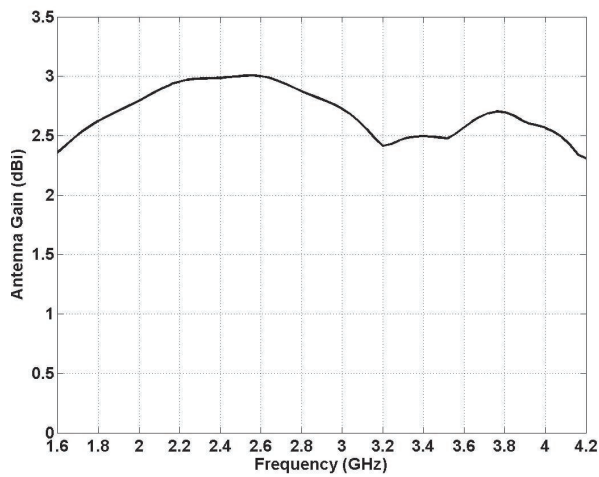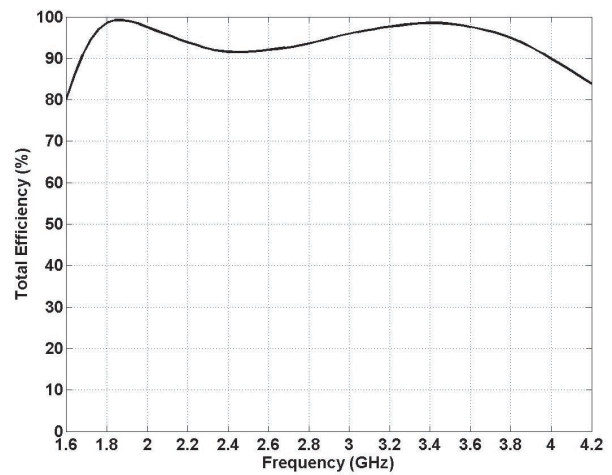

Figure 10: Gain of the proposed antenna.

Figure 11: Total efficiency of the proposed antenna.

The proposed antenna was also fabricated as can be seen in Fig. 7. It was measured by Agilent vector network analyzer. The dashed lines in Figs. 5 and 6 represent the measured VSWR and return loss of the proposed antenna. The experimental results agree well with the computed results. Moreover, the radiation patterns of the proposed antenna in free space are also studied. Figs. 8 and 9 depict the radiation patterns of the presented antenna at central frequencies of every communication system in E-plane and H-plane, respectively. It can be clearly seen that the radiation patterns of the proposed antenna are approximately omni-directional.

In addition, the gain and efficiency of the proposed antenna are investigated too. Figs. 10 and 11 exhibit the computed gain and efficiency of the presented antenna. It can be concluded that the gain and efficiency of the designed antenna meet the demands required by mobile terminals.

5. CONCLUSIONS

A compact design of a wideband PIFA antenna for seven-band (DCS/PCS/WCDMA/UMTS/WiBro/WLAN /DMB) mobile applications is proposed in this paper. The antenna with a very low profile and a compact structure meets the bandwidth requirements of mobile systems. The radiation patterns of the proposed antenna are approximately omni-directional in free space. Gain and efficiency of the antenna also satisfy the needs of mobile terminals. Good agreement between the measurement and simulation results can be achieved. All the features above confirm that the presented antenna is alternative in use for mobile multi-system applications.

REFERENCES

1. Kim, B. C. and J. H. Yun, "Small wideband PIFA for mobile phones at 1800 MHz," *IEEE International Conference on Vehicular Technology*, 27–29, Daejeon, South Korea, May 2004.
2. Wang, F., Z. Du, Q. Wang, and K. Gong, "Enhanced-bandwidth PIFA with T-shaped ground plane," *Electronics Letters*, Vol. 40, 1504–1505, 2004.
3. Ji, Z. H. and Y. C. Nai, "Design of a compact practical PIFA antenna," *Radio Communications*, Vol. 32, 33–34, 2006.
4. Zhu, X. W., X. X. He, and J. Liu, "Design of planar inverted-F antenna for mobile 3G applications," *Mobile Communications*, Vol. 31, 79–81, 2007.
5. Li, H., J. Yin, and J. H. Wang, "A novel wideband antenna for WCDMA mobile terminals," *Mobile Communications*, Vol. 31, 79–81, 2007.
6. Omar, A. S., M. Javwardence, and P. Mcevoy, "L and S shape PIFA antenna for triple-band (DCS/PCS/UMTS) mobile handsets," *IEEE International Symposium on Antennas and Propagation Society*, Vol. 3, 3107–3110, 2004.
7. Song, C. T. P., P. S. Hall, and H. Ghafouri-Shiraz, "Triple-band planar inverted-F antenna for handheld devices," *Electronics Letters*, Vol. 36, 112–114, 2000.
8. Ciais, P., R. Staraj, and G. Kossiavas, "Compact internal multi-band antenna for mobile phone and WLAN standards," *Electronics Letters*, Vol. 40, 920–921, 2004.
9. Nepa, P., G. Manara, and A. A. Serra, "Multiband PIFA for WLAN mobile terminals," *IEEE Antennas and Wireless Propagation Letters*, Vol. 4, 349–350, 2005.

Interaction between Two Photorefractive Bright Solitons in Different Dimensions

A. Keshavarz

Department of Physics, Faculty of Science, Shiraz University of Technology
P. O. Box 71555-313, Shiraz, Iran

Abstract— Optical solitons are self-trapped and localized wave packets existed by an exact balance between the diffraction or dispersion that tends to expand the wave pockets and the non linear effect. Nowadays many model equations of nonlinear phenomena are known to express soliton generation, and many methods of solution are introduced to solve them mathematically. Among optical solitons, photorefractive spatial solitons are more attractive than other types due to the fact that they are interesting for application in optics and photonics, also solving governed equations in mathematics. In this paper we introduced a suitable numerical method according to the Crark-Nicholson scheme to solve coupled nonlinear equations in one and two dimensions and simulated the interaction between two solitons in different dimensions. Results exhibited very interesting phenomena and show how we can control light by light.

1. INTRODUCTION

Solitons are one of the interesting topic in nonlinear optics, because these waves can be propagate without diffraction and or dispersion in fiber or crystal. Among this photorefractive (PR) spatial solitons (PRSS) have been shown to exhibit very interesting behavior. PRSS results from the nonlocal and nonlinear characteristics of photorefractive effect in photorefractive crystal, such as strontium barium niobate (SBN). At present, three types of steady-state PR solitons have been predicted: screening soliton, photovoltaic solitons, and screening-photovoltaic solitons. PRSS was found in both transverse dimensions and that these solitons can be observed at microwatt and lower power level. Thus PRSS have the key rule in photonic devices where light guides itself, and control of light by light. Progress in this field shows other interesting phenomena such as interaction between them. In this paper, we briefly present a physical model of PRSS generation, and simulate the interaction between one dimension with two dimension solitons (1D-2D interaction), as a new kind of PRSS interaction [1–6].

2. PHYSICAL MODEL

Generation of solitons in PR crystal emerges from nonlinear response of PR material under applied external field E_0. The material response of PR medium is described by the band transport model of Kukhtarer et al. [1, 8].

According to this model beside Maxwell's equations in the paraxial approximation, in anisotropic media, coupled wave equation and potential in normalized coordinates ($\frac{x}{x_0}$, $\frac{y}{y_0}$ and $\frac{z}{L_d}$ where ($L_d = kn_0x_0^2$) is diffraction length) introduced by:

$$\partial_z \overrightarrow{A} - \frac{i}{2}\nabla_\perp^2 \overrightarrow{A} = \frac{i}{2}\gamma(\partial_x\varphi - E_0)\overrightarrow{A} \tag{1}$$

$$\nabla_\perp^2 \varphi + \overrightarrow{\nabla} Ln(1+I) \cdot \overrightarrow{\nabla}\varphi = E_0\partial_x Ln(1+I) \tag{2}$$

where $\overrightarrow{A} = \overrightarrow{A}(x, y, z)$ is slowly varying amplitude of the beam propagates in the z-axis, $\gamma = k^2 n_0^4 x_0^2 r_{33}$ is the PR coupling constant which consists of the vacuum wave number k, and the unperturbed refractive index n_0. Here r_{33} is the effective electro-optic tensor.

The power intensity I is measured in units of the dark intensity I_d. The dark intensity is a material parameter that is proportional to the conductivity of the space-charge field in Kukhtarev model, and E_0 is the external field which is applied along the c-axis perpendicular to the propagation direction.

In one dimensional case, after some algebra, we can see the potential equation satisfy in $\partial_x\varphi = (\frac{I}{1+I})E_0$, and thus the wave equation written as:

$$\partial_z \overrightarrow{A} - \frac{i}{2}\partial_{xx}\overrightarrow{A} = -\frac{i}{2}\gamma(\frac{E_0}{1+I})\overrightarrow{A} \tag{3}$$

3. INTERACTION OF SOLITONS IN DIFFERENT DIMENSIONS

Interaction of soliton is one of the most interesting phenomena in modern optics. Till now interaction between PR solitons in one and two dimension are studied. Results show that incoherent screening solitons in one-dimensions (1D) have an isotropic nature and exhibited only attraction, when the solitons field is being overlapped. The situation is more different in two-dimension (2D). The launching of incoherent solitons along the direction of applied electric field leads to both repulsive and attractive effects corresponding to separation of the overlapping beams. In contrast if the solitons propagate in the plane perpendicular to the direction of the applied field always attracts each other. These results offer a potential for applications in photonic devices [8].

In order to control of light by light we investigated and simulated incoherent interaction of 1D screening PR soliton with 2D counterpart. In follow, we employed the crank-Nicholson scheme [7], which was accompanied by the central difference method to solve numerically the coupled wave and potential equations that govern the generation and interaction of PR screening solitons.
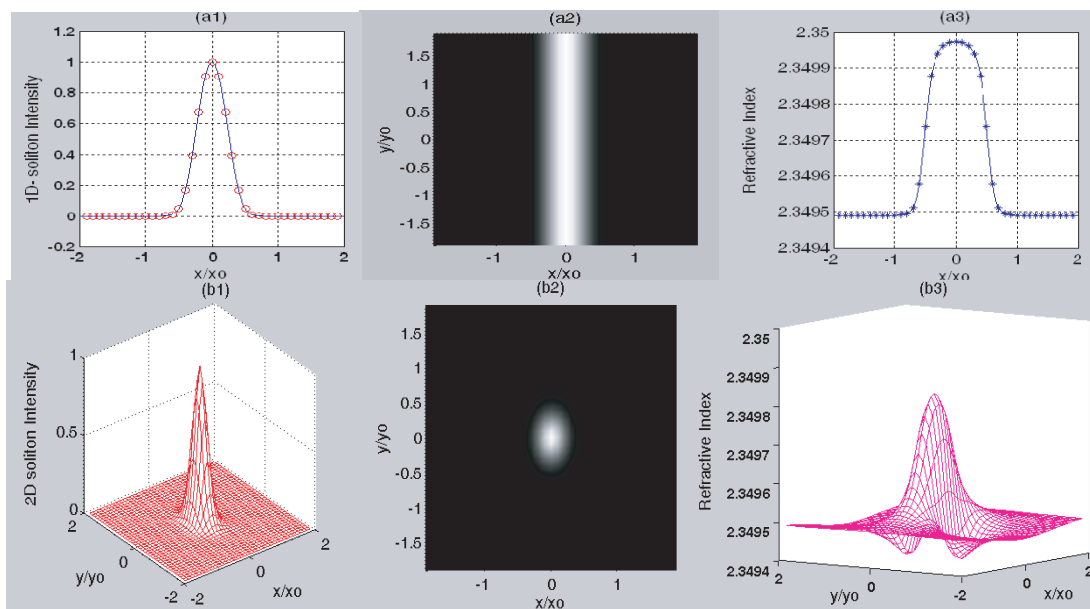
Figure 1: Beam profile, transverse soliton intensity distribution and modulated refractive index in one dimension (top row), and two dimension (bottom row) are shown from left to right.
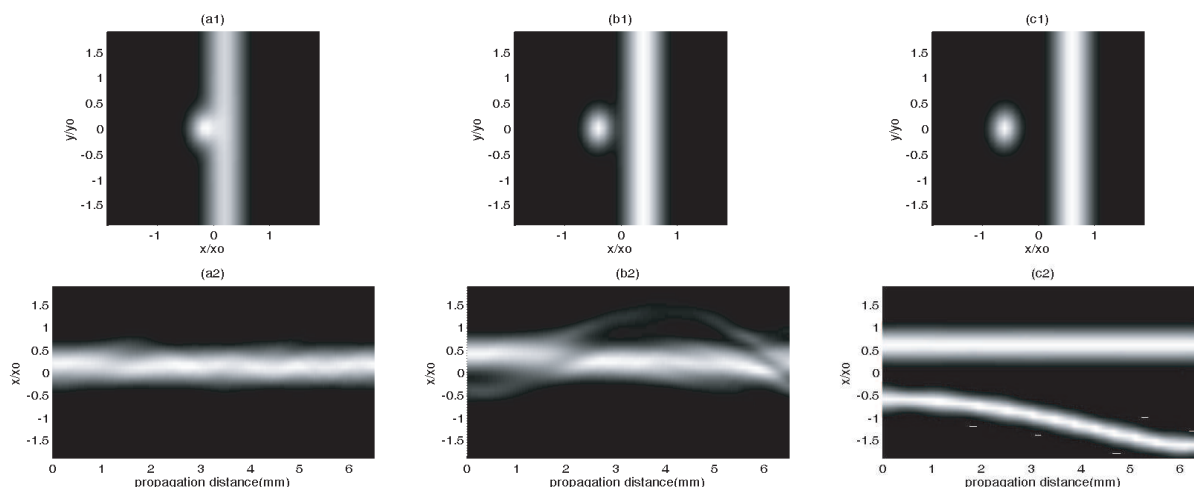
Figure 2: Numerical simulation of 1D-2D PRSS interaction. Top row shows transverse field distribution in the entrance face of the crystal (x-y plane) with three arbitrary separation distances, and bottom row shows the propagation of the solitons under interaction (x-z plane).

As an experimental data, our simulation is performed for the case of SBN crystal with $n_0 = 2.35$, $r_{33} = 180 \frac{pm}{V}$ and 6.5 mm length. The dark intensity is chosen as $I_d = 10^{-2}$, and the wavelength of the incident beam is chosen as $\lambda = 488$ nm, because the PR medium is sensitive to this wavelength. With these choices x_0 is obtained as 14.66 μm.

Soliton solution of Equations (1)–(3) are shown in Fig. 1. In this figure beam profile, transverse soliton intensity distribution and modulated refractive index by the soliton field in one and two dimension are presented.

For studying incoherent interaction between 1D and 2D PRSS, let us employing the condition $I = |A_1|^2 + |A_2|^2$ where A_1 and A_2 represents beam amplitude in one and two dimension. simulation results are depicted in Fig. 2. This Figure exhibited transverse field distribution and show how the field interacts with each other under propagation with respect to initial sepration of the field.

4. CONCLUSION

In this paper, we have studied the generation PRSS soliton and then we have investigated the interaction of 1D with 2D of such solitons. At the first we solved the coupled wave and potential equation numerically in order to obtain soliton beam profile in one and two dimensions. Then the interaction of 1D with 2D soliton was simulated. The results show that the attraction and repulsion of solitons depends on the initial separation of the optical field. We see the soliton attract in the initial distance condition and if the initial separation is bigger than the beam diameter, 2D soliton repel by 1D soliton. The strong of interaction can be controlled by the change in their initial separation. This soliton bending can be used in a read situation when more than two output ports exist. Then outputs from selected ports of spatial switching devices can be made available. Another result of our simulation is the stability of one dimension PR soliton with respect to two dimension counterpart. It more clears the real aspect of this solitons.

ACKNOWLEDGMENT

REFERENCES

1. Kuroda, K., *Progress in Photorefractive Nonlinear Optics*, Taylor and Francis, 2002.
2. Stegeman, G., "Optical spatial solitons: Historical prespectives," *IEEE J. Select. Top. Ouantum Electron.*, Vol. 6, 1419–1427, 2000.
3. Shi, T. and S. Chi, "Nonlinear photonic switching by using the spatial soliton collision," *Opt. Lett.*, Vol. 15, 1123–1125, 1990.
4. Shih, M., M. Segev, G. Valley, G. Salamo, G. Crosignani, and P. Di-Porto, "Observation of two-dimensional steady-state photorefractive screening soliton," *Electron. Lett.*, Vol. 31, 826–827, 1995.
5. Krolikowski, W., C. Denz, A. Stepken, M. Saffman, and B. Luther-Davies, "Interaction of spatial photorefractive solitons," *Quantum Semiclass Opt.*, Vol. 10, 823–837, 1998.
6. Evans, G., J. Blackledge, and P. Yardley, *Numerical Methods for Partial Differential Equations*, Springer Verlag, Berlin, 2000.
7. Yeh, P., *Introduction to Photorefractive Nonlinear Optics*, John Wiley, New York, 1995.
8. Zakery, A. and A. Keshavarz, "Simulation of the incoherent interaction between two bright spatial photorefractive screening solitins in one and two dimentions," *J. Phys. D: Appl. Phys.*, Vol. 37, 3409–3418, 2004.

Structural and Magnetic Properties of Mn Implanted GaN

Abdul Majid[1,2], **Akbar Ali**[1], **Rehana Sharif**[3], **J. J. Zhu**[2], **and X. F. Han**[3]

[1]Advance Materials Physics Lab, Physics Department
Quaid-i-Azam University, Islamabad, Pakistan
[2]State Key Laboratory on Integrated Optoelectronics
Institute of Semiconductor, Chinese Academy of Sciences, Beijing 100083, China
[3]State Key Laboratory of Magnetism
Institute of Physics, Chinese Academy of Sciences, Beijing 100083, China

Abstract— (Ga, Mn)N with Mn concentration of 0.04–5 at. % has been achieved by Mn ion implantation into MOCVD grown GaN. Structural and magnetic properties of the material were studied by X-ray diffraction and vibrating sample magnetometer respectively. Ferromagnetic properties of the samples at room temperature have been observed. The saturation magnetization reached to its maximum value with Mn concentration of 2 at. %.

1. INTRODUCTION

Transition metal (TM) doped wide band gap Diluted Magnetic Semiconductors (DMS) earned an intensive research interest during recent years due to their potential applications in spintronic-devices. 3d transition metal-impurities in III–V semiconductors preferably occupy the substitutional sites at low and moderate concentrations [1]. It is reported in literature that Mn atoms can occupy substitutional or interstitial sites. It can also exist in the form of precipitates and clusters [4]. In the case of its position on substitutional sites it form 'A$_{1-x}$Mn$_x$B' DMS alloy and in case of precipitates it exists as Mn$_4$N, Mn$_x$Ga$_y$ and GaMn$_3$N in (Ga, Mn)N system [4–7]. The location and distribution of impurity atoms into the host lattice have a strong correlation with the structural, optical and magnetic properties of the material. The location of Mn in GaMnAs and GaMnN lattice sites has strong impact on curie temperature [2, 3]. The coupling between Mn and host cations provides strong driving force for the Mn to group together to form the nanoclusters [4]. The coupling between ions of doped Mn and host GaN has been found to be ferromagnetic in nature [5]. High curie temperature of (Ga, Mn)N and related systems has been speculated due to coherent nanoclusters of magnetic impurities [6]. Though a sufficient data on (Ga, Mn)N system is available in literature to explain the magnetic properties of the system yet a question about the mechanism responsible for placing the TM impurity into one of the above mentioned forms to induce the ferromagnetic properties in host material still remained unanswered. The present study gives an insight to understand the structural and magnetic properties of Mn implanted GaN thin films.

2. EXPERIMENTAL

Wurtzite GaN thin films grown under low pressure by metal organic chemical vapor deposition (MOCVD) technique on c-plane sapphire substrates have been used in this work. Trimethylgallium (TMGa) and Ammonia (NH$_3$) were used as a source of Ga and N while hydrogen is used as a carrier gas. Firstly a 25 nm thick buffer layer of GaN was grown at 510°C with TMGa flow rate of 21.8 sccm/min. Then temperature of the buffer layer, was ramped up to 1040°C and ~3 μm thick GaN layer was grown with TMGa flow rate 51 sccm/min. Flow rate of ammonia and chamber pressure were kept constant at of 2500 sccm/min 500 Torr respectively. Crystalline quality of as-grown samples was checked by XRD by measuring FWHM of symmetric (0002) and asymmetric (10–12) scans. The values were found to be 244 arcsec and 273 arcsec respectively. Carrier concentration and carrier mobility of as grown samples have been determined by Hall measurement at room temperature and are found to be $7.71 \times 10^{16}\,\mathrm{cm}^{-3}$ and $219\,\mathrm{cm}^2\mathrm{V}^{-1}\mathrm{S}^{-1}$ respectively. Samples of the same size scribed from the same wafer were uniformly implanted with different Mn doses of 1×10^{14}, 2×10^{15}, 5×10^{15}, 9×10^{15}, 2×10^{16} and 5×10^{16} ions/cm at room temperature^2 accelerated under 250 KeV. The Mn concentrations were found to be ~0.01%, 0.2%, 0.5%, 0.9%, 2% and 5% respectively in DMS layers. Implantation was done at 7° to the c-axis of wurtzite GaN samples. The estimated depth of the implanted ions by TRIM for peak concentration was found to be 150 nm from sample surface. Following the implantation, samples were RTA annealed at 800°C for 30 seconds in nitrogen ambient. To reduce the possible decomposition of the samples during annealing, they

were faced down on a GaN wafer. High resolution X-ray diffraction (HRXRD) measurements have been carried out using Rigaku SLX-1A X-ray diffractometer to study the structural properties of the implanted samples. Vibrating Sample Magnetometer (VSM) of ADE Technologies (Model DMS 4HF) was used to investigate the magnetic properties of the implanted samples. Magnetic hysteresis loops were measured at room temperature for all the samples using 5000 Oe in-plane and out-of-plane applied magnetic field to saturate the samples. The correction for diamagnetic contribution of substrate has been made.

3. RESULTS AND DISCUSSION

Double crystal XRD spectra of the as-grown and implanted samples are shown in Figure 1. The GaN (0002), GaN (0004) and sapphire (0006) peaks are clearly seen in XRD ($\omega - 2\theta$) scans. Though there are no extra peaks visible but due to resolution limit of XRD spectrometer, the possibility of the contribution of second phases (Mn_xN_y, MnGa etc.) to the magnetic properties of our samples can not be ruled out.
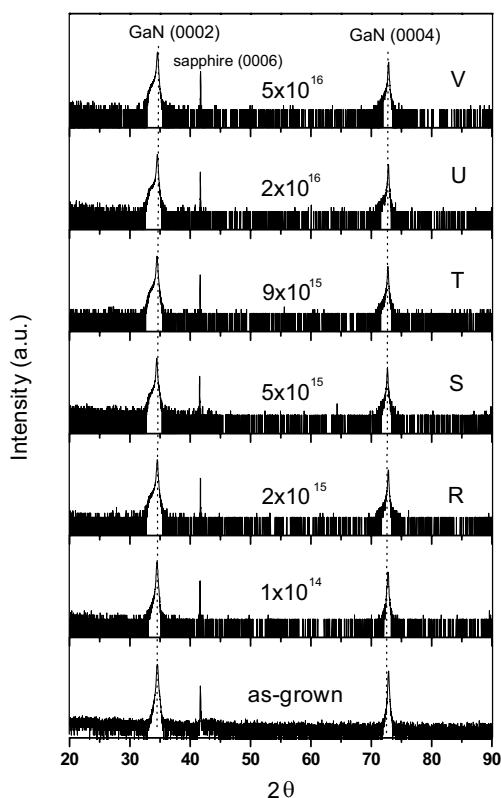
Figure 1: XRD ($\omega - 2\theta$) scans for as-grown and Mn implanted GaN with dose from 10^{14} to 5×10^{16} ions/cm^2 at 250 KeV.

Symmetric (0002) $\omega - 2\theta$ diffraction curves of as-grown and implanted samples are shown in Figure 2. In the scans of as-grown sample only a main peak of GaN at $2\theta = 34.56°$ having symmetrical shape is found present whereas in the scans of implanted samples extra features on lower angle side of the main peak are also visible.

Sample implanted with 1×10^{14} Mn ions cm^{-2} shows a clear peak around $2\theta = 34.47°$, which indicates the lattice expansion due to implantation induced disorder. The scans of the samples implanted with higher dose of 2×10^{15} cm^{-2} show a broad feature due to overlapping of many small peaks on the lower angle side of the spectrum with decreasing trend in intensity with decrease in angle. A similar pattern shown in Figure 2 has also been observed for other samples implanted with higher doses. During ion implantation process material is removed from the surface by sputtering which may be a cause of reduction in X-ray intensity. The other reason that can be given to support the reduction in intensity is the defects generated during ion implantation. Appearance of additional peak on the left side of the GaN peak is assumed due to the lattice expansion, damages and appearance of amorphous phase in the host lattice. The presence of magnetic phase of GaMnN may also be the cause of this peak [11].
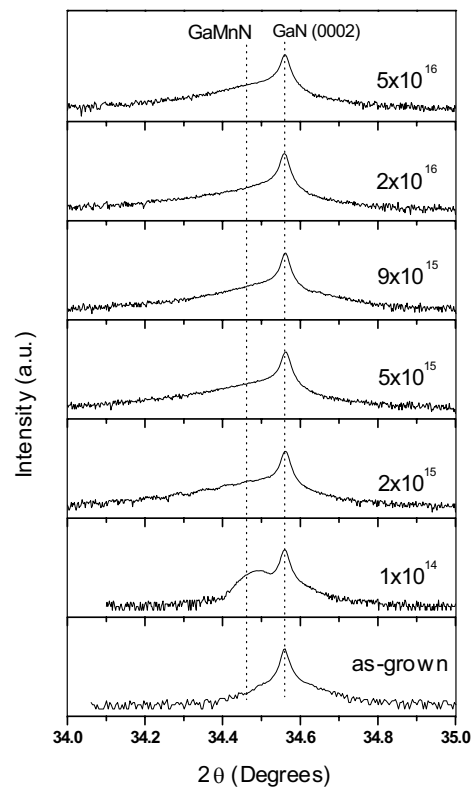
Figure 2: XRD $\omega - 2\theta$ scan of the as-grown and Mn implanted annealed GaN samples at various doses.

The ratio of the X-ray intensity of the peaks corresponding to GaMnN (around $2\theta = 34.47°$) and GaN for as-grown samples (at $2\theta = 34.56°$) has been plotted in Figure 3 against dose. Samples implanted with dose 2×10^{16} ions/cm^2 show the lowest intensity ratio indicating the best crystalline quality of the implanted samples.
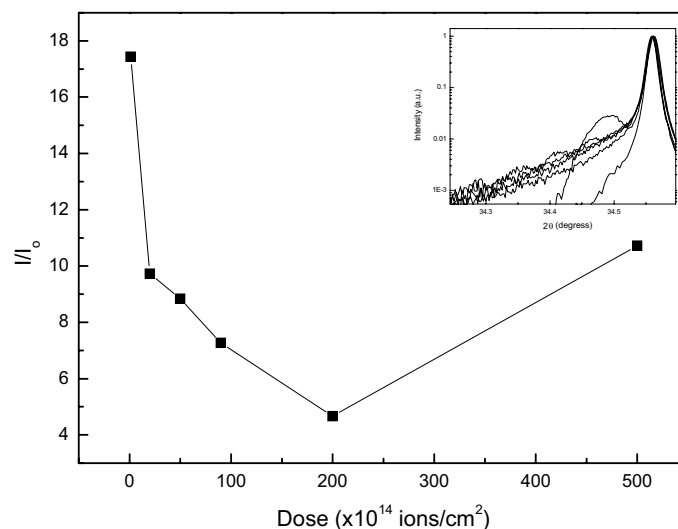

Figure 3: Dose dependence of the intensity ratio of implanted (I) and as-grown (I_o) samples at the GaMnN peak position in symmetric (0002) X-ray diffraction. Inset shows the GaMnN peak structure on left side of GaN peak at different implantation doses.

Figure 4 shows the FWHM for (0002) and (0004) peaks of GaMnN as a function of implantation dose. In both the cases FWHM reached to maximum value at the dose of 2×10^{16} ions/cm^2. FWHM of (0002) reflection before annealing is also given for comparison. The FWHM values of the peaks for implanted samples after annealing have also been plotted against dose in Figure 4. This figure

shows that samples having dose 2×10^{16} ions/cm^2 exhibit maximum value of FWHM when compared with all other samples.
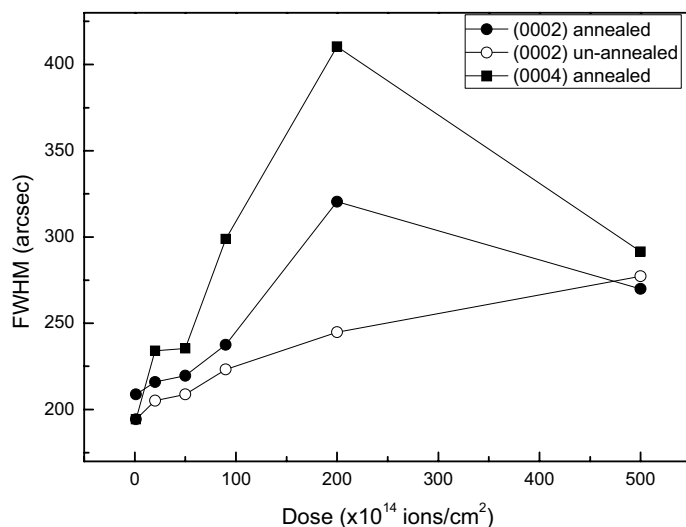
Figure 4: Variation in FWHM of (0002) and (0004) GaMnN peaks.

Similarly saturation magnetization due to parallel and perpendicular magnetic fields to the surface of the samples has been plotted in Figure 5. The figure shows that the variation in the saturation magnetization for the implanted samples is different for parallel magnetic field as compared to perpendicular magnetic field. The samples with plane orientation parallel to the field show large magnetization which indicates that this is an easy axis for the samples.
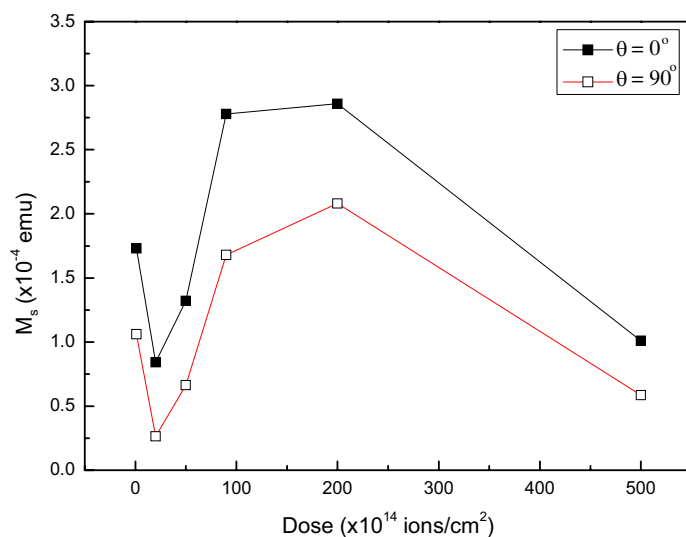
Figure 5: Variation in saturation magnetiztion (for magnetic field along parallel and perpendicular to the sample) surace with different implantation doses.

The ferromagnetic ordering in our samples by Mn implantation into GaN can be interpreted by the formation of clusters, Mn related secondary phases or homogeneous diluted alloys. More work is required to investigate the microstructures and possible origin of ferromagnetism in this system.

ACKNOWLEDGMENT

REFERENCES

1. Zunger, A., *Solid State Physics*, Vol. 39, 275, edited by F. Seitz, H. Ehrenreich, and D. Turnbull, Academic Press, New York, 1986.
2. Yu, K. M., W. Walukiewicz, T. Wojtowicz, I. Kuryliszyn, X. Liu, Y. Sasaki, and J. K. Furdyna, *Phys. Rev. B*, Vol. 65, 201303(R), 2002.
3. Kim, N., S. J. Lee, and T. W. Kang, *Phys. Lett. A*, Vol. 329, 226, 2004.
4. Van Schilfgaarde, M. and O. N. Mryasov, *Phys. Rev. B*, Vol. 63, 233205, 2001.
5. Das, G. P., B. K. Rao, and P. Jena, *Phys. Rev. B*, Vol. 68, 035207, 2003.
6. Dietl, T., *Nature Mater.*, Vol. 5, 673, 2006.
7. Liu, C., F. Yun, and H. Morkoc, *JOMS: Mat. Electron.*, Vol. 16, 555, 2005.
8. Coey, J. M. D., M. Venkatesan, and C. B. Fitzgerald, *Nature Mater.*, Vol. 4, 73, 2005.
9. Liu, C., B. Mensching, K. Volz, and B. Rauschenbach, *Appl. Phys. Lett.*, Vol. 71, 2313, 1997.
10. Pong, B. J., C. J. Pan, Y. C. Teng, G. C. Chi, W.-H. Li, K. C. Lee, and C.-H. Lee, *J. Appl. Phys.*, Vol. 83, 5992, 1998.
11. Teraguchi, N., et al., *Solid State Communications*, Vol. 122, 651, 2002.
12. Wang, Y. and N. Herron, *Phys. Rev. B*, Vol. 42, 7253, 1990.

Virtual Antenna Method as Applied to the Study of the Scattering by 2-dimensional Non-linear Metamaterials

Frédéric Zolla, **Pierre Godard**, and **André Nicolet**

Institut Fresnel, Marseille, France

Abstract— We are interested in the electromagnetic scattering by a finite set of parallel nonlinear rods (optical Kerr-effect, for instance) of any shape. Associated with perfectly matched layers, the Finite Element Method (FEM) is well suited for this kind of problems. Nevertheless, when using the FEM, the sources have to be put inside the meshed area; it is then clear that this method fails whenever the sources are far from the obstacles (for instance, when dealing with plane waves). In this paper, a new route for obtaining the scattered field by non-linear obstacles is proposed. The basic idea consists in simulating the real incident field by a virtual field emitted by an appropriate antenna, located in the meshed domain, and encompassing or lying above the obstacles. This general procedure is of course adapted to the diffraction by non-linear metamaterials. Some results are given in order to illustrate the versatility of our method: transmission through a finite Kerr photonic crystal, Kerr gratings, etc.... We check the numerical results via a verification of the power balance.

1. DIFFRACTION BY AN OPTICAL KERR MEDIUM

We study the scattering by a nonlinear rod $\mathcal{R}$, in which a photonic crystal has been grooved. The system is invariant along one direction, taken as the z-axis. The electromagnetic field is supposed to be harmonic in time, and for the sake of simplicity only TM fields are tackled. A function u: $\mathbb{R}^2 \to \mathbb{C}$ can thus be defined such that $\mathbf{E}(x, y, z, t) = \Re e\{u(x, y)e^{iwt}\}\hat{z}$. The rod $\mathcal{R}$, considered as being nonmagnetic, is surrounded by a vacuum. The non-linearity is an optical Kerr effect (see, for example, [1]). For the time being, we restrict ourselves to an isotropic medium, so that we are concerned only with the $(\varepsilon_r)_{zz}$ component (indices are dropped from now on). Thus, in $\mathcal{R}$, $\varepsilon_r(u) := \varepsilon_r^{(0)} + \chi^{(3)}|u|^2$, with $(\varepsilon_r^{(0)}, \chi^{(3)}) \in \mathbb{C}^2$, and hence the equation we have to solve is

$$\left(\Delta + k_0^2 \varepsilon_r(u)\right) u = \rho, \tag{1}$$

with $u := u^d + u^i$, where u^d is the unknown scattered field satisfying an outgoing wave condition (OWC) and u^i is a given incident field that satisfies

$$(\Delta + k_0^2)u^i = \rho. \tag{2}$$

The source generating u^i described by ρ can be currents, or it vanishes in case of incident plane waves.

We handle this study by numerical simulation. The finite element method (FEM) revealed to be appropriate, for its ability to treat inhomogeneous permittivities (hence this method seems more general than, for example, [2]). We used the *Comsol Multiphysics* software, in which the non-linearity is treated by an iterative scheme (damped Newton method).

The OWC is implemented by perfectly matched layers (PML) bounding the region of physical interest.

2. IMPLEMENTING THE FAR FIELD: THE VIRTUAL ANTENNA METHOD

When using methods like FEM, we have to put the source ρ in the meshed area. This can be very inconvenient: if the currents are far from the scattering objects, precision decreases or a higher data storage has to be allowed because a large domain has to be considered. Besides, we know that plane waves exist in vacuum; we have to find a new route to implement this incident field.

A usual method to get round these difficulties is to work with the scattered field, namely u^d ([3], or [4] — to be published). In this way, the sources of the problem are automatically conveyed in the obstacle, which is in the meshed area. However, in our case, the equations satisfied by the fields u and u^d are non-linear; as a consequence, the equation satisfied by the scattered field is almost intractable. A new method has been developed to solve the equation for the total field (Equation (1)) and to simulate the incident field u^i by a current $\jmath$ located on a simple curve $\partial\Omega$

(the interior of which is denoted by Ω) in the meshed area. More precisely, we find $\jmath$ such that it radiates a field u^0 satisfying an OWC,

$$(\Delta + k_0^2)u^0 = \jmath\delta_{\partial\Omega} \tag{3}$$

and such that u^0 has the following fundamental property

$$u^0|_\Omega = u^i|_\Omega. \tag{4}$$

The current $\jmath$ is (uniquely) determined by

$$\jmath = \frac{-1}{i\omega\mu_0}\left[\frac{dv}{dn}\right]\bigg|_{\partial\Omega},$$

where v is the total field existing in the system in which a perfectly conductor fits in Ω and is illuminating by u^i. In a general case, $\jmath$ cannot be computed in a closed form, but, as far as we are concerned in the following section, Ω is a closed disk (say, of radius R and centered at the origin) and u^i is a plane wave oscillating in a vacuum. Here we obtain (all the details will appear soon in [4])

$$\jmath(R, \theta) = \sum_{n\in\mathbb{Z}} \frac{i^n k_0}{2i\omega\mu_0}\left\{\frac{J_n(k_0 R)}{H_n^{(2)}(k_0 R)}\left(H_{n-1}^{(2)} - H_{n+1}^{(2)}\right)(k_0 R) - (J_{n-1} - J_{n+1})(k_0 R)\right\}e^{in\theta},$$

where J_n and $H_n^{(2)}$ are respectively the Bessel functions and the Hankel functions (of the second kind) of order n.

We have called this process a *virtual antenna*. It is able to simulate almost any incident field in a bounded region.

3. SOME NUMERICAL RESULTS ABOUT A HOLEY NONLINEAR ROD

A particular simulation is now more detailed. We propose the following system to study: there is one big rod, $\mathcal{R}$, made of a dielectric of relative permittivity $\varepsilon_r = 8.41$. Inside $\mathcal{R}$ is grooved an air lattice. A plane wave, of amplitude A^i, is coming from the right. A picture (Figure 1(a)) of a cross-section of the system under study is presented.
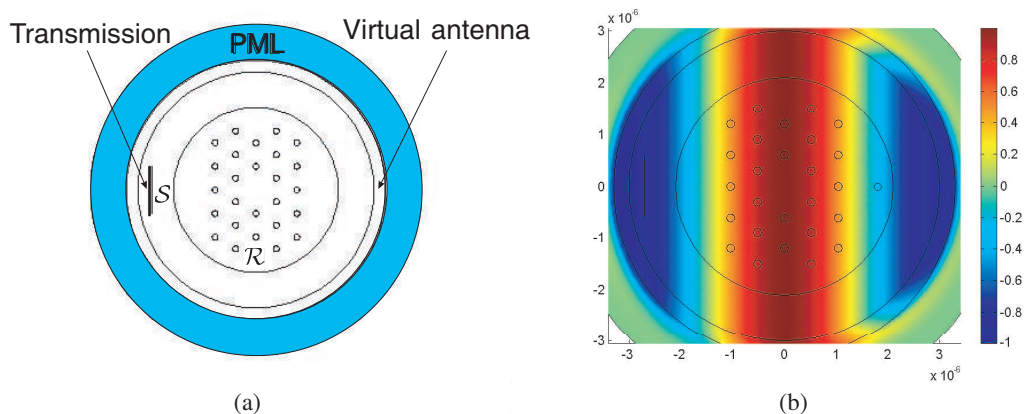

Figure 1: (a) A cross-section of the studied system. The segment $\mathcal{S}$ is used for extrapolation of the transmission coefficient. The cluster of small circles stands for the holes inside the big rod $\mathcal{R}$. The four circles centered on the origin are, from the smallest to the largest: 1. $\partial\mathcal{R}$, the boundary of the bulk, 2. $\partial\Omega$ on which the current of the virtual antenna flows, 3. the inner boundary of the PML, 4. the outer boundary of the PML; (b), The real part of the incident electric field, as simulated by the virtual antenna's current. We see that, when restricted to Ω, the field is a plane wave, but out of Ω, the two fields are different.

We note $\mathbf{P}_{A^i, \chi^{(3)}}$ (respectively $\mathbf{P}_{A^i, \chi^{(3)}}^{inc}$) the complex Poynting vector associated to the total (respectively the incident) field, when the amplitude of the incident field is A^i and the nonlinear

coefficient $\chi^{(3)}$. The units are the ones of the international system: A^i is in V/m and $\chi^{(3)}$ in m^2/V^2. Then we define the coefficient transmission $T_{A^i,\,\chi^{(3)}}^{\mathcal{S}}$ by

$$T_{A^i,\,\chi^{(3)}}^{\mathcal{S}} = \frac{\int_{\mathcal{S}} \Re e\{\mathbf{P}_{A^i,\,\chi^{(3)}}\} \cdot \hat{n} \; dl}{\int_{\mathcal{S}} \Re e\{\mathbf{P}_{A^i,\,\chi^{(3)}}^{inc}\} \cdot \hat{n} \; dl}$$

$\hat{n}$ being the unit normal vector, and $\mathcal{S}$ is a segment located "behind" $\mathcal{R}$. Of course, if $\chi^{(3)}$ vanishes, then the transmission is independent of A^i.

The transmission $T_{1,0}^{\mathcal{S}}$ of this system is presented in the Figure 2(a). This result may seem curious: $T_{1,0}^{\mathcal{S}}$ can be greater than unity (i.e., $\mathcal{R}$ focuses the field just behind it) or negative (indeed, we can see that for some resonant wavelengths, the Poynting vector flows through the segment from left to right). If we change the shape or place of the rod, this behavior changes quantitatively but not qualitatively.

(a) $T_{1,\,0}^{\mathcal{S}}$.   (b) $T_{10^{-8},\,-10^{-3}}^{\mathcal{S}}$ - $T_{1,\,-10^{-3}}^{\mathcal{S}}$.
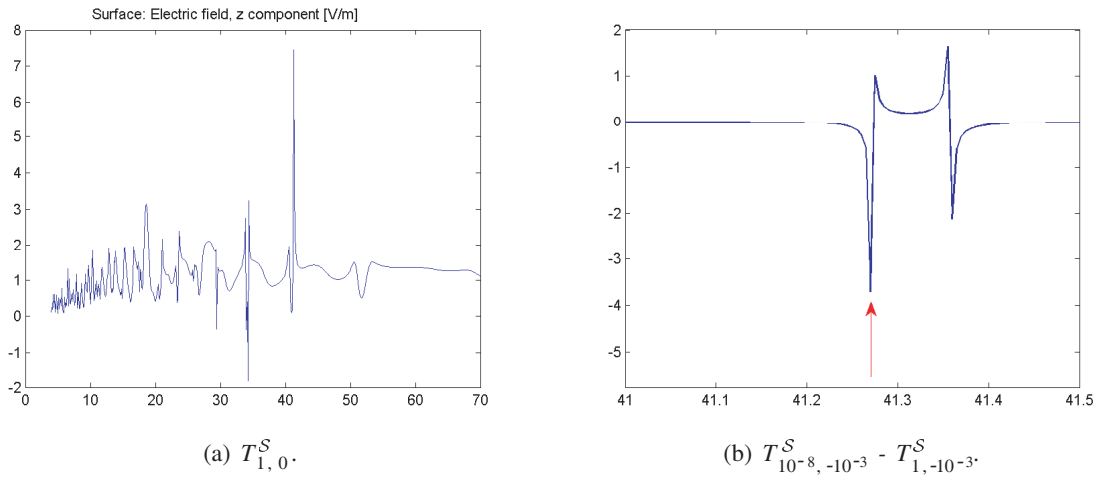
Figure 2: (a) Transmission versus normalized wavelength λ/d, where d is the diameter of one hole. Here the host rod $\mathcal{R}$ is assumed to be linear; (b) The difference ($T_{10^{-8},\,-10^{-3}}^{\mathcal{S}} - T_{1,\,-10^{-3}}^{\mathcal{S}}$) of the transmission, with respect to the normalized wavelength λ/d.

We then look for the alteration that a Kerr nonlinearity in $\mathcal{R}$ can induce on $T_{A^i,\,\chi^{(3)}}^{\mathcal{S}}$. In order to have a spectacular disturbance, we choose to see what happens at the largest resonance wavelength. The nonlinearity coefficient is set to the usual $\chi^{(3)} = -10^{-3}\,\text{m}^2/\text{V}^2$ ([2, 5], etc.). Two simulations are done: the first one with an amplitude of the incident field of $A^i = 10^{-8}\,\text{V/m}$ (the amplitude is very low and therefore the effects due to the nonlinearity have to pass unnoticed), the second one with $A^i = 1\,\text{V/m}$. The result is presented on the Figure 2(b). At the resonance frequency, the nonlinear coefficient has huge consequences on the field. We show two maps (Figure 3), in the linear or nonlinear regimes, of the modulus of the electric field (we choose $\chi^{(3)} = -0.5\,\text{m}^2/\text{V}^2$ to have large differences).

In order to check the model coherence, we study the dissipated power; from now on a lossy material is considered: $\varepsilon_r^{(0)} = 8.41 + 2i$. Let Σ be a disk enclosing $\mathcal{R}$ which does not intersect the PML domain. Since $\partial\Sigma$ (the boundary of Σ) is in the vacuum area, the (line density of the average over a time period of the) electromagnetic power $\mathcal{P}_e^{harm}$ flowing through it can be easily derived:

$$\int_{\Sigma} \mathcal{P}_e^{harm} ds = -\int_{\partial\Sigma} \Re e(\mathbf{P}) \cdot \hat{n} \; dl. \tag{5}$$

Denoting by ε_r'' the imaginary part of the relative permittivity, we have

$$\int_{\Sigma} \mathcal{P}_e^{harm} ds = -\frac{\varepsilon_0 \omega}{2} \int_{\Sigma} \varepsilon_r''(u) |u|^2 ds. \tag{6}$$

This expression is the electromagnetic power lost inside Σ, i.e., in $\mathcal{R}$.

(a) $\chi^{(3)} = 0$ m^2/V^2.
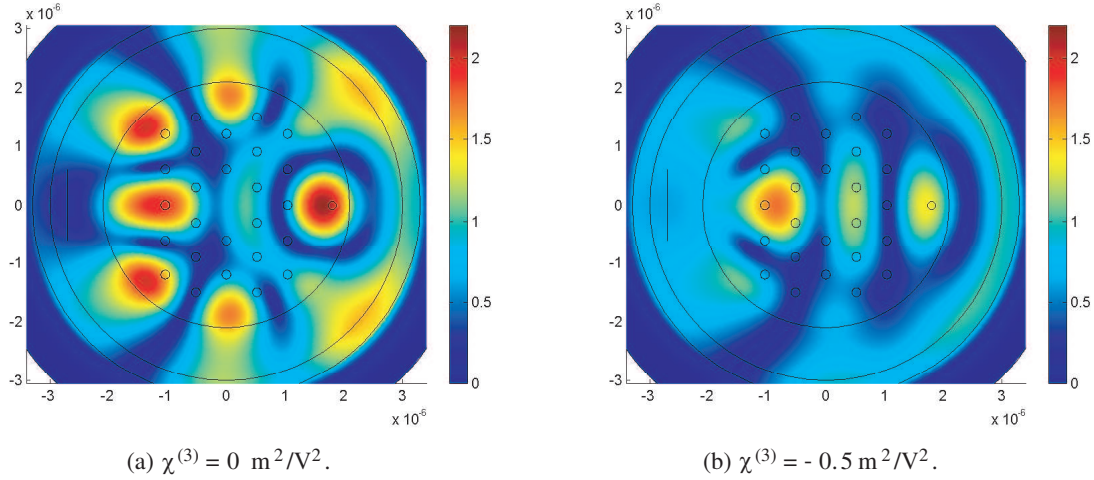
(b) $\chi^{(3)} = -0.5$ m^2/V^2.

Figure 3: The modulus $|u|$ of the electric field in the (a) linear or (b) nonlinear regimes, at the largest resonance wavelength: $\lambda/d = 41.27$ (which corresponds to the arrow on the Figure 2(b). Note that the scales are the same.

The difference of the two expressions for $\int_\Sigma \mathcal{P}_e^{harm} ds$ gives, when divided by $\int_{\partial\Sigma} |\Re e(\mathbf{P}^{inc}) \cdot \hat{n}| dl$ (to "normalize" the error), 1.2×10^{-4}, for linear and for non-linear crystals as well. From the numerical point of view, this is highly acceptable in view of the fact that one expression integrates $u\nabla\bar{u}$ on a line and the other one integrates $\varepsilon_r(u)|u|^2$ on a surface.

4. CONCLUDING REMARKS

The optical parameters used in this paper correspond to stronger non-linearity than the ones usually found, and thus we think we can now safely simulate more realistic experiments. In particular, we are interesting to study how several fields with different frequencies interact. For example, if a field with a time dependance in $e^{i\omega t}$ interacts with a non-linear medium, a field with pulsation 2ω is generated. The fields at 2ω and at $-\omega$ interact and give a contribution to the field with pulsation ω. This is often neglected but this approximation seems not really justified in more recent experiments.

We also wish to find materials with new optical or geometrical properties that exhibit important differences between the linear and nonlinear regimes. This is why we turn to the study of nonlinear metamaterials.

REFERENCES

1. Boyd, R. W., *Non Linear Optics*, 2nd edition, Academic Press, Amsterdam, 2003.
2. Centeno, E. and D. Felbacq, "Optical bistability in finite-size nonlinear bidimensional photonic crystals doped by a microcavity," *Physical Review B*, Vol. 62, No. 12, 7683, 2000.
3. Demésy, G., F. Zolla, A. Nicolet, M. Commandré, and C. Fossati, "The finite element method as applied to the diffraction by an anisotropic method," *Optics Express*, Vol. 15, No. 26, 18089, 2007.
4. Godard, P., F. Zolla, and A. Nicolet, " Scattering by a 2-dimensional doped photonic crystal presenting an optical Kerr effect," *Compel*, 2009, (to appear).
5. Xie, P. and Z. Q. Zhang, "Multifrequency gap solitons in nonlinear photonic crystals," *Physical Review Letters*, Vol. 91, No. 21, 213904, 2003.

Coupling of Terahertz Surface Plasmon Polaritons in Corrugated Stacks of Dielectric and Semiconductor

Xin Wu, **De Li**, **Wei-Hua Sun**, **Feng Gao**, **Zhi-Jian Zhang**, and **Ru-Wen Peng**

National Laboratory of Solid State Microstructures and Department of Physics
Nanjing University, Nanjing 210093, China

Abstract— We present a theoretical approach that terahertz surface plasmon polaritons (THz-SPPs) are tuned by temperature in a stack of dielectric and semiconductor with periodic corrugations. Based on Rayleigh hypothesis, we show that when THz electromagnetic wave illuminates the waved stack, temperature-dependent THz-SPPs are excited. At resonant modes, reflection dips or Fano-type resonance shape are found. With increasing the temperature difference of the upper and lower semiconductor layers in the stack, transmissions increase and reflections decrease significantly. Our investigation indicates that such stacks may achieve potential applications in thermally controlled THz devices.

1. INTRODUCTION

When metallic nanostructures are illuminated, the incoming radiation may couple to surface charge oscillations and excite the surface plasmon polaritons (SPPs) [1]. It is well known that SPPs are responsible for the near-field enhancement, which may have potential applications in optics and photonics [2–5]. Up to now, most investigations on SPPs have been focused on the patterned metal surfaces in the visible and infrared regions.

However, it is found that the real part of the permittivity of some semiconductors can be negative at terahertz frequencies and they can also support SPPs [6–8]. For example, the thermal switching of THz SPPs scattering has been studied in groove arrays of indium antimonide (InSb) [6, 7]. The THz-enhanced transmission has also been observed through the slit surrounded by periodic grooves of silicon wafer by optically modifying the propagation lengths of THz SPPs [8]. As we know, terahertz science and technology can bridge the gap between photonics and electronics, which provides a powerful tool for the characterization of semiconductor and biomolecule materials [9]. And THz spectroscopy and imaging may achieve a wide range of applications in biology and medicine [10–13]. Therefore, the further research on THz SPPs will benefit the improvement of THz sensing and imaging.

In this work, we theoretically study the normal transmission and reflection influenced by THz SPPs in a periodically corrugated stack of three layers (InSb/Silicon/InSb) when it is illuminated by p-polarized THz electromagnetic waves. The temperature difference between the upper and lower InSb layer can be changed in order to tune the reflection and transmission properties. It is shown that temperature-dependent THz SPPs are excited. The first order and the second order resonant modes are observed. At those modes, reflection dips or Fano-type resonance shape are found. Time averaged magnetic field distributions are also given to illustrate the influence of temperature on these resonant modes. With increasing the temperature difference of the two InSb layers, transmissions increase and reflections decrease significantly. Our investigation indicates that such stacks may achieve potential applications in thermally controlled THz devices.

2. THEORETICAL APPROACH

In order to excite THz SPPs, the stacks of InSb and silicon are designed with periodic corrugations (as shown in Fig. 1). The average thickness of the InSb layer d and the average thickness of the silicon layer D are set to be indentical in our calculation. The interfaces can be written in the form of $y_j = h_j + a\sin(k_g x)$ at the xy plane, and $h_j = (5/2 - j)d$ $(j = 1, 2, 3, 4)$. Here a is the corrugation height, $k_g = 2\pi/\lambda_0$ is the grating vector, and λ_0 is the corrugation period.

The THz electromagnetic wave illuminates upon the stack in normal incidence. Based on Rayleigh hypothesis [14], the reflection and the transmission spectra can be obtained theoretically. The theoretical treatment includes the following processes: (i) The magnetic fields in each media of the stack are expressed as Rayleigh expansions in terms of spatial harmonics with periodic boundary condition. (ii) An infinite set of coupled amplitude equations is obtained. (iii) We truncate the superposition of all the spatial harmonics and solve the coupled amplitude equations. (iv) The reflectivity and the transmittivity are calculated. This theoretical treatment is similar to that in Ref. [15], and Rayleigh hypothesis has been made to be valid [16, 17] in our calculation.

3. NUMERICAL CALCULATION AND DISCUSSIONS

Due to the fact that InSb has a high electronic mobility (about $7.7 \times 10^4 \, \text{cm}^2\text{V}^{-1}\text{s}^{-1}$) and a small band-gap (about $0.17 \, \text{eV}$) [18], when the temperature varies from $225 \, \text{K}$ to $325 \, \text{K}$, there are a significant number of thermally excited carriers in InSb, which makes InSb to behave as a metal at the THz region [6, 7]. Thereafter, the dielectric functions of the InSb film is characterized by a Drude-type function

$$\varepsilon(\omega, T) = \varepsilon_\infty - \frac{\omega_p^2(T)}{\omega \left[\omega + i\Gamma(T)\right]} \tag{1}$$

where ε_∞ is the high-frequency permittivity, $\omega_p(T)$ is the plasma frequency and $\Gamma(T)$ is the temperature-dependent collision rate. Therefore, at this temperature range, the real part of permittivity for InSb becomes negative in the THz range, and the InSb film presents the metallic characteristic. While for $10 \, \text{K}\Omega\text{cm}$ silicon from $0.1 \, \text{THz}$ to $2.0 \, \text{THz}$, the refraction index is about 3.418 which is independent of frequency and temperature [19, 20]. The loss in $10 \, \text{K}\Omega\text{cm}$ silicon is very small and neglected in our calculation. Therefore, THz SPPs may be excited at the InSb/air or InSb/Si interface and the resonant modes can be tuned by temperature.
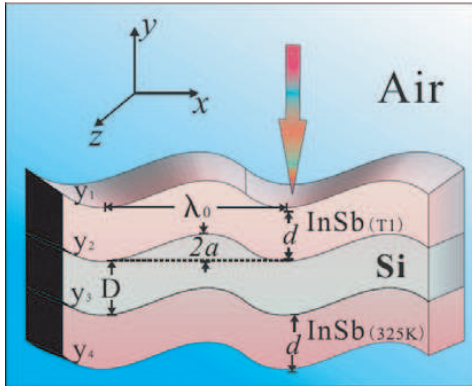
Figure 1: The geometry of the corrugated stack of InSb/Si/InSb. Here d is the average thickness of the InSb layer, D is the average thickness of the silicon layer, a is the corrugation height, $k_g = 2\pi/\lambda_0$ is the grating vector, and λ_0 is the corrugation period. The interfaces are assumed to be smooth and invariable in the z direction.
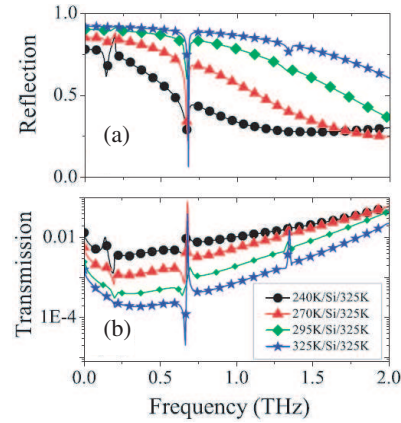
Figure 2: The calculated (a) reflection spectra and (b) transmission spectra in normal incidence. The circle, triangle, diamond and pentacle symbols are indicated for the upper InSb layer at temperatures $240 \, \text{K}$, $270 \, \text{K}$, $295 \, \text{K}$, and $325 \, \text{K}$, respectively.

In our calculation, the parameters of the stack are set as $\lambda_0 = 440.0 \, \mu\text{m}$, $d = D = 7.0 \, \mu\text{m}$, and $a = 15.4 \, \mu\text{m}$. Besides, the permittivity of InSb is obtained from Eq. (1) by using the data for both $\omega_p(T)$ and $\Gamma(T)$ in Ref. [6]. The temperature of the lower InSb layer is set as $325 \, \text{K}$, and we change the temperature T_1 of the upper InSb layer. Thereafter, the temperature difference ΔT of the two InSb layers can be defined as $\Delta T = 325 - T_1$. The calculated reflection and transmission spectra are shown in Fig. 2.

The incident radiation can be coupled to the THz SPPs in the stack because the periodic corrugations provide additional momentum. The THz SPPs are resonantly excited in the stack, which happens at the momentum matching of

$$k_{SPP} \equiv \frac{2\pi}{\lambda} \sqrt{\frac{\varepsilon_i \cdot \varepsilon(\omega, T)}{\varepsilon_i + \varepsilon(\omega, T)}} = k_{//} \pm n k_g. \tag{2}$$

Here, λ is the wavelength of incident light, and ε_i represents the permittivity of the air or silicon, $\varepsilon(\omega, T)$ is given by Eq. (1). $k_{//}$ is the in-plane wave vector, which is zero in normal incidence. In the terahertz region from $0.1 \, \text{THz}$ to $2.0 \, \text{THz}$, the magnitude of real part of $\varepsilon(\omega, T)$ is far more than ε_i. Hence, the square root in Eq. (2) can be set as 1, and the resonant wavelength is just related to the period of the stack. From Fig. 2, we can find that the 1st order InSb/Si SPPs modes, 1st order InSb/air SPPs modes and 2nd order InSb/air SPPs modes are excited at the frequencies of

0.17 THz, 0.68 THz and 1.34 THz, respectively. The magnitude of the 2nd order InSb/Si SPPs mode is too small to be observed in our model. At those resonant modes, reflection dips or Fano-type resonance shape are found.

Time averaged magnetic field distributions are also given to illustrate the influence of temperature on those resonant modes in Fig. 3. From Fig. 3, we can find that for low temperature of the upper InSb layer, the field is mainly focused in the middle silicon layer as shown in Figs. 3(a) and (b); while for high temperature, the field mainly exists in the upper and lower InSb layer as shown in Figs. 3(c) and (d).

It is possible to tune significantly the reflection and the transmission by changing the temperature difference in the stack. Fig. 4 presents the temperature-dependent reflection and transmission when 1.0 THz electromagnetic wave illuminates normally on the stack. It is shown that when the temperature difference of the two InSb layers increases from 0 K to 100 K, the reflectivity decreases from 86.5% to 29.5%, and the transmission increases from 0.07% to 1.2%. This feature originates from the fact that the permittivity of InSb is changed by varying the temperature (as shown in the inset of Fig. 4). Obviously, the corrugated stacks provide a convenient way to control electromagnetic properties of the THz devices simply by changing temperature instead of by changing geometrical parameters of the structure.
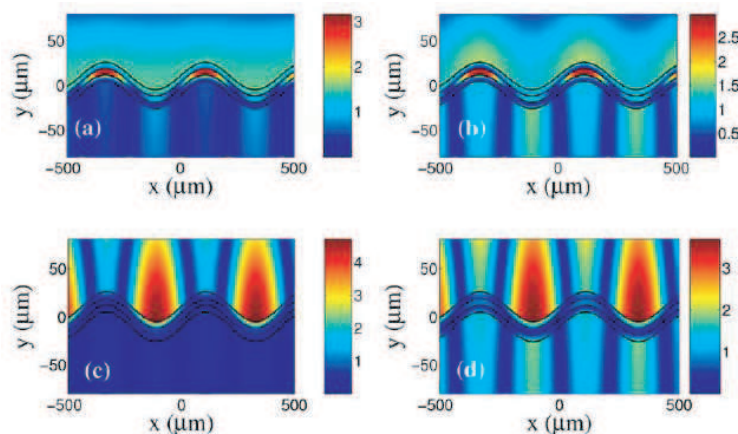
Figure 3: The time-averaged magnetic field H_z distributions at the frequency 0.68 THz and at the temperature of (a) 240 K, (b) 270 K, (c) 295 K and (d) 325 K for the upper InSb layer, respectively.
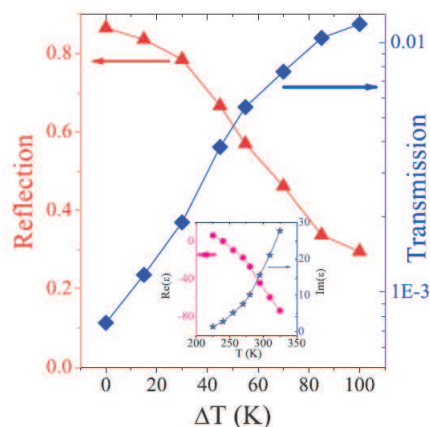
Figure 4: Temperature dependence of the reflection (triangle) and the transmission (diamond) in the stack, which is illuminated by 1.0 THz electromagnetic wave in normal incidence. The inset illustrates the real part (circle) and the imaginary part (pentacle) of the permittivity of InSb as a function of temperature at the frequency of 1.0 THz.

4. CONCLUSIONS

Based on Rayleigh hypothesis, we study the transmission and the reflection influenced by THz SPPs in the periodically corrugated stack of three layers (InSb/Silicon/InSb) when it is illuminated by

THz electromagnetic waves. Starting from the coupled amplitude equations of electromagnetic waves, we obtain the reflectivity and the transmittivity in the perpendicular incidence. It is shown that temperature-dependent THz SPPs are excited, the first-order and the second-order modes are observed. At those resonant modes, the reflections are obviously suppressed, which leads to the reflection dips or Fano-type resonance shape. With increasing the temperature difference of the two InSb films, transmissions increase and reflections decrease significantly. Our investigation indicates that such stacks may achieve potential applications in thermally-controlled Terahertz devices.

ACKNOWLEDGMENT

REFERENCES

1. Rather, H., *Surface Plasmon*, Springer, Hamburg, 1989.
2. Ebbesen, T. W., H. J. Lezec, H. F. Ghaemi, T. Thio, and P. A. Wolff, "Extraordinary optical transmission through sub-wavelength hole arrays," *Nature*, Vol. 391, No. 6668, 667–669, 1998.
3. Barnes, W. L., A. Dereux, and T. W. Ebbesen, "Surface plasmon subwavelength optics," *Nature*, Vol. 424, No. 6950, 824–830, 2003.
4. Genet, C. and T. W. Ebbesen, "Light in tiny holes," *Nature*, Vol. 445, No. 7123, 39–46, 2007.
5. Tang, Z. H., R. W. Peng, Z. Wang, X. Wu, Y. J. Bao, Q. J. Wang, Z. J. Zhang, W. H. Sun, and M. Wang, "Coupling of surface plasmons in nanostructured metal/dielectric multilayers with subwavelength hole arrays," *Phys. Rev. B*, Vol. 76, No. 19, 195405.1–8, 2007.
6. Sánchez-Gil, J. A. and J. Gómez Rivas, "Thermal switching of the scattering coefficients of terahertz surface plasmon polaritons impinging on a finite array of subwavelength grooves on semiconductor surfaces," *Phys. Rev. B*, Vol. 73, No. 24, 205410.1–8, 2006.
7. Gómez Rivas, J., M. Kuttge, H. Kurz, P. H. Bolivar, and J. A. Sánchez-Gil, "Low-frequency active surface plasmon optics on semiconductors," *Appl. Phys. Lett.*, Vol. 88, No. 8, 082106.1–3, 2006.
8. Hendry, E., F. J. Garcia-Vidal, L. Martin-Moreno, J. G. Rivas, M. Bonn, A. P. Hibbins, and M. J. Lockyear, "Optical control over surface-plasmon-polariton-assisted THz transmission through a slit aperture," *Phys. Rev. Lett.*, Vol. 100, No. 12, 123901.1–4, 2008.
9. Ferguson, B. and X. C. Zhang, "Materials for terahertz science and technology," *Nat. Mater.*, Vol. 1, No. 1, 26–33, 2002.
10. Wu, D., N. Fang, C. Sun, X. Zhang, W. J. Padilla, D. N. Basov, D. R. Smith, and S. Schultz, "Terahertz plasmonic high pass filter," *Appl. Phys. Lett.*, Vol. 83, No. 1, 201–203, 2003.
11. Dragomana, D. and M. Dragoman, "Terahertz fields and applications," *Prog. Quant. Electron.*, Vol. 28, No. 1, 1–66, 2004.
12. Siegel, P. H., "THz technology in biology and medicine," *IEEE Trans. Microwave Theory Tech.*, Vol. 52, No. 10, 2348–2447, 2004.
13. Battula, A., Y. Lu, R. J. Knize, K. Reinhardt, and S. Chen, "Tunable transmission at 100 THz through a metallic hole array with a varying hole channel shape," *Opt. Express*, Vol. 15, No. 22, 14629–14635, 2007.
14. Rayleigh, L., "On the dynamical theory of gratings," *Proc. R. Soc. London, Ser. A*, Vol. 79, No. 532, 399–416, 1907.
15. Dutta Gupta, S., G. V. Varada, and G. S. Agarwal, "Surface plasmons in two-sided corrugated thin films," *Phys. Rev. B*, Vol. 36, No. 12, 6331–6335, 1987.
16. Watanabe, T., Y. Choyal, K. Minami, and V. L. Granatstein, "Range of validity of the Rayleigh hypothesis," *Phys. Rev. E*, Vol. 69, No. 5, 056606.1–5, 2004.
17. Elfouhaily, T. and T. Hahn, "Rayleigh's hypothesis and the geometrical optics limit," *Phys. Rev. Lett.*, Vol. 97, No. 12, 120404.1–4, 2006.
18. Madelung, O., *Physics of III-V Compounds*, Wiley, New York, 1964.
19. Van Exter, M. and D. Grischkowsky, "Optical and electronic properties of doped silicon from 0.1 to 2 THz," *Appl. Phys. Lett.*, Vol. 56, No. 17, 1694–1696, 1990.
20. Van Exter, M. and D. Grischkowsky, "Carrier dynamics of electrons and holes in moderately doped silicon," *Phys. Rev. B*, Vol. 41, No. 17, 12140–12149, 1990.

Advancements in Active Multimodal Microwave (SAR) Remote Sensing

Wolfgang-Martin Boerner and Jorge J. Morisaki

ECE/CSN Laboratory, University of Illinois at Chicago, USA

Abstract— Very decisive progress was made in advancing fundamental POL-IN-SAR theory and algorithm development during the past decade, which was based on the underlying accomplishments of fully polarimetric SAR and differential SAR interferometry and its current merger. This was accomplished with the aid of airborne & shuttle platforms supporting single-to-multi-band multi-modal POL-SAR and also some POL-IN-SAR sensor systems, which will be compared and assessed with the aim of establishing the hitherto not completed but required missions such as tomographic and holographic imaging. Because the operation of airborne test-beds is extremely expensive, aircraft platforms are not suited for routine monitoring missions; those are better accomplished with the use of drones (UAV). Such unmanned aerial vehicles (drones) were hitherto developed for defense applications, however currently lacking the sophistication for implementing advanced forefront POL-IN-SAR technology.

1. INTRODUCTION

Very decisive progress was made in advancing fundamental POL-IN-SAR theory and algorithm development during the past decade [1], which was based on the underlying accomplishments of fully polarimetric SAR [2, 3] and differential SAR interferometry [3, 4] and its current merger [5]. This was accomplished with the aid of airborne & shuttle platforms supporting single-to-multi-band multi-modal POL-SAR and also some POL-IN-SAR sensor systems, which will be compared and assessed with the aim of establishing the hitherto not completed but required missions such as tomographic and holographic imaging. Because the operation of airborne test-beds is extremely expensive, aircraft platforms are not suited for routine monitoring missions; those are better accomplished with the use of drones (UAV). Such unmanned aerial vehicles (drones) were hitherto developed for defense applications, however currently lacking the sophistication for implementing advanced forefront POL-IN-SAR technology. This shortcoming will be thoroughly scrutinized resulting in the finding that we do now need to develop most rapidly also POL-IN-SAR drone-platform technology especially for environmental stress-change monitoring subject to severe operational constraints due to adverse unsafe flight conditions with a great variance of applications beginning with flood, bush/forest-fire to tectonic-stress (earth-quake to volcanic eruptions) for real-short-time hazard mitigation. However, for routine global monitoring purposes of the terrestrial covers neither airborne sensor implementation — aircraft and/or drones — are sufficient; and there-fore multi-modal and multi-band space-borne POL-IN-SAR space-shuttle and satellite sensor technology needs to be further advanced at a much more rapid pace. The existing ENVISAT and ALOS-PALSAR with the forthcoming RADARSAT-2, and the TERRASAR 1 & 2 will be compared, demonstrating that at this phase of development the fully polarimetric and polarimetric-interferometric SAR modes of operation must be treated as preliminary algorithm verification support, and at this phase of development are still not to be viewed as routine modes. The same considerations apply to the near future implementation of any satellite-cluster bi/multi-static space-borne tomographic imaging modes, which must however be developed concurrently in collaboration of all major national or joint continental efforts in order to reduce proliferation of space-platforms and for cost-cutting reasons. Prioritization of developmental stages will be assessed according to applications, and will differ for air-borne to space-borne sensors with the aim of developing a permanently orbiting fleet of equidistantly space-distributed satellites — similar to the GPS configuration, however each equipped with the identical set of multi-band POL-IN-SAR sensors.

2. ADVANCES IN SAR POLARIMETRY AND POL-IN-SAR TECHNOLOGY

Radar polarimetry and polarimetric SAR theory, algorithm development and technology have developed to a highly matured state although not yet fully driven to the limits of physical realizability [1]. It has been clearly demonstrated beyond an iota of doubt that fully polarimetric (scattering matrix) SAR image data take acquisition — as complicated as it is regarding calibration and validation — provides input for highly improved environmental image feature interpretation

although lacking depth information [2, 3]. Similarly, non-polarimetric (single amplitude) SAR interferometry has provided reasonable Digital Elevation Maps (DEM) however lacking the ability of differentiating the origin of the backscattering returns from which the interferograms are being constructed [6]. This deficiency was overcome with the implementation [7] of the POL-IN-SAR *"polarimetric-interferometric contrast phase optimization methods"* for delineating the canopy, from the under-store versus ground returns so enabling three-dimensional SAR-Imaging. This 3-dim imaging method was further enhanced with the implementation of multiple bistatic (repeat-pass) fully polarimetric *"tomographic"* TOMO-SAR image data take acquisition, which in the limit results in polarimetric SAR holography, from which three-dimensional voluminous imagery of vegetation structures can be reconstructed subject to the sensor frequency and bandwidth [1, 8]. However, what has not yet been demonstrated is how *"fully polarimetric Differential SAR interferometry"* — based on multiple repeat-pass POL-IN-SAR imagery — will improve the three-dimensional depiction of lateral, sheared and torsionally skewed surface and volumetric underburden deformations, which is one of the major unresolved research topic to be addressed in the forthcoming decade [9].

3. COMPARISON OF AIRBORNE MULTI-BAND POL-SAR & POL-IN-SAR TEST PLATFORMS

There by now exist about 15 or more aircraft-platforms for supporting POL-SAR and some also POL-IN-SAR imaging capabilities, but not a single one of them was designed to satisfy the ideal performance conditions for conducting Multi-band POL-IN-SAR Imaging. This is truly a very sore dilemma and ought to be removed by realizing the design of the ideally designed *POL-IN-SAR Aircraft Imaging Platforms*. From a thorough comparison it seems that currently the DLR ESAR, the CRL PISAR and the ONERA RAMSES multi-band POL-(IN)-SAR are leading in advancing this vital remote sensing technology, and also have integrated high-precision repeat-pass GPS co-registration capabilities. In order for realizing fully Polarimetric (scattering matrix) Differential SAR Interferometry both the ideal platform design for sustaining on-board POL-IN-SAR imaging and highest possible precision of GPS co-registration become paramount [1, 3, 9]. Definitely, for the testing of novel multi-modal imaging algorithms aircraft platforms will be required for a long time to come, and therefore design of aircraft dedicated for SAR-imaging missions is fully justified.

4. NEED FOR DEVELOPING DRONES (UAV) MONITORING PLATFORMS WITH MULTI-BAND POL-SAR AND POL-IN-SAR REPEAT-PASS IMAGING CAPABILITIES

The maintenance and operation of any sophisticated imaging test-aircraft platform requiring crews of three to twelve pilots including the sensor operators such as for Multi-band POL-IN-SAR is extremely costly; and therefore it is justified and necessary to develop rapidly mission dedicated drones (UAV) for carrying out regional routine remote sensing and environmental stress-change monitoring missions. However, the design of such multi-purpose drones must accommodate the most advanced Multi-band POL-SAR and POL-IN-SAR operational modes that had been tested and performance-hardened previously with the aid of the aircraft test-platforms, and also with the aid of the highly successful shuttle SIR-C/X-SAR mission. Under no circumstance must we regress to a *'venerable Landsat technology of the 1970-ies'* as impressive as those products truly are; and the remote sensing SAR user's community must wake up and be challenged to utilize the immense additional novel monitoring capabilities *Multi-band POL-IN-SAR* sensors have to offer, and especially with the aid of less costly drones. Indeed, we do now need to develop most rapidly the most advanced POL-IN-SAR drone-platform technology especially for environmental stress-change monitoring subject to severe operational constraints due to adverse unsafe flight conditions with a great variance of applications beginning with flood, bush/forest-fire to tectonic-stress (earth-quake to volcanic eruptions) for real-short-time hazard mitigation.

5. ACCELERATION OF ADVANCEMENT OF MULTI-BAND POL-SAR AND POL-IN-SAR SENSOR TECHNOLOGY FOR SHUTTLE AND SATELLITE DEPLOYMENT

One of the most successful and ingenious space-borne remote sensing accomplishments was that of the two SIR-C/X-SAR missions of April and September/October 1994 demonstrating at C-Band & L-Band how useful and irreplaceable fully polarimetric SAR image acquisition also from space truly is. More so, its well co-registered sets of repeat-pass C&L-Band POL-SAR image data takes along the Baikal rift zone of Inner Asia made possible the testing and verification of the novel POL-IN-SAR algorithms developed by Cloude and Papathanassiou [6] at DLR. In hindsight,

some of us be-mourn (*or are still weeping bitterly about*) the fact that it was not possible to make the otherwise rather successful SRTM mission also fully polarimetric because so much more could have been gained on properly determining global vegetation cover and in highly improved soil parameter acquisition [9]. Therefore, we desire to have that SRTM mission concept be enlarged and extended to include a fully polarimetric X/C/L/P-multi-band POL-IN-SAR performance capability and to have it redone at the earliest possible date. In fact, all of the brilliantly designed and *executed "SAR Remote Sensing Shuttle Missions"* were so successful and irreplaceable for the rapid advancement of satellite-borne SAR technology so that those must not be abandoned but continued. As regards the advancement of Space-SAR technology a crucial milestone was achieved during the recent ESA POLinSAR-03 Workshop [8] during which the implementation of fully polarimetric (scattering matrix) SAR modes for all future satellite-born SAR systems of ESA, DLR, NASA and also NASDA was in essence decided, and the first step in this direction was achieved with the successful launches of ENVISAT (ASAR) and of ALOS (PAL-SAR), and then towards Fall 2006 RADARSAT-2 and of TERRASAR following soon thereafter. Here, it needs to be emphasized that to consider the implementation of the fully polarimetric POL-SAR and the POL-IN-SAR capabilities to be just another *"technology push"* is absolutely unacceptable in that it has been demonstrated beyond any further doubt that proper and more correct biomass and soil estimation parameters [9–12] can only be obtained with multi-band POL-IN-SAR imagery. Similarly it will be shown shortly that more correct and complete lateral, sheared and torsion-twisted surface and volumetric underburden deformations can only be recovered with onboard POL-IN-SAR satellite sensors operated in contiguous repeat-pass orbital modes.

6. BI-STATIC MULTI-BAND POL-IN-SAR SATELLITE CLUSTERS & DEVELOPMENT OF PERMANENT FLEET OF MULTI-BAND POL-IN-SAR SATELLITES

In order to improve the detection capability of objects occluded under vegetation cover from space, it is necessary to implement tomographic and holographic imaging principles — next to frequency diversity — and for space-SAR satellite implementation that asks for the design of orbiting clusters of equidistantly gyrating satellites as proposed with the ESA Cartwheel and the USAF High-Tech Space-SAR concepts. Although somewhat more sophisticated, the implementation of fully polarimetric POL-SAR sensors for each of the symbiotic cluster sub-satellites must also be developed and it is feasible. The space SAR cartwheel concept can only be viewed as the a partial forerunner of developing the orbiting fleet of equidistantly grid-distributed multi-modal multi-band POL-IN-SAR satellites very similar to the configuration of equidistantly grid-distributed GPS satellites; however in the imaging case replacing each of the orbiting individual satellites by a cluster of three to eight parasitic satellites gyrating around a central POL-IN-SAR Transceiver Satellite and each one carrying a set of multi-modal multi-band POL-IN-SAR sensors.

7. CONCLUSION

By means of placing such an orbiting fleet of satellites into space — *in the long run* — will reduce the exorbitant cost for establishing a viable *"home-globe security protection"* technology. It will provide rather accurate global change data E eventually on an hourly basis accessible to all who need to know. The pertinent National and International airborne and space borne multi-modal, multi-band SAR remote sensing and security conflict surveillance support agencies are herewith invited for co-sponsoring our proposal as time proceeds, in that it is timely and POLinSAR platforms are urgently required to be placed into space [1–3, 8–12].

REFERENCES

1. Boerner, W.-M., "Recent advances in extra-wideband polarimetry, interferometry and polarimetric interferometry in synthetic aperture remote sensing and its applications," *IEE Proceedings, Radar Sonar and Navigation*, Special Issue EUSAR-02, June 2003.
2. Boerner, W.-M., H. Mott, E. Lüneburg, C. Livingston, B. Brisco, R. J. Brown, and J. S. Paterson with contributions by S. R. Cloude, E. Krogager, J. S. Lee, D. L. Schuler, J. J. van Zyl, D. Randall P. Budkewitsch, and E. Pottier, "Polarimetry in radar remote sensing: Basic and applied concepts," *Principles and Applications of Imaging Radar*, F. M. Henderson and A. J. Lewis, (Eds.), Ch. 5, *Manual of Remote Sensing*, R. A. Reyerson, (Ed.), 3rd Ed., Vol. 2, 940, John Willey & Sons, New York, 1998.
3. Massonet, D. and K. L. Feigl, "Radar interferometry and its application to displaying stress-changes in the earth's crust," *Review of Geophysics*, Vol. 36, No. 4, 441–500, Nov. 1998.

4. Pottier, E., S. R. Cloude, and W.-M. Boerner, "Recent development of data processing in polarimetric and interferometric SAR," *Proc., URSI-GA-02*, Maastricht, NL, (edited by R. W. Stone); Also see: ibid, Invited Paper, Radio Science Bulletin No. 304, 48–59, March 2003.

5. Ouchi, K., *Principles of Synthetic Aperture Radar for Remote Sensing*, Tokyo Denki University Press, Tokyo, 2004.

6. Cloude, S. and K. Papathanassiou, "Polarimetric SAR interferometry," *IEEE Trans. Geosci. Remote Sensing*, Vol. 36, No. 4, 1551–1565, 1998; (also see: Papathanassiou, K. P., "Polarimetric SAR interferometry," Ph.D Thesis, Tech. Univ. Graz (ISSN 1434-8485 ISRN DLR-FB-99-07), Graz, Austria, 1999).

7. Reigber, A. and A. Moreira, "First demonstration of airborne SAR tomography using multi-baseline L band data," *IEEE Transactions on Geosciences and Remote Sensing*, Vol. 38, No. 5, 2142–2152, September 2000; (see: Reigber, A., "Polarimetric SAR tomography," Dissertation, Uni. Stuttgart, October 15, 2001).

8. Yajima, Y., Y. Yamaguchi, H. Yamada, and W.-M. Boerner, "POLSAR image analysis of wetlands using modified four-component scattering power decomposition," *IEEE-GRSS Trans.*, submitted, March 12, 2007; (Yamaguchi, Y., Radar Polarimetry from Basics to Applications, Lecture Monograph, Niigata University, in Japanese, January 1, 2007).

9. Park, S.-E., J.-S. Kim, W. M. Moon, and W.-M. Boerner, "Inversion of surface parameters from NASA/JPL AIRSAR polarimetric SAR data takes," *Proceedings POLinSAR-07*, 6, ESA-ESRIN, Frascati, Italy, in print, January 22–26, 2007.

10. Chen, K. S., T. D. Wu, L. Tsang, Q. Li, J. C. Shi, and A. K. Fung, "The emission of rough surfaces calculated by the integral equation method with a comparison to a three-dimensional moment method simulations," *IEEE Trans. GRSS*, Vol. 41, No. 1, 1–12, 2003.

11. Lee, J. S., W.-M. Boerner, D. L. Schuler, T. L. Ainsworth, I. Hajnsek, K. P. Papathanassiou, and E. Lüneburg, "A review of polarimetric SAR algorithms and their applications," *Journal of Photogrammetry and Remote Sensing*, Vol. 9, No. 3, 31–80, September 2004.

Target Detection beneath Canopy Using PolSAR Images

C. F. Hu[1, 2], J. D. Xu[1], N. J. Li[2], and L. X. Zhang[2]

[1]Electronic Engineering Department, Northwestern Polytechnic University, China
[2]National Key Laboratory of UAV Specialty Technique
Northwestern Polytechnic University, China

Abstract— Polarization information is applied to detect target underneath forest by synthetic aperture imaging. At first, hard-in-loop PolSAR system is constructed in an anechoic chamber, then the resolution and sampling interval of system are analyzed. In order to obtain accurate polarization data, polarization scattering matrix measurement and calibration method are used. The data of echoes are processed by an improved back-projection algorithm. After comparing the difference of images, target beneath canopy is detected according to the best combination polarization information. In the experiment, a PNA transmits two signals by wide-band antennas, and another two antennas receive returned signals coming back to the PNA. The antennas maintain downward at an incident angle of 20 degrees with ground. The area of scene is $1\,\mathrm{m}^2$, which consists of three fir trees and a scaled tank. The height of trees is about 1meter, and the scaled tank is located beneath trees. The frequency is working at L-band, and the frequency sampling interval is 12.5 MHz. Scanner moves 3 meters along the center of scene, and the spatial sampling interval is 1.5 cm. The resolutions of cross-range and ground-range are 0.17 m and 0.15 m respectively. The results show that HH polarization image has a good effect for target detection beneath canopy at L-band.

1. INTRODUCTION

Microwave sensors are often used to detect targets for its advantage of penetrability, as well as being able to work all daylong [1]. Generally, forest vegetation exhibits different properties in different polarization of electromagnetic waves [2]. Therefore, it's important to investigate mutilpolarization information for knowing characteristics of spatial distribution, and then recognize the targets beneath canopy according to the appropriate combination of polarization [3, 4].

Synthetic Aperture Radar (SAR) is a kind of high resolution radar system [5]. After dealing with the echoes at many regular positions, a high resolution microwave image of irradiated area is got, and if some transcendental knowledge is known, we can recognize the targets. In this paper, the hard-in-loop PolSAR system is constructed in an anechoic chamber, then a scaled tank beneath three firs is measured on L-band. Four polarization images are obtained by improved back-projection algorithm. Finally, some crucial conclusions are given.

2. THE HARD-IN-LOOP POLSAR SYSTEM

The system was constructed in the anechoic chamber of National Key Laboratory of UAV Specialty Technique (shown in Figure 1). It consists of four parts: scanner, vector network analyzer, wideband antennas, and scene. The scanner can move along three mutual vertical axes, which simulates the airborne SAR flight path. A vector network and four wideband antennas constitute the entire radar system that can transmit and receive signals on two different channels simultaneously. The antennas maintain downward at an incident angle of 20 degrees with ground. The area of scene is 1 square meter, which consists of three fir trees and a scaled tank beneath the trees. The experiment performed on L-band. The frequency sampling interval is 12.5 MHz. The scanner moves 3 meters along the centre of scene, and the spatial sampling interval is 1.5 cm.

Back-projection arithmetic is a kind of time-domain processing method, which can reconstruct two-dimension image accurately [6], so it's practical to obtain exact imaging in laboratory. However, it requires the sampling data on a circular arc; therefore, the echoes gained from linear path must be interpolated into an arc route whose center is where the target locates, and its radius is distance from target to the middle of linear path. Then the relationship between image and the measured electric field is shown in Equation (1):

$$\hat{g}(x, y) = \int\limits_{\theta_{\min}}^{\theta_{\max}} \int\limits_{k_{\min}}^{k_{\max}} kG(k, \theta) \exp[j2\pi k(y \cos \theta - x \sin \theta)] \mathrm{d}k \mathrm{d}\theta \tag{1}$$

where, the coordinate x-y is fixed on target, $\hat{g}(x,y)$ is the two-dimension image of target.

Note that integral restrict cannot be satisfied when FFT is used, so $k_{\min}$ must be moved to zero, let $B' = k_{\max} - k'_{\min}$, B' is the bandwidth of spatial frequency k, then

$$P_\theta(l) = \int_0^{B'} (k + k_{\min}) \, G\left(k + k_{\min}, \theta\right) \exp(j2\pi kl) \mathrm{d}k \tag{2}$$

$$\hat{g}(x,y) = \int_{\theta_{\min}}^{\theta_{\max}} P_\theta(l) \exp\left(j2\pi k_{\min} l\right) \mathrm{d}\theta \tag{3}$$

$$l = y \cos\theta - x \sin\theta \tag{4}$$

As the frequency of signal is discrete, therefore, $k = n \cdot B'/N$, $n = 0, 1, 2, \ldots, N-1$, where N is the points of frequency. Then Equation (2) can be described as follows:

$$P_\theta(l) = \sum_{k=0}^{(N-1)B'/N} \left(\frac{B'}{N} \cdot n + k_{\min}\right) G(n,\theta) e^{j2\pi \frac{B'}{N} \cdot n \cdot l} \tag{5}$$

The summation can be done by a FFT, and the image is obtained after integral at all angles.

$$\hat{g}(x,y) = \int_{\theta_{\min}}^{\theta_{\max}} P_\theta(l) \exp\left(j2\pi k_{\min} l\right) \mathrm{d}\theta = \sum_\theta P_\theta(l) e^{j2\pi k_{\min} l} \tag{6}$$
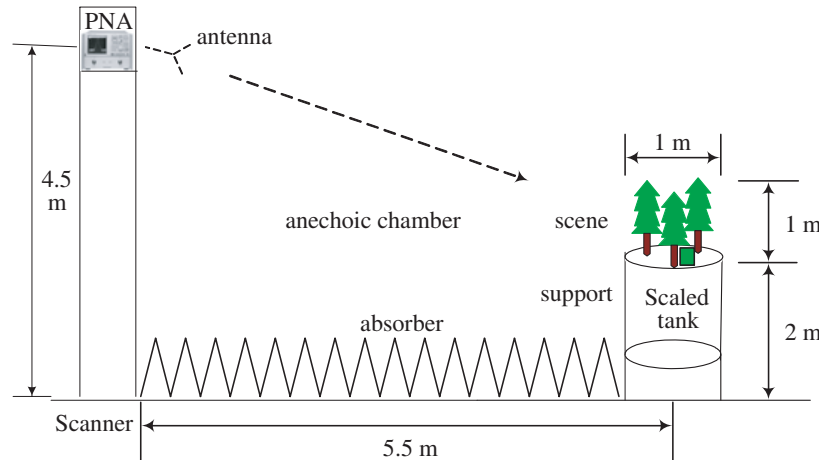
Figure 1: The hard-in-loop PolSAR system.

3. EXPERIMENTAL RESULTS

Four combination of different polarization are got by the hard-in-loop PolSAR system, moreover, the canopy with scaled tank and without it inside are given in the following figures. The range resolution of images is $0.15\,\mathrm{m}$ according to the bandwidth of L-band used, and the azimuth resolution is $0.17\,\mathrm{m}$ determined by the moved distance of scanner.

Some conclusions can be made as follows:

(1) The scattering of leaves and branches does not appear in all the images, so it shows that microwave at L-band has good penetrability in forest.

(2) The strong echoes of each image mainly result from the scattering of soil at bottom of trees and repetition reflection between the soil and branches, and they produce lots of cross-polarization energy. However, the returns of tank are mostly identical-polarization wave.

(3) The quality of images is coarse because the resolution of L-band is low. However, compared to the canopy without scaled tank, the location of tank can be recognized from the HH polarization image when it hides beneath the trees. The tank lies on the middle of back trees, takes up two cells at cross-range and one cell at ground-range. The size and position is identical to the information set before. These characteristics will not be seen in other pictures. They manifest the advantage of mutil-polarization that we can choose the best combination of polarization when scene is complex.

(a) fir trees   (b) scaled tank hidden in the trees
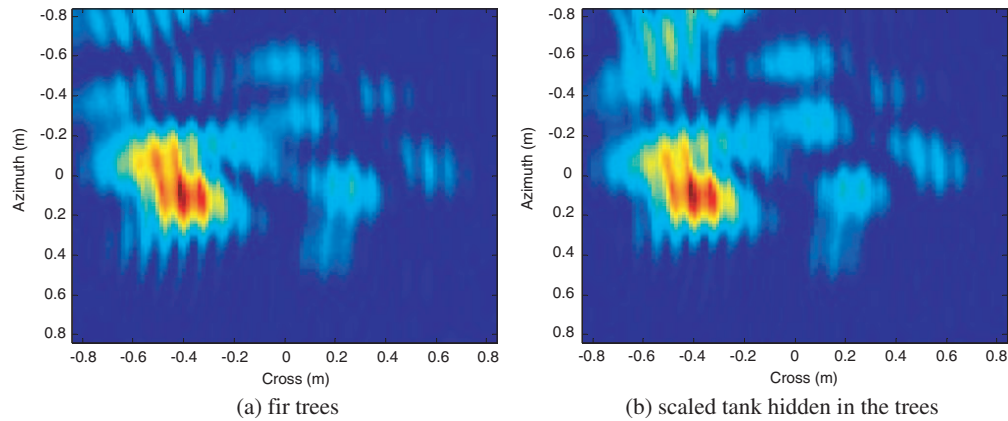
Figure 2: Image of VV polarization on L-band.

(a) fir trees   (b) scaled tank hidden in the trees
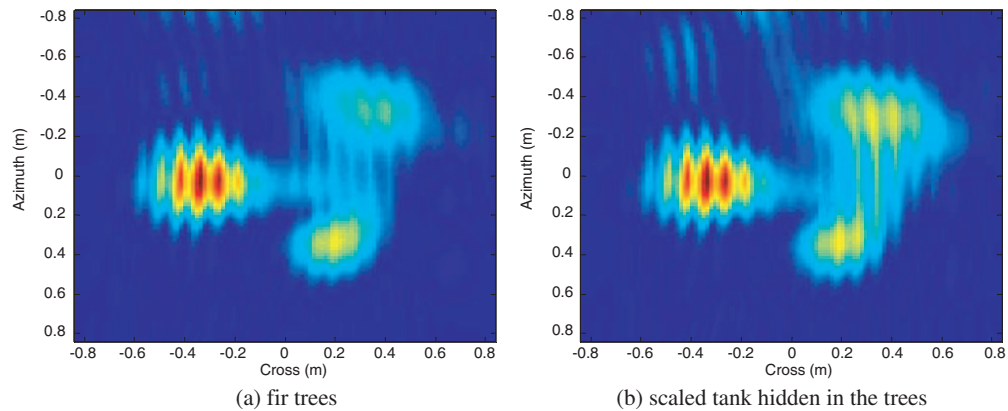
Figure 3: Image of VH polarization on L-band.

(a) fir trees   (b) scaled tank hidden in the trees
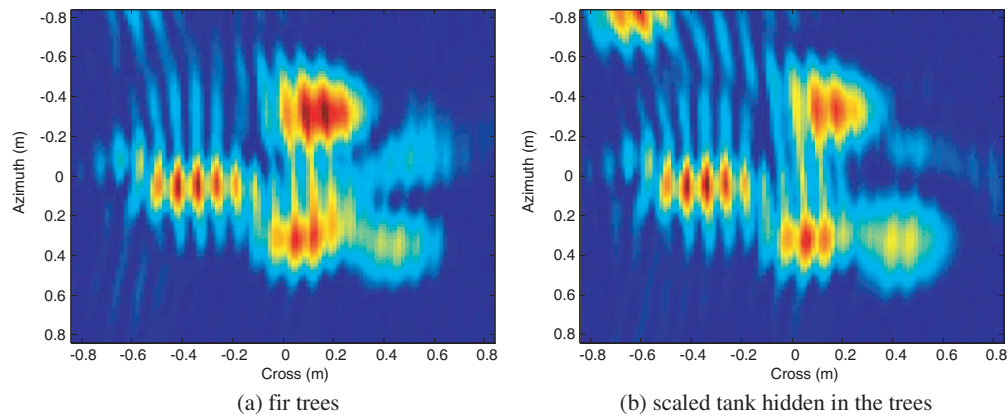
Figure 4: Image of HV polarization on L-band.

(a) fir trees

(b) scaled tank hidden in the trees
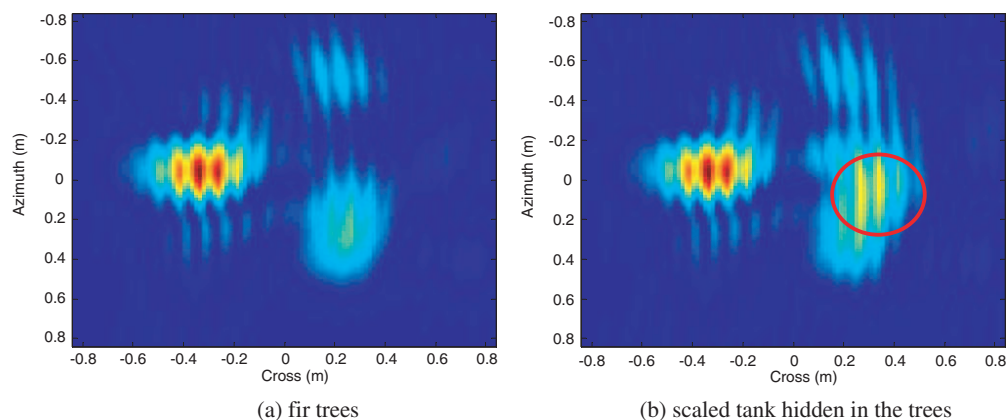
Figure 5: Image of HH polarization on L-band.

4. CONCLUSION

From the former description, it's natural to see that the microwave on L-band has good penetrability in forest, and which can be applied to detect metal target beneath canopy, moreover, when the polarization information are used, the veracity of reorganization can be obviously improved. This paper also provides some basic data of soil and fir tree on L-band. The polarization characteristics of other bands will be investigated for the future.

ACKNOWLEDGMENT

REFERENCES

1. Elachi, C., *Introduction to the Physics and Techniques of Remote Sensing*, Wiley, New York, 1987.

2. Hirosawa, H., Y. Matsuzaka, and O. Kobayashi, "Measurement of microwave backscatter from a cypress with and without leaves," *IEEE Geosci. Remote Sensing*, Vol. 27, No. 6, 698–701, 1989.

3. Cloude, S. R., D. G. Corr, and M. L. Williams, "Target detection beneath foliage using polarimetric SAR interferometry," *Waves Random Media*, Vol. 14, No. 2, 393–414, 2004.

4. Cloude, S. R. and M. L. Williams, "The negative alpha filter: A new processing technique for polarimetric SAR interferometry," *IEEE Geosci. Remote Sensing*, Vol. 2, No. 2, 187–191, 2005.

5. Curlander, J. C. and R. N. McDonough, *Synthetic Aperture Rader Systems & Signal Processing*, Wiley, New York, 1991.

6. Hu, C. F., P. Li, N. J. Li, and L. X. Zhang, "The modeling and simulation of a near-distance microwave imaging system," *Proceeding of 5th International Conference on Microwave and Millimeter Wave Technology (ICMMWT)*, 472–474, Guilin, China, 2007.

An Inverse Model for Sea Ice Thickness Retrieval Using Active Microwave Remote Sensing

Y. J. Lee[1], **W. K. Lim**[1], **H. T. Ewe**[2], **and H. T. Chuah**[2]

[1]Multimedia University, Malaysia
[2]Tunku Abdul Rahman University, Malaysia

Abstract— Sea ice encompasses a large area within the polar region and greatly influences the earth's climate system. One particular sea ice parameter of interest in understanding the dynamics of the sea ice cover and the heat exchange between the ocean and the atmosphere is its thickness. Due to this, there has been an increase in interest towards research in the polar region. Yet the harsh environment proves a great challenge to scientists doing research in those regions. The use of microwave remote sensing to retrieve physical data of the polar region, in particular sea ice thickness serves as a practical solution to the problem. In this paper, an RT-DMPACT Inverse Model to retrieve sea ice thickness from active microwave remote sensing data is presented. The inverse model is a combination of the Radiative Transfer Theory with Dense Medium Phase and Amplitude Correction Theory (RT-DMPACT) forward model and the Levenberg-Marquardt Optimization algorithm. The RT-DMPACT forward model is an improved forward model and is applied to generate the radar backscatter data, where the DMPACT is included to account for the close spacing effect among the scatterers within the medium. The Levenberg-Marquardt Optimization algorithm is then applied to improve on the set of input parameters until the sea ice thickness can be estimated. Data from ground truth measurements carried out in Ross Island, Antarctica, such as sea ice surface roughness and temperature, together with radar backscatter data extracted from purchased satellite images, are used as inputs to estimate the sea ice thickness in an area. The estimated sea ice thickness is then compared with the ground truth measurement data to verify its accuracy. The results from the simulation show promise towards the use of the RT-DMPACT inverse model to retrieve sea ice thickness from actual conditions in the polar region.

1. INTRODUCTION

In recent years, the study of the earth's polar region has grown dramatically, driven by a variety of reasons. With the increasing awareness on global climate change and the fact that sea ice, covering up to 25% of the earth's surface, plays a critical role in balancing the world climate, many studies are being directed towards the sea ice extent and the heat exchange between the ocean and the atmosphere [1]. Yet, such research can be both costly and dangerous, due to the extremity of the polar region's climate and weather [2]. The application of microwave remote sensing in the polar region offers a practical means to monitor and retrieve data from the harsh continent. In order to do this however, an inverse model needs to be first developed to retrieve the sea ice parameters from the radar backscatter data obtained from remote sensing.

From various reports in the literature, it is known that the sea ice thickness plays an important factor in understanding the dynamics of the sea ice cover as well as the air-ocean heat exchange. Several methods of inverse scattering algorithms for the recovery of sea ice thickness have been explored and reported [3]. Four approaches to recover sea ice thickness were presented: Radiative Transfer-Thermodynamic Model for Thickness Retrieval from Time-Series Scattering Data, Neural Network Inversion for Sea Ice Thickness, Reflectivity Inversion for Sea Ice Thickness and Proxy Indicators for Sea Ice Thickness.

In this paper, an inversion algorithm that is a combination of the Radiative Transfer-DMPACT Forward Model and the Levenberg Marquardt Optimization Algorithm is presented. The forward model is an improved model that is applied to calculate the expected backscatter data. It considers the sea ice as an electrically dense random discrete media [4], where the Dense Medium Phase and Amplitude Correction Theory (DMPACT) is included in the phase matrix of the scatterers to take into account the close spacing effect among the scatterers [5]. The Levenberg Marquardt Optimization Algorithm is then applied to reduce the error between the results from the forward model and the radar backscatter data extracted from satellite images. Finally, a comparison is made between the inversed sea ice thickness and the actual sea ice thickness measured during the ground truth measurements carried out in Ross Island, Antarctica.

2. RT-DMPACT INVERSE MODEL FOR SEA ICE THICKNESS RETRIEVAL

This model is based loosely on the Radiative Transfer-Thermodynamic Inverse Model for Sea Ice Thickness from Time-Series Scattering Data [6]. The original model utilized the Radiative Transfer Theory to provide the relationship between the expected backscatter measurements to the radar parameters and the sea ice characteristics. A growth model for saline ice is also applied to more accurately predict the evolution of the sea ice growth through the use of time-series measured data. The Levenberg Marquardt Optimization method is then used to adjust the parameters and estimate the sea ice thickness.

However, while the algorithm was successful towards the reconstruction of sea ice thickness from time series electromagnetic measurements of laboratory grown sea ice [7], it has yet to be tested under actual conditions. In addition, the collection of time series measurements using active microwave remote sensing can be tedious and expensive. Therefore, the new algorithm developed is a variation of the above model and aims to explore the possibility of inverting sea ice thickness through the use of the Radiative Transfer Theory without the use of time series measurements.

The flow chart of the developed RT-DMPACT inverse model is shown in Figure 1 below.
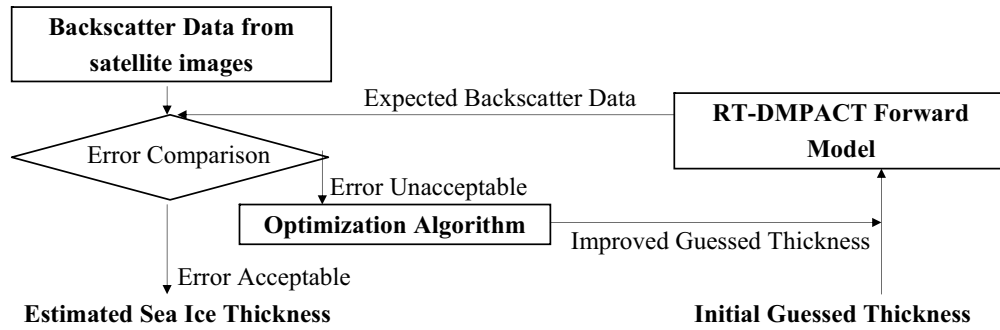
Figure 1: Flow chart of inversion algorithm using RT-DMPACT.

For the developed inverse model, the RT-DMPACT Forward Model is used to calculate the expected backscatter data from a set of sea ice parameters. The output from the forward model is used to compare with actual radar backscatter data extracted from Synthetic Aperture Radar (SAR) measurements using satellites, like the RADARSAT. The configuration for the RT-DMPACT Model is shown in Figure 2.
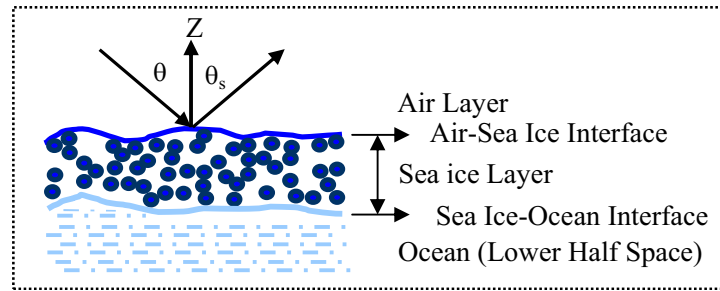
Figure 2: Model configuration for RT-DMPACT forward model.

The classical formulation of the Radiative Transfer equation, is given by:

$$\cos\theta \frac{d\overline{I}}{dz} = -\overline{\overline{\kappa}}_e \overline{I} + \int \overline{\overline{P}}\,\overline{I}\,d\Omega \tag{1}$$

where I, κ_e, P, $d\Omega$ and z are the Stokes vector, extinction matrix, phase matrix of the medium, solid angle and vertical direction, respectively [8]. The phase matrix P has the following expression:

$$\overline{\overline{P}}(\theta, \phi; \theta', \phi') = \langle |\psi|^2 \rangle_n \cdot \overline{\overline{S}} = \begin{bmatrix} P_{vv} & P_{vh} \\ P_{hv} & P_{hh} \end{bmatrix} \tag{2}$$

where $\langle|\psi|^2\rangle_n$ is the dense medium phase correction factor and S is the Stokes' matrix for Mie scatterers with the Close Spacing Amplitude Correction [9]. From the previous equation, $\langle|\psi|^2\rangle_n$ can be further expressed as:

$$\langle|\Psi|^2\rangle_n = \frac{1 - e^{-k_{si}^2\sigma^2}}{d^3} + \frac{e^{-k_{si}^2\sigma^2}}{d^3} \sum_{q=1}^{\infty} \frac{(k_{si}^2\sigma^2)^q}{q!} \cdot \left[\left(\sqrt{\frac{\pi}{q}}\left(\frac{l}{d}\right)\right)^3 \exp\left(\frac{-k_{si}^2l^2}{4q}\right) - a(k_x)a(k_y)a(k_z)\right] \quad (3)$$

where

$$a(k_r) = \sqrt{\frac{\pi}{q}}\left(\frac{l}{d}\right)\exp\left(\frac{-k_r^2l^2}{4q}\right)\mathrm{Re}\left\{erf\left(\frac{(qd/l) + jk_rl}{2\sqrt{q}}\right)\right\} \quad (4)$$

The inverse model utilizes the Levenberg Marquardt Optimization Method to reduce the sum of squares of the deviation between the simulated radar backscatter data (σ_{HH}) and the actual radar backscatter data from the satellite so that it becomes minimal. The optimization algorithm achieves this by improving on the guess of the sea ice thickness.

In the retrieval process, a set of sea ice parameters is first input into the RT-DMPACT Forward Model. Among these parameters, one of them is the sea ice thickness, which is initially guessed. The other parameters are assumed as known parameters and are obtained from the ground truth measurement. The forward model will then calculate the expected backscatter coefficient. A comparison is then made between the simulated backscatter coefficient with another set of backscatter coefficient extracted from satellite images purchased from the Canadian RADARSAT. The Levenberg Marquardt Optimization Algorithm is then applied to improve on the sea ice thickness guess and reduce the deviation between the two sets of backscatter coefficient. This process will repeat itself until the simulated backscatter coefficient from the forward model matches as close as possible to the satellite backscatter coefficient. The final estimated sea ice thickness is then compared with the sea ice thickness recorded during the ground truth measurement to verify its accuracy.

3. RESULTS AND DISCUSSION

In order to test the effectiveness of the developed inverse model in estimating the sea ice thickness from radar backscatter data, simulations were carried out using ground truth measurement data from the years 2006 and 2007. As the satellite image acquired for both years were from RADARSAT, only HH polarization radar backscatter data was utilized. For the simulations, the frequency is fixed at 5.3 GHz and the incident angle at 25°. Due to the single layer configuration of the forward model, only first year sea ice sites were used for the simulation as these sites were absent of the snow layer, thus matching the model configuration.

Four first year sea ice sites were chosen during the ground truth measurement for 2006. Figure 3 displays the results of the sea ice thickness estimation compared with the actual sea ice thickness obtained from the ground truth measurement for the year 2006. The graph shows a good match between both sets of sea ice thickness.
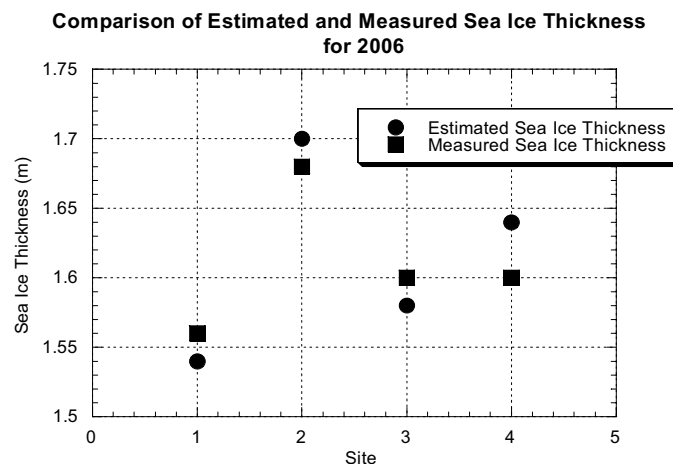

Figure 3: Sea ice thickness estimation results for sites from 2006.

Figure 4 shows the result of the sea ice thickness estimation for the year 2007. Again, the graph shows a close match between the estimated and actual sea ice thickness. However, for 2007, only one first year sea ice site is shown due to two factors. The first factor is the change in measurement procedure compared to 2006. For 2007, the data for each site contains the average values of three measurements collected at three points in close proximity within the site, as opposed to just a single measurement at one point in each site as done in 2006. This is to obtain better accuracy of the data from the measurements. The second factor is due to bad weather, which caused the measurement trip to be abandoned midway and as a result fewer sites were visited.
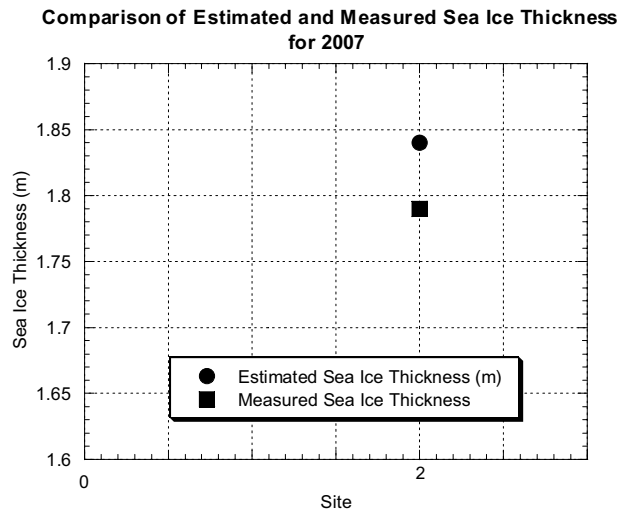
Figure 4: Sea ice thickness estimation results for sites from 2007.

4. CONCLUSION

In this paper, a RT-DMPACT inverse model for sea ice thickness retrieval is presented. From simulations with data obtained from ground truth measurement carried out in Ross Island in the years 2006 and 2007, the model has shown promising results towards the retrieval of sea ice thickness using single polarization active microwave remote sensing data.

ACKNOWLEDGMENT

REFERENCES

1. Haykin, S., E. O. Lewis, R. K. Raney, and J. R. Rossiter, *Remote Sensing of Sea Ice and Iceberg*, John Wily & Sons, Inc., 1994.

2. Veysoglu, M. E., H. T. Ewe, A. K. Jordan, R. T. Shin, and J. A. Kong, "Inversion algorithms for remote sensing of sea ice," *IEEE IGARSS*, 626–628, Pasadena, USA, August 1994.

3. Golden, K. M., D. Borup, M. Cheney, E. Cherkaeva, M. S. Dawson, K. H. Ding, A. K. Fung, D. Isaacson, S. A. Johnson, A. K. Jordan, J. A. Kong, R. Kwok, S. V. Nghiem, R. G. Onstott, J. Sylvester, D. P. Winebrenner, and I. H. H. Zabel, "Inverse electromagnetic scattering models for sea ice," *IEEE Transactions on Geoscience and Remote Sensing*, Vol. 36, No. 5, 1675–1704, 1998.

4. Albert, M. D., H. T. Ewe, and H. T. Chuah, "A theoretical and measurement study of sea ice and ice shelf in antarctica as electrically dense media," *Journal of Electromagnetic Waves and Applications*, Vol. 19, No. 14, 1973–1981, 2005.

5. Chuah, H. T., S. Tjuatja, A. K. Fung, and J. W. Bredow, "A phase matrix for a dense discrete random medium: Evaluation of volume scattering coefficient," *IEEE Transactions on Geoscience and Remote Sensing*, Vol. 34, No. 5, 1137–1143, 1996.

6. Shih, S. E., K. H. Ding, S. V. Nghiem, C. C. Hsu, J. A. Kong, and A. K. Jordan, "Thickness retrieval using time series electromagnetic measurements of laboratory grown saline ice," *Proceedings IEEE IGARSS*, 1208–1210, Lincoln, USA, May 1996.

7. Shih, S. E., K. H. Ding, S. V. Nghiem, C. C. Hsu, J. A. Kong, and A. K. Jordan, "Saline ice thickness retrieval using time series C-band polarimetric radar measurements," *IEEE Transactions on Geoscience and Remote Sensing*, Vol. 36, No. 5, 1589–1598, 1998.

8. Chandrasekhar, S., *Radiative Transfer*, Dover, New York, 1960.

9. Fung, A. K. and H. J. Eom, "A study of backscattering and emission from closely packed inhomogenous media," *IEEE Transactions on Geoscience and Remote Sensing*, Vol. 23, No. 5, 761–767, 1985.

Monitoring Crop Phenology with MERIS Data — A Case Study of Winter Wheat in North China Plain

Jihua Meng, **Bingfang Wu**, **Qiangzi Li**, **Xin Du**, and **Kun Jia**

Institute of Remote Sensing Applications, Chinese Academy of Sciences, China

Abstract— Crop phonology monitoring is an important part of growth monitoring. On the other hand, the analysis on crop phenology can improve the accuracy of crop classification and crop yield estimation. Crop phenology mainly has relation not only to weather variety, but also to the regional planting habit. Crop phonological stages and growth period vary in different areas and different years. With the development of remote sensing technique, the detection of crop phenology and it s mechanism using remote sensing data on regional or global scales have become popular topics in remote sensing applications. The MERIS data can provide time-serial terrestrial parameters at a several-day frequency, with which we can track the growing process of crops (take winter wheat for example) and study its variation in the growing season. The normalized different vegetation index (NDVI) derived from red band and near infrared band of MERIS sensor is a directly remote sensing indicator that reflects crop growth situation. However, due to reasons such as the influence of cloud and atmospheric conditions, the residual noise in the time-series NDVI derived from MERIS will induce erroneous result in crop phenology monitoring. Thus in this study, after the time-series NDVI was computed from MERIS data, a Savitzky-Golay filter was used to smooth out noise in NDVI time-series at pixel scale, and a time-series NDVI dataset at day frequency was produced (reconstructed). Then indicators such as the peak were extracted from the crop NDVI profile for each pixel. After that the relation between these indicators and different phonological stages for winter wheat was analyzed and a model to estimate certain phonological stage for winter wheat was developed from the analysis. The model was validated with the field observation data collected from Fengqiu, Henan province and Yucheng, Shandong province. The validation result shows that the error in monitoring result for Heading Date and Flowering date of winter wheat is less than 3 days.

1. INTRODUCTION

Identification of important phenological stages of crops is essential input to model crop condition and productivity. On the other hand, the analysis on crop phenology can improve the accuracy of crop classification and crop yield estimation. Crop phenology mainly has relation not only to weather variety, but also to the regional planting habit. Crop phonological stages and growth period vary in different areas and different years. With the development of remote sensing technique, the detection of crop phenology and it s mechanism using remote sensing data on regional or global scales have become popular topics in remote sensing applications.

Remote sensing has become the main tool for detecting seasonal vegetation changes at regional or global scale. Various methods using daily Normalized Difference Vegetation Index (NDVI) data have been developed for monitoring crops and natural vegetation (Akiyama et al., 2002; Saito et al., 2002; Xiao et al., 2002). A lot of studies on monitoring the phenological stages of crops have been carried out using AVHRR, VEGETATION and MODIS (Toshihiro, 2005). this article is going to explore the potential of MERIS in this field.

2. STUDY AREA AND DATA DESCRIPTION

2.1. Study Area

Wheat crop monitoring has global importance due to its key position in food security. At the same China is the biggest wheat producing countries in the world whose wheat production accounts for nearly 20% of that of the whole world. Shandong and Henan are the biggest two wheat producing provinces in China, the wheat production of Shandong and Henan province accounts for over 40% of China's total winter wheat production. Due the above reasons, Shandong and Henan are chosen as the monitoring area of the study.

The land use in the area is dominated by the intensive dual-cropping system based on winter wheat and autumn crops, including maize, millet, soybean, cotton and sorghum. Despite a variety of crops in autumn, winter wheat is the dominant summer crop in most areas. According to the traditional tillage practice, winter wheat is sown in early October, harvested in early or mid June next year, and autumn crops are planted in early to mid June and harvested at the end of September

or the beginning of October, from where the cycle is repeated. Due to the large extension of the study area, the phenophase of winter wheat in different places vary in a broad range.

Annual precipitation is about 600 mm, more than 50% of which arrives during the summer monsoon between July and September. Due to the limited and variable precipitation, in spring the winter wheat productivity is only guaranteed by irrigation.

2.2. RS Data

The RS data used in the study is MERIS (MEdium Resolution Imaging Specrometer Instrument). MERIS is one of the sensors on ENVIronmental SATellite (ENVISAT) which was launched by the European Space Agency (ESA) on March 2002. Although MERIS was primarily dedicated to ocean color, its bands configuration broadened its application to vegetation monitoring (Laura Dente, 2008).

The MERIS data can provide time-serial terrestrial parameters at a several-day frequency, with which we can track the growing process of crops (take winter wheat for example) and study its variation in the growing season.

The normalized different vegetation index (NDVI) derived from red band and near infrared band is a directly remote sensing indicator that reflects crop growth situation. The NDVI for each pixel were calculated using red and near infrared (NIR) reflectance as follows

$$NDVI = (NIR - RED)/(NIR + RED) \tag{1}$$

where RED and NIR is canopy reflectance at red and near infrared. As for MERIS, band13 (855–875) and band8 (677.5–685) are assigned as near infrared and red bands.

MERIS data since February to July 2008 covering Shandong and Henan was collected in the frame of the Dragon 2 Program. These data was pre-processed after which NDVI was computed from each scene of MERIS data.

2.3. Basic Data

The 1 : 100,000 land use/cover digital data and land use map is the most important basic data in the study. The land use/cover digital data was derived from Landsat Thematic Mapper (TM) images and was used to identify arable fields.

2.4. Observation Data

Two 5 Km × 5 Km experimental areas are selected in Fengqiu (114 31 32E–35 00 58N, in Henan province) and Yucheng (116 34 09E–36 49 52N, Shandong province). 25 observing points (in 5 300 m × 300 m plots) are distributed in each experimental area. Key phenophases of winter wheat such as heading, flowering and harvesting date were observed and recorded. These data was used not only to calibrate the model, but also to validate the monitoring result.

3. METHODS

The implementation of monitoring key phenophase of winter wheat is described in flowchart shown in Fig. 1.
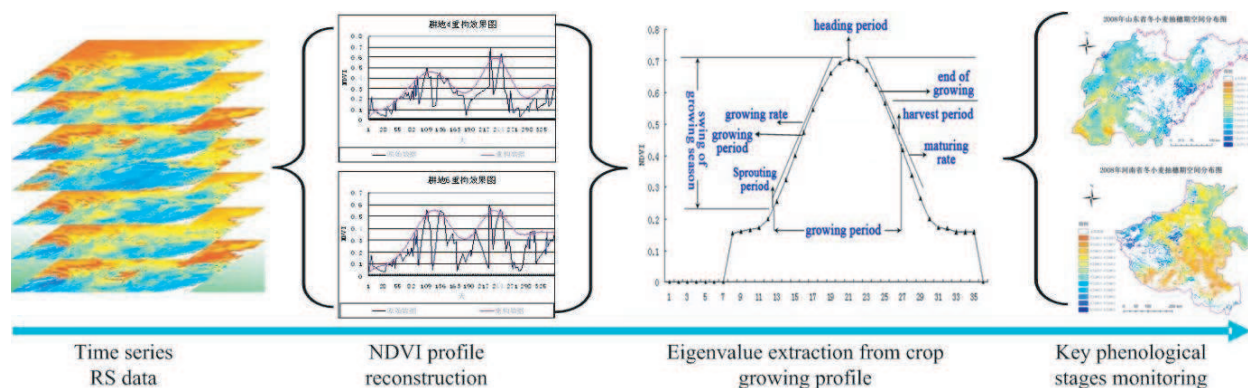

Figure 1: Process flow chart of monitoring winter wheat phenophase.

3.1. Reconstruction of Time Series NDVI

Due to reasons such as the influence of cloud and atmospheric conditions, the residual noise in the time-series NDVI derived from MERIS will induce erroneous result in crop phenology monitoring like other NDVI products (RAO M.V.K, 1982). Thus a Savitzky-Golay filter was used to smooth out noise in NDVI time-series at pixel scale (Jin Chen, 2004), and a time-series noise-free NDVI dataset at day frequency was produced.

One modification was made to the original NDVI-reconstructing algorithm. The changing trend of fitting-effect index we found in this study is different from that in Chen's study (Jin Chen, 2004), which is shown in Fig. 2. So a new threshold was defined to end the iteration of the NDVI profile fitness.

$$\sum_{i=1}^{n} \text{ABS}(\text{NDVI}_{k+1}^{i} - \text{NDVI}_{k}^{i})/n < \text{Threshold}_{\text{dist}} \tag{2}$$

where NDVI_{k+1}^{i} is the ith NDVI value produced in the $(k+1)$th curve fitness, NDVI_{k}^{i} is the ith NDVI value produced in the kth curve fitness, n is the length of time series, $\text{Threshold}_{\text{dist}}$ is the predefined threshold. When the condition in formula (2) was met, the iteration will end and output the reconstructed NDVI curve.
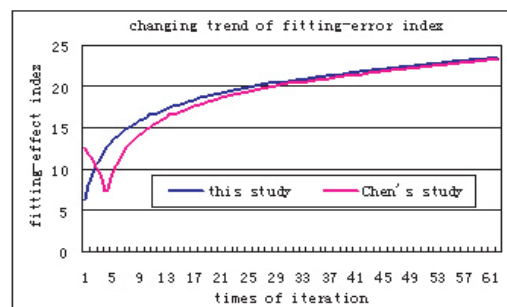
3.2. Determination of Key Phonological Stages

Peak is the most obvious eigenvalue from the crop NDVI profile and it is easy to extract. So the relationships between the date when crop NDVI profile reaches its peak and the key phenological stages were analyzed. Based on the observation data of Fenqiu, we found that the heading date of winter wheat is always 4–5 days later than the date when crop NDVI profile reaches its peak and a model was build to extract the heading data of winter wheat. The similar relationships were analyzed for flowering date and harvest date and models to extract these key phenological stages were also built.

4. RESULTS

Figure 2 shows the monitoring result of heading date (similar to that of flowering and harvesting) for winter wheat in Shandong and Henan.
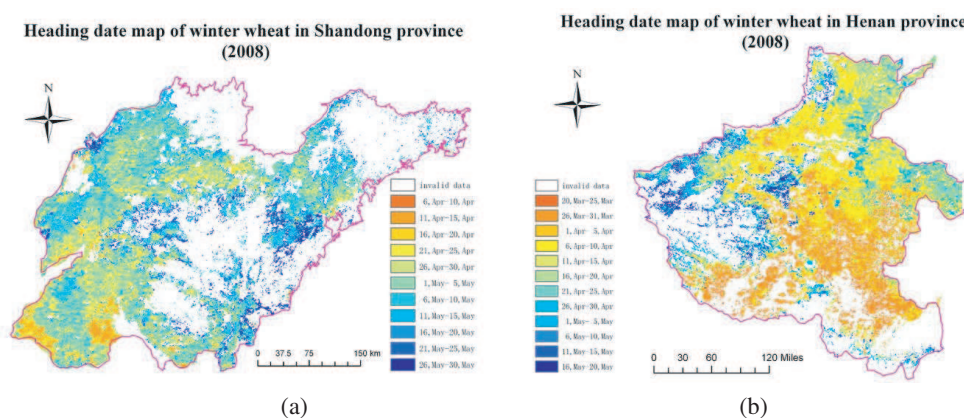
Figure 2: Heading date for winter wheat in Shandong and Henan, (a) Shandong province, (b) Henan province.

In Shandong province, the heading date of winter what is generally earlier in the west than that in the east. While the heading data in Caoxian and Jinxiang can be as early as the middle of April, that of Jiaozhou and Gaomi could be as late as the late of May. A variation of more than one month's in heading date could be found in the province.

As for Henan province, a general trend of earlier in the east and later in the west could be found. The earliest heading date appears in a big area of southeast Henan at the end of March, the latest appears in the east of Henan at the middle of May. A variation of more than one and half a month's in heading date could be found in the province. The heading date of winter wheat in Henan is generally earlier than that in Shandong.

5. CONCLUSION

We have developed a method for detecting the key phenological stages of winter wheat in North China Plain from time series MERIS data. The method consists of three procedures: (i) pre-processing of time series MERIS data; (ii) reconstruct the time series MERIS NDVI by pixel to a day-frequency; and (iii) specifying the key phenological stages from the reconstructed NDVI profile.

This method can determine the heading and flowering harvesting dates for winter wheat with a high precision. As crop calendars are not available in many regions, this method is particularly useful for determination of regional characteristics of winter wheat phenology. We believe that this method also has potential in application to other crops and some natural vegetation.

It was proved that the MERIS data also has an immense potential in time series monitoring of crops. The influence of mixed pixel on the monitoring result and the application of crop phenophase monitoring in crop condition assessment and crop yield forecast are going to be addressed in our future study.

REFERENCES

1. Akiyama, T., K. Kawamura, A. Fukuo, and Z. Z. Chen, "Sustainable grassland management using GIS, GPS and remote sensing data in Inner Mongolia," In S. Uchida, C. Youqi, and G. Saito (Eds.), *Application on Remote Sensing Technology for the Management of Agricultural Resources*, 13–19, Beijing' China Agricultural Scientech Press, 2002.

2. Saito, G., N. Mino, Y. Q. Li, and Y. Yasuda, "Seasonal changes of vegetation index obtained from NOAA/AVHRR data in China and Japan," In S. Uchida, C. Youqi, and G. Saito (Eds.), 107–114, Beijing' China Agricultural Scientech Press, 2002.

3. Xiao, X., S. Boles, S. Frolking, W. Salas, B. III Moore, L. He, et al., "Observation of flooding and rice transplanting of paddy rice field at the site to landscape scales in China using VEGETATION sensor data," *International Journal of Remote Sensing*, Vol. 23, 3009–3022, 2002.

4. Sakamoto, T., M. Yokozawa, H. Toritani, M. Shibayama, N. Ishitsuka, and H. Ohno, "A crop phenology detection method using time-series MODIS data," *Remote Sensing of Environment*, Vol. 96, No. 3–4, 366–374, 2005.

5. Rast, M., J. L. Bezy, and S. Bruzzi, "The ESA medium resolution imaging spectrometer MERIS — A review of the instrument and its mission," *International Journal of Remote Sensing*, Vol. 20, 1681–1702, 1999.

6. Dente, L., G. Satalino, F. Mattia, and M. Rinaldi, "Assimilation of leaf area index derived from ASAR and MERIS data into CERES-Wheat model to map wheat yield," *Remote Sensing of Environment*, Vol. 112, No. 4, 1395–1407, 2008.

7. Rao, M. V. K, R. S. Ayyangar, and P. P. N. Rao, "Role of multispectral data in assessing crop management and crop yield," *Machine Processing of Remote Sensed Data Symposium*, 1982.

8. Chen, J., P. Jonsson, and M. Tamura, et al., "A simple method for reconstructing a high-quality NDVI time-series data set based on the Savitzky-Golay filter [J]," *Remote Sensing of Environment*, Vol. 91, 332–344, 2004.

Passive Microwave Remote Sensing for Sea Ice Thickness Retrieval Using Neural Network and Genetic Algorithm

H. J. Yap[1], **W. K. Lim**[1], **H. T. Ewe**[2], **and H. T. Chuah**[2]

[1]Multimedia University, Malaysia
[2]Tunku Abdul Rahman University, Malaysia

Abstract— Over the years, global warming has gained much attention from the global community. The fact that the sea ice plays an important role and has significant effects towards the global climate has prompted scientists to conduct various researches on the sea ice in the Polar Regions. One of the important parameters being studied is the sea ice thickness as it is a direct key indication towards the climate change. However, to conduct studies on the sea ice scientists are often facing with tough challenges due to the unfavorable harsh weather conditions and the remoteness of the Polar Regions. Thus, microwave remote sensing offers an attractive mean for the observation and monitoring of the changes of sea ice in the Polar Regions for the scientists. In this paper, we will be presenting 2 approaches using passive microwave remote sensing to retrieve sea ice thickness. The first approach involves the training and testing of the neural network (NN) by using data sets generated from the Radiative Transfer Theory with Dense Medium Phase and Amplitude Correction Theory (RT-DMPACT) forward scattering model. Once training is completed, the inversion for sea ice thickness could be done speedily. The second approach utilizes a genetic algorithm (GA) which would perform a search routine to identify possible solutions in sea ice thickness that would match the corresponding brightness temperatures profile of the sea ice. The results obtained from both approaches are presented and tested by using Special Scanning Microwave Imager (SSM/I) data with the aid of the sea ice measurements in the Arctic sea.

1. INTRODUCTION

In order to understand the interactions between the wave and sea ice medium, a forward scattering model based on Radiative Transfer Theory was constructed. This forward scattering model was further improved by incorporating Dense Medium Phase and Amplitude Correction Theory (RT-DMPACT) to take into account of the effect of the closely placed scatterers in the sea ice medium. This forward scattering model formed the basis of our inverse model for the sea ice thickness retrieval process. For the NN approach, multiple pairs of data set consist of different sea ice parameters and thicknesses with the corresponding brightness temperatures are first generated using the forward scattering model. This data set will be provided to the NN to create a range of sea ice thickness profile to be used for NN training. The training process is completed when the error generated by NN is acceptably small. After that, inversion is done by providing the brightness temperature profiles of the sea ice to obtain the corresponding sea ice thicknesses. As for GA, a pool of chromosomes representing sea ice thicknesses is created to be fed into the forward scattering model. The chromosomes are then evolved and carried forward to the next generation according to the natural selection concept, whereby the fittest candidate is more likely to survive and to reproduce. The generation and creation continues until the one of the chromosomes has been found to be suitable to be the thickness solution for a given brightness temperature profile.

2. DATA TRAINING AND SEA ICE THICKNESS INVERSION BY NN

The RT-DMPACT Model mentioned above is used to calculate the passive microwave returns in terms of brightness temperatures of vertically (T_{Bv}) and horizontally (T_{Bh}) polarized wave. The Neural Network (NN) constructed consists of an input layer, two hidden layers and an output layer. Each layer employs several neurons, which are connected to other neurons in the adjacent layer with different weights. The signals propagate from input layer, through hidden layers and to the output. The network is trained by the input-output data generated from the RT-DMPACT Model. The training process is carried out by changing the values of the interconnecting weights of the neurons in the layers by using Levenberg-Marquardt Algorithm (Martin H. & Mohammad B. M. 1994), according to the error generated. The weights in the NN are then changed in each iteration to reduce the error to an acceptable margin.

The inversion process by NN is divided into 2 parts as illustrated in Figure 1. At the training stage, the NN is being characterized by the training data provided by the forward model. At the

testing stage, the NN is ready to do the inversion when it is fully trained, using the data from the Special Scanning Microwave Imager (SSM/I) on a Defense Meteorological Satellite Program (DMSP) satellite.
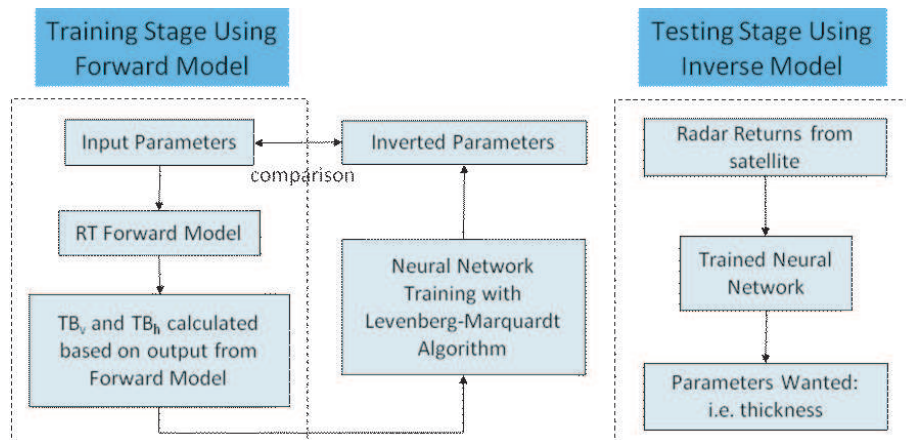

Figure 1: The training stage and the testing stage involving the Neural Network for the sea ice thickness inversion process.

3. SEA ICE THICKNESS RETRIEVAL BY GA

The Genetic Algorithm (GA) is a random search technique that would provide an optimal solution to a problem. The GA encodes the candidate solutions from the existing population into sequence of numbers that are called chromosomes. These chromosomes undergo the process of natural selection where the fitter chromosomes are more likely to survive and pass their traits to the next generation by a reproduction process called crossover. Crossover happens between 2 chromosomes to create new off springs by switching genes at a random point in the chromosomes. Mutations cause small random changes in a chromosome and introduce diversity to the population at a small probability of P_m. The chromosomes are evaluated with an objective function to determine their fitness. The process repeats until a solution has been found. The process flow of the GA is shown in Figure 5. Again, the Special Scanning Microwave Imager (SSM/I) on a Defense Meteorological Satellite Program (DMSP) satellite is utilized for validation of the inversion result.
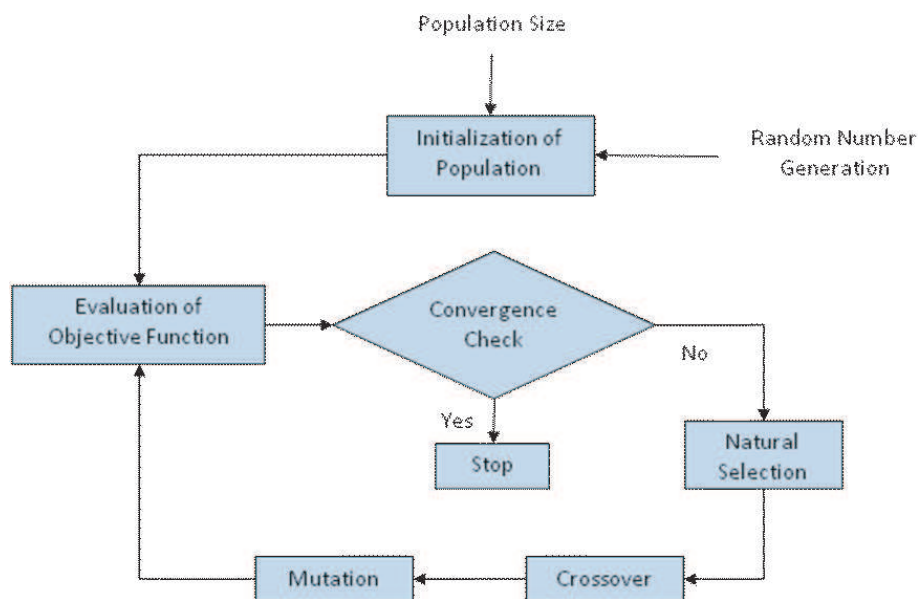
Figure 2: The process flow of the genetic algorithm.

4. RESULT COMPARISON OF NN AND GA

Simulation was first carried out by using the RT-DMPACT model at a frequency of 19 GHz to calculate the various brightness temperatures data set for different sea ice parameters as shown in Table 1, by varying the sea ice thickness.

Table 1: Estimated input parameters for the RT forward model.

Volume fraction	5–10%
Scatterer radius	0.25–0.50 mm
Effective dielectric constant of top layer (air)	$1.0 + j0.00$
Scatterer dielectric constant (brine)	$18.4 - j28.2$
Background dielectric constant (sea ice)	$3.17 - j0.06$
Effective dielectric constant of bottom layer (lower half space)	$18.4 - j30.2$

These data sets are then provided to the NN for training purpose before the inversion process could be made. The inversion result (thickness) is compared to that of the training data sets for validation, shown in Figure 3. For GA, a search routine is setup to look for suitable sea ice thickness with the corresponding brightness temperatures profile. The inversion result from GA is shown in Figure 4.

Figures 3 and 4 show the comparison of the inversion result from NN and GA to that of the theoretical result from the forward scattering model. The general trend is that both approaches yield similar results in terms of sea ice thickness in meters. To further test them in real sea ice cases, we have decided to pick the test sites located to the North West of Beaufort Sea, in the Arctic Ocean around the longitude of 152.641487W–155.436310W and the latitude of 80.591475N–80.648062N.
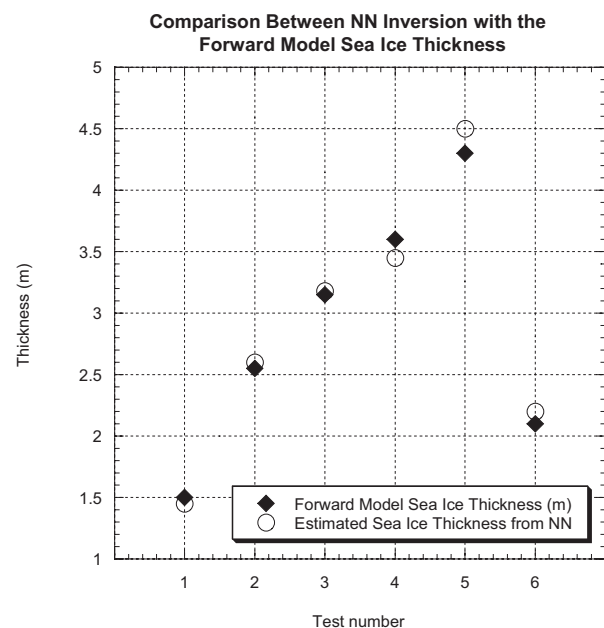
Figure 3: Inversion result from NN compared to that of the forward model.
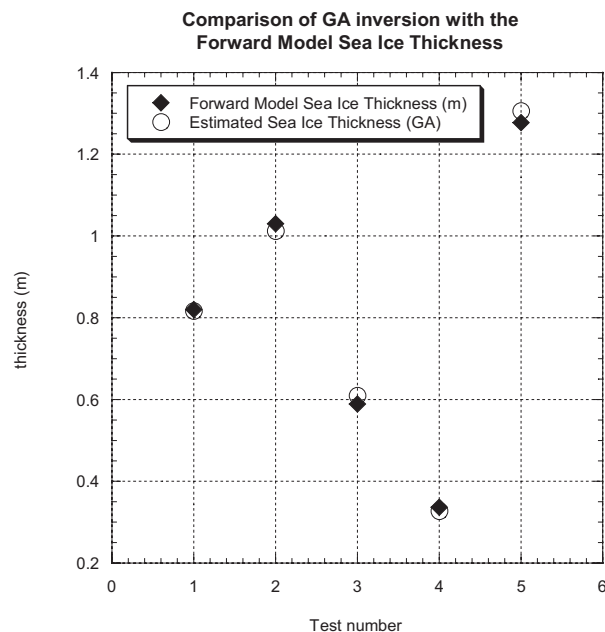
Figure 4: Inversion result from GA compared to that of the forward model.

Figure 5 shows inversion result for both NN and GA by using brightness temperature profile from the Special Scanning Microwave Imager (SSM/I) on a Defense Meteorological Satellite Program (DMSP) satellite dated 19th September 1997. The Arctic sea ice thickness is collected from the submarine upward looking sonar measurement data. The measurement data can be found in the SCICEX-97 data on National Snow and Ice Data Center website http://nsidc.org/data/g01360.html. We can see that the inversion results from NN and GA are quite close to that of the thickness measurement data.
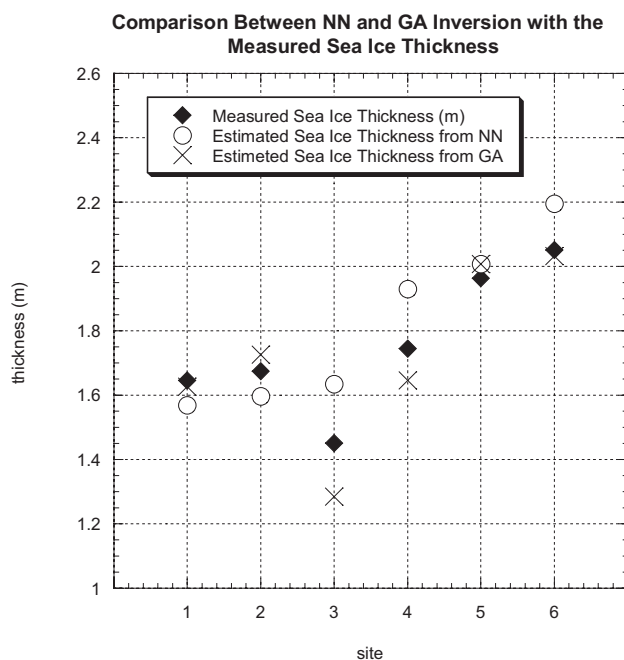
Figure 5: Inversion result from NN and GA compared to the forward model result.

5. CONCLUSIONS

In this paper, two approaches for sea ice thickness retrieval is been presented, one being the NN approach and the other by using GA. These two approaches are used to retrieve sea ice thickness from passive microwave remote sensing. The applicability for both approaches has also been studied. The results from the two approaches show interesting and promising results and indicate that sea ice thickness retrieval using passive microwave remote sensing is possible.

REFERENCES

1. Albert, M. D., T. E. Tan, H. T. Ewe, and H. T. Chuah, "A theoretical and measurement study of sea ice and ice shelf in antarctica as electrically dense media," *Journal of Electromagnetic Waves and Applications*, Vol. 19, No. 14, 1973–1981, 2005.
2. Arthur, K. J. and E. V. Murat, "Electromagnetic remote sensing of sea ice," *Inverse Problems*, Vol. 10, 1041–1058, 1994.
3. Chuah, H. T., S. Tjuatja, A. K. Fung, and J. W. Bredow, "A phase matrix for a dense discrete random medium: Evaluation of volume scattering coefficient," *IEEE Transactions on Geoscience and Remote Sensing*, Vol. 34, No. 5, 1137–1143, 1996.
4. Dawson, M. S., J. Olvera, A. K. Fung, and M. T. Manry, "Inversion of surface parameters using fast learning neural networks," *Geoscience and Remote Sensing Symposium, 1992, IGARSS'92*, 910–912, 1992.
5. Ewe, H. T., H. T. Chuah, and A. K. Fung, "A backscatter model for a dense discrete medium: Analysis and numerical results," *Remote Sensing of Environment*, Vol. 65, No. 2, 195–203, 1998.
6. Fung, A. K., *Microwave Scattering and Emission Models and Their Applications*, Artech House Norwood, MA, 1994.
7. Golden, K. M., D. Borup, M. Cheney, E. Cherkaeva, M. S. Dawson, K. H. Ding, A. K. Fung, D. Isaacson, S. A. Johnson, A. K. Jordan, J. A. Kong, R. Kwok, S. V. Nghiem, R. G. Onstott, J. Sylvester, D. P. Winebrenner, and I. H. H. Zabel, "Inverse electromagnetic scattering models

for sea ice," *IEEE Transactions on Geoscience and Remote Sensing*, Vol. 36, No. 5, 1675–1704, 1998.

8. Golden, K. M., M. Cheney, K. H. Ding, A. K. Fung, T. C. Grenfell, D. Isaacson, J. A. Kong, S. V. Nghiem, J. Sylvester, and D. P. Winebrenner, "Forward electromagnetic scattering models for sea ice," *IEEE Transactions on Geoscience and Remote Sensing*, Vol. 36, No. 5, 1655–1674, 1998.

9. Kamal, S. and S. L. Eric, "Characterization of optimum polarization for multiple target discrimination using genetic algorithms," *IEEE Transactions on Antenna and Propagation*, Vol. 45, No. 12, 1810–1817, 1997.

10. Leung, T., C. Zhangxiao, O. Seho, J. M. Roberts, and A. T. C. Chang, "Inversion of snow parameters from passive microwave remote sensing measurements by a neural network trained with a multiple scattering model," *IEEE Transactions on Geoscience and Remote Sensing*, Vol. 30, No. 5, 1015–1024, 1992.

11. Martin, T. H. and B. M. Mohammad, "Training feedforward networks with the marquardt algorithm," *IEEE Transactions on Neural Network*, Vol. 5, No. 6, 989–993, 1994.

12. Randy, L. H., "An introduction to genetic algorithm for electromagnetics," *IEEE Antenna and Propagation Magazine*, Vol. 37, No. 2, 7–15, 1995.

13. Veysoglu, M. E., H. T. Ewe, A. K. Jordan, R. T. Shin, and J. A. Kong, "Inversion algorithms for remote sensing of sea ice," *Geoscience and Remote Sensing Symposium 1994, IGARSS'94, Surface and Atmospheric Remote Sensing: Technologies, Data Analysis and Interpretation*, Vol. 1, 626–628, August 8th–12th, 1994.

Interpolation Techniques to Improve RIO Boundary Detection

Avijit Hira, **Shaik Ashraf Hossain**, and **Md Ishfaqur Raza**

Department of Electrical and Electronic Engineering, East West University
43 Mohakhali C/A, Dhaka-1212, Bangladesh

Abstract— Non-invasive detection of boundary separating different media using radiation imaging operators is dependent on the reliable reconstruction of scattered waves caused by variations in material characteristics. Reverse simulation used in scattered wave reconstruction uses recorded data as source signal. The physical limitations of density of field recorders is complemented using numerical interpolation schemes to approximate data fields between recorders. Here the technique is extended to detecting boundary separating media with different electromagnetic characteristic parameters.

1. INTRODUCTION

A wide range of methods, such as Kirchoff's Integral method, have been widely used to recreate images in a wide range of applications, such as ultrasound medical imaging and geophysical exploration [1–3]. An approach using finite difference time domain (FDTD) numerical method has been earlier effectively used to detect objects with varying density using the radiation imaging operators (RIO) [3]. In this paper the FDTD method is again used to detect boundaries separating constitutive properties, such as permittivity and permeability. The RIO for a 2D electromagnetic (EM) media is derived for use in the analysis.

The physical setup of the model to detect object boundary using RIO is shown in Fig. 1. It is assumed that the primary reflection originates from the object boundary. The unknown object is embedded in a region of known physical characteristics. A source excitation is placed near the outer surface of the area of interest. A set of recorders is placed closed to the source. Location of the source and the object to be imaged is on opposite sides of the recorders. An approach to increase the density of the data at the recorder line is introduced here. Different interpolation algorithms in a generic mathematical tool were used here to estimate the field data.

2. ELECTROMAGNETIC RADIATION IMAGING OPERATOR

Wave propagation in rectangular coordinate system is defined by the wave equation. A simplified two dimensional (2D) wave propagation case is studied in this paper (see Fig. 1). Assume constant field distribution in the z direction, i.e., $\partial_z = 0$ and a 2D electromagnetic (EM) field problem in the TM mode, i.e., $H_Z = 0$. The EM field components are E_z, H_x, and H_y. Considering field propagation in y direction and D for partial differential operator, the wave equation satisfying EM wave distribution in the object (medium 2) with velocity $c_2 = (\varepsilon_2 \mu_2)^{-1/2}$ is given by

$$\left(D_{xx}^2 + D_{yy}^2 - \frac{1}{c^2} D_{tt}^2 \right) E_z = 0$$

$$\text{or} \quad \left(D_{yy}^2 - \left(\frac{1}{c^2} D_t \sqrt{1 - c_2^2 \frac{D_{xx}^2}{D_{tt}^2}} \right)^2 \right) E_{2z} = 0$$

$$\text{or} \quad \left(c_2 D_{yt}^2 + D_{tt}^2 - \frac{1}{2} c_2^2 D_{xx}^2 \right) E_{2z} = 0$$

where 1st order Taylor series expansion is used to rewrite the square root term.

The EM field boundary conditions dictate that the tangential electric fields ($\mathbf{E}_{\text{tan}}$) are same on both sides of the boundary of the object. These conditions are necessary to derive the RIO. For this TM problem, E_z in medium 1 and 2 is tangential to boundary, irrespective of object orientation in x-y plane. The RIO for $+ve$ y going waves is

$$\left(c_2 D_{yt}^2 + D_{tt}^2 - \frac{1}{2} c_2^2 D_{xx}^2 \right) E_{1z} \Big|_{boundary} = 0 \tag{1}$$

The RIO is applied to the sum of the source field and the reconstructed scattered field. Equation (2) operating on E_{1z} returns a minimum value at the boundary (see Fig. 1). This premise is used to detect the object boundary.
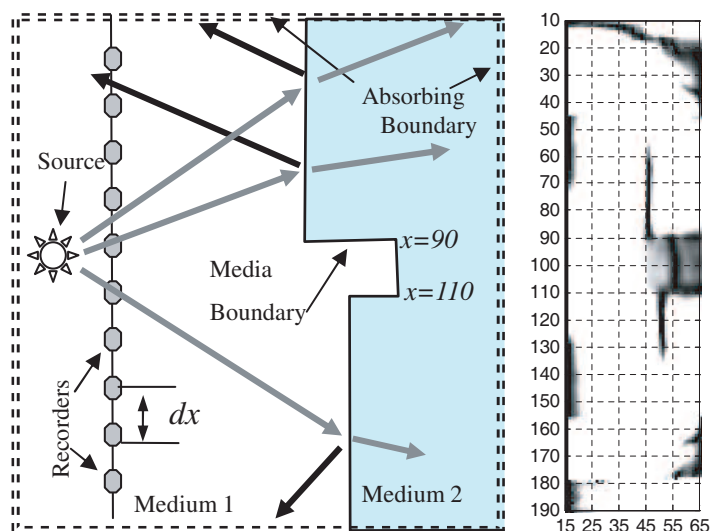
Figure 1: 2D problem space for non-invasive boundary detection (model and RIO detected boundary).

3. IMAGE CONSTRUCTION PROCESS

The process of creating the image of the object boundary primarily consists of four steps. The first step is based on field data collection and also numerical modelling of the region (shown on left in Fig. 1). The source used in this experiment is defined by a pulse. It is assumed that the region is 'quiet' at time $t = 0$. When the source is turned on, a string of recorders begins to record field components on the recorder line. The data is recorded for a certain length of time until EM field distribution in the model space becomes sufficiently quiet. This first step of data acquisition is simulated for this paper. The next steps will however, have to be always numerical modelled.

In the second step, the region of interest is modelled excluding the object, the void filled with the known material (as an extension of the area surrounding it). A source, similar to the one used in step 1 is used here. Wave distribution at all the nodes in the simulated space is stored. The recorders are also used in this step to store E_Z.

In step 3, reverse wave propagation is implemented. The source is the scattering data extracted from data at the recorder line stored in steps 1 and 2. During backward propagated, fields at all the nodes in simulation space are also recorded. Sum of reconstructed scattered waves from step 3 and the source signal from step 2 recreates field distribution at every time-step, which is only valid in the region between the recorders and the boundary but invalid in the object. The final step is detection of object boundary. Here the RIO is applied on the reconstructed data. The result shows a minimum at the boundary (dark line, right image Fig. 1).

Reconstruction of the scattered wave is implemented using the FDTD numerical method [3]. The scattered data stored at the recorder locations are played backwards in time. Simulation starts at the final recorded time step and decrements towards zero. The greater the density of the recorders used in the field data acquisition state the better the information available for back propagation in the scattered wave reconstruction phase. However, it is neither always easy nor feasible to have sufficient recorders. In this paper different numerical interpolation schemes are used to mathematically predict the electrical field distribution in between the recorder nodes.

4. IMAGE SPACE SIMULATION AND ANALYSIS

The FDTD method is used to generate all the numerical data in both forward and backward wave propagation simulation. The following Maxwell's equations model the EM fields for this TM mode problem.

$$\varepsilon_0 \frac{\partial E_{zx}}{\partial t} + \sigma_{ex} E_{zx} = \frac{\partial H_y}{\partial x} \qquad \mu_0 \frac{\partial H_x}{\partial t} + \sigma_{my} H_x = -\frac{\partial (E_{zx} + E_{zy})}{\partial y}$$
$$\varepsilon_0 \frac{\partial E_{zy}}{\partial t} + \sigma_{ey} E_{zy} = -\frac{\partial H_x}{\partial y} \quad \text{and} \quad \mu_0 \frac{\partial H_y}{\partial t} + \sigma_{mx} H_y = \frac{\partial (E_{zx} + E_{zy})}{\partial x}$$

For the detection of boundary, the RIO is discretized using 2nd order finite difference (FD),

which is

$$\partial_{yt}^2 Ez_{i,j}^{n+1} = \frac{Ezr_{i,j+1}^{n+2} - Ezr_{i,j+1}^{n} - Ezr_{i,j-1}^{n+2} + Ezr_{i,j-1}^{n}}{4\delta_t \delta_y} + \frac{Ezs_{i,j+1}^{n+2} - Ezs_{i,j+1}^{n} - Ezs_{i,j-1}^{n+2} + Ezs_{i,j-1}^{n}}{4\delta_t \delta_y} \quad (2)$$

$$\partial_{tt}^2 Ez_{i,j}^{n+1} = \frac{Ezr_{i,j}^{n+2} - 2Ezr_{i,j}^{n+1} + Ezr_{i,j}^{n}}{\delta_t^2} + \frac{Ezs_{i+1,j}^{n+2} - 2Ezs_{i,j}^{n+1} + Ezs_{i-1,j}^{n}}{\delta_t^2} \quad (3)$$

$$\partial_{xx}^2 Ez_{i,j}^{n+1} = \frac{Ezr_{i+1,j}^{n+1} - 2Ezr_{i,j}^{n+1} + Ezr_{i-1,j}^{n+1}}{\delta_x^2} + \frac{Ezs_{i+1,j}^{n+1} - 2Ezs_{i,j}^{n+1} + Ezs_{i-1,j}^{n+1}}{\delta_x^2} \quad (4)$$

$$\Im_{i,j} = \frac{c_0}{\sqrt{\varepsilon_r}} \partial_{xx}^2 Ez_{i,j}^{n+1} - \partial_{xx}^2 Ez_{i,j}^{n+1} + \frac{c_0^2}{2\varepsilon_r} \partial_{xx}^2 Ez_{i,j}^{n+1} \quad (5)$$

The description of the model and the simulation problem is as follows.

Time step	dt = 5 ps		Modeled space (x, y)	$(200dx, 80dy) = (240 \text{ cm}, 96 \text{ cm})$
Spatial interval	(dx, dy) = 12 cm		Recorders line	$y = 12dy$
Total simulation time	$T = 300dt$ = 1.5 ns		Source Location	$(100dx, 10dy)$

A Gaussian voltage pulse is used as hard source signal, given by $S(t) = Ke^{-(t-A)/B}$. Both A and B are set to 20 dt. It is designed such that its significant frequencies have wavelength several times smaller then the object features. Berenger's perfect latched layer (PML) absorbing boundary is used here [4]. PML layer depth is 6.

5. INTERPOLATION SCHEME

The accuracy of the detection of the object boundary is a function of the 'goodness' of the reverse simulation numerical scheme. To reconstruct the image to its finer details, the distance between recorders need to be small compared to the wavelengths of the source signal. As recorder density cannot be increased easily, general numerical interpolation techniques are proposed. This estimates the details of the recorded waveforms between the recorders.

Using interpolation schemes, a finer distribution of EM fields at the recorder line over time is derived. The interpolation data is then back propagated over the finer grid enabling the methodology to image finer details of the boundary surface. This reduces the level of noise in the image. In this paper, three different interpolation methods are used — spline, linear, and next state [5]. The Interpolations are done using Matlab routines [6].
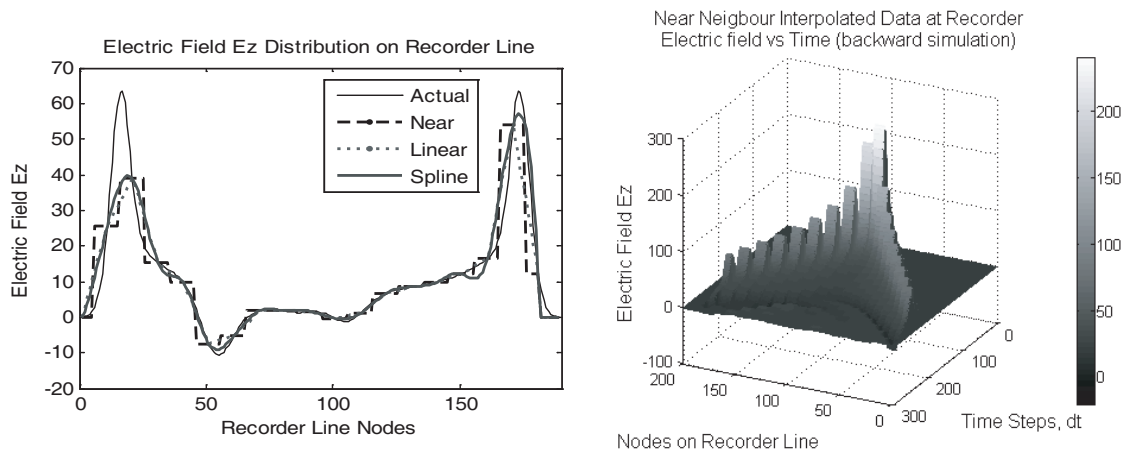

Figure 2: Reconstructed field on recorder line for different interpolation scheme, interpolation intervals 10 (left), and near neighbor interpolation wave distribution on the recorder line vs time (right).

Of the different interpolation schemes, spline is more accurate as it ensures continuity of the 1st and 2nd order derivative of the known data at the known data at the recorders. If the object being detected is expected to have lower radii of curvature, the linear or near neighbour interpolation technique will be sufficient. In field

distribution with frequent changes and fluctuations, use of near neighbour or linear (low order) interpolation techniques have a low pass filter effect on the data. This attenuates oscillations in the reconstructed waveform [7]. For such electric field data, spline interpolation method is preferable, despite the cost of extra computation and algorithm complexity.
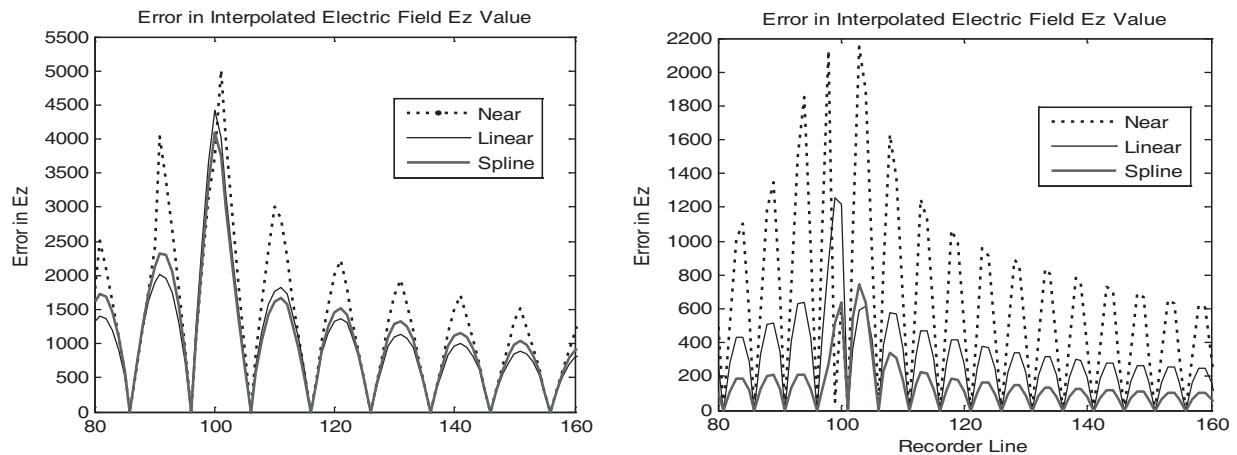

Figure 3: Interpolation errors for different techniques — interval 10 steps (left), interval 5 steps (right).

The accuracy of the wave reconstruction can be characterized by summing the absolute error at every node. This error grows when fewer recorder points. Simulation data is shown in Fig. 3. Error is significant irrespective of the interpolation technique when intervals are large (10 vs. 5, Fig. 3). The error is also large near the nodes where the staircase steps are close, (near node = 100). This is where scattering is complex. It is also noted that error is higher with spline over linear interpolation due to the over compensation with splines when intervals are small (right of Fig. 3). It increases oscillations where little should exist. Such systems are better modelled using linear interpolation.
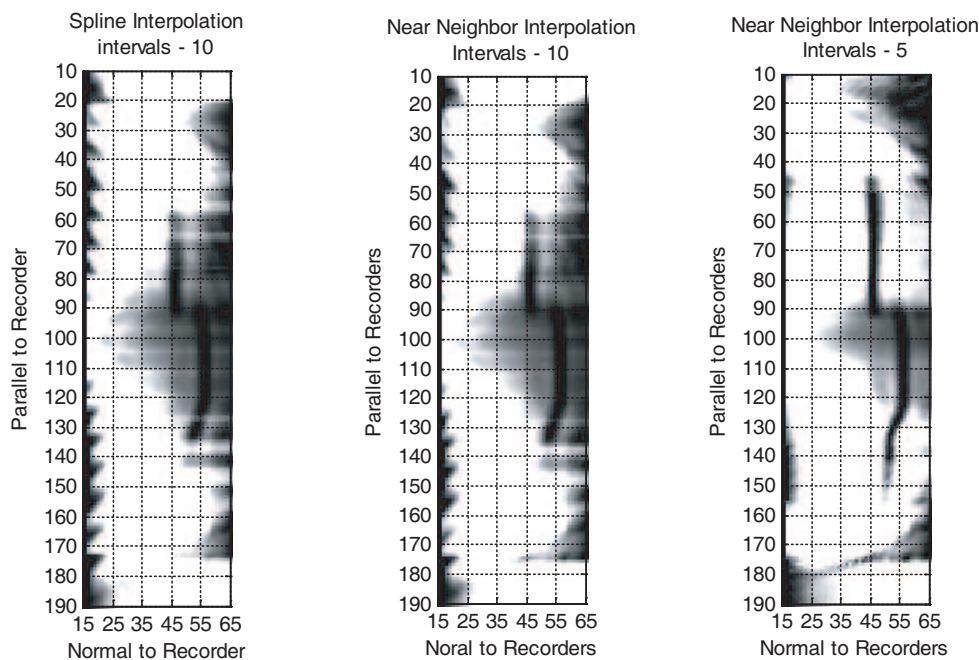
Figure 4: Image reconstructed using interpolated data (Figures: left, center, right).

6. IMAGE RECONSTRUCTION AND DISCUSSION

Several matlab scripts were written to simulate wave propagation and RIO boundary detection. In this paper a staircase structure is experimented with (Fig. 1). With all the recorder data available

(interpolation not needed), the top and bottom ends of image are not captured due to absence of scattered data. The rest of the edges facing the recorders are detected, excluding the faces of the object that are almost vertical to the recorder line. Scattering waves are not available from these edges, hence no edges detected. Then some of the recorders were turned off to allow experimentation of the interpolation schemes. First only the 5th recorder was kept on and then only the 10th recorder was kept on. Interpolation method was then used to estimate the data at the recorder nodes where recorders were off.

The data plots in Fig. 3 show that the E_Z field reconstruction in the 5 step interval has significantly less error then the 10 step interval. These interpolated data is then used to reconstruct the object shown in Fig. 1. The left and centre images of Fig. 4 show the boundary of the object using two different interpolation schemes for 10 step interval. The boundary is blurred with noise but it is still recognizable. The right figure in Fig. 4 shows the image with 5 step interval. This image is sharper and the top and bottom part is better detected. If interpolation was not done then in the 10 step interval case only one node would have defined the staircase notch. This would have been a very coarse reconstruction of the boundary. Also significant amount of scattered data propagates in directions where recorders are not present (top and bottom edges). These field waves are lost and not available for wave reconstruction.

7. CONCLUSION AND FUTURE WORK

This work has focused on applying the RIO concept into the electromagnetic domain. The object boundary was detected using a non-invasive technique. All detection were accurate, however, due to loss of scattered waves that were not incident on the recorder strings, object edges closer to the radiation boundary could not be detected. The paper also introduced the concept of performing numerical interpolation to increase the grid density of the simulation domain to detect object boundaries. This has allowed better reconstruction of the object boundary.

REFERENCES

1. Blackledge, J. M. and L. Zapalowski, "Quantitative solutions to the inverse scattering problem with applications to medical imaging," *Inverse Problems*, Vol. 1, 17–32, 1985.
2. Stolt, R. H., "Migration by Fourier transform," *Geophysics*, Vol. 43, 23–48, Feb. 1978.
3. DuBroff, R. I., M. I. Raza, and T. J. Herrick, "Remote detection of acoustic boundaries using radiation imaging operators," *IEEE Trans. Ultrason., Ferroelect., Freq. Contr.*, Vol. 42, 1012–1019, Nov. 1995.
4. Berenger, J. P., "Perfect latched layer for the FDTD solution of wave-structure interaction problems," *IEEE Antennas Propagat.*, Vol. 44, 110–1, Jan. 1996.
5. Stoer, J. and R. Bulirsch, *Introduction to Numerical Analysis*, 3rd edition, Springer, 2002.
6. www.mathworks.com, MATLAB®, version 7, release 14.
7. Fomel, S., "Stanford exploration project," *Report Sergey*, Nov. 9, 179, 2000.

A Microwave Scattering Model for the Remote Sensing of Oil Palm Plantations

Jun-Yi Koay[1], Tuck-Yew Yan[1], Ka-Sing Lim[2], and Hong-Tat Ewe[1]

[1]Universiti Tunku Abdul Rahman, Malaysia
[2]Multimedia University, Malaysia

Abstract— The alarming rate of expansion of oil palm plantations in Southeast Asian countries in recent years is expected to have an impact on the environment and global climate change. This is due to the massive reduction of tropical rainforests and the use of large-scale burning for the clearing of land. Microwave remote sensing is a viable method for the monitoring of the large expanses of oil palm plantations in the region, yet research in this area is insignificant at present. In this study, a theoretical model is developed based on a dense medium radiative transfer method to simulate the backscattering coefficient of 4 year old oil palm canopies. Needles are used to represent the leaves instead of elliptic disks, which were used in an earlier preliminary study. Initial comparisons of simulation results with measurement data obtained using a C-band scatterometer show a good match, but do not show much improvement over the model employing elliptic disks. The model will need to be further verified through the collection of more data from scatterometer measurements and satellite images. It is hoped that these initial theoretical studies and data collection will provide the impetus for future research work in the development of oil palm monitoring applications, of which some possible areas are explored in this paper.

1. INTRODUCTION

The soaring prices of palm oil in the world markets in the last few years have, up till recently, lead to a boom in the palm oil industry in South East Asian countries such as Malaysia and Indonesia [1]. With the rapid increase and expansion of oil palm plantations in these regions, there is a need for local authorities to monitor their growth, since these regions are also rich in biodiversity. Rainforests, as well as being critical to the survival of many species, serve as carbon sinks for the removal of CO_2 in the atmosphere; yet they are continually sacrificed to make way for oil palm plantations, with detrimental effects on the Earth's environment and climate [2, 3]. Although there are some who argue that oil palm plantations are also capable of serving the same purpose, it is clear that they are no substitute for tropical rainforests developed over hundreds of millions of years. Another adverse effect of oil palm plantations on the global climate stems from the mismanagement of these plantations, where many agriculturalists have resorted to burning for land clearance and preparation [4]. Microwave remote sensing is thus expected to play a crucial role in the monitoring of these large expanses of plantations in the near future by providing relevant information to decision makers so that a balance can be struck between economic development and environmental concerns.

However, research in the remote sensing of oil palm is almost insignificant at present, with only a few brief studies conducted on the backscattering coefficient of oil palm canopies obtained from satellite data [5]. A preliminary scattering model has been developed based on the radiative transfer approach with the phase matrix of the leaves obtained from the scattered field of elliptic disks [6]. In this study, a similar model will be developed, but needle-shaped scatterers will be used instead for the development of the phase matrices of the leaves. This scattering model is described in Section 2 and will be used in the simulation of the backscattering coefficient of oil palm canopies based on ground truth parameters measured at plantations in Bangi, Selangor, Malaysia. The simulation results of the model developed in this study will be compared with that obtained using elliptic-disks [6] to determine if needle-shaped scatterers provide a better match with C-band scatterometer measurements. These results are shown in Section 3, together with detailed analysis of the backscattering behavior of oil palm canopies at various angles of incidence and polarizations. These theoretical model simulations and analysis will provide a platform for future work in the development of monitoring applications in the remote sensing of oil palm, of which some possibilities are discussed in Section 4.

2. DEVELOPMENT OF THEORETICAL MODEL

The theoretical model developed for this study is based on the multi-layer second order iterative solutions [7] of the radiative transfer equations [8]. The oil palm canopy is configured as two layers

above a slightly rough soil surface, in which the top layer consists of leaves and fronds, while the bottom layer is made up of the tree trunks. The leaves are modeled as needles, while the fronds and trunks are modeled as cylinders. This model is shown alongside an actual photograph of an oil palm tree in Figure 1. The generalized Rayleigh-Gans approximation [9] and the infinite cylinder approximation [10] are used in the development of the phase matrices of the needles and cylinders. The amplitude and Fresnel phase corrections [11], as well as the Dense Medium Phase and Amplitude Correction Theory (DM-PACT) [12], are also included to consider the near field and coherent effects of closely spaced scatterers.
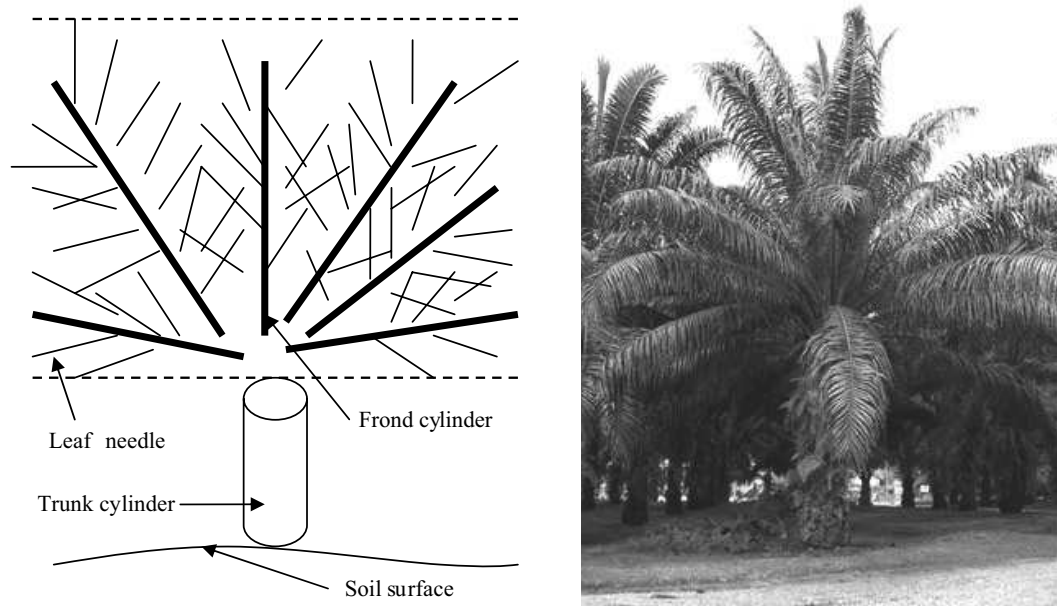
Figure 1: Configuration of oil palm canopy in the theoretical model, together with a photograph of an oil palm tree in Bangi, Selangor, Malaysia.

3. COMPARISONS AND ANALYSIS

The theoretical model is used to simulate the backscattering coefficient of 4 year old oil palm canopies over a range of incident angles at a frequency of 5.3 GHz. This frequency is similar to the frequency used in [6] for comparisons with C-band scatterometer measurements. Input parameters for the theoretical model are obtained from ground truth data collected in Bangi, Selangor, Malaysia in July 2007 at the same time the scatterometer measurements were obtained. The simulation results are shown in Figure 2 in comparison with data measured using the scatterometer. Generally, the simulated backscattering coefficients provide a good match with the measured values. There is not much improvement to the overall matching as compared with the previous model based on elliptic disks (which will not be shown here). This is because the leaves do not seem to contribute much to the overall backscattering coefficient of the canopy in both models. Figure 3 demonstrates that at this frequency, the fronds provide the largest contribution to the overall HH volume backscattering of the canopy, instead of the leaves. The backscattering from the tree trunk and soil surface is negligible based on the simulations. The small difference between measured and simulated values of the backscattering coefficient can probably be attributed to the slight curvature of the fronds, which can be seen in the photograph in Figure 1.

There is not much difference between the backscattering coefficients at VV and HH polarizations. Both measured and simulated data also show that the backscattering coefficient of the oil palm canopy does not vary much with the angles of incidence, since the fronds are distributed over all angles of orientation. However, these results will need to be further verified with satellite data, since the footprint of the scatterometer antenna is smaller than the size of a single oil palm tree and the measurement results are obtained as averages of multiple measurements over randomly selected points in the canopy.
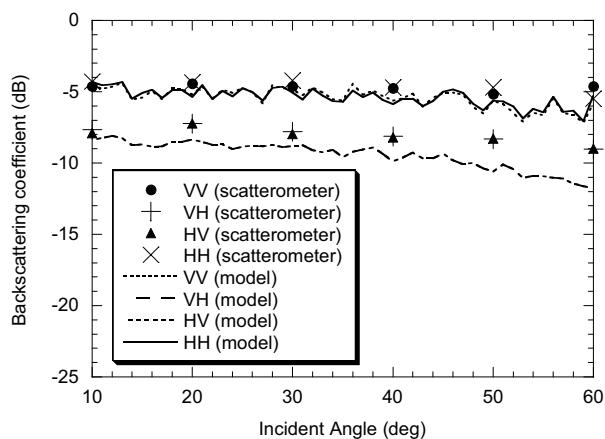
Figure 2: Measured and simulated backscattering coefficient of oil palm canopies at various angles of incidence and polarizations.
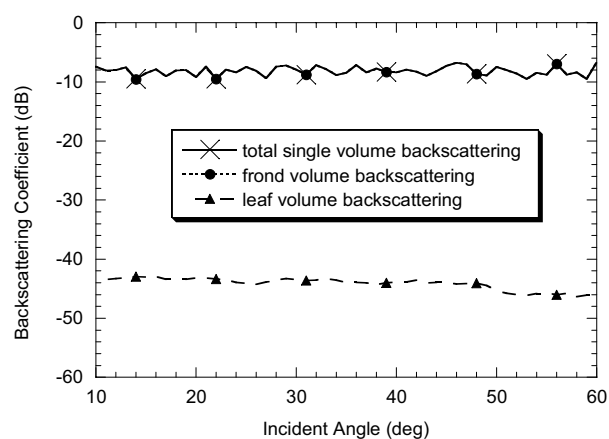
Figure 3: Simulated HH volume backscattering coefficient of oil palm canopies at various angles of incidence demonstrating the contribution from various components of the canopy.

4. POSSIBLE DIRECTIONS FOR FUTURE RESEARCH WORK

The theoretical model developed for oil palm canopies in this study is a simple model that needs to be further verified via comparisons with more scatterometer measurements as well as actual satellite data. This will allow the model to be further refined for theoretical studies, with some suggestions for the improvement of the model already proposed in [6]. An experimentally validated model will offer much needed assistance in the selection and optimization of satellite parameters (i.e., frequency, incident angle and polarization) for the monitoring of oil palm plantations. It is proposed that the next step should involve the collection of large quantities of data on the backscattering coefficients of oil palm canopies of various ages as obtained from scatterometers and satellites at various incident angles, frequencies and polarizations. These data, together with the theoretical model, will hopefully be able to uncover some correlation or trends in the backscattering coefficient of oil palm canopies that can pave the way for the development of monitoring applications. Some probable applications include:

- *classification of oil palm plantations from rainforests and other forms of land cover* — This will be critical for land-use management purposes, and to ensure that oil palm plantations do not grow unchecked at the expense of tropical rainforests.

- *detection and control of oil palm diseases* — Basal Stem Rot (BSR) has been identified as the most widespread disease affecting oil palm plantations today [13]. Since this disease leads to the drying up and reduction of oil palm fronds, it is possible that the disease can be detected and monitored through microwave remote sensing. Proper control of such diseases will greatly increase the yield without the need to enlarge plantations.

- *monitoring of oil palm growth* — Oil palm trees above 25 years of age have a much reduced yield. Clearing old trees to make way for new ones is more conducive for the environment and makes more effective use of the land. The challenge is to develop novel techniques to classify oil palm trees of different ages so that trees beyond their peak production age can be distinguished in remote sensing images. Some initial work in this area can be found in [14].

- detection of large-scale burning for land clearance and preparation — large-scale burning to clear land for agricultural use should be easily detectable using remote sensing (particularly at optical and infra-red frequencies), thus enabling the relevant authorities to take necessary action.

5. CONCLUSIONS

The remote sensing of oil palm is very inadequately researched at the moment. Yet, it holds much promise as one of the key techniques that can be used to monitor oil palm plantations — part of an industry that is controversially linked to issues of the environment and global climate change. In

this study, a theoretical model is developed for the simulation of the backscattering coefficient of oil palm canopies. Comparisons of simulated and measured backscattering coefficients show a good match, although more data will need to be collected for further validation of the model. These data, together with the model, will provide a platform for the development of various applications to monitor oil palm plantations. It is hoped that these applications will help to increase palm oil yield per square area, thus negating the need to continually expand plantations, while also providing necessary information for proper land management and law enforcement.

ACKNOWLEDGMENT

REFERENCES

1. "Historical crude palm oil prices," Available: http://www.palmoil.com.
2. Tilman, D., J. Fargione, B. Wolff, C. D'Antonio, A. Dobson, R. Howarth, D. Schindler, W. H. Schlesinger, D. Simberloff, and D. Swackhamer, "Forecasting agriculturally driven global environmental change," *Science*, Vol. 292, 281–284, 2001.
3. Watkins, K., *United Nations Human Development Report 2007/2008 — Fighting Climate Change: Human Solidarity in a Divided World*, Palgrave Macmillan, New York, 2007.
4. Fitzherbert, E. B., M. J. Struebig, A. Morel, F. Danielsen, C. A. Brühl, P. F. Donald, and B. Phalan, "How will oil palm expansion affect biodiversity?" *Trends in Ecology and Evolution*, Vol. 23, No. 10, 538–545, 2008.
5. Rosenqvist, A. and H. Oguma, "Phenological characteristics of cultivated vegetation covers in JERS-1 and ERS-1 synthetic aperture radar data," *Proceedings of International Symposium on Vegetation Monitoring*, 194–195, 1995.
6. Koay, J. Y., K. S. Lim, H. T. Ewe, H. T. Chuah, H. Jamil, and S. Bahari, "Preliminary study in the backscattering measurements and theoretical modeling of oil palm canopies," *Proceedings of the Asian Conference on Remote Sensing*, Kuala Lumpur, Malaysia, November 12–16, 2007.
7. Karam, M. A., A. K. Fung, R. H. Lang, and N. S. Chauhan, "A microwave scattering model for layered vegetation," *IEEE Transactions on Geoscience and Remote Sensing*, Vol. 30, No. 4, 767–784, 1992.
8. Chandrasekhar, S., *Radiative Transfer*, Dover, New York, 1960.
9. Schiffer, R. and K. O. Thielheim, "Light scattering by dielectric needles and disks," *Journal of Applied Physics*, Vol. 50, No. 4, 2476–2483, 1979.
10. Karam, M. A. and A. K. Fung, "Electromagnetic scattering from a layer of finite length, randomly oriented, dielectric, circular cylinders over a rough interface with application to vegetation," *International Journal of Remote Sensing*, Vol. 9, No. 6, 1109–1134, 1988.
11. Ewe, H. T. and H. T. Chuah, "A study of Fresnel scattered field for non-spherical discrete scatterers," *Progress In Electromagnetics Research*, PIER 25, 189–222, 2000.
12. Chuah, H. T., S. Tjuatja, A. K. Fung, and J. W. Bredow, "A phase matrix for a dense discrete random medium: Evaluation of volume scattering coefficient," *IEEE Transactions on Geoscience and Remote Sensing*, Vol. 34, No. 5, 1137–1143, 1996.
13. Idris, A. S. and D. Ariffin, "Basal stem rot — Biology, detection and control," *Proceedings of the International Conference on Pests and Diseases of Importance to the Oil Palm Industry*, No. 10, 134–165.
14. Nordin, L., "Application of AIRSAR data to oil palm tree characterization," *Proceedings of the Asian Conference on Remote Sensing*, Kathmandu, Nepal, November 5–9, 2002.

EM Scattering from Multiple Cylinders

W. Z. Yan[1], D. W. Liu[1], H. T. Ewe[2], and Y. Du[1]

[1]The Electromagnetics Academy at Zhejiang University
Zhejiang University, Hangzhou 310058, China
[2]Tunku Abdul Rahman University, Petaling Jaya 46200, Malaysia

Abstract— In this paper we propose to extend the recently proposed iterative technique with extension to the T-matrix approach to the problem of electromagnetic scattering from a cluster of parallel dielectric circular cylinders. The overall treatment is separated into two stages: at the first stage, scattering from a single cylinder is obtained as the first-order solution; and at the second stage, a recursive process that accounts for multiple scattering, where the scattered field from one cylinder is considered as the illuminating wave for the other cylinder and vice verse, is formed. The validity of the proposed method has been verified by good agreement between model results and numerical simulations.

During the last several decades, electromagnetic scattering from multiple cylinders has been an active research topic of in many areas, such as microwave remote sensing, theory of photonic crystals, atmospheric sciences, and so on. Rigorous theoretical treatment is therefore of critical importance.

Using the multi-scatterer equation, varying technical delicacy could be attached to the solution process. Based the T-matrix approach introduced by Waterman [1], examples include the special cases of the problems of multi-sphere scattering in the iterative algorithms by Mackowski [2] or the recursive T-matrix algorithm (RTMA) by Chew [3]. Yet regardless of the underlying technical details, several benevolent features hold for such setting, including fulfillment of the mutual exclusive condition of the circumscribing spheres of each scatterer (actually the sphere itself in these cases) and the favorable behavior of the T matrix for spheres. It is not the case when scattering from multiple cylinders is considered. On one hand, the mutual exclusive condition of the circumscribing spheres is often found violated (as in the case when any pair of reasonably long cylinders are close to each other); on the other hand, the T matrix of a dielectric cylinder of arbitrary length, equivalent volumetric radius, and dielectric contrast with the ambient environment can have poor convergent property or even fail to converge. Therefore, partly for these reasons, in [4], the 3D problem was first converted to a 2D problem by assuming infinite length of the cylinders to obtain the exciting fields and then to use the Huygen's principle to bring back the 3D scattering. Yet such convenience for technical treatment may compromise the rigorousness and fidelity of the scattering characterization. Another approach without resorting to the multi-scatterer equation in studying scattering from two scatterers was based on the reciprocity theorem to obtain scatterer coupling up to the second order [5]. Yet this method, an approximated one in its nature, may not be suitable for situations where more rigorous treatment is required.

For electromagnetic scattering from a single dielectric cylinder of finite length, we have recently proposed a new iterative technique with extension to the T-matrix approach [6]. The appealing feature of this approach is its capability of dealing with dielectric cylinder of arbitrary length, hence overcoming the limitation inherent in the conventional T-matrix approach where the algorithm may fail to converge if the length is larger than several times of the radius. In this approach, a long cylinder is divided into a cluster of N identical sub-cylinder by using N-1 hypothetic surfaces, for each the T matrix can be calculated stably in the numerical sense. Therefore, special care should be paid to both rigorously fulfill the boundary conditions at the hypothetical division interfaces and cast the coupling among sub-cylinder into a rigorous formulism. For the purpose of clarity of the approach, we will first consider the case of two sub-cylinder division which is depicted in Fig. 1. Since the EBCM involves surface integrals and since cylinder division generates hypothetical interfaces, before we proceed we need to denote these surfaces carefully. Each sub-cylinder will contain a primary surface and an interface. The primary surface of sub-cylinder $j(j = 1, 2)$, S_{jp} includes its surface without the division interface. The center of sub-cylinder j is r_j. The common interface is denoted by S_d.
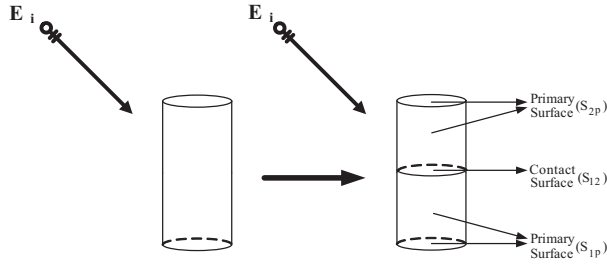
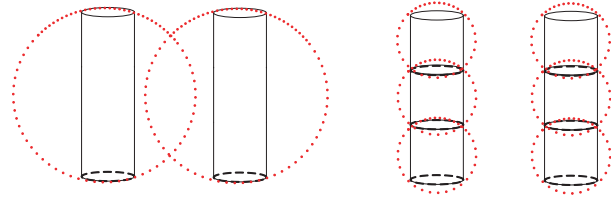Figure 1: Division of a cylinder into two identical sub-cylinder.

Figure 2: Model of two adjacent cylinders with the circumscribing spheres.

Now for fields expanded in terms of vector spherical waves with different origins, we introduce the following intermediate variables:

$$
\begin{bmatrix} a_{mn}^{(M)(j)h} \\ a_{mn}^{(N)(j)h} \end{bmatrix} = -ik(-1)^m \int_{S_{jh}} dS i\omega\mu\hat{n}_j \times \mathbf{H}_j(\mathbf{r}) \cdot \begin{bmatrix} \bar{M}_{-mn}(\overline{rr_j}) \\ \bar{N}_{-mn}(\overline{rr_j}) \end{bmatrix} + k\hat{n}_j \times \mathbf{E}_j(\mathbf{r}) \cdot \begin{bmatrix} \bar{N}_{-mn}(\overline{rr_j}) \\ \bar{M}_{-mn}(\overline{rr_j}) \end{bmatrix} \tag{1}
$$

$$
\begin{bmatrix} a_{mn}^{s(M)(j)h} \\ a_{mn}^{s(N)(j)h} \end{bmatrix} = ik(-1)^m \int_{S_{jh}} dS i\omega\mu\hat{n}_j \times \mathbf{H}_1(\mathbf{r}) \cdot \begin{bmatrix} Rg\bar{M}_{-mn}(\overline{rr_j}) \\ Rg\bar{N}_{-mn}(\overline{rr_j}) \end{bmatrix} + k\hat{n}_j \times \mathbf{E}_j(\mathbf{r}) \cdot \begin{bmatrix} Rg\bar{N}_{-mn}(\overline{rr_j}) \\ Rg\bar{M}_{-mn}(\overline{rr_j}) \end{bmatrix}, \tag{2}
$$

where the superscript h respectively represents the primary part from the primary surface of jth sub-cylinder denoted by p and from common interface denoted by d. S_{jh} is thus appropriately selected between S_{jp} and S_d. s denotes the scattered field. In the above, $\hat{n}_j$ is the outward pointing unit normal vectors on the surface S_j of sub-cylinder j. These intermediate variables are not arbitrary quantities but have specific physical meanings. They represent the expansion coefficients of the exciting fields and scattered fields due to the primary surfaces and the interface of these sub-cylinder, respectively. Therefore, utilizing T matrix, the expanded coefficients $\bar{a}_{mn}$ and $\bar{a}_{mn}^s$ for each part are related as follows

$$
\begin{bmatrix} a_{mn}^{s(M)(j)p} \\ a_{mn}^{s(N)(j)p} \end{bmatrix} + \begin{bmatrix} a_{mn}^{s(M)(j)d} \\ a_{mn}^{s(N)(j)d} \end{bmatrix} = \bar{\bar{T}} \cdot \left\{ \begin{bmatrix} a_{mn}^{(M)(j)p} \\ a_{mn}^{(N)(j)p} \end{bmatrix} + \begin{bmatrix} a_{mn}^{(M)(j)d} \\ a_{mn}^{(N)(j)d} \end{bmatrix} \right\}. \tag{3}
$$

Since the terms $\bar{a}_{mn}^{(1)d}$ and $\bar{a}_{mn}^{s(2)d}$ are expressed in terms of the tangential fields on the interface, it is natural to relate them with the aid of translational addition theorem. For the case of vector spherical wave functions, the vector addition theorems have the form [7]

$$
\begin{bmatrix} Rg\bar{M}_{mn}(\bar{r}_j) \\ Rg\bar{N}_{mn}(\bar{r}_j) \end{bmatrix} = \sum_{\mu,\nu} \left\{ \begin{bmatrix} RgA_{\mu\nu}^{mn}(\bar{r}_{ji}) \\ RgB_{\mu\nu}^{mn}(\bar{r}_{ji}) \end{bmatrix} \cdot Rg\bar{M}_{\mu\nu}(\bar{r}_i) + \begin{bmatrix} RgB_{\mu\nu}^{mn}(\bar{r}_{ji}) \\ RgA_{\mu\nu}^{mn}(\bar{r}_{ji}) \end{bmatrix} \cdot Rg\bar{N}_{\mu\nu}(\bar{r}_i) \right\} \tag{4}
$$

and

$$
\begin{bmatrix} \bar{M}_{mn}(\bar{r}_j) \\ \bar{N}_{mn}(\bar{r}_j) \end{bmatrix} = \sum_{\mu,\nu} \left\{ \begin{bmatrix} A_{\mu\nu}^{mn}(\bar{r}_{ji}) \\ B_{\mu\nu}^{mn}(\bar{r}_{ji}) \end{bmatrix} \cdot Rg\bar{M}_{\mu\nu}(\bar{r}_i) + \begin{bmatrix} B_{\mu\nu}^{mn}(\bar{r}_{ji}) \\ A_{\mu\nu}^{mn}(\bar{r}_{ji}) \end{bmatrix} \cdot Rg\bar{N}_{\mu\nu}(\bar{r}_i) \right\} \tag{5}
$$

for the condition $\bar{r}_i < \bar{r}_{ji}$, where the vector spherical waves with and without the prefix Rg stand for regular and outgoing waves, respectively.

Through rotation of coordinates, the numerical advantages to a common z axis can be exploited. A transformation from j to i could thus be accomplished by the three steps as follows

(i) The coordinate system of j is rotated so that the z axis of j points towards the origin of i. The Euler angles for this rotation are $\alpha = \phi^{ji}$, $\beta = \theta^{ji}$ and $\gamma = 0$,

$$
\bar{M}_{mn}(\overline{r'r_j}) = \sum_k D_{mk}^n(\theta^{ji}) \bar{M}_{kn}(\overline{r'r_j}) e^{ik\phi^{ji}} \tag{6}
$$

and the transformation yields

$$a_{mn}^{s(M)(j)'} = \sum_k D_{mk}^n(\theta^{ji}) a_{kn}^{s(M)(j)} e^{ik\phi^{ji}}$$

$$a_{mn}^{(M)(j)'} = \sum_k D_{mk}^n(\theta^{ji}) a_{mn}^{(M)(j)} e^{ik\phi^{ji}}. \tag{7}$$

(ii) The rotated coefficients at j are axially translated along z axis to the origin of i. Therefore, we can have

$$a_{mn}^{(M)(ji)} = \sum_\nu \left\{ a_{m\nu}^{s(M)(j)'} A_{mn}^{m\nu}(\overline{r_j r_i}) + a_{m\nu}^{s(N)(j)'} B_{mn}^{m\nu}(\overline{r_j r_i}) \right\}$$

$$a_{mn}^{(N)(ji)} = \sum_\nu \left\{ a_{m\nu}^{s(M)(j)'} B_{mn}^{m\nu}(\overline{r_j r_i}) + a_{m\nu}^{s(N)(j)'} A_{mn}^{m\nu}(\overline{r_j r_i}) \right\}. \tag{8}$$

(iii) The coefficients are rotated back to the original orientation. For this, $\alpha = 0$, $\beta = -\theta^{ji}$ and $\gamma = -\phi^{ji}$. This completes the translation transformation. Thus,

$$a_{mn}^{s(M)(ji)} = (-1)^m e^{-im\phi^{ji}} \sum_k (-1)^k D_{mk}^n(\theta^{ji}) a_{kn}^{s(M)(j)}$$

$$a_{mn}^{(M)(ji)} = (-1)^m e^{-im\phi^{ji}} \sum_k (-1)^k D_{mk}^n(\theta^{ji}) a_{mn}^{(M)(j)} \tag{9}$$

where in this transformation, the identity $D_{mk}^n(-\beta) = (-1)^{m+k} D_{mk}^n(\beta)$ is used. The vector translational addition coefficients and rotated coefficients can be found in [7].

For the cases of single constituent cylinder, we have the convenience of reducing the double summation over m and ν to single summation over ν because the translation is along the z axis. By shifting the origin from r_1 to r_2 and making use of the intermediate variables of sub-cylinder 2, the term $\bar{a}_{mn}^{(1)d}$ can thus be expressed as

$$\begin{bmatrix} a_{mn}^{(M)(1)d} \\ a_{mn}^{(N)(1)d} \end{bmatrix} = \sum_\nu \left\{ A_{-mn}^{-m\nu}(\overline{r_1 r_2}) \begin{bmatrix} a_{m\nu}^{s(M)(2)d} \\ a_{m\nu}^{s(N)(2)d} \end{bmatrix} + B_{-mn}^{-m\nu}(\overline{r_1 r_2}) \begin{bmatrix} a_{m\nu}^{s(N)(2)d} \\ a_{m\nu}^{s(M)(2)d} \end{bmatrix} \right\}. \tag{10}$$

Note that for a single scatterer, the incident field is equal to the exciting field. In our case, the virtual partition shall not change this property. Now if we let the global origin coincidence with r_1, by applying transformation of origin on the vector spherical waves and making use of the intermediate variables we have

$$\begin{bmatrix} a_{mn}^{(M)} \\ a_{mn}^{(N)} \end{bmatrix} = \begin{bmatrix} a_{mn}^{(M)(1)p} \\ a_{mn}^{(N)(1)p} \end{bmatrix} - \sum_\nu \left\{ A_{-m\nu}^{-mn}(\overline{r_1 r_2}) \begin{bmatrix} a_{m\nu}^{s(M)(2)p} \\ a_{m\nu}^{s(N)(2)p} \end{bmatrix} + B_{-m\nu}^{-mn}(\overline{r_1 r_2}) \begin{bmatrix} a_{m\nu}^{s(N)(2)p} \\ a_{m\nu}^{s(M)(2)p} \end{bmatrix} \right\}. \tag{11}$$

Combining the above two equations, yields

$$\begin{bmatrix} a_{mn}^{(M)} \\ a_{mn}^{(N)} \end{bmatrix} = \begin{bmatrix} a_{mn}^{(M)(1)} \\ a_{mn}^{(N)(1)} \end{bmatrix} - \sum_\nu \left\{ A_{-m\nu}^{-mn}(\overline{r_1 r_2}) \begin{bmatrix} a_{m\nu}^{s(M)(2)} \\ a_{m\nu}^{s(N)(2)} \end{bmatrix} + B_{-m\nu}^{-mn}(\overline{r_1 r_2}) \begin{bmatrix} a_{m\nu}^{s(N)(2)} \\ a_{m\nu}^{s(M)(2)} \end{bmatrix} \right\}. \tag{12}$$

Similarly, we can also establish the following system of equations by focusing on the cylinder 2 as follows

$$\begin{bmatrix} a_{mn}^{(M)} \\ a_{mn}^{(N)} \end{bmatrix} \cdot e^{ikh\cos\theta_i} = \begin{bmatrix} a_{mn}^{(M)(2)} \\ a_{mn}^{(N)(2)} \end{bmatrix} - \sum_\nu \left\{ A_{-m\nu}^{-mn}(\overline{r_2 r_1}) \begin{bmatrix} a_{m\nu}^{s(M)(1)} \\ a_{m\nu}^{s(N)(1)} \end{bmatrix} + B_{-m\nu}^{-mn}(\overline{r_2 r_1}) \begin{bmatrix} a_{m\nu}^{s(N)(1)} \\ a_{m\nu}^{s(M)(1)} \end{bmatrix} \right\}, \tag{13}$$

where h is the height of each sub-cylinder.

The scattered field can be treated similarly. Therefore, the total scattered coefficients of whole constituent cylinder in the primary coordinate system are

$$
\begin{bmatrix} a_{mn}^{s(M)} \\ a_{mn}^{s(N)} \end{bmatrix} = \begin{bmatrix} a_{mn}^{s(M)(1)} \\ a_{mn}^{s(N)(1)} \end{bmatrix} + \sum_{\nu} \left\{ RgA_{-m\nu}^{-mn}(\overline{r_1 r_2}) \begin{bmatrix} a_{m\nu}^{s(M)(2)} \\ a_{m\nu}^{s(N)(2)} \end{bmatrix} + RgB_{-m\nu}^{-mn}(\overline{r_1 r_2}) \begin{bmatrix} a_{m\nu}^{s(N)(2)} \\ a_{m\nu}^{s(M)(2)} \end{bmatrix} \right\}. \quad (14)
$$

It is clear that the solutions of these coupled, linear, simultaneous equations can be easily obtained by iterative method.

For the electromagnetic scattering from a cluster of parallel dielectric circular cylinders, we propose to extend the above method to such kind of problems. Moreover, it can be clearly seen from Fig. 2 that the intersection volume of the circumscribing spheres is strongly reduced by using division of the elongated cylinders. Such convenience holds the potential for the cases of closely positioned constituent cylinders.

The modification to the formulation for multi-cylinder scattering is that the scattered field is now taken to be the superposition of scattered fields resulting from the interaction between the incident wave and each scatterer on one hand, and between the scatterers on the other hand. Consider a cluster of N_c isotropic and homogeneous cylinders with the radius a_l ($l = 1, \ldots, N_c$), length h_l, relative dielectric constant ε_l, and located at a point $\bar{r}_l$ where the origin of the primary coordinate system is at the center of the constituent cylinder 1.

Based on the above analysis which has already represented each field component by an infinite series of spherical harmonic waves, and then the first order solution can be easily obtained by calculating the response of each single constituent cylinder and expressed as

$$
\begin{bmatrix} a_{mn}^{s(M)1st} \\ a_{mn}^{s(N)1st} \end{bmatrix} = \begin{bmatrix} a_{mn}^{s(M)(1)} \\ a_{mn}^{s(N)(1)} \end{bmatrix} + \sum_{l=2}^{N_c} \sum_{\mu, \nu} \left\{ \begin{bmatrix} A_{mn}^{\mu\nu}(\overline{r_1 r_l}) & B_{mn}^{\mu\nu}(\overline{r_1 r_l}) \\ B_{mn}^{\mu\nu}(\overline{r_1 r_l}) & A_{mn}^{\mu\nu}(\overline{r_1 r_l}) \end{bmatrix} \begin{bmatrix} a_{mn}^{s(M)(l)H} \\ a_{mn}^{s(N)(l)H} \end{bmatrix} \right\} \quad (15)
$$

where $\bar{a}^{s(l)H}$ is the expanded coefficients of scattered field by the constituent cylinder l. For the higher order solution associated with the multiple scattering effects between arbitrary pair of cylinders (cylinder i and j), the scattered field from one cylinder is considered as the illuminating wave for the other cylinders whose expanded coefficients should be translated from $\bar{r}_i$ to $\bar{r}_j$ and vice verse. Therefore, we can establish the similar system of equations and repeat the procedure to get each order of scattering field. As all the coefficients converge, the total expanded coefficients of scattered field by the multi-cylinder system is thus obtained. Moreover, we use a method similar to the successive over-relaxation method (SOR), which takes the form of a weighted average between the previous iterate and the computed new iterate successively for each component. An extrapolation factor w ($0 \leq w \leq 1$) is used to speed up the convergency procedure.

To verify our proposed method, we compare the theoretical predictions of the proposed approach with numerical simulations, as well as measurements for scattering from multiple dielectric circular cylinders with finite length. As an example, we would like to first present the computed scattering
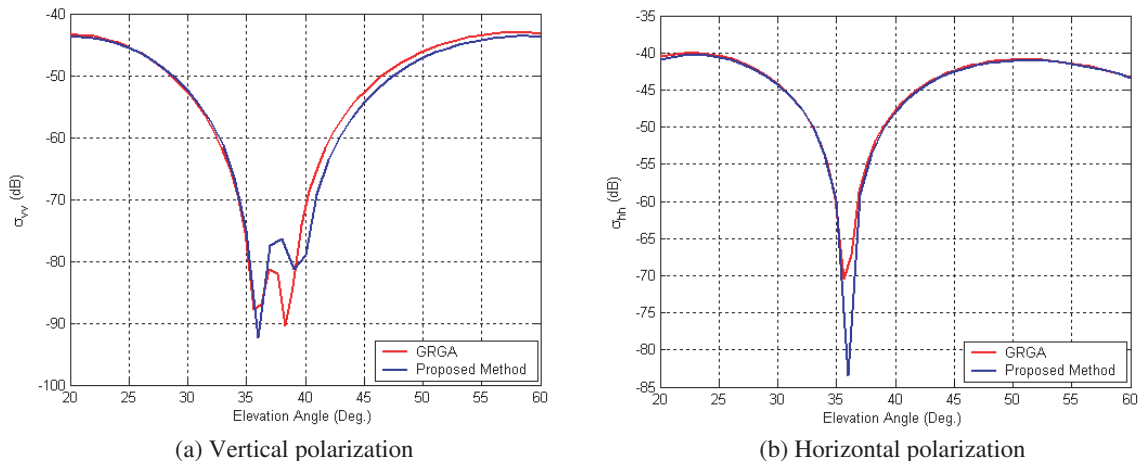

(a) Vertical polarization   (b) Horizontal polarization

Figure 3: Forward scattering cross section of two adjacent dielectric cylinder, 4 cm separation.

(a) Vertical polarization
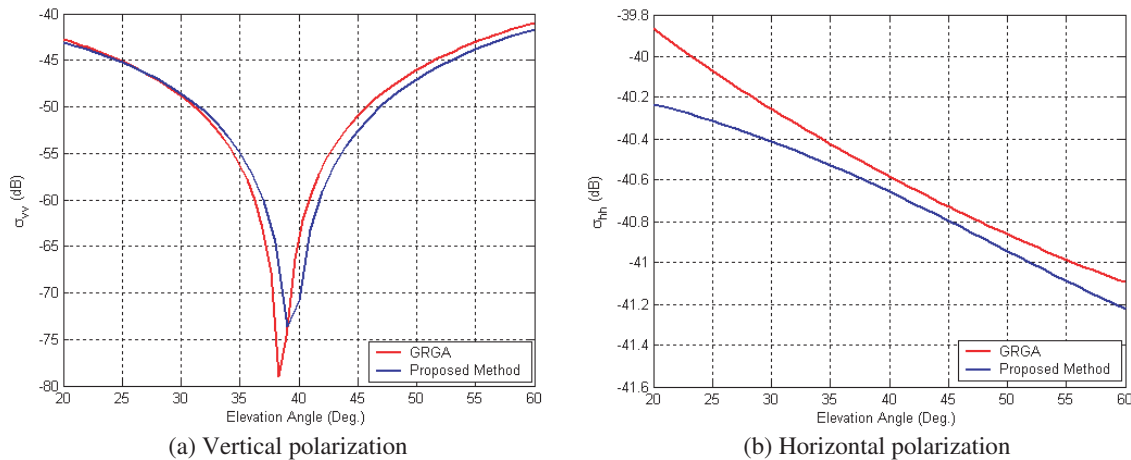
(b) Horizontal polarization

Figure 4: Forward scattering cross section of two adjacent dielectric cylinder, 4 cm separation.

results for two adjacent cylinders. Both cylinders have a diameter-to-length aspect ratio ρ of 10 and a refractive index of $m_r = 1.5 + 0.02i$. The radius of cylinders is fixed to 2 cm. The frequency of the excitation wave is 5.3 GHz. The azimuthal incidence angle is $180°$.

Comparison between the theoretical predictions by our method and that by Li [8] for both vertical and horizontal polarizations is shown in Fig. 3, where the method of Li is an extension of [5] to the cylindrical case. The second cylinder is arranged in x axis with 4 cm separation. The overall agreement is good except at peak where our results are reasonably higher. Similar observations can be made from Fig. 4, where the second cylinder is arranged in y axis with the same separation.

It should be noted that since no approximation is introduced in the procedure, this approach is thus more rigorous. The procedure is also found to converge very fast except for the case when any pair of cylinders is very close to each other. Additionally, the formalism is general and can be readily applied to cylinders with cross section other than circular so long as the T matrix of each sub-cylinder can be accurately obtained. Further verification may be carried out when measurement data are available from our collaborators.

ACKNOWLEDGMENT

REFERENCES

1. Waterman, P. C., "Matrix formulation of electromagnetic scattering," *Proc. IEEE*, Vol. 53, 805–811, 1956.
2. Mackowski, D. and M. Mishchenko, "Calculation of the *T*-matrix and the scattering matrix for ensembles of spheres," *J. Opt. Soc. Am. A*, Vol. 13, 2266–2278, 1996.
3. Chew, W. C., *Waves and Fields in Inhomogeneous Media, IEEE Press Series on Electromagnetic Waves*, 1990.
4. Tsang, L., K. H. Ding, G. F. Zhang, C. C. Hsu, and J. A. Kong, "Backscattering enhancement and clustering effects of randomly distributed dielectric cylinders overlying a dielectric half space based on Monte-Carlo simulation," *IEEE Trans. Antennas Propag.*, Vol. 43, 488–499, 1995.
5. Sarabandi, K. and P. F. Polatin, "Electromagnetic scattering from two adjacent objects," *IEEE Trans. Antennas Propag.*, Vol. 42, 510–516, 1994.
6. Yan, W. Z., Y. Du, H. Wu, D. W. Liu, and B. I. Wu, "EM scattering from a long dielectric circular cylinder," *Progress In Electromagnetics Research*, PIER. 85, 39–67, 2008.
7. Mackowski, D. W., "Analysis of radiative scattering for multiple sphere configurations," *Proc. R. Soc. Lond. A*, 599–614, 1991.
8. Li, S. Q., J. Fang, and W. B. Wang, "Electromagnetic scattering from two adjacent cylinders," *IEEE Trans. Geosci. Remote Sensing*, Vol. 36, 1981–1985, 1998.

Analysis of the Electromagnetic Properties of High Impedance Surfaces Using Genetic Synthesis

N. Lassouaoui, **H. Hafdallah Ouslimani**, **and A. Priou**

Applied Electromagnetism Group (GEA), Scientific and Technical Pole
University of Paris Ouest Nanterre La Defense
50, rue de SEVRES 92410, Ville d'AVRAY, France

Abstract— In this paper, we are interested by the analysis and the synthesis of the high impedance surfaces (HIS), based on periodic arrays of planar conducting elements (FSS) on a dielectric slab backed by a metal surface. The self-resonant grid model is used to analyze the HIS, which allows computing the surface impedance, reflection phases and the propagation properties of the surface waves along the HIS. The synthesis with genetic algorithms (GAs), we search the material characteristics of the electromagnetic structure that ensured the desired performances. Here in, we hope to find the characteristics of the substrate and the grid of FSS which ensure a resonance at a desired frequency and its stability according the angles and the polarisation of the incident wave. Numerical results are presented.

1. INTRODUCTION

Periodic structures, such as frequency-selective surfaces and photonic band-gap materials, exhibit total reflection in specific frequency bands while total transmission in other bands. They find numerous applications in a large field of the electromagnetic (EM) spectrum. Here in, we are interested by an artificial high-impedance surface (HIS) based on a thin 2D dimensional lattice of plates deposited in a dielectric substrate and attached to ground planes by metal-plated via. The HIS was proposed [1] as a new simplest example of textured electromagnetic surface having thickness lower than the traditional quarter-wavelength deep, with an interesting characteristic is that the electromagnetic wave is not reflected shifted to 180° compared to the incident wave, this is resulted from the resonance property of the impedance surface of HIS.

To analyze the surface impedance, the phase of the reflection parameter and the propagation properties of the surface waves along the HIS, we used the analytical model where the surface can be described using a lumped parameter circuit model, which accurately predicts many of its electromagnetic properties [1–4]. We recall that the models of planar array of metal elements excited by plane waves can be roughly split into two categories [1, 4]: computational and analytical methods.

However, it is not easy to define the characteristics of the HIS (period, distance between the elements, etc) which:

- Check the behaviour of HIS in a desired frequency band.
- Ensure a resonant frequency stable; indeed, it varies according to the polarization and the incidence angles.
- Allow a good bandwidth.

Here in, we propose to use the genetic algorithms [5] to search the best material characteristics of the HIS which ensure the resonance at desired frequency and a large bandwidth. For that, a multi objective function has been proposed and used to direct the genetic research to the best configuration.

In following section, we present the analytical model of HIS. In Section 3, we present the genetic algorithms and how we adapt them to our problem. Then, we present application results. Finally, we give our conclusion.

2. ANALYSIS OF HIGH IMPEDANCE SURFACE

Sievenpiper and Simovski [1–3] have presented analytical models for HIS with and without via. These analytical formulas give the impedance at the interface between air and the structure (Z_s) depending on the incidence angles, the polarization of the wave as well as all the properties of the substrate and the metallic grid. These models are valid only if the grid period D is small compared to the wavelength in the dielectric medium λ_d, indeed the tangential component of electric field

in the grid plane averaged over the grid periods is simply proportional to the averaged current induced in the grid [1–3].

In terms of the transmission-line approach, the surface impedance (Z_s) can be expressed as a parallel connection of the grid impedance Z_g and the surface impedance of the dielectric shield Z_d as detailed in [1–3]:

$$Z_s = \frac{Z_g Z_d}{Z_g + Z_d} \tag{1}$$

The resonance at which the structure behaves as a magnetic wall corresponds to the case:

$$\text{Im}(Z_g) + \text{Im}(Z_d) = 0 \tag{2}$$

We are interested by analyzing a HIS with Jerusalem crosses patches (Figure 1).
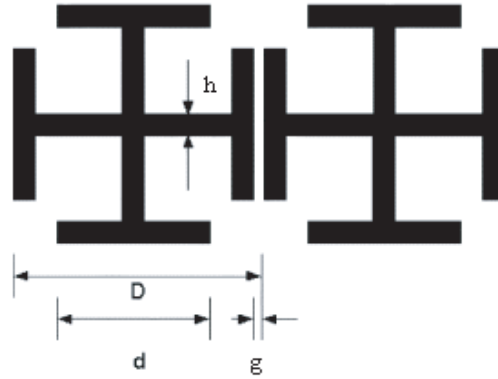
Figure 1: Jerusalem crosses patches.

The theory of the grid of metal Jerusalem crosses is presented [3]. The mesh unit cell contains both effective capacitance C (due to the strong capacitive coupling of adjacent crosses) and inductance L (due to straight portions of crosses). A formula for the effective capacitance of the grid of Jerusalem crosses which takes into account the full-wave interaction of the grid elements is given by [3]:

$$C = \frac{2}{\pi}\varepsilon\varepsilon_0 d \left[\log \cos ec \left(\frac{\pi g}{2D}\right) + F\right] \tag{3}$$

with

$$F = \frac{Qu^2}{1 + Q(1-u)^2} + \left(\frac{du(3u-2)}{4\lambda'}\right)^2 \quad Q = \sqrt{1 - \left(\frac{d}{\lambda'}\right)^2} \quad u = \cos^2 \frac{\pi g}{2d} \quad \lambda' = \frac{2\pi}{k'} \tag{4}$$

with k' is the wavenumber of the effective medium $k' = \omega\sqrt{\varepsilon_0\mu_0(\varepsilon+1)/2}$. These formulas are valid when $h \ll d$ (Figure 1).

The resonance of the grid is determined by the inductive L and the capacitance C. L is given by: $L = \eta'\alpha/2\omega$ with α is the grid parameter and is depended by the capacitive loading of the wire mesh [3]. We note that the grid parameter expressed in terms of circuit parameters C and L does not depend on the incidence angle θ.

The grid impedance of the Series-Resonant-Grids for the TM and TE cases are [3]:

$$Z_g^{TM} = \cos^2\theta\left(j\omega L + \frac{1}{j\omega C_g}\right) \quad Z_g^{TE} = \left(j\omega L + \frac{1}{j\omega C_g}\right) \tag{5}$$

Knowing the grid impedance and the dielectric shield Z_d [1–4], we deduce the surface impedance Z_s (1), and the reflection coefficient R [1–4].

In what follows, we use the reflection coefficient in genetic optimisation to direct the research to the configuration for which the phase of the reflection parameter is equal to zero at desired resonant frequency and incidence angle.

3. GENETIC SYNTHESIS

The genetic algorithms GAs are applied in several works [6–9] in electromagnetic and antenna fields; they begin [4] with a random generation of the population (solution candidates) and evaluate their fitness (adaptability to the problem). Then, the genetic operators (selection, crossover and mutation) are iteratively applying to the population to produce a new which is revaluated and the process begins anew with selection. The GAs are stopped when a design goal is reached. Here in, we propose to use the GAs to search the characteristics of the substrate and the FSS structure which ensure a stable resonant frequency. To adapt the GAs to our problem, we take:

1. A representation of the solutions: An array of bits which facilitates the genetic operations is chosen. Here in, each component in chromosome defines a real value of one characteristic of HIS (ε_r, ε_i, T_L, D, g, d, h), with:

   - T_L, ε_r and ε_i are respectively the thickness, real and imaginary parts of the permittivity of the dielectric layer.
   - D, g, d and h are respectively the period, the slit, the length of the small arms and the thickness of the arms h of the cross.

2. We have used the phase of the reflection parameter as fitness function to direct the genetic research to the configuration for which the phase is equal to zero at desired resonant frequency and incidence angle.

A multi-objective function is chosen for the fitness function. For each chromosome, we compute for the desired incidence angle θ:

- The resonant frequency f_o of the configuration corresponded to the chromosome.
- The phase φ_o of the chromosome at the desired resonant frequency f_d.

Then, with GAs, we search the characteristics which allow decreasing:

- The deviation of the obtained resonant frequency f_o to the desired frequency f_d: $\Delta f = |f_o - f_d| \to 0$.
- The deviation of the phase $\varphi_o \to 0$ at the desired resonant frequency f_d.

In what follows, we present the application results of genetic optimization of the Jerusalem crosses patches.

4. APPLICATION RESULTS

The application of the genetic synthesis with the analytic model to Jerusalem cross patch (Figure 1) to search the characteristics which ensure a resonance at 6 GHz for normal incidence are given by Figure 2. Figures 2(a), (b), (c) present the evolution of the optimization criteria, each level corresponds to a configuration of the best solution in the population. We note that from generation to other, the solution candidate resonates near to the desired frequency (Figure 2(a)), the maximal angular error φ_0 decreases to zero (Figure 2(b)). And from the generation 33, we obtain a solution which resonates at the desired frequency 6 GHz with a good bandwidth of 35%, computed from $-\pi/2$ to $\pi/2$.

At the last level, we obtain these characteristics.

- The permittivity and the thickness of the dielectric layer are: $\varepsilon = 1.01 - i * 0.2$, $T_L = 3.89$ mm.
- The period D, the slit g, d and h of the cross are respectively $D = 10.4$ mm, $g = 1$ mm, $d = 7$ mm, $h = 3.15$ mm.

The Figures 2(d), (e), (f) present the surface impedance (d), the phase of the reflection parameter (e) and the propagation properties of the surface wave (f). We obtain a resonance at desired frequency 6 GHz with a large bandwidth of 35%, computed from $-\pi/2$ to $\pi/2$. Good analytical results are obtained.
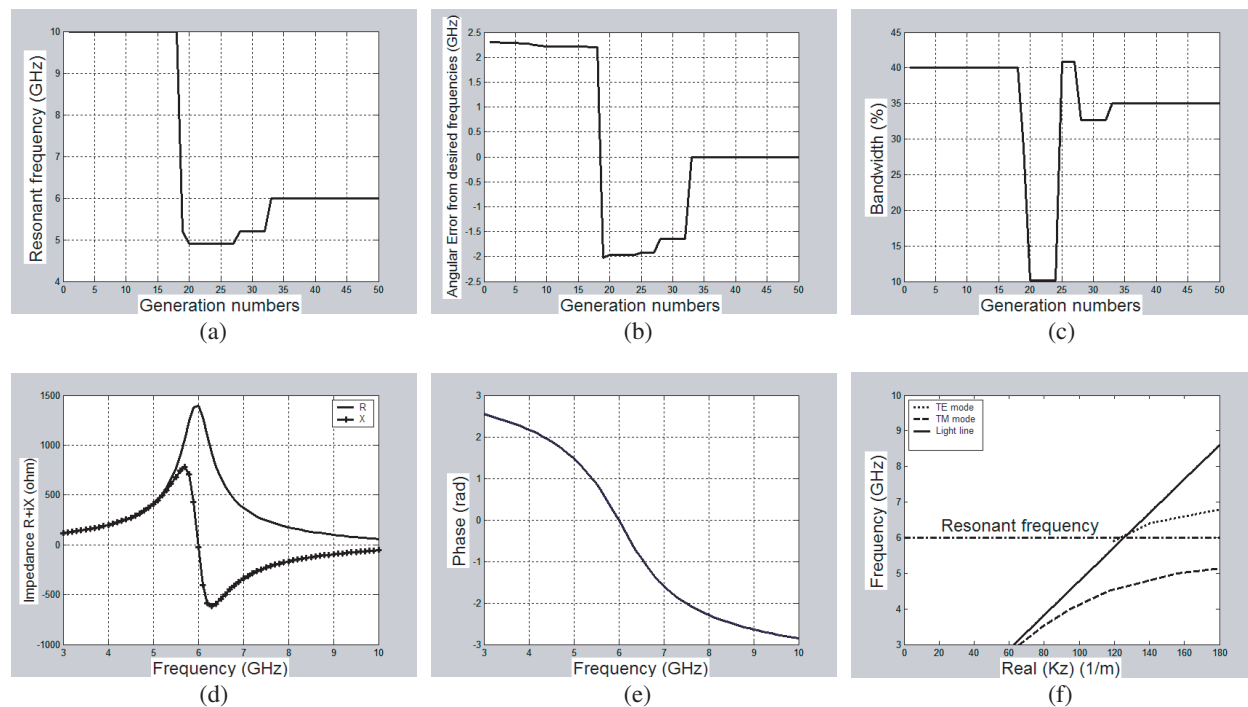
Figure 2: Results of the genetic optimisation of the HIS with the Jerusalem crosses patches, evolution according the generation of (a) The resonant frequency; (b) The deviation of the phase; (c) The bandwidth computed from $-\pi/2$ to $+\pi/2$ of the best configuration (chromosome) in the population. The frequency behaviour of the configuration at generation 50: (d) Real and imaginary parts of impedance; (e) The phase; (f) The propagation properties of the surface waves along the HIS.

5. CONCLUSION

The paper deals with the analysis of the series resonant grids to create the high impedance surface with the search the characteristics of the HIS (period, distance between the elements, etc) which ensure: The zero reflection at the desired resonant frequency and its stability according to the polarization and the incidence angles.

For the analysis, we have used the theory of wire meshes and the self-resonant grid model to analyze respectively the grid and the HIS.

The genetic algorithms are used to find the characteristics which ensure good frequency behaviour of the high impedance surface with the grid of metal Jerusalem crosses. A multi objective function has been proposed to direct the genetic research to the best configuration. Good results are obtained.

REFERENCES

1. Sievenpiper, D. F., "High-impedance electromagnetic surfaces," Doctorate thesis, University of California, 1999.

2. Sievenpiper, D, F., "Review of theory fabrication and applications of HIS ground planes," *Metamaterials: Physics and Engineering, Explorations*, Chap. 11, 287–311, Edited by N. Engheta and R. Ziolkowski, Wiley Interscience, 2006.

3. Simovski, C. R., P. D. Maagt, and I. V. Melchakova, "High-impedance surfaces having stable resonance with respect to polarization and incidence angle," *IEEE Transactions on Antennas and Propagation*, Vol. 53, No. 3, 908–914, March 2005.

4. Luukkonen, O., C. Simovski, G. Granet, G. Goussetis, D. Lioubtchenko, A. V. Räisänen, and S. A. Tretyakov, "Simple and accurate analytical model of planar grids and high-impedance surfaces comprising metal strips or patches," 1–20, May 2008. http://arxiv.org/

5. Goldberg, D. E., *Genetic Algorithms in Search, Optimization and Machine Learning*, Addison-Wesley, 1989.

6. Samii, Y. R. and E. Michielssen, *Electromagnetic Optimization by Genetic Algorithms*, Wiley Interscience, 1999.

7. Lassouaoui, N., H. Ouslimani, A. Priou, and Z. Hu, "On the improvement of stability of artificial magnetic conductor based on genetic algorithms," *Metamaterials 2008*, Pamplona, 2008.

8. Lassouaoui, N., H. Ouslimani, and A. Priou, "Development of genetic algorithms and c-method for optimizing a scattering by rough surface," *European Computing Conference*, Springer Verlag Book, Greece, September 25–27, 2007.

9. Lassouaoui, N., H. Ouslimani, and A. Priou, "Genetic algorithms for automated design of the multilayer absorbers in the X-band and incident angle range," *PIERS Proceedings*, 509–513, Hangzhou, China, March 24–28, 2008.

Meander-line Antenna Design for UHF RFID Tag Using a Genetic Algorithm

D. Zhou, **R. A. Abd-Alhameed**, **C. H. See**, **M. S. Alkhambashi**,
Z. Zainal Abidin, **K. N. Ramli**, **M. M. Abusitta**, and **M. Usman**

Mobile and Satellite Communications Research Centre
University of Bradford, Bradford, West Yorkshire, BD7 1DP, UK

Abstract— In this paper, a simple planar meander-line tag antenna for RFID application at UHF band designed and optimized using genetic algorithms (GA). The meander-line tag antenna dimensions were optimized and evaluated using GA in collaboration with NEC-2 source code. Configuration of optimal antenna with excellent impedance value at 900 MHz frequency band was found within the maximum generation. The simulated input impedance of the GA-optimised tag antenna has shown good agreement with the targeted impedance value. Moreover, the capabilities of GA are shown as an efficient optimisation tool for selecting globally optimal parameters to be used in simulations with an electromagnetic antenna design code, seeking convergence to designated specifications.

1. INTRODUCTION

In recent years Radio Frequency Identification (RFID) has become very popular in many commercial applications such as access control, animal tracking, security, and toll collection, because of its ability to track moving objects and its low-cost implementation [1, 2]. A typical RFID system is always made up of two components, including the tags (transponders) and readers (interrogators). A tag comprises an antenna and an application-specific integrated circuit (ASIC, or microchip) that is given a unique electronic product code. The antennas, as a key part of the system, enable the tag or reader to send and receive the signals. Readers are devices that read tags, and they equipped with antennas, a transceiver, and a processor (server with software system). The tag antenna design is quite challenging. This is because tag antenna is required directly connected to the tag IC, whose input impedance always presents capacitive reactance in nature. It means that the reactance part of tag antenna has to be designed and optimised to be complex conjugate impedance of tag IC in order to realize the maximum transmission using RF power induced from the antenna tag.

In this paper, an approach of using Genetic Algorithm (GA) in cooperation with an electromagnetic simulator was adopted to design and optimise the RFID tag antenna for UHF band. The benefit of applying GA is that it provides fast, accurate and reliable solutions for antenna structures. Genetic algorithm driver [3], written in Fortran, was adopted in this work in conjunction with the industry-standard NEC-2 Fortran source code [4], which was used to evaluate the randomly generated antenna samples. A meander-line antenna configuration was proposed in this study in order to achieve a tag design with compact size at UHF band. A Higgs IC [5], designed to follow EPCglobal Class-1 Gen-2 specification, was selected for the tag IC, input impedance of which was found to be $(12.2 - j135)\,\Omega$ at 900 MHz.

2. GENETIC ALGORITHM

Genetic algorithms are stochastic search procedures orchestrated by natural genetics, selection and evolution. They are modelled on Darwinian concepts of natural evolution thus making them more inspiring during use [6]. After it's first introduction in 1960's by J. Holland, it has become an efficient tool for search, optimization and machine learning, but in the pre-GA era, concepts of it had been looming and applied in game playing and pattern recognition [7]. Over the recent years, it has proven to be a promising technique for different optimizations, designs and control applications.

An approach of using GA in cooperation with an electromagnetic simulator has been introduced for antenna designs and has become increasingly popular recently [8]. For example, GA have been employed to design wire antennas [9, 10] and microstrip antennas [11]. The benefit of applying GA is that they provide fast, accurate and reliable solutions for antenna structures. Genetic algorithm driver [3], written in Fortran, was adopted in this work in conjunction with the industry-standard NEC-2 Fortran source code [4], which was used to evaluate the randomly generated antenna samples.

Several antenna designs using GA in authors' previous study [12, 13] has shown that the GA was successfully proved as an efficient optimizer tool that can be adopted and used to search and find the quicker solutions for complex antenna design geometries.

A flow chart to represent the easiest way in which the GA optimizer coordinates its functions is represented in Fig. 1. The algorithm randomly initiates its population and converts the parameters of the initiated individuals into a file in a card format which can be called by NEC-2 to determine the performance of these individuals. The results from NEC-2 are fed again to the GA engine to evaluate individual fitness if the maximum value is obtained for convergence, if otherwise the whole process is repeated until optimal results are produced.
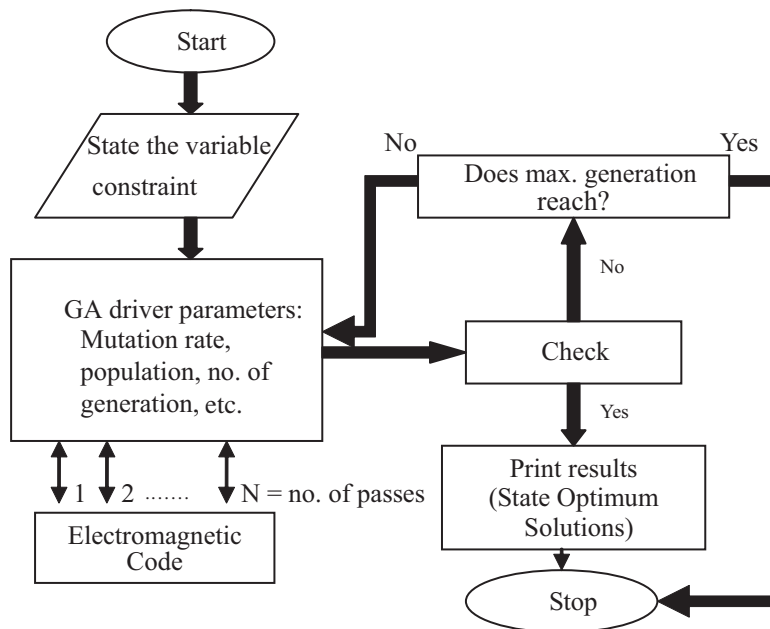
Figure 1: Flow chart of the genetic algorithm adopted in this study.

3. SIMULATION RESULTS AND DISCUSSION

A meander-line antenna configuration, as shown in Fig. 2, was proposed in this study in order to achieve a tag design with compact size at UHF band. Moreover, a paralleled meander line arrangement was used to enhance the impedance bandwidth for the proposed design. A Higgs IC [5], designed to follow EPCglobal Class-1 Gen-2 specification, was selected for the tag IC, input impedance of which was found to be $(12.2 - j135)\,\Omega$ at 900 MHz.
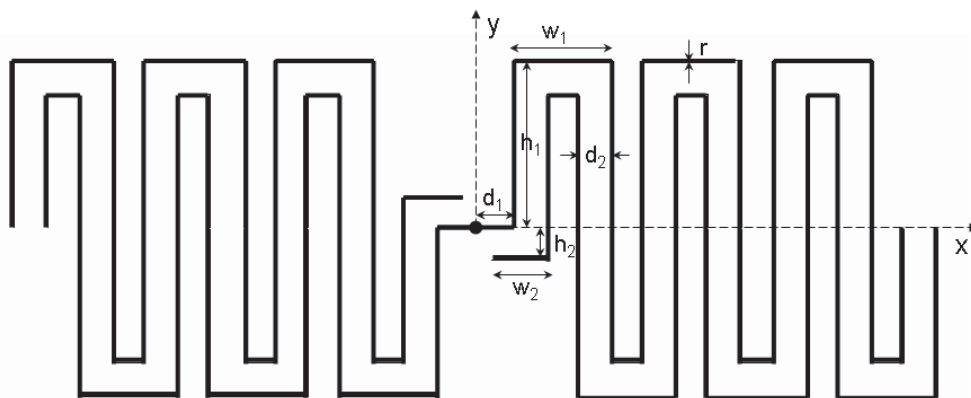
Figure 2: The new RFID antenna tag model.

Table 1 presents the GA input parameters in which the possible range of parameters magnitudes

were shown. There are seven parameters used to define the proposed tag antenna, including a matching circuit (i.e., parameters w_2 and h_2). For this optimisation, real-valued GA chromosomes were used. The optimisation of input impedance of the proposed tag antenna at 900 MHz band is considered inside the GA cost function. The randomly generated antenna configurations were evaluated for maximum fitness using a cost function. The computation time consumed for each of the erratically generated antenna samples only took a few seconds, according to the different combination of length, width and height of the patch antenna selected for comprising the antenna configuration. This was achieved by using a PC: 2.8 Pentium IV of 1 GB RAM.

Table 1: Summary of GA input parameters, antenna variables and best solutions.

GA parameters	GA-optimised RFID passive tag antenna	
	Parameters (m)	Optimal (m)
	Feeding wire length (d_1) (0.0025–0.0025)	0.0025
No. of population size = 4,	Spacing between wires (d_2) (0.001–0.003)	0.00222
No. of parameters = 7,	Outer wire width (w_1) (0.006–0.01)	0.00651
Probability of mutation = 0.02,	Matching wire width (w_2) (0.0015–0.0055)	0.00372
Maximum generation = 250,	Outer wire height (h_1) (0.005–0.015)	0.01110
No. of possibilities = 32768,	Matching wire height (h_2) (0.001–0.003)	0.00214
	Wire radius (r) (0.0002–0.0002)	0.0002

The geometry configuration of the optimal antenna was found within the maximum generations and the best solutions are listed in Table 1. It is notable the overall dimension ($l \times w$) of the optimal tag antenna is 62×22 mm. The obtained input impedance of the optimal tag antenna was found to be $(10.5 + j135.2)\,\Omega$. For validation, the performance of the GA-optimised tag antenna was evaluated and validated with another commercial EM simulator and simulated results of the antenna input impedance from 800 MHz to 1000 MHz was analysed and presented in Fig. 3. Moreover, comparison of the simulated return loss of the GA-optimised RFID tag antenna was shown in Fig. 4. As can be seen, the optimal tag antenna features wide impedance bandwidth with respect to the tag IC impedance and enables to fully cover the allocated UHF frequency band for RFID application from 860 MHz to 960 MHz. Radiation patterns of the proposed tag antenna were also investigated. The radiation patterns in the zx plane and zy plane at 900 MHz were studied and the corresponding normalised results were presented in Fig. 5. As can be see, the optimal antenna has a dipole-like pattern, as expected. The maximum antenna gain was found to about 1.5 dB. The results are encouraging for practical implementation of this tag antenna.
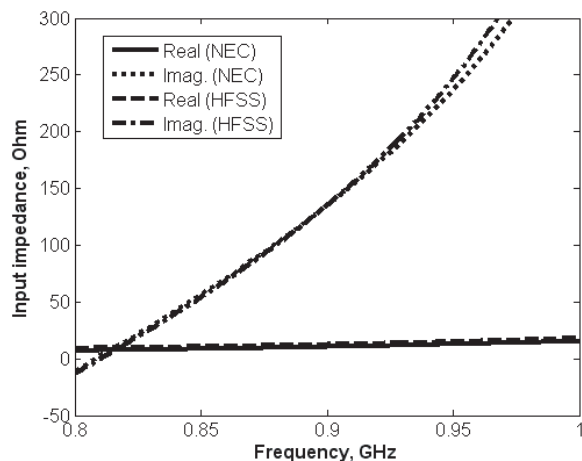

Figure 3: Simulated input impedance of the optimal RFID tag antenna.
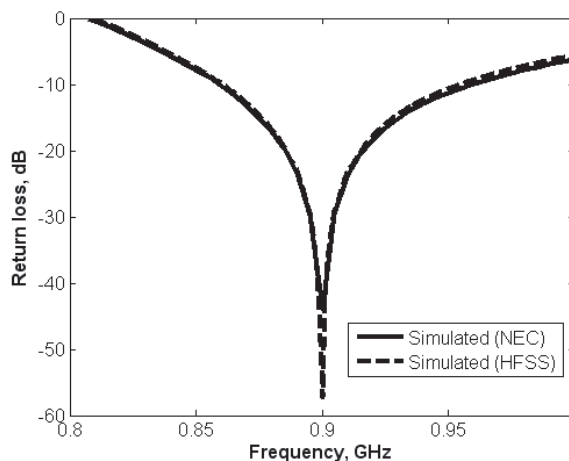
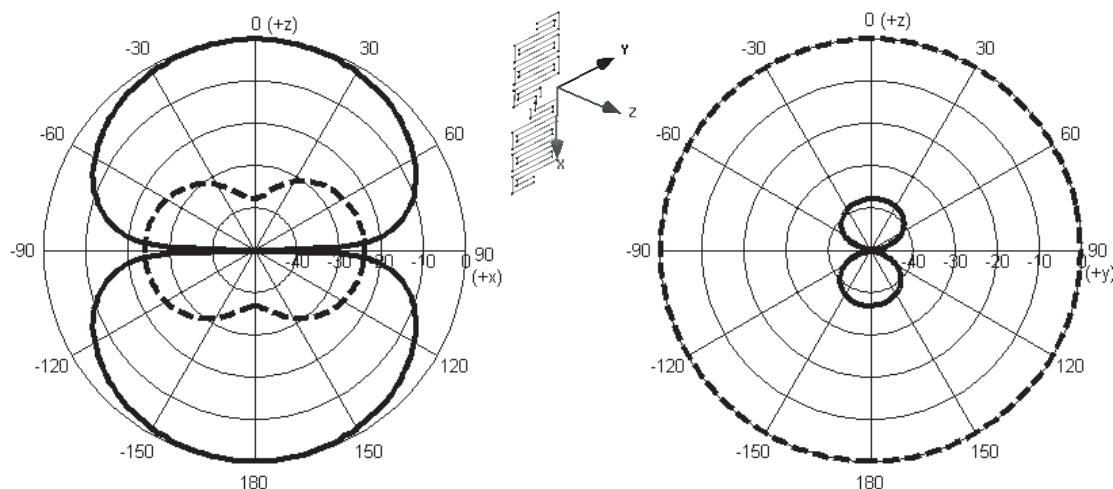Figure 4: Comparison of return loss for the optimal RFID tag antenna.

Figure 5: Radiation patterns of the proposed GA-optimized tag antenna for 900 MHz at: (left) zx plane; (right) zy plane; '—' measured E_θ and '- - - -' measured E_ϕ.

4. CONCLUSIONS

A novel design for the design and optimisation of RFID tag antennas with linear polarisation by use of genetic algorithms has been presented. A FORTRAN code genetic algorithm driver was adopted in this work in conjunction with the industry-standard NEC-2 FORTRAN source code, which was used to evaluate the randomly generated antenna samples. The results of the optimum designs of the proposed antennas exhibit good input impedance matching as required by the RFID IC. The presented examples show the capability of the proposed program in antenna design using GA and the results are encouraging for practical implementation of this tag antenna for UHF RFID applications.

REFERENCES

1. Finkenzeller, K., *RFID Handbook*, 2nd ed., John Wiley & Sons, Chichester, Ltd., 2004.
2. Bhatt, H. and B. Glover, *RFID Essentials*, O'Reilly, January 2006.
3. Carroll, D. L., FORTRAN Genetic Algorithm Driver, Version 1.7, download from: http://www.staff.uiuc.edu/ carroll/ga.html, 12/11/98.
4. Burke, G. L. and A. J. Poggio, "Numerical Electromagnetics Code (NEC)-method of moments," Lawrence Livermore Laboratory, Livermore, CA, 1981.
5. http://www.alientechnology.com.
6. Coley, D. A., *An Introduction to Genetic Algorithms for Scientists and Engineers*, World Scientific, Singapore, 1999.
7. Ammar, H. H. and Y. Tao, "Fingerprint registration using genetic algorithms," *IEEE Symposium on Applications Specific Systems and Software Engineering Technology*, 148–154, March 2000.
8. Rahmat-Samii, Y. and E. Michielssen, "Electromagnetic optimization by genetic algorithms," John Wiley & Sons, Canada, 1999.
9. Altshuler, E. E. and D. S. Linden, "Wire-antenna designs using genetic algorithms," *IEEE Antennas Propag. Mag.*, Vol. 39, 33–43, 1997.
10. Jones, E. A. and W. T. Joines, "Design of Yagi-Uda antennas using genetic algorithms," *IEEE Transactions on Antennas and Propagation*, Vol. 45, No. 9, 1386–1392, 1997.
11. Liu, W.-C., "Design of a CPW-fed notched planar monopole antenna for multiband operations using a genetic algorithm," *IEE Proc. — Microw. Antennas Propag.*, Vol. 152, No. 4, 273–277, 2005.
12. Zhou, D., R. A. Abd-Alhameed, C. H. See, P. S. Excell, and E. A. Amushan, "Design of quadrifilar helical and spiral antennas in the presence of mobile handsets using genetic algorithms," *Proceedings of the European Conference on Antennas and Propagation: EuCAP 2006*, Session 3PA1, No. 122, Nice, France, November 6–10, 2006.
13. Zhou, D., R. A. Abd-Alhameed, and P. S. Excell, "Bandwidth enhancement of balanced folded loop antenna design for mobile handsets using genetic algorithms," *PIERS Online*, Vol. 4, No. 1, 136–139, 2008.

A Miniature Chip Antenna Design for a Passive UHF RFID Tag to Be Built in a Portable Device

Yu-Shu Lin, **Hsien-Wen Liu**, **Kuo-Hsien Wu**, and **Chang-Fa Yang**

Department of Electrical Engineering
National Taiwan University of Science and Technology
Taipei, Taiwan

Abstract— In this paper, a miniature antenna for a passive UHF RFID tag is designed, which may be built in a portable device. Matching techniques for a Gen2 tag IC are employed to enhance the readable distance of the tag for long-range reading purposes, where quasi-lumped and lumped elements are used to match the chip antenna to the tag IC having complex input impedance. A commercial simulator, HFSS$^{\text{TM}}$ is used to analyze the performance of the antenna. Also, measurements in an anechoic chamber of the RFID education and research center at National Taiwan University of Science and Technology are performed to evaluate the readable range of the chip tag, which is more than 5 m for a reader with an EIRP equal to 4 W. The chip antenna operating in the 900 MHz RFID band proposed here has dimensions of only $10 \times 9.5 \times 0.8$ mm^3. Thus, this miniature tag may be flexibly built in a portable device to allow long-range reading.

1. INTRODUCTION

In recent years, Radio Frequency Identification (RFID) has been developed for many applications, such as supply chain managements, retail store applications, etc. For UHF passive RFID systems, the passive tags need to have good impedance matching to achieve efficient power transfer between the tag IC and antenna. Usually, tag antennas in ordinary half-wave dipole forms were designed [1–6]. In this paper, a miniature chip antenna having a size of only $10 \times 9.5 \times 0.8$ mm^3 for the UHF RFID passive tag is presented, which can be easily built in a portable device. An impedance matching approach by using quasi-lumped components is also investigated and is compared with that by applying lumped elements. A commercial simulator, HFSS$^{\text{TM}}$ [7] has been employed to analyze the electrical characteristics of the tag antenna and quasi-lumped elements.

2. RESULTS

As shown in Fig. 1, a miniature chip tag operating in the RFID UHF band is proposed here, which has antenna dimensions of only $10 \times 9.5 \times 0.8$ mm^3. To have a low cost design, this tag antenna is fabricated on an FR4 substrate with a relative permittivity $\varepsilon_r = 4.4$ and loss tangent $\delta = 0.02$. Performance of the proposed tag antenna having an input impedance of $26 + j3\,\Omega$ is demonstrated in Fig. 2, where a 100×48 mm^2 test board is used here. The input impedance of the Monza Gen2 tag IC we have used is equivalent to that of an RC series circuit with $R = 33$ ohm and $C = 1.58$ pF. To achieve a conjugated match with this tag IC, as shown in Fig. 3(a), a lumped inductance of 18 nH is serially connected between the proposed antenna and tag IC. Also, another matching circuit, composed of two compact quasi-lumped elements, is applied to obtain the conjugated match, as shown in Fig. 3(b). This quasi-lumped circuit consists of a series inductance and a shunt inductance, where the equivalent values of the inductances are extracted to be 12.3 nH and 12.5 nH, respectively.
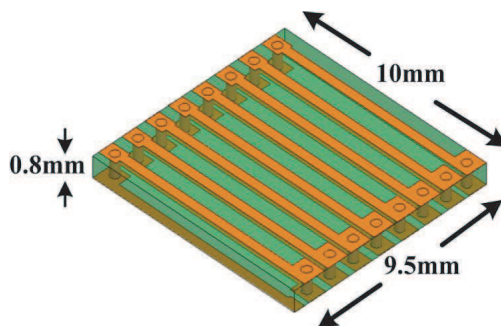

Figure 1: Geometry of the proposed miniature chip tag antenna.

Fig. 4 shows the measured input impedances and reflections of the lumped and quasi-lumped designs for the proposed chip antenna. The quasi-lumped design has a wider bandwidth in the RFID UHF band.
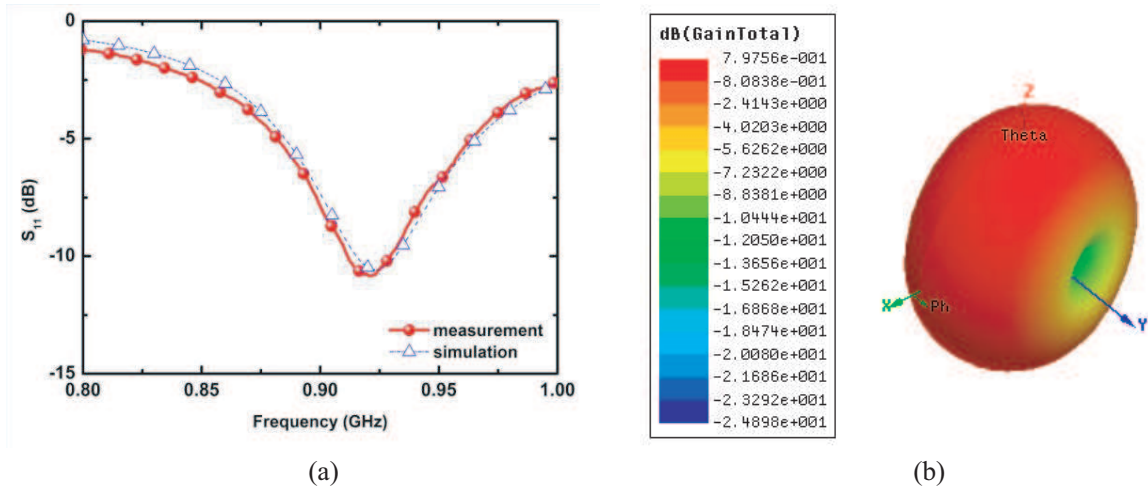

(a) (b)

Figure 2: The performance of the proposed passive tag antenna. (a) Return loss; (b) Simulated far-field radiation pattern at 922 MHz.
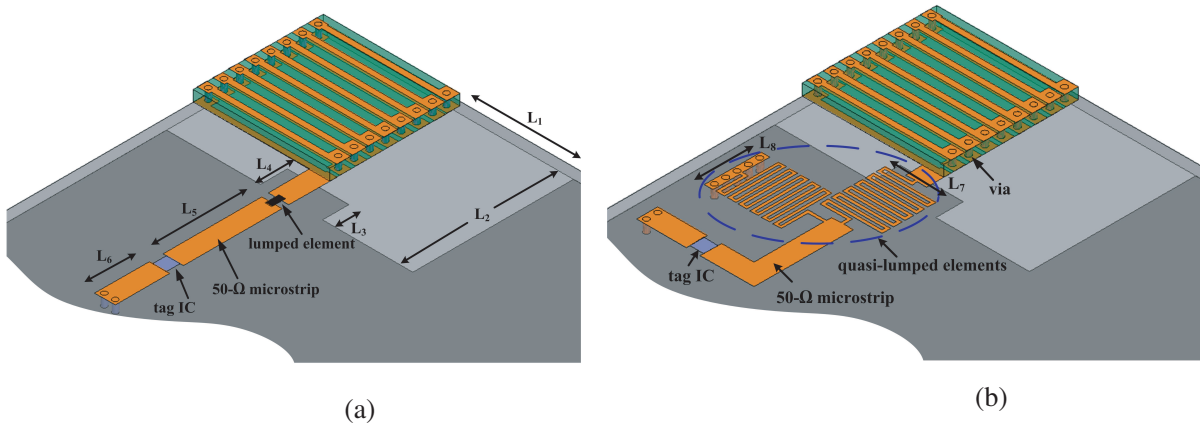

(a) (b)

Figure 3: Configurations of the lumped and quasi-lumped matching circuits. (a) Lumped circuit with $L_1 = 8\,\text{mm}$, $L_2 = 11.75\,\text{mm}$, $L_3 = 1.95\,\text{mm}$, $L_4 = 2.25\,\text{mm}$, $L_5 = 7.2\,\text{mm}$ and $L_6 = 4\,\text{mm}$; (b) Quasi-lumped circuit with $L_7 = 4\,\text{mm}$ and $L_8 = 4\,\text{mm}$.

The readable range of the tag was tested in an antenna measurement anechoic chamber, as shown in Fig. 5. A transmitting horn antenna with a gain G_t was fed by an RFID reader via a connecting cable with loss L_c. The proposed tag antenna, attached on a Styrofoam, was oriented to obtain the maximum power from the reader antenna. Since RF charging of the passive tag by the reader is the critical part for a success reading, the maximum readable range for a given $EIRP$ can be determined by the following formula [6]:

$$r_{\max} = d\sqrt{\frac{EIRP}{P_{\min}G_t L_c}} \tag{1}$$

where d is the distance between the tag and the transmitting antenna, $P_{\min}$ is the minimum power of the reader to be able to read the tag, $G_t = 5.7\,\text{dBi}$ and $L_c = -1.5\,\text{dB}$ at 922 MHz for the chamber system. In those measurements, d was fixed at 3.6 m, and the measured $P_{\min}$ for lumped and quasi-lumped designs were individually obtained to be 29 dBm and 28 dBm. Therefore, if the $EIRP$ of the reader is set to 4 W, the maximum readable ranges with the lumped and quasi-lumped

designs will be 5 m and 5.5 m, respectively. Besides, read-range experiments were also performed in a corridor to compare with those from chamber measurements, as listed in Table 1. Due to multi-path contributions, the distances measured in the corridor were longer in this test case.

Table 1: Experimental results of readable range measurements.

Matching circuit Readable range	Maximum range in the corridor	Maximum range in the anechoic chamber
Lumped elements	5.8 m	5 m
Quasi-lumped elements	6 m	5.5 m
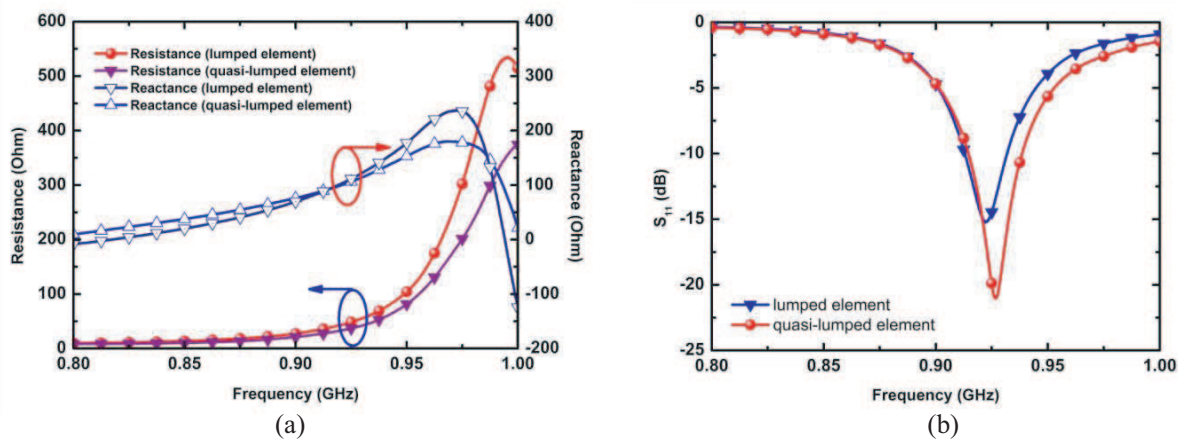
Figure 4: Measured input impedances and return losses of the proposed tag antenna with the lumped and quasi-lumped matching circuits. (a) Input impedance; (b) Return loss.
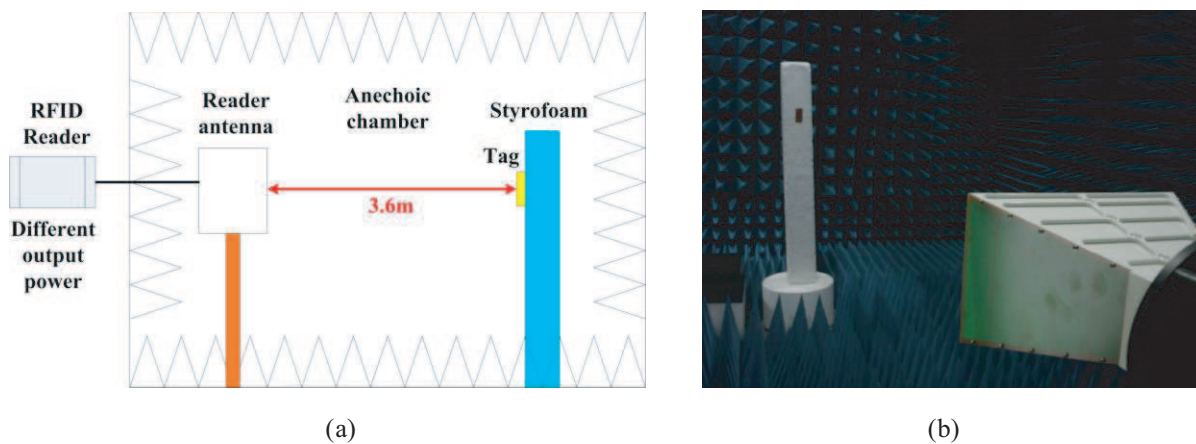
Figure 5: The readable range measurements in an anechoic chamber. (a) Measurement setup; (b) Chamber environment.

3. CONCLUSIONS

In this paper, we have proposed and analyzed a miniature chip antenna with lumped and quasi-lumped matching circuits for passive UHF RFID tag applications. The performance of the proposed tag antenna was examined through the readable range measurements in an anechoic chamber. The

compact chip tag with either quasi-lumped or lumped matching circuits can have a readable range more than 5 m with a 4 W *EIRP* reader.

REFERENCES

1. Rao, K. V. S., P. V. Nikitin, and S. F. Lam, "Antenna design for UHF RFID tags: A review and a practical application," *IEEE Trans. Antennas Propag.*, Vol. 53, No. 12, 3870–3876, Dec. 2005.
2. X. Qing and N. yang, "A folded dipole antenna for RFID," *Proc. IEEE AP-S Int. Symp. Dig.*, 97–100, Jun. 2004.
3. Ahn, J., H. Jang, H. Moon, J.-W. Lee, and B. Lee, "Inductively coupled compact RFID tag antenna at 910 MHz with near-isotropic radar cross-section (RCS) patterns," *IEEE Ante. and Wireless Propag. Lett.*, Vol. 6, 518–520, Jun. 2007.
4. Son, H.-W. and C.-S. Pyo, "Design of RFID tag antennas using an inductively coupled feed," *Electronics Lett.*, Vol. 41, No. 18, 994–996, Sept. 2005.
5. Liu, Y.-W., S.-Y. Chen, and P. Hsu, "Short-ended coplanar strip antenna for UHF RFID tags," *Proc. IEEE AP-S Int. Symp. Dig.*, 1773–1776, Jun. 2007.
6. Kurokawa, K., "Power waves and the scattering matrix," *IEEE Trans. Microw. Theory Tech.*, Vol. 13, No. 3, 194–202, Mar. 1965.
7. HFSS, *User's guide 9.2*, Ansoft Corp., USA.

A Metal Tag Antenna for Passive UHF RFID Applications

Hsien-Wen Liu, **Yu-Shu Lin**, **Kuo-Hsien Wu**, and **Chang-Fa Yang**

Department of Electrical Engineering
National Taiwan University of Science and Technology
Taipei, Taiwan

Abstract— In this paper, a passive tag antenna operating in RFID UHF band is presented, which may be mounted on a metallic object. This metal tag antenna design is composed of a slot radiator, a capacitive coupling structure and a coplanar waveguide (CPW) feed to provide a good power transfer to the tag IC. No additional matching network is required to achieve a conjugated matching between the tag IC and the proposed tag antenna. A commercial simulator, HFSS is used to analyze the proposed antenna performance. This tag antenna for the 900 MHz RFID band has dimensions of only $93(L) \times 20(W) \times 3.4(H)\,mm^3$, and therefore can be easily attached on metal surfaces, such as license plates for vehicle managements. Also, the antenna with low cost, easy fabrication and high efficiency are achieved by using a 0.4 mm FR4 PCB attached on a 3 mm PP substrate. For the metal tag mounted on the license plate, the maximum readable range measured in an anechoic chamber is more than 7 m for a reader with an EIRP equal to 4 W.

1. INTRODUCTION

In recent years, Radio Frequency Identification (RFID) has rapidly attracted high attention in many commercial applications, such as supply chain managements, retail store applications and tracking goods. For UHF passive RFID systems, the passive tags must have a good impedance matching to achieve efficient power transfer between the tag IC and antenna. Many literatures [1–5] have investigated the tag antennas for various RFID applications. In this paper, we propose a passive UHF tag antenna having dimensions of only $93(L) \times 20(W) \times 3.4(H)\,mm^3$, which may be mounted on a metal object, such as being attached on a license plate for vehicle managements. A commercial simulator, HFSS[TM] [6] has been applied to analyze the electrical characteristics of the metal tag antenna. Also, the readable range of the metal tag has been measured in an anechoic chamber of the RFID education and research center at National Taiwan University of Science and Technology.

2. RESULTS

As shown in Fig. 1, the proposed metal tag antenna consists of a slot radiator, a capacitive coupling structure and a coplanar waveguide (CPW) feed, which has dimensions of only $93(L) \times 20(W) \times 3.4(H)\,mm^3$. This tag antenna is fabricated on a 0.4 mm FR4 PCB and attached on a 3 mm polypropylene (PP) substrate, where the FR4 substrate has a relative permittivity $\varepsilon_r = 4.4$ and loss tangent $\tan\delta = 0.02$, and the PP substrate has $\varepsilon_r = 2.3$ and $\tan\delta = 0.006$. Also, Impinj Monza Gen2 tag IC with an input impedance of $33 - j112$ ohm is used here. To achieve a conjugated match
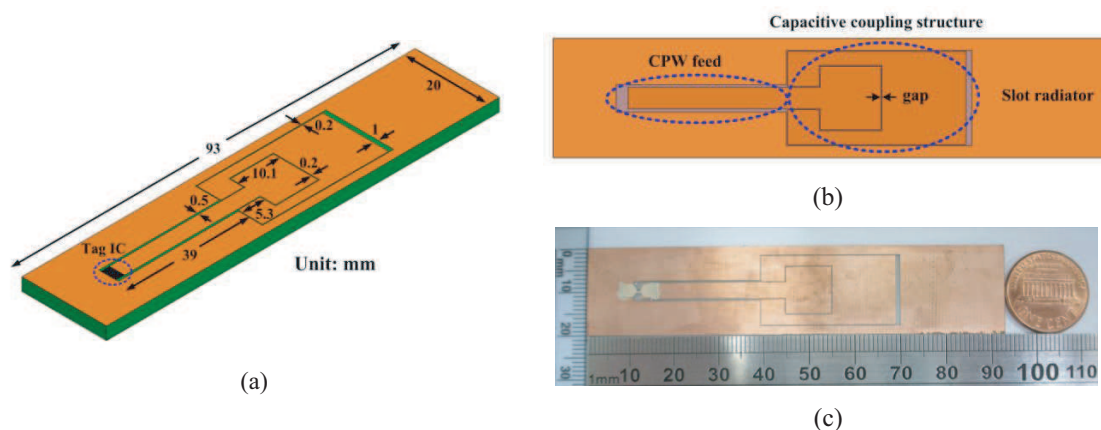

Figure 1: The proposed passive metal tag antenna. (a) Geometry; (b) Antenna structure; (c) Photograph.

with the tag IC, the gap width of the capacitive coupling structure was varied to tune the input impedances of the tag antenna, as shown in Fig. 2(a). Note that the return loss of the proposed antenna can be obtained by the following equation

$$20 \log |\Gamma| = 20 \log \left| \frac{Z_L - Z_S^*}{Z_L + Z_S} \right| \tag{1}$$

where Z_L is the impedance of tag IC and Z_S is the input impedance of tag antenna.

Both simulations and measurements for the return loss of the antenna terminated with the tag IC are plotted in Fig. 2(b), which show a good matching in the RFID UHF band. Also, fair agreements between simulated and measured results are observed, although the measurements indicate a wider bandwidth. This difference may be due to measurement errors caused by a probing cable connecting the antenna input terminal. For examining the antenna performance, the proposed metal tag is attached on a metal plate with dimensions of $30 \times 15\,\mathrm{cm}^2$, as shown in Fig. 3(a). The simulated 3D far-field pattern of the metal tag on the plate at 922 MHz is plotted in Fig. 3(b), where a main beam in the upper forward direction is obtained as desired.
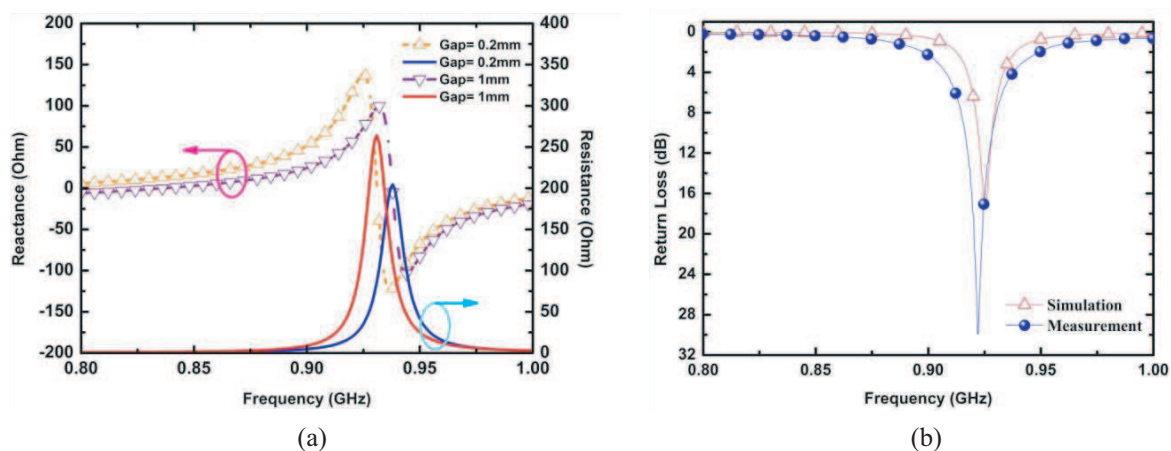
Figure 2: Input impedance and return loss of the metal tag antenna for different gap widths in the capacitive coupling structure. (a) Input impedance; (b) Return loss.
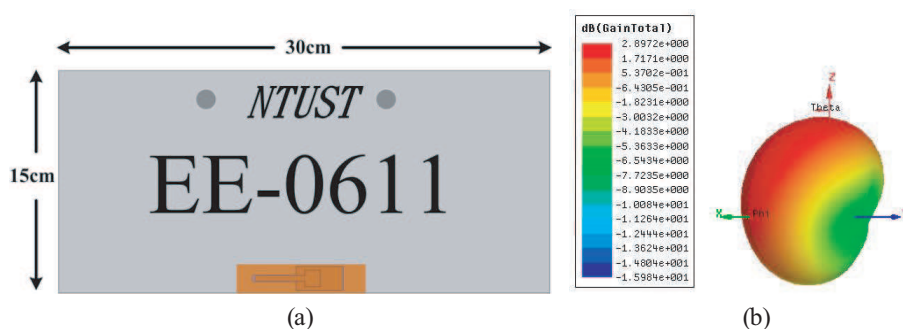

Figure 3: The metal tag mounted on a license plate. (a) Geometry; (b) Simulated far-field radiation pattern at 922 MHz.

The readable range of the proposed tag was tested by using the far-field antenna measurement anechoic chamber, as shown in Fig. 4. A transmitting horn antenna with a gain G_t was fed by an RFID reader via a connecting cable with loss L_c. The proposed tag antenna, attached on a Styrofoam with or without the metal plate, was oriented to obtain the maximum power from the reader antenna at a fixed distance d. Since RF charging of the passive tag by the reader is the critical part for a success reading, the maximum readable range in free space can be determined by the following Friis transmission formula [5]:

$$r_{\max} = d \sqrt{\frac{\mathrm{EIRP}}{P_{\min} G_t L_c}} \tag{2}$$

where d is the distance between the tag and the transmitting antenna, $P_{\min}$ is the minimum power of the reader to be able to read the tag, $G_t = 5.7\,\text{dBi}$ and $L_c = -1.5\,\text{dB}$ at $922\,\text{MHz}$ in our chamber. Since the measured $P_{\min}$'s with and without the metal plate are $25.5\,\text{dBm}$ and $29.5\,\text{dBm}$, the maximum readable ranges are $7.3\,\text{m}$ and $4.6\,\text{m}$, respectively. Also, the readable range was tested in a corridor. Comparisons of the results obtained in the chamber and corridor are given at Table 1, where the distance measured in the corridor for the metal tag alone is longer than that obtained in the chamber. However, for the metal tag attached on the plate, the readable distances are about the same. The longer-distance reading is caused by multi-path contributions in the corridor, which are more significant for the metal tag without the plate due to its omni-directional pattern.

(a)   (b)
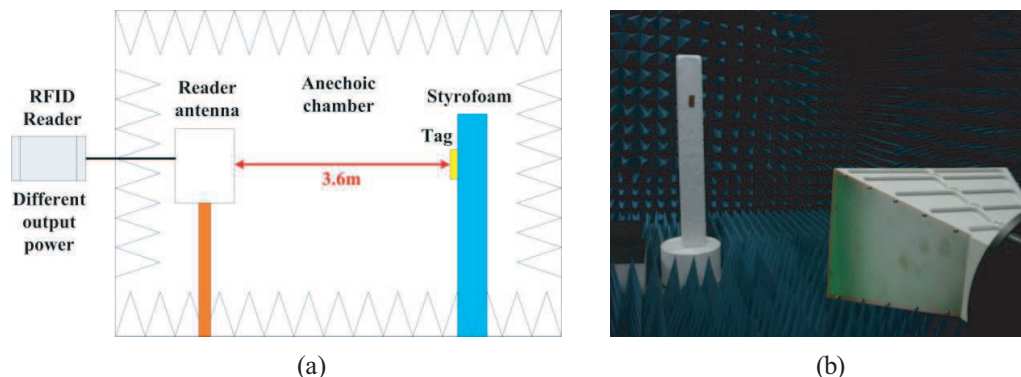
Figure 4: The readable range measurements in an anechoic chamber. (a) Measurement setup (b) Chamber environment.

Table 1: Readable range measurements of the metal tag with a 4 W EIRP reader.

Site \\ Tag	Anechoic chamber	Corridor
Alone	4.6m	6.5m
On a metal plate	7.3m	7.4m

3. CONCLUSIONS

A compact metal tag antenna for passive UHF RFID applications has been proposed and analyzed in this paper. This metal tag may be easily mounted on a metal object. Performance of the tag was examined with simulations and measurements. The maximum readable distance of the metal tag on a metal plate measured in an anechoic chamber is more than $7\,\text{m}$ for a reader with an EIRP equal to $4\,\text{W}$.

REFERENCES

1. Rao, K., S.-F. Lam, and P. V. Nikitin, "Wideband metal mount UHF RFID tag," *2008 IEEE AP-S Int. Symp. Dig.*, 1–4, Jul. 2008.
2. Sim, D.-U., D.-H. Kim, J.-I. Choi, and H.-D. Choi, "Design of novel dipole-type tag antennas using electromagnetic bandgap (EBG) surface for passive RFID applications," *2007 IEEE AP-S Int. Symp. Dig.*, 1333–1336, Jun. 2007.
3. Cho, C., H. Choo, and I. Park, "Design of novel RFID tag antennas for metallic objects," *2006 IEEE AP-S Int. Symp. Dig.*, 3245–3248, Jul. 2006.
4. Son, H.-W. and C.-S. Pyo, "Design of RFID tag antennas using an inductively coupled feed," *Electronics Lett.*, Vol. 41, No. 18, 994–996, Sept. 2005.
5. Rao, K. V. S., P. V. Nikitin, and S. F. Lam, "Antenna design for UHF RFID tags: A review and a practical application," *IEEE Trans. Antennas Propag.*, Vol. 53, No. 12, 3870–3876, Dec. 2005.
6. HFSS, *User's guide 9.2*, Ansoft Corp., USA.

Dual-frequency Balanced Mobile Antenna for WLAN and Short Range Communication Systems

D. Zhou[1], **R. A. Abd-Alhameed**[1], **C. H. See**[1],
S. W. J. Chung[1], **A. G. Alhaddad**[1], **and P. S. Excell**[2]

[1]Mobile and Satellite Communications Research Centre
University of Bradford, Bradford, West Yorkshire, BD7 1DP, UK
[2]Glyndwr University, Wrexham, LL11 2AW, Wales, UK

Abstract— In this paper, a balanced antenna for mobile handset applications with dual-frequency performance, that covers 2.4-GHz and 5.2-GHz WLAN bands, is investigated. The antenna is a thin-strip planar dipole with folded structure and a dual-arm on each monopole. Performance of the proposed antenna was analysed and optimised against the targeted two frequency bands. For validation, a prototype of the antenna was fabricated and tested. The performance of this balanced antenna was verified and characterised in terms of the antenna return loss, radiation pattern and power gain. The predicted and measured results show fairly good agreement and the results also confirm good impedance bandwidth characteristics for the proposed balanced antenna with dual-band operation.

1. INTRODUCTION

The need to expand the bandwidth of antennas in mobile handheld devices follows from the ever-increasing data rates, and hence spectrum requirements, of mobile devices. Antennas are a major part of the complete design in mobile device design. Conventionally, the unbalanced planar inverted F antenna (PIFA) is one of the most popular candidates for compact built-in antennas for mobile handsets. PIFAs use the ground plane as a part of the radiator, which enables very small antennas to achieve sufficient gain and bandwidth [1–4]. In almost all cases, radiating currents are induced on both the ground plane and the antenna element. In use, however, these antennas exhibit poor performance when held by users. This is mainly because the user holding the mobile phone largely takes the place of the ground plane resulting in currents flowing on the human body, which degrade the performance of the antenna's radiation properties and introduce losses and uncertainty in its matching.

Balanced antenna is a good alternative candidate since balanced currents only flow on the antenna element in this type of antenna, thus dramatically reducing the effect of current flow on the ground plane. As a result, balanced antennas should have good efficiency and more important to maintain their performance when in use adjacent to the human body [5]. In recent years, several novel mobile antennas designed with the balanced technique have demonstrated the enhanced stability of antenna performance, compared to the unbalanced type, when the handset is approximately placed next to the human head and/or hand [6–8].

This paper presents and analyses a new design of a built-in dual-frequency balanced-dipole antenna for WLAN and short range wireless communications. The characteristics of this balanced folded dipole antenna with a novel dual-arm structure for mobile handsets are analysed. In the analysis, an electromagnetic simulator based on the finite integration technique was applied to calculate return loss and radiation patterns [9].

2. ANTENNA DESIGN CONCEPT

Basically, the first antenna design attempted was designed in free space and then several modifications were introduced to achieve a dual-band feature for mobile handset applications. The antenna, as shown in Fig. 1, is mounted on the top of a rectangular conductor plate ($45 \times 100\,\mathrm{mm}$), which can be regarded as the mobile handset chassis or ground plane of a practical mobile phone.

The design concept for producing dual-band balanced mobile antennas was applied and implemented in the authors' previous work, as illustrated in [10], where a technique to generate another resonant frequency was employed by inserting an additional thin-strip arm in one of the arms of the planar dipole; as a result, the single resonant antenna was modified and developed as a wideband dual-resonant variant for multi-band operation. In this study, the new proposed antenna was developed using the same design principle, but designed with simpler configuration for different

applications in WLAN and short range communication systems. Initially, a folded antenna with single arm, operating at around 2.4 GHz, was designed and optimized using the EM simulator. Subsequently, a new technique was applied by inserting an additional thin-strip arm (see Fig. 1) that will be used to obtain the resonant frequency for 5.2 GHz band.

The proposed antenna features a compact design, with dimension ($l \times w \times h$) of $38 \times 8 \times 8$ mm. The length and location of the additional arm, including other parameters of the proposed antenna, were adjusted and further optimised to ensure that the design entirely covered the required two frequency bands (i.e., 2400–2485 MHz & 5150–5350 MHz) at VSWR ≤ 2.5.
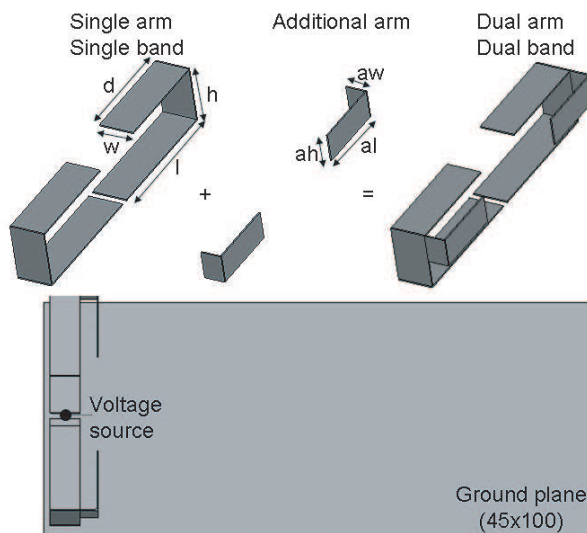
Figure 1: Balanced mobile antenna configuration studied.

3. SIMULATION AND MEASUREMENT RESULTS

The optimal antenna configuration studied in terms of return loss, radiation patterns and power gain was found with aid of CST simulator ($l = 18.5$, $d = 14.5$, $w = 5$, $h = 8$, $al = 10$, $aw = 3$, $ah = 4$; dimensions are in mm). For the hardware realisation, copper sheet with 0.15 mm thickness was used for fabricating the proposed balanced antenna (see Fig. 2). For a balanced antenna (e.g., dipole) system, a balun is usually required as a support feeding network, to provide a balanced feed from an unbalanced source. A commercially hybrid junction from ET Industries [11] that operates from 2 to 12 GHz has been utilized in this work. Fig. 3 presents the measured and simulated return loss of the prototype antenna. As can be seen, taking into account the errors caused by

Figure 2: Photograph of prototype of the proposed balanced antenna design.
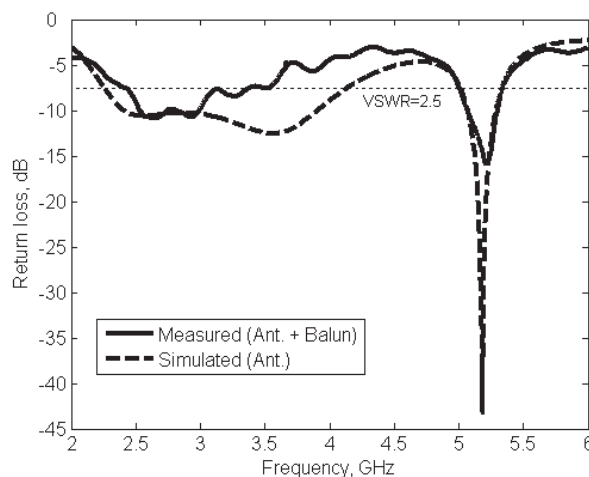

Figure 3: Comparison of simulated and measured return loss.

manufacturing the proposed antenna, a fairly good agreement between the calculated and measured return loss was observed.

Measurements of the radiation patterns of the prototype were carried out in a far-field anechoic chamber. Two pattern cuts were taken for two selected operating frequencies that cover the designated whole bandwidth in this study. The radiation patterns in the xz plane and yz plane for the balanced folded dipole at 2450 MHz and 5200 MHz were measured, as presented in Fig. 4. The measured patterns at the lower band shown asymmetrical radiation, which is mainly due to the asymmetrical antenna structure in fabrication and imbalanced outputs from the balun device in testing. It is worth mentioning that the measured patterns of the prototype at higher frequencies in the lower band (e.g., 2600 MHz, 3000 MHz and 3200 MHz) are similar to the ones at 2450 MHz presented in Fig. 4, as observed. This is because antenna impedance matching at those frequencies were all generated and controlled by the single-arm folded dipole containing; whereas, the proposed antenna at 5200 MHz tends to radiate at the $+z$ direction in both plane cuts. In this case, the ground plane in this band acts as a good reflector.
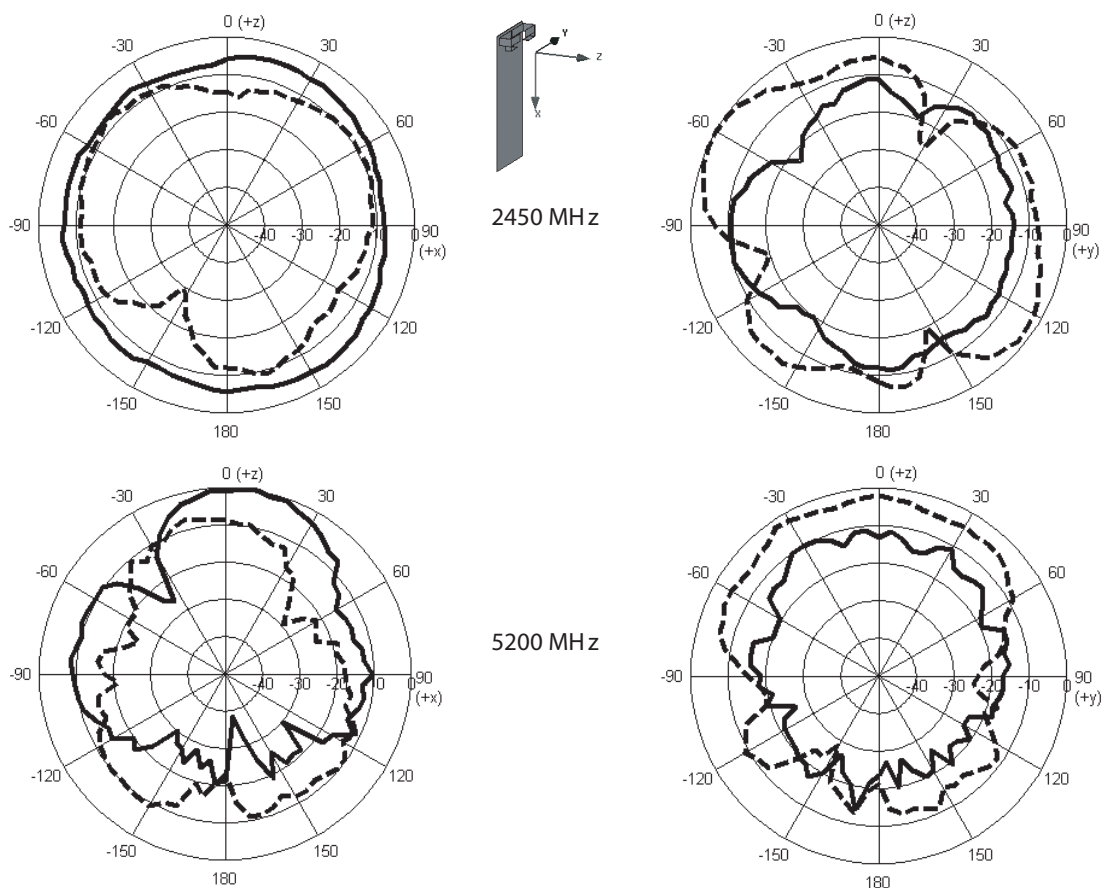
Figure 4: Radiation patterns of the proposed antenna for 2450 MHz and 5200 MHz at: (left) xz plane; (right) yz plane, where '——' measured E_θ and '- - -' measured E_ϕ.

Measured broadside antenna power gain for the frequencies across the 2.4 GHz and 5.2 GHz WLAN bands were also investigated. It is notable that the insertion loss of the feeding network was subsequently compensated for each measured power gain over all bands. It was found that the maximum measured antenna gain at lower and upper WLAN bands were 2.3 dBi and 6.2 dBi, respectively.

In addition, current distribution on the mobile phone ground plane was analyzed using the EM simulator: it was observed that most of the current induced on the ground plane concentrated in the area beneath the antenna and minimum current distribution appeared on the rest of the ground plane, as expected. This proves the model advantage of using a balanced antenna in designs for mobile handsets. The results are encouraging for practical investigation of this antenna in finding the performance of radiation and SAR of this new development.

4. CONCULSIONS

A dual-band balanced folded dipole antenna with novel structure for mobile devices operated over 2.4 GHz and 5.2 GHz WLAN bands has been presented. The proposed antenna model was experimentally verified in terms of antenna return loss, radiation pattern and power gain. The simulated and measured results over all frequency bands considered, show a good agreement and this made the proposed antenna an attractive candidate for mobile handset applications.

ACKNOWLEDGMENT

REFERENCES

1. Li, Z. and Y. Rahmat-Sammii, "Optimization of PIFA-IFA combination in handset antenna designs," *IEEE Trans. on Antennas and Propagation*, Vol. 53, No. 5, 1770–1778, May 2005.
2. Wang, Y.-S., M.-C. Lee, and S.-J. Chung, "Two PIFA-related miniaturized dual-band antennas," *IEEE Trans. on Antennas and Propagation*, Vol. 55, No. 3, 805–811, March 2007.
3. Janapsatya, J., K. P. Esselle, and T. S. Bird, "A dual-band and wideband planar inverted-F antenna for WLAN applications," *Microwave and Optical Technology Letters*, Vol. 50, 138–141, January 2008.
4. Huynh, M.-C. and W. Stutzman, "Ground glane effects on planar inverted-F antenna (PIFA) performance," *IEE Proc.-Microw. Antennas Propag.*, Vol. 150, 209–213, August 2003.
5. Zhou, D., R. A. Abd-Alhameed, and P. S. Excell, "Wideband balanced folded dipole antenna for mobile handsets," *Proceedings of The European Conference on Antennas and Propagation: EuCAP 2007*, Paper No. MoPA.012, Edinburgh, UK, November 11–16, 2007.
6. Morishita, H., H. Furuuchi, and K. Fujimoto, "Performance of balance-fed antenna system for handsets in vicinity of a human head or hand," *IEE Proc.-Microw. Antennas Propag.*, Vol. 149, No, 2, 85–91, April 2002.
7. Morishita, H., S. Hayashida, J. Ito, and K. Fujimoto, "Analysis of built-in antenna for handset using human (heand,hand,finger) model," *Electronics and communications in Japan*, Part 1, Vol. 86, No. 9, 35–45, 2003.
8. Abd-Alhameed, R. A., P. S. Excell, K. Khalil, R. Alias, and J. Mustafa, "SAR and radiation performance of balanced and unbalanced mobile antennas using a hybrid formulation," Invited paper, *IEE Proceedings-Science, Measurement and Technology special issue on Computational Electromagnetics*, Vol. 151, No. 6, 440-444, November 2004.
9. Computer Simulation Technology Corporation, CST Microwave Studio, Version 5.0, Germany.
10. Zhou, D., R. A. Abd-Alhameed, C. H. See, and P. S. Excell, "Design of multiband balanced folded dipole antenna based on a dual-arm structure for mobile handsets," *PIERS Online*, Vol. 4, No. 8, 821–824, 2008.
11. ET Industries, USA, http://www.etiworld.com/.

Enhanced-bandwidth PIFA Antenna with a Slot on Ground Plane

Xingyu Zhang and Anping Zhao

Nokia Research Center, Beijing 100176, China

Abstract— In order to overcome the shortcoming of narrow bandwidth for conventional planar inverted-F antenna (PIFA), a novel bandwidth enhancement approach for internal multi-band handset antennas is proposed in this paper. In particular, a rectangular slot with an appropriate location and a proper size is introduced into the ground plane of the system printed circuit board to improve the bandwidths of handset antennas in both the low (GSM850/GSM900) and high (DCS1800/PCS1900) bands. The influences of the slot with different locations and sizes on antenna bandwidth are investigated. A prototype that can cover the frequency bands of GSM850, GSM900, DCS1800 and PCS1900 simultaneously was fabricated and measured. Good agreement between the measurement and simulation results is achieved.

1. INTRODUCTION

Nowadays, modern wireless communication technologies are in the process of rapid development. Multi-system applications have been used explosively. Owing to this, it bas been a necessity to design antennas with the characteristics of multiband and wideband for mobile terminals. At present, planar inverted-F antenna (PIFA) is being adopted extensively as handset antennas because of its advantages of compact structure, low profile, easy fabrication, low manufacturing cost and easy integration with portable devices. However, a major disadvantage of the PIFA antenna is its narrow impedance bandwidth. Hence, it is desirable to find methods that can enhance the bandwidths of the PIFA antennas. The bandwidth of the PIFA antenna described in [1] is broadened by using a tapered-type radiating patch. Multi-layer patches and a folded stub are introduced into the internal PIFA to improve its bandwidth [2]. The bandwidth enhancement approaches mentioned above both focus on making modifications on the radiating elements of PIFA antennas. There are also other bandwidth improvement methods concentrating on making modifications on the system ground plane of mobile terminals. For example, a T-shaped ground plane is reported to broaden the bandwidth of the PIFA antenna [3]. A slotted ground plane for handset devices is described to lower the profile and improve the bandwidth of PIFA antennas [4, 5]. The bandwidth of the PIFA antenna designed in [6] is enhanced by using quarter-wavelength wavetraps.

In this paper, a novel technique that is used to broaden the impedance bandwidth of traditional multi-band PIFA antennas is presented. In particular, a rectangular slot is introduced into the ground plane of mobile chassis. By varying the location and size of the slot, the equivalent length of the ground plane can be adjusted to the optimal lengths of the low and high bands, which thus enhance the bandwidths of PIFA antennas for both the low and high bands. The influences of different slot locations and sizes on the bandwidths of the low and high bands are studied and analyzed. Based on this study, a compact internal quad-band (GSM850/GSM900/ DCS1800/PCS1900) PIFA antenna with only a volume of $20 \times 40 \times 6 \, \text{mm}^3$ was constructed and measured. The measurement results agree well with the simulation ones.

2. ANTENNA DESIGN AND RESULTS ANALYSIS

The geometry of the PIFA antenna under consideration is shown in the left figure of Fig. 1, where the volume of the antenna with two small folded arms is $20 \times 40 \times 6 \, \text{mm}^3$. The system printed circuit board with a volume of $40 \times 100 \times 1 \, \text{mm}^3$ is comprised of a very thin metal plate and a lossy FR-4 substrate (with permittivity of 4.9 and loss tangent of 0.025). For comparison, the PIFA antenna without the slot on the mobile chassis is used as reference antenna; and the return loss of the reference antenna is plotted in Fig. 2. It can be seen from Fig. 2 that the reference antenna is a dual-band PIFA antenna with two resonant frequencies at 0.87 GHz and 1.81 GHz. In order to broaden the bandwidth of this dual-band PIFA antenna, a rectangular slot is introduced onto the mobile chassis. The location and dimension of the slot are described by parameters S, L and W.

Effect of the location and size of the slot on the impedance bandwidth (here $-6 \, \text{dB}$ is used as the criteria) of the low band is studied first. Fig. 2 plots the bandwidth of the PIFA antenna varying as a function of W for the case where $S = 50 \, \text{mm}$ and $L = 35 \, \text{mm}$. One can see from Fig. 2 that the impedance bandwidth of the low band is gradually improved first and then becomes
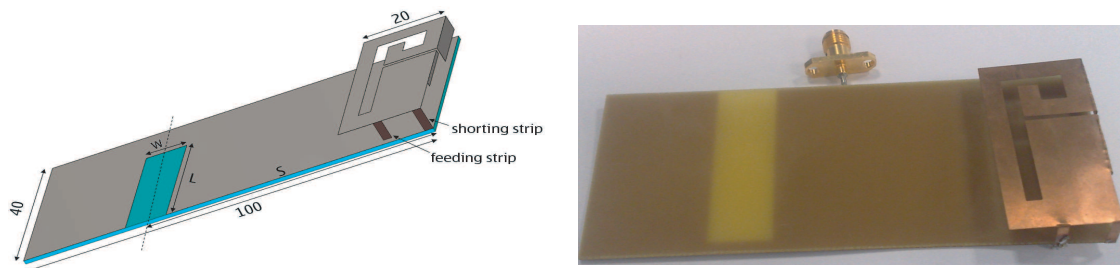
Figure 1: Geometry of the studied PIFA antenna (in mm) and prototype of the finalized fabrication antenna.

worse while W increases from 2 mm to 26 mm. In particular, when W increases from 2 mm (note that in this case there is still a single-resonant mode in the low band) to 10 mm, a dual-resonant mode starts to appear in the low band; and a balanced dual-band mode appears when $W = 12$ mm. But, when W increases from 12 mm, the balanced dual-resonant mode begins to be distorted; and the impedance bandwidth of the low band does not meet the -6 dB criteria anymore, e.g., while $W = 26$ mm. Obviously, the antenna performance of the low band reaches its optimal at the balanced dual-resonant mode. Hence, $W = 12$ mm can be defined as the optimal value of W for the case where $S = 50$ mm and $L = 35$ mm. It can also be seen from Fig. 2 that, compared to the reference antenna, the antenna bandwidth of the low band obtained with the optimal parameters (i.e., $S = 50$ mm, $L = 35$ mm and $W = 12$ mm) is significantly broadened.

In order to further investigate the antenna bandwidth property for the low band, different optimal situations of the PIFA antenna for the case of $S = 50$ mm are depicted in Fig. 3. One can see from Fig. 3 that for a fixed value of S the optimal cases are obtained while W increases greatly with a slight decrease of L. One can also see from Fig. 3 that for a fixed slot location (described by S) an unlimited number of (different) optimal cases for the low band can be obtained by adjusting the slot size (described by L and W). In addition, results in Fig. 3 indicate that for a fixed value of S better performance is obtained for the high band (the bandwidth in the low band is almost unchanged) when L is bigger. Moreover, the cases for $S = 60$ mm and $S = 70$ mm are also studied; and similar phenomenon is observed for $S = 60$ mm and $S = 70$ mm cases.
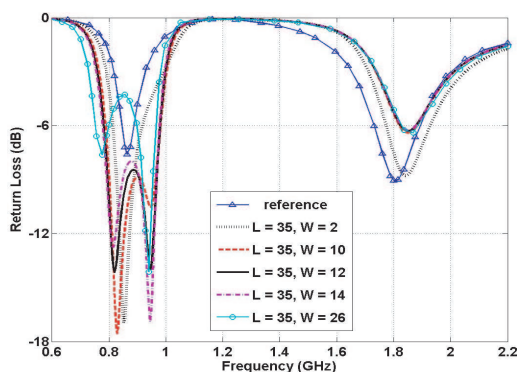

Figure 2: Bandwidth variations with different values of W ($S = 50$ mm).
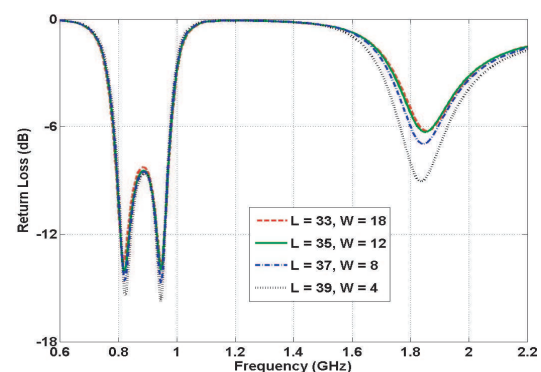
Figure 3: Different optimal cases in the low band for $S = 50$ mm.

The influences of the slot location on antenna bandwidths of both the low and high bands are investigated next. Fig. 4 denotes the comparison between different optimal situations with different values of S while $L = 37$ mm. It can be seen from Fig. 4 that, when S increases from 50 mm to 80 mm, the antenna bandwidth of the low band slightly decreases while the bandwidth of the high band is obviously improved. Especially, the bandwidth of the high band is improved even significantly when S increases from 50 mm to 70 mm. The above study indicates that the optimal performances of the low and high bands are highly dependent on the slot location and size. Also, the optimal slot location and size of the low band are different from those of the high band. Hence, to broaden the bandwidths for the low and high bands simultaneously, a compromised solution for the slot location and size should be selected. In addition, the following conditions should also be taken into consideration while the compromised solution is selected: i) all the GSM850, GSM900,

DCS1800 and PCS1900 bands should be covered; and ii) the size of the slot should not be too big as enough space should be accommodated for other electronic components on the mobile chassis. To this end, the slot location and size with values of $S = 70\,\text{mm}$, $L = 37\,\text{mm}$ and $W = 12\,\text{mm}$ are selected as the compromised solution, which is defined as the proposed antenna in this paper. A prototype for the proposed antenna was manufactured, as exhibited in the right figure of Fig. 1. Fig. 5 shows the simulated and measured return losses of the proposed antenna. For comparison, the computed and experimental return losses of the reference antenna are also depicted in Fig. 5. One can see from Fig. 5 that quite good agreement between the measurement and the simulation results is obtained. In addition, the measured impedance bandwidth (defined at $-6\,\text{dB}$ level) of the low band ranges from $0.7\,\text{GHz}$ to $0.98\,\text{GHz}$ and for the high band it is between $1.65\,\text{GHz}$ and $2.02\,\text{GHz}$, which completely covers the required quad-band operational bandwidth. Compared with the bandwidth of the reference antenna, the measured bandwidth of the proposed antenna improves by 543% and 133% in the low and high bands, respectively. The simulated radiation patterns of the proposed antenna are shown in Figs. 6 and 7. It can be seen that the radiation patterns of the proposed antenna is approximately omni-directional. Figs. 8 and 9 plot the gain and efficiency of the presented antenna. It is illustrated from Fig. 8 and Fig. 9 that the gain and efficiency of the fabrication antenna meet the requirements of mobile terminals.
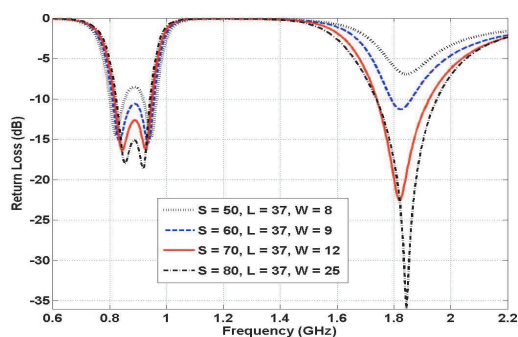

Figure 4: Comparison of various optimal cases with different S ($L = 37\,\text{mm}$).
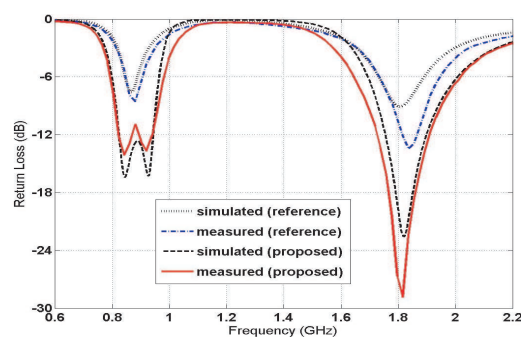
Figure 5: Measured and simulated antenna return losses.

Figure 6: Radiation patterns of the proposed antenna at central frequencies in E-plane, (a) $0.859\,\text{GHz}$, (b) $0.92\,\text{GHz}$, (c) $1.795\,\text{GHz}$, (d) $1.92\,\text{GHz}$.

Furthermore, the reason for getting such big bandwidth improvement for both the low and high bands is also explored. As discussed in [7], to reach the maximum bandwidth for a PIFA antenna with a chassis of about $40\,\text{mm}$ wide, the optimum lengths for the low band and high bands are about $120\,\text{mm}$ and $70\,\text{mm}$, respectively. This means that the length $100\,\text{mm}$ in the reference antenna is either too short for the low band or too long for the high band. Fig. 10 depicts E-field and surface current distributions of the proposed antenna at the resonant frequencies of the low and high bands, where the arrowed lines indicate part of the current paths flowing on the chassis. It can be seen from Fig. 10(a) that the effective length for the low band is lengthened. This is why the first resonance frequency of the low band is shifted from $0.87\,\text{GHz}$ (reference antenna) to $0.844\,\text{GHz}$. Another important reason for getting such a wider bandwidth in the low band is that an equivalent dipole resonant mode (at $0.924\,\text{GHz}$) shown in Fig. 10(b) is created by the slot. On the other hand, one can see from Fig. 10(c) that for the high band almost no current could reach

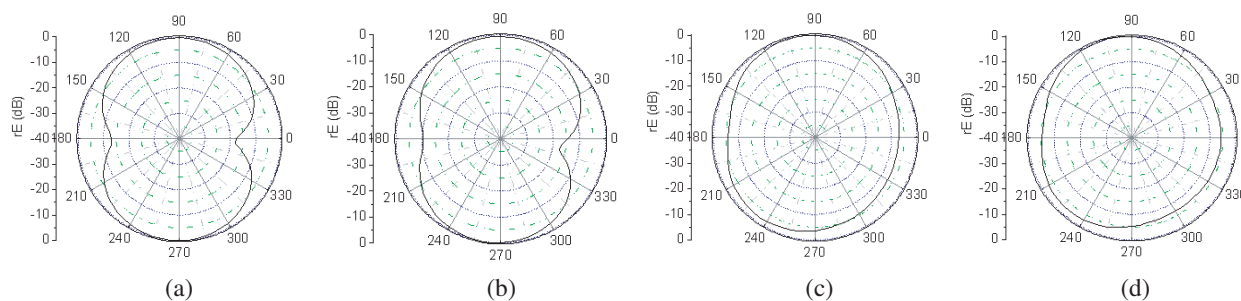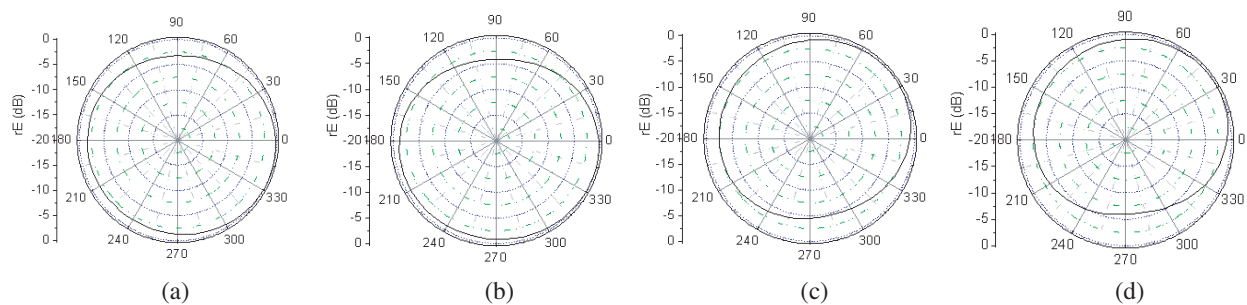(a)   (b)   (c)   (d)

Figure 7: Radiation patterns of the proposed antenna at central frequencies in H-plane, (a) 0.859 GHz, (b) 0.92 GHz, (c) 1.795 GHz, (d) 1.92 GHz.
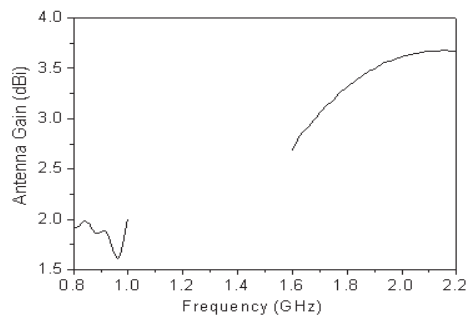

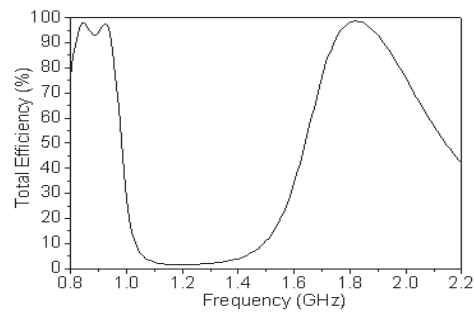Figure 8: Gain of the proposed antenna.

Figure 9: Total efficiency of the proposed antenna.

the area below the slot on the chassis. This implies that for the high band the effective length of the chassis is shortened and it is close to its optimal length, which just explains why a very significant bandwidth improvement is obtained for the high band. The above analysis clearly demonstrates that the bandwidths of the PIFA antenna in both the low and high bands can be significantly improved by the slot with a proper location and a suitable size.
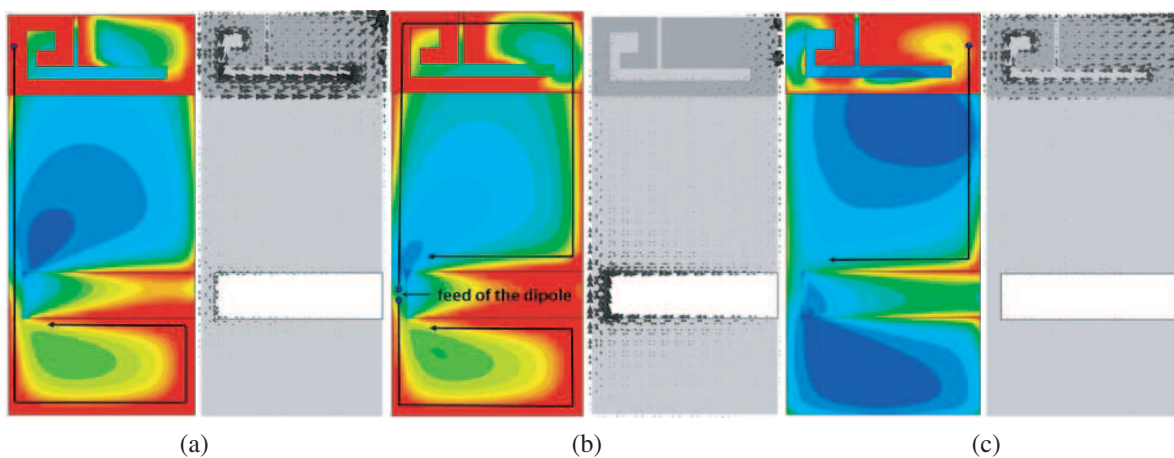

(a)   (b)   (c)

Figure 10: E-field and surface current distributions of the proposed antenna at the resonant frequencies, (a) E-field and current distributions at 0.844 GHz, (b) E-field and current distributions at 0.924 GHz, (c) E-field and current distributions at 1.82 GHz.

3. CONCLUSIONS

In this paper, a novel bandwidth enhancement solution for the conventional multi-band PIFAs is proposed. It has been demonstrated that by introducing a rectangular slot with an appropriate location and a proper size on the mobile chassis, the bandwidths of the PIFA antenna in both the low and high bands can be significantly broadened and optimized. In fact, for a typical mobile chassis with an area of 40 mm × 100 mm, its length (100 mm) is not optimized for either the low band or high

band. The slot opened appropriately on the chassis can effectively adjust the electrical lengths of the chassis to the optimal lengths required by the low and high bands. With the help of the proposed technique, a compact internal antenna for a quad-band operation covering GSM850, GSM900, DCS1800 and PCS1900 bands can be simply designed. Furthermore, the proposed approach is also suitable for any other types of internal mobile antennas.

REFERENCES

1. Kim, B. C., J. H. Yun, and H. D. Choi, "Small wideband PIFA for mobile phones at 1800 MHz," *IEEE International Conference on Vehicular Technology*, 27–29, Daejeon, South Korea, May 2004.
2. Guo, Y. X. and H. S. Tan, "New compact six-band internal antenna," *IEEE Antennas and Wireless Propagation Letters*, Vol. 3, 295–297, 2004.
3. Wang, F., Z. Du, Q. Wang, and K. Gong, "Enhanced-bandwidth PIFA with T-shaped ground plane," *Electronics Letters*, Vol. 40, 1504–1505, 2004.
4. Hossa, R., A. Byndas, and M. E. Bialkowski, "Improvement of compact internal antenna performance by incorporating open-end slots in ground plane," *IEEE Microwave and Wireless Components Letters*, Vol. 14, 283–285, 2004.
5. Abedin, M. F. and M. Ali, "Modifying the ground plane and its effect on planar inverted-F antennas (PIFAs) for mobile handsets," *IEEE Antennas and Wireless Propagation Letters*, Vol. 2, 226–229, 2003.
6. Lindberg., P. and E. Ojefors, "A bandwidth enhancement technique for mobile handset antennas using wavetraps," *IEEE Transactions on Antennas and Propagation*, Vol. 54, 2226–2232, 2006.
7. Kivekas., O., J. Ollikainen, T. Lehtiniemi, and P. Vainikainen, "Bandwidth, SAR, and efficiency of internal mobile phone antennas," *IEEE Transactions on Electromagnetic Compatibility*, Vol. 46, 71–86, 2004.

Design of Multi-band Antenna Using Different Radius Wires

Tsutomu Yokoyama[1], **T. Hoashi**[2], **K. Murata**[2],
S. Egashira[2], **K. Egashira**[3], **and T. Nakamiya**[4]

[1]Department of General Education, Sojo University, 4-22-1 Ikeda, Kumamoto 860-0082, Japan
[2]Department of Electronics, Computer and Network, Sojo University
4-22-1 Ikeda, Kumamoto 860-0082, Japan
[3]Saga Denshi Kogyo Co., Ltd., 2-7-13, Kaisei, Saga, Japan
[4]Department of Electronics and Intelligent Systems Engineering, Tokai University
9-1-1, Toroku, Kumamoto 862-8652, Japan

Abstract— A novel design method for multi band antenna using different radius wires for mobile communication and Digital communications System is presented. We made a trial two-band antenna, with operating frequencies of 800 MHz and 2.1 GHz and examined the design method by comparing measured VSWR and current of the antenna and the simulation results of the antenna.

We have also analyzed the trial antenna using simulation (using WIPL-D Microwave) for a different radius wires antenna mounted on a finite ground plane. The simulation results of the current and VSWR are in good agreement with the experimental results.

1. INTRODUCTION

Multi-function and mass transmission of both still pictures and animated images become indispensable in telecommunication technology of recent years. In particular, there have been remarkable improvements in mobile phone technology. However, there have been on-going difficulties in making compact antenna with multi band function.

Up to now, an analytical method of a linear antenna has been performed using transmission line approximation [1, 2] and integral equations [3].

Egashira et al. showed that current distribution of different radius antenna was represented equivalently by current distribution of the impedance loadings antenna and the characteristics of antennas with wires of the different radii could be analyzed using equivalent loaded antennas.

In this paper, we propose a novel design method for two-band antenna using wires of different radii. This design method is simple, easy to make and cheap. First, using antenna analysis software Nec-2, we estimated the radii and lengths of the three wires necessary to have two operating frequencies of 800 MHz and 2.1 GHz, available on a mobile phone antenna. This frequency band can be applied to a mobile phone antenna. Second, the current distribution of this antenna was measured using a shield loop [4] (current probe) and compared with the simulation result. Thirdly, we measured VSWR of the antenna with the network analyzer and compared it with the obtained using Nec-2. Finally, the directivity of the antenna was obtained using Microwave.

2. DESIGN OF TWO-BAND ANTENNA

We designed a two-band antenna with wires of three different radii for the two operating frequency bands. Here, we chose the radius and length of three wires parameters so as to be smaller than 1.5 for VSWR of the two band antenna

Figure 1 shows the structure of the trial two-band antenna constructed using wires of tree different radii mounted on the horizontal conductive plane. We selected 800 MHz and 2.1 GHz as the operating frequencies of the test antenna suitable for a cellular phone. This antenna was constructed of three wires and the radii and length of wire 1, 2 and 3 respectively, were as shown in Fig. 1. These values were selected as VSWR of the antenna became smaller than 1.5 at operating frequencies.

3. MEASUREMENTS

We measured VSWR and current distribution to examine the characteristics of the trial antenna and to compare them with the simulation results of the antenna.
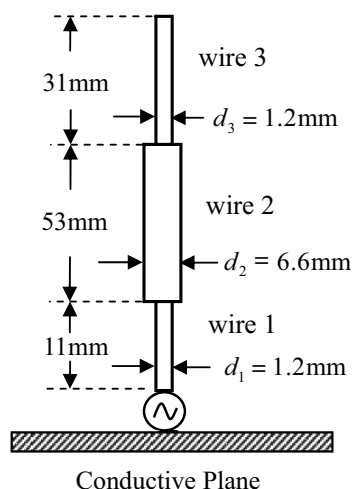
Figure 1: Structure of two band antenna with three different radius wires.
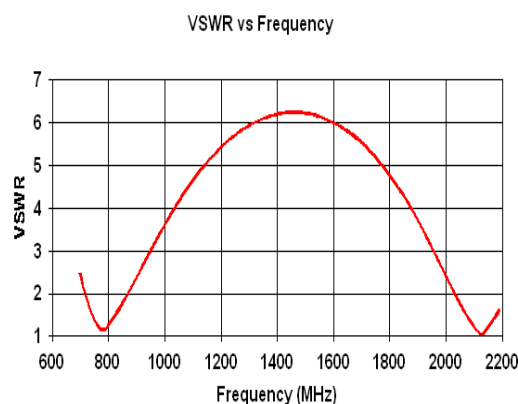

Figure 2: VSWR of two band antenna of the operating frequencies at 800 MHz and 2.1 GHz.

3.1. Measurement of VSWR

We measured VSWR of the antenna using the Hewlett Packard 8753D Network Analyzer. Fig. 3 shows the measured VSWR against the frequency of the antenna. This antenna has good characteristics at both 800 MHz and 2.1 GHz. It seems that this antenna is suitable for making two-band antenna. These operating frequencies are agreed well with the frequencies in the Fig. 1 estimated using Nec-2 simulation software.

3.2. Measurement of Current Distribution

Figure 4 shows the measurement system of current distribution of the antenna. We measured the current distribution of the test antenna when the operating frequency was 800 MHz and compared the result with the simulation results obtaining using WIPL-D Microwave.
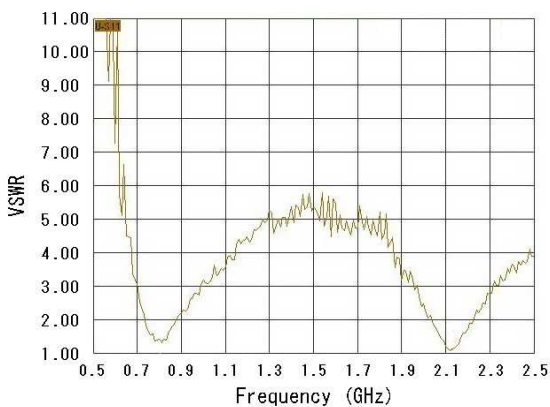

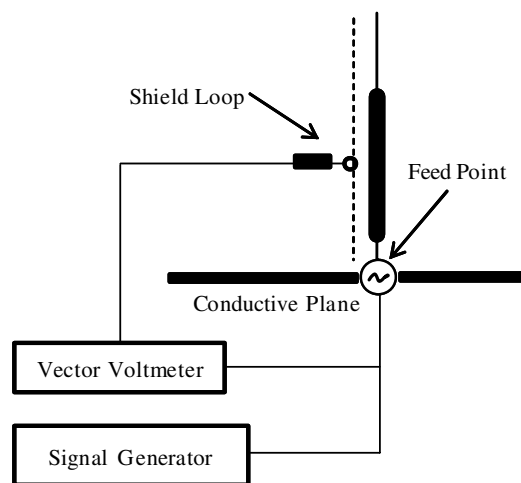Figure 3: Measurement of VSWR.

Figure 4: Measurement system of current distribution.

Signals from the generator were fed in to the antenna. While the same was fed in to one channel of the vector voltmeter as shown in Fig. 2. The other channel of the vector voltmeter was fed by the voltage induced on the shield loop [4–7].

We measured the relative amplitude and the phase of the current distribution on the antenna using the electromotive force induced on the shield loop by moving the shielded loop 5.0 mm along the antenna.

Figure 5 shows the measured and simulated relative amplitude of current distribution on the antenna. The upper line is the electromotive force induced on the shield loop and the lower line is

the simulation value of amplitude of magnetic field at a point 4.5 mm away from the test antenna center. The simulated and measured current distributions seem to be almost equal.
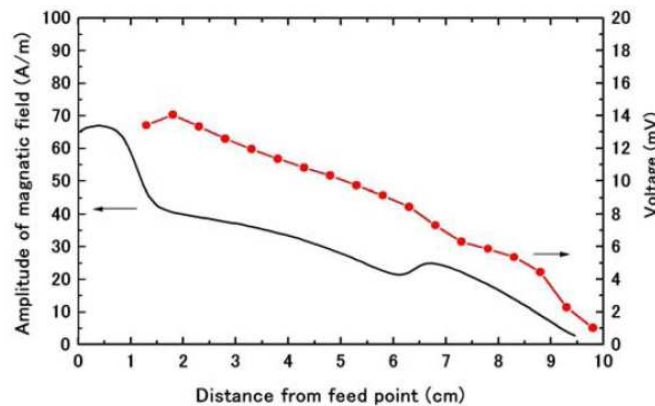

Figure 5: Measurement and simulation of current distribution of test antenna at 800 MHz.

We measured the current distribution of the test antenna and compared with the simulation results obtained using WIPL-D Microwave. This software is based on the method of moments and can analyze the antenna with the ground of the arbitrary shape.

Figure 6 shows the directivities of the test antenna. Here, the feeding point is at the starting point and the antenna is in the direction of the z axis and the ground is in the X-Y plane We simulated the antenna as shown in Fig. 1, mounting it on a square conductive plane (150×150 mm).
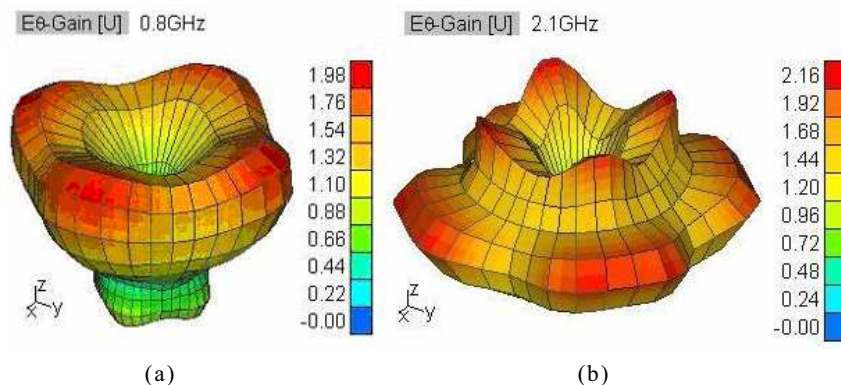

Figure 6: Radiation pattern of test antenna at (a) 800 MHz and (b) 2.1 GHz.

4. CONCLUSION

A novel design method for two band antennas using different radius wires, operating at 800 MHz and 2.1 GHz suitable for mobile handsets has been proposed. The simulated results for the two operating frequency bands agreed well with measurement results of VSWR and current distribution. These results show that the antennas designed using wires of different radii are good candidates for multi-band antenna applications.

REFERENCES

1. Schelkunoff, S. A., *Electromagnetic Wave*, Chap. 11, D. von Nostrand Co. Inc., 1952.
2. Schelkunoff, S. A. and H. T. Friis, *Antennas Theory and Practice*, Chap. 3.5 and Chap. 8 28, John Wiley and Sons Inc., 1952.

3. Hallen, E., "Theoretical investigation into the transmitting and receiving qualities of antennas," *Nova Acta Upssala*, Vol. 11, No. 4, 1938.
4. Egashira, S., M. Yaguchi, and A. Sakitani, "Consideration on the measurement of current distribution on bent wire antenna," *IEEE Trans. Antennas Propagat.*, Vol. 6, No. 7, 918–926, July 1988.
5. Edwardes, H. N., "The measurement of current distribution in Aerials at VHF," *Proceedings of the I.R.E. Australia*, 351–354, April 1963.
6. Yokoyama, T., K. Koga, and S. Egashira, "Estimation of radiation pattern by near field measurement of linear antenna," *International Conference on Microwave and Millimeter Wave Technology*, 357–360, 2002.
7. Nakamura, T., S. Yamaguchi, T. Yokoyama, and S. Egashira, "Ladder antenna," *3rd International Conference on Microwave and Millimeter Wave Technology*, 396–372, Bejjing, August 2002.

Balanced MIMO Antenna for Mobile Phones

Muhammad Usman, **Raed A. Abd-Alhameed**, and **D. Zhou**

Mobile Satellite Communications Research Centre, University of Bradford
Richmond Road, Bradford, West Yorkshire, BD7 1DP, UK

Abstract— The paper presents a new modeling and design concept of antennas using polarization diversity of 2×2 Multiple Input Multiple Outputs (MIMO) balanced antenna that is proposed for future mobile handsets. The balanced MIMO antenna is designed and its coupling has been investigated. The results are compared to the constraints capacity limits in which the maximum capacity observed.

1. INTRODUCTION

MIMO for short, which stands for Multiple Input, Multiple Output) systems are theoretically able to provide increased throughput, and better error performance than traditional systems [1–5]. The particular aspect that is used by MIMO systems is called *Multi*-Path propagation [2, 5]. This effect occurs when the radio signals sent from the transmitter bounce off intermediate objects before reaching the receiver. Some of these reflected signals may travel along entirely separate paths, and even reach the receiver at different times. Currently, there are a number of MIMO applications, development platforms, and tools that are showing great promise in the quest for wireless systems with higher bandwidth and greater capabilities. The major advantage of MIMO technology is the digital beam forming, which is now making its way out of research laboratories and into real-world applications with great speed. Spatial corrrelation using polarization issues for MIMO applications has great interest since the size of the actual radiating elements can be reduced [6–12]. This study has great advantages if a MIMO system needs to be implemented on a mobile handset. This paper will consider the implementation of balanced antennas for mobile handset the will increase the channel capacity and will reduce the coupling between the handset and body.

2. MATHEMATICAL INTERPRETATION

We start our assumption that our system under consideration consists of short dipoles and we are not taking mutual coupling between the multiples dipoles in account, then the channel capacity is given as

$$c = E \left| \log 2 \left\{ I + \frac{Pt}{nt\sigma} HH^* \right\} \right| \tag{1}$$

In the above equation HH^* is given as

$$[HH^*]^{1/2} = \rho_r \frac{1}{2} G$$

where as ρ_r elements is given as:

$$\rho_{i,j} = \frac{\oint\limits_{s} (E_{ai}.E_i)(E_{aj}.E_i)\, d\Omega}{\sigma_1 \sigma_2} \tag{2}$$

where

$$\sigma_1 = \oint\limits_{s} (E_{ai}.E_i)^2 d\Omega$$

$$\sigma_2 = \oint\limits_{s} |E_{aj}.E_i|^2 d\Omega$$

where we have: $d\Omega = \sin\theta_\theta^d d_\phi$ and $\oint\limits_{s} = \int_{\phi 1}^{\phi 2} \int_{\theta 1}^{\theta 2}$.

Substituting the values of σ_1, σ_1 and $d\Omega$ into the Eq. (2) the following can be given:

$$\rho_{i,j} = \frac{\oint_s (E_{ai} \cdot E_i)(E_{aj} \cdot E_i) \sin \theta_\theta^d d_\phi}{\sqrt{\oint_s (E_{ai} \cdot E_i)^2 \sin \theta_\theta^d d_\phi \oint_s |E_{aj} \cdot E_i|^2 \sin \theta_\theta^d d_\phi}} \tag{3}$$

The correlation coefficients will form the spatial matrix which is given as

$$\rho = \begin{bmatrix} \rho_{11} & \rho_{12} & \rho_{1n} \\ \rho_{21} & \rho_{22} & \rho_{2n} \\ \rho_{n1} & \rho_{n2} & \rho_{nn} \end{bmatrix} \tag{4}$$

The channel capacity can also be given as:

$$C = \sum_{i=1}^{n} \left(I + \frac{P}{n_T N} \lambda_i \right) \tag{5}$$

where Li is the ith eigen value of the HH^* matrix.

3. BALANCED MIMO ANTENNA AND RESULTS

The main aim of this present work was to design two elements antenna structure having a ground plane whose dimensions are compatible with a mobile phone at 5 GHz band for MIMO applications of the future wireless mobile communications. The antenna proposed here is made of two wideband balanced antenna elements and placed in parallel, as shown in Figs. 1 and 2. The proposed 2×2 MIMO balanced antenna system was designed optimized using commercial simulator HFSS (High Frequency Structure Simulator), which uses a 3D full-wave finite element Method (FEM). The antenna geometry and location on the ground plane can be found in Fig. 2. As can be seen, the antenna is fed at the centre with differential feeding which provide equal magnitude but 180 degree out of phase current for the two arms of the antenna. The input impedance of the antenna is 50 Ω.
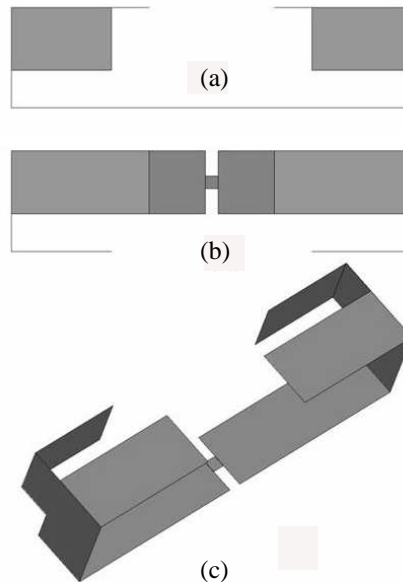

Figure 1: Antenna design. (a) Front view, (b) Top View, (c) 3D view.

The optimal configuration of the elements was chosen to minimize the coupling between elements. The two balanced antenna elements were placed inside the limits of the ground plane and the distance between them is 24 mm (see Fig. 2).

Figure 3 presents the simulated results of return loss and isolation performance of this 2×2 antenna system. As can be observed in the 5 GHz band range, the return loss is lower than 8 dB and the isolation lower than -13 dB for both elements.
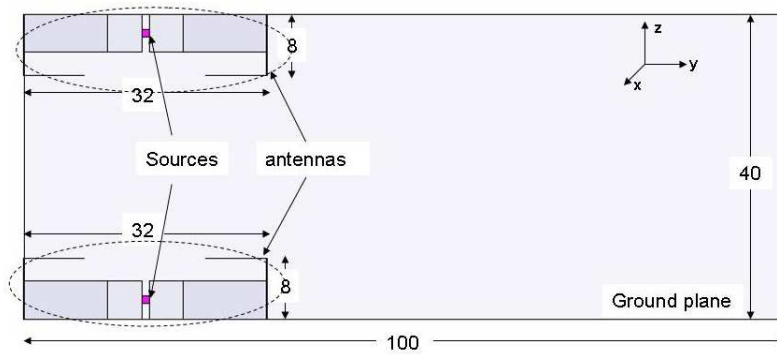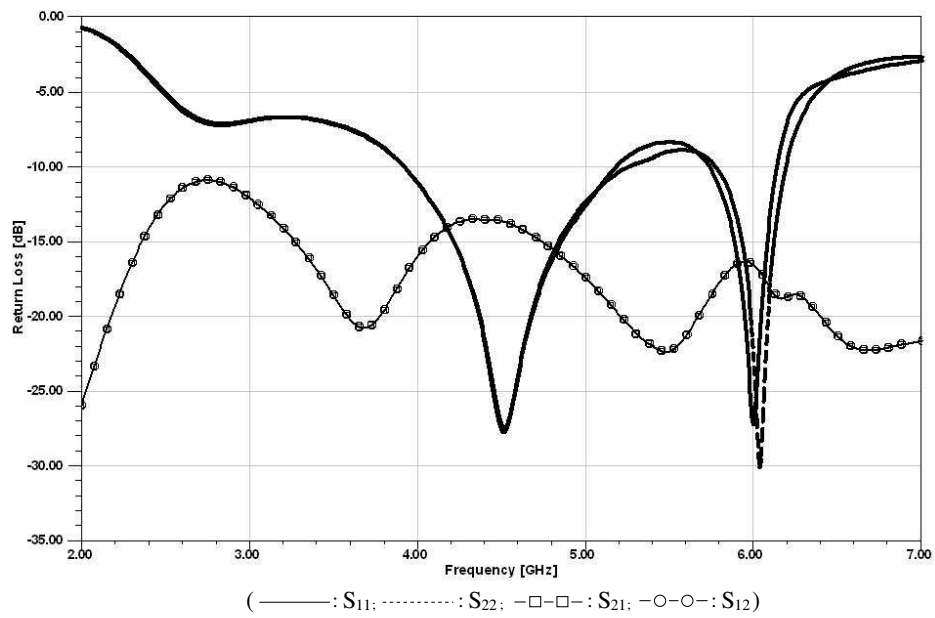
Figure 2: 2×2 Balanced MIMO antenna.

(——— : $S_{11;}$ ·········· : $S_{22;}$ $-\square-\square-$: $S_{21;}$ $-\circ-\circ-$: S_{12})

Figure 3: Simulated S-Parameters for 2×2 Balanced MIMO antenna.

$-\square-\square-$: represents $E_{\varphi;}$ $-\circ-\circ-$: is $E_{\theta;}$
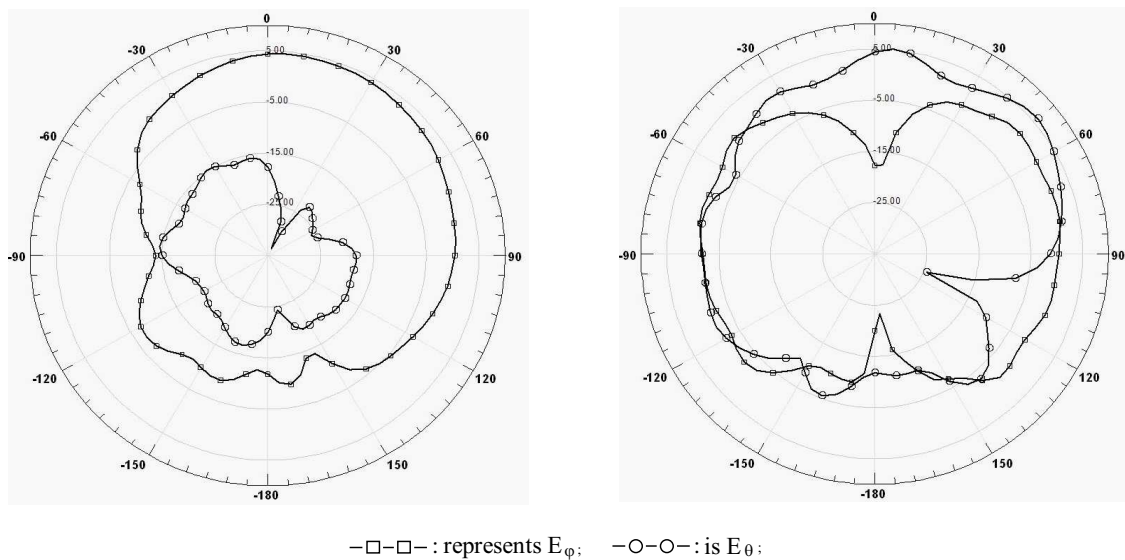
Figure 4: Radiation pattern at 5.8 GHz for xz plane (left) and yz plane (right).

The radiation property of the proposed 2×2 MIMO balanced antennas was also investigated. Two pattern cuts were taken for four selected operating frequencies that cover the designated whole bandwidth in this study. The radiation patterns in the xz plane and yz plane for the antenna systems at 5.2 GHz and 5.8 GHz were measured. The results in simulation were shown in Figs. 4 and 5, where the patterns of the prototype antenna show to be quite similar to each other for the both cases considered. The maximum power was found at around $\theta = 60°$ direction with peak gain of 5 dBi.

4. CONCLUSIONS

The simulation results using HFSS shows that the coupling between the antennas can be reduced with enhanced channel capacity. The balanced MIMO design discussed in this paper can be used for mobile handsets. The 2×2 balanced MIMO antenna systems with less volume can be incorporated efficiently into mobile phones. This design can also be used for PDAs and small handheld wireless devices.

REFERENCES

1. Foschini, G. J. and R. A. Valenzuela, "Initial estimation of communication efficiency of indoor wireless channel," *Wireless Networks*, Vol. 3, 141–154, 1997.
2. Winters, J. H., J. Salz, and R. D. Gitlin, "The impact of antenna diversity on the capacity of wireless communication systems," *IEEE Trans. Commun.*, Vol. 42, 1740–1751, Feb. 1994.
3. Andrews, M. R., P. P. Mitra, and R. deCarvalho, "Tripling the capacity of wireless communications using electromagnetic polarization," *Nature*, Vol. 409, No. 6818, 316–318, Jan. 2001.
4. Svantesson, T., "On capacity and correlation of multi-antenna systems employing mulTiple polarizations," *IEEE Int. Antennas Propagation Symp. Digest*, 202–205, San Antonio, TX, June 2002.
5. Stancil, D. D., A. Berson, J. P. Van't Hof, R. Negi, S. Sheth, and P. Patel, "Doubling wireless channel capacity using co-polarised, co-located electric and magnetic dipoles," *Electron. Lett.*, Vol. 38, No. 14, 746–747, July 2002.
6. Andersen, J. B. and B. N. Getu, "The MIMO cube — A compact MIMO antenna," *5th Int. Symp. Wireless Personal Multimedia Communications*, 112–114, Honolulu, HI, Oct. 2002.
7. Winters, J. H., J. Salz, and R. D. Gitlin, "The impact of antenna diversity on the capacity of wireless communication systems," *IEEE Trans. Commun.*, Vol. 42, 1740–1751, Feb. 1994.
8. Andrews, M. R., P. P. Mitra, and R. deCarvalho, "Tripling the capacity of wireless communications using electromagnetic polarization," *Nature*, Vol. 409, No. 6818, 316–318, Jan. 2001.
9. Svantesson, T., "On capacity and correlation of multi-antenna systems employing multiple polarizations," *IEEE Int. Antennas Propagation Symp. Digest*, 202–205, San Antonio, TX, June 2002.
10. Stancil, D. D., A. Berson, J. P. Van't Hof, R. Negi, S. Sheth, and P. Patel, "Doubling wireless channel capacity using co-polarised, co-located electric and magnetic dipoles," *Electron. Lett.*, Vol. 38, No. 14, 746–747, July 2002.
11. Andersen, J. B. and B. N. Getu, "The MIMO cube — A compact MIMO antenna," *5th Int. Symp. Wireless Personal Multimedia communications*, 112–114, Honolulu, HI, Oct. 2002.
12. Xu, H., M. J. Gans, N. Amitay, and R. A. Valenzuela, "Experimental verification of MTMR system capacity in controlled propagation environment," *Electron. Lett.*, Vol. 37, No. 15, 936–937, July 2001.

Design of RFID Reader Antenna for Exclusively Reading One Single Tag

Chi-Fang Huang and I-Feng Huang
Graduate Institute of Communication Engineering, Tatung University
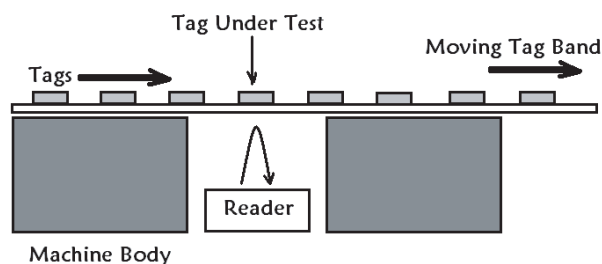40, Chung-Shan N. Rd., Sec. 3, Taipei 104, Taiwan

Abstract— This paper presents a design of RFID reader antenna, which is equipped on a chip-attaching machine producing the RFID tags. Such an antenna is constrained to read exclusively one tag only for the purpose of functional check of the whole tag when it passes the reader antenna, namely, the other neighbour tags on the same rolling band are ignored that time. A wideband microstrip antenna is designed and a fixture with shielding material is set up for such a reading constraint.

1. INTRODUCTION

Even invented and applied initially during the World War II, RFID (Radio Frequency Identification) [1] has attracted much attention recently. Precisely speaking, RFID has been applied very widely in some proprietary or closed systems, for example, animal control, portal control (access badges), etc. in last decades. The main advantages of RFID application are, storing item data in an electronic way, data access by electromagnetic wave, and allowing multiple accesses to RFID tags. Based on the diverse applications, different spectrum bands are allocated, for example, LF (125–134.2 kHz and 140–148.5 kHz) for animal control, HF (13.56 MHz) for electronic ticket, and UHF (868 MHz–928 MHz) for logistics, etc. Most of the frequencies are located in the ISM (Industrial, Scientific and Medical) bands [1].

However, RFID was emphasized again mainly because of the need of supply chain [2]. By proposing a standard for the format of electronic data used for goods items, of which EPC (Electronic Product Code) [3] is an example, the products can be registered at once when they are shipped out from the factories, and be released when they are checked out at the counter of a supermarket. This is called "product tracking" and is to be carried out in an "Internet of Thing" [4].

The RFID tags of supply chain are assumed to be very low-cost, either are the RFID chips. Therefore, usually the chips for tags do not afford to be 100% quality assurance after fundray and package. Consequently, the risk of producing tags with chips which probably do not work does exist. Such a sort of tags is termed as dead or silent tags. This kind of potential risk is not acceptable after the tag is made by attaching the chip on the tag antenna. Hence, the cost should be paid by carrying a functional check one by one by a reader after the chip is attached on the antenna as a tag, just as shown in Fig. 1. That means, the production machine should be able to exclusively read the tag under test only, and the other neighbor tags are not allowed to response when reading.

Figure 1: Set-up for exclusively reading one single tag on a production machine.

This paper addresses a design of a fixture containing a reader antenna to meet the purpose mentioned above. This reader antenna is also designed in this work. This fixture is installed on

a production machine of RFID tags. Measurement of the proximate-field strength on this fixture is done to verify the field distribution which is for the present reading constraint. For reference, Fig. 2 shows a typical RFID tag printed on a paper substrate, where the chip is attached at the center of tag antenna [4].

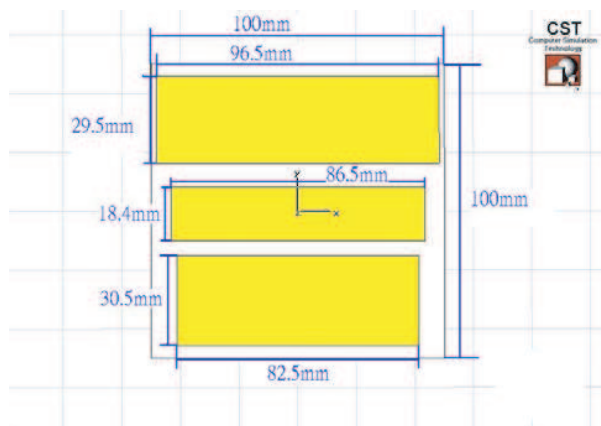
Figure 2: A tag using paper substrate.

Figure 3: Simulation model of the wideband reader antenna

2. DESIGN OF READER ANTENNA

Firstly, the reader antenna is designed. The concept of microstrip antenna [5] is adopted for this task. The reasons of choosing microstrip antenna are: a) low profile, so not occupying not much room in machine, b) easy to fabricate, because it can be etched on a Printed Circuit Board (PCB), and c) its fundamental mode is naturally to have a boresight radiation pattern, which is suitable for the present application as shown in Fig. 1. A microstrip antenna can be seen as a loosy resonator due to radiation [6]. However, the obvious disadvantage of microstrip antenna is its narrow band. The target bandwidth of this work is about 860 MHz–960 MHz which is for covering all RFID standards worldwide. The RFID bands used in the world are: 866–869 MHz in Europe, 902–928 MHz in North and South America, and 950–956 MHz in Japan and some Asian countries. The RFID's band used in Taiwan is 902–928 MHz. Consequently, special design technique is supposed to be necessary to have such a broadband design of microstrip antenna.
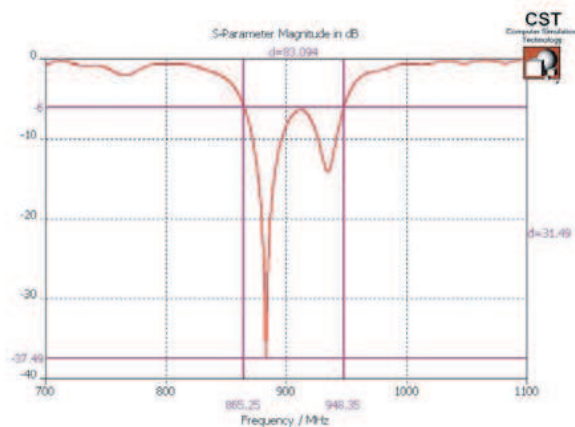

Figure 4: The simulated frequency response of return loss.

Figure 5: Realized antenna.

The electromagnetic package CST [7] is employed for the simulation before fabricating the antenna, which is a full 3-D tool for antenna simulation. Fig. 3 is the simulation model, and it is also the final determination of the geometrical and material parameters. FR4 is used as the substrate. The central rectangle is the main microstrip antenna, whose horizontal side 86.5 mm approximately follows the theoretical resonant length of half wavelength in substrate. The other upper and lower

rectangles play the parasitic parts which have strong coupling effect with the central radiator. This technique had been widely used [8] for broadening the bandwidth of microstrip antenna. However, usually, parasitic parts are set at the ends of the resonant side. Putting them along the resonant sides is an unique feature in the present work.

It should be reminded that, the present design of RFID communication is a short-range one, therefore, we trade off in obtaining the broadband while scarifying the performance of return loss. We set the -5 dB as the index for the matching condition in this design, and it predicts in simulation an 865 MHz–948 MHz bandwidth as for -6 dB as shown in Fig. 4. After simulation, the antenna is realized by being etched on a PCB with a substrate thickness 4 mm as shown in Fig. 5. Its measured return loss is shown in Fig. 6. Referring to the bandwidth requirement, the lower band is quite meeting the target, but the upper band is not so satisfied in terms of the necessary band. Anyway, this antenna is to be installed on a machine fixture which may influence the antenna performance, and the final result will be further discussed.

3. FIXTURE DESIGN FOR READING

As shown in Fig. 1, in the fast process of attaching chips on the RFID tags, the moving band is supported by a mechanical fixture. For simulating the fixture of a real machine in lab, a non-metal fixture is assembled as shown in Fig. 7. The top platforms are made of plastics and serves to support the tag band. Furthermore, the reader antenna designed above sits under the platforms and sits at the central position as well.
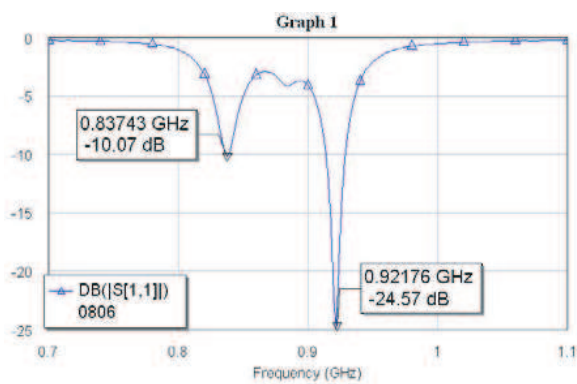
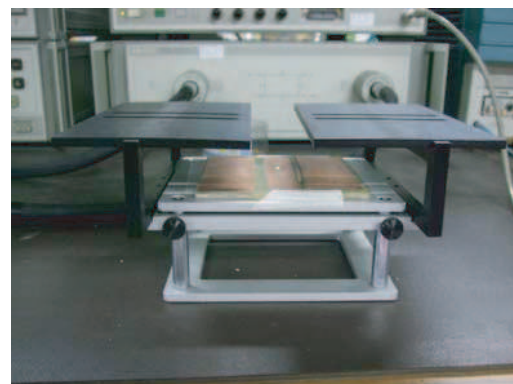

Figure 6: Measured return loss.

Figure 7: The laboratory fixture for testing.

From the first idea, for depressing the response of the neighbour tags, we adopt the shielding sheets of Nanonix [9], and put them on and beneath the platforms. The left and right sliding platforms are adjustable to find an optimal window width for antenna below to read as the purpose, see Fig. 7 and Fig. 8. In Fig. 8, there are three tags side by side, yet only the middle one is readable.
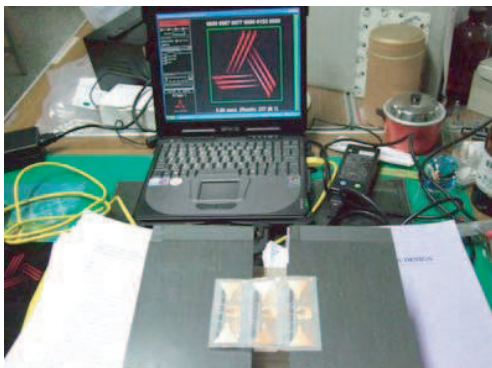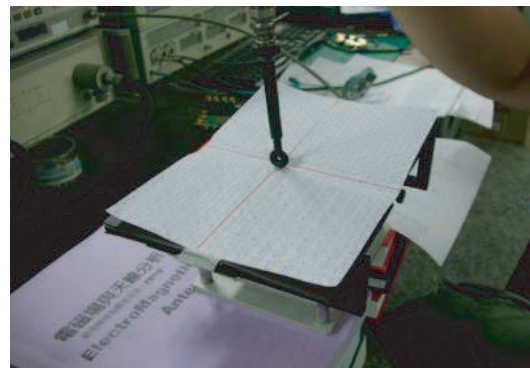

Figure 8: Test of exclusive reading.

Figure 9: Measurement of the proximity field on the platform surface.

4. ANALYSIS OF PROXIMITY FIELD AND DISCUSSION

For analyzing the field distribution on the surface of the platforms, a set-up of the proximity field measurement is also designed. By drawing grids in advance on a paper which is fixed on the platforms, a field probe is used point-by-point to measure on the surface the proximity field radiated from the reader antenna, see Fig. 9.

Three configurations are under evaluation, namely, no shielding sheets, with shielding sheets as described above, and lowering the sheets which were attached beneath the platforms down to the surface of the reader antenna. As examples, the measurement results of 910 MHz are shown in Fig. 10. By a quantity comparison, configuration (c) is indeed to make the field lower on the region of side tags than that above the central window. However it is easy to affect the antenna's designed characteristics than configuration (b). Of course, configuration (a) is not able to meet the function as required. Choosing (b) or (c) needs engineering evaluation on site.
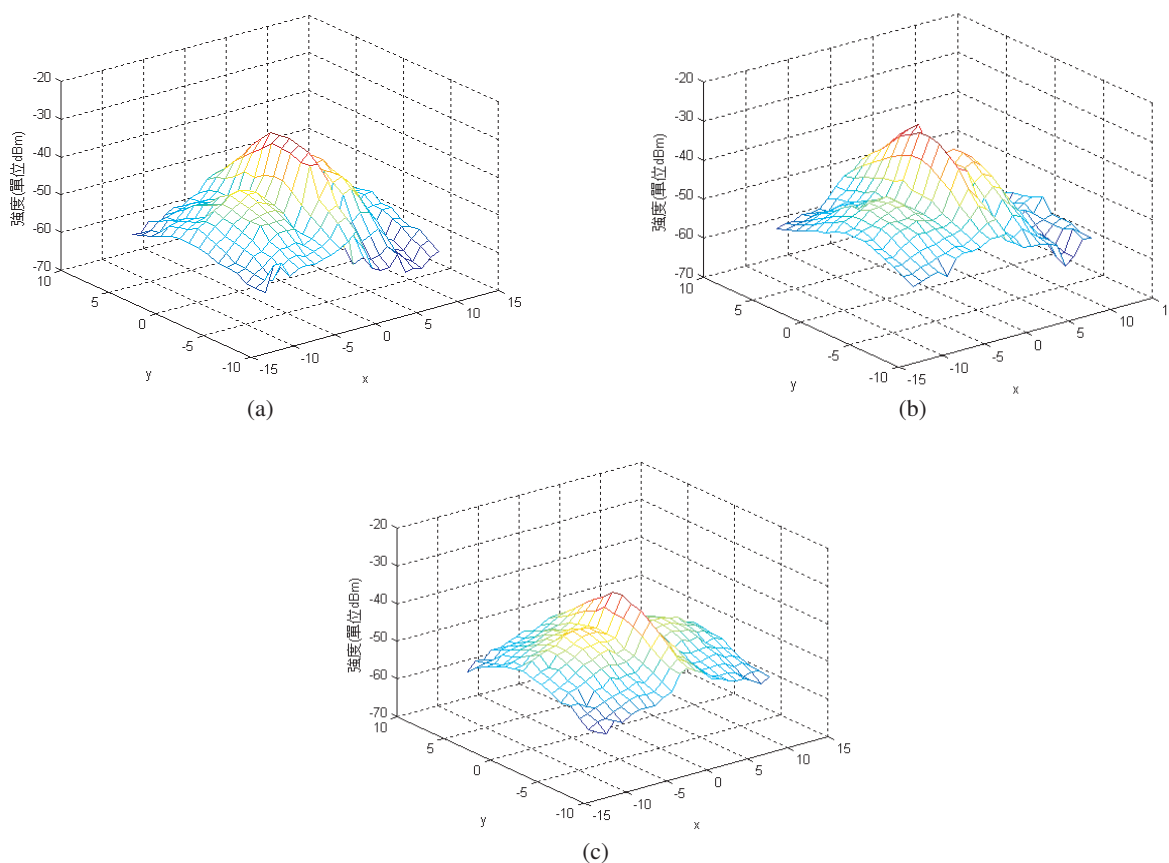

Figure 10: Distribution of proximity field (a) no shielding sheets, (b) sheets beneath the platforms, and (c) sheets on the reader antenna's surface.

5. CONCLUSIONS

In this paper, we have proposed a design of fixture for the machines of tag production. After attaching the chips on antennas of a band of tags, this machine needs to check each tag if its chip does work or not at the end of production procedure. A broadband microstrip antenna is also designed for this fixture. By using the shielding sheets on the fixture, the requirement of reading exclusively only one tag is achieved. Measurement of the proximity fields which is radiated from the designed reader antenna, are measured as well on the surface of fixture platforms to evaluate the proper configuration of shielding sheets. This present work has demonstrated itself as a reference design for production machines of RFID tags, which needs to have a functional check for each tag described in this work.

REFERENCES

1. Finkenzeller, K., *RFID Handbook: Fundamentals and Applications in Contactless Smart Cards and Identification*, 2nd edition, Wiley & Sons Ltd. New York, 2003.
2. Bansal, R., "Coming soon to a Wal-Mart near you," *IEEE Antennas Propag. Mag.*, Vol. 45, 105–106, 2003.
3. Sarma, S., D. Brock, and D. Engels, "Radio frequency identification and the electronic product code," *IEEE Micro.*, 50–54, 2001.
4. Huang, C.-F., J.-Q. Zhan, S.-F. Yang, and Y.-C. Lin, "Low-cost solution for RFID tags by the manufacture of printing technologies," Submitted to *IEEE Antennas Propagat. Mag.*.
5. Carver, K. R. and J. W. Mink, "Microstrip antenna technology," *IEEE Trans. Antennas Propagat.*, Vol. 29, No. 1, 2–24, Jan. 1981.
6. Lo, Y. T., et al., "Theory and experiment on microstrip antennas," *IEEE Trans. Antennas Propagat.*, Vol. 27, 137–146, Mar. 1979.
7. The CST website, [On line], Available: http://www.cst.com, 2008.
8. James, J. R., P. S. Hall, and C. Wood, "Microstrip antenna: Theory and design," *IEE Electromagnetic Waves Series*, Vol. 12, 1981.
9. The Nanonix website, [On line], Available: http://www.nanonix.com/nanonix_china/company/index.htm, 2008.
10. The Highlight Tech Corp. website, [On line], Available: http://www.high-light.com.tw, 2008.

An All Optical XOR Logic Gate for NRZ Based on TOAD

Yaping Wang, **Chongqing Wu**, **Xiaojun Shi**,
Shuangshou Yang, and **Yongjun Wang**

Key Lab of Education Ministry on Luminescence and Optical Information Technology
Institute of Optical Information, Beijing Jiaotong University, Beijing 100044, China

Abstract— All-optical XOR logic gate is a basic and crucial element for optical signal processing. With introducing assistant light, we proposed and simulated a novel all optical XOR gate for NRZ based on teraherz optical asymmetric demultiplexer (TOAD). Simulation results shows that this program can get 13.29 dB extinction ratio (ER) of XOR logic operation output. The analysis of impact of nonlinear phase shift difference departure from π and 2π in actual system shows that when a fluctuant rang of nonlinear phase shift difference is confined within 0.1 rad, 13 dB extinction ratio of output is still obtained with assistant light injection. Its validity is confirmed through experiments and simulation at 2.5 Gb/s and 40 Gb/s, respectively.

1. INTRODUCTION

For high-speed optical communication networks, all-optical logic devices required in optical add-drop multiplexers and optical cross connects perform networking functions [1], such as clock extraction [2], signal regeneration, addressing, header recognition [3], data encoding, encryption, etc. Recently, the XOR logic gate has attracted particular attention because it is a key element to perform a wide range of operations such as packet header processor, label swapping, counting, pattern matching, decisior and comparison, pseudo-random bit generation and so on [4, 5]. In order to realize all optical XOR gate, various configurations have been reported that utilize the ultrafast nonlinear properties of the semiconductor optical amplifier (SOA) including from 10 Gb/s to 160 Gb/s all optical XOR gate based on the single SOA structure using cross gain modulation (XGM), and interferometric structures such as the terahertz optical asymmetric demultiplexer (TOAD), the ultrafast nonlinear interferometer (UNI) and Mach-Zehnder interferometer (MZI), etc [6–9]. XOR gate using SOA MZI and differential packet format have been deployed to overcome the strong speed limitations, but its structure is complicated and requires precise synchronization. XOR scheme based on UNI has been demonstrated at 100 Gb/s, but it needs accurate control of polarization. Sokoloff et al. demonstrated XOR gate based on TOAD. TOAD exploits the strong, slow optical nonlinearities present in semiconductor and permits control and signal pulses to be distinguished by polarization or wavelength, and it requires less than 1 pJ switching energy. But this structure which input the clock as probe light and requires clock synchronization between signal and clock only realize XOR gate for RZ. To the best of our knowledge, there is no report for all optical XOR gate for NRZ based on TOAD. This paper proposes a scheme for all optical XOR gate for NRZ based on TOAD. The feasibility of this scheme is theoretically analyzed with the principle of TOAD. Based on this, All optical XOR gate operation at 40 Gb/s is successfully simulated. The experiment give chance to demonstrate all of the possibilities of XOR gate.

2. OPERATION PRINCIPLE

Figure 1 illustrates the configuration of the all optical XOR gate. When two synchronizing signals as control beams are introduced into loop via WDM, control level will send out frame synchronizing signal as the probe beam at different wavelength from the two signals. The probe injected into the loop from port 1 is split into two components that propagate clockwise (CW) and counterclockwise (CCW) and recombining at the base 50 : 50 coupler.

An SOA used as a nonlinear element is placed at the center of the loop, while tunable fiber delay lines (DL) are used to introduce the desired displacement of SOA. Therefore, the whole CW component passes the SOA before the arrival of CCW component. Assumed E_i and E_i' ($i = 1, 2, 3, 4$) are input and output the light electric field of coupler, then

$$\begin{bmatrix} E_3 \\ E_4 \end{bmatrix} = \begin{pmatrix} \sqrt{2}/2 & j\sqrt{2}/2 \\ j\sqrt{2}/2 & \sqrt{2}/2 \end{pmatrix} \begin{bmatrix} E_1 \\ E_2 \end{bmatrix} \tag{1}$$

When the signals (P_C) and probe beam (P_p) through the SOA, the two counterpropagating probes obtain a differential phase shift $\varphi_{cw}(t)$, $\varphi_{ccw}(t)$ and gain G_{cw}, G_{ccw} via cross-phase modulation and
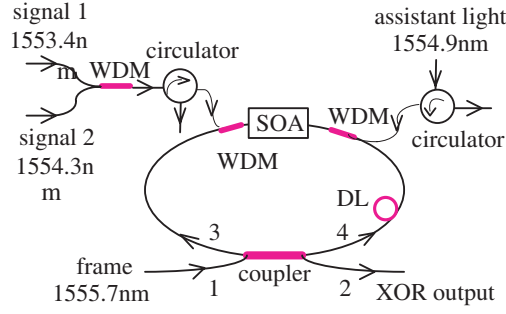
Figure 1: The configuration of XOR gate using TOAD.

cross-gain modulation in the SOA, where P_{sat} is saturation power, G_{cw} and

$$G_{cw} = G_0 \exp\left[(1 - G_{cw})\frac{P_c + P_p}{P_{sat}}\right], \tag{2}$$

$$G_{ccw} = G_0 \exp\left[(1 - G_{ccw})\frac{P_p}{P_{sat}}\right], \tag{3}$$

G_{ccw}, $\varphi_{cw}(t)$ and $\varphi_{ccw}(t)$ are the gain and phase shift of CW and CCW probes in the SOA, respectively. The relation of gain and phase shift is shown as Eq. (2)

$$\varphi(\tau) = -\frac{1}{2}\alpha \ln[G(\tau)] \tag{4}$$

the nonlinear phase shift difference will be:

$$\Delta\varphi = -\frac{\alpha}{2}\left[(1 - G_{cw})(P_c + P_p) - (1 - G_{ccw})P_p\right] \tag{5}$$

where α is line width enhancement factor, G_0 is the small signal gain, P_s is the saturation power. The light electric fields which travel along the ring for a round trip and then reenter the coupler can be expressed as:

$$\begin{bmatrix} E_3' \\ E_4' \end{bmatrix} = \begin{bmatrix} \frac{\sqrt{2}}{2}j\sqrt{G_{ccw}k}E_1 \\ \frac{\sqrt{2}}{2}\sqrt{G_{cw}k}E_1 \exp(-j\Delta\varphi) \end{bmatrix} \tag{6}$$

where k is the loss of the loop. The output from port 2 is the interference of E_3' and E_4', and shown as

$$E_2' = -\frac{1}{2}\left(\sqrt{G_{ccw}k} - \sqrt{G_{cw}k}\exp(-j\Delta\varphi)\right)E_1 \tag{7}$$

$$P_2' = \frac{1}{4}kP_{clk}\left[G_{ccw} - 2\sqrt{G_{ccw}}\sqrt{G_{cw}}\cos\Delta\varphi + G_{cw}\right] \tag{8}$$

It can be seen that the output power depends on the gain and the nonlinear phase difference. According to the Eqs. (5) and (8), when signals 1 and 2 are different, nonlinear different phase shift is $\Delta\varphi_1 = \pi$ and the gain of count-propagating components are G_{cw1} and G_{ccw}. As they recombine

Table 1.

Signal 1	Signal 2	$\Delta\varphi$	XOR
0	0	0	0
1	0	π	1
0	1	π	1
1	1	2π	0

and interfere, the output power of port 2 achieve maximum. When signals 1 and 2 are both "1", nonlinear different phase shift is $\Delta\varphi_2 = 2\pi$ and the gain of count-propagating components is G_{cw2}, G_{ccw}, respectively. They will be reflected from the coupler. When signals 1 and 2 are both "0", phase shift and the gain of count-propagating components are equal. They also will be reflected from the coupler. Thus, the XOR function is realized. The truth table of the XOR is shown in the Table 1.

Based on the analyzes above and Eq. (5),

$$(1 - G_{cw2})(P_{tal} + P_p) - (1 - G_{ccw})P_p = 2\left[(1 - G_{cw1})(P_{c1} + P_p) - (1 - G_{ccw})P_p\right]. \qquad (9)$$

where $P_{tal} = P_{c2} + P_{c1}, P_{c1}, P_{c2}$ is the power of signals pulse, spectively. According to Eq. (2), $G_{cw2} > G_{cw1}$, so $P_{c2} > P_{c1}$. In order to avoiding competition of two signal with differential power in the SOA, the assistant light P_{ass} is introduced into devise. At this time, the Eq. (9) comes into existence with $P_{tal} = 2P_{c1}$.

The comparison between with and without the assistant light shown in Fig. 2, when the nonlinear phase shift difference is π, 2π, respectively. According to the gain curve in Fig. 2 and the relationship between gain and phase shift in the Eqs. (3) and (4), a, b are the dots which give rise to π, 2π
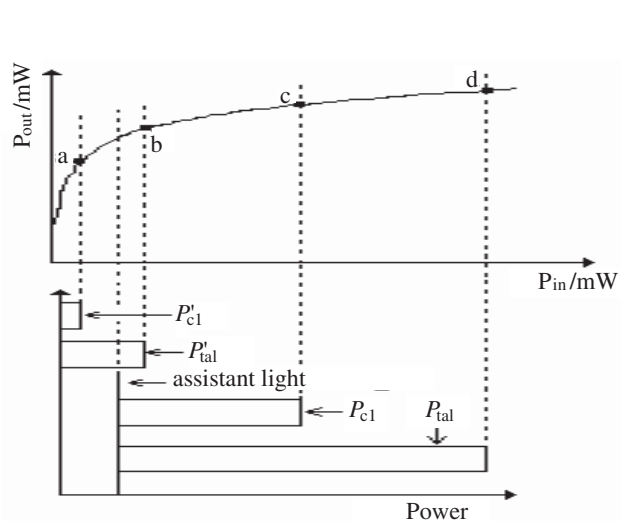
Figure 2: The comparison between with and without the assistant light.
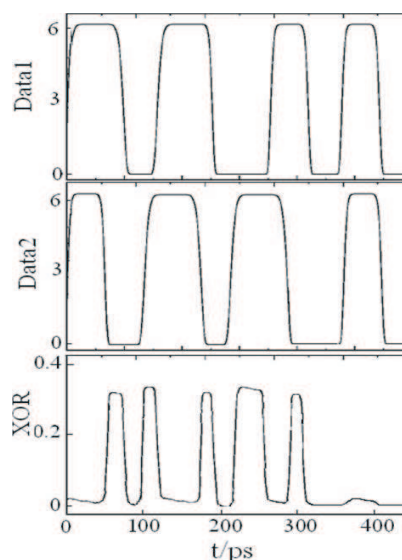
Figure 3: Output of XOR.

Table 2.

Parameters	values
SOA length	500 μm
SOA spontaneous lifetime	16 ps
SOA small signal gain	20 dB
SOA transparent carrier density	$10^{24}\,\mathrm{m}^{-3}$
SOA line-width enhancement	5
SOA active area	$3 \times 10^{-13}\,\mathrm{m}^2$
SOA saturation power	11.6 mW
probe pulse width (FWHM)	10 ps
Probe pulse power	0.2 mW
Assitant light power	2.597 mW
Dual signal pulse power	6.415 mW
SNR of input	20 dB

phase shift without assistant light, and c, d are the dots which give rise to π, 2π phase shift with assistant light. Obviously, the power of two signal pulses is equal by introducing assistant light.

3. SIMULATION

A data stream 11100111000 110011 is compared with data stream 11001110011100011. The main parameters are shown in the Table 2.

The simulation results at 40 Gb/s are shown in Fig. 3. The extinction ratio of output will achieve 13.29 dB.

It is impossible to fix the power of assistant light and signals on the precise value in experiment. Therefore, on the supposition $P_{tal} = 2P_{c1}$, P_{ass} and P_{c1} will be adjusted with the considerations of $\Delta\varphi_1 + \Delta\varphi_2 = 3\pi$ and $\Delta\phi_1 - \Delta\phi_2 < \pi - 2\delta$, where δ is a fluctuant rang of nonlinear phase shift difference. Fig. 4 shows the curve of $\Delta\varphi_1$, $\Delta\varphi_2$ against P_{ass}, and Fig. 5 shows the curves of P_{c1} against P_{ass} and ER of output against P_{ass}.
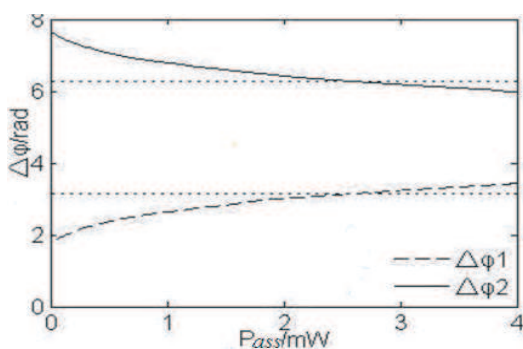
Figure 4: Phase shift difference against the power of assistant light with consideration of $\Delta\varphi_1 + \Delta\varphi_2 = 3\pi$ and $\Delta\phi_1 - \Delta\phi_2 < \pi - 2\delta$.
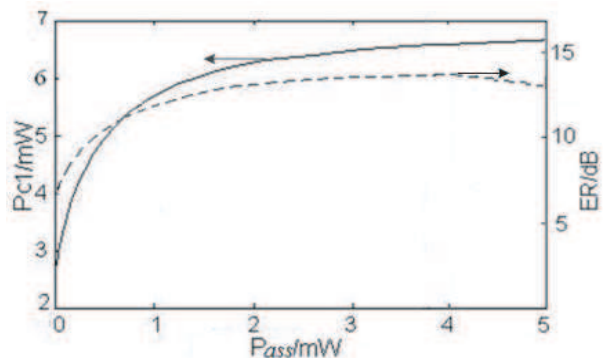
Figure 5: The power of siganl pulse and ER against the power of assistant light with consideration of $\Delta\varphi_1 + \Delta\varphi_2 = 3\pi$ and $\Delta\phi_1 - \Delta\phi_2 < \pi - 2\delta$.

As can be seen in Fig. 4 and Fig. 5, when $P_{ass} = 2.597$ mW and $P_{c1} = 6.415$ mW, the nonlinear phase shift difference $\Delta\varphi_1 = \pi$, $\Delta\varphi_2 = 2\pi$. If fluctuant rang of nonlinear phase shift difference is restricted within 0.1 rad, the rangs of P_{ass} is from 2.017 mW to 3.095 mW and of P_{c1} is from 6.289 mW to 6.514 mW. The ER of output is more than 13 dB and increasing with the $P_{ass} \in [2.017$ mW, 3.095 mW].

Figure 6: The output of XOR in experimrntation.

Figure 7: The power of signal pulse and ER against the power of assistant light in experimrntation.

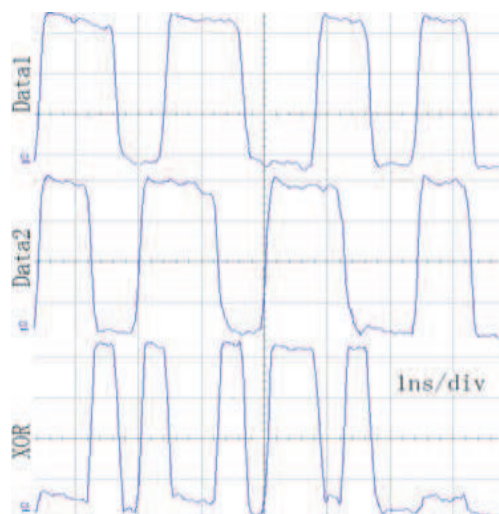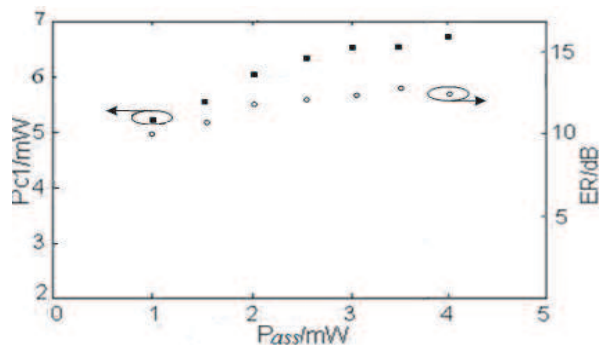## 4. EXPERIMENTATION

The experimental setup for the all optical XOR logic gate 2.5 Gb/s is shown in the Fig. 1. The main parameters of SOA are agrees with that of simulation. The wavelength and the power of signals, assistant light, frame synchronizing signal is 1553.4 nm, 1554.3 nm, 1554.9 nm, 1555.7 nm, 6.415 mW, 2.597 mW, 0.4 mW. The output of XOR is shown in the Fig. 6. This result is a good agree with the truth table of logic XOR as shown in Table 1 and the simulation result as shown in Fig. 3.

We fixed the frame synchronizing signal power at 0.4 mW and adjusted the signal power with the assistant light power increasing from 1 mW to 4 mW. In Fig. 7, it is clearly shown that the signal power and output ER are increased with the assistant light $P_{ass} \in [2.017\,\text{mW}, 3.095\,\text{mW}]$, and the experimental result is consistent with that of theoretic analysis. Therefore, the demander of debugging is degraded in experimentation.

5. CONCLUSION

A novel optical XOR logic gate based on TOAD is proposed. The successful demonstration shows the potential of this scheme to process XOR gate operation for NRZ by inputting assistant light and frame synchronizing signal as probe beam and adjustting the position of SOA in the loop advisably. With common SOA, the results of simulation and experimentation shows that this program can get 13.29 dB extinction ratio of output by introduceing advisable assistant light. When fluctuant rang of the nonlinear phase shift difference is confined within 0.1 rad, the more than 13 dB extinction ratio of XOR operition still be obtained. Therefore, the demander of debugging is degraded.

REFERENCES

1. Li, P., D. X. Huang, and X. Zhang "Novel all-optical AND and NOR gates based on semiconductor fiber ring later [J]," *Acta Photonica Sinica*, Vol. 56, No. 2, 871–877, 2007.
2. Hong, W. and D. X. Huang, "Numerical simulation of clock component extraction of NRZ signal using SOA loop mirror [J]," *Acta Photonica Sinica*, Vol. 33, No. 1, 43–46, 2004.
3. Martinez, J. M., F. Ramos, and J. Marti, "All-optical packet header processor based on cascaded SOA-MZIs [J]," *Elect. Lett.*, Vol. 40, No. 14, 894–895, 2004.
4. Fjelde, T., A. Kloch, D. Wolfson, et a1., "Novel scheme for simple label swapping employing XOR logic in an integrated interferometric wavelength converter [J]," *Photonics Tech. Lett.*, Vol. 13, No. 7, 750—752, 2001.
5. Poustie, A. J., K. J. Blow, R. J. Manning, et a1., "All optical pseudorandom number generator [J]," *Optics Communications*, Vol. 159, No. 4, 208—214, 1999.
6. Soto, H., D. Erasme, and G. Guekos, "5-Gb/s XOR optical gate based on cross-polarization modulation in semiconductor optical amplifiers [J]," *Photonics Tech. Lett.*, Vol. 13, No. 4, 335–37, 2001.
7. Houbavlis, T., K. Zoiros, A. Hatziefremidis, et al., "10 Gbit/s all-optical boolean XOR with SOA fiber sagnac gate [J]," *Elect. Lett.*, Vol. 35, No. 19, 1650–1652, 1999.
8. Webb, R. P., R. J. Manning, G. D. Maxwell, et al., "40 Gbit/s all-optical XOR gate based on hybrid-integrated Mach-Zehnder interferometer [J]," *Elect. Lett.*, Vol. 39, No. 1, 79–81, 2003.
9. Randel, S., A. M. de Melo, K. Petermann, et al., "Novel scheme for ultrafast all-optical XOR operation [J]," *Lightwave Tech.*, Vol. 22, No. 12, 2808–2815, 2004.

Ultra-low Power Frequency Conversion in Two-photon-absorption Free Micro Ring Resonator

M. Ferrera[1], **L. Razzari**[1, 2], **D. Duchesne**[1], **R. Morandotti**[1],
Z. Yang[3], **M. Liscidini**[3], **J. E. Sipe**[3], **S. Chu**[4], **B. E. Little**[4], and **D. J. Moss**[5]

[1]INRS-EMT, 1650 Boulevard Lionel Boulet, Varennes, Québec J3X 1S2, Canada
[2]Dipartimento di Elettronica, Università di Pavia, via Ferrata 1, 27100 Pavia, Italy
[3]Department of Physics and Institute for Optical Sciences, University of Toronto
60 St. George St., Toronto, Ontario M5S 1A7, Canada
[4]Infinera Corp., 9020 Junction Dr., Annapolis, Maryland 94089, USA
[5]CUDOS, School of Physics, University of Sydney, New South Wales 2006, Australia

Abstract— All-optical integrated circuits bring the promise to vastly increase the bandwidth, improve the flexibility as well as reduce the cost of future communication networks. All optical integrated components, like switches and wavelength converters, must meet fundamental requirements such as low optical losses, strong nonlinear response and ease of fabrication. To date, however, research on these devices has been based either on semiconductors, such as silicon and GaAs, or highly nonlinear glasses, such as chalcogenides which, although exhibit a Kerr nonlinearity (n2) of 100x–400x silica glass, also present limitations such as remarkable linear and nonlinear losses and, for certain applications, a not developed fabrication techniques. Specifically, the possibility to rely upon a mature technology recently has proved itself to be a powerful solution to fabricate micrometric resonant structures which are able to locally enhance the desired nonlinearities. In this work we present the first example of nonlinear optics in silica glass waveguides using continuous wave (CW) light. We achieve wavelength conversion via four wave mixing (FWM) at ultra-low ($\approx 5\,$mW CW) power levels in C-MOS compatible micro-ring resonator.

1. INTRODUCTION

Traditional material systems for the development of all-optical and optoelectronic devices have primarily been based on semiconductors [1, 2]. Typically these materials exhibit a strong nonlinear response when shaped as waveguides, thanks to their large nonlinear coefficients, high index contrast and small effective area. On the other hand they are often linked with some significant drawbacks such as large linear and nonlinear losses [3] that prevent optimal efficiency for high pump power applications. Contrarily, regarding glass (fused silica) technology, traditional silica waveguides are low index contrast structures and thus results in poor confinement and large bend radii, making all-optical signal processing on a single chip unfeasible, not withstanding their extremely low nonlinear response. Sometimes, when the fabrication process are particularly developed and mature, the strategy is that one of fabricating ultra high Q resonant cavities in order to increase the local intensity and consequently the nonlinearities of the device [4]. However, this solution could avoid the applicability of the phenomenon under investigation in fast communication systems, since a huge value of the Q factor drastically narrows the bandwidth.

As alternative approach, using nonlinear glasses such as chalcogenides and Ta_2O_5, has been developed to offer a substantial nonlinear response comparable to semiconductors. However, such glasses are also prone to linear and nonlinear losses for small device footprints, and for certain applications, their fabrication technology is still quite immature [5]. Here we present a high-index silica glass material (Hydex®) which offers an excellent compromise between the best properties of semiconductors (high nonlinearities and tight field confinement) together with the low loss values of silica glass. Hydex® glass is a high index material ($n = 1.7$) whose developed fabrication technique admits the possibility to vary the index contrast between the core and the silica cladding from 1 to 25% [6] making possible tight bends on the order of $5\,\mu$m in radius and hence, the fabrication of complex resonant microstructures [7, 8].

Furthermore the deposition process using Chemical Vapor Deposition (CVD) and the waveguide core patterned by reactive ion etching makes the entire fabrication process of Hydex totally compatible with current silicon technology [6]. The versatility of high-index glass waveguides have already been largely proved by numerous accomplishments in many applications including optical sensing of bio-molecules using ring resonators [7], and high-order filters with an $80\,$dB rejection ratio [9] but the study of the nonlinear properties of this material has never been addressed.

Since the wavelength conversion is a fundamental nonlinear process for future all optical communication systems we decide to perform the nonlinear investigation of Hydex® starting from the Four Wave Mixing experiment (FWM).

2. EXPERIMENTS

The FWM is a parametric process that is used here to generate a new frequency of light from two existing ones [10, 11]. This kind of wavelength conversion process can be an important tool for wavelength-agile optical networks, where wavelength division multiplexing and demultiplexing, signal regeneration and switching/routing applications are required. Recently, ultra-low power CW FWM wavelength conversion was reported in silicon by using micro-ring resonators [2]. It is of fundamental importance, however, to investigate other material systems since silicon is well known to suffer from two-photon absorption (TPA) and induced free carrier losses that can affect performances at high pump powers [11]. Indeed, the intrinsic nonlinear figure of merit for silicon still remains low even if we eliminate this undesirable effect by means of pin junctions to sweep carriers out [12].

Figure 1 is a scheme of the ring resonator used in our experiment. The ring has a Q-factor of 65000, a free-spectral range of 575 GHz, a radius of 48 μm and a cross-section of 1.5 μm × 1.5 μm. The bus waveguides, which have the same cross section as the ring, are buried underneath a SiO_2 layer and they are used to couple light inside and outside the resonator itself.
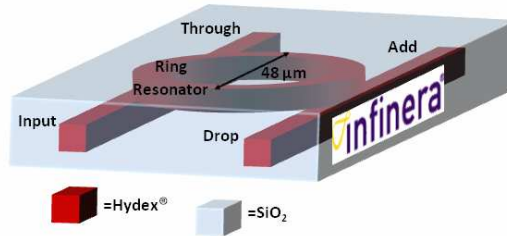

Figure 1: Schematic of the micro-ring resonator.

Two wavelength-tunable CW lasers were used in this experiment; the pump laser (at the INPUT port) was set in such way to provide a power of 5 mW inside the ring and tuned to a TM ring resonance at 1553.38 nm, whereas the signal laser (at the ADD port) had a power of 550 μW and was tuned to an adjacent resonance at 1558.02 nm. The outputs were analyzed using either a power meter or a spectrum analyzer.

3. RESULTS

By the FWM process two idlers are generated according the following formulas:

$$\omega_{\text{1st Idler}} = 2\omega_{\text{Pump}} - \omega_{\text{Signal}} \quad \text{and} \quad \omega_{\text{2nd Idler}} = 2\omega_{\text{Signal}} - \omega_{\text{Pump}}$$

The output power spectra, as recorded at the through channel, are reported below (Fig. 2-Left) as well as the 1st-idler power as a function of the square of the pump power (Fig. 2-Right). The latter shows a good linear dependence, as expected from theory, and demonstrates that our device does not exhibit saturation due to nonlinear absorption, for pump power up to 20 mW.

The first idler was determined to be exactly on resonance at 1548.74 nm, as it is also clearly shown by the idler detuning curve (Fig. 3-Left). This condition is the best to take advantage of the FWM resonance enhancement factor [13, 14] and is made possible tanks to the negligible dispersion of the system that is proved by the strictly linear behavior of the plot that represents the resonance frequencies spacing (Fig. 3-Right).

In order to quantitatively estimate our device performances, we used a theoretical model that takes into account the resonant enhancement factor due to the cavity geometry [13]:

$$\eta \equiv \frac{P_{\text{idler}}}{P_{\text{signal}}} = |2\pi R\gamma|^2 P_{\text{pump}}^2 \cdot (FE_p)^4 \cdot (FE_s)^2 \cdot (FE_i)^2 \tag{1}$$

$$FE = \frac{\sqrt{2(1-\sigma)}}{2(1-\sigma) + \alpha\pi R} \quad \sigma = \left(1 - \frac{\pi}{2Finesse}\right)\exp\left(\frac{\alpha\pi R}{2}\right)$$
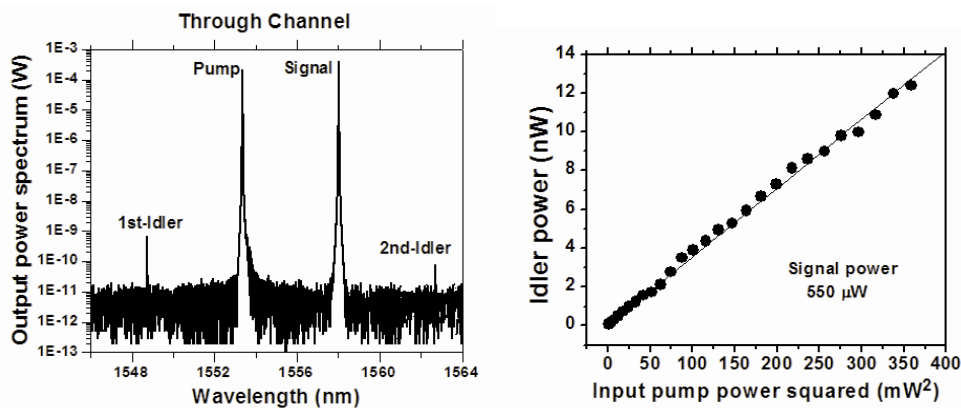
Figure 2: (Left): Output power spectra at the through port. (Right): 1st Idler power as a function of the Pump power squared.
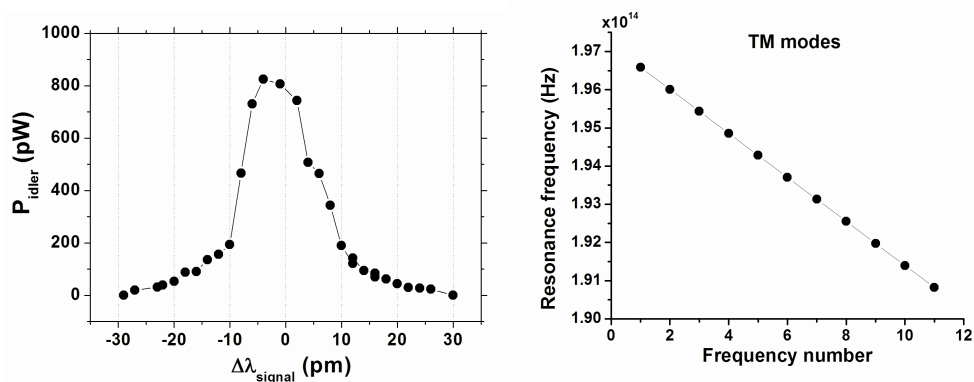

Figure 3: (Left): Power of the 1st idler as a function of the signal detuning from its corresponding resonance. (Right): Resonance frequencies Vs resonance positions (arbitrary frequency location number).

where R is the ring radius, α is the linear loss coefficient and γ is the nonlinear parameter. From the measured input and output powers, and by using Equation (1), the nonlinear parameter can be deduced to be $\sim 233\,\text{W}^{-1}\text{Km}^{-1}$. Our results are comparable to the best results recently reported in silicon structures [2], moreover our glass-based platform offer other advantages such as the ability to produce very good quality high order filters [7, 9], ultra-low losses, as well as the absence of two-photon absorption near $\lambda = 1.5\,\mu\text{m}$, a property which is highly desirable for nonlinear optical applications. Furthermore, the total insertion loss (from laser input to device output) is approximately 3 dB, due to the very good coupling efficiencies between the bus waveguides and the ring resonator ($\sim 100\%$ in resonance). Such coupling efficiencies and throughput are not readily seen for integrated semiconductor waveguides and devices, where coupling efficiencies can be extremely poor [2, 15].

Finally by means of transmission measurements in different length waveguides, we also determined the linear propagation losses to be as little as 0.06 dB/cm. This extremely low loss value is orders of magnitude better than in similar semiconductor waveguides, where values greater than 1 dB/cm are typically seen in AlGaAs and SOI monomode waveguides [3, 15].

4. CONCLUSIONS

In conclusion, the strong non linearity together with the absence of nonlinear losses and the large reduction in linear losses, reveal some great advantages of our material over the silicon counterpart, especially when re-amplification processes have to be avoided. The estimated γ value together with the intrinsic benefits related with the micro ring resonator technology bring us a step forward toward the realization of integrated multifunctional nonlinear all-optical devices. This kind of micro-metric optical package could perform fundamental communication system operations like optical amplification and regeneration, wavelength filtering, conversion and switching. We strongly believe that our waveguides can open new frontiers in ultra-fast all-optical signal processing as well

as in total secure transmission networks based on entangled photons with the promise of reducing development timescale.

REFERENCES

1. Radic, S., D. J. Moss, and B. J. Eggleton, "All-optical photonic signal processing," *Optical Fiber Telecommunications*, Ch. 20, Elsevier Press, Oxford, UK, 2008.
2. Turner, A. C., et al., *CLEO*, post-deadline paper, CPDA3, Baltimore, Md, 2007.
3. Siviloglou, G. A., et al., "Enhanced third-order nonlinear effects in optical AlGaAs nanowires," *Optics Express*, Vol. 14, No. 20, 9377–9384, 2006.
4. Kippenberg, T. J., et al., "Kerr-nonlinearity optical parametric oscillation in an ultrahigh-Q toroid microcavity," *Phys. Rev. Lett.*, Vol. 93, 083904, 2004.
5. Ta'eed, V. G., et al., "Ultrafast all-optical chalcogenide glass photonic circuits," *Optics Express*, Vol. 15, 9205, 2007.
6. Little, B. E., "A VLSI photonics platform," *Optical Fiber Comm. Conf.*, Vol. 2, 444, 2003.
7. Yalcın, A., et al., "Optical sensing of biomolecules using microring resonators," *IEEE J. Sel. Top. Quant. Elec.*, Vol. 12, 148–155, 2006.
8. Tong, L. M., et al., "Subwavelength-diameter silica wires for low-loss optical wave guiding," *Nature*, Vol. 426, 816–819, 2003.
9. Little, B. E., et al., "Very high-order microring resonator filters for WDM applications," *IEEE Photon. Technol. Lett.*, Vol. 16, 2263–2265, 2004.
10. Fukuta, H., et al., "Four-wave mixing in silicon wire waveguides," *Optics Express*, Vol. 13, No. 12, 4629–4637, 2005.
11. Rong, H., Y. Kuo, A. Liu, and M. Paniccia, "High efficiency wavelength conversion of 10 Gb/s data in silicon waveguides," *Optics Express*, Vol. 14, No. 3, 1182–1188, 2006.
12. Liang, T. K. and H. K. Tsang, "Role of free carriers from two-photon absorption in Raman amplification in silicon-on-insulator waveguides," *Appl. Phys. Lett.*, Vol. 84, No. 15, 2745–2747, 2004.
13. Absil, P. P., et al., "Wavelength conversion in GaAs micro-ring resonators," *Opt. Lett.*, Vol. 25, 554–556, 2000.
14. Van, V., et al., "Optical signal processing using nonlinear semiconductor microring resonators," *IEEE J. Sel. Top. Quant. Elec.*, Vol. 8, 705, 2002.
15. Vlasov, Y. A. and S. J. McNab, "Losses in single-mode silicon-on-insulator strip waveguides and bends," *Optics Express*, Vol. 12, 1622–1631, 2004.

Highly Birefringent Hybrid Photonic Crystal Fiber

S. Arismar Cerqueira, Jr., **H. E. Hernandez-Figueroa**, and **H. L. Fragnito**
Optics and Photonics Research Center, UNICAMP, Brazil

Abstract— The Hybrid Photonic Crystal Fiber is a novel type of microstructured fiber, in which for the first time, light was guided and manipulated simultaneously by two different propagation mechanisms: modified total internal reflection from an array of air holes and antiresonant reflection from a line of high-index inclusions. We present an experimental investigation of the birefringent properties of a Highly Birefrigent Hybrid Photonic Crystal Fiber.

1. INTRODUCTION

Highly birefringent fibers provide strong birefringence deliberately introduced during the fiber fabrication process. There are two ways to achieve the required birefringence: the shape of the refractive-index profile that defines the waveguide can be made noncircular (form or shape birefringence); or the material that forms the fiber can itself be made birefringent, typically by introduction of stresses as in bow-tie or PANDA fibers.

Photonic Crystal Fiber technology allows light to be controlled within the fiber in ways not previously possible or even imaginable [1]. They have been intensively explored in the last decade in an effort to understand and exploit their broad potential. Light in a PCF core can be guided by two different mechanisms depending on the photonic crystal formed in their cladding and the type of core used. In index-guiding PCFs, light is confined to a solid core by total internal reflection from a reduced-effective-index cladding material formed from glass shot through with an array of air holes. On the other hand, in photonic bandgap PCFs, light can be confined to a low-index region, even an air hole, by reflection from a 2-dimensional array of high-index scatterers.

The Hybrid Photonic Crystal Fiber or Hybrid PCF [2, 3] is a novel type of microstructured fiber, in which for the first time, light was guided and manipulated simultaneously by two different propagation mechanisms: modified total internal reflection from an array of air holes and antiresonant reflection from a line of high-index inclusions. The Hybrid PCF is composed of air holes and Germanium-doped silica rods disposed around an undoped silica core. The air holes are arranged in a hexagonal pattern as in index-guiding PCFs, whereas the high-index rods replace a single row of air holes along one of the PCF axes. These unique properties make Hybrid PCF naturally high birefringent, since light is guided along its two orthogonal polarization states by two different propagation mechanisms. This work presents an experimental investigation of the birefringent properties of a Highly Birefrigent Hybrid PCF.

2. HYBRID PCF

The Highly Birefringent Hybrid Photonic Crystal Fiber is like that shown in Fig. 1. It has the following parameters: air hole diameter $d = 4.34 \, \mu\text{m}$, interhole spacing $\Lambda = 8.00 \, \mu\text{m}$, germanium rod diameter $D = 6.38 \, \mu\text{m}$ and gradual refractive index with maximum step $\Delta n = 2.03\%$. The white inclusions are Germanium-doped rods, whereas the black circles are air holes.

In order to measure the fiber photonic bandgaps, a supercontinuum source, pumped at 1064 nm, has been coupled to the hybrid fiber using a $20\times$ objective lens. The output was analyzed using an optical spectrum analyzer. Fig. 2 shows the transmitted spectrum recorded with a fiber sample of 1.0 m length. There are five antiresonant regions in silica transmission window, which are represented by the low-attenuation windows in the transmitted spectrum.

3. MEASUREMENT OF BIREFRINGENCE PROPERTIES

The experimental setup is shown in Fig. 3 and is based on the following pieces of equipment: a tunable external cavity laser (ECL), a fiber polarization controller (PC), some objective lenses and an optical spectrum analyzer (OSA). PC and OSA have been used to change the polarization at the fiber input and to measure the output power, respectively. We have analyzed the birefringence properties in the second photonic bandgap around 1500 nm, which is the wavelength range of our ECL.

Figure 4 displays the polarization dependent loss measurement of the Hybrid PCF as a function of wavelength. It demonstrates the fiber birefringence is much more intense on the photonic bandgap edges, where power variation between the two orthogonal polarization states (ΔP) is about 21 dB.
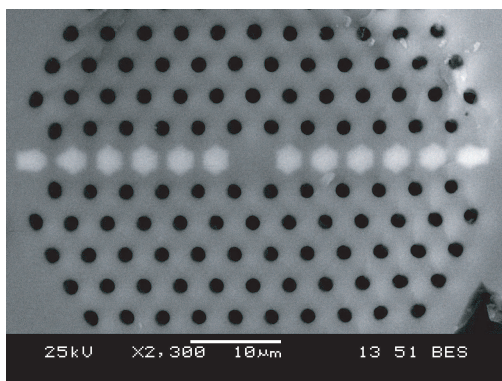
Figure 1: Hybrid photonic crystal fiber.
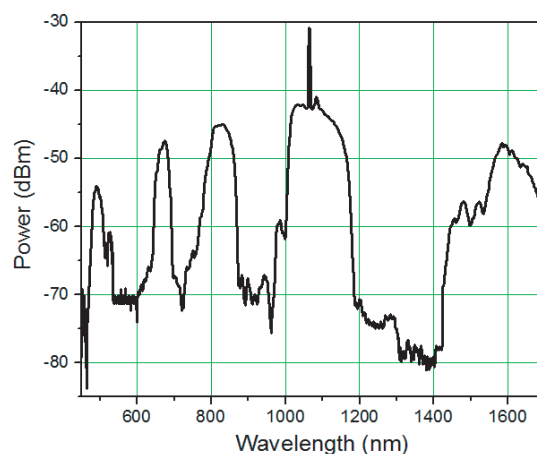
Figure 2: Transmission spectrum measurement.
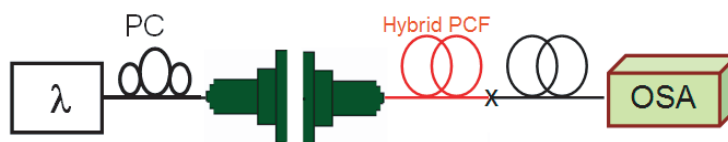
Figure 3: Experimental setup.
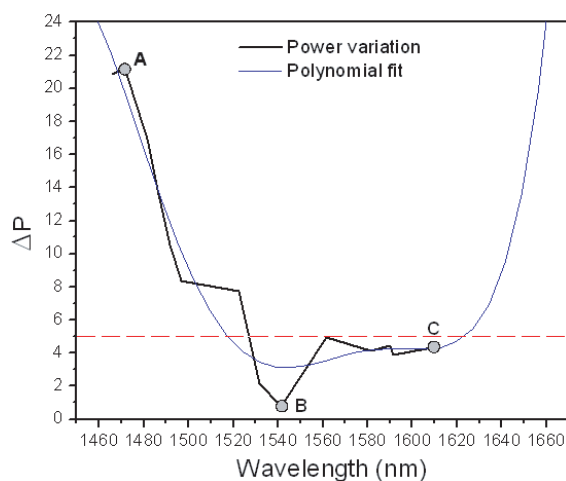
Figure 4: PDL measurement.

The very strong birefringence of Hybrid PCFs comes from the significant stress field produced by Ge inclusions; and since they are positioned along a line through the structure, they give rise to an asymmetric stress field within the core that induces a sizeable birefringence [4]. The asymmetric stress distribution will split the two polarization modes and cause a polarization dependent loss. The same behavior is expected for the other bandgaps.

4. CONCLUSIONS

A highly birefringent Hybrid photonic crystal fiber has been proposed and experimentally investigated. It provides very strong birefringence that comes from the significant stress field produced by Ge inclusions positioned along a line through the structure. Polarization dependent loss as high as 21 dB has been reported on the photonic bandgap edges. Hybrid PCFs can be efficiently applied to the development of gyroscopes, fiber polarizers, and fiber lasers and amplifiers to ensure linearly polarized output.

REFERENCES

1. Knight, J. C., "Photonic crystal fibres," *Nature*, Vol. 424, 847–851, August 2003.
2. Arismar Cerqueira, Jr., S., F. Luan, C. M. B. Cordeiro, A. K. George, and J. C. Knight, "Hybrid photonic crystal fiber," *Opt. Express*, Vol. 14, 926–931, 2006.
3. Arismar Cerqueira, Jr., S., C. M. B. Cordeiro, F. Biancalana, P. J. Roberts, H. E. Hernandez-Figueroa, and C. H. Brito Cruz, "Nonlinear interaction between two different photonic bandgaps of a hybrid photonic crystal fiber," *Opt. Letters*, Vol. 33, September 2008.
4. Schreiber, T., et al., "Stress-induced single-polarization single-transverse mode photonic crystal fiber with low nonlinearity," *Opt. Express*, Vol. 13, 7621–7630, 2005.

Efficient Generation of Cascaded Four-wave Mixing in Very Short Optical Fibers

S. Arismar Cerqueira, Jr., **J. D. Marconi**, **H. E. Hernandez-Figueroa**, and **H. L. Fragnito**

Optics and Photonics Research Center, UNICAMP, Brazil

Abstract— This work presents a three-pump technique for generating cascaded four-wave mixing spaced by only 0.8 nm or 100 GHz, which is the standard separation between Dense-Wavelength Division Multiplexing channels. It consists of using very short optical fibers, few meters, and three closely pumps (100–200 GHz), but unequally spaced in frequency, and relatively close to the zero-dispersion wavelength of the fiber. It has obtained 275 FWM products locked to the 100 GHz standard telecommunications grid.

1. INTRODUCTION

Four-wave mixing (FWM) is a nonlinear phenomenon, based on optical Kerr effect, which is very attractive for developing nonlinear devices. FWM occurs when four different waves interact in such way that their energy and momentum are conserved. The momentum conservation is often referred to as phase matching and depends strongly on the chromatic dispersion of the nonlinear medium. As the waves propagate through the fiber, FWM processes may occur involving the new generated waves, creating in this manner photons at further new frequencies. This is referred to as cascaded or multiple FWM [1, 2]. For the simultaneous propagation of multiple intense pulses, FWM can provide an efficient mechanism for broadband redistribution of the energy to new wavelengths. This frequency cascading is formed by signals with well-defined frequency and phase differences [3].

We have previously proposed a two pumps-based method for generating broadband four-wave mixing products [1]. By using this method large bandwidths of FWM products spaced by large spectral spacing, such as 2.5 and 6.5 nm, have been reported. This work presents an efficient technique for generating cascaded four-wave mixing spaced by only 0.8 nm or 100 GHz, which is the standard separation between Dense-Wavelength Division Multiplexing channels. It consists of using very short optical fibers, few meters, and three not equally spaced pumps launched near their zero-dispersion wavelengths. The advantages of using very short optical fibers result from three effects: reducing the relative phase difference $\Delta\Phi$ of non-polarization maintaining fibers; avoiding undesirable variation of the zero-dispersion wavelength and preserving the phase matching condition by keeping the product $\Delta\beta L$ small. On the other hand, the use of three pumps instead of two pumps, as in the previous publication, has been shown extremely interesting for improving the cascaded FWM efficiency.

2. ANALYSIS OF MULTIPLE FOUR-WAVE MIXING EFFICIENCY

The experimental setup is shown in Fig. 1. Three external cavity lasers (ECL), with a nominal linewidth of 120 KHz, are coupled together with a 33% coupler and passed through a Mach-Zehnder amplitude modulator (AM) to obtain 40 ns pulses at a repetition rate of 100 KHz. Two erbium doped fiber amplifiers (EDFAs) in tandem boost the pulses to ~ 20 W total peak power. In Fig. 1, EDFA 1 is a low noise pre-amplifier with an average output power up to 15 mW, whereas EDFA 2 is a booster amplifier with 1 W average output power. Polarization controllers (PC) guarantee the parallelism among the states of polarization the pumps, thus optimizing the FWM efficiency. We used an optical spectrum analyzer (OSA) with 0.01 nm resolution bandwidth to measure the Optical Signal to Noise Ratio (OSNR) of the generated sidebands. The individual lasers were approximately equal in peak power, and we monitored the resulting optical pulse (after the EDFA booster) using a fast photodiode and an oscilloscope with combined rise-time response of < 1 ns.

3. RESULTS

In order to investigate experimentally the efficiency of multiple four-wave mixing in our three-pump technique, we fixed the optical frequencies of lasers 1 and 2 at $\nu_1 = 194.3$ THz (1542.94 nm) and $\nu_2 = 194.2$ THz (i.e., $\nu_1 - \nu_2 = 100$ GHz), respectively, and tuned the third laser (ν_3) so that the spacing between lasers 2 and 3, $\Delta\nu_{23} = \nu_2 - \nu_3$, was varied between 100 GHz and 200 GHz. The total peak power was kept constant at ~ 20 W for all cases.
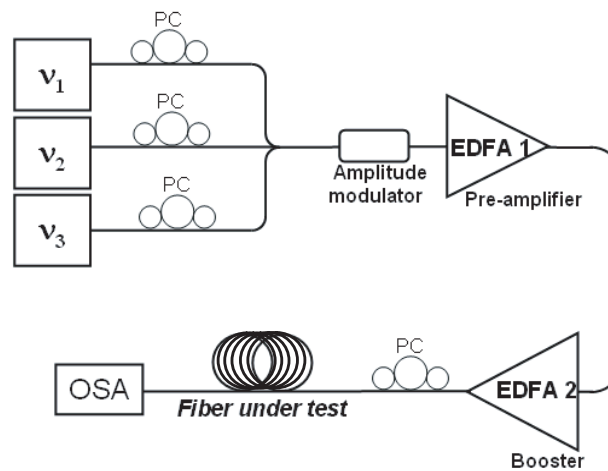
Figure 1: Experimental setup for three pumps.

Figure 2 presents a comparison between two and three pump schemes equally spaced to 100 GHz. The efficiency enhancement is clearly obtained when three pumps are used. It is important to highlight the pump wavelength spacing should be carefully tuned in order to ensure FWM products are going to be equally spaced. Otherwise the efficiency of CFWM process can be degraded. Particularly in this experiment, our precision was limited by the resolution of our OSA (0.01 nm). It has been shown that FWM within the booster EDFA plays an important role as seed for the CFWM in this type of experiments [1]. Consequently, the insets of Fig. 2 show the measured spectrum at the input of the HNLF for each case. The measured OSNR is limited by the high stray light from our OSA.

(a) Two pumps   (b) Three pumps equally spaced
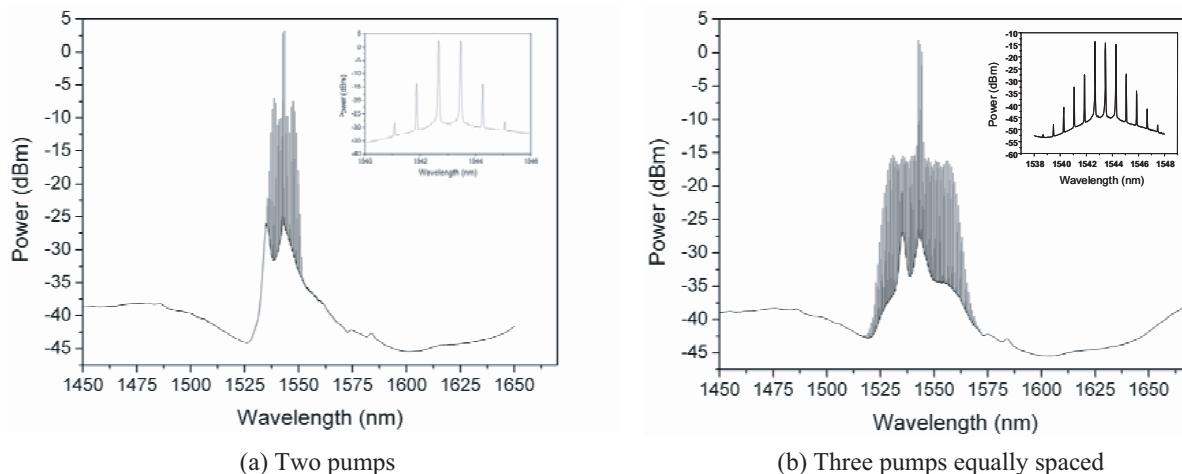
Figure 2: Comparison between two and three pump schemes.

Figure 3 shows the multiple FWM efficiency can be further improved by using not equally spaced pumps ($\Delta\nu_{23} = 200\,\text{GHz}$), where as many as 275 FWM products locked to the 100 GHz standard telecommunications grid have been generated. Among then, 136 FWM products with OSNR > 10 dB were generated from 1500 to 1609 nm.

Figure 4 displays a zoomed spectrum near the pumps for this case, and reveals clearly that the generated sidebands present a good OSNR and have a small variation of spectral power (7 dB) among the 40 FWM products displayed. Furthermore, the output spectrum is very stable; remaining unchanged for several hours. Note that the spectral window in Fig. 4 exceeds the full C-band of DWDM systems (1530–1565 nm). With further improvements in the fiber design, our result shows that our three-pump technique it should be possible to generate frequency combs covering the bands of DWDM with good channel equalization and OSNR. One should notice that the noise pedestal observed in the spectra from Figs. 2 and 3 arises from the ASE emitted by the EDFAs

(and partially from parametric amplification in the HNLF). Therefore, it is not a fundamental limitation and can be greatly reduced by using separate EDFAs, spectral filters, and polarization filtering (the sidebands have will defined polarization, whereas the ASE is randomly polarized). As a last comment, one can in principle use four or more pumps to try to produce even better results than with our 3-pump scheme, but at the expenses of more complexity and cost.
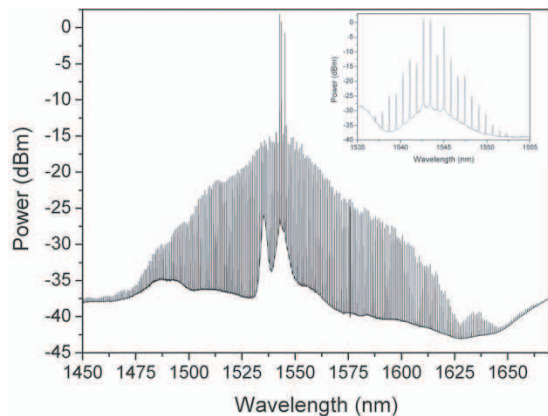
Figure 3: 275 FWm products obtained by using $\Delta\nu_{23} = 200\,\text{GHz}$.
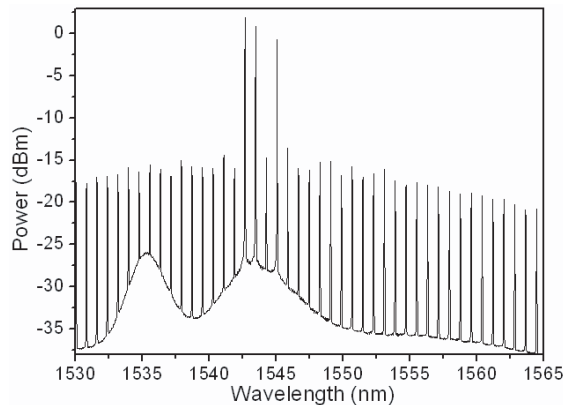
Figure 4: Zoom at the C band for $\Delta\nu_{23} = 200\,\text{GHz}$.

4. CONCLUSIONS

A three-pump technique has been proposed and demonstrated for efficient generation of frequency combs in the standard DWDM grid. By properly spacing the pumps we obtained a total of 275 FWM products, such that 136 FWM products have an OSNR $> 10\,\text{dB}$ spanning over 109 nm, from 1500 to 1609 nm. This frequency comb exceeds the C-band of DWDM. This technique can be useful as broadband multi-wavelength source for DWDM test & measurement, WDM multicasting, high bit rate systems ($> 100\,\text{Gb/s}$), and scientific applications of frequency combs.

REFERENCES

1. Arismar Cerqueira, Jr., S., J. M. Chavez Boggio, A. A. Rieznik, H. E. Hernandez-Figueroa, H. L. Fragnito, and J. C. Knight, "Highly efficient generation of broadband cascaded four-wave mixing products," *Opt. Express*, Vol. 16, 2816–2828, February 2008.
2. Cruz, F. C., "Optical frequency combs generated by four wave mixing in optical fibers for astrophysical spectrometer calibration and metrology," *Opt. Express*, Vol. 16, 13267–13275, 2008.
3. Liu, X. M., "Theory and experiments for multiple four-wave -mixing processes with multifrequency pumps in optical fibers," *Phys. Rev. A*, Vol. 77, 043818, 2008.

High Performance, Low-loss Nonlinear Integrated Glass Waveguides

D. Duchesne[1], M. Ferrera[1], L. Razzari[1, 2], R. Morandotti[1],
M. Peccianti[1], B. Little[3], S. T. Chu[3], and D. J. Moss[4]

[1]INRS-EMT, 1650 Boulevard Lionel Boulet, Varennes, Québec, J3X 1S2, Canada
[2]Dipartimento di Elettronica, Università di Pavia, via Ferrata 1, Pavia 27100, Italy
[3]Infinera Corp., 9020 Junction Dr, Annapolis, Maryland 94089, USA
[4]CUDOS, School of Physics, University of Sydney, New South Wales 2006, Australia

Abstract— Using a novel high-index glass material platform, integrated low-loss waveguides were fabricated and are shown to have excellent nonlinear properties. Through self-phase modulation measurements in a 45 cm long spiral waveguide, the Kerr nonlinearity is determined, and is estimated to be more than 200 times larger than that of single mode fibers. The excellent linear transmission together with absence of multi-photon absorption, for peak intensities up to $25\,GW/cm^2$, offers a promising alternative for the fabrication of future nonlinear all-optical devices.

1. INTRODUCTION

Photonic research for telecommunications has become an important subject of investigation largely due to the high bandwidth and low energy costs of signal processing performed using photonics over electronics. The future development of all-optical networks will require optical materials that have attractive linear and nonlinear properties. Many signal processing application will require the use of nonlinear optical devices, such as wavelength converters and switches, for basic logic functions, as well as for routing and wavelength division (de) multiplexing schemes. There are still many challenges prior to the implementation of these devices, which ultimately will depend on the choice of a suitable optical material.

Conventional nonlinear materials include AlGaAs, $LiNbO_3$, BBO and SOI [1–3]. Recently, very high index nonlinear glasses, such as Chalcogenides have also been explored as a nonlinear medium [4]. Whereas most of these materials have large nonlinear coefficients, many of them are also plagued by high scattering losses, nonlinear absorption and/or expensive/immature fabrication technologies [1–4]. Waveguides made from these materials usually have a high index contrast. Whereas this is beneficial for tight bend radii and increased intensity levels (due to modal confinement), this also results in small structural dimensions required for the guides to maintain single mode operation, which in turn leads to increased scattering losses and a decrease in the butt-coupling efficiency to optical fibers. On the other hand, standard glass (fused silica) is not often viewed as a potential optical material due to its very weak nonlinear optical properties and low index, in spite of the excellent ease of fabrication and control of losses. In this paper we report a novel high-index glass waveguide having the attractive linear properties of conventional silica optical fibers, such as the absence of nonlinear absorption and small propagation losses, but also a moderately large Kerr nonlinearity, leading to a nonlinear parameter (γ) more than 200 times higher than that of optical fibers.

Moreover, we employ a 45 cm long waveguide confined in a $2.5 \times 2.5\,mm$ area chip with high energetic efficiency that is also fully pigtail for immediate fiber integration.

2. DEVICE

Hydex$^{\circledR}$ is a high optical index ($n = 1.7$) glass material developed by Little Optics in 2003 [5]. High index contrast waveguides are formed by surrounding a rectangular core of Hydex$^{\circledR}$ with fused silica. The high index contrast ($\Delta n = 0.26$) allows for tightly confined modes down to ~1 μm dimensions. In addition to this, tight bends of less than 30 μm in radius are possible with negligible losses [6]. These waveguides have excellent sidewall verticality (< 1 degree), which in turn reduces scattering losses considerably. Hydex$^{\circledR}$ is deposited using Chemical Vapor Deposition (CVD); the waveguide cores are patterned using reactive ion etching and the stepper optical lithography tolerance far exceeds 100 nm. The unique character of our glass system is the CMOS fabrication compatibility that does not require any post-annealing, unlike similar glass systems such as SiON where temperatures greater than 1000 degrees are required to reduce losses [5]. These high-index

glass waveguides have already shown much success in many applications including optical sensing of biomolecules using ring resonators [7], and high-order filters with an 80 dB rejection ratio [6].

In spite of the recent success associated to the use of Hydex® waveguides, the nonlinear properties of this material have not been characterized yet. To determine the nonlinear properties of this material we used the 45 cm long spiral waveguide previously mentioned. The cross-sectional area of the core is 1.45 μm by 1.5 μm and is surrounded on all sides by silica. In order to optimize the coupling efficiency between the small $2.0\,\mu m^2$ effective area of the waveguide mode to that of a single mode fiber, tapers (fiber pigtails) were used. The designed mode converters have a low loss of 1.5 dB, a great improvement over inverse or horn tapers which often require complicated fabrication procedures and result in smaller conversion efficiencies [8].

3. TRANSMISSION RESULTS

From low power transmission measurements (performed using a CW tunable laser) in different length waveguides, linear propagation losses for the waveguide were determined via a cut-back style procedure, and were determined to be as small as 0.06 dB/cm. Note that this extremely low loss is orders of magnitude better than what is available from current technological processes for high-index contrast AlGaAs and Si monomode waveguides, which have loss values on the order of a few dB/cm or more [1–3]. The total device insertion loss was determined to be 6 dB. Recent four-wave mixing experiments in the C-band in similar waveguides also implied that the total dispersion is expected to be quite low [9]. The low propagation losses, high throughput of the device and low dispersion present ideal characteristics for pulse propagation.

To understand if these low propagation losses would be maintained in the high power pulsed regime, the nonlinear transmission of the 45 cm waveguide was investigated using pulses of ∼450 fs duration from a mode-locked fiber laser. An erbium-doped fiber amplifier was used to amplify the pulse power, followed by an inline fiber attenuator to control the input power coupled into the waveguide, while the output average power was measured. Autocorrelation measurements were taken immediately before the waveguide input, from which we deduced the pulse duration and approximate shape. This was then used to relate the average power measured at the input of the waveguide to the peak power. The results, presented in Figure 1, show a pure linear dependence with the output average power, implying that no multi-photon absorption was present up to the maximum power of 500 W ($25\,GW/cm^2$) attainable with our laser system. Absence of nonlinear absorption, especially two-photon absorption, is of great importance in nonlinear signal processing. In particular, nonlinear absorption is often detrimental in many semiconductor waveguides such as in silicon-on-insulator [2, 10, 11].

4. SPECTRAL BROADENING EXPERIMENT

A particularly important parameter for nonlinear optical applications is the nonlinear-index coefficient, n_2, and the nonlinear parameter, γ. Whereas n_2 is a material property which determines the effective nonlinear shift in the refractive index of the material, γ depends on the waveguide parameters and describes the strength of the Kerr nonlinear interactions within the waveguide ($\gamma = 2\pi n_2/\lambda A_{eff}$, where λ is the pulse central wavelength, c is the speed of light and A_{eff} is the effective area). We determine these parameters through self-phase modulation experiments, which have often been employed as a tool to measure both these parameters [2, 3].

Pulses of 50 W peak power and 1.2 ps duration from a mode locked fiber laser were injected inside the 45 cm waveguide and output power spectra measurements were obtained using an optical spectrum analyzer. The results for the self-phase modulation are shown in Figure 2. Simulations for the pulse propagation were performed according to the nonlinear Schrödinger equation:

$$i\frac{\partial A}{\partial z} + i\frac{\alpha}{2}A - \frac{\beta_2}{2}\frac{\partial^2 A}{\partial T^2} + \gamma \left|A\right|^2 A = 0, \tag{1}$$

where A is the slowly varying envelope of the electric field, α are the measured propagation losses, z is the propagation direction, T is the travelling time coordinate and β_2 is the group velocity dispersion. By varying the dispersion and nonlinear parameter, it was possible to fit the experimental data. The input pulse for the simulation was obtained from the experimentally measured input spectrum (by an inverse Fourier operation), with knowledge that the fiber laser emits almost transform limited pulses. A quadratic chirp was added to the temporal input pulse in order to match the evolution of the spectrum as a function of power (not shown here). The best fit was

obtained when the nonlinear index coefficient was set to $1.1 \times 10^{-19} \, \text{m}^2/\text{W}$, which is approximately 5 times larger than the value found in silica glass. Finally, the dispersion was deduced to be small with minimal effect on the spectral broadening. From the measured value of n_2, the nonlinear parameter was deduced to be $220 \, \text{W}^{-1}/\text{Km}$, more than 200 times larger than in single mode fibers $(1 \, \text{W}^{-1}/\text{Km})$. This result agrees well with previous four-wave mixing experiments in a micro-ring resonator composed of the same waveguides [7]. It is important to note that the value of γ in typical semiconductors can far exceed this value ($\sim$200,000 in SOI [2, 3, 11]) due to smaller waveguide geometries and larger intrinsic nonlinear-index coefficients, but typical silicon based waveguides have strong nonlinear absorption, high linear propagation losses/insertion losses, as well as large dispersion values for non-tailored geometries [2, 11].
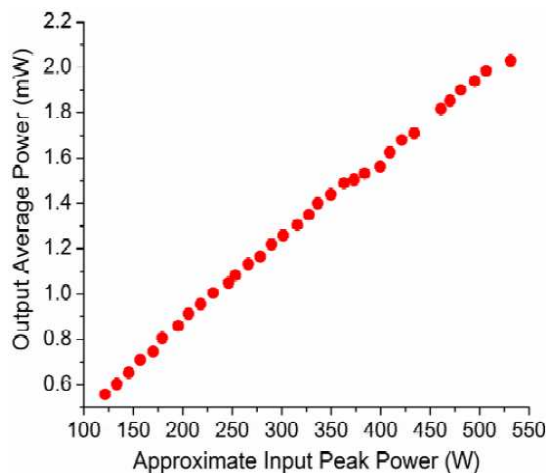
Figure 1: High power transmission of 450 fs pulses in a 45 cm waveguide show absence of nonlinear absorption.
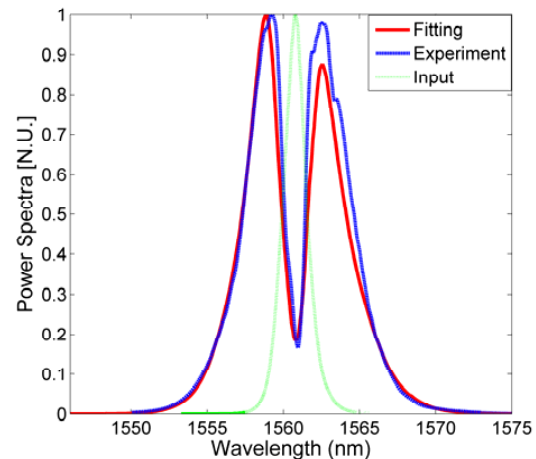
Figure 2: Self-phase modulation spectral broadening as experimentally measured (blue curve) and the corresponding fit (red) based on simulations. The input pulse spectrum is also shown (green curve).

Significantly larger spectral broadening was obtained using 350 fs pulses of 240 W peak power. As it is shown in Figure 3, from an input spectral width of 25 nm (at 1% power level) we obtain an output spectrum more than ten times larger. This interesting result suggests that possible supercontinuum and frequency mixing applications may be possible in this waveguide.
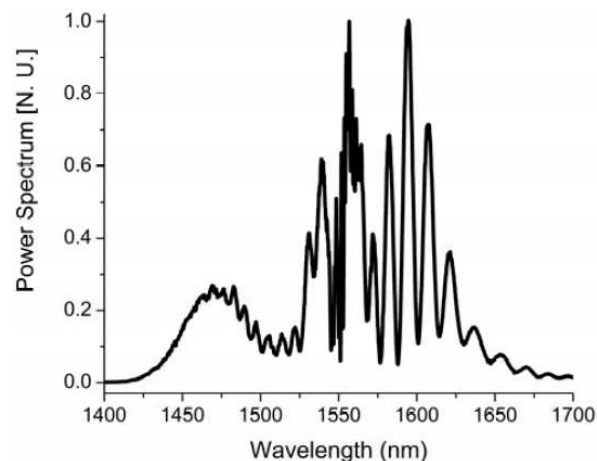
Figure 3: Large spectral broadening at the output of the 45 cm waveguide.

5. CONCLUSIONS

Low-loss, high-index, integrated glass waveguides were shown to have excellent linear properties, with losses as low as 0.06 dB/cm and low dispersion in the C-band. The low cost, mature fabrication technology, fully CMOS compatible integration, coupled with already developed and low loss fiber pigtails shows promise for signal processing applications where moderate nonlinear interactions are required.

REFERENCES

1. Vlasov, Y. A. and S. J. McNab, "Losses in single-mode silicon-on-insulator strip waveguides and bends," *Opt. Expr.*, Vol. 12, 1622–1631, 2004.
2. Dulkeith, E., Y. A. Vlasov, X. Chen, N. C. Panoiu, and R. M. Osgood, Jr., "Self-phase-modulation in submicron silicon-on-insulator photonic wires," *Opt. Expr.*, Vol. 14, 5524–5534, 2006.
3. Siviloglou, G. A., S. Suntsov, R. El-Ganainy, R. Iwanow, G. I. Stegeman, D. N. Christodoulides, R. Morandotti, D. Modotto, A. Locatelli, C. De Angelis, F. Pozzi, C. R. Stanley, and M. Sorel, "Enhanced third-order nonlinear effects in optical AlGaAs nanowires," *Opt. Expr.*, Vol. 14, 9377–9384, 2006.
4. Ta'eed, V. G., N. J. Baker, L. Ful, K. Finsterbusch, M. R. E. Lamont, D. J. Moss, H. C. Nguyen, B. J. Eggleton, D. Y. Choi, S. Madden, and B. Luther-Davies, "Ultrafast all-optical chalcogenide glass photonic circuits," *Opt. Expr.*, Vol. 15, 9205–9221, 2007.
5. Little, B. E., "A VLSI photonics platform," *Optical Fiber Communication Conference*, 444–445, Atlanta, USA, March 2003.
6. Little, B. E., S. T. Chu, P. P. Absil, J. V. Hryniewicz, F. G. Johnson, F. Seiferth, D. Gill, V. Van, O. King, and M. Trakalo, "Very high-order microring resonator filters for WDM applications," *IEEE Photon. Technol. Lett.*, Vol. 16, 2263–2265, 2004.
7. Yalcın, A., K. C. Popat, J. C. Aldridge, T. A. Desai, J. Hryniewicz, N. Chbouki, B. E. Little, O. King, V. Van, S. Chu, D. Gill, M. Anthes-Washburn, M. S. Unlu, and B. B. Goldberg, "Optical sensing of biomolecules using microring resonators," *IEEE J. Sel. Top. Quant. Elec.*, Vol. 12, 148–155, 2006.
8. Moerman, I., P. P. Van Daele, and P. M. Demeester, "A review on fabrication technologies for the monolithic integration of tapers with III–V semiconductor devices," *IEEE J. Sel. Top. Quant. Elec.*, Vol. 3, 1308–1320, 1997.
9. Ferrera, M., L. Razzari, D. Duchesne, R. Morandotti, Z. Yang, M. Liscidini, J. E. Sipe, S. Chu, B. Little, and J. Moss, "Low power continuous-wave nonlinear optics in doped silica glass integrated waveguide structures," *Nat. Phot.*, (to be published).
10. Yin, L. and G. P. Agrawal, "Impact of two-photon absorption on self-phase modulation in silicon waveguides," *Opt. Lett.*, Vol. 32, No. 14, 2031–2033, 2007.
11. Hsieh, I.-W., X. Chen, J. I. Dadap, N. C. Panoiu, and R. M. Osgood, Jr., "Cross-phase modulation-induced spectral and temporal effects on co-propagating femtosecond pulses in silicon photonic wires," *Opt. Expr.*, Vol. 15, No. 3, 1135–1146, 2007.

Birefringence Vector Computation and Measurement for Fiber with Polarization Dependent Loss

Zhengyong Li, Chongqing Wu, Qingtao Zhang, and Huiyuan Zhang

Key Lab of Education Ministry on Luminescence and Optical Information Technology
Institute of Optical Information, Beijing Jiaotong University, Beijing 100044, China

Abstract— Based on polar decomposition of the Mueller matrix, the birefringence vector is computed for the fiber with polarization dependent loss (PDL) with the validity confirmed by experiment. A computer-controlled measure system is employed to measure the Mueller matrix of a 2.5-km fiber for 5-mm length under lateral press. By comparison we find the differential rotation method is applicable to large rotations with accurate results. Further experiments in pressure vector measurement show the linearity of birefringence magnitude to pressure is excellent ($R^2 > 0.999$) with average error ~ 0.25 N, and the press orientation can be determined by birefringence vector with average error $\sim 1.05°$. Our conclusions are applicable to long time measurement of the fiber in complicated environment with great perturbation such as the fiber-based remote pressure sensing.

1. INTRODUCTION

The semiconductor optical amplifier (SOA) has highly nonlinear optical properties and its refractive nonlinearity is very large ($> 10^8$ times larger than an equivalent length of optical fiber) [1]. Recently the nonlinear polarization properties in SOAs are receiving considerable interest for their promising applications in optical signal processing such as wavelength conversion, optical time domain demultiplexing, and all-optical logic [2–4]. The key technology of these applications is the polarization switching (PS) caused by polarization rotation (PR) in the SOA. Chen and Liu early performed PS in an InGaAsP/InP laser by control of the injected current [5], while it is inapplicable for high-speed optical communications due to the limited speed of current modulation. In this paper, we introduce a polar decomposition method of Mueller matrix to analyze the polarization activities of SOAs and demonstrate the relationship between PR and mode gains. Then we realize the orthogonal PR by control of a high-intensity pump laser, and perform the PS based on photoinduced PR with data rate at 2.5 G-bit/s.

2. MEASUREMENT AND COMPUTATION OF BIREFRINGENCE VECTOR

The principle of birefringence vector measurement is shown in Fig. 1, where the lower part is the pressure vector generator (PVG) made of a force gauge and a rotatable PZT-based squeezing device, which squeezes 5-mm length fiber in the middle of a 2.5-km fiber system. A computer-controlled measure system is employed to obtain the Mueller matrix of the fiber under different pressure.
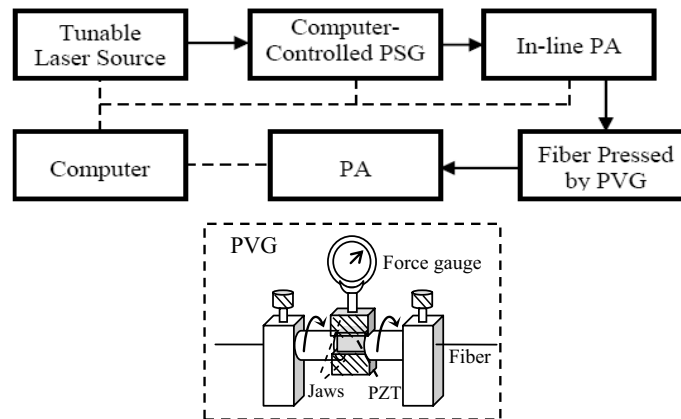

Figure 1: Experimental setup for birefringence vector measurement based on Mueller matrix method.

The polarization state generator (PSG) produces four kinds of linear independent states of polarization (SOPs) $\vec{S}_1$, $\vec{S}_2$, $\vec{S}_3$ and $\vec{S}_4$ measured by Polarimeter 1 which form a matrix $S_{\text{in}} =$

$[\vec{S}_1 \, \vec{S}_2 \, \vec{S}_3 \, \vec{S}_4]$, while the corresponding output SOPs obtained by Polarimeter 2 form another matrix S_{out}. Since output and input SOPs are related by $S_{\text{out}} = MS_{\text{in}}$, the Mueller matrix can be obtained by $M = S_{\text{out}}(S_{\text{in}})^{-1}$. Actually besides the birefringence the system contains the polarization dependent loss (PDL) so matrix M should include both birefringence term M_B and PDL term M_D. However the pressure P mainly relates to the birefringence. We use the decomposing method described in [4] to obtain this pressure dependent birefringence matrix M_R

$$
M_B = MM_D^{-1}, \quad M_D = m_{11} \begin{pmatrix} 1 & \vec{D}^T \\ \vec{D} & m_D \end{pmatrix},
$$
$$
\vec{D} = D\hat{D} = D\vec{D}/|\vec{D}| = m_{11}^{-1}(m_{12}, \, m_{13}, \, m_{14})^T \tag{1}
$$
$$
m_D = \sqrt{1 - D^2} \, \text{diag}\,[1, \, 1, \, 1] + (1 - \sqrt{1 - D^2})\hat{D}\vec{D}^T
$$

here m_{ij} denotes the component of matrix M. Then the birefringence vector can be computed by [5]

$$
\vec{B} = \theta\hat{B} = \theta(S_1, \, S_2, \, S_3)^T,
$$
$$
\theta = |\vec{B}| = \cos^{-1}[Tr(M_B)/2 - 1],
$$
$$
S_1 = (m_{34}^B - m_{43}^B)/(2\sin\theta), \tag{2}
$$
$$
S_2 = (m_{42}^B - m_{24}^B)/(2\sin\theta),
$$
$$
S_3 = (m_{23}^B - m_{32}^B)/(2\sin\theta),
$$

where $Tr(M_B)$ and m_{ij}^B $(i, \, j = 1, \, 2, \, 3, \, 4)$ are the trace and components of matrix M_R.

3. DIFFERENTIAL ROTATION METHOD

In this section we will discuss three kinds of computation results related to absolute rotation, relative rotation, and differential rotation method. By Mueller matrix method described in Section 2 the Mueller matrixes are measured for the fiber under different presses with fixed squeezing direction. After the birefringence matrixes M_R are decomposed by Eq. (1), firstly they are directly used to calculate the birefringence vectors, which we call the absolute rotation method. The results are shown in Fig. 2. In general the direction of birefringence vector is invariable when the press direction is fixed [6]. While in Fig. 2(b) the result is far from this conclusion. So this method should be modified.
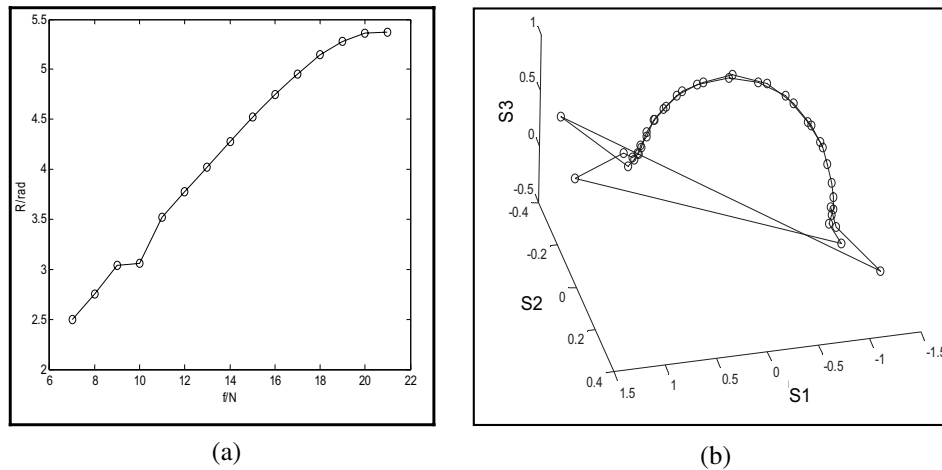
Figure 2: Measurement results of birefringence vector $\vec{B}$ by absolute rotation method, (a) $\theta \sim f$; (b) $S_1 \sim S_3$.

To obtain better result we choose the birefringence matrix under initial press as a reference (M_{R0}), and calculate the relative matrixes $M_R^r = M_R M_{R0}^{-1}$ for other matrixes under different presses. Then the matrixes M_R^r are utilized to compute corresponding birefringence vectors instead of M_R. Since the polarization rotation induced by birefringence is relative to a reference, it can be called a relative rotation method. The calculation results are presented in Fig. 3, where we can

find the birefringence magnitude θ is linear to press with high linearity ($R^2 = 0.9995$). However the direction of the birefringence vector is just invariable within a small range of press (~ 10 N), while it has periodic jump every 10 N or π radian increase of birefringence (polarization rotation). Therefore we should further improve it.
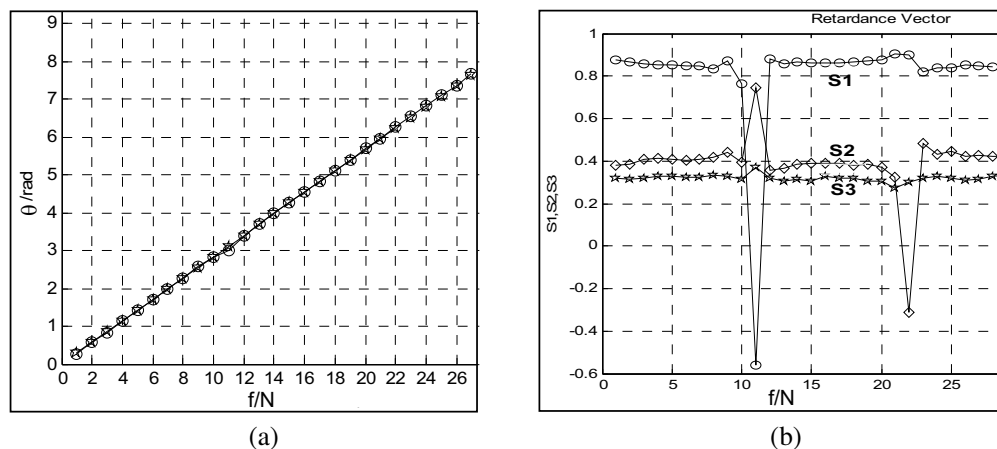
Figure 3: Measurement results of $\vec{B}$ by relative rotation method, (a) $\theta \sim f$; (b) $S_1 \sim S_3$.

Furthermore we select the adjacent birefringence matrix as a reference (M_R^{i-1}) instead of the unified M_{R0}, while employ the differential matrixes $\Delta M_R^i = M_R^i M_R^{i-1}$ to compute corresponding birefringence vector instead of M_R^r, which we call the differential rotation method since it is a differential polarization rotation. Fig. 4 gives the calculation results, from which we can find the birefringence magnitude θ is linear to press with high linearity ($R^2 = 0.9998$), while the direction of the birefringence vector is nearly invariable within the whole range of press. Statistical analysis shows the average deviation of the Stokes parameter is less than 2.5%.
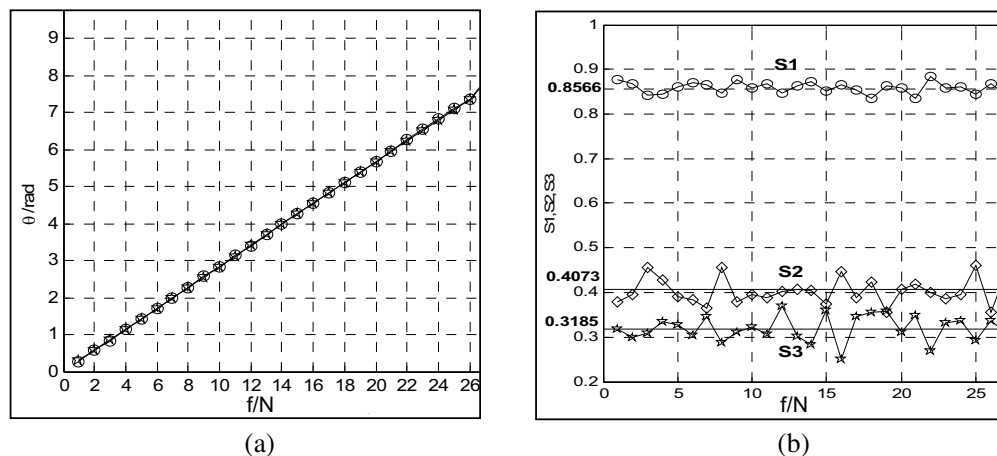
Figure 4: Measurement results of $\vec{B}$ by differential rotation method, (a) $\theta \sim f$; (b) $S_1 \sim S_3$.

Compare above results (Figs. 2–4), we can draw the conclusion that the differential rotation method is optimal for measurement of fiber with PDL. Since most of the error is reduced by data differential, it is applicable to long time measurement of fiber in complicated environment with great perturbation as long as the differential interval is small enough.

4. EXPERIMENT OF PRESSURE VECTOR MEASUREMENT

According to Ref. [5], the pressure vector can be computed by its induced birefringence vector, and the press azimuth is determined by $\alpha = \cos^{-1}(\hat{B} \cdot \hat{B}_0)/2$ in which $\hat{B}_0$ corresponds to the pressing azimuth at $0°$, while the press magnitude is linear to the birefringence. Thus based on this relationship we can perform the pressure vector measurement by employment of differential rotation method to the scheme described in Fig. 1. To get the initial value $\hat{B}_0$, squeezing the fiber vertically with press $P = 1$ N while measuring the corresponding birefringence we obtain $B_0 = 0.2839$ and

its unit vector $\hat{B}_0 = [-0.6218, 0.4995, -0.6045]^T$. Then we change the magnitude of pressure and measure the birefringence while recording the practical pressure values to analyze the error, we get the pressure and plot them in Fig. 5(a). By linear regression we get

$$P = 3.54\theta - 0.046, \quad R^2 = 0.9996 \tag{3}$$

and the average error between calculated and practical pressure is ~ 0.25 N.

Furthermore, we rotate the device in Fig. 1 to press the fiber at different orientation determined by geometrical method. Then we calculate birefringence vectors by Eq. (2) and the pressure azimuthes according to $\alpha = \cos^{-1}(\hat{B} \cdot \hat{B}_0)/2$. Some results are shown in Fig. 5(b). By statistical analysis we find the average deviation is $\sim 1.05°$.
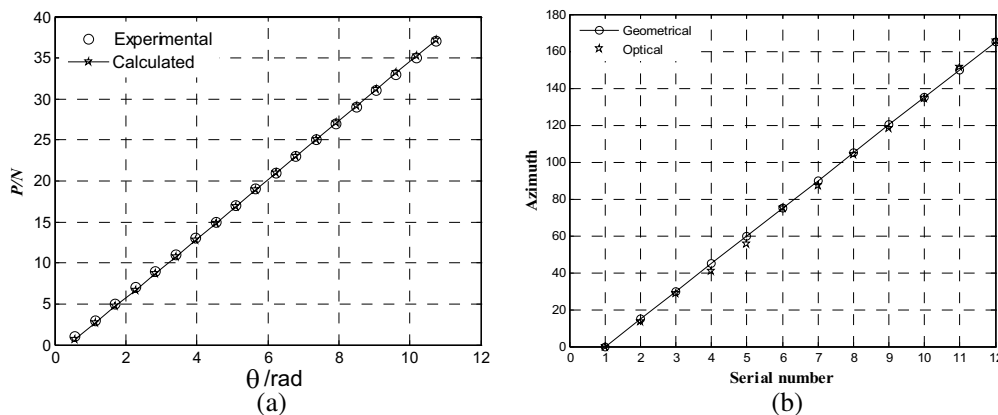
Figure 5: (a) Experimental and calculated results of pressure magnitude, (b) comparison for calculated and practical azimuthes of presses.

5. CONCLUSIONS

By polar decomposition of the Mueller matrix with a computer-controlled measure system, the birefringence vector is computed for the fiber with polarization dependent loss (PDL). To reduce the measurement error a differential rotation method is proposed which is applicable to large rotations with precise results. Further experiments in pressure vector sensing show the linearity of birefringence magnitude to pressure is excellent ($R^2 > 0.999$) with average error ~ 0.25 N, and the press orientation is determined by birefringence vector with average error $\sim 1.05°$. Our conclusions are applicable to fiber-based remote pressure sensing.

ACKNOWLEDGMENT

REFERENCES

1. Chowdhury, D. and D. Wilcox, "Comparison between optical fiber birefringence induced by stress anisotropy and geometric deformation," *IEEE J. Sel. Topics Quantum Electron.*, Vol. 6, 227–232, 2000.
2. Sakai, J. and T. Kimura, "Birefringence and polarization characteristics of single mode optical fibers under electric deformations," *IEEE J. Quantum Electron.*, Vol. 17, 1041–1051, 1981.
3. Park, Y., U. C. Paek, and D. Y. Kim, "Determination of stress-induced intrinsic birefringence in a single-mode fiber by measurement of the two-dimensional stress profile," *Opt. Lett.*, Vol. 27, 1291–1293, 2002.
4. Lu, S. Y. and R. A. Chipman, "Interpretation of Mueller matrices based on polar decomposition," *J. Opt. Soc. Am. A*, Vol. 13, 1106–1113, 1996.
5. Li, Z., C. Wu, H. Dong, P. Shum, C. Y. Tian, and S. Zhao, "Stress distribution and induced birefringence analysis for pressure vector sensing based on single mode fibers," *Optics Express*, Vol. 16, 3955–3960, 2008.
6. Theocaris, P. and E. Gdoutos, *Matrix Theory of Photoelasticity*, Springer-Verlag, 1979.

Spectrum Property of 6.5 W Multi-mode Output Laser Diode

Lanlan Liu, **Chongqing Wu**, **Guodong Lin**, and **Luyao Zhai**

Key Laboratory of Luminescence and Optical Information, Ministry of Education
Institute of Optical Information, School of Science, Beijing Jiaotong University
Beijing 100044, China

Abstract— LD is attracting widespread attention due to the advantages of small volume, simple structure, high efficiency, long life and high electricity-photo conversion efficiency. Especially, with the appearance of high-power Laser Diode, it has been an important research direction to use it as the laser's pumping source. However, due to the low coupling efficiency of LD laser and single-mode fiber, the application of LD is limited. With the appearance of the high-power multi-mode output laser diode and the consummation of double-clad fiber manufacture techniques, high-power fiber amplifier and fiber laser have been developed rapidly. We have developed an amplifier based on the hybrid Er-Yb double-clad fiber, which use the multi-mode output LD with nominal peak wavelength 975 nm and nominal power 6.5 W as the pumping source, and have obtained a gain over 30 dB. Because the pumping source LD's spectrum property has obvious influence on the fiber amplifier and laser, we have conducted the experimental study to the spectrum property of the 6.5 W multi-mode output LD. The LD's threshold current is 0.3 A. With the rise of the LD's temperature and the increase of the injection drive current, the peak wavelength of the LD's output laser drift to the longer wavelength direction. LD's emission spectrum in different injection currents was obtained in the experiment. When the drive current increased from 0.3 A to 5 A, the peak wavelength of the LD's output laser drifted from 964.2 nm to 972.5 nm.

1. INTRODUCTION

There are three kinds of light sources used in optical communication, laser diode (LD), light-emitting diode (LED) and non laser diode. Non laser diodes, such as, gas lasers, solid-state lasers and so on, are too huge to match fibers, and they are only used in some special occasions presently. LED is a kind of non-coherent light source, and is suitable for short distance and small or medium-capacity optical fiber communication systems. Laser Diode is a kind of semiconductor device whose working style is semiconductor diode stimulated luminescence. It sends out laser and plays an important role in the optical communication system. Since Laser Diode was developed, people have kept on improving its structure. Luminescence only happened in low temperature initially driven by impulse current. Continuous luminescence in room temperature was realized later. Afterward, the quantum well laser diode was published and the luminescence efficiency was improved greatly. With the amelioration of LD's structure, its performance has been improved evidently. The great progress of laser diode promoted the fiber communication and other application greatly. Because of the advantages of small volume, low power consuming, long life span, high electricity-photo conversion efficiency and apt modulation, LDs are used in many fields of optical communication, optical storage, optical gyro, laser print, laser forgery-proof, medical treatment and measure [1].

These years, the study of high power laser diode draws people's high attentions. Using high-power LDs as other lasers' pumping sources can save much holistic power dissipation of lasers, brief the structures, and reduce the volumes. With the development of double-clad pumping technology and the consummation of high-power multi-mode LD's manufacture techniques, double-clad fiber lasers draw people's attention more and more [2, 3]. Presently, high power LDs have been applied as the pumping sources of fiber lasers and fiber amplifiers widely [4, 5].

We used a 6.5 W multi-mode output LD as the pumping source, and developed a double-clad fiber amplifier with a gain over 30 dB. It was found in the experiment that the spectrum property of the pumping LD had a very clear impact to the fiber amplifier, and the amplification difference could reach above 10 times. Therefore, we made an experimental study to the spectrum property of the 6.5 W LD, and obtained the change regularity of LD's emission spectrum and wavelength, which provided an important foundation for the study and utilization of fiber amplifier and fiber laser.

2. THE RELATIONS OF THE 6.5 W MULTI-MODE OUTPUT LD AND THE DOUBLE-CLAD FIBER AMPLIFIER

We used a 6.5 W multi-mode output LD as the pumping source in the hybrid Er-Yb double-clad fiber amplifier. The LD's nominal peak wavelength is 975 nm. Laser was outputted from a 105/125 multi-mode fiber with power above 6.5 W. The LD's working temperature is 15–45°C, maximal working current is 8.5 A, and the threshold current is 300 mA. Figure 1 is the schematic diagram of the double-clad fiber amplifier using LD as the pumping source.
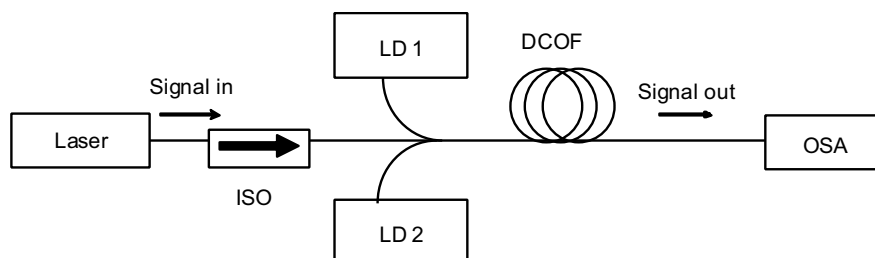
Figure 1: Schematic diagram of the double-clad fiber amplifier.

In the experiment of the fiber amplifier, all the signal wavelengths were 1550.136 nm. For comparison, in the case of the identical LD's injection currents, such as $I = 6$ A, the fiber amplifier's maximal gain was 32.15 dB, the minimal gain was 20.15 dB, and the difference was over 10 times, due to the different temperature. That shows the LD's characteristic has a very noticeable effect to the double-clad fiber amplifier.

3. EXPERIMENTAL RESULTS AND DISCUSSION

3.1. Spectrum Property

Because LD's output wavelength is easily affected by temperature and injection current, we analyzed the LD's spectrum property using spectrum analyzer by changing the drive current in the case of
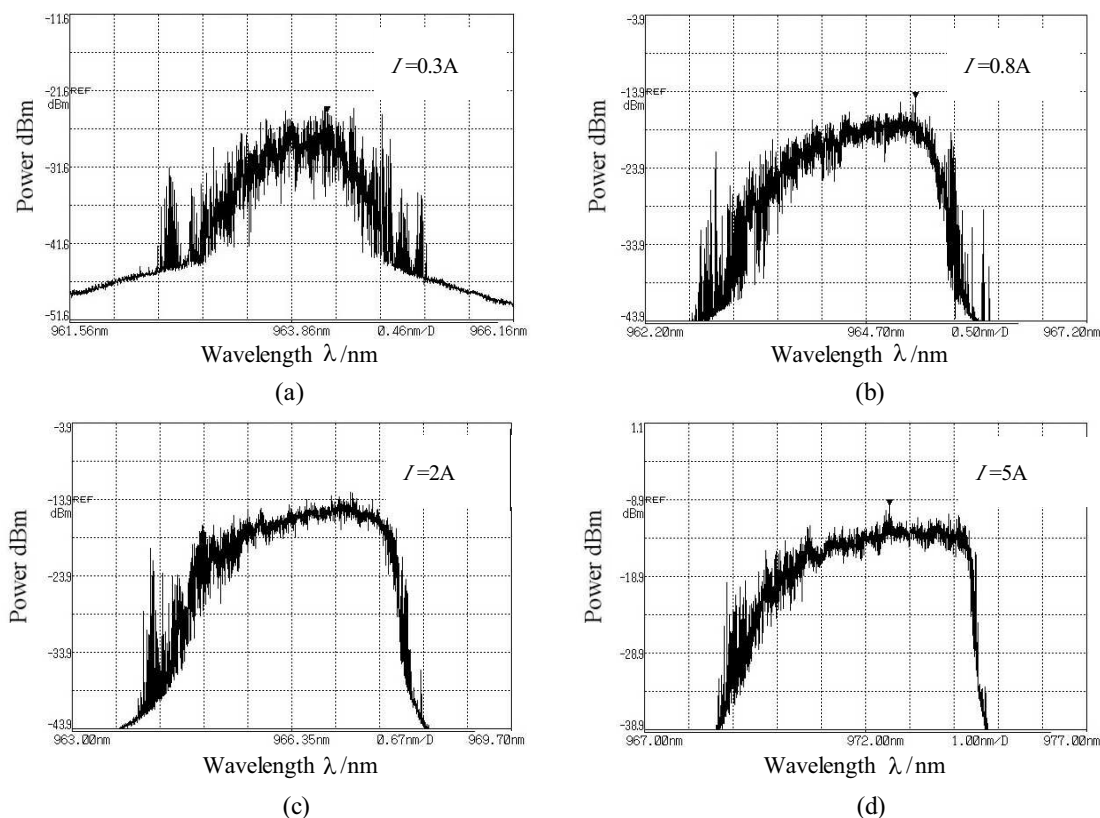
Figure 2: LD emission spectrum.

ensuring the laser's normal operating and stable temperature. Figure 2 is high-power LD's laser spectrum curve varying with the different injection currents.

It was found through experiments that LD's threshold current was 300 mA, LD emission peak wavelength drifted to the longer wavelength, and LD's central wavelength was not 975 nm, which was Yb-doped quartz-fiber's nominal absorption peak, but between 964 nm to 973 nm. When the drive currents were 0.3 A and 5 A, the laser peak wavelengths were 964.2 nm and 972.5 nm respectively.

3.2. *P-I* Emission Characteristic

P-I characteristic means the relations between LD's injection forward current and output optical power. LD is a kind of device which converts electric energy to optical energy directly, so electro-optical conversion efficiency is an important parameter of the device. LD's electro-optical conversion efficiency is defined by

$$\eta_e = \frac{\phi_e}{P_e} = \frac{\phi_e}{IV} \tag{1}$$

where η_e is LD's electro-optical conversion efficiency, ϕ_e is LD's radiation power, and P_e is LD's electric power, whose numerical value is the product of forward current and voltage. LD's output power curve vary with the drive current, namely *P-I* emission characteristic curve, can show the laser's capability visually.

In the experiment, LD's output optical power rose rapidly along with the increase of the drive current. We obtained the LD's output optical power curve vary with the drive current, shown as Figure 3.
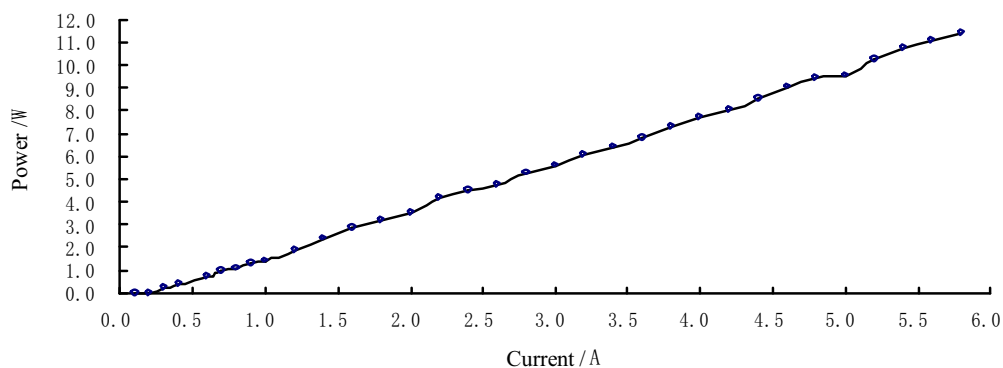
Figure 3: *P-I* characteristic curve.

From the LD's *P-I* emission characteristic curve, LD's threshold current is 300 mA, when the LD's optical power is 0.2 W, and the drive voltage is 1.4 V. The LD's emission characteristic curve of output optical power vary with the drive current is similar to be a straight line. Calculation shows the LD's electro-optical conversion efficiency can reach 68.4%. LD's emission characteristic curve helps us choose proper drive current to obtain an ideal output when we design and use the double-clad fiber amplifier and laser.

4. CONCLUSIONS

A 6.5 W multi-mode output LD's spectrum property was studied through experiments. Spectrum property of the LD's output laser in different drive currents was obtained. When the injection drive current increased from 0.3 A to 6 A, the LD's peak wavelength drifted to the longer wavelength from 964.2 nm to 972.5 nm. The LD's *P-I* emission characteristic curve was obtained metrically. From the emission characteristic curve, the laser's electro-optical conversion efficiency can be counted. The research results provided important basis for the design and utilization of the double-clad fiber amplifier and laser.

REFERENCES

1. Sun, X.-M., *Theory and Application of Interferometry Using Laser Diode*, 5–8, National Defence Industry Press, Beijing, China, 1998.
2. Jeong, Y., J. K. Sahu, and D. N. Paync, "Ytterbium-doped large-core fiber with 1 KW of continuous-wave output power," *Electron. Lett.*, Vol. 40, No. 8, 470–471, 2004.

3. Limpert, J., A. Liem, and S. Hofer, "150 W Nd/Yb codoped fiber laser at 1.1 µm," *CLEO*, 590–591, CThx1, Long Beach, USA, May 2002.

4. Zhang, Q., J. Yao, and W. Wen, "High power laser diode pumped Nd : YAG continuous wave dual-wavelength laser," *Chin. J . Lasers*, Vol. 33, No. 5, 577–581, 2006.

5. Stickley, C. M., E. Mark, and E. P. Filipkowski, "Overview of progress in super high efficiency diodes for pumping high energy lasers," *Proceedings of SPIE*, Vol. 6104, 610405-1–610405-10, San Jose, USA, February 2006.

Evolution of Beat Signal in a Nonlinear PCF Considering the Stability of the Light Source

L. M. Zhang, **Z. Wang**, **K. L. Yu**, and **C. Q. Wu**

Key Laboratory of Luminescence and Optical Information, Ministry of Education, China
Institute of Optical Information, School of Science, Beijing Jiaotong University, China

Abstract— The spectrum evolution of the beat signal can be used to measure the nonlinear coefficient of the fiber. By theoretical simulations, for the first time, we analyzed the effect of the stability of the output power, the frequency and the linewidth of the laser on the measurement of the nonlinear coefficient. The simulations show good agreement with the experiments in which all impacts are involved. The transmission process and the evolution spectra of the beat signal propagating along the PCF are analyzed by using the Split-Step Fourier Method with the consideration of self-phase modulation, fiber loss and dispersion. The results show that the stability of the laser output power has little effect on the measurement of the nonlinear coefficient, but the linewidth and the stability of the central wavelength have more effects on it.

1. INTRODUCTION

The photonic crystal fibers (PCFs) [1] with special dispersion and nonlinear properties have been used in optical communications and optical signal processing [2–4]. If two beams of continuous light wave with a particular frequency difference are injected into a fiber, a beat signal will be generated. When the beat signal propagates along the fiber, its spectrum will broaden due to the group velocity dispersion (GVD) and self-phase modulation (SPM). By measuring the intensities of the zero- and first-order harmonics, the nonlinear phase shift, hence then the nonlinear coefficient can be calculated [5].

However, because there is a certain randomicity in the laser, it is hard to acquire a perfect beat signal. At present, there is not any report about the effect of the stability of the laser on the measurement of the nonlinear coefficient. In this paper, with the consideration of SPM, fiber loss and group velocity dispersion (GVD), the transmission properties of the beat signal propagating along a kind of nonlinear PCF are investigated, and the effects of the stability of the output power, the frequency and linewidth of the laser on the measurement of the nonlinear coefficient are discussed in detail.

2. SPM PROCESS OF THE BEAT SIGNAL

The photonic crystal fiber we studied is a kind of big air hole TIR-PCF made by Yangtze Optical Fibre and Cable Company Ltd. Its SEM image is shown in Fig. 1, and the propagation properties are simulated by the compact supercell method [6]. The calculated nonlinear coefficient γ is about 18.8/w·km, and the GVD is 80 ps/nm·km at 1550 nm. The measured fiber loss α is 45 dB/km. A beat signal will be affected by the GVD, SPM and the loss while propagating in such a PCF.

Both electric fields of the beat signal can be written as:

$$E_1(t) = \sqrt{\frac{P_0}{2}} \cos(\omega_1 t), \quad E_2(t) = \sqrt{\frac{P_0}{2}} \cos(\omega_2 t), \tag{1}$$

where $P_0/2$ is the optical power of each beam, ω_1 and ω_2 ($\omega_1 > \omega_2$) are the angular frequencies, respectively. Then the electric field of the beat signal is given by:

$$E_0(t) = E_1(t) + E_2(t) = \sqrt{2P_0} \cos(\Delta\omega t/2) \cos(\omega_{avg} t), \tag{2}$$

where $\omega_{avg} = (\omega_1 + \omega_2)/2$ is the average frequency, and $\Delta\omega = (\omega_1 - \omega_2)$ is the beat frequency. The evolution of this beat signal satisfies the nonlinear Schrodinger equation [7]:

$$i\frac{\partial A}{\partial z} = -\frac{i}{2}\alpha A + \frac{1}{2}\beta_2 \frac{\partial^2 A}{\partial T^2} - \gamma |A|^2 A, \tag{3}$$

where $A(0,T) = \sqrt{2P_0} \cos(\Delta\omega T/2)$ is the slowly varying amplitude, α is loss coefficient, $\beta_2 = d^2\beta/d\omega^2$ is the second-order dispersion coefficient, and only the fiber losses, GVD and SPM are

included in Eq. (3). The Split-Step Fourier Method [7] is employed to solve the equation and then to get the evolution of the beat signal in the PCF.

Figure 2 shows the simulated output spectrum of the beat signal after it propagates along a 200-meter long PCF. The two wavelengths of beat signal are 1552.42 nm and 1552.54 nm, respectively, and the power P_0 is 0.5 w. When the beat signal propagates along the fiber, besides both original components at frequencies ω_1 and ω_2, more and more new components at frequencies $\omega_1 + m\Delta\omega$ and $\omega_2 - m\Delta\omega$ are generated. Because of the continuous SPM effect, new frequencies are generated gradually with the increase of the fiber length, which results in the spectrum broadening and the signal power decreasing.

From Fig. 2, measuring I_0 and I_1, which are the intensities of the components at frequencies ω_1 and $\omega_1 + \Delta\omega$ or ω_2 and $\omega_2 - \Delta\omega$, we can calculate the nonlinear phase-shift φ_{SPM} caused by SPM according Eq. (4), where J_n is the nth-order Bessel function.

$$\frac{I_0}{I_1} = \frac{J_0^2\left(\varphi_{\mathrm{SPM}}/2\right) + J_1^2\left(\varphi_{\mathrm{SPM}}/2\right)}{J_1^2\left(\varphi_{\mathrm{SPM}}/2\right) + J_2^2\left(\varphi_{\mathrm{SPM}}/2\right)}, \tag{4}$$

The nonlinear coefficient γ can be obtained from the formula $\varphi_{\mathrm{SPM}} = 2\gamma L_{eff} P_0$, in which P_0 is the average power of the beat signal, L_{eff} is the effective length of the fiber. From Fig. 2, the calculated nonlinear coefficient is about 19.60/w·km, which has a certain difference from the value 18.8/w·km used in the simulations. The reason is that SPM, fiber loss and dispersion are all included in Eq. (3) while the dispersion is excluded in Eq. (4). So, when measuring the nonlinear coefficient with the Eq. (4), the smaller the dispersion is, the more accurate the result is.

Figure 3 shows the experimental spectrum of the beat signal propagating along the 200-meter long PCF. In our experiment, the central wavelength difference between both signals is 0.12 nm. It is obvious that the zero- and first-order harmonics can be measured easily, and the nonlinear coefficient is about 16.98/w·km after some calculations.
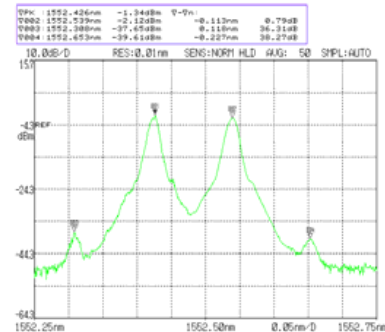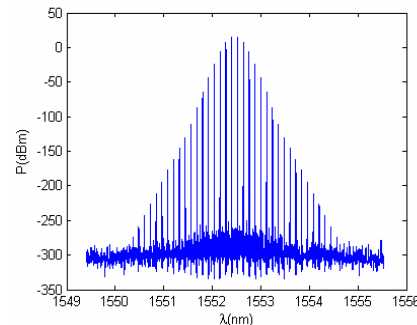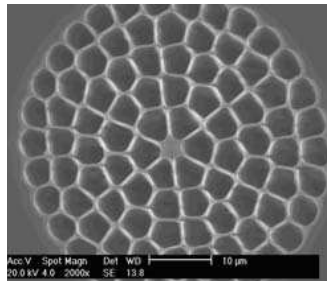
Figure 1: SEM image of the PCF.

Figure 2: Spectrum of the beat signal after propagating along the 200 meters PCF.

Figure 3: Experimental spectrum of the beat signal.

3. THE EFFECT OF THE LASER STABILITY ON THE SPECTRUM EVOLUTION

Comparing Fig. 2 with Fig. 3, it is found that the number of the new generated components in experiment is much less than in the simulation, and the experimental figure has some differences from the theoretical one. The effects of the output power, the frequency and line width of the lasers on the evolution of the beat signal in the PCF are investigated in this section.

3.1. The Stability of the Laser Power

In order to study the effect of stability of the output power on the propagating of the beat signal in the nonlinear PCF, a random disturbance is added on the power while simulating. The disturbance is normally distributed, the average of which is 0, and the standard deviation is S_p. S_p/P is defined as the stability of the power. Fig. 4 shows the simulation results of the spectra when S_p/P is supposed to be 1% and 10% respectively. It is found that the magnitude of the random disturbance has some effect on the order number of the new components. But, for the two disturbances, the intensities of the zero-order and first-order harmonics have little changes, which means I_0/I_1 has little changes. The nonlinear coefficients, calculated from Fig. 4, are 19.49 and 19.57/w·km for

both cases. So there is only a very weak effect of the stability of the output power on the nonlinear coefficient measurements.

3.2. The Stability of the Central Wavelength

The instabilities of the wavelengths of the lasers will induce the instability of beat frequency, and generate random phase differences. In simulation, a random disturbance is added on the beat frequency, which is normally distributed, and the variance is S_ω. $S_\omega/\Delta\omega$ is defined as the stability of the frequency. Fig. 5 shows the simulation results of the spectra when $S_\omega/\Delta\omega$ is supposed to be 1% and 10% respectively. Even though the stability is 10%, the first-order frequency is clear enough to be used to measure the nonlinear coefficient. However, for the two disturbances, the intensities of the zero-order and first-order harmonics both have some changes, which means I_0/I_1 has changes. The nonlinear coefficients, calculated from Fig. 5, are 19.61 and 15.47/w·km for both cases. It can be seen that the more stable the laser wavelength is, the smaller the effect on the measurement is.
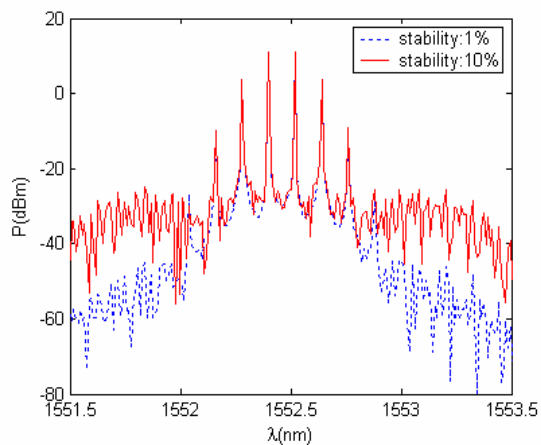
Figure 4: Output spectrum of the beat signal when the stability of the power is 1% and 10%.
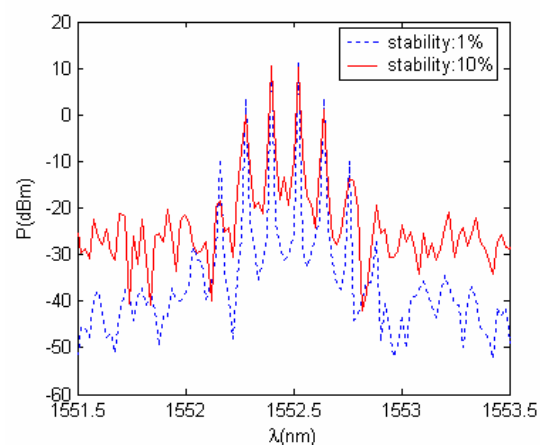
Figure 5: Output spectrum of the beat signal when the stability of the frequency is 1% and 10%.

3.3. Linewidth of the Laser

The linewidth of the laser has some effects on the SPM spectrum evolution. The output spectrum of the laser is approximated to be a Gaussian shape, and the linewidths of both lasers are $\Delta\lambda$. Fig. 6 shows the simulated results of the spectra when $\Delta\lambda$ is supposed to be 0.015 nm and 0.03 nm respectively. It can be found that there are also a certain linewidth in the new components, which is determined by the linewidth of the laser. And I_0/I_1 also has some changes. The greater the linewidth is, the greater the change is. The calculated nonlinear coefficients are 18.06/w·km and 14.14/w·km for both cases. It can be seen that the linewidth has obvious effect on the result because it changes the spectrum character of the beat signal.

3.4. The Output Spectrum Considering the Three Aspects

As a laser used in experiments, those three factors discussed above will do effects at the same time, and the simulated spectrum is shown in Fig. 7. In the simulations, the power stability is 3%, the wavelength stability is 3%, and the linewidth is 0.02 nm. The nonlinear coefficient is calculated to be 15.25/w·km from Fig. 7.

In order to obtain a clear spectrum of the beat signal and to accurately measure the data for calculating the nonlinear coefficient, one should use the small linewidth laser with high stability of power and wavelength. In fact, the experimental result of Fig. 3 is obtained on the condition that the laser output power is about 20 mw, the power stability is about 3%, the wavelength stability is about 3%, and the laser linewidth is about 0.02 nm.

3.5. Some Discussions

In this paper, there are several values of the nonlinear coefficient, which are different from each other. The main reasons are as follows: first, there are some approximations to the real fiber when the compact supercell method is employed to calculate the nonlinear coefficient. Second, the fiber is dispersive in the experiment, while the dispersion is neglected in Eq. (4). These factors result in
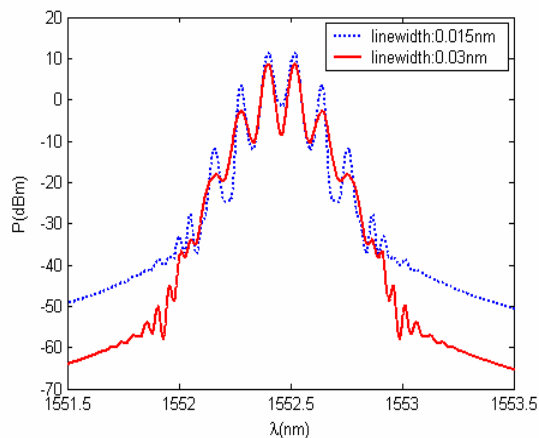
Figure 6: Output spectrum when the laser's linewidth is 0.015 nm and 0.03 nm.
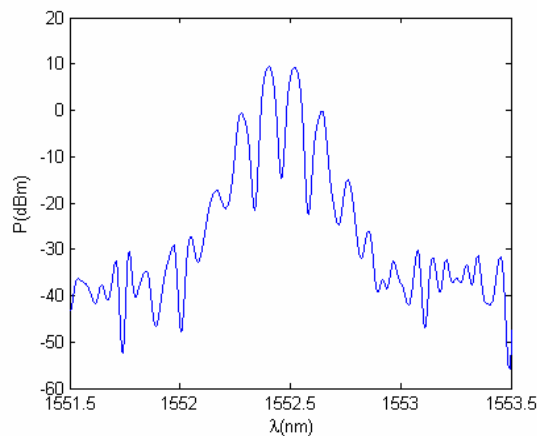
Figure 7: Output spectrum considering laser's linewidth and disturbance of power and frequency.

some differences between the theory and the experiments. With the consideration of the stability of the laser, the value of the nonlinear coefficient varies a little, but even if the disturbance is much greater, the beat signal can still be used to measure the nonlinear coefficient of the fiber.

4. CONCLUSIONS

The transmission properties of the beat signal propagating along a PCF are investigated. The spectrum properties of the beat signal after propagating along the fiber are obtained by theory analysis and simulation calculations. The effects of the stability and linewidth of the laser on measuring the nonlinear coefficient of the fiber are analyzed. It is found that the stability of the laser output power has little effect on the measurement, but the linewidth and the stability of the central wavelength have more effects. As to measure the nonlinear coefficient, two high stable lasers with rather narrow linewidth should be employed.

REFERENCES

1. Russell, P., "Photonic crystal fibers," *Science*, Vol. 299, 358–362, 2003.
2. Belardi, W., J. H. Lee, K. Furusawa, Z. Yusoff, P. Petropoulos, M. Ibsen, T. M. Monro, and D. J. Richardson, "A 10 Gbit/s tuneable wavelength converter based on four-wave mixing in highly nonlinear holey fiber," *European Conference on Optical Communication*, Copenhagen, Denmark, September 2002, PD1.2.
3. Sharping, J. E., M. Fiorentino, P. Kumar, and R. S. Windeler, "All-optical switching based on cross-phase modulation in microstructure fiber," *IEEE Photon. Technol. Lett.*, Vol. 14, 77–79, 2002.
4. Matsumoto, M., Y. Shimada, and H. Sakaguchi, "Wavelength-shift-free SPM-based 2R re-generation by bidirectional use of a highly nonlinear fiber," *Optical Fiber Communication*, Anaheim, California, March 2007, OME5.
5. Boskovic, A., S. V. Chernikov, and J. R. Taylor, "Direct continuous-wave measurement of n2 in various types of telecommunication fiber at 1.55 µm," *Opt. Lett.*, Vol. 21, 1966–1968, 1996.
6. Wang, Z., G. B. Ren, S. Q. Lou, W. J. Liang, and S. P. Guo, "Compact supercell method based on opposite parity for bragg fibers," *Opt. Express*, Vol. 11, 3542–3549, 2003.
7. Agrawal, G. P., *Nonlinear Fiber Optics*, Academic Press, San Diego, 2001.

Investigation on Traffic Grooming of OPS Edge Node Base on FDLs

Kai-Qiang Gao, **Chong-Qing Wu**, **Xin-Zhi Sheng**, and **Kai Chen**
Key Laboratory of Luminescence and Optical Information, EMC
School of Science, Beijing Jiaotong University, China

Abstract— Based on the structure of FDLs, a novel model has been built for edge node of optical packet switching network. The method of active queue management has been put forward to investigate the performance of the edge node. The efficiency of packet switching node has been evaluated by parameters of Load, FDL and Packet Length under self-similar data traffic load. Because the model can describe the node switching performance in detail, a lot of new results will be revealed.

1. INTRODUCTION

FDL (Fiber Delay Lines) is an applied method to solve the problem of port competition in OPS (Optical Packet Switch) network node. However, each switching structure with a different scheme and can be applied to various networks, which will lead to the great difference of analysis models and scheduling algorithms. There are two main aspects of the research based on the switching structure of FDLs at present. One is the research of scheduling algorithms on special switch structure and application field. In the documents [1, 2] the author presented three kinds of scheduling algorithms based on sharing the multiple input and output port of FDLs which is applicable to synchronous network, fixed packet length format, and sharing FDLs switch structure. The other is the theoretical analysis of statistics which based on features of FDLs. Theoretical analysis model based on the mean value, probability and the number of port was proposed in documents [3–5], which described the performance of FDLs synoptically.

However, considering the actual application of scheduling algorithms of FDLs there are still two major problems. Firstly, system structure may restrict the length of optical signal transmission. Documents [1, 6, 7] mentioned a operate method which made one packet repeated access into FDLs in one switching process. Thus it must add the optical amplifier and noise suppression device in loop line to achieve finite cycle propagation of optical signal. And in the process of cycle, whether the packet need to enter in FDLs again is decided by the identification of packet head and the operation of scheduling algorithm, which must induce the attenuation of optical power. Besides, this kind of operation not only consumes the resources of hardware and all-optical device, but also increases the average delay of packets. Secondly, it's hard to establish mathematical models with precise description of actual FDLs' scheduling process. For example, when a packet passes through a certain port, the description of occupation on this port, input port, and output port, etc. is not precise. It is lead to the neglect of packet loss calculation.

Consequently, we establish a model based on the research of edge node in OPS (Optical Packet Switching) network, which describes the work property of FDLs more concretely. Considering packet asynchronous arrival, variable packet length and self similar datum traffic with strong burst propertythe model is build up with first fit scheduling algorithm to achieve the traffic grooming process of edge node. The rest of paper is organized as follow. Part two introduces the structure and function of edge node based on FDLs. Part three describes the simulation model. In part four, the performance of edge node under different condition are analyzed. And part five draws the conclusion.

2. THE STRUCTURE AND FUNCTION OF DEGE NODE FOR TRAFFIC GROOMING

Because the identifying technique of optical packet header is immature, the header extraction needs photo-electric conversion both in OPS and OBS (Optical Burst Switching) network. And the header information is provided to the core processing unit, but the switching and buffering packet is still completed in optical field.

When datum resource is connected into edge aggregation node from port 0 to port N, the arrival packet is split into two series of optical signal which optical power ratio is $2:8$. The optical signal with 20% optical power accesses into a receiver for header processing. According to header information and the scheduling algorithms, the core processing unit controls the switching matrix and assigns packet to a certain FDL channel with a given delay to avoid output port competition.

The packets are queued up when passing through aggregation node, and therefore all of the FDLs' output ports can be connected to a coupling device which assembled the packets' data from multiple FDLs channels into one output link fiber to finish the process of traffic grooming. It's necessary to add fiber delay line between beam splitters and switching matrix for time delay, because the module of header recognition needs time to process. When the packet with 80% optical power accesses into switching matrix, information of the same packet has been extracted, and the scheduling process will be carried on without any mistake.
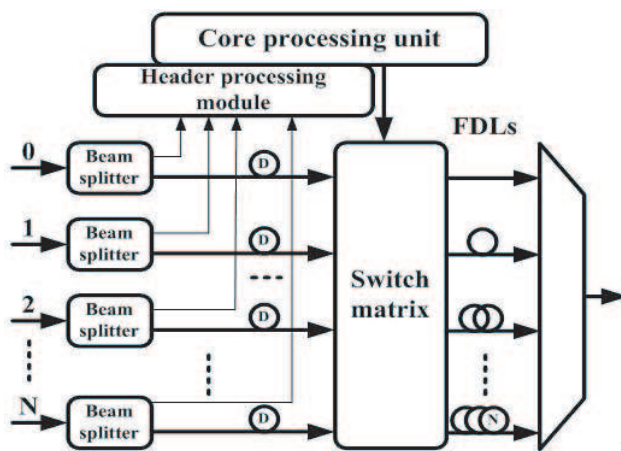
Figure 1: The structure of edge node for traffic grooming based on FDLs.

3. DESCRIBE SUMULATION MODEL OF EDGE AGGREGATION NODE BASED ON FDLS

A model of edge aggregation node based on simple FDLs structure with a special management mechanism has been put forward to this paper. The mechanism of output port reservation will regulate the port occupation. Meanwhile, the state of main buffer array and input/output port will be updated in real-time. To consider that the occupation time of packet access into and get out the FDLs make the input/output port busy, the model of FDLs node which can show the real performance of FDLs under different traffic load is build up, and it has great physical meaning.

The scheduling algorithm proposed in this paper is based on mechanism of output port reservation. Because of the difficulty of scheduling conflict packets, some of them are dropped before access into FDLs. This kind of operation saved the FDLs buffer recourses. The structure of scheduling algorithm model has been shown in Fig. 2.
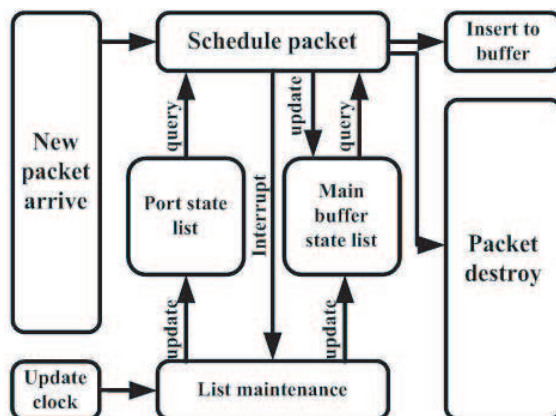
Figure 2: The relationship of functional module in scheduling algorithm model.

The scheduling process includes three operation stages. When new packet arrives in, the first stage operation begins. The packet scheduling module traverses the state list of main buffer array to find available time slot which can insert the arrival packet. Taking account of time slot packet

insert time and state of channel port, the scheduling process picks up a certain channel from which the packet will be send out or destroyed. At the same time the state of channel is changed to busy and the buffer array is queued up and updated. The maintenance of buffer array is the second stage. The packet position recorded in main buffer array is updated at intervals. New packet is inserted into and old packet is moved out. The third stage is to update the channel work state. The duration of packet passing through port is set as the time when channel state keeps busy. Packet scheduling module changes the port state to busy. According to channel port state, the interrupt delay is set. At last the list maintenance module alternates the port state to idle.

As shown in Fig. 3, packets access into FDLs and queue up in main buffer array based on the mechanism of port reservation. There is a packet sequence diagram which is arranged without interference in the whole buffer depth. When buffer array has saved four packets, the arrival of the fifth packet provokes the process of traversing main buffer array. First find out all of time slot in packet sequence diagram. Second compared with packet length, the longer time slot will be recorded as available slot. Obviously Slot 0 is shorter than the length of fifth packet, and it is not a usable slot. Third calculate the real available slot with reference to available slot and the packet insert time. Slot 1 is kept away from real available slot. At last insert the packet in Slot 2 which is one of real slots.
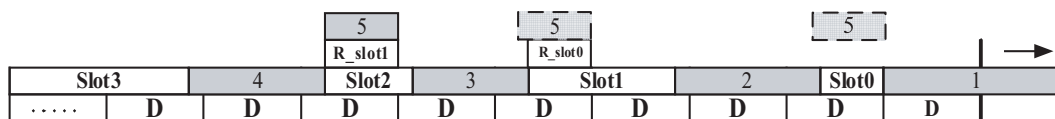

Figure 3: Main buffer array schematic diagram.

4. ANALYSES ON CHARACTERISTIC OF AGGREGATION NODE

There are a few important factors on the network efficiency and the key parameters involved include: throughput capacity, packet lost rate, average delay time, buffer array size [8]. As the main function of FDLs is traffic grooming in the model, the lost rate and average delay time play more important role than other parameters. And from computer simulation we can get some statistics results.

The variable fdl_unit stands for the granularity of FDL, and pk_len_average represents the packet average length. Let D be the ratio of fdl_unit/pk_len_average. The relationship between packet lost rate and D has been shown in Fig. 4, and the different traffic load results different curve.
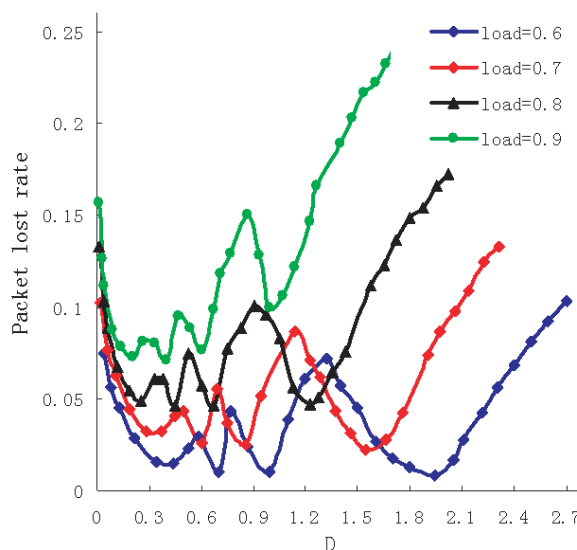
Figure 4: Relationship between packets lost rate and D.

With the increase of traffic load the packet lost rate grows up. But the result is different from previous research such as document [4]. With the growth of D the packet lost rate experiences a series of swinging up and down but not a single stationary wave hollow. The amount of available

slot and available port influent the relationship between D and packet lost rate. The increase of D prolongs the packet's delay time and provides more available slot, but the average packet length is fixed which induced the periodic vibration of the curve. According to the several valley floors in the chart, D can be configured to different value which can decrease the packet lost rate.

Figure 5 showed that packet lost rate, average packet delay and the amount of FDLs have some relativities. With the increase of B packet lost rate and packet average delay have the different trend. Both of them should be take into account when FDL was configured.
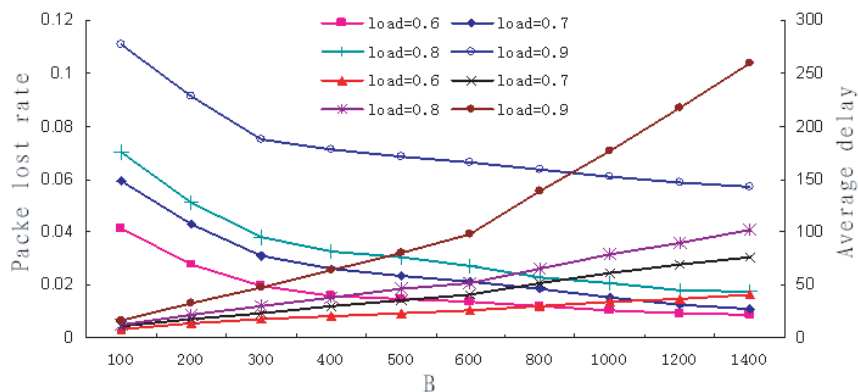
Figure 5: Relativities among FDLs amount, packet lost rate and average delay.

As shown in Fig. 6, the statistical chart of port utilization coefficient with delay time unitary is drawn under First-Fit Scheduling Algorithm. The document [1] mentioned a FDLs' configuration in which the FDLs length with exponential distribution. Indeed taking out some FLD with low port utilization coefficient can reduce the complexity of switching node.
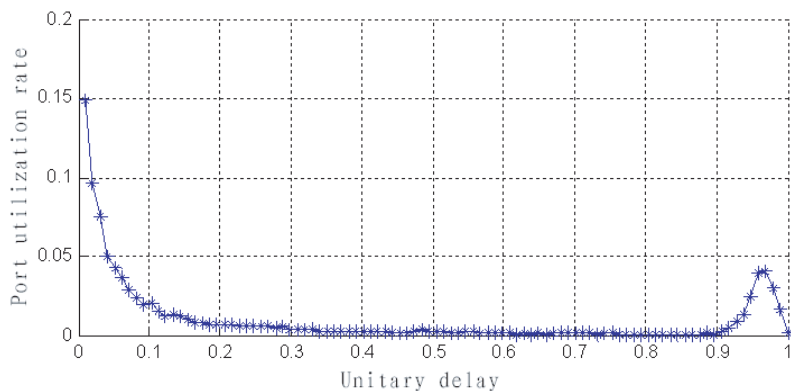
Figure 6: The statistical chart of port utilization coefficient with delay unitary.

5. CONCLUSION

A new model of aggregation edge node based on FDLs is presented in this paper. The active scheduling method managed the switching process. Modelling and Simulating give us key parameters with reference values which are important to design an optical network edge node. From the analysing result physical node can be established for special network demand.

ACKNOWLEDGMENT

REFERENCES

1. Liew, S. Y. and G. Hu, "Scheduling algorithms for shared fiber-delay-line optical packet switches — Part I the single-stage case [J]," *Journal of Lightwave Technology*, Vol. 23, No. 4, 1586–1600, 2005.

2. Jiang, S. and G. Hu, "Scheduling algorithms for shared fiber-delay-line optical packet switches — Part II the three-stage clos-network case [J]," *Journal of Lightwave Technology*, Vol. 23, No. 4, 1601–1609, 2005.

3. Zhang, T. and K. Lu, "An analytical model for shared fiber-delay line buffers in asynchronous optical packet and burst switches [A]," *ICC 2005 [C]*, Vol. 3, 1636–1640, Korea, Seoul, 2005.

4. Callegati, F., "On the design of optical buffers for variable length packet traffic [A]," *ICCCN 2000 [C]*, 448–452, 2000.

5. Fayoumi, A. G. and A. P. Jayasumana, "Performance model of an optical switch using fiber delay lines for resolving contentions [A]," *Local Computer Networks 2003 [C]*, 178–186, Bonn, Germany, 2003.

6. Li, L. and S. D. Scott, "A novel fiber delay line buffering architecture for optical packet switching [A]," *GLOBECOM '03, IEEE [C]*, Vol. 5, 2809–2813, California, USA, 2003.

7. Chlamtac, I. and A. Fumagalli, "Multi-buffer delay line architectures for efficient contention resolution in optical switching nodes [J]," *IEEE Transactions on Communications*, Vol. 48, No. 12, 2089–2098, 2000.

8. Huang, A., T. Yang, O. Kabranov, and D. Makrakis, "QoS performance in IP over PetaWeb optical network," *IEEE 2002 International Conference on Communications, Circuits and Systems and West Sino Expositions*, Vol. 1, 664–668, June 29–July 1, 2002.

Three-dimensional Surfaces of Inorganic Materials Fabricated by Femtosecond Laser Lithography

H. Nishiyama[1], M. Mizoshiri[1], J. Nishii[2], and Y. Hirata[1]

[1]Division of Materials and Manufacturing Science, Graduate School of Engineering
Osaka University, Japan
[2]National Institute of Advanced Industrial Science and Technology, Japan

Abstract— Three-dimensional (3D) surfaces of inorganic optical materials were created by a combined process of nonlinear lithography and plasma etching. 3D patterns were directly written inside a KMPR-1050, which is chemically amplified negative-tone resists, on convex lenses by femtosecond laser-induced nonlinear optical absorption. Then, the patterns were transferred to the underlying substrates by CHF_3 plasma. The fabrication of silica-based diffractive-refractive hybrid microlenses was demonstrated. We obtained micro-Fresnel lenses with smooth surfaces even on curved substrates. When 632.8-nm-wavelength laser light was coupled to the hybrid lens, the primary focal length was 614 μm. This result well agreed with theoretical value 617 μm. Our combined process was useful for the precise fabrication of 3D surfaces based on inorganic materials.

1. INTRODUCTION

Micro-optical elements are recognized as key components for various photonic systems such as optical interconnections, optical pickups, photonic integrated sensors, and so on [1–3]. In these applications, three-dimensional (3D) surface profiles of the elements strongly affect their optical performances. For example, maximum diffraction efficiency of a blazed grating is more than two times higher than that of a binary counterpart.

The semiconductor technology including photo/electron-beam lithography and various etching processes is often used for the fabrication of micro-optical elements. This technology is a powerful tool for micro/nanofabrication. However, it is rather difficult to create 3D surfaces because of planar features of the technology. For example, the cross-sectional profiles of structures are limited to be rectangular shapes, and we can fabricate structures only on planar substrates. If we form slope or curved relief structures on wafers, complicated multiple exposure process or gray-scale mask method are required [4, 5]. In order to obtain structures onto non-flat substrates such as convex lenses and steps, highly accurate control of exposure dose and position alignments are needed even with specially-modified systems because of the difficulty in achieving uniform resist coating [6]. These techniques are based on single-photon process. Therefore, complicated setups and systems are indispensable.

On the other hand, femtosecond laser polymerization has attracted much attention. When femtosecond laser pulses are tightly focused into transparent photopolymers, nonlinear optical processes such as two-photon absorption occur only near the focal spot. This phenomenon enables the fabrication of actual 3D polymeric structures only by scanning the laser-spot inside the polymer. To date, various microstructures such as bulls and springs have been reported using photopolymerizable resins, photoresists and so on [7–9]. Recently, we developed the technique that form 3D surfaces of inorganic optical materials by a combined process of the femtosecond laser induced nonlinear lithography and plasma etching [10, 11]. This technique can fabricate structures even on non-flat substrates. Thereby, complex 3D surface profiles can be obtained. In this paper, the fabrication of silica-based diffractive-refractive hybrid lenses is demonstrated by our combined process.

2. EXPERIMENTAL

A femtosecond fiber laser system was used for lithography process. This system delivers laser pulses of 780 nm wavelength with a pulse duration of 68 fs and repetition rate of 50 MHz. The laser beam was focused by an objective lens with numerical aperture of 0.5. Laser power was controlled using a neutral density filter. Laser writing was carried out by translating a 3D stage with samples. An epoxy based chemically amplified negative-tone photoresist KMPR-1050 was used. Silica glass plates of 1 mm thickness and microlens arrays were used. The diameter, height, curvature radius, and focal length of each lens were 240, 18.9, 380, and 830 μm, respectively. Etching was performed by electron cyclotron resonance (ECR) plasma with CHF_3 gas.

3. FEMTOSECOND LASER LITHOGRAPHY FOR 3D SURFACES

Figure 1 schematically shows femtosecond laser lithography assisted micromachining (FLAM) for fabrication of 3D surfaces from inorganic materials. First, the resist is spin-coated on non-flat substrates. Then, 3D patterns are written directly inside the resist by using femtosecond laser-induced nonlinear optical absorption. The resist patterns are transferred to the underlying substrates by ECR ion beam etching after baking and development treatments. In FLAM, the pattern width is kept to be constant even when the laser pulses are focused into any region inside resists, unlike conventional single-photon lithography, because absorption occurs only near the focal volume. By using this highly advantageous feature, we can form well-defined patterns even in resists deformed by surface tension on non-flat substrates. Although 3D microfabrication was reported by single-photon absorption, much higher spatial resolution below 100 nm is achievable by using femtosecond laser pulses. we can obtain various 3D surfaces of inorganic materials by FLAM [12].
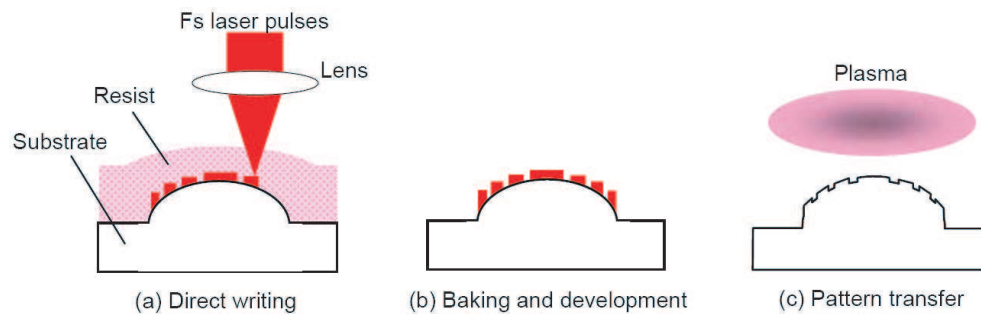
Figure 1: Schematic illustration of femtosecond laser lithography assisted micromachining.

Formation of polymeric fiber-like patterns by ultraviolet laser exposure was previously reported, and the authors explained this phenomenon in terms of self-trapping based on photopolymerization [13]. This phenomenon enables us to expose a high-aspect-ratio region of materials. Figure 2 shows an SEM image of filamentary rods of the resist formed by femtosecond laser exposure. These rods were written by exposure from above along the optical axis in 50-μm-thick resist. The dotted line in Figure 2 indicates the surface of the resist film before development, meaning that the rods were directly formed inside the resist. Maximum height of the rods was 47 μm, which was more than three times longer than the focal depth of laser setup. Such rod formation is due to channel propagation of femtosecond laser pulses based on local photothermal polymerization [10].
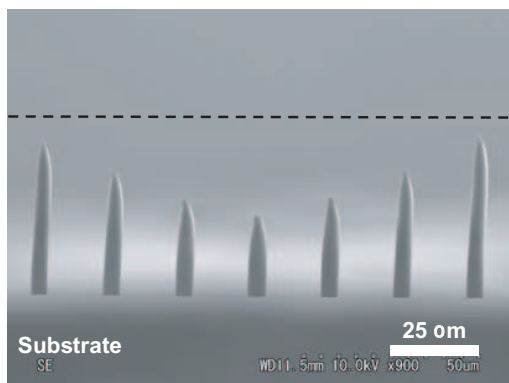
Figure 2: SEM image of filamentary rods of the resist.
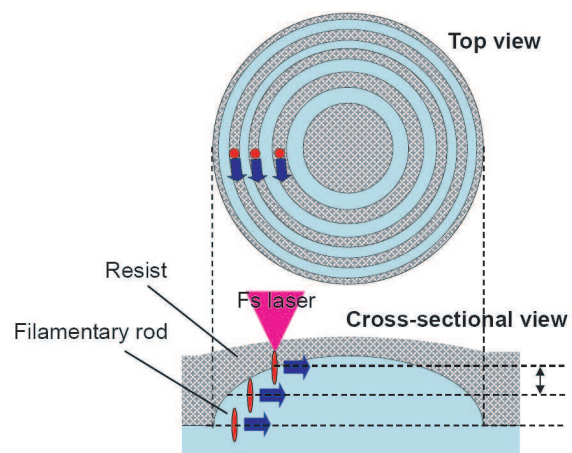
Figure 3: Laser writing procedure for hybrid microlens structures.

By using this lithographic process, micro-Fresnel lens patterns were written inside the resists of 20 μm thickness on convex lenses to form silica-based diffractive-refractive hybrid lenses. Figure 3 shows the writing procedure for obtaining such hybrid structures. We scanned the laser-induced rod three-dimensionally inside the resist. The laser writing speed and average power were 300 μm/s and 33 mW, respectively. The rods have sharp ends, as shown in Figure 2. For example, the diameters

of the top and central parts of the rods were measured to be 0.5 and 2.0 μm, respectively, in the case of the writing speed of 100 μm/s and average power of 27.4 mW. Therefore, the distance between adjacent circles was fixed to be 300 nm, which was less than the diameter of the top part of the end. The focal length of the hyrbrid lens is expressed by Eq. (1):

$$\frac{1}{f_h} = \frac{1}{f_m} + \frac{1}{f_F} \tag{1}$$

where f_h, f_F, and f_m are the primary focal lengths of a hybrid lens, a Fresnel lens, and a convex lens, respectively. From Eq. (1), the focal length of the hybrid lens should be 617 μm when a Fresnel lens with a focal length of 2400 μm onto the convex lens. The radius r_m of the m-th zone of the Fresnel lens can be expressed by $r_m \approx \sqrt{m f_F \lambda_0}$ for incident laser wavelength λ_0 632.8 nm. Figure 4 shows SEM images of (a) a resist lens pattern on a convex lens before pattern transfer (b) a silica-based diffractive-refractive hybrid microlens. The gas pressure in the process chamber, ECR power, and bias voltage were 2.0×10^{-2} Pa, 100 W, and 700 V, respectively. We can see that well-defined structures with smooth surfaces were obtained even on curved substrates. The primary focal length was measured to be 614 μm when the hybrid lenses were illuminated from the back by a He-Ne laser light with a wavelength of 632.8 nm. This result means that primary focal spot was shifted to the lens side by 216 μm due to the hybridization of refractive and diffractive lenses. This shift amount well agrees with theoretical value 213 μm.
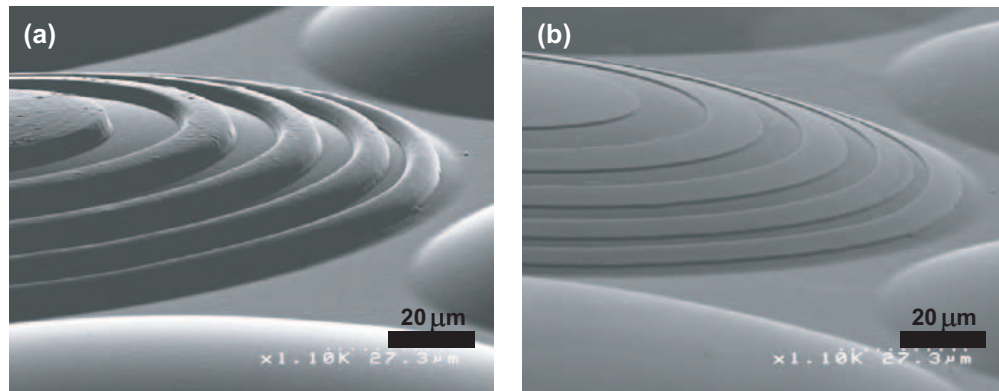
Figure 4: SEM images of a resist lens pattern on a convex lens before pattern transfer (b) a silica-based diffractive-refractive hybrid microlens.

4. CONCLUSIONS

We reported the technique that creates 3D surfaces of inorganic materials by a combined process of femtosecond laser lithography and plasma etching. Micro-Fresnel lens patterns were written directly inside the resist on convex lenses. Here, the filamentary rod patterns of the resist were found to be induced without translating the laser spot. We obtained silica-based diffractive-refractive hybrid microlenses with smooth surfaces after the pattern transfer by use of CHF_3 plasma. When He-Ne laser light was normally coupled to the hybrid lens, the primary focal length was measured to be 614 μm, which well agreed with theoretical value. Our combined process will be useful for the formation of more functional optical components.

REFERENCES

1. McFadden, M. J., M. Iqbal, T. Dillon, R. Nair, T. Gu, D. W. Prather, and M. W. Haney, "Multiscale free-space optical interconnects for intrachip global communications: motivation, analysis, and experimental validation," *Appl. Opt.*, Vol. 45, 6358–6366, 2006.

2. Chang, S. and J.-B. Yoon, "A 3-D planar microlens for an effective monolithic optical inter-connection system," *IEEE Photon. Technol. Lett.*, Vol. 18, No. 7, 814–816, 2006.

3. Pan, J.-W., C.-M. Wang, H.-C. Lan, W.-S. Sun, and J.-Y. Chang, "Homogenized LED-illumination using microlens arrays for a pocket-sized projector," *Opt. Express*, Vol. 15, No. 17, 10483–10491, 2007.

4. Stern, M. B., M. Holz, M. M. Medeiros, and R. E. Knowlden, "Fabricating binary optics: Process variables critical to optical efficiency," *J. Vac. Sci. Technol.*, Vol. B9, 3117–3121, 1991.

5. Suleski, T. J. and D. C. O'Shea, "Gray-scale masks for diffractive-optics fabrication: I. Commercial slide imagers," *Appl. Opt.*, Vol. 34, 7507–7517, 1995.

6. Radtke, D. and U. D. Zeitner, "Laser-lithography on non-planar surfaces," *Opt. Express*, Vol. 15, 1167–1174, 2007.

7. Kawata, S., H.-B. Sun, T. Tanaka, and K. Takada, "Finer features for functional microdevies," *Nature*, Vol. 412, 697–698, 2001.

8. Maruo, S., O. Nakamura, and S. Kawata, "Three-dimensional microfabrication with two-photon-absorbed photopolymerization," *Opt. Lett.*, Vol. 22, 132–134, 1997.

9. Serbin, J., A. Egbert, A. Ostendorf, and B. N. Chichkov, "Femtosecond laser-induced two-photon polymerization of inorganic-organic hybrid materials for applications in photonics," *Opt. Lett.*, Vol. 28, 301–303, 2003.

10. Nishiyama, H., M. Mizoshiri, J. Nishii, and Y. Hirata, "SiO$_2$-based nonplanar sutructures fabricated using femtosecond laser lighography," *Opt. Express*, Vol. 16, No. 22, 17288–17294, 2008.

11. Nishiyama, H., M. Mizoshiri, J. Nishii, and Y. Hirata, "Nonplanar surface structures of inorganic optical materials fabricated by femtosecond laser lithography," *Proc. SPIE*, Vol. 6883, Art. No. 68830E, 2008.

12. Maruo, S. and K. Ikuta, "Three-dimensional microfabrication by use of single-photon-absorbed polymerization," *Appl. Phys. Lett.*, Vol. 19, 2656–2658, 2000.

13. Kewitsch, A. S. and A. Yariv, "Self-focusing and self-trapping of optical beams upon photopolymerization," *Opt. Lett.*, Vol. 21, 24–26, 1996.

Integral Equations for 3-D Scattering: Finite Strip on a Substrate

Egon Marx

National Institute of Standards and Technology
Gaithersburg, MD 20899-8212, USA

Abstract— Singular integral equations that determine the exact fields scattered by a dielectric or conducting finite strip on a substrate are presented. The computation of the image of such a scatterer from these fields by Fourier optics methods is also shown.

1. INTRODUCTION

The simulation of the microscope image of a finite strip on an infinite substrate is based on the solution of the three-dimensional Maxwell equations reduced to singular integral equations. This applies to a line on a wafer as used by the semiconductor industry, often simulated by assuming an infinite line on a substrate [1], which is a two-dimensional scattering problem. The three-dimensional scattering problem is a special case of the scattering by a finite body located in the plane interface of two semi-infinite regions, shown in Fig. 1. This interface can be deformed near the scatterer to represent imperfections or roughness of the surface.

The homogeneous reflected and refracted fields are determined by the substrate from the incident field in the absence of the scatterer. These plane monochromatic waves do not satisfy the radiation condition at infinity. The total electromagnetic field is decomposed into the sum of homogeneous and scattered fields, which do satisfy the radiation condition at infinity and are expressed in terms of unknown tangential vector fields defined on the interfaces between the homogeneous media, shown in Fig. 1. Once the integral equations are solved, the electromagnetic fields are obtained by integration. For the two-dimensional configuration the unknown functions diverge at the edges [2], which we expect to be the case in the three-dimensional problem as well. At the vertices P_i the divergences could be worse. The image at a selected focus height is computed from the electromagnetic fields by Fourier methods.

Figure 1: Finite scatterer in a plane interface.

Figure 2: Finite strip on an infinite substrate.

2. FIELDS SCATTERED FROM A FINITE BODY IN A PLANE INTERFACE

The homogeneous fields determined for a plane interface are the sum of the incident and reflected fields in V_1, $\vec{E}^{\mathrm{h}1}(\vec{x}) = \vec{E}^{\mathrm{in}}(\vec{x}) + \vec{E}^{\mathrm{refl}}(\vec{x})$ and $\vec{H}^{\mathrm{h}1}(\vec{x}) = \vec{H}^{\mathrm{in}}(\vec{x}) + \vec{H}^{\mathrm{refl}}(\vec{x})$, and in V_2 they are the refracted fields, $\vec{E}^{\mathrm{h}2}(\vec{x}) = \vec{E}^{\mathrm{refr}}(\vec{x})$ and $\vec{H}^{\mathrm{h}2}(\vec{x}) = \vec{H}^{\mathrm{refr}}(\vec{x})$. Each of these fields is defined in all of space. They are combined into $\Delta\vec{E}^{\mathrm{h}} = \vec{E}^{\mathrm{h}1} - \vec{E}^{\mathrm{h}2}$ and $\Delta\vec{H}^{\mathrm{h}} = \vec{H}^{\mathrm{h}1} - \vec{H}^{\mathrm{h}2}$.

Auxiliary fields that are equal to the scattered fields in V_1 and V_2 and to the total field in V_3 are expressed in terms of the jumps across the boundaries, the surface vector fields $\vec{\eta}_{ij}$ and $\vec{\phi}_{ij}$, where the index i refers to the surface S_i and the index j refers to the medium in V_j, as shown in Fig. 1.

The equations for the unknown tangential fields, $\vec{\chi}_{ji} = \hat{n}_i \times \vec{\eta}_{ji}$ and $\vec{v}_{ji} = \hat{n}_i \times \vec{\phi}_{ji}$, are

$$\left[\left(\frac{1}{2}+\vec{L}^{\text{t1}}_{21}\right)\vec{M}^{\text{t1}}_{11}+\vec{M}^{\text{t1}}_{21}\left(\frac{1}{2}+\vec{L}^{\text{t1}}_{11}\right)\right]\{\vec{\chi}_{11}\}+\left[\left(\frac{1}{2}+\vec{L}^{\text{t1}}_{21}\right)\vec{M}^{\text{t1}}_{12}+\vec{M}^{\text{t1}}_{21}\vec{L}^{\text{t1}}_{12}\right]\{\vec{\chi}_{12}\}-\vec{L}^{\text{t1}}_{23}\{\vec{v}_{23}\}-\vec{M}^{\text{t1}}_{23}\{\vec{\chi}_{23}\}$$

$$= -\left(\frac{1}{2}+\vec{L}^{\text{t1}}_{21}\right)\left\{\hat{n}_1\times\Delta\vec{E}^{\text{h}}\right\}-\vec{M}^{\text{t1}}_{21}\left\{\hat{n}_1\times\Delta\vec{H}^{\text{h}}\right\}, \tag{1}$$

$$\left[\vec{L}^{\text{t3}}_{21}\vec{M}^{\text{t1}}_{11}+\vec{M}^{\text{t3}}_{21}\left(\frac{1}{2}+\vec{L}^{\text{t1}}_{11}\right)\right]\{\vec{\chi}_{11}\}+\left[\vec{L}^{\text{t3}}_{21}\vec{M}^{\text{t1}}_{12}+\vec{M}^{\text{t3}}_{21}\vec{L}^{\text{t1}}_{12}\right]\{\vec{\chi}_{12}\}+\left(\frac{1}{2}-\vec{L}^{\text{t3}}_{23}\right)\{\vec{v}_{23}\}-\vec{M}^{\text{t3}}_{23}\{\vec{\chi}_{23}\}$$

$$= -\vec{L}^{\text{t3}}_{21}\left\{\hat{n}_1\times\Delta\vec{E}^{\text{h}}\right\}-\vec{M}^{\text{t3}}\left\{\hat{n}_1\times\Delta\vec{H}^{\text{h}}\right\}, \tag{2}$$

$$\left[\left(\frac{1}{2}+\vec{L}^{\text{t2}}_{32}\right)\vec{M}^{\text{t2}}_{11}+\vec{M}^{\text{t2}}_{32}\vec{L}^{\text{t2}}_{11}\right]\{\vec{\chi}_{11}\}+\left[\left(\frac{1}{2}+\vec{L}^{\text{t2}}_{32}\right)\vec{M}^{\text{t2}}_{12}+\vec{M}^{\text{t2}}_{32}\left(\frac{1}{2}+\vec{L}^{\text{t2}}_{12}\right)\right]\{\vec{\chi}_{12}\}+\vec{L}^{\text{t2}}_{33}\{\vec{v}_{23}\}+\vec{M}^{\text{t2}}_{33}\{\vec{\chi}_{23}\}$$

$$= -\left(\frac{1}{2}+\vec{L}^{\text{t2}}_{32}\right)\left\{\hat{n}_2\times\vec{E}^{\text{h1}}\right\}-\vec{M}^{\text{t2}}_{32}\left\{\hat{n}_2\times\vec{H}^{\text{h1}}\right\}-\vec{L}^{\text{t2}}_{33}\{\hat{n}_3\times\vec{E}^{\text{h2}}\}-\vec{M}^{\text{t2}}_{33}\{\hat{n}_3\times\vec{H}^{\text{h2}}\}. \tag{3}$$

$$\left(\vec{L}^{\text{t3}}_{32}\vec{M}^{\text{t2}}_{11}+\vec{M}^{\text{t3}}_{32}\vec{L}^{\text{t2}}_{11}\right)\{\vec{\chi}_{11}\}+\left[\vec{L}^{\text{t3}}_{32}\vec{M}^{\text{t2}}_{12}+\vec{M}^{\text{t3}}_{32}\left(\frac{1}{2}+\vec{L}^{\text{t2}}_{12}\right)\right]\{\vec{\chi}_{12}\}+\left(\frac{1}{2}+\vec{L}^{\text{t3}}_{33}\right)\{\vec{v}_{23}\}+\vec{M}^{\text{t3}}_{33}\{\vec{\chi}_{23}\}$$

$$= -\vec{L}_{32}\left\{\hat{n}_2\times\vec{E}^{\text{h1}}\right\}-\vec{M}_{32}\left\{\hat{n}_2\times\vec{H}^{\text{h1}}\right\}-\left(\frac{1}{2}+\vec{L}^{\text{t3}}_{33}\right)\{\hat{n}_3\times\vec{E}^{\text{h2}}\}-\vec{M}^{\text{t3}}_{33}\{\hat{n}_3\times\vec{H}^{\text{h2}}\}. \tag{4}$$

The tangential parts of the functionals are defined by

$$\vec{L}^{\text{t}}\{\vec{\phi}\}(\vec{x}) = \hat{n}\times P\oint_S dS'\frac{(1-ikR)\vec{\phi}(\vec{x}')\times\vec{R}}{4\pi R^3}\exp(ikR), \tag{5}$$

$$\vec{M}^{\text{t}}\{\vec{\phi}\}(\vec{x}) = -i\omega\mu\hat{n}\times P\oint_S dS'\left[\frac{(1-ikR)\nabla'_s\cdot\vec{\phi}(\vec{x}')\vec{R}}{4\pi k^2 R^3}-\frac{\vec{\phi}(\vec{x}')}{4\pi R}\right]\exp(ikR), \tag{6}$$

where $\hat{n}_i$ is the unit normal to S_i at $\vec{x}$, k is the wave number of the light used in the microscope, and $\vec{R} = \vec{x}-\vec{x}'$, $R = |\vec{R}|$, $\hat{n}' = \hat{n}(s')$, $\vec{x}' \in S$. The numerical superindices correspond to the surface S where the field point $\vec{x}$ is located. The computation of the partial derivatives to evaluate the surface divergence $\nabla'_s\cdot\vec{\phi}(\vec{x})'$ in the functional $\vec{M}^{\text{t}}$ may be complicated unless the patches into which each surface of the interface is subdivided are uniformly distributed. An alternative is to use a divergence theorem to do an integration by parts, which eliminates the derivatives but makes the integral hypersingular. To eliminate $\vec{v}_{33}$ and $\vec{\chi}_{33}$ we use

$$\vec{v}_{33} = -\hat{n}_3\times\vec{E}^{\text{h2}}-\vec{v}_{23}, \quad \vec{\chi}_{33} = -\hat{n}_3\times\vec{H}^{\text{h2}}-\vec{\chi}_{23}. \tag{7}$$

The integral equations (1) to (4) are obtained using the boundary conditions and the vanishing of some of the auxiliary fields at the boundaries.

Once the boundary functions are computed by converting the integral equations into algebraic equations by, for instance, the point-matching method, and solving the equations, the scattered fields in V_1 can be computed by integration from

$$\vec{E}^{\text{sc}}(\vec{x}) = -\sum_{j=1}^{2}\oint_{S_j} dS'i\omega\left[\frac{(1-ikR)\nabla'_s\cdot\vec{\chi}_{1j}(\vec{x}')\vec{R}}{4\pi k^2 R^3}-\frac{\vec{\chi}_{1j}(\vec{x}')\vec{R}}{4\pi R}\right]\exp(ikR), \tag{8}$$

$$\vec{H}^{\text{sc}}(\vec{x}) = \sum_{j=1}^{2}\oint_{S_j} dS'\frac{(1-ikR)\exp(ikR)\vec{\chi}_{1j}(\vec{x}')\times\vec{R}}{4\pi R^3}. \tag{9}$$

These fields are then added to the reflected fields to construct an image. More details about scattering by a finite body are found in [3].

3. FIELDS SCATTERED BY A FINITE STRIP

A special case of the configuration discussed in Section 2 is the finite strip shown in Fig. 2 together with the chosen coordinate system. The interface S_3 is part of the plane at the top of the substrate

and the interface S_2 is divided into five parts, S_{21}, S_{22}, S_{23}, S_{24}, and S_{25}, that form the interface between V_1 and V_3. The unknowns then are

$$\vec{\chi}_{11}(\vec{x}) = \chi_{11x}(x,\, 0,\, z)\hat{e}_x + \chi_{11z}(x,\, 0,\, z)\hat{e}_z, \quad \vec{x} \in S_1, \tag{10}$$

$$\vec{\chi}_{12}(\vec{x}) = \begin{cases} \chi_{121x}(x,\, h,\, z)\hat{e}_x + \chi_{121z}(x,\, h,\, z)\hat{e}_z, & \vec{x} \in S_{21}, \\ \chi_{122y}(\tfrac{1}{2}w,\, y,\, z)\hat{e}_y + \chi_{122z}(\tfrac{1}{2}w,\, y,\, z)\hat{e}_z, & \vec{x} \in S_{22}, \\ \chi_{123y}(-\tfrac{1}{2}w,\, y,\, z)\hat{e}_y + \chi_{123z}(-\tfrac{1}{2}w,\, y,\, z)\hat{e}_z, & \vec{x} \in S_{23}, \\ \chi_{124x}(x,\, y,\, \tfrac{1}{2}l)\hat{e}_x + \chi_{124y}(x,\, y,\, \tfrac{1}{2}l)\hat{e}_y, & \vec{x} \in S_{24}, \\ \chi_{125x}(x,\, y,\, -\tfrac{1}{2}l)\hat{e}_x + \chi_{125y}(x,\, y,\, -\tfrac{1}{2}l)\hat{e}_y, & \vec{x} \in S_{25}, \end{cases} \tag{11}$$

$$\vec{\chi}_{23}(\vec{x}) = \chi_{23x}(x,\, 0,\, z)\hat{e}_x + \chi_{23z}(x,\, 0,\, z)\hat{e}_z, \quad \vec{x} \in S_3, \tag{12}$$

$$\vec{v}_{23}(\vec{x}) = v_{23x}(x,\, 0,\, z)\hat{e}_x + v_{23z}(x,\, 0,\, z)\hat{e}_z, \quad \vec{x} \in S_3, \tag{13}$$

where h is the height, w is the width, and l is the length of the finite strip.

4. MICROSCOPE IMAGE SIMULATION

The illumination of the sample in a microscope can be simulated by a series of plane waves with varying directions of incidence and polarization defined by a circle in the back focal plane defined by the illumination numerical aperture. The image is formed by the sum of the intensities of the scattered plus reflected fields of these waves. The fields are calculated at a chosen height y_0 above the substrate, but we can propagate them to a different focus height because each field component satisfies the wave equation. We decompose each wave into Fourier components and keep those that propagate in a direction inside the collection numerical aperture and that are not evanescent waves.

In the three-dimensional case, we fix the distance y from the substrate and define the Fourier transform in the x- and z-coordinates of a function $f(x,\, y,\, z)$ to get the hybrid field

$$\tilde{f}(k_x,\, k_z;\, y) = [1/(2\pi)] \int_{-\infty}^{\infty} \int_{-\infty}^{\infty} dx dz f(x,\, y,\, z) \exp(-ik_x x - ik_z z). \tag{14}$$

The function at an arbitrary height y can be determined from the function and its normal derivative at y_0 by

$$f(x,\, y,\, z) = [1/(2\pi)] \int_{-\infty}^{\infty} \int_{-\infty}^{\infty} dk_x dk_z \left[\tilde{f}_{0+}(k_x,\, k_z)\exp(ik_y y) + \tilde{f}_{0-}(k_x,\, k_z)\exp(-ik_y y) \right]$$
$$\cdot \exp(ik_x x + ik_z z), \tag{15}$$

where

$$\tilde{f}_{0\pm}(k_x,\, k_z) = \frac{1}{2}\left[\tilde{f}(k_x,\, k_z;\, y_0) \mp (i/k_y)d\tilde{f}(k_x,\, k_z;\, y_0)/dy \right]\exp(\mp ik_y y_0), \tag{16}$$

$$k_y = \begin{cases} +\sqrt{k^2 - k_x^2 - k_z^2}, & \text{for } k_x^2 + k_z^2 < k^2, \\ +i\sqrt{k_x^2 + k_z^2 - k^2}, & \text{for } k_x^2 + k_z^2 > k^2. \end{cases} \tag{17}$$

The top value corresponds to propagating waves and the bottom value to evanescent waves, that decrease exponentially away from the interface as shown by the first term in Eq. (15). The second term corresponds to incoming and exponentially increasing fields. The former do not contribute to the radiation field and are limited to the induction zone. The latter are unphysical and have to be eliminated by setting the coefficient $\tilde{f}_{0-}(k_x,\, k_z)$ equal to zero for an imaginary k_y.

To use Eq. (16) we need to know the electromagnetic field components and the derivatives with respect to y at the height y_0 to determine the fields at an arbitrary height y. We can relate these normal derivatives to the fields and the tangential derivatives using Maxwell's equations. We have

$$\begin{aligned} \partial E_x(x,\, y,\, z)/\partial y &= -i\omega\mu_1 H_z(x,\, y,\, z) + \partial E_y(x,\, y,\, z)/\partial x, \\ \partial E_y(x,\, y,\, z)/\partial y &= -\partial E_x(x,\, y,\, z)/\partial x - \partial E_z(x,\, y,\, z)/\partial z, \\ \partial E_z(x,\, y,\, z)/\partial y &= i\omega\mu_1 H_x(x,\, y,\, z) + \partial E_y(x,\, y,\, z)/\partial z, \\ \partial H_x(x,\, y,\, z)/\partial y &= i\omega\varepsilon_1 E_z(x,\, y,\, z) + \partial H_y(x,\, y,\, z)/\partial x, \\ \partial H_y(x,\, y,\, z)/\partial y &= -\partial H_x(x,\, y,\, z)/\partial x - \partial H_z(x,\, y,\, z)/\partial z, \\ \partial H_z(x,\, y,\, z)/\partial y &= -i\omega\varepsilon_1 E_x(x,\, y,\, z) + \partial H_y(x,\, y,\, z)/\partial z. \end{aligned} \tag{18}$$

Once the fields are computed at y_0, the fields at an arbitrary focus height can be computed using Eq. (16) to determine the coefficients in the inverse Fourier transform (15). We limit the components included in the inverse transform to those components that are captured by the lens in terms of the collection numerical aperture. The propagation vectors and the amplitudes of these components are further modified by the magnification of the lens [1]. Once these radiation fields are determined, we obtain the image by adding, for instance, the intensities of the electric fields or the normal components of the Poynting vectors.

5. CONCLUDING REMARKS

We have extended the methods used to obtain images of infinite lines to finite lines. The main difficulty is the increase of the number of unknowns in each boundary surface, which is now two-dimensional. Consequently, it becomes more important to determine the behavior of the unknown functions at edges and corners to take into account the divergences in the numerical integrations. Computer memory and running times are important factors in these simulations.

REFERENCES

1. Marx, E., "Images of strips on and trenches in substrates," *Appl. Opt.*, Vol. 46, 5571–5587, 2007.
2. Marx, E., "Scattering of an arbitrary plane wave by a dielectric wedge: Integral equations and fields near the edge," *Radio Sci.*, Vol. 42, RS6S09, 2007, doi:10.1029/2006RS003568.
3. Marx, E., "Integral equation for scattering by a dielectric," *IEEE Trans. Antennas Propagat.*, Vol. 32, 166–172, 1984.